JAEA-Research
2019-009
DOI:10.11484/jaea-research-2019-009

JAEA-Research

Phase 1 Code Assessment of SIMMER-III, A Computer Program for LMFR Core Disruptive Accident Analysis

(Eds.) Satoru KONDO and Yoshiharu TOBITA

Fast Reactor Cycle System Research and Development Center
Oarai Research and Development Institute
Sector of Fast Reactor and Advanced Reactor Research and Development

March 2020

Japan Atomic Energy Agency

日本原子力研究開発機構

本レポートは国立研究開発法人日本原子力研究開発機構が不定期に発行する成果報告書です。
本レポートの入手並びに著作権利用に関するお問い合わせは、下記あてにお問い合わせ下さい。
なお、本レポートの全文は日本原子力研究開発機構ホームページ（https://www.jaea.go.jp）
より発信されています。

国立研究開発法人日本原子力研究開発機構 研究連携成果展開部 研究成果管理課
〒319-1195 茨城県那珂郡東海村大字白方 2 番地4
電話 029-282-6387, Fax 029-282-5920, E-mail:ird-support@jaea.go.jp

This report is issued irregularly by Japan Atomic Energy Agency.
Inquiries about availability and/or copyright of this report should be addressed to
Institutional Repository Section,
Intellectual Resources Management and R&D Collaboration Department,
Japan Atomic Energy Agency.
2-4 Shirakata, Tokai-mura, Naka-gun, Ibaraki-ken 319-1195 Japan
Tel +81-29-282-6387, Fax +81-29-282-5920, E-mail:ird-support@jaea.go.jp

JAEA-Research 2019-009

Phase 1 Code Assessment of SIMMER-III, A Computer Program for LMFR Core Disruptive Accident Analysis

(Eds.) Satoru KONDO and Yoshiharu TOBITA

Fast Reactor Cycle System Research and Development Center
Oarai Research and Development Institute
Sector of Fast Reactor and Advanced Reactor Research and Development
Japan Atomic Energy Agency
Oarai-machi, Higashiibaraki-gun, Ibaraki-ken

(Received November 14, 2019)

The SIMMER-III computer code, developed at the Japan Atomic Energy Agency (JAEA, the former Power Reactor and Nuclear Fuel Development Corporation), is a two-dimensional, multi-velocity-field, multi-component fluid-dynamics code, coupled with a space- and time-dependent neutron kinetics model. The code is being used widely for simulating complex phenomena during core-disruptive accidents (CDAs) in liquid-metal fast reactors (LMFRs). In parallel to the code development, a comprehensive assessment program was performed in two phases: Phase 1 for verifying individual fluid-dynamics models; and Phase 2 for validating its applicability to integral phenomena important to evaluating LMFR CDAs. The SIMMER-III assessment program was participated by European research and development organizations, and the achievement of Phase 1 was compiled and synthesized in 1996.

This report has been edited by revising and reproducing the original 1996 informal report, which compiled the achievement of Phase 1 assessment. A total of 34 test problems were studied in the areas: fluid convection, interfacial area and momentum exchange, heat transfer, melting and freezing, and vaporization and condensation. The problems identified have been reflected to the Phase 2 assessment and later model development and improvement. Although the revisions were made in the light of knowledge base obtained later, the original individual contributions by the participants, both positive and negative, are retained except for editorial changes.

Keywords: Multi-component Flow, Multi-phase Flow, Fluid Dynamics, Heat and Mass Transfer, SIMMER-III, V&V, Severe Accidents, CDA, LMFR Safety

---

This work has been performed in JAEA (the former Power Reactor and Nuclear Fuel Development Corporation) in collaboration with Forschungszentrum Karlsruhe, Germany and Commissariat à l'Énergie Atomique, France.

JAEA-Research 2019-009

高速炉炉心崩壊事故解析コードSIMMER-IIIの第1期検証

日本原子力研究開発機構　高速炉・新型炉研究開発部門　大洗研究所
高速炉サイクル研究開発センター

（編）近藤　悟、飛田　吉春

（2019年11月14日受理）

日本原子力研究開発機構（旧動力炉・核燃料開発事業団）が開発したSIMMER-IIIは、2次元・多速度場・多成分流体力学を空間・時間依存の核動特性モデルと結合した計算コードであり、液体金属高速炉の炉心崩壊事故の解析に広く利用されている。コードの開発と並行して、包括的なコード検証プログラムを、第1期（流体力学個別モデルのverification）及び第2期（炉心崩壊事故における複雑かつ重要な現象についてのvalidation）の2段階に分けて実施してきた。SIMMER-III検証プログラムには欧州の研究開発機関が参加し、第1期の成果は1996年に総合的にとりまとめられた。

本報告書は元の1996年の非公式の文書を再生・改訂することにより、第1期検証の研究成果を再編集したものである。第1期検証プログラムでは、流体対流、境界面積及び運動量交換、熱伝達、溶融・固化、蒸発・凝縮の分野で計34のテスト問題の解析が参加機関により分担して実施された。第1期プログラムで明らかとなった課題についてはその後のモデル開発・改良及び第2期プログラムに反映した。本報告書は新たに得られた研究知見に基づいて改訂しているが、参加者による元の解析結果と結論は、批判的な内容を含めて、そのまま記載している。

本研究は日本原子力研究開発機構（旧動力炉・核燃料開発事業団）がカールスルーエ研究センター（ドイツ）及び原子力庁（フランス）との協力により実施したものである。
大洗研究所：〒311-1393　茨城県東茨城郡大洗町成田町4002

Contents

目　次

Authors of the Original Internal Document in 1996

Sa. Kondo (compiler), Y. Tobita, K. Morita, K. Kamiyama
(Power Reactor and Nuclear Fuel Development Corporation*1, Japan)

D. J. Brear (compiler), E. A. Fischer
(International Fellows, Power Reactor and Nuclear Fuel Development Corporation*1, Japan)

W. Maschek, C. -D. Munz, M. Flad, S. Kleinheins, G. Arnecke,
E. Hesselschwerdt, M. Göz, H. Jacobs, B. Stehle,
(Forschungszentrum Karlsruhe*2, Germany)

T. Jeanne
(Institut de Protection et de Sûreté Nucléaire *4, France)

P. Coste, D. Wilhelm, F. Boulanger, S. Vandroux-Koenig
(Commissariat à l'Énergie Atomique *4, France)

Organizations as of 2019

*1 Japan Atomic Energy Agency (JAEA), Japan

*2 Karlsruhe Institute of Technology (KIT), Germany

*3 Institut de Radioprotection et de Sûreté Nucléaire (IRSN), France

*4 Commissariat à l'Énergie Atomique et aux énergies alternatives (CEA), France

Nomenclature

a	Binary-contact area per unit volume
a	Fitting constant in EOS equations
A	Convectible interfacial area per unit volume
e	Specific internal energy
g	Gravitational acceleration
h	Heat-transfer coefficient
$H(x)$	Heaviside unit function
i	Enthalpy
k_c	Microscopic thermal conductivity
k_T	Turbulent thermal conductivity
K	Inter-field momentum exchange function
p	Pressure
q	Heat transfer rate
q_c	Intra-cell conductive heat flux
Qic	Energy source term by intra-cell heat transfer
Q_N	Nuclear heating rate
Q_{MF}	Rate of energy interchange due to melting/freezing
Q_{VC}	Rate of energy interchange due to vaporization/condensation
Q_{HT}	Rate of energy interchange due to heat transfer
S	Interfacial area source term
t	Time
T	Temperature
$\boldsymbol{v}$	Velocity
$\boldsymbol{VM}$	Virtual mass

Greek symbols

α	Volume fraction
α_0	Maximum void fraction in a "single-phase" cell
α_B	Maximum void fraction for bubbly flow in a cell
α_D	Maximum void fraction for dispersed flow in a cell
ρ	Microscopic density
$\bar{\rho}$	Macroscopic density
ν	Specific volume

ΔT	Temperature difference between components
Γ	A mass-transfer rate per unit volume
Γ_m	Total mass-transfer rate per unit volume from component m
$\Gamma_{qq'}$	Mass-transfer rate from q to q'
Γ_{MF}	Melting or freezing rate for mass interchange
Γ_{VC}	Vaporization or condensation rate for mass interchang

Subscripts and superscripts

B	Bubbly flow regime
Crt	Critical point
D	Dispersed flow regime
G	Gas/vapor mixture
I	Interfacial quantity
GL	Terms existing at interfaces between vapor and an averaged liquid velocity
M	Energy component
m	Density component
q, q'	Velocity fields
qq'	Terms existing at interfaces between velocity field q and q'
qS	Terms existing at interfaces between velocity field q and structure
S	Structure
S	Structure-field energy component
s	Structure-field density component

This is a blank page.

1. Introduction

1.1 Notes to the Present Publication

The SIMMER-III liquid-metal fast reactor (LMFR) safety analysis computer code was developed at the Power Reactor and Nuclear Fuel Development Corporation (PNC) in the 1990s.[1)] After the completion of Version 1 of SIMMER-III, a code having all the fluid-dynamics models originally intended at the start of the Project, the code assessment (validation and verification, or V&V) program was initiated, in collaboration with the European research organizations, in two phases: Phase 1 mostly for verification and Phase 2 for validation. In the early Agreement on this joint study, publication of technical achievement was restricted rather strictly. For this reason the Phase 1 study completed in 1996 was compiled only as an informal document of PNC, even though Phase 1 is basic study oriented and essentially involves no proprietry imformation.

The above restriction was later relaxed and the Phase 2 study completed in 2000 was documented as an open report[2)]. The Phase 1 document, after two decdes since its original compilation in 1996, is believed to retain its original archival value even today, and therefore it is strongly recommended that the Phase 1 document be re-produced and published as an open report. Moreover, combined Phase 1 and Phase 2 reports could complete the first comprehensive study for SIMMER-III V&V efforts. The purpose of the present report is to compile the achievement of the Phase 1 assessment program, by re-producing the most parts of the original document.

Not all the results and conclusions of Phase 1 are valid at present any longer, since only early code versions were used in the study. Many of the problem areas identified in Phase 1 had alreacy been reflected to later model imrovement or addition. Some of the test problems were re-visted in Phase 2 to further validate new versions of the code and evaluate its applicability to reactor cases. Section 1.3 gives additional remaks on these points. Section 1.2 comes from the intruduction to the original Phase 1 document.

1.2 Historical Perspective and Purposes

The consequences of postulated core disruptive accidents (CDAs) have been and still is one of major concerns in the safety LMFRs. Although the extensive safety design effort for accident prevention has made the occurrence of such an event extremely unlikely, the importance of CDAs is still emphasized from the viewpoint of safety design and evaluation to appropriately mitigate and accommodate the consequences and thereby to minimize the risk to the public. A recent comprehensive assessment of an unprotected loss-of-flow accident, a representative CDA, shows that a recriticality and resultant energetics potential during the so-called transition phase is one of the most important risk contributors[3), 4)]. Complexities of evaluating the transition phase, together with limited direct experimental data in comparison with the initiating phase of CDAs, tend to introduce relatively large uncertainties in the safety analysis.

In this area, the SIMMER-II code was developed at the Los Alamos National Laboratory (LANL) starting in the 1970s as the first tool of its kind,[5)] and has been used in many experimental and reactor analyses.[6)] The code has played a pioneering role, especially in studying the transition phase phenomenology, and was extensively tested, used and improved worldwide. However, extensive

application also revealed several serious limitations in virtually all the major areas of fluid dynamics, particularly in: heat, mass and momentum constitutive relationships; the multiphase-flow numerical solution methods; the multicomponent equation-of-state (EOS) formalism; and the fuel-pin and structure models. These deficiencies and shortcomings have limited the code applicability and reliability, and the code can no longer be considered as a state-of-the-art tool for reactor safety analysis.

The next historical step was the development of a small prototype fluid dynamics code, AFDM (Advanced Fluid Dynamics Model) [7]. It used advanced solution methods and models, but its scope is for model testing, rather than reactor application. Therefore there was still the need for developing an advanced reactor code. Based on the past experiences, the development of such a next-generation code, SIMMER-III, was initiated at around 1990 at PNC, initially in collaboration with LANL. Although the code still retains an LANL originated naming of “SIMMER”, it is not an extention of or improvement from the former SIMMER-II. SIMMER-III has been designed and coded from zero. The SIMMER-III effort at PNC was later participated by AEA Technology, United Kingdom, Forschungszentrum Karlsruhe (FZK), Germany, and Commissariat a l'Énergie Atomique (CEA), France.

The purpose of SIMMER-III is to alleviate some of the above limitations and thereby to provide a next-generation tool for more reliable analysis of the transition phase. SIMMER-III is a two-dimensional, three-velocity-field, multiphase, multicomponent, Eulerian, fluid-dynamics code coupled with a space- and energy-dependent neutron dynamics model. The scope of the code development effort is determined primarily from the needs of the accident-analysis point of view and is optimized so as to utilize either existing or achievable technologies. The achievement and experience gained in the AFDM development are used to maximum extent. The advanced features of the code resolve many of the problems associated with SIMMER-II, as summarized in Table 1-1. SIMMER-III is intended to be a generalized code that is useful for analyzing relatively short-time-scale multiphase flow problems with or without neutronics. Although the original objective of SIMMER-III is primarily to resolve some of the key LMFR CDA issues, its flexible framework enables us to apply the code to various areas of interest which are consistent with the SIMMER-III modeling framework. It is believed, therefore, that the future application of the code will possibly include: accident analyses of any types of future or advanced fast reactors, steam-explosion problems in current- and future-generation light water reactors, and general types of multiphase flow problems.

The development of the SIMMER-III code has successfully reached the milestone that integrated code application has been initiated.[1] Major physical models have been completed and they have been integrated into a fluid-dynamics code system, that is Version 1. A number of functional and verification tests performed during its development have been very promising, demonstrating that the advanced features of the code can reasonably simulate some of the phenomena not treated by the previous codes. Since SIMMER-III is expected to become a standard tool for LMFR safety analysis with likely application to licensing calculations, the models must be extensively validated as far as appropriate. For this reason, the partners of the SIMMER-III program agreed to conduct a systematic and comprehensive validation of the code. This effort, termed more generally as "the assessment program", consists of two phases: Phase 1 for fundamental or separate-effect code assessment of individual models; and Phase 2 for integral code assessment for key physical phenomena relevant to LMFR safety.

The Phase 1 assessment program has several objectives. First the code must be validated on an individual model basis. Second even though SIMMER-III can model complex interacting phenomena, the code still has to simulate simple problems such as single-phase flows and water two-phase flows. From these aspects, SIMMER-III can be compared with existing state-of-the-art fluid-dynamics codes used for multi-phase flow simulation. Third model by model validation in Phase 1 assessment is ideal for checking and debugging complex programming of SIMMER-III. Fourth simple test problems are easier to set up, and hence the users can easily become familiar with the code.

A total of 34 test problems were defined for the Phase 1 assessment, which has been jointly conducted by PNC, FZK and CEA. Roughly half of the test calculations were performed in Europe, based on their technical expertise and own experimental data. This gives the program a character of "independent assessment". This report is intended to be a synthesis document of the Phase 1 code assessment, describing all the results of the test problems defined. Each problem is documented as “summeary report” in the same format to facilitate readers' understanding.

1.3 Additional Remarks

The models of SIMMER-III are concisely described in Chapter 2, so that the results of assessment can be understood in relation to the models. In Chapter 3, the overall approach to the SIMMER-III Phase 1 and Phase 2 assessment programs is described. The Phase 1 test problems are described as the summary reports in Appendix to this report. The summary reports contain the results of the Phase 1 assessment, where the contributions from participants is included with minimal editorial modification. Positive and negative views by each contributor are included as they were originally written. Chapter 4 is an attempt to evaluate the achievement of Phase 1 assessment, and synthesizes the views on the present SIMMER-III performance and desired future model improvement. Even though many of the test problems are for basic validation of fluid dynamics, the implications from the Phase 1 assessment for the Phase 2 assessment and reactor application are also discussed in Chapter 4.

The Phase 1 assessment study was performed from 1993 to 1996, and Version 1 of SIMMER-III (Veresions 1.A to 1.J) was used. The error corrections and model improvement recommended from Phase 1 were made to develop Version 2 of SIMMER-III[8], which was used in Phase 2 assessment. It was confirmed that many of the problem areas were resolved in Version 2. The challenges still remaining are described in the Phase 2 report[2]. The code has further evolved to Version 3[9]. Yet the shortcomings arrising from the basic framework of the code cannot be resolved. Concerning one of the most important examples of such shortcomings, dimensionality, was actually improved by development of three-dimensinal SIMMER-IV code, Version 1 in 2000[10] and Version 2 in 2003[11]. In SIMMER-IV, the fluid convection equatations are solved in three dimensions and the four lateral mesh cell boundaries are defined. The physical models of local heat and mass transfers and momentum coupling are identical in the two codes. This means the results of code assessent studies with SIMMER-III are applicable to SIMMER-IV as well. Furthermore the limitations coming from the numbers of components were improved by increasing the number of velocity field and adding new components in the latest code verisons.

Table 1-1. Accident analysis aspects of advanced SIMMER-III features

Key Accident Phenomena (Current Problem Areas)	Advanced SIMMER-III Features (Improvement from SIMMER-II)
Pool boil-up exaggerated due to instantaneous interfacial areas	Interfacial area convection with time-dependent source terms
Liquid interface smeared due to numerical diffusion	Higher-order differencing for better resolution
No fuel/ steel separation nor fuel penetration into coolant	Three-field model allows liquid relative motion
Liquid/vapor coupling overestimated in low void fraction pool	Modeling a bubbly flow with smooth transition between flow regimes
Instantaneous fission gas release upon pellet breakup	Accommodate fission gas in liquid/ particulate fuel and model its release
Can wall melt-out treated unphysically	Separated left/ right walls with 2-node representation
Instability upon single/two phase transition	Consistent treatment of single-phase cells with new analytic EOS
Pressure drop along a pin bundle underestimated	Modeling proper channel flow regimes with smooth change
No fuel/ steel vapor condensation on coolant	Modeling all the important mass-transfer processes
Instabilities of vaporization/condensation and EOS at high temperature	A new model with improved solution procedure and consistent/accurate EOS
Poor conservation of mass and energy	Improved by semi-implicit method and consistent single-phase treatment
Maintainability, structure, user friendliness, vectorization, etc.	Improved and optimized in totally new programming

2. Scope and Outline of SIMMER-III Models

2.1 Code Framework and Geometry

The conceptual overall framework of SIMMER-III is shown in Fig. 2-1. The entire code consists of three elements: the fluid-dynamics model, the structure (fuel pin) model, and the neutronics model. The fluid-dynamics portion, which constitutes about two thirds of the code, is interfaced with the structure model through heat and mass transfer at structure surfaces. The neutronics portion provides nuclear heat sources based on the mass and energy distributions calculated by the other code elements. Without the neutronics, nuclear heat source can still be provided by power-versus-time table, based on input specification and specific power density distribution.

To increase the computational efficiency, an optimized hierarchy of three-level time-step control is implemented; that is, the fluid-dynamics, reactivity (and fuel pin heat transfer), and flux-shape time steps in the order from the smallest. This time-step control scheme is shown in Fig. 2-2, and the overall computational flow in Fig. 2-3.

The basic geometric structure of SIMMER-III is a two-dimensional R-Z system as shown in Fig. 2-4, although optionally an X-Z or one-dimensional system can also be used for various fluid-dynamics calculations. The neutronics mesh is a sub-region of the fluid-dynamics computational mesh. In each mesh cell, the structure-field volumes are defined for the fuel pin and can wall components, which are stationary and provides walls containing fluid flow. Unlike SIMMER-II, the can walls with refrozen crust fuel attached on them are distinguished between left and right cell boundaries for improved simulation of a core melt-out behavior. In addition, the structure surface nodes are separated from the interior nodes to improve thermal response from contact with the fluid.

The remaining volume $(1-\alpha_S)$ is occupied by fluid having three velocity fields. When the cell vapor volume fraction falls below a certain non-zero value α_0, the mesh cell is regarded as single phase. This treatment is necessary, even in SIMMER-III, for the numerical reason that a vapor state is explicitly treated even in a single-phase liquid cell. The treatment of single-phase cells consistent with two-phase cells eliminates such problems observed in SIMMER-II as vapor mass non-conservation and unphysical pressure behavior upon phase transition. The value of α_0 can be made reasonably small (for example, 10^{-4}), compared with the former codes, such that any errors associated with this approximation are negligible.

2.2 SIMMER-III Components

The complete lists of the structure-, liquid- and vapor-field components are shown in Tables 2-1 through 2-3. In these tables, the lower-case subscripts denote density components while the upper-case subscripts denote energy components commonly used throughout SIMMER-III. The fuel components are divided into fertile and fissile in their mass (density components) to represent different enrichment zones in the core. However, the two materials are assumed to be mixed intimately, and hence the single temperature is assigned (energy components). Namely, the macroscopic (smeared) densities of a fuel component has the following equivalence:

$$\bar{\rho}_{S1} = \bar{\rho}_{s1} + \bar{\rho}_{s2} \tag{1}$$

Since the component specific volumes (not microscopic densities) are used in the SIMMER-III EOS model, macroscopic densities are converted to volume fractions by:

$$\alpha_{S1} = \bar{\rho}_{S1} v_{S1} \tag{2}$$

The pin fuel interior component is not included in Table 2-1, because it is treated only in the fuel-pin model. The pin interior is modeled by one-point temperature node in a standard simple model, whereas an optional detailed model calculates the radial temperature distribution. The fuel pin related components are listed in Table 2-4. The intra-granular and inter-granular fission gas in the pin fuel, separately modeled in SIMMER-II, are not distinguished in SIMMER-III, because such detailed treatment is judged to be beyond the scope of this code. Improvement exists, however, in the modeling of fission gas in the liquid-field fuel components (see Table 2-2) and this eliminates a problem of instantaneous release and unphysical pressurization observed in SIMMER-II.

The default assignment of fluid components to the three velocity fields is also shown in Tables 2-2 and 2-3. The present selection is made such that the relative motion of fuel with either steel or coolant can be simulated. This assignment can be changed through user-specified input.

Finally the vapor species are assumed to be completely mixed and a single energy is assigned to the vapor field.

2.3 Fluid-Dynamics Model

2.3.1 Fundamental differential equations

In SIMMER-III, conservation equations are written for independent variables in a unit volume. and the mass and energy are represented by macroscopic density and specific internal energy, respectively. The conservation equations involving fluid mass, momentum and internal energy are:

$$\frac{\partial \bar{\rho}_m}{\partial t} + \nabla \cdot \left(\bar{\rho}_m \boldsymbol{v}_q\right) = -\Gamma_m \tag{3}$$

$$\begin{aligned} \frac{\partial \bar{\rho}_q \boldsymbol{v}_q}{\partial t} + \sum_{m \in q} \nabla \cdot \left(\bar{\rho}_m \boldsymbol{v}_q \boldsymbol{v}_q\right) + \alpha_q \Delta p - \bar{\rho}_q \boldsymbol{g} + K_{qS} \boldsymbol{v}_q - \sum_{q'} K_{qq'} \left(\boldsymbol{v}_{q'} - \boldsymbol{v}_q\right) - \boldsymbol{VM}_q \\ = \sum_{q'} \Gamma_{qq'} \left[H\left(\Gamma_{qq'}\right) \boldsymbol{v}_q + H\left(\Gamma_{q'q}\right) \boldsymbol{v}_{q'}\right] \end{aligned} \tag{4}$$

$$\frac{\partial \bar{\rho}_M e_M}{\partial t} + \sum_{m\in M} \nabla\cdot\left(\bar{\rho}_m e_m \boldsymbol{v}_q\right) + p\left[\frac{\partial \alpha_M}{\partial t} + \nabla\cdot\left(\alpha_M \boldsymbol{v}_q\right)\right] - \frac{\bar{\rho}_M}{\bar{\rho}_m}\left[\sum_q K_{q'q}\left(\boldsymbol{v}_q - \boldsymbol{v}_{q'}\right)\cdot\left(\boldsymbol{v}_q - \boldsymbol{v}_{q'q}\right) + K_{qS}\boldsymbol{v}_q\cdot\left(\boldsymbol{v}_q - \boldsymbol{v}_{qS}\right) + \boldsymbol{VM}_q \cdot\left(\boldsymbol{v}_q - \boldsymbol{v}_{GL}\right)\right] = Q_N + Q_M(\Gamma_M) + Q_H(h, a, \Delta T) \tag{5}$$

In the above equations, the density components are subscripted by *m*, the energy components by *M*, the velocity components by *q*, and $\bar{\rho}_m = \alpha_M/v_M$ (other symbols are described in Nomenclature of this report). Similar to the former codes, component mass and energy are represented by macroscopic density and specific internal energy in SIMMER-III, such that the equations are written for a unit volume. The mass and energy equations for the fuel-pin and can-wall components, which are stationary, have similar expressions but do not involve the convection terms. The momentum treatment in Eq. (4) for the vapor field includes a virtual mass term to provide a significant stability improvement. The AFDM manual discusses this effect and other conceptual assumptions of these basic equations[12]. In addition to the above equations, a model for convecting interfacial areas is attempted in SIMMER-III to better follow phenomenological histories, as described in Section 2.3.4.

2.3.2 Overall solution procedure

The overall fluid-dynamics solution algorithm is based on a time-factorization approach developed for AFDM, in which intra-cell interfacial area source terms, heat and mass transfer, and momentum exchange functions are determined separately from inter-cell fluid convection. There are four steps in this algorithm as shown in Table 2-5 and Fig. 2-5.

Step 1 of the fluid-dynamics algorithm solves Eqs. (3) - (5) for intra-cell transfers whilst ignoring the convection terms. The computational flow through Step 1 has the following parts:

1. Perform energy and mass transfer operations associated with fuel-pin or can-wall breakup whenever the break-up criterion is satisfied.
2. Determine structure configuration and calculate structure heat-transfer coefficients.
3. Update convectible interfacial areas with source terms and determine binary contact areas between energy components.
4. Calculate momentum-exchange functions.
5. Calculate fluid heat-transfer coefficients.
6. Calculate fission-gas release from liquid and particulate fuel.
7. Update internal energies due to nuclear heating.
8. Perform heat and mass transfer operations due to non-equilibrium melting/freezing and vaporization/condensation.
9. Calculate can-wall heat transfer.
10. Calculate inter-cell heat transfer.
11. Update velocities and interfacial areas based on mass transfers.

This extremely complex procedure of Step 1 operations is a central reason why the intra-cell transfer is decoupled with the inter-cell convection.

2.3.3 Fluid convection algorithm

Steps 2, 3 and 4 solve fluid convection by integrating Eqs. (3) - (5) whilst ignoring the source terms on the right hand sides. First Step 2 explicitly estimates the end-of-time-step variables to initialize for the pressure iteration. While the first-order donor-cell differencing scheme is optionally used, a higher-order spatial differencing is the standard scheme to reduce numerical diffusion. The latter was based on the AFDM formulation.

Step 3 performs the so-called pressure iteration that obtains consistent end-of-time-step velocities and pressure using a multivariate Newton-Raphson method. During the pressure iteration, selected sensitive variables are allowed to change from the Step 2 estimates to make their residuals to zero. These variables are: the total density of liquid 1, the density of steel, the density of sodium (and control particles), the total density of vapor mixture, the vapor temperature, and the difference between EOS pressure and cell pressure. In addition, an advantage over the previous AFDM approach is the elimination of an inefficient internal EOS iteration to obtain mechanical equilibrium among compressible fluid components. This is done by defining the EOS pressure as a function of the cell pressure, and the latter is related to the amount of liquid compression.

The matrix solution methods currently used for the pressure iteration are: a direct inversion method and an ILUBCG (Incomplete LU-decomposition Bi-Conjugate Gradient) method. The latter is more advantageous for larger problems, typically with more than 1500 mesh cells. A simple tri-diagonal matrix solver is used for one-dimensional problems.

Finally Step 4 performs consistent mass, momentum and energy convection based on the semi-implicit algorithm. The interfacial areas are also convected consistently in this step.

Although this modularized, four-step method is advantageous and flexible enough to allow future improvement or exchange of different intra-cell models, problems can arise from decoupling intra-cell mass transfer from the inter-cell fluid convection. Practically this is known to introduce time-step-size sensitivity problems, when the fluid convection is strongly driven by the intra-cell source terms. A completely integrated fully-implicit approach is obviously impractical in a complex multiphase, multicomponent framework of SIMMER-III. However, an additional time step control has been implemented by monitoring the pressure change between the intra- and inter-cell transfers, and it was shown that this problem is partially, but reasonably, mitigated.

2.3.4 Interfacial area model

The interfacial area modeling successfully attempted in AFDM[13] was extended to the SIMMER-III multicomponent system, with slightly simpler but more comprehensive representation of flow topologies. To obtain the mass, momentum, and energy transfer terms, the binary contact areas must be determined for 42 possible contact interfaces among seven fluid energy components and three structure surfaces (a fuel pin,

left can wall and right can wall). These binary contact areas are determined based on the convectible interfacial areas and a flow regime which describes the topology of the multiphase flow.

Flow regimes are modeled for both pool flow, in which the effect of the structure is negligible, and channel flow, which is confined by structure. The present flow-regime representation is rather simple; for instance, only bubbly, dispersed and in-between transition regimes are modeled for the pool flow (see Fig. 2-6) [14]. The upper limit of the bubbly regime and the lower limit of the dispersed regime are defined by user-specified void fractions, α_B and α_D, respectively, with the typical values being 0.3 and 0.7. In the SIMMER-III flow-regime modeling, it is generally assumed that a cell consists of two local regions: a bubbly and a dispersed regions[12]. This is schematically illustrated in Fig. 2-7. In Fig. 2-6, the transition regime is defined as a combination of the two regions, which always have the void fractions α_B and α_D. This means that the transition regime, more commonly called a churn-turbulent flow regime, is defined non-mechanistically as an interpolated flow regime. However, this treatment is very advantageous because the flow characteristics can be determined continuously over the entire void fraction range, without abrupt change upon flow-regime transition.

The modeling approach taken for the channel flow regimes is essentially the same, but special flow characteristics resulting from the effects of channel walls also have to be considered. The channel flow-regime map is shown in Fig. 2-8 for the nine flow regimes modeled as the functions of the vapor volume fraction and the liquid entrainment fraction. The latter is related to the inter-phasic velocity difference, taking into account the flooding criterion for a liquid film on structure. Since we cannot distinguish a liquid film on a fuel-pin surface from one on a can wall, there remain some uncertainties. No geometric picture is given for the interpolated flow regime, where the quantities are estimated purely by mathematical interpolation.

This multiple flow-regime treatment in SIMMER-III significantly improves the code applicability to reactor and experiment analyses over the previous SIMMER-II, in which only a dispersed droplet flow is modeled. It is also intended to provide a consistent framework of the flow regime map, over the entire range of void fraction, with smooth and stable transitions between flow regimes.

The interfacial area convection model improves the flexibility of SIMMER-III by tracing transport and history of interfaces, and thereby better represents physical phenomena. Ishii[15] proposed a convection equation for the interfacial areas per unit volume in a general form:

$$\frac{\partial A_M}{\partial t} + \nabla \cdot (A_M \boldsymbol{v}) = \sum_k S_{M,k} \tag{6}$$

where A_M is the interfacial area of component M per unit volume and $S_{M,k}$ denotes the source terms of the interfacial area. This formulation is difficult to be implemented into a Eulerian code such as SIMMER-III because the real velocity of an interface cannot be determined easily. Therefore, we made a compromise that a convective interfacial area is defined as a surface area of an energy component and is convected with the same velocity. A total of nine interfacial areas associated to moving energy components are presently defined. These are: the surface areas of real liquids (fuel, steel and sodium) in the bubbly region; the surface areas of real liquids in the dispersed region; the surface areas of fuel and steel particles; and the surface area

of bubbles in the bubbly region. A special treatment is modeled to avoid abrupt changes in such situations that the area convection occurs into a cell having a different void fraction. This is done by additional local convection (diffusion) terms between the bubbly and dispersed regions[14]:

$$\frac{\partial A_{M,B}}{\partial t} + \nabla \cdot \left(A_{M,B}\boldsymbol{v}\right) = \sum_{k} S_{M,B,k} - A_{M,B\to D} \tag{7}$$

$$\frac{\partial A_{M,D}}{\partial t} + \nabla \cdot \left(A_{M,D}\boldsymbol{v}\right) = \sum_{k} S_{M,D,k} - A_{M,D\to B} \tag{8}$$

where $A_{M,B}$ and $A_{M,D}$ are the convective interfacial areas of component M in the bubbly and dispersed regions, respectively. The second term on the right side denotes the diffusion between the two regions. The changes of interfacial areas due to hydrodynamic breakup, flashing, turbulence-driven breakup, coalescence, and production of droplets or bubbles are treated as "source terms" in the interfacial area convection equation.

The binary contact areas are then calculated using the convective interfacial areas, structure surface areas, component volume fractions, physical properties, etc. The present model basically calculates the contact areas based on the volume fractions of the fluids and a "summation rule" that the sum of binary contact areas over a component should be equal to the convective interfacial area (surface area) of the component. For the fluid-fluid contacts between moving discontinuous components, a theory developed for SIMMER-II is used.

2.3.5 Momentum exchange functions

Since both theoretical and experimental knowledge is limited for a multicomponent three-velocity flow, the developed formulations are based on engineering correlations of steady-state two-velocity flow. Fluid-structure, fluid-fluid drag and liquid-vapor virtual mass effects are formulated.

The momentum exchange function between velocity fields q and q', $K_{qq'}$, in the momentum equation is a function of the drag coefficient and interfacial areas. Between the continuous and the discontinuous fields, the momentum exchange function consists of laminar and turbulent terms. The laminar term is described by Stoke's law, and the turbulent term is proportional to the inter-phase velocity difference with the drag coefficient based on Ishii's drag similarity hypothesis[16]. Since standard two-phase pressure drop correlations are not applicable in the three-field situations, the momentum exchange functions between continuous fluids and the structure are calculated separately by Reynolds number correlations. Here the effective hydraulic diameters are defined by the respective binary contact areas and the fluid volume fractions. The validity of this treatment was confirmed by comparing the two-phase pressure drop in a bubbly flow in a pipe with the traditional treatment using Lockhart-Martinelli multiplier. For the momentum exchange function between two discontinuous velocity fields or between a discontinuous field and the structure, only a turbulent term is considered and a constant drag coefficient is employed.

The momentum exchange functions are defined separately for the bubbly and dispersed regions. To smooth the transition between liquid and vapor continuous flows, these two values are averaged

logarithmically, since the momentum exchange function may differ by several orders of magnitude between the two regions.[12)]

Solid mobile particles in a flow require a special consideration, since since the presence of particles, depending on their volume fraction, should significantly increase the hydrodynamics resistance of the flow. Therefore the concept of effective particle viscosity is introduced to particle components as a function of particle volume (packing) fraction and it is used in defining the total viscosity of each liquid velocity field. This model is crucial when the fuel blockage formation due to particle jamming is simulated.

2.3.6 Heat-transfer coefficients

Heat-transfer coefficients (HTCs) are required to perform the heat and mass transfer calculations. The heat and mass transfer paths between the fluid energy components are illustrated in Fig. 2-9. HTCs are defined for 42 binary contacts between the energy components and contribute to 30 vaporization/condensation (V/C) paths and 20 melting/freezing (M/F) paths. The coefficients control heat transfer between the bulk and interface temperatures for each liquid energy component and for the gas/vapor mixture.

The HTCs are based on quasi-steady state heat transfer correlations. The correlations take account of the Prandtl number range of the interacting fluids, which is particularly important when calculating heat transfer in liquid metals.

Solid particles are treated as rigid spheres, and heat transfer is controlled by conduction. Liquid droplets and gas bubbles were also treated as rigid spheres but the effects of internal circulation and oscillation of fluid particles are also treated. In the latter case conduction is augmented by convection in the fluid particles. In the dispersed flow regime the heat transfer between moving droplets can be calculated as a function of the contact times.

Forced convection heat transfer from continuous phase liquids or gas to solid particles is calculated using correlations obtained from forced flow over spheres. Fluid spheres are treated as rigid spheres at low Reynolds number, but at higher Reynolds numbers alternative correlations are used to take account of internal circulation in the fluid particles. When the velocity difference between the continuous and dispersed phases is low the forced convection heat transfer can be augmented by natural convection heat transfer. Heat transfer between continuous phase liquid or gas and structure is calculated using correlations obtained for forced convection single-phase flow in pipes.

A model to calculate HTCs in the event of film boiling around a hot droplet or particle in a continuous phase coolant liquid is also available in SIMMER-III. The model can significantly reduce heat fluxes due to the insulating effect of the vapor blanket.

The HTCs are defined for the bubbly, annular and dispersed flow regimes. HTCs in intermediate flow regimes are computed by interpolation between well-defined flow regimes. The interpolation is performed using logarithmic averaging to smooth the transition between flow regimes. In addition the HTCs of two liquid components are interpolated between the continuous and discontinuous phase HTCs

when neither liquid forms a dominant continuous phase. This avoids sudden changes in heat transfer caused by small alterations in volume fractions of the components.

2.3.7 Heat and mass transfer model

After the interfacial areas and heat-transfer coefficients are determined, the conservation equations without convection are solved for intra-cell heat and mass transfer in two steps. The first step calculates the phase transition processes occurring at interfaces, described by a non-equilibrium heat-transfer-limited model. This is a non-equilibrium process because the bulk temperature does not generally satisfy the phase-transition condition when the mass transfer occurs at the interface. The second step of mass and energy transfer is through an equilibrium process occurring when the bulk temperature satisfies the phase-transition condition. At 42 possible interfaces defined in SIMMER-III, all the important non-equilibrium mass-transfer processes are modeled, including 30 V/C paths and 20 M/F paths. Note that in the V/C transfers condensation processes of fuel or steel vapor on other colder liquids are included to avoid the SIMMER-II/AFDM problem of nonphysical presence of supercooled vapor. The M/F transfers include the crust formation on a can wall that furnishes thermal resistance, and steel ablation and particle formation that contribute to fluid quenching and bulk freezing. In addition, 8 equilibrium M/F transfers are performed to eliminate supercooled liquids or metastable solids as a result of heat transfer and nuclear heating. The mass-transfer processes actually modeled are selected in consideration of their importance in and effects on the behavior of materials in the transition-phase.

The basic concept of the non-equilibrium mass transfer model is described using Fig. 2-10, in which a binary contact interface of the energy components A and B is shown. This is a heat-transfer-limited process where the phase transition rate is determined from energy balance at the interface. The heat transfer rates from the interface are:

$$q_{A,B} = a_{A,B} h_{A,B} \left(T^I_{A,B} - T_A \right) \tag{9}$$

$$q_{B,A} = a_{A,B} h_{B,A} \left(T^I_{A,B} - T_B \right) \tag{10}$$

where $T^I_{A,B}$ is the instantaneous contact interface temperature due to heat conduction without phase transition. The net energy transfer rate from the interface is defined as:

$$q^I_{A,B} = q_{A,B} + q_{B,A} \tag{11}$$

If the net heat flow $q^I_{A,B}$ is zero, sensible heat is exchanged without phase transition.

If $q^I_{A,B}$ is positive, namely the energy loss at the interface, either a liquid component freezes or a vapor component condenses. Then the mass transfer rate for this case is determined from:

$$\Gamma^I_{A,B} = \frac{q^I_{A,B}}{i_A - i^I_B} \quad \text{if the component } B \text{ is formed by phase transition, or} \tag{12}$$

$$\Gamma^I_{A,C} = \frac{q^I_{A,B}}{i_A - i^I_C} \quad \text{if the component } C \text{ is formed by phase transition.} \tag{13}$$

If $q^I_{A,B}$ is negative, on the other hand, namely the energy gain at the interface, either a solid component melts or a liquid component vaporizes. Then the mass transfer rate for this case is determined from:

$$\Gamma^I_{B,A} = \frac{q^I_{A,B}}{i^I_A - i_B} \quad \text{if the component } A \text{ is formed by phase transition, or} \tag{14}$$

$$\Gamma^I_{B,D} = \frac{q^I_{A,B}}{i^I_D - i_B} \quad \text{if a new component } D \text{ is formed by phase transition.} \tag{15}$$

In the above four equations, the heat of phase transition (the effective latent heat) is defined as the difference between the enthalpy at the interface and the bulk enthalpy of a component undergoing a phase-transition process.

In the non-equilibrium V/C model, the mass-transfer rates are determined from net energy gain or loss at an interface divided by the effective latent heat. The interfacial energy loss means that condensation must occur to conserve energy, while the interfacial energy gain means that the energy is going into vaporization. The energy- and mass-conservation equations coupled with EOSs are then solved iteratively using the mass-transfer rates obtained. In the solution procedure, based on a multivariate Newton-Raphson method, five sensitive variables (three condensable vapor densities, coolant energy and vapor temperature) are updated implicitly, whereas the remaining less sensitive variables are updated explicitly following the convergence of the iteration. In a single-phase cell, vapor is assumed to always exist in a non-zero small volume, $\alpha_0(1-\alpha_S)$, so its density and energy are calculated consistently with two-phase cells to avoid numerical difficulties. Currently, the single-phase V/C calculations are performed using the same procedure as two-phase cells except for the energy transfer between liquids. At a liquid/liquid interface, such as fuel/sodium contact in a two-phase cell, vaporization can occur, and in this case the interface temperature is defined as the saturation temperature of a vaporizing material. In a single-phase cell, however, the interface temperature of the liquid/liquid contact is defined so that no vaporization is caused by the energy transfer between the liquids. Instead phase transition occurs only when the liquid temperature increases sufficiently to cause vaporization at a liquid/vapor interface.

The M/F calculation is also based on the two modes: non-equilibrium and equilibrium processes. The former is similar to the V/C processes; however all the variables are updated explicitly except for the coolant energy, which is identified as sensitive. After calculating the heat and mass transfer resulting from non-equilibrium processes and structure heat transfer, the equilibrium M/F rates are determined by comparing the updated component energy with its liquidus energy for freezing or its solidus energy for melting.

The intra-cell heat and mass transfer calculations result in updated component volume fractions and masses. The convective interfacial areas and velocities are then adjusted consistently.

2.3.8 Inter-cell heat transfer

SIMMER-III, like its preceding codes SIMMER-II and AFDM, originally calculated only intra-cell heat transfer, and could not transfer energy between cells except for the energy transfer by convection. However, a treatment of inter-cell heat transfer was essential to analyze small-scale pool boiling behavior

correctly and hence a new model to calculate the inter-cell heat conduction was developed and implemented in SIMMER-III.

The generalized energy conservation equation including the inter-cell heat conduction term is written as:

$$\frac{\partial \bar{\rho}_M e_M}{\partial t} + \nabla \cdot \left(\bar{\rho}_M e_M \boldsymbol{v}_q\right) = Q + \nabla \cdot q_c \tag{16}$$

where Q is the energy source other than the inter-cell heat conduction, which is shown as the second term of RHS. In SIMMER-III/SIMMER-IV the energy transfer due to fluid convection is separately treated in Steps 2 to 4. Therefore, the evaluation of the conductive heat transfer is to be performed in Step 1 using the temperature at the beginning of time step. The heat flux which appears in Eq. (16) is calculated by Fourier's law and includes the turbulent thermal conductivity:

$$q_c = -f_I(k_c + k_T)\ \nabla T_M \tag{17}$$

where the turbulent thermal conductivity k_T depends on the position, direction, and the nature of the turbulent flow. The turbulent heat flux is evaluated by a combination of Prandtl's mixing length theory and experimental correlations.

2.3.9 Equations-of-state model

An EOS model is required to close and complete the fluid-dynamic conservation equations. Moreover it is crucial from the viewpoints of numerical accuracy and stability, and computing efficiency. Neither SIMMER-II nor AFDM were satisfactory from these aspects. Based on past experiences, therefore, an improved analytic EOS model using the flexible thermodynamic functions has been developed for SIMMER-III[17]. The model treats the basic reactor-core materials: mixed-oxide fuel, steel, sodium, control (B_4C) and fission gas. These materials are assumed to be immiscible, such that a unique EOS for each material can be defined.

A modified Redlich-Kwong (MRK) equation is used for the vapor phase[18]. The MRK EOS has the form:

$$p_{Gm} = \frac{R_M T_M}{v_{Gm} - a_{G1,M}} - \frac{a(T_G)}{v_{Gm}\left(v_{Gm} + a_{G3,M}\right)} \tag{18}$$

where

$$a(T_G) = a_{G2,M}\left(\frac{T_G}{T_{Crt,M}}\right)^{a_{G4,M}}, \text{for } T_G < T_{Crt,M}$$

$$a(T_G) = a_{G2,M}\left[1 + a_{G4,M}\left(\frac{T_G}{T_{Crt,M}} - 1\right)\right], \text{for } T_G \geq T_{Crt,M}$$

and $a_{G1,M}$, $a_{G2,M}$, $a_{G3,M}$ and $a_{G4,M}$ are the EOS parameters.

The above equation is similar to the van der Waals equation, but it can be made reasonably accurate especially at high temperatures. It was found, however, that this EOS poorly reproduces the evaluated

data[19] of the internal energy and the heat capacity of sodium vapor. Therefore the MRK EOS was extended to a reacting system, which describes the dimerization process of sodium vapor molecules, and thereby satisfactory agreement was obtained.

In AFDM, an inner EOS iteration was implemented to obtain mechanical equilibrium to compress each liquid to a state that is consistent with an identical pressure, and thereby to define the vapor volume fraction. This treatment turned out to be less computing cost effective and made the pressure iteration, a main element of fluid convection algorithm, very slow. In SIMMER-III, an improved method is introduced to eliminate the inner EOS iteration by defining the EOS as a function of the cell pressure, and thereby the mechanical equilibrium among liquid components with the cell pressure is automatically guaranteed when the pressure iteration is converged.

The EOS functions are fitted using the most up-to-date and reliable data sources available[19), 20)]. The present SIMMER-III/SIMMER-IV EOS model has adequate accuracy at high temperature and high pressure and consistently satisfies basic thermodynamic relationships over the wide temperature range from the solid to supercritical state.

2.4 Fuel Pin and Structure Model

2.4.1 Fuel pin configuration and heat-transfer model

The fuel-pin and can wall model not only represents the stationary structure in the core, but also traces time-dependent disintegration. The standard fuel-pin model is rather simple with a pellet interior modeled by a single temperature node and with breakup modeled only by a thermal (melt fraction) criterion. However the separated treatment of a pellet surface node provides better thermal coupling with the fluid. Because of the relatively large thermal inertia of the pellet interior, the fuel-pin heat-transfer calculation can be performed with time steps larger than the fluid-dynamics steps. This simplified model is considered to be sufficient for simulating the fuel-pin behavior in a voided channel typical in a loss-of-flow accident.

Radial and axial fuel-pin geometries are represented as shown in Figs. 2-11 and 2-12. The axial blanket and fission-gas plenum regions can be placed both above and below the core region. The heat-conduction equation in a cylindrical geometry is solved implicitly for specific internal energies of up to three fuel-pin components (interior, surface and cladding). Pellet-cladding gap conductance is modeled by an input constant in this simple model. The pin surface node (either pin fuel surface or cladding) exchanges mass and energy with the fluid. In the fission-gas plenum region, the gas temperature is represented by one point and the heat transfer is solved explicitly because of its slow thermal response. For a control subassembly, the pin fuel is replaced by the control material (B_4C), which is modeled by one node.

The breakup of the pin fuel and cladding is determined from input threshold melt fractions, typically 0.5 for pin fuel and the solidus energy for the cladding. The mass and energy transfer upon breakup is instantaneous and this operation is included in fluid-dynamics Step 1. Similar to SIMMER-II, a special model can be selected by user input to simulate the mobilization of unsupported pin fuel. Namely, the pin fuel is assumed to break up when both the cladding and can walls in a cell are lost, or when the cladding is

lost and the pin fuel structure below is lost. The control is assumed to break up into particles when the cladding is lost. The control particles are only modeled in fluid in SIMMER-III.

As explained in Section 2.2, the fission-gas components in the liquid-field fuel (liquid and particles) are modeled in SIMMER-III. Upon breakup of the pin fuel, the fission gas mass is transferred to the liquid field and no direct path to the vapor field is allowed. Then later release from the liquid and particulate fuel is modeled based on user-specified release time constants. This significantly improves the modeling of the important effect of fission gas on fuel motion during the transition phase.

2.4.2 Can wall configuration and heat-transfer model

The can wall model treats separated left and right can walls assumed to be located at the mesh cell boundaries. The presence of the can wall at a cell boundary eliminates radial fluid convection. Fuel crust can grow on a can wall when the heat and mass transfer model predicts this. Inter-cell heat transfer is also calculated when one of the two can walls at a cell interface is missing. When the can wall becomes thin, then the two nodes are merged into a single interior node.

The above requires a complex procedure to define the can-wall structure configuration. The detailed structure of a mesh cell with all the can-wall components is shown in Fig. 2-13. Let us consider a mesh cell boundary. If this is the left boundary of the first radial cell or the right boundary of the last radial cell, or a boundary where two can-wall interior nodes are present, then the two cells adjacent at this boundary are thermally decoupled. Each can wall is treated separately in each cell. On the other hand, if one of the can walls at this boundary is missing, then the two cells are coupled thermally through the remaining can wall. Four cases exist in this situation depending on whether the can wall is thick (two nodes) or thin (a single interior node), and whether the crust fuel is present or not.

The can-wall heat transfer is modeled considering the above combinations of geometric configuration and heat transfer paths. The calculation is performed implicitly with fluid time steps based on heat conduction in a slab geometry between up to five structure-component layers. The can walls undergo heat and mass transfer with the fluid through non-equilibrium and equilibrium M/F processes.

2.5 Neutronics Model

No neutronics model was available in Version 1 of SIMMER-III. A simple heat source model was available, in which power distribution and a power-versus-tie talble are specified by user input.

The neutronics model being developed for SIMMER-III is based on two optional models. One is similar to the neutronics model in SIMMER-II which models the space dependence of neutron flux by a multi-group S_n transport theory with a coarse-mesh rebalancing scheme based on TWOTRAN code. Another new model is based on a TWODANT code which takes advantage of a diffusion-synthesis acceleration method and improves both the robustness and calculational efficiency. The transient neutron kinetics is treated by an improved quasi-static method. Coupling with the fluid-dynamics portion is carefully designed, because the neutronic state of an LMFR core during a CDA is determined primarily from time-dependent mass and energy distribution of the core materials. It is because of this time dependence that the calculations of shielded (effective) macroscopic cross sections are also performed in the code. To

connect with the initiating phase calculations, a capability of transient-state neutronics initialization is available, similar to SIMMER-II.

Additional features included in SIMMER-III, not available in SIMMER-II, are: an optional use of PCG matrix solvers for the rebalance equation; a simple decay heating model, which provides a consistent treatment with the SAS-series initiating-phase analysis code[21)] ; the model improvement for applying the code to a thermal or epi-thermal reactor. The latter includes: the treatment of neutron up-scattering, the treatment of cell heterogeneity in calculating the macroscopic cross sections, and the special acceleration for thermal neutron energy groups.

2.6 Status of SIMMER-III Development

The Phase 1 assessment program has concentrated to verification and validation of the fluid-dynamixs model. During the course of the assessment in 1994 through 1996, the code versions have evolved from Version 1.A to 1.K with a numcer of major and minot model changes and error corrections. The Phase 1 assessment program proved to be very useful not only for model validataion but slso for debugging its coding.

Version 2 of SIMMER-III is to be completed in 1996 The neutronics model has been coupled with the fluid-dynamics and structure models, and the steady-state and transient capabilities have been tested successfully. All the recent improvement in fluid-dynamics and structure models are included. One of the most important features available in Version 2, which was not included in the original scope of SIMMER-III, is the viscous term in the momentum equation. The viscous term is believed to be important in small-scale problems where inter-cell momentum coupling is important.

Table 2-1. SIMMER-III fluid-dynamics structure-field components.

Density components (MCSR)		Energy components (MCSRE)	
*s*1	Fertile Pin Fuel Surface Node	*S*1	Pin Fuel Surface Node
*s*2	Fissile Pin Fuel Surface Node		
*s*3	Left Fertile Fuel Crust	*S*2	Left Fuel Crust
*s*4	Left Fissile Fuel Crust		
*s*5	Right Fertile Fuel Crust	*S*3	Right Fuel Crust
*s*6	Right Fissile Fuel Crust		
*s*7	Cladding	*S*4	Cladding
*s*8	Left Can Wall Surface Node	*S*5	Left Can Wall Surface Node
*s*9	Left Can Wall Interior Node	*S*6	Left Can Wall Interior Node
*s*10	Right Can Wall Surface Node	*S*7	Right Can Wall Surface Node
*s*11	Right Can Wall Interior Node	*S*8	Right Can Wall Interior Node
*s*12	Control	*S*9	Control

Table 2-2. SIMMER-III fluid-dynamics liquid-field components.

Density components (MCLR)		Energy components (MCLRE)		Velocity fields
*l*1	Liquid Fertile Fuel	*L*1	Liquid Fuel	*q*1
*l*2	Liquid Fissile Fuel			*q*1
*l*3	Liquid Steel	*L*2	Liquid Steel	*q*2
*l*4	Liquid Sodium	*L*3	Liquid Sodium	*q*2
*l*5	Fertile Fuel Particles	*L*4	Fuel Particles	*q*1
*l*6	Fissile Fuel Particles			*q*1
*l*7	Steel Particles	*L*5	Steel Particles	*q*1
*l*8	Control Particles	*L*6	Control Particles	*q*2
*l*9	Fission Gas in Liquid Fuel			*q*1
*l*10	Fission Gas in Fuel Particles			*q*1

Table 2-3. SIMMER-III fluid-dynamics vapor-field components.

(All vapor components have the same temperature and assigned to the velocity field *q3*)

Density components (MCGR)		Material components (MCGM1)	
*g*1	Fertile Fuel Vapor	*G*1	Fuel Vapor
*g*2	Fissile Fuel Vapor		
*g*3	Steel Vapor	*G*2	Steel Vapor
*g*4	Sodium Vapor	*G*3	Sodium Vapor
*g*5	Fission Gas	*G*4	Fission Gas

Table 2-4. SIMMER-III fuel-pin components.

Simple model (standard)		**Detailed model (optional)**	
a	Pin Fuel Interior Node	(k)	Pin Fuel Radial Nodes
b	Pin Fuel Surface Node (= *S*1)	(NT)	Pin Fuel Surface Node (= *S*1)
c	Cladding (= *S*4)	(NT+1)	Cladding
	Fission Gas in Pin Fuel	(k)	Fission Gas in Pin Fuel
		Fuel-Pin Cavity	
		*c*1	Fertile Cavity Fuel
		*c*2	Fissile Cavity Fuel
		*c*3	Dissolved Fission Gas in Cavity
		*c*4	Free Fission Gas in Cavity

Table 2-5. Update procedure in four-step algorithm

Step 1: Calculate intra-cell transfers from the end of the previous time step.

$$\left(\bar{\rho}^{(1)}, \boldsymbol{v}^{(1)}, e^{(1)}\right) \leftarrow (\bar{\rho}^{n}, \boldsymbol{v}^{n}, e^{n})$$

Step 2: Estimate end-of-time-step values $\left(\bar{\rho}^{(2)}, \boldsymbol{v}^{(2)}, e^{(2)}\right)$ without intra-cell source terms.

$$\frac{\bar{\rho}^{(2)} - \bar{\rho}^{(1)}}{\Delta t} + \nabla \cdot \left(\bar{\rho}^{(1)} \boldsymbol{v}^{(1)}\right) = 0$$

$$\frac{\bar{\rho}^{(2)} \boldsymbol{v}^{(2)} - \bar{\rho}^{(1)} v^{(1)}}{\Delta t} + \nabla \cdot \left(\bar{\rho}^{(1)} \boldsymbol{v}^{(1)} v^{(1)}\right) + \nabla p^{n} = 0$$

$$\frac{\bar{\rho}^{(2)} e^{(2)} - \bar{\rho}^{(1)} e^{(1)}}{\Delta t} + \nabla \cdot \left(\bar{\rho}^{(1)} e^{(1)} \boldsymbol{v}^{(1)}\right) + p^{n} \nabla \cdot \boldsymbol{v}^{(1)} = 0$$

Step 3: Solve for $\left(\bar{\rho}^{(3)}, \boldsymbol{v}^{(3)}, e^{(3)}\right)$ by pressure iteration.

$$\frac{\bar{\rho}^{(3)} - \bar{\rho}^{(1)}}{\Delta t} + \nabla \cdot \left(\bar{\rho}^{(1)} \boldsymbol{v}^{(3)}\right) = 0$$

$$\frac{\bar{\rho}^{(3)} \boldsymbol{v}^{(3)} - \bar{\rho}^{(1)} \vec{\boldsymbol{v}}^{(1)}}{\Delta t} + \nabla \cdot \left(\bar{\rho}^{(1)} \boldsymbol{v}^{(1)} \boldsymbol{v}^{(3)}\right) + \nabla p^{(3)} = 0$$

$$\frac{\bar{\rho}^{(2)} e^{(3)} - \bar{\rho}^{(1)} e^{(1)}}{\Delta t} + \nabla \cdot \left(\bar{\rho}^{(1)} e^{(1)} \boldsymbol{v}^{(1)}\right) + p^{(3)} \nabla \cdot \boldsymbol{v}^{(3)} = 0$$

Step 4: Calculate final end-of-time-step values $(\bar{\rho}^{n+1}, \boldsymbol{v}^{n+1}, e^{n+1})$.

$$\frac{\bar{\rho}^{(3)} \boldsymbol{v}^{(4)} - \bar{\rho}^{(1)} \boldsymbol{v}^{(1)}}{\Delta t} + \nabla \cdot \left(\bar{\rho}^{(1)} \boldsymbol{v}^{(1)} \boldsymbol{v}^{(3)}\right) + \nabla p^{(3)} = 0$$

$$\frac{\bar{\rho}^{(3)} e^{(4)} - \bar{\rho}^{(1)} e^{(1)}}{\Delta t} + \nabla \cdot \left(\bar{\rho}^{(1)} e^{(1)} \boldsymbol{v}^{(3)}\right) + p^{(3)} \nabla \cdot \boldsymbol{v}^{(3)} = 0$$

$$(\bar{\rho}^{n+1}, \boldsymbol{v}^{n+1}, e^{n+1}) \leftarrow \left(\bar{\rho}^{(3)}, \boldsymbol{v}^{(4)}, e^{(4)}\right)$$

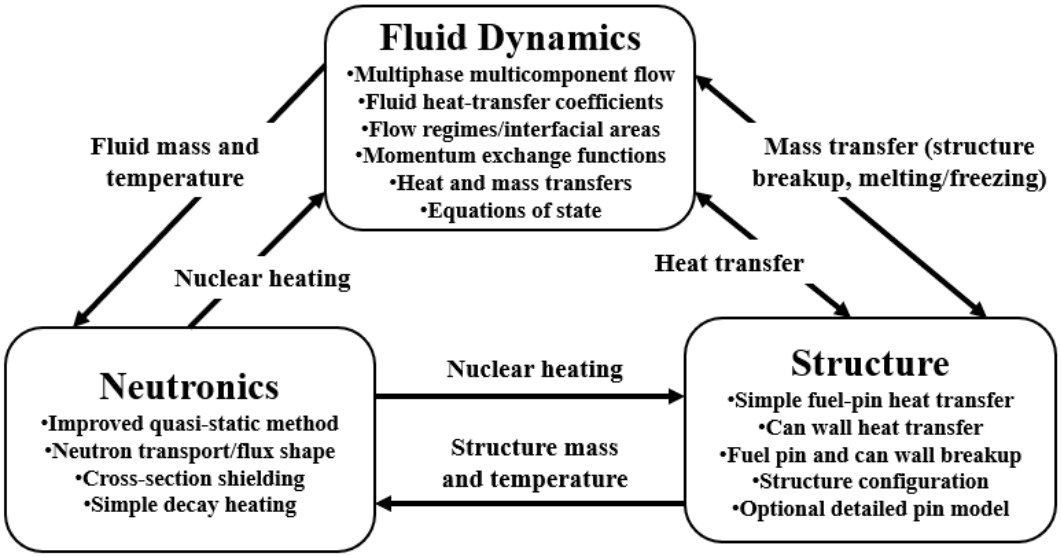

Fig. 2-1. SIMMER-III overall code structure

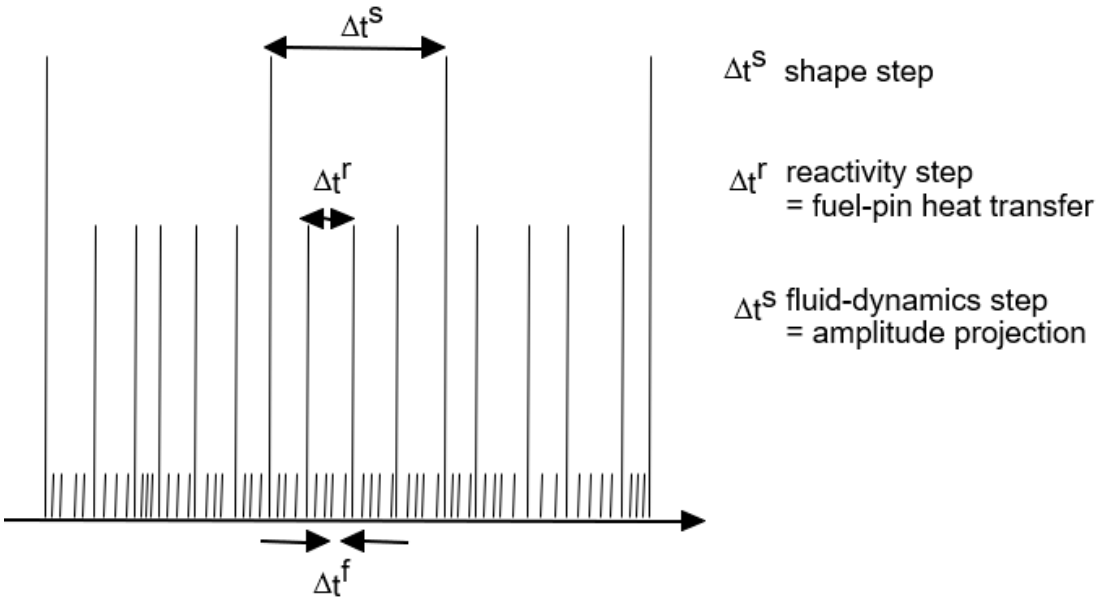

Fig. 2-2. SIMMER-III time step hierarchy

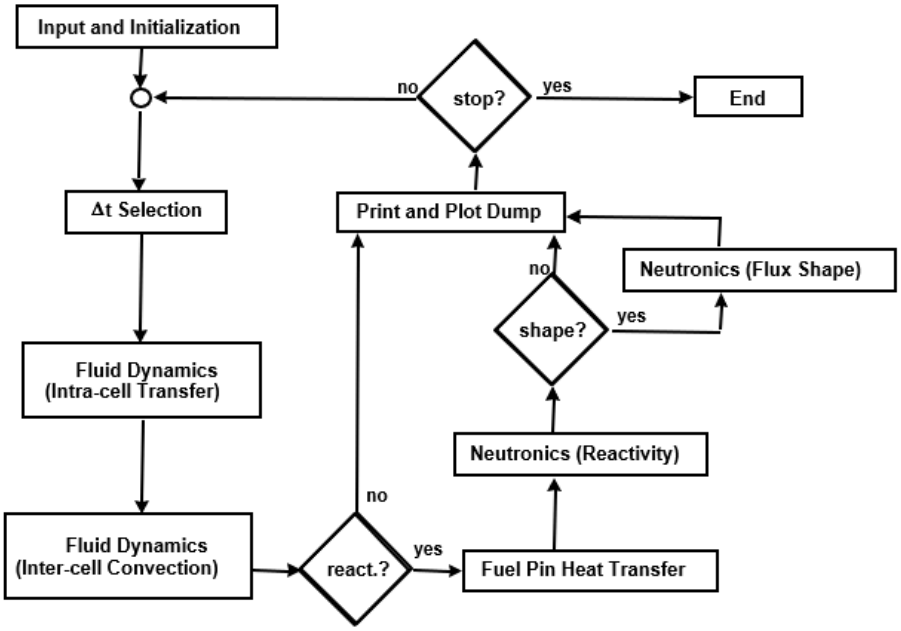

Fig. 2-3. SIMMER-III calculational flow

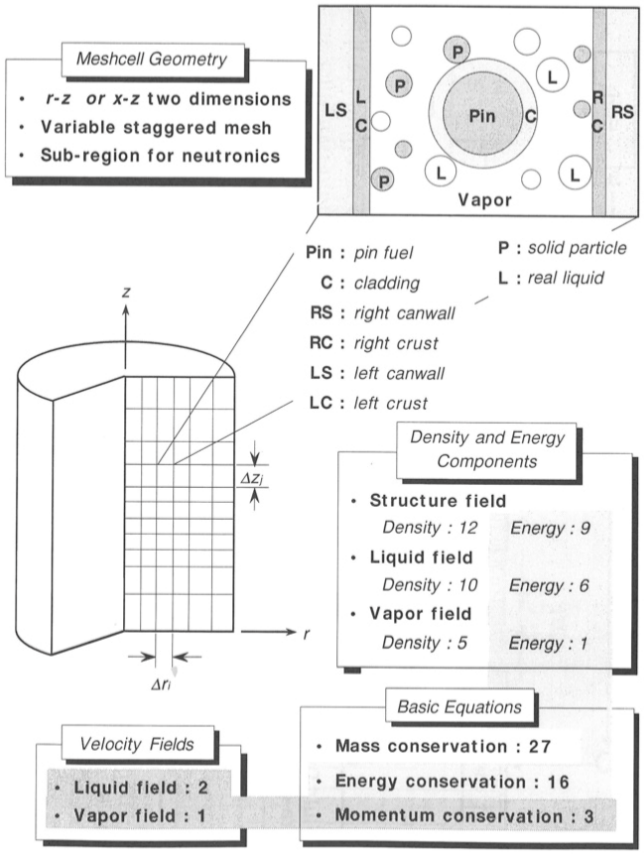

Fig. 2-4. SIMMER-III geometric framework

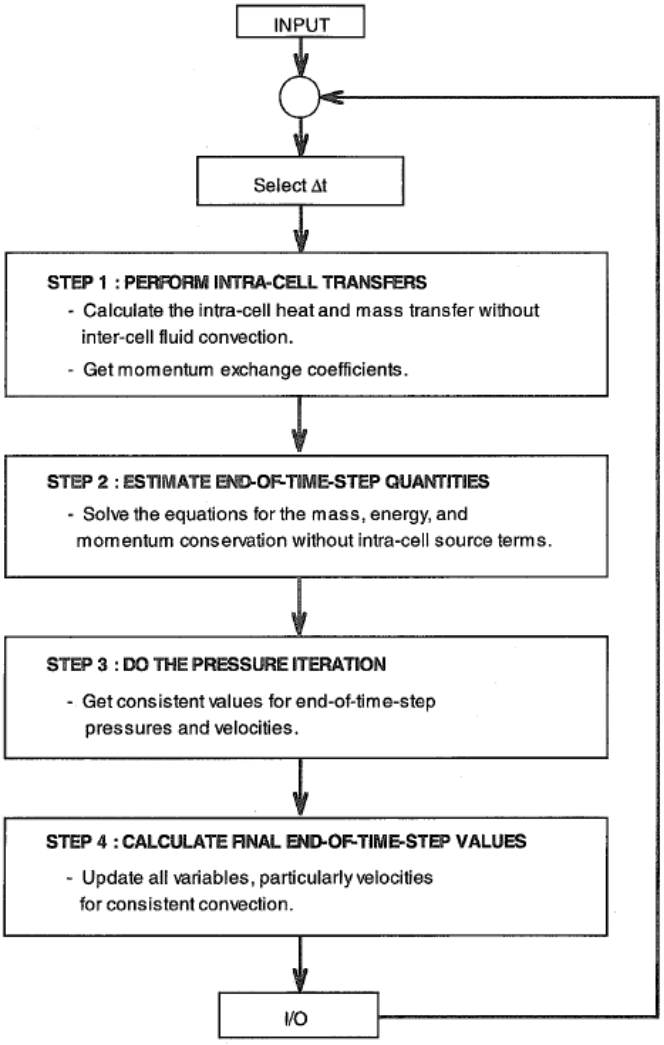

Fig. 2-5. Schematic diagram of the four-step method

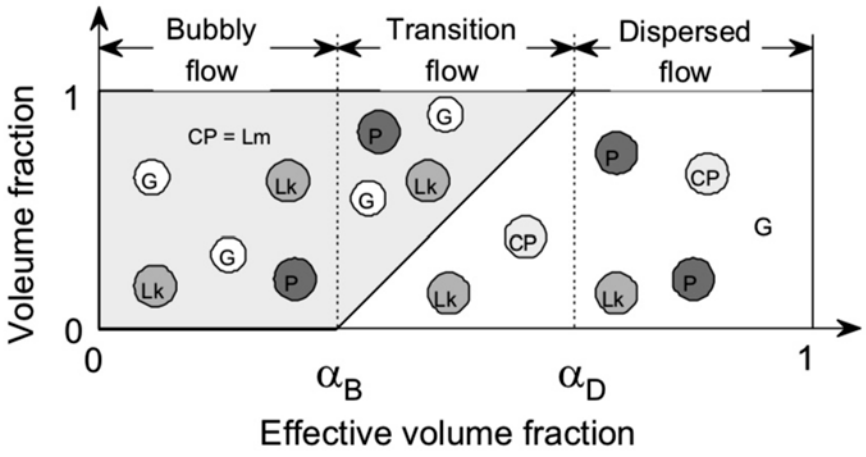

Fig. 2-6. SIMMER-III pool flow regime map

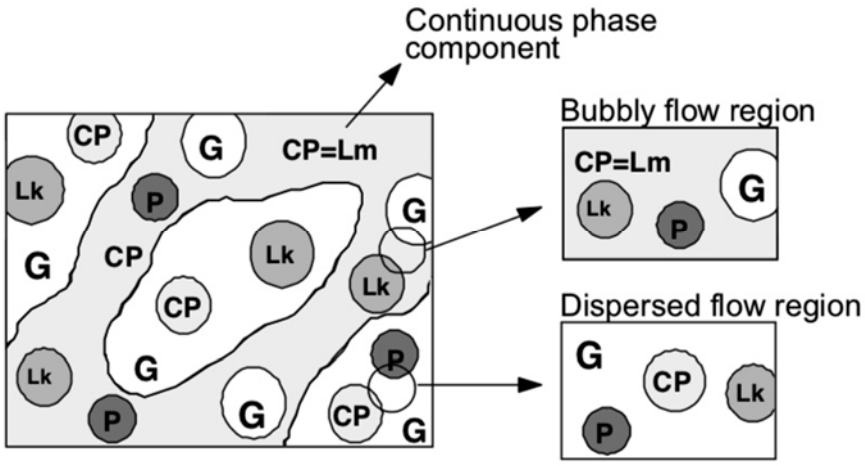

Fig. 2-7. Schematic concept of separating bubbly and dispersed regions

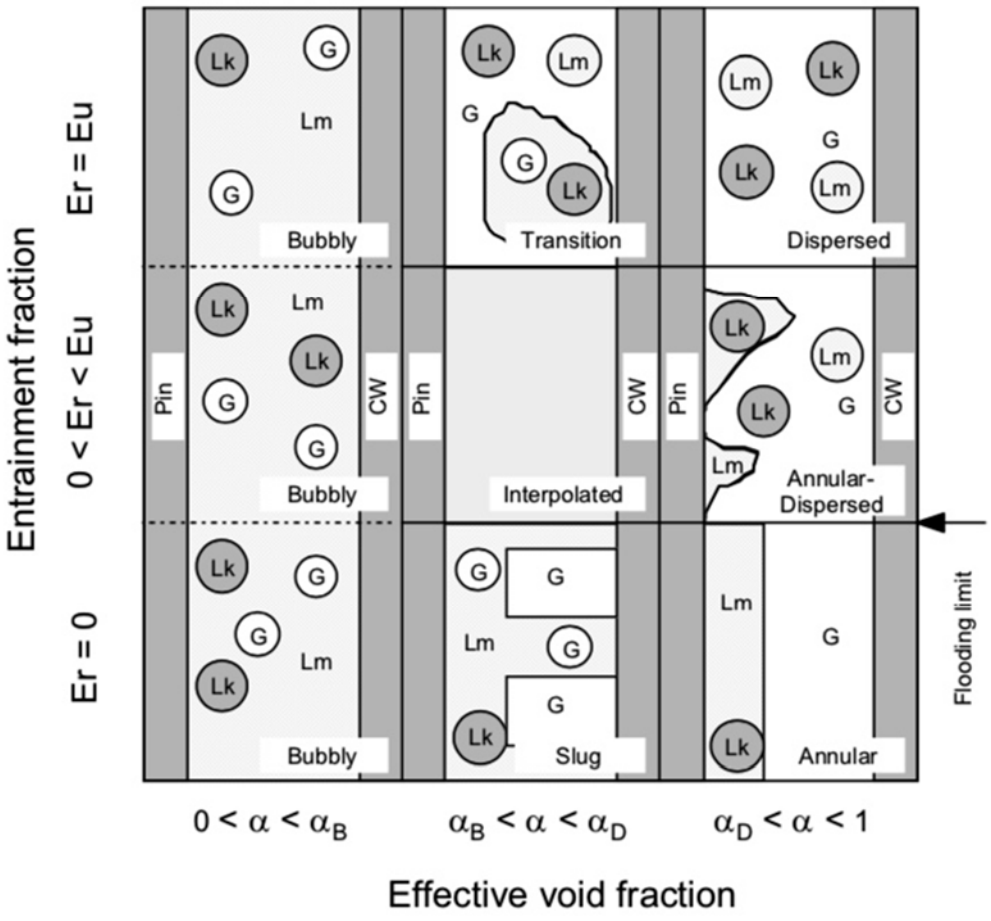

Fig. 2-8. SIMMER-III channel flow regime map

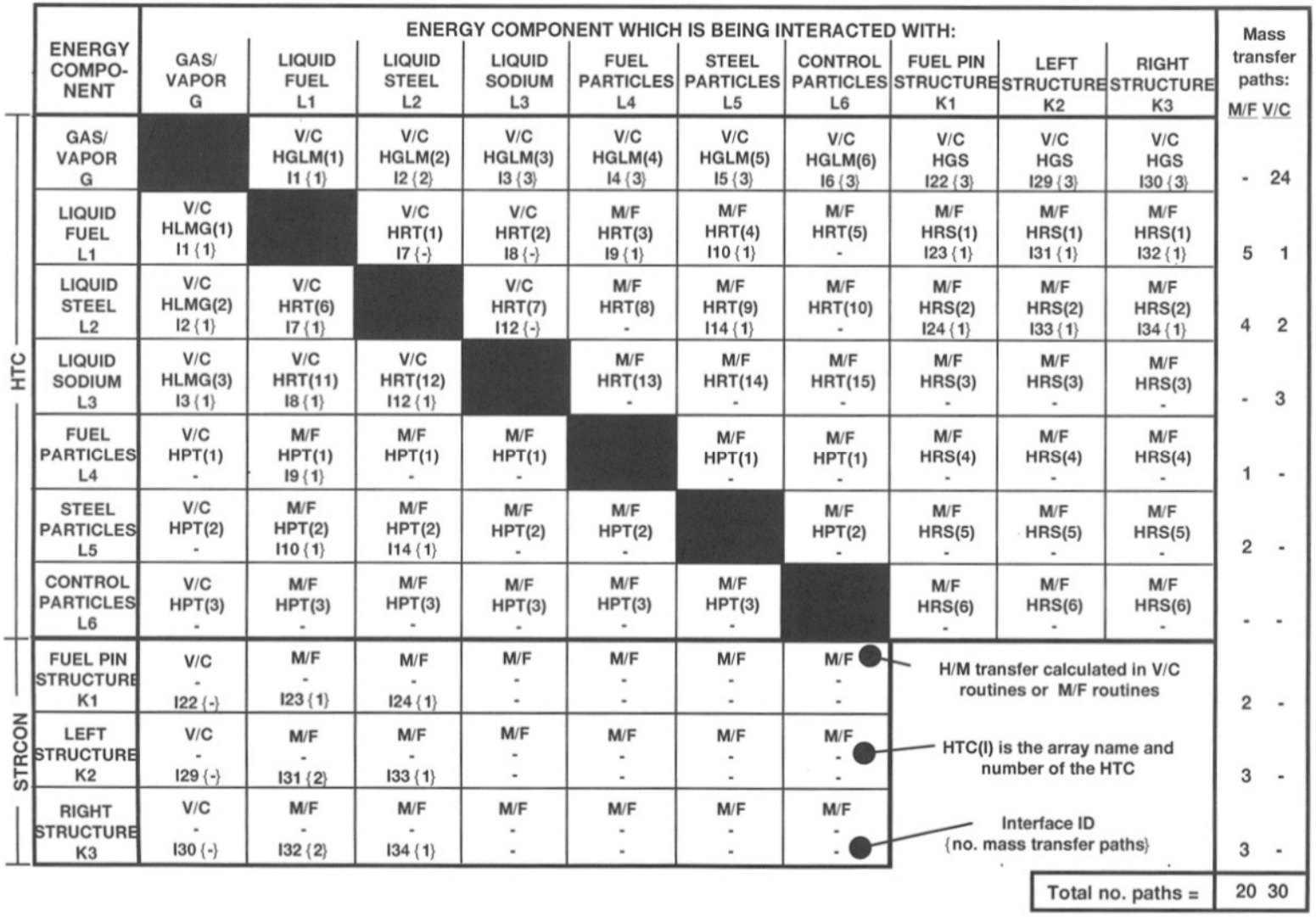

Fig. 2-9. Role of IITCs in SIMMER-III heat and mass transfer

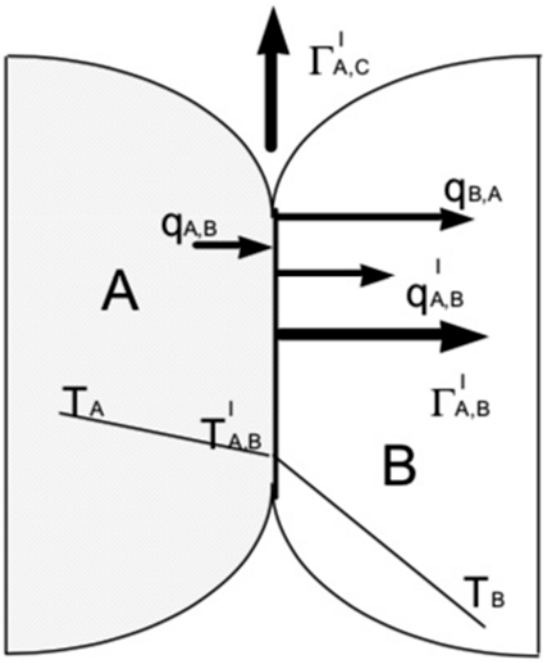

Mass transfer possibilities at an (A,B) interfaces with net heat flow to the interface from Component A

- Component A condenses or freezes

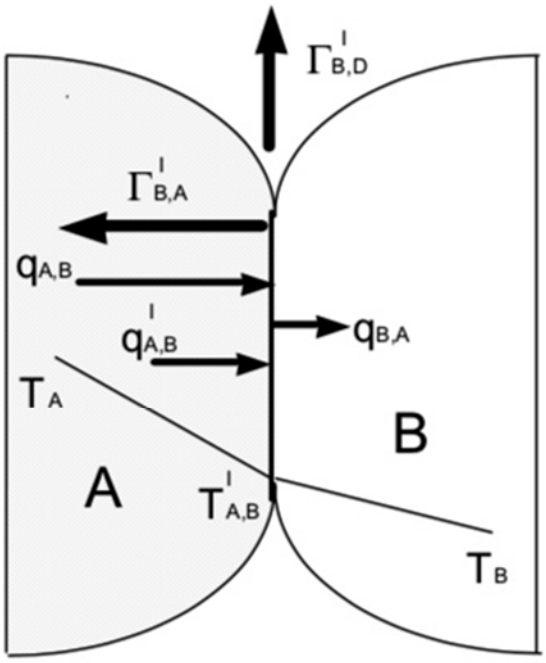

Mass transfer possibilities at an (A,B) interfaces with net heat flow to the interface from Component A

- Component B vaporizes or melts

Fig. 2-10. Interface treatment in non-equilibrium transfer

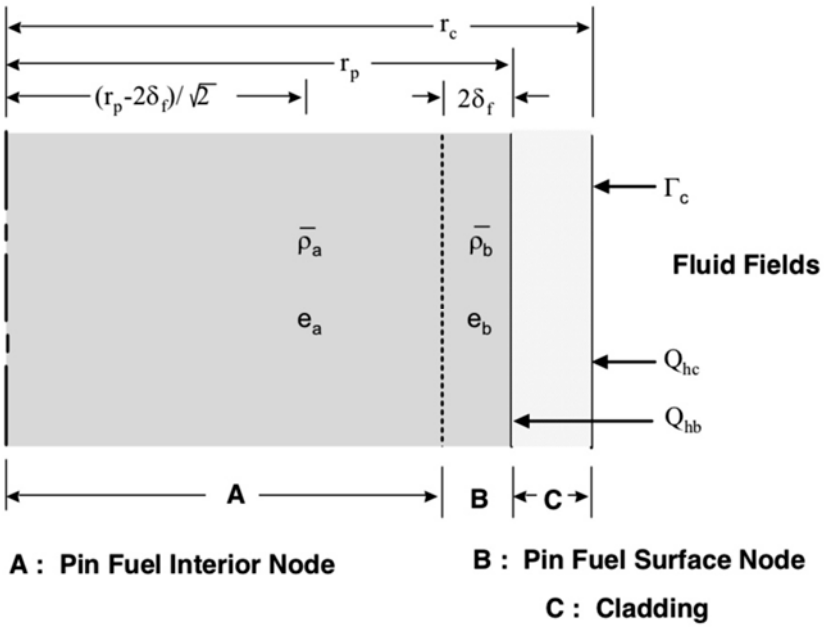

Fig. 2-11. Radial fuel-pin cross section in SIMMER-III (Simple model)

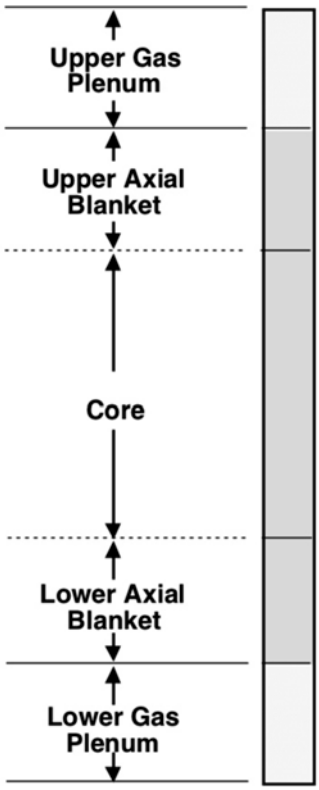

Fig. 2-12. Axial fuel-pin representation in SIMMER-III (Simple model)

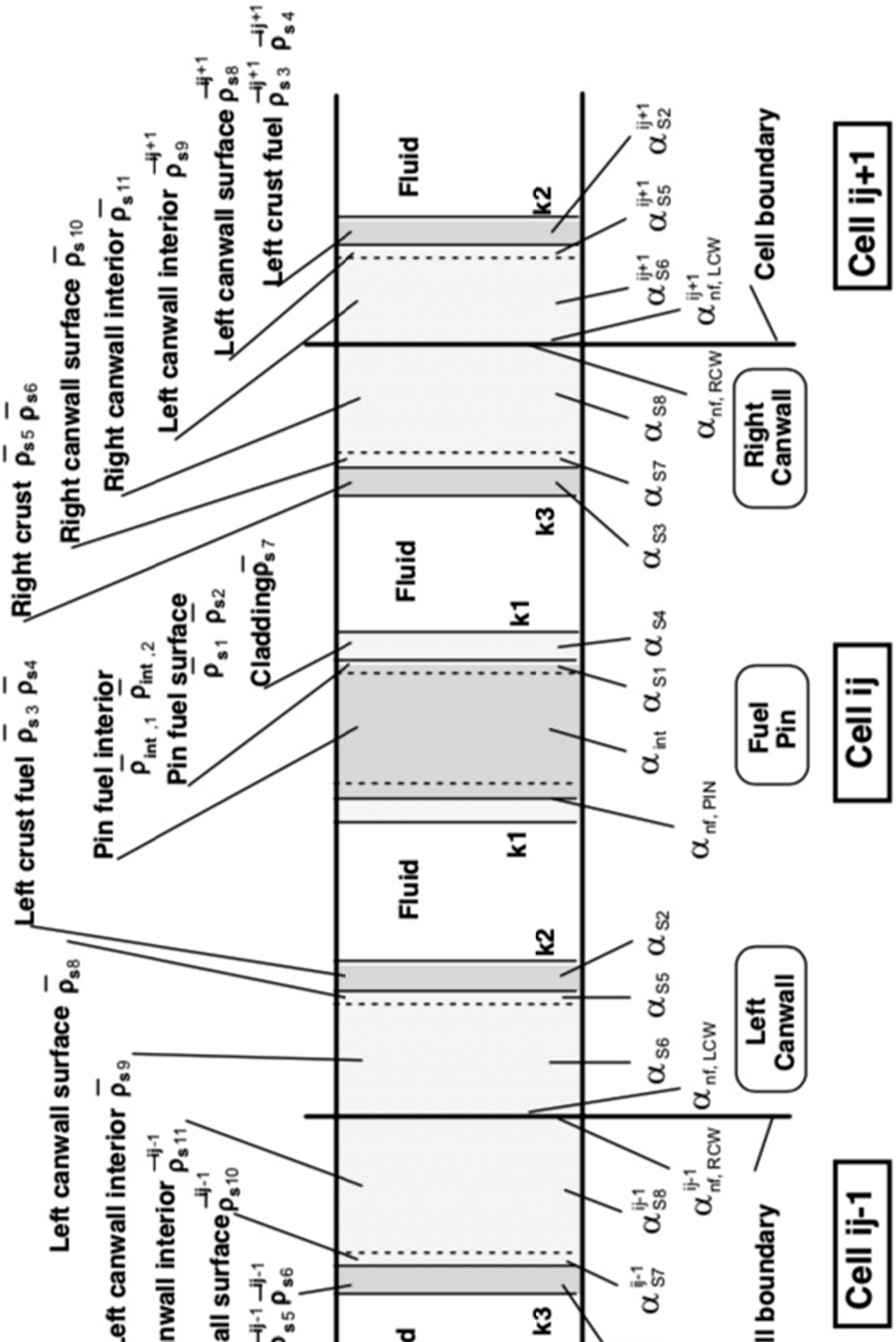

Fig. 2-13. Fuel-pin and can-wall configuration in a mesh cell

3. Approach to Code Assessment Program

3.1 Overview of SIMMER-III Assessment Program

The ultimate goal of the SIMMER-III project is to provide a reliable and standard tool for LMFR safety analysis. To make the code sufficiently reliable to be applied to reactor cases, it must be capable of simulating the relevant phenomena which may occur during the course of an accident. At the same time, and more importantly, it is highly desirable that the physical models of the code be validated against available experimental data and known physics that are relevant to reactor accident phenomenology.

In the past an extensive effort was made worldwide to validate SIMMER-II, since its first application to an energy partition problem in the post-disassembly expansion phase of a CDA showed significant potential mitigation of mechanical energy release[22]. The United States NRC proposed an international validation program named as a "qualification testing program" [23], but this was not actually conducted. Then the application of SIMMER-II to the transition phase necessitated that the code be validated against experiments relevant to the transition phase[24]. Many of these applications demonstrated that the code could simulate, to some extent, accident sequences reasonably. Nevertheless the status and level of SIMMER-II validation were limited, mainly because of limitations in the code framework, such as the two-velocityfield fluid dynamics, single flow regime and simplified equations of state. Also the validation study was not systematic and was restricted to those areas where a limited knowledge base was available. As a result, SIMMER-II has been applied to reactor cases more or less prudently and conservatively.

The AFDM program was intended to rectify some of the known code limitations of SIMMER-II. Because of the complexity of AFDM modeling and its application problems, it was planned to confirm the plausibility of calculated results. This program was not actually conducted because of the limited resources available and because, among the partners of AFDM, PNC and LANL decided to go ahead with the development of a next reactor code, SIMMER-III, in preference to further validating AFDM.

A validation program for SIMMER-III has been discussed since the initiation of the code development program. Furthermore so-called "developmental assessment" has been conducted as new models were proposed and developed. A good example is the interfacial area model development, where a simple test code was first developed and extensively tested for single-cell (zero-th dimension) problems before the models were actually programmed in SIMMER-III. The fluid convection algorithm and boundary conditions were also tested thoroughly in an early adiabatic version of the code without models for heat and mass transfer. By this time, the German FZK and French CEA organizations had become partners in SIMMER-III development and assessment. So when SIMMER-III Version 1 was made available it was decided to conduct a more systematic validation program within a framework of international cooperation.

Two different terminology are commonly used in computer code development: "verification" ensures that the code is programmed and performing calculations according to its specification; whilst "validation" confirms that the code predictions are physically valid by comparison against experimental data or other validated codes. In the SIMMER-III project, the terminology of "assessment" is used consistently to give

the program a more general meaning, similar to that used in NRC-sponsored light water reactor safety codes such as TRAC[25].

The SIMMER-III code assessment program has several objectives. First the models of the code must be as applicable to accident sequence simulation as they are designed to be. Second the coding must be checked and debugged such that the quality of the program is assured. The quality assurance of large and complex codes like SIMMER can only be done through extensive testing for various problems under a variety of initial and boundary conditions. These test calculations, and the resultant model refinement, are effective for making the code robust and reliable, both numerically and physically. Third SIMMER-III must be practically useful: the computing cost of application calculations must be acceptable. Fourth the validity of the code must be confirmed for the key accident phenomena which the code is intended to simulate. Key LMFR accident phenomena includes fuel relocation behavior, boiling fuel/steel behavior, fuel-coolant interactions (FCIs) and disrupted core neutronics. In addition, even though SIMMER-III is to be applied to analyses of complex and integrated problems in the CDAs, the code at the same time must be applied to simple problems such as water two-phase flows. The last point is especially important since potential peer reviewers will not be satisfied by the applications to complex problems only. Rather it is highly desired that the code should be comparable, at least, with other existing state-of-the-art computer codes, for example those used in light water reactor safety analysis or water two-phase flow calculations.

Based on the above considerations and the general objectives of the code assessment, it was decided to conduct the SIMMER-III assessment program in two steps, Phase 1 and Phase 2. The Phase 1 assessment is intended to validate individual fluid-dynamics models of the code, whilst Phase 2 is for comprehensive validation for integral and inter-related accident phenomena, such as transient fuel motion during the transition phase and high-pressure CDA bubble expansion in the post-disassembly expansion phase. Direct application of the code to complex accident phenomena involves many inter-related processes to be solved simultaneously and is not always productive. It can result in crude parametric adjustments without assuring the general validity of major individual models. Thus the present stepwise approach is considered to be advantageous, since in Phase 1 the coding is largely debugged and verified, and each major model is validated separately. At the end of Phase 1, it is intended that the code is sufficiently robust and numerically stable for the application to integral phenomena in Phase 2. The Phase 1 and 2 assessment programs are discussed in more detail in the following sections.

3.2 Phase 1 Assessment Program

In Phase 1 of the assessment program, SIMMER-III has been applied to various separate effect problems in order to debug and verify its coding and validate individual models. Only the fluid-dynamics portion of the code was tested (the fuel-pin and neutronics models are out of the scope of Phase 1, but should be addressed in Phase 2). These calculations include many small-scale test problems, which as a whole cover the major models of the code. The test problems defined in Phase 1 include: simple test calculations to demonstrate the code can simulate known physics plausibly; single- and multi-phase flow benchmark problems to confirm the code is comparable with other state-of-the-art codes; and analyses of simple experiments with unambiguous data available. Some of the experimental analyses are fairly complex and

hence will be further studied in the subsequent Phase 2 assessment. Many of the Phase 1 problems were taken from the DOE/EPRI benchmark cases proposed in the late 1980s[26].

The Phase 1 assessment may well be regarded as a basic research. However this research is not the ultimate goal of the program, but should instead be regarded as an important step in the overall code assessment program, as discussed in the previous section. Phase 1 is intended to demonstrate that SIMMER-III is not only a useful tool for LMFR safety analysis but also that the code should be regarded as sufficiently advanced in the area of multi-phase flow computational technology, which will make the code more widely accepted among various technical communities outside the LMFR safety. Calculations of simple problems in Phase 1 are also beneficial with respect to user familiarization since they are easy to set up and run, and have short computing times. The user experience gained in Phase 1 wll be effectively used in future Phase 2 or reactor calculations. ·

The Phase 1 assessment of SIMMER-III covers a variety of fluid-dynamics test problems with the objective that the individual models are validated separately as far as possible. The test problems therefore are categorized as follow:

1 . Fluid convection algorithm,

2. Interfacial area and momentum exchange models,

3. Heat transfer,

4. Melting and freezing, and

5. Vaporization and condensation.

A complete list of the 34 test problems defined and analyzed is given in Table 3-1. The relationship with the code models are also shown. During the course of Phase 1 assessment, conducted from 1993 to 1996, the SIMMER-III code itself has been improved significantly, in part reflecting errors identified and additional needs raised by code application. This is a practice undertaken especially at PNC where the code development and improvement is performed in parallel. Therefore the assessment study at PNC has, more or .less, a character of developmental assessment. On the other hand, the active participation of the European organizations, FZK and CEA, have provided an independent character to the overall Phase 1 study. Their (unedited) critical views are included in this report, which can therefore be considered as an objective documentation of the study.

3.3 Phase 2 Assessment Program

Although the main objective of this report is to give the results and a synthesized view on the Phase 1 assessment program, an overview of the forthcoming Phase 2 assessment is also useful. Phase 2, as defined in Section 3.1, is intended to validate the code for integral accident phenomena, and hence is relevant to the future application of SIMMER-III to reactor calculations. The Phase 2 assessment will document the appropriateness (or conservatism) of SIMMER-III calculations of reactor cases. This aspect is especially important when the code is to be applied to licensing or risk assessment.

The scope of Phase 2 assessment must be carefully defined to cover key phenomena involved in accident sequences relevant to a CDA analysis. The transition phase of CDAs is an extended core disruption

stage following the initiation phase, which starts from an intact core at steady-state operation and evolves into initial core disruption. As the core melts, a large-scale motion of core materials, namely molten fuel and steel if the core is voided of sodium, will take place with a reactivity swing potentially leading to a recriticality event. Since the boiling point of steel is close to the melting point of fuel, a molten core will behave as a boiling pool, in which the heat generated neutronically in fuel is transferred to steel to heat up and vaporize it. The dynamic behavior of the boiling pool caused by steel vaporization plays a crucial role in determining the reactivity effect of material motion. Fuel removal from the core, on the other hand, can effectively mitigate the recriticality potential. The behavior of fuel relocation and freezing in an escape path is therefore a key phenomenon to be investigated. The potential contact between relocating fuel and sodium coolant raises a concern about the influence of fuel-coolant interactions (FCIs). Additionally at the beginning the transition phase, parts of the core fuel pins and most of subassembly can walls are still intact but they successively undergo disruption. Thus fuel disruption and post-failure fuel motion, as well as can wall melt-out, can have an important influence on the overall core behavior.

When an energetic recriticality event is postulated to occur, high-temperature core materials resulting from a neutronic power burst expand into a sodium pool in the reactor upper plenum through the above-core structures. This accelerates the sodium pool and results in a mechanical energy release. This energy conversion process is also an important area of SIMMER-III application, and hence the key phenomena involved in the post-disassembly expansion phase must be validated, including high-speed multi-phase flow dynamics in a narrow channel and expansion of a multi-phase bubble into a coolant pool. In a longer-term scenario of a CDA, including post-accident downward melt progression, FCIs become a concern, because they may generate mechanical loading on a reactor boundary structure and the resultant melt quenching behavior is important with respect to post-accident heat removal.

The above discussion briefly sketches a typical CDA accident scenario, and is intended to introduce key accident phenomena on which the Phase 2 assessment program should focus. In summary the areas of current interest in Phase 2 are:

1. Boiling pool dynamics (single and multi-component, steady and transient),
2. Fuel relocation and freezing (various channels with or without structure melting),
3. Material expansion (through a channel and into a pool),
4. FCIs (in a channel and a pool),
5. Structure disintegration (can walls and fuel pins), and
6. Disrupted core neutronics.

It is agreed among the SIMMER-III partners that the Phase 2 assessment program should be conducted in a similar way to Phase 1 under PNC-FZK/CEA collaboration. The program includes integral calculations of rather complex experiments, which have been conducted at various research laboratories. It is generally agreed that the partner having the best access to experimental information and data is responsible for the relevant assessment. Since different laboratories performed similar experiments in the past, such as material freezing, some of the effort may be closedly related each other. With collaboration the confidence level of the validated code should be much improved, hopefully reaching technical consensus among the partners.

With the completion of Phase 1 assessment, SIMMER-III is available for reactor application, and actually such an effort has been already initiated. Since Phase 2 is directly relevant to LMFR safety analysis, interaction and feedback between the two areas of application will be beneficial.

3.4 Features of SIMMER-III from Assessment Viewpoint

In this section, some characteristics of SIMMER-III which influence code assessment are highlighted, in particular the modeling scope, numerical robustness and structure of the code. From the beginning of the code development program, SIMMER-III was designed such that the models could be validated as efficiently and practically as possible. The code design features and philosophy are discussed below in comparison with SIMMER-II.

The first salient feature of SIMMER-III is a modularized code design. The physical models for local (intra-cell) phenomena of heat and mass transfer processes are completely separated from fluid convection calculations. This has a significant merit in Phase 1 assessment and the resultant model improvement. This also facilitates future possible replacement with a further advanced model. Currently only a simple fuel-pin model is included in the code, but it is coded separately from the fluid-dynamics portion, allowing future elaboration or straightforward replacement. The functions for EOSs and thermophysical properties (TPPs) are independently programmed such that revisions can be easily made. All the modeling options and parameters are specified by user input flags, such that a user can test different model options without re-compilation from the source file.

The second feature is improved numerical accuracy. SIMMER-II was often criticized for its rather poor conservation of mass and energy. SIMMER-III improves significantly upon SIMMER-II due to the following three modeling approaches. First a consistent fluid convection algorithm based on a semi-implicit method minimizes the mass and energy nonconservation associated with fluid convection. Second the explicit treatment of the vapor state in a single-phase liquid cell eliminates the vapor mass losses in the former code. Third careful treatment of missing components has eliminated remaining sources of mass non-conservation. In a multi-component framework of SIMMER-III, not all the components are present in a cell. Macroscopic densities of missing components are given a small value (10^{-30}) for numerical reasons, but their volume fractions are set to zero and they are not explicitly treated. From a number of calculations performed thus far, the conservation of mass is considered to be highly satisfactory, although there still remains some energy non-conservation of the order of 10^{-5} or slightly more. This is caused mainly by convergence precision in heat and mass transfer calculations and this level of residual error in internal energies is thought to be acceptable.

Four additional points should be noted with respect to improved numerical accuracy. First the SIMMER-III approach allows a very small value (10^{-4}) to be assigned to a so-called minimum vapor volume fraction (α_0) which significantly reduces errors associated with this treatment. Second the accuracy and thermodynamic consistencies of EOSs and TPPs have been significantly improved over the entire temperature ranges of interest. Third mechanical equilibrium between cell pressure and fluid compression is suitably treated, and is effective for simulating a single-phase liquid cell. Fourth a higher-order spatial

differencing scheme reduces numerical diffusion associated with fluid convection in an Eulerian staggered mesh.

The third feature of SIMMER-III is improved numerical stability. Many numerical instability and non-convergence problems encountered in SIMMER-II seriously limited the applicability and credibility of the code. The basic fluid convection algorithm employed in SIMMER-III is based on a semi-implicit method that has been widely used in current generation two-phase flow codes. The numerically stable, four-step algorithm, which separates intra-cell heat and mass transfer from inter-cell fluid convection, was successfully used in AFDM before being implemented in SIMMER-III. Furthermore the SIMMER-III algorithm for pressure iteration has been improved from AFDM based on experiences with this code. The convergence characteristics were also improved by implementing a special acceleration technique, and convergence of a complex iteration scheme in a vaporization and condensation model reflects the many lessons learned and experiences accumulated from SIMMER-II and AFDM. In addition many special-case treatments necessary for missing or small-mass components have been successfully implemented. Another feature of the code to improve numerical convergence is a time-step re-calculation capability: when non-convergence is detected in any step of the fluid-dynamics calculation, the same cycle is re-calculated with an automatically reduced time step size. These features, together with consistent EOSs and TPPs, have significantly improved the numerical stability of the code.

Another advantageous feature of SIMMER-III is its generalized framework and modeling flexibility. A rather arbitrary geometry with flexible boundary conditions can be set up within a two-dimensional R-Z or X-Z framework. Any material can be used provided that EOS and TPP functions are available. For isothermal problems, a simplified analytic EOS (SAEOS) model is also available. For combinations of various materials, the concept of EOS regions provides a means for users to specify any number of materials in different regions. Liquid components can be assigned to different velocity fields and multiple flow regime modeling allows a variety of multi-phase flow problems to be simulated over the entire range of void fraction for both the pool and channel flow geometries. SIMMER-III models the most important paths for mass transfer and can simulate those mass-transfer processes which cannot be treated in SIMMER-II, such as fuel vapor condensation on liquid sodium. Finally a structure wall is represented by two temperature nodes, which better simulates heat losses to the structure, especially in a small-scale experiment. Many of these features have been used in the code assessment calculations to model various experimental geometries and non-LMFR materials.

From the computer technology point of view, the portability of the code has been significantly improved. SIMMER-III has been developed on an IBM-compatible mainframe computer and standard Unix workstations. This has eliminated unnecessary effort of code conversion between different machines and improved overall productivity. The main disadvantage of SIMMER-III from a computational aspect is its computing costs. Even though the code is programmed to be as efficient as possible, SIMMER-III requires roughly an order of magnitude more computer time than SIMMER-II. Advanced and detailed modeling and threevelocity-field treatment inevitably increases the computing workload.

Table 3-1. List of test problems for SIMMER-III Phase 1 assessment (1/2)

No	Title	Organization	Conv.	IA/MX	HTC	M/F	V/C	EOS	Str.
Category 1: Fluid convection algorithm									
1.1	Ideal gas shock tube	PNC	×						
1.2	Two-phase shock tube	FZK	×	×					
1.3	Oscillating manometer	IPSN	×						
1.4	One-dimensional sedimentation	PNC	×						
1.5	Two-dimensional sedimentation	PNC	×						
1.6	One-dimensional sodium boiling	PNC	×	×			×		
1.7	Liquid sloshing with particles	FZK	×	×					
1.8	Water hammer	PNC	×					×	
1.9	Impact of liquid slugs	FZK	×	×					
1.10	Steam expulsion by subcooled water	PNC	×						
1.11	Stability of one-dimensional bubble column	PNC	×	×					
Category 2: Interfacial area and momentum exchange models									
2.1	Zero-th dimensional pool flow	PNC		×					
2.2	One-dimensional isothermal bubble column	CEA-G	×	×					
2.3	Two-dimensional isothermal bubble column	CEA-G	×	×					
2.4	Pressure drop in fully developed flow	CEA-G	×	×					
2.5	Momentum exchange in pipe flow	PNC	×	×					
2.6	Developing annular flow	PNC	×	×					
Category 3: Heat transfer									
3.1	Can-wall heat transfer	PNC							×
3.2	Structure axial heat transfer	PNC							×
3.3	Film boiling in sodium	PNC			×		×		
Category 4: Melting and freezing									
4.1	Fuel freezing: GEYSER experiments	CEA-G	×	×	×	×			×
4.2	Fuel freezing: SMPR experiments	CEA-G	×	×	×	×			×
4.3	Freezing of hot melts in tubes: THEFIS	FZK	×	×	×	×			×

Table 3-1. List of test problems for SIMMER-III Phase 1 assessment (2/2)

Category 5: Vaporization and condensation									
5.1	Condensation of steam on droplet	PNC			×		×		
5.2	Droplet evaporation	PNC			×		×	×	
5.3	Vapor bubble collapse	PNC			×		×	×	
5.4	Rapid fuel vaporization	FZK		×	×		×	×	
5.5	Boiling in a pipe	PNC	×	×	×		×	×	
5.6	Vapor condensation on structure	CEA-G	×	×	×		×	×	×
5.7	Boiling pool with wall heat transfer	CEA-G	×	×	×		×	×	×
5.8	Two-phase blowdown: Bartak's pipe	CEA-G	×	×	×		×	×	
5.9	Two-phase blowdown: Edwards' pipe (1)	CEA-G	×	×	×		×	×	
5.10	Two-phase blowdown: Edwards' pipe (2)	PNC	×	×	×		×	×	
5.11	Thermite injection into sodium: THINA	CEA-G	×	×	×	×	×	×	

Conv.: Fluid convection algorithm

IA/MX: Interfacial area and momentum exchange function models

HTC: Heat transfer coefficient model

M/F: Melting and freezing model

V/C: Vaporization and condensation model

EOS: Equation of state model

Str.: Structure model

4. Achievement of Phase 1 Code Assessment

This chapter draws together the results and conclusions described in the individual summary reports documented in Appendix. The synthesis of the Phase 1 assessment is attempted in Section 4.1, which summarizes the validation status of SIMMER-III models. The Phase 1 assessment has highlighted areas where modeling can be improved, and some of the code features were not sufficiently tested by the Phase 1 assessment. Therefore, problem areas and needs for further code assessment are reiterated in Section 4.2. The impact of Phase 1 on the Phase 2 assessment program is addressed in Section 4.3.

4.1 Synthesis of Phase 1 Results

The synthesis is organized to describe the validation status of each distinctive code model as far as possible, since this is the basic aim of the Phase 1 assessment. However many topics, such as phenomena in a boiling pool, are integral and cannot be discussed comfortably in the context of individual models. The section attempts to draw conclusions based on all of the Problems, and therefore inevitably conflicts with some of the conclusions expressed in the individual summary reports. The Problems are referred to by the Problem numbers listed in Table 3-1.

4.1.1 Fluid-dynamics algorithm

(1) Stability of the fluid-dynamics convection algorithm

All the Problems in Category 1 contribute to the assessment of the fluid-dynamics convection algorithm. SIMMER-III calculated fluid convection in all the Problems satisfactorily, though some calculations exhibited numerical pressure spikes (discussed below). Nevertheless, even when pressure spikes did occur the overall results of the calculation were usually satisfactory.

Although not part of this assessment study, Ruel of EC Joint Research Center, Ispra has investigated the properties of the fluid-dynamics equations used in AFDM. Essentially the same equations set with the same spatial differencing scheme is used in SIMMER-III. He found, based on an extensive deduction of finite-differenced equations, that an AFDM (and SIMMER-III) higher-order differencing scheme contains second-order errors. In other words, fluid convection in a diagonal direction is not suitably represented. This is not a major problem unless a diagonally-dominant flow is to be simulated.

The test problems in Category 1 indicated that the fluid-dynamics convection algorithm is basically valid, accurate, numerically stable and robust. There are no serious problems in simulating isothermal multi-phase flows.

(2) Decoupling of intra-cell transfer from convection

There is a concern about the fluid dynamics four-step algorithm that the decoupling of intra-cell transfer from inter-cell transfer (convection) introduces a sensitivity to timestep size. Namely heat and mass transfer is calculated based on a beginning-of-cycle cell state without taking into account the change in the cell state due to convection. Such a decoupling effect can be especially important when the mass transfer due to vaporization or condensation competes with fluid convection. In the case of vaporization, intra-cell

vaporization can result in pressure buildup which is not relieved by fluid convection until the next cycle. This concern has been addressed by Problem 1.6.

Problem 1.6 illustrates the timestep sensitivity due to intra-cell decoupling and suggests that the most effective way to mitigate the error is to restrict the maximum timestep size. For cases involving rapid vaporization it is recommended that timestep sizes be restricted to 10^{-4} or 10^{-5} s.

Methods for mitigating the intra-cell decoupling problem are available optionally in SIMMER-III and are being tested. However, there will remain a fundamental limitation on timestep size due to the assumption of linearization in temporal discretization of the fluid dynamics equations.

(3) Numerical diffusion

Spatial discretization of the fluid dynamics equations in Eulerian codes like SIMMER-III inevitably gives rise to numerical diffusion. It is essential to have a differencing scheme which mitigates numerical diffusion such that the motion of fluids can be followed sufficiently accurately. SIMMER-III contains both a first-order donor-cell differencing scheme and a higher-order differencing scheme. The effectiveness of these schemes in mitigating numerical diffusion was explicitly investigated in Problems 1.1, 1.3, 1.4, 1.5, 1.7 and 1.9.

The conventional donor-cell differencing scheme, whilst giving satisfactory results in many cases, also exhibited unacceptably large numerical diffusion in some applications. In comparison the higher-order differencing scheme proved to be very effective in mitigating numerical diffusion, and was considered essential for the correct simulation of the features seen in some tests (e.g. the liquid sloshing in Problem 1.7).

The large numerical diffusion associated with donor-cell differencing was actually found to be advantageous in reducing numerical instability in Problem 1.4. However, this is because no friction (no physical damping) was present in this Problem. Most SIMMER-III applications involve friction.

Higher-order differencing is the preferred option in SIMMER-III. It is considered that residual numerical diffusion, using the higher-order scheme, is acceptable.

(4) Liquid surface and interpenetration of liquids

A multi-phase code like SIMMER-III, which is based on volume- and time-averaged equations, does not explicitly track the gas-liquid surface. This means that a moving liquid surface is smeared to some extent, and the physics of the surface cannot be fully modeled.

The smearing of the gas-liquid interface due to numerical diffusion is discussed above; it is considered to be acceptably small if the higher-order differencing scheme is used. Problems 1.3, 1.7 and 1.9 indicate that the gas-liquid interface can be modeled sufficiently accurately, whilst the interpenetration of two liquids was reasonably simulated in Problems 1.4 and 1.5. SIMMER-III calculations of liquid sloshing of Problem 1.7 are particularly impressive demonstrations that the code can capture the essential features of a complex liquid motion. On the other hand, in the summary report for Problem 1.9 it is noted that the hydrodynamic instabilities observed on the surface of falling slugs of liquid cannot be properly represented by SIMMER-III because the free surface of the slug is not explicitly modeled.

The Phase 1 calculations indicate that SIMMER-III adequately tracks the location of the gas-liquid surface when higher-order differencing is used. However, the Taylor or Kelvin-Helmholtz instabilities which can arise on the free surfaces of liquids are not fully modeled. This may be a limitation if the code is applied, for example, to an expanding vapor bubble in the post-disassembly phase of a CDA.

(5) Waterpacking

"Waterpacking" is a well-known phenomenon associated with the representation of the liquid-gas interface in an Eulerian code like SIMMER-III. When liquid flows upward into a mesh cell, the liquid velocity at the top edge of the cell first decreases and then reverses direction under the influence of gravity. The negative velocity is forced positive again just before the cell fills with liquid, and this is affected by a (spurious) pressure spike. The waterpacking problem is common to all multi-phase codes using a Eulerian staggered mesh. The phenomenon was explicitly investigated in Problem 1.10, and was also probably the cause of the pressure spikes noted in the summary report of Problem 1.3.

Problem 1.10 confirmed that the waterpacking phenomenon can occur in SIMMER-III calculations, and that the magnitudes of the pressure spikes are sensitive to the momentum coupling between liquid and vapor. The waterpacking was mitigated to some extent by condensation in Problem 1.10, but the degree of mitigation depends on the condensation rate. The influence of the pressure spikes on the overall fluid motion was not significant. Similarly, in the oscillating manometer of Problem 1.3 the calculated pressure spikes had negligible effect on the overall behavior of the liquid.

In the summary report for Problem 1.10 it is remarked that the numerical techniques available to scale down pressure spikes calculated due to waterpacking. No attempt has been made to implement the techniques into SIMMER-III because it is not envisaged that waterpacking will be a major problem in key application areas of the code, and the above applications indicate that waterpacking has a negligible effect on the overall behavior of the liquid motion.

(6) Compression of single-phase cells

Problems 1.8 and 1.9 examined SIMMER-III predictions for liquid slugs impacting a rigid wall. Both Problems indicate that momentum transfer from, and compression of, single-phase liquid cells are accurately treated by the code. The propagation of a decompression wave in liquid was also successfully modeled in Problems 5.9 and 5.10 (Edwards' pipe).

These applications indicate that the SIMMER-III treatment of single-phase cells is valid, and that liquid properties such as compressibility are calculated correctly by the EOS functions. However, an appropriate simulation of single-phase cells requires a reduction in the time step size such that sonic propagation can be represented.

(7) Overpacking in single-phase cells

Overpacking occurs in a single-phase mesh cell when thermal expansion of liquid, structure or particles, combined with convection of liquid into the cell, rapidly reduces the void volume and gives rise to single-phase pressure spikes. Such single-phase pressure spikes seem to have been present in Problem 4.3

(melt penetration in a tube) at least, although the pressure spikes do not seem to have affected the overall results of that calculation.

The main problem with overpacking is its effect on run time for a computation. Overpacking is currently dealt with in the fluid dynamics algorithm by reducing the timestep size to avoid an excessive change in pressure. However, in some test problems this results in excessively small timestep sizes. A simple practical remedy for this is to instantaneously transfer overfilled liquid components to surrounding mesh cells using a kind of donor-acceptor method. This remedy is available in Version 2.A and initial applications suggest it is effective in cases where pressurization due to Step 1 intra-cell transfer is important. (The modification does not alter the compression of single-phase cells resulting from fluid convection.)

(8) Inter-cell momentum coupling and turbulence modeling

Problem 1.7 identified the lack of momentum exchange between adjacent mesh cells in SIMMER-III as a plausible reason for differences between the calculation and observations of a liquid sloshing. Simulations of two-dimensional bubble columns and boiling pools (discussed below) should also benefit from the introduction of radial inter-cell momentum coupling in the code. Furthermore, the introduction of a diffusion term in a momentum equation is known to improve numerical characteristics of the basic equations set from a numerical fluid-dynamics point of view.

Inter-cell radial momentum coupling is undoubtedly required to simulate two-dimensional two-phase flow in small-scale geometries with small mesh sizes. However, in the reactor application of SIMMER-III the mesh size used is fairly coarse, typically of the order of 5-10 cm, and the effect of structure walls on radial momentum coupling is less important, so such modeling detail is not as essential. Nevertheless, it is considered prudent to provide SIMMER-III with inter-cell momentum coupling because the code is also applied to small-scale reactor cases, such as simulating a fuel subassembly in two dimensions, and the code validation is to be performed against small-scale experiments. The radial momentum coupling is modeled through a viscous (or diffusion) term in the momentum equation. Modeling of the momentum diffusion term is being implemented and tested in SIMMER-III.

In Problem 2.3 it is recommended that a turbulence model should also be introduced into SIMMER-III. A turbulence model is undoubtedly desirable, but its implementation would require a major modeling effort. It is therefore considered prudent to first assess the effectiveness of the momentum diffusion term being implemented into SIMMER-III before concluding whether a turbulence model is actually needed.

(9) Assignation of velocity fields

Problem 1.7 examined the interaction of a liquid and particles during a sloshing behavior. The ratio of the particle-to-liquid density was similar to the density ratio for fuel particles in liquid fuel, and so the particles were assigned to the same velocity field as the liquid. The redistribution of the liquid and particles are reported to be well-calculated, indicating that the assumption of assigning fuel particles to the liquid fuel velocity field is reasonable.

(10) Three-dimensional effects

The application of SIMMER-III to the two-dimensional bubble column (discussed below) and liquid sloshing (Problem 1.7) have suggested that three-dimensional effects may be present in these experiments. Three-dimensional modeling is out of the scope of SIMMER-III.

4.1.2 Flow regimes, momentum exchange and IFA modeling

(1) Zero-dimensional pool flow (Problem 2.1)

SIMMER-III explicitly represents the bubbly and dispersed pool flow regimes, whilst the intermediate regime is modeled by a transition flow where a mesh cell is treated as a combination of a bubbly region and a dispersed region. Problem 2.1 compiles experimental data on pool flow regimes, and indicates criteria for the transitions between bubbly, churn-turbulent and dispersed flows. The churn-turbulent regime is identified with the transition flow regime in SIMMER-III modeling. Experimental data shows a dependence of the bubbly-churn transition on pool height (or bubble duration in the pool), but a 30 % void fraction criterion represents the data reasonably. A 70 % void fraction criterion for the dispersed flow regime is also compatible with the experimental data. These criteria are default values in SIMMER-III.

The zero-th order calculations of pool flow also addressed the IFA modeling and momentum exchange in the different pool flow regimes. The momentum exchange functions in SIMMER-III are based on the Ishii-Zuber formulation for bubbly and dispersed flow, and a zero-th order calculation has shown that the interpolation scheme used by SIMMER-III for the transition (churn-turbulent) regime is also consistent with the Ishii-Zuber formulation. The interpolation ensures that the code simulates a smooth transition across bubbly, churn-turbulent and dispersed flows. The data compiled in Problem 2.1 shows that SIMMER-III can simulate gas fluxes well in bubbly flow. Gas fluxes in the churn-turbulent flow regime are also reasonably well modeled by SIMMER-III, particularly when the scatter in experimental data for this flow regime is taken into account.

SIMMER-III not only treats flow regime transition as a function of void fraction, the transition from one continuous liquid to a second continuous liquid as a function of volume fraction is also explicitly modeled. Problem 2.1 indicated that the code can treat reasonably the change from bubbly to transition flow for different continuous liquids (water and mercury). The transition was measured to take place at a volume fraction of 40 %. However, the momentum exchange in the multi-component transition flow regime has not yet been validated.

In summary, the framework of multi-phase pool flow topology is sound. The multiple flow regime modeling in SIMMER-III is a significant advance on SIMMER-II, improving especially on SIMMER-II's poor simulation of the bubbly flow regime. Furthermore, the capability to treat the transition from one continuous liquid to another continuous liquid is a feature not available in most other codes.

Problem 2.1 verifies the momentum exchange functions in SIMMER-III, and shows that a smooth transition between flow regimes is modeled. It is the first step in understanding the one- and two-dimensional analyses of bubble column behavior discussed below. However, the behavior of a real pool is

influenced by internal circulation and the spatial distribution of void fraction, especially in the churn-turbulent regime, which cannot be fully taken into account by zero-th order calculations.

(2) The 1-D bubble column

Problem 2.2 addressed IFA modeling and momentum exchange in the one-dimensional bubble column. For the bubbly flow regime SIMMER-III simulates superficial gas velocities and interfacial areas well. However, the study found that the gas velocities tend to be underestimated at average void fractions greater than about 30 %, and that the IFA calculated by SIMMER-III increases significantly in the chum-turbulent flow regime. The increase in IFA has al.so been observed in a preliminary analysis of the Scarabee BF2 boiling pool for the Phase 2 assessment. The mechanism is thought to be the relatively high gas-liquid slip velocity predicted by SIMMER-III at high void fractions, which promotes Weber break-up of bubbles. In churn-turbulent flow, bubbles are entrained in the wake of other bubbles and the effective slip velocity to be used in the break-up model should be the vapor drift velocity rather than the calculated slip velocity. The preliminary analysis of BF2 has also indicated the need to model the drag between vapor continuous and liquid continuous regions of transition flow, to enhance the momentum coupling between vapor and liquid. Model improvements to represent these effects in SIMMER-III are being examined.

A linear stability analysis of the SIMMER-III two-phase flow equations in a one-dimensional bubble column is reported in Problem 1.11. The study showed that the equations set of SIMMER-III is well-posed when inter-phasic momentum coupling is suitably modeled. This means that the physical oscillations (chugging) predicted by the code in a one-dimensional system are consistent with a numerically stable solution.

In summary, although the SIMMER-III modeling of IFA and momentum exchange is shown to be valid for the bubbly flow regime, some improvements to the modeling of the IFA and inter-phase drag in the churn-turbulent regime are considered to be desirable, and are being examined. As noted in the summary report for Problem 2.2, other discrepancies with data are probably due to the influence of internal circulation and the radial spatial distribution of void fraction, which cannot be treated satisfactorily by a one-dimensional calculation.

(3) The 2-D bubble column (Problem 2.3)

A two-dimensional calculation of an isothermal bubble column can in principle address the behavior of a multi-phase pool more realistically, since effects such as internal circulation and the spatial distribution of void fraction can be modeled. Such a calculation was performed in Problem 2.3. The application was not encouraging: the calculated flow circulation and void distribution did not reflect experimental observations at all. The first point to make is that the modeling deficiencies identified above for the one-dimensional bubble column, and some other Problems, were also present in the two-dimensional calculation i.e. lack of a momentum diffusion term and deficiencies in modeling bubble break-up and gas-liquid drag in the chum-turbulent flow regime. However, in addition, a two-dimensional R-Z system might not be the best geometry to analyze a bubble column due to the center-line problem (see below). A complementary calculation in X-Z geometry would also be beneficial. A further comment is that the IFA model in SIMMER-III underwent important improvements for the release of SIMMER-III Version 1.J, and these

improvements were not available when this Problem was analyzed. It is worthwhile recalculating this Problem to assess the effect of these improvements.

The second point is that there are undoubtedly further difficulties to be encountered when modeling bubble columns. One is the effect of the centrifugal force in a real (three-dimensional) pool, which cannot be modeled by a two-dimensional fluid dynamics algorithm; this is the so-called "centerline" problem, in which the liquid component tends to collect along the centerline in a two-dimensional R-Z system. In a two-dimensional bubble column this could promote the non-physical radial void distribution currently calculated by SIMMER-Ill. Another influence is turbulence: some authors consider it necessary to use a turbulence model to simulate a bubble column. Nevertheless, it seems sensible to first investigate the influence of the code modifications described above before concluding whether such additional major model developments are warranted.

(4) Channel flow regime modeling

The channel flow regime map in SIMMER-III is a major advance on previous codes. SIMMER-III recognizes bubbly, slug, annular, annular-dispersed and dispersed flows, which greatly enhances its application area. The simulation of channel flow regimes in steady-state flow is studied in Problems 2.4 and 2.6. The code exhibits no numerical difficulties in annular-droplet flow. However, Problem 2.4 encountered unphysical pressure oscillations in the transition from annular to chum-annular flow. In Problem 2.6 similar oscillations seem to have been encountered in fully developed annular flow. The reason for these oscillations is not clear, though a linear stability analysis of the SIMMER-III two-phase flow equations for a one-dimensional bubble column (Problem 1.11) indicates that the chugging motion predicted for the chum-turbulent regime can be a physical, not merely numerical, phenomenon. In Problem 2.6 a steady-state condition was achieved by applying a multiplication factor to the liquid-vapor momentum exchange function.

Problems 2.4 and 2.6 highlight code limitations in simulating an annular-droplet flow. In this flow regime, high-velocity vapor flow tends to entrain liquid droplets from the liquid film. The dispersed droplets in reality have much higher velocities than the liquid film. However, SIMMER-III models both droplets and film using the same velocity field, so the code can only simulate this flow regime in an averaged way. This results in too strong coupling between the vapor and liquid, and too high film flowrates. The summary reports for Problems 2.4 and 2.6 both concluded that momentum exchange between gas and liquid in annular dispersed flow needs to be improved. In Problem 2.6 this was partly resolved by the application of an empirical multiplication factor to the liquid-vapor momentum exchange functions.

Problem 5.9 examined the flow regime transition between bubbly and dispersed flow under highly transient conditions in a pipe. In rapidly expanding systems the transition from bubbly to slug or chum flows can be inhibited until quite large void fractions, of over 70%, are achieved. The default transition criterion in SIMMER-III, which is based on zero-th dimensional calculations for pool flow, is 30%. Nevertheless, even the default flow regime map in SIMMER-III could simulate the blowdown behavior in the Problem fairly well.

In summary, the Phase 1 assessment has identified areas for improvement in channel flow regime modeling. Firstly, unphysical oscillations are encountered on the transition to churn-annular flow. Secondly the annular dispersed flow regime treats the liquid film on structure and the entrained droplets in the same velocity field, which results in a poor approximation of the liquid behavior. Thirdly foam flow, which occurs in some transient situations, is not explicitly modeled. Nevertheless, the simulation of channel flow regimes in SIMMER-III is a significant improvement on previous codes.

(5) Momentum exchange functions

The momentum exchange functions are based on quasi-steady state engineering correlations for well-defined topologies. They are modeled separately for each velocity field and for each flow regime. An assessment of momentum exchange in pool flow is obtained from the zero-th order calculations of pool flow and the bubble column discussed above. The momentum exchange functions in the bubbly and dispersed flow regimes are considered to be satisfactory, and the interpolation procedure is believed to provide a sufficiently smooth and valid means of treating the transition flow regime. However, the need to model the drag between vapor-continuous and liquid-continuous regions of transition flow was also identified. A model improvement to do this is being tested.

It is noted in one summary report (Problem 5.7) that instabilities can arise in calculations of a boiling pool. and that the instabilities may be due to an imperfect description of the large differences in momentum exchange functions in going from liquid-continuous to vapor continuous at the pool surface. This has been concluded from the application of other multiphase codes, as well as SIMMER-III, to the boiling pool. However, SIMMER-III calculations have also been performed in which such instabilities were triggered from the center of a two-phase pool, suggesting that the oscillations are not a numerical artifact but might be a physical phenomenon. The linear stability analysis of the SIMMER-III two-phase flow equations for a one-dimensional bubble column (Problem 1.11) supports this interpretation. The role of the gas-liquid surface in causing numerical instabilities remains unresolved.

Problem 2.5 was a zero-th order calculation of momentum exchange function between liquid and structure in pipe flow, as was done in Problem 2.1 for pool flow. The pressure drop in pipe flow was underestimated by the original code model due to the lack of a proper treatment of turbulent enhancement in the liquid phase by the relative motion of vapor. An improvement to the liquid-structure momentum exchange function to take account of this effect enabled SIMMER-III to reproduce the pressure drop characteristics in pipe flow well. This improvement is available in Version 2.A.

Problems 2.4 and 2.6 show that the momentum exchange between gas and liquid in annular dispersed flow needs to be improved to compensate for the large difference between droplet and film velocities. Problems 2.4 and 2.6 also found that SIMMER-III underestimates the vapor-liquid film momentum coupling in pure annular flow. This is probably because the formation of ripples on the surface of liquid films enhances the momentum coupling, and this effect is not currently modeled by the code. These modeling deficiencies have not yet been addressed.

The momentum exchange functions also influence melt penetration lengths in pipes and tubes. In the case of conduction-limited freezing (Problem 4.3) the reduction of cross-sectional area due to crust growth

reduces the driving pressure for liquid penetration. In Problem 4.3, the calculated pressure loss is considered to be satisfactory, though it was noted that discrepancies in pressure loss would arise for a sudden constriction with an areal change of more than 50 %. In bulk freezing the formation of solid particles enhances the viscosity of the liquid/solid mixture, and it is the viscous slurry which brings penetration to a halt. This effect was studied to some extent in Problems 4.1 and 4.2, but heat transfer from liquid to wall was the dominant factor determining penetration lengths in these experiments. In Problem 4.3, the flow is reported to be stopped by an unphysically low particle volume fraction. This should be resolved by recent modifications to the SIMMER-III particle jamming model which have been implemented into SIMMER-III Version 2.A.

The momentum exchange between sloshing liquid and initially stationary particles (Problem 1.7) seems to have been successfully reproduced by SIMMER-III. Problem 1.7 also identified the absence of friction at the bottom of a sloshing pool as a possible difference between calculation and observation, but there are currently no plans to model this. Some momentum exchange modeling has not been examined by the Phase 1 test calculations, for example in complex interpolated flow regimes and flows with high void fractions. The effect of momentum exchange in fuel freezing and plugging will be studied further in the Phase 2 assessment.

(6) Interfacial areas modeling

The flow topologies are modeled by a generalized interfacial area (IFA) convection concept, which was first implemented in AFDM. SIMMER-III is more complex, treating a total of nine convectible IFAs. This provides a means to better simulate transient multi-phase flows because the multi-phase flow history can be modeled rather than determining properties from instantaneous local flow conditions alone. The IFA convection model includes source terms due to liquid flashing, turbulence breakup, hydrodynamic breakup (or fragmentation), bubble nucleation and droplet/bubble coalescence. Each source term is generally characterized by an equilibrium value (for steady-state) and a time constant (for transients). These have to be estimated from experimental data.

Most of the Phase 1 assessment Problems have examined steady state IFAs. IFAs in pool flow are discussed more fully above, with respect to the bubble column. The conclusions are that steady-state IFAs in bubbly flow are considered to be satisfactory, but bubble break-up in transition flow is believed to be excessive. A means to improve the break-up model has been proposed (using the vapor drift velocity rather than the calculated slip velocity) and is being examined.

The two-phase blowdown problems (Problems 5.8, 5.9 and 5.10) investigated IFA source terms in highly transient conditions. SIMMER-III calculations of Edwards' pipe problem (Problems 5.9 and 5.10) gave good agreement with experimental results without modification, but it is considered that the result is very sensitive to input parameters. In the summary report for Problem 5.10 it is shown that SIMMER-III also calculates good agreement using a more physically-based bubble nucleation model. However, it is considered that this nucleation model has insufficient general applicability to warrant its implementation in SIMMER-III (see also the discussion below on water properties).

The discrepancies in the SIMMER-III calculation of Bartak's pipe (Problem 5.8) might be due to deficiencies in the IFA modeling, and the analysis could benefit from the lessons learned from Problem 5.10. However, it should also be noted that the transient IFA model in SIMMERIII has seen some important developments throughout Version 1, particularly with Version 1.J, and Problems 5.8 and 5.9 were conducted without the benefit of these improvements.

In general, the overall framework of IFA modeling in SIMMER-III seems sound, though the assessment has specifically identified the need to refine the model for bubble break-up in the pool transition flow regime. The two-phase blowdown problems partly validate the IFA source term modeling, although further validation of IFA source terms is clearly desirable. Fragmentation in FCIs is a phenomenon which is sensitive to the steady-state and transient IFA modeling, and it is planned to study this topic further in the Phase 2 assessment.

4.1.3 Heat and mass transfer

(1) Structure heat transfer

Heat transfer in structure is by conduction. SIMMER-III calculates radial heat transfer in structure using two can wall nodes (a surface and an interior node) which is an improvement on previous codes. The thickness of the surface node is determined by a user-input thermal time constant. Problem 3.1 examined the temperature response of the structure for the boundary conditions of constant heat flux and constant temperature. The model was verified for the constant heat flux condition, but it can only reproduce the temperature response for a constant temperature boundary condition on the timescale dictated by the thermal time constant. It is currently recommended that the time constant should be selected to reflect the timescale of the phenomenon being modeled.

Axial heat transfer in structure is modeled for cladding and left/right can walls. This model was compared with an analytical solution for transient heat transfer in Problem 3.2 and showed excellent agreement.

(2) Fluids heat transfer coefficients

Fluids heat transfer coefficients are modeled by quasi-steady state Nusselt number heat transfer correlations for selected fluid configuration and flow topologies. SIMMER-III calculations of mass transfer during melting/freezing and vaporization/condensation also rely on the heat transfer coefficients. Transient heat transfer coefficients are not modeled. This is known to be inaccurate on short timescales for rigid particles and droplets, and was highlighted by condensation on a subcooled droplet in Problem 5.1. However, it is not considered feasible to implement transient correlations into SIMMER-III, and besides it was shown in Problem 5.1 that the steady-state formulation can be used parametrically to investigate the effect of enhancing the condensation rate.

Problem 5.3 shows that SIMMER-III can approximately simulate the rate of collapse of subcooled vapor bubbles. The summary report for the Problem also concluded that the collapse could be better simulated if heat transfer correlations took account of the internal circulation and mixing in the bubble. This capability has subsequently been implemented in SIMMER-III Version 2.

The liquid-structure heat transfer coefficients contributed successfully to the conduction freezing calculated in Problem 4.3. However, calculations of bulk freezing of fuel (Problems 4.1 and 4.2) indicate the need to model an additional contact thermal resistance between liquid and structure. It is anticipated that the implementation of the interface resistance will require modifications to the liquid, as well as structure, heat transfer coefficients.

The analysis of the boiling pool (Problem 5.7) did not result in specific recommendations concerning liquid-wall heat transfer modeling. However, a preliminary analysis of the SCARABEE BF2 boiling pool for the Phase 2 assessment indicates that it is desirable to improve the calculation of the local length scale and velocity used in the heat transfer correlations. Improvements in modeling the liquid-wall heat transfer in a boiling pool are being investigated.

The SIMMER-III film-boiling model is intended for liquid-liquid heat-transfer, but was successfully applied for a solid sphere in liquid sodium (Problem 3.3). The application helps to calibrate the model, but also highlighted the fact that there is no physical representation of the boiling curve in SIMMER-III. It is intended to use the film boiling model to model FCIs in the Phase 2 assessment. No thermal radiation heat transfer is currently modeled in SIMMER-III, and no Phase 1 calculations have suggested the need for such modeling. However, the temperatures which can be reached by LMFR materials in a CDA easily exceed the temperatures achieved in most of the Phase 1 assessment Problems. The implementation of thermal radiation heat transfer in SIMMER-III is being examined.

The Phase 1 test calculations have not properly tested the effect of flow regime interpolation on the heat transfer coefficients, which could be done for channel (pipe) flow.

(3) Melting and freezing

Melting and freezing of liquid fuel on structure is a key phenomenon in LMFR safety analysis since the dynamics of fuel freezing plays an important role in determining fuel removal from the core. Problems 4.1 to 4.3 help to assess the current SIMMER-III modeling, whilst fuel freezing will be further studied in the Phase 2 assessment program. SIMMER-III can simulate conduction-limited freezing, with fuel crust formation on a structure wall. In this case the crust effectively insulates the liquid fuel from the wall, and the liquid fuel cannot be cooled below its liquidus temperature. A fuel crust forms if the heat flux to the structure exceeds the heat flux from the liquid fuel at the liquid-structure interface. If a fuel crust does not form (and the steel structure melts) the bulk enthalpy of molten fuel flow can be lowered below its liquid us energy, and the code allows liquid fuel to solidify into solid particles. The particles enhance the viscosity of the liquid/particle mixture, which can bring penetration to a halt. SIMMER-III can therefore in principle treat both the conduction and bulk freezing mechanisms.

In Problem 4.3, which involved the penetration of an Al_2O_3 melt in a vertical tube, the mode of freezing was conduction-limited freezing with crust formation. With slight modifications to input variables SIMMER-III reproduced the conduction-limited freezing mode and was able to predict the penetration length to within 10%. The SIMMER-III calculation was also consistent with a previous SIMMER-II calculation. The application indicates that the SIMMER-III melting/freezing model is adequate for simulating melt penetration with conduction-limited freezing.

Problems 4.1 and 4.2 analyzed the penetration of tubes by pure UO_2 and a UO_2/Mo mixture respectively. In contrast with Problem 4.3, the freezing mechanism was predominantly bulk freezing, though crust formation occurred in at least some tests. The experimental results contradict the SIMMER-III freezing model in that bulk freezing occurred without melting of the steel wall. The SIMMER-III prediction for crust formation/wall melting was found to be undesirably sensitive to the (user-input) value of the structure time constant. Furthermore, even when SIMMER-III calculations were performed with only slight steel melting the penetration lengths predicted by the code were much too short, indicating excessive heat transfer from the liquid to the wall. The insertion of a thermal resistance between the molten fuel flow and the wall significantly improves the predicted fuel penetration lengths. This treatment is included as a non-standard option in SIMMER-III Version 2.A.

The bulk freezing model incorporating a contact thermal resistance currently gives the best estimate of fuel penetration lengths in tubes. However, uncertainties still remain as to how the thermal resistance should be implemented in SIMMER-III such that the code can predict bulk freezing, conduction freezing and wall melting correctly for given local temperature and flow conditions. Furthermore, fuel freezing environments during LMFR CDAs may be quite complex, involving: wall melting simultaneously upon fuel freezing, entrainment of ablated wall material and its heat transfer enhancement, the effect of solidified fuel particles on penetration of pin bundles, etc. It is therefore necessary to continue studying fuel freezing as part of the Phase 2 assessment.

(4) Vaporization and condensation

The SIMMER-III vaporization and condensation algorithm has been tested by several separate-effect calculations (Problems 5.1 through 5.3). Problem 5.2 verifies that energy transfers are consistent for two different condensation processes. The discrepancies between code calculation and experimental results, where they arise, are ascribed to the heat transfer coefficients (discussed above). It is considered that the basic calculation of vaporization or condensation of a single component has been verified.

Problem 5.4 examined rapid vaporization of liquid fuel in both a vacuum and in the presence of a non-condensable gas. The computed fuel temperature response for vaporization in a vacuum is in agreement with theoretical results. In the presence of a non-condensable gas the exact pressure development could not be reproduced by SIMMER-III because the code does not have a sufficiently detailed bubble dynamics model. Nevertheless, it is considered that SIMMER-III reproduces the vaporization process with sufficient accuracy.

The effect of non-condensable gas on vapor condensation on a wall was studied in Problem 5.6. SIMMER-III could simulate the rate of condensation in a vacuum sufficiently accurately, but the condensation rate in the presence of an inert gas is overestimated. In rapid condensation the non-condensable gas accumulates at the condensation surface and retards the flux of vapor molecules to the surface. In these circumstances condensation is governed (limited) by the diffusion of vapor molecules through a layer of non-condensable gas. A simple diffusion-limited model has been proposed to simulate this effect, and it is intended to implement this model in a future version of SIMMER-III.

Problems 5.8 through 5.10 examined vaporization of water following rapid depressurization. In the summary report for Problem 5.10 it is considered that the rapid vaporization induces a non-equilibrium, local

cooling of liquid surrounding vapor bubbles, which is not modeled by SIMMER-III. Nevertheless, a SIMMER-III calculation which did not explicitly account for this effect gave quite reasonable results. Problems 5.9 and 5.10 indicate that SIMMER-III can reasonably simulate rapid vaporization. Discrepancies in the calculation of Bartak's pipe (Problem 5.8) may be caused by similar phenomena, or else from deficiencies in the IFA modeling (discussed above).

Problem 1.6 showed that SIMMER-III can plausibly calculate the rapid vaporization of superheated sodium without numerical difficulties.

SIMMER-III is in principle able to simulate vaporization and condensation in a multicomponent environment. This includes vaporization at a liquid-liquid interface and condensation of a vapor species on a different liquid component. The former type of mass transfer path is important for modeling FCIs and a fuel/steel boiling pool, whilst the latter path occurs in a post-disassembly expansion where a fuel/steel vapor bubble condenses in a sodium pool. These capabilities have not been tested in Phase 1 calculations and should be studied in the Phase 2 assessment.

(5) The vaporization/condensation iteration

The vaporization and condensation model require a complex iteration procedure to implicitly update sensitive variables. Many special-case treatments are necessary, mainly for handling missing components or components with very small heat capacity. The model is also tightly coupled to the EOSs, since a small change in the vapor thermodynamic state strongly influences the rate of phase transition. Furthermore, a smooth and physically consistent transition from single- to two-phase flow must be modeled. In general, the Phase 1 calculations (such as Problems 1.6, 5.9 and 5.10) have shown that the iteration is sufficiently stable and robust, for example in modeling boiling onset from a single-phase condition.

(6) The boiling pool (Problem 5.7)

A fuel/steel boiling pool is a key phenomenon in LMFR safety studies, and will be studied further in the Phase 2 assessment program. In the Phase 1 assessment water boiling pools have been examined (Problem 5.7). Since the calculation of a boiling pool relies to some extent on the representation of a bubble column, reference will also be made to the above discussion of two-dimensional calculations of the bubble column. The physical phenomena which occur in a boiling pool are sketched in the summary report for Problem 5.7.

The application of SIMMER-III to water boiling pools (Problem 5.7) was not encouraging: in general, the flow patterns observed in the boiling pools were not reproduced by the code calculation, the pool hold-up was underestimated and the pool surface was unusually calm. These discrepancies in flow behavior are considered in the summary report for Problem 5.7 to be the cause of the incorrect heat flux distribution calculated along the wall.

The points made about the two-dimensional bubble column calculation need to be reiterated here. Deficiencies identified above regarding modeling of momentum exchange and IFAs in the churn-turbulent flow regime also apply to this Problem. Important code developments have been implemented in SIMMER-III since this calculation was performed, specifically the IFA modeling has been refined and the momentum

diffusion term has been implemented. Furthermore, a preliminary analysis of the SCARABEE BF2 boiling pool for the Phase 2 assessment showed that it was essential to model inter-cell heat transfer in order to realistically model a boiling pool. Otherwise an excessively large radial temperature profile is calculated in the pool. An inter-cell heat transfer model has been implemented in SIMMER-III for Version 2.A, and is expected to influence the calculation of a water boiling pool. In addition, the discrepancies in flow behavior may be partly caused by the incorrect heat flux distribution along the wall. A recalculation using the observed heat loss to the wall is required to confirm whether or not this is the case.

In addition to the above comments, the calculation in Problem 5.7 was performed using "symmetric box", which may not be appropriate to the transient flow pattern in the pool. A complementary calculation in the usual X-Z geometry would be beneficial. In summary, it is worthwhile recalculating this Problem to investigate the effect of model improvements.

(7) Properties of water

Many of the Phase 1 assessment problems involve water, and of course water is the coolant for light water reactors (LWRs). Water is usually modeled in SIMMER-III by substituting it for liquid sodium as the coolant. Although SIMMER-III is intended to be sufficiently flexible to model a wide variety of liquids, and in fact the Phase 1 assessment as a whole confirms this capability, the code is primarily designed to analyze the behavior of LMFR core materials in a CDA. This means there are some code limitations in modeling water.

Water has a very low thermal conductivity in comparison to sodium, so its bulk temperature tends to respond relatively slowly and it can support higher temperature gradients. In the summary report for Problem 5.10, which involved the rapid depressurization of subcooled water, it was concluded that the system pressure was governed by the liquid temperature local to the vapor bubbles, rather than the liquid bulk temperature. This transient effect is not modeled within the current SIMMER-III framework, and it is expected to be less applicable to sodium than for water. However, applications of the code to water in transient conditions need to consider the consequences of effects like this.

Another characteristic of SIMMER-III is that some mass transfer paths which are important in LWR accident studies, such as coolant boiling on solid particles and walls, are not treated by the code. These mass transfer paths are not important for LMFR CDA analyses, but their absence can limit the application area of the code, such as in the analysis of steam explosions. Nevertheless, it is not planned to expand the mass transfer paths currently modeled.

4.1.4 Overall features of the code

(1) Portability of the code

SIMMER-III has been successfully installed and applied to a wide variety of problems at four different research centers, using at least as many types of computer. Although the Phase 1 Problems were not explicitly checked for machine-dependency of the results, experience with other test problems indicates that machine-dependency is negligible. The code is considered to be portable and robust.

(2) Code run times

Problem 4.3, melt penetration in a tube, is reported to have taken a large CPU time. This can be attributed partly to small timesteps associated with the overpacking problem (discussed above). However, it also seems that the run time can be reduced by adjusting user-input variables associated with the pressure iteration. Calculation of a steady-state bubble column or boiling pool also requires relatively small timesteps in order to simulate local vapor transport. The vaporization/condensation iteration is known to consume significant amounts of CPU time, as are calls to EOS subroutines. In-line expansion of these subroutine calls can noticeably improve run times. ·

Some effort was devoted during the development of Version 1 to optimizing run times, and several modifications have resulted in more efficient computation. Nevertheless, the advanced and detailed modeling in SIMMER-III inevitably increases the computing workload in comparison with previous codes.

4.1.5 Summary

SIMMER-III has a sound scientific basis for simulating a variety of multi-phase flows. The four-step fluid dynamics algorithm has been demonstrated to be numerically accurate, sufficiently stable and robust. Advanced features such as interfacial area convection and generalized heat and mass transfer models have provided a sufficiently flexible framework to simulate transient multi-phase phenomena. Accurate and consistent EOSs help eliminate uncertainties and numerical problems. In short, SIMMER-III has proved to be a reliable and genuine state-of-the-art multi-phase fluid-dynamics code.

This is not to say that there are no problems. The Phase 1 assessment has been extremely valuable in highlighting problem areas, and in fact the above synthesis refers to many modeling deficiencies and errors that were addressed a d solved whilst the Phase 1 assessment was being conducted. Remaining problem areas which have been identified through Phase 1 calculations are summarized in the following section. These areas help guide future model development.

4.2 Problem Areas and Desirable Improvements

Problem areas identified in the Phase 1 assessment have already been discussed to some extent in Section 4.1. For some of the problems, code improvement is already in progress and they should be resolved in a future version of SIMMER-III. In addition, there are limitations of the code which were not tackled in the Phase 1 assessment calculations but are known from the modeling framework or other applications. Below, the problem areas are collated and the status of improvements is summarized.

(1) Dimensionality: A fundamental limitation to the application of SIMMER-III is its two-dimensional framework. Some of the experimental setups used in the code assessment are difficult to simulate in an axi-symmetric cylindrical geometry. In addition, reactor application may have to simulate three-dimensional mitigation mechanisms, such as off-centered whole core sloshing and fuel removal through control-rod guide tubes. Extension of the SIMMER-III algorithm to three dimensions is rather straightforward, and indeed a preliminary study has been initiated.

(2) Basic equations set and algorithm: One concern with the fluid dynamics equations is an instability occurring with higher-order differencing when no dissipative mechanism is present. However, in practice numerical damping due to drag forces is usually present, so this is not considered to be an important problem. More practical concerns are the influences of intra-cell transfer decoupling and overpacking on timestep size. Methods to compensate for these effects have been implemented and are being tested.

(3) Liquid free surfaces: There are no practical proposals to better model hydrodynamic instabilities on the free surfaces of liquids in SIMMER-III, and the Phase 1 applications have given no compelling reasons to do so. However, this conclusion may be revised by future application to, for example, an expanding vapor bubble in the post-disassembly phase of a CDA.

(4) Momentum diffusion term: It is recommended that viscous diffusion terms be modeled in the momentum equations in order to hydrodynamically couple radial cells. The inclusion of a diffusion term (second-order derivative) is known to be effective for making the equations set unconditionally stable. This code modification is being implemented and a preliminary version is available in SIMMER-III Version 2.A.

(5) Turbulence modeling: It has long been desired that a turbulence model be implemented in SIMMER-III. However, there is no practical turbulence model available for such complex multi-phase codes as SIMMER-III. It seems prudent to first test the effect of the viscous diffusion terms (item (4)) before concluding whether a turbulence model is really required. If a turbulence model is attempted a simplified approach should be considered. Proposals, based on experience from other codes, are welcome.

(6) Channel flow regimes: It is desirable to better represent the annular-droplet flow regime, which is currently not treating the behavior of dispersed droplets and liquid films satisfactorily, and to avoid the unphysical oscillations experienced in one-dimensional calculations of churn-annular flow. However, these problems have not yet been addressed.

(7) Interfacial area source terms: It is recommended to maintain the current framework of interfacial area convection with source terms. Improvements to the calculation of bubble break-up in pool transition flow are being examined. Validation of source terms models should be further conducted during the Phase 2 assessment.

(8) Momentum exchange functions in pool flow: The modeling of drag between the liquid-continuous and vapor-continuous regions of transition flow is being improved. It is recommended to further test the momentum exchange functions in intermediate and high void fraction range.

(9) Momentum exchange functions in channel flow: It is desirable to improve the momentum exchange between liquid and vapor in annular and annular-dispersed flow regimes, but no model development is currently planned. The effect of momentum exchange on fuel freezing and plugging behavior needs to be studied further in the Phase 2 assessment.

(10) Heat transfer coefficients: The contact resistance between liquid fuel and structure needs to be implemented appropriately in SIMMER-III. Alternative methods for calculating heat transfer to the wall of a boiling pool are being investigated. Further assessment of the influence of vaporization at liquid-liquid interfaces on heat transfer coefficients is desirable, particularly with respect to fuel/steel boiling pools. It is not recommended to model transient heat transfer coefficients.

(11) Thermal radiation heat transfer: Though not identified by the Phase 1 assessment, it is believed to be desirable to have this modeling capability. Existing models in multi-phase codes are being reviewed and it is believed a suitable model can be implemented in SIMMER-III in the future.

(12) Fuel freezing: The SIMMER-III melting and freezing model requires modification to suitably treat the thermal contact resistance and non-equilibrium conditions at the liquid-structure interface. The model needs to predict bulk freezing, conduction-limited freezing and wall melting correctly for the given local temperature and flow conditions. Validation of such a model will require further application to separate effects experiments of material freezing and wall melting. In addition, the complex freezing mechanisms to be studied in Phase 2 or in reactor application may also drive future model elaboration.

(13) Vaporization and condensation: It is desirable to model diffusion-limited vapor condensation in the presence of non-condensable gas. A suitably simple model has been proposed, and it is intended to implement it in a future version of SIMMER-III. Further model improvement may be driven by future application to more complex multicomponent phase transition problems.

4.3 Implication for Phase 2 Assessment and Reactor Application

SIMMER-III is now ready for Phase 2 assessment and reactor application. The two application areas of Phase 1, melting/freezing and vaporization/condensation, both involve integral problems relevant to LMFR safety, and so there are many common features. Below, the experience from the Phase 1 assessment is discussed with reference to each of the key CDA phenomena identified in Section 3.3. Suggestions are made as to how the Phase 2 assessment should be tailored to meet the concerns identified in the Phase 1 assessment.

(1) Boiling pools

SIMMER-III will play an important role in investigating the stability of the fuel/steel boiling pool against internal and external disturbances. Key models are the IFA modeling, which determines the time-dependent surface area evolution, momentum exchange functions in bubbly and chum-turbulent flow, and non-equilibrium vaporization and condensation. It is considered straightforward to apply SIMMER-III to a fuel/steel boiling pool problem with internal heat generation. However, the Phase 1 assessment of various bubble column and single-component boiling pool problems indicated the need for improvements to the modeling, particularly with respect to the IFAs and momentum exchange. As reported in Sections 4.1 and 4.2 many of these improvements have already been incorporated into the code: errors in the IFA modeling have already been corrected, improvements to modeling the IFAs and inter-phase drag in the transition flow regime have been identified and are being tested, and treatments of the momentum diffusion term and inter-cell heat transfer are both available in SIMMER-III Version 2.A.

A preliminary simulation of the SCARABEE BF2 experiment has been very encouraging and has been the source of many model improvements. There is already a need to recalculate Phase 1 assessment problems associated with the bubble column and the single-component boiling pool to assess the effect of the above model changes. Furthermore, the Phase 2 assessment will undoubtedly result in additional improvements to SIMMER-III modeling. To assess these model developments, it is important to have strong feedback and interaction between the Phase 2 applications and relevant Phase 1 calculations, particularly of the bubble column and water boiling pools.

(2) Fuel relocation and freezing

Phase 2 assessment problems should be closely relevant to reactor accident analysis and hence must suitably address, in addition to basic fuel freezing mechanisms, potential fuel escape paths and their specific geometric configurations. Three potential fuel escape (fuel relocation) paths are discussed briefly. For an intra-subassembly pin bundle, fuel freezing and penetration is affected by rapid cladding ablation, fuel particle formation, remaining pellet breakup, etc.

The effect of viscosity enhancement and potential jamming due to presence of solid particles are expected to be important. An inter-subassembly gap channel in the axial and radial blanket regions is a simple slab geometry and is characterized by relatively low structure temperature, so wall melting is expected. Fuel relocation into a control-rod guide tube is influenced by the timing of structure wall melting (or failure) and the effect of FCIs with liquid sodium remaining in the channel.

The main SIMMER-III models which are involved in calculating fuel relocation are the melting/freezing model, and the fluids and structure heat transfer coefficients. The modeling of particle jamming and viscosity enhancement of a liquid-solid mixture by particles is also expected to be influential. The Phase 1 assessment concentrated on fuel freezing in tubes, which is the most basic geometry yielding the least ambiguous data. The applications have proved to be extremely useful for assessing individual key models. The SIMMER-III conduction-limited freezing model has been shown to be valid, providing the conditions for conduction-limited freezing are satisfied. The penetration lengths in the bulk freezing tests analyzed in Phase 1 are more sensitive to the rate of heat loss from the liquid rather than particle jamming, and so help to resolve uncertainties in the liquid-structure heat transfer rates. This has resulted in recommendations for model improvements, specifically with regard to treating interfacial contact resistance between liquid and structure. However, some fundamental uncertainties remain, particularly as to how the contact resistance and non-equilibrium conditions at the liquid-structure interface should be modeled in SIMMER-III such that bulk freezing, conduction-limited freezing and wall melting are correctly calculated for given local temperature and flow conditions. These uncertainties can only be resolved by further Phase 1-type assessment.

It is desirable to assess the fuel relocation and freezing calculated by SIMMER-III in more prototypic geometries than were analyzed in the Phase 1 assessment. At the same time, it is desirable to resolve some of the fundamental issues raised by the Phase 1 assessment before embarking on a large-scale assessment program in prototypic geometries. It seems sensible to continue to carry out Phase 1-type analyses of test problems in parallel with the Phase 2 applications to more prototypic conditions.

(3) Post-disassembly expansion

The post-disassembly expansion phase of CDAs involves the following event sequences: high-speed, multi-phase flows through narrow channels (or pin bundles) interacting with structure walls (with or without wall melting); and multi-phase bubble expansion into a cold coolant pool. Key phenomena include the effect of non-condensable gas on rapid vapor condensation and the effect of hydrodynamic instabilities on the free liquid (or bubble) surface.

SIMMER-III was not applied to an expansion phase problem in the Phase 1 assessment. Nevertheless, the Phase 1 assessment has validated the SIMMER-III multi-phase convection algorithm. Phase 1 also highlighted the need to treat diffusion-limited vapor condensation in the presence of non-condensable gas, and it is intended to implement a simple model in a future version of SIMMER-III. Also, the way liquid surfaces are treated in a Eulerian code like SIMMER-III means that the physics of instabilities on the bubble surface cannot be fully modeled.

SIMMER-III can be directly used to simulate the post-disassembly expansion phase of an LMFR CDA. However, it is also worthwhile studying separate-effects phenomena relevant to the expansion phase, for example using data for nitrogen expansion into a water pool.

(4) Fuel-Coolant Interactions (FCIs)

FCIs could occur at various stages of a CDA progression. Classically there are four stages to the FCI: (a) pre-mixing: formation of a coarse melt/coolant mixture, (b) triggering, (c) propagation of a pressure pulse accompanied by fragmentation of the melt droplets, and (d) expansion of the melt/coolant mixture. The pre-mixing stage generally requires that the film boiling condition is satisfied, which is believed to be less likely in an LMFR than in an LWR because of the high conductivity of sodium coolant compared to water. Nevertheless, FCIs remain a concern in LMFR safety analysis.

Virtually all of the SIMMER-III fluids dynamics models are involved in modeling FCIs. However, the triggering event can involve local microphysical phenomena, and modeling of microphysical processes is beyond the scope of SIMMER-III. Furthermore, some nonequilibrium mass transfer paths which are present in steam explosions, such as coolant boiling on solid particles, cannot be fully treated by SIMMER-III. Nevertheless, apart from these caveats the code can be used to perform an integral simulation of an FCI.

The Phase 1 assessment demonstrated that SIMMER-III could successfully simulate some aspects of an FCI in a sodium system (e.g. analysis of THINA - Problem 5.11; validation of the film boiling model - Problem 3.3). In addition, a comparison of SIMMER-III IFA modeling with other FCI codes has led to improvements in the IFA source terms. Furthermore SIMMER-III has recently been applied to steam explosion experiments, including the FARO ST experiment for the pre-mixing phase and the KROTOS-28 experiment for the propagation phase. The Phase 2 assessment should include and expand on these applications.

(5) Structural disintegration

In the transition phase of a CDA, disintegration of remaining fuel pins and can walls is important for assessing core melt-out behavior and stability of a fuel/steel boiling pool. Fission gas released from disrupted fuel could have a significant effect on fuel motion. Structural disintegration was not treated in the Phase 1 assessment. Moreover, a detailed plan for assessing these mechanisms has not been formulated yet.

(6) Summary

The main purpose of the Phase 2 assessment program is to significantly improve the confidence level of SIMMER-III for future reactor application. However, both the Phase 2 assessment and reactor application will undoubtedly suggest new areas for code improvement. Feedback from future reactor application of SIMMER-III will undoubtedly do likewise, and will be used to guide and prioritize future code development and assessment.

The Phase 1 assessment is a solid foundation upon which the application of the code to integral phenomena in Phase 2 and reactor conditions can be assessed. Nevertheless, recalculation of relevant Phase 1 test problems should continue to be performed as model improvements are implemented in SIMMER-III. Future code assessment is expected to further narrow down the remaining limitations and applicability ranges of the code. The information and experience gained will be essential for guiding future CDA analysis, and for identifying rational uncertainty ranges for input model parameters.

Future code application may also suggest new areas of future safety research. New experimental programs, both in- and out-of-pile, may well be proposed on the basis of SIMMER-III calculations. Thus, future assessment may also be utilized to guide and prioritize long-term programs for LMFR safety research.

5. Conclusion

The completion of SIMMER-III Version 1, a two-dimensional, three-velocity-field, multiphase, multicomponent, Eulerian, fluid-dynamics system code, enabled the integrated code to be applied to fluid dynamics problems for the first time. SIMMER-III has been designed with many advantageous code features from the viewpoint of validation. These include: its modularized and flexible code design and programming, numerical accuracy and stability. With the release of Version 1 the development and assessment of the code has been internationally participated by Forschungszentrum Karlsruhe, Germany and Commissariat a l'Energie Atomique, France. To advance the code as the next-generation standard tool for LMFR safety analysis, it was agreed that a joint assessment program should be conducted amongst the partners in a comprehensive and systematic way.

The SIMMER-III assessment program consists of two stages: Phase 1 for fundamental and separate-effect code assessment of individual models; and Phase 2 for code application to integral experiments describing key physical phenomena directly relevant to LMFR safety. This report documents the results of the Phase 1 assessment. A total of 34 test problems have been modeled, including: simple test calculations to verify the code; single- and two-phase flow benchmark problems to confirm the code is competitive to other state-of-the-art multi-phase codes; and analyses of small-scale experiments where unambiguous data is available. Such an assessment effort is essential for making the code reliable, and to promote its widespread acceptance. The results and achievements of the Phase 1 assessment, and the impact of Phase 1 on future model development and the Phase 2 assessment, are synthesized in this report. The major conclusions are summarized below.

(1) The fluid-dynamics convection algorithm is basically valid for a variety of one- and two-dimensional isothermal problems. The solution method is numerically stable and accurate. Numerical diffusion is sufficiently mitigated by the higher-order differencing scheme.

(2) There is a fundamental timestep-size limitation because the intra-cell heat and mass transfer is decoupled from fluid convection in the four-step fluid dynamics algorithm. However, this limitation is acceptable for most code application areas.

(3) Some of the test problems identified a need to model radial inter-cell momentum coupling, which is lacking in the current SIMMER-III and in its predecessors SIMMER-II and AFDM. This concern should be resolved by the momentum diffusion terms which are being implemented in Version 2 of SIMMER-III. A turbulence model is also desirable but, since the implementation of a turbulence model would require a major modeling effort, it is considered prudent to first examine the influence of the momentum diffusion term.

(4) The multiple flow regimes in SIMMER-III enable a variety of multi-phase flows in both a pool and a channel geometries to be modeled, which is a significant improvement on previous codes. The only major disappointment is the annular-dispersed channel flow regime, where the treatment of a liquid film and entrained droplets in the same velocity field is proving to be a poor approximation.

(5) The test problems have identified areas for improvement in the momentum exchange functions. A treatment of the momentum coupling between the liquid-continuous and vapor-continuous regions in pool transition flow is being tested. The treatment of liquid vapor momentum coupling in annular and annular-dispersed flows is unsatisfactory, but this is not considered a major problem for the main application areas of SIMMER-III.

(6) The generalized interfacial area convection model in SIMMER-III has proved to be promising, and is a major advance on SIMMER-II. Some of the interfacial area source terms have been validated by the Phase 1 applications but further validation is necessary.

(7) The basic framework of the heat and mass transfer modeling has been verified. The modeling of melting/freezing in SIMMER-III is an advance on SIMMER-II, but the Phase 1 applications have indicated the need for further sophistication, particularly with regard to modeling a liquid/structure contact resistance. Further assessment of freezing in more prototypic geometries, is desirable.

(8) Single-component vaporization/condensation was validated, but the need was identified to model diffusion-limited condensation model in the presence of non-condensable gas. A suitably simple model has been proposed, and it should be implemented in a future version of SIMMER-III. Validation for complex phase transition processes is desirable.

(9) SIMMER-III has proved to be a useful tool for simulating a variety of multi-phase flows. The code has a stable and robust numerical framework, and is portable, having been successfully used at four research centers. The accurate and thermodynamically consistent functions of equations of state and thermophysical properties have contributed to the accuracy, stability and validation of heat and mass transfer model.

(10) The Phase 1 assessment is a solid foundation upon which the application of the code to integral phenomena in Phase 2 and reactor conditions can be assessed. Nevertheless, recalculation of relevant Phase 1 test problems should continue to be performed as model improvements are implemented in SIMMER-III.

In summary, the Phase 1 assessment was a great success. A time and man power consuming effort to perform numerous calculations for the code assessment was made possible by the framework of international collaboration between PNC and European FZK and CEA. The Phase 1 study has confirmed that SIMMER-III is now ready for application to integral phenomena. The code can be profitably used to investigate such key accident phenomena as: boiling-pool dynamics, fuel relocation and freezing, post-disassembly material expansion and fuel-coolant interactions. These applications will form the backbone of the Phase 2 assessment program.

The development of the SIMMER-III code has reached the stage where reactor safety analyses can be conducted. The fluid dynamics models of Version 1 have been coupled with a space- and energy-dependent neutron kinetics model, to create Version 2 of the code. The outcome of this program is expected to significantly improve the reliability of future LMFR safety analyses.

Acknowledgments

The initial two years of the SIMMER-III code development was performed under the agreement between the United States Nuclear Regulatory Commission and PNC. The authors are grateful to W.R. Bohl of the Los Alamos National Laboratory for his indispensable and pioneering contribution to germinating the technological basis for SIMMER-III. The code assessment study performed and documented in this report relies greatly on the experience and knowledge accumulated during the development of former codes, SIMMER-II and AFDM. For this reason, the past efforts of many contributors to these former codes are also acknowledged.

This study has been conducted under the international agreement between PNC and German FZK and French CEA. Since the participation of the European research organizations was essential for both the quality and quantity of the assessment program, their management supports are sincerely acknowledged. Also appreciated is the participation of the UK AEA Technology, which participated in the program during an early stage. The support from PNC's management, both at Oarai and Tokyo, was also a key element to the success of this study. This has been a happy example of successful international cooperation in a field of joint software development.

A key member of the SIMMER-III development team at PNC Oarai was N. Shirakawa of Toshiba corporation. Mr. Shirakawa's contribution to SIMMER-III is reflected by the success of the fluid dynamics algorithm described in this report.

Finally, the untiring support of PNC programming staff, F. Inoue and M. Sugaya, is deeply appreciated, especially for undertaking numerous assessment calculations.

References

1) Sa. Kondo, et al.: "SIMMER-III: An Advanced Computer Program for LMFBR Severe Accident Analysis", Proc. Int. Conf on Design and Safety of Advanced Nuclear Power Plants (ANP'92), Tokyo, Japan, Oct. 25-29, 1992.

2) Sa. Kondo, et al.: " PHASE 2 CODE ASSESSMENT OF SIMMER-III, A COMPUTER PROGRAM FOR LMFR CORE DISRUPTIVE ACCIDENT ANALYSIS", JNC TN9400 2000-105, 2000.

3) Sa. Kondo, et al.: "Integrated Analysis of In-Vessel and Ex-Vessel Severe-Accident Sequences", Proc. 1990 Int. Fast Reactor Safety Mtg. Snowbird, Utah, U.S.A., Aug. 12-16, 1990.

4) N. Nonaka, O. Miyake and S. Kondo: "Characterization of LMFBR Severe Accident Progression", Proc. Int. Conf on Design and Safety of Advanced Nuclear Power Plants (ANP'92), Tokyo, Japan, Oct. 25-29, 1992.

5) W.R. Bohl and L.B. Luck: "SIMMER-II: A Computer Program for LMFBR Disrupted Core Analysis", LA-11415-MS, Los Alamos National Laboratory (1990).

6) L. L. Smith, et al.: "The SIMMER Program: Its Accomplishment", Proc. Int. Top. Mtg. on Fast Reactor Safety, Knoxville, Tennessee, U.S.A., Apr. 21-25, 1985.

7) W.R. Bohl, et al.: "AFDM: An Advanced Fluid Dynamics Model", LA-11692-MS, Los Alamos National Laboratory (1990).

8) Sa. Kondo, et al.: "SIMMER-III: A Computer Program for LMFR Core Disruptive Accident Analysis – Version 2.H Model Summary and Program Description –", JNC TN9400 2001-002, 2000, 318p.

9) H. Yamano, et al.: " SIMMER-III: A Computer Program for LMFR Core Disruptive Accident Analysis – Version 3.A Model Summary and Program Description –", JNC TN9400 2003-071, 2003, 340p.

10) Sa. Kondo, et al.: "SIMMER-IV: A Three-Dimensional Computer Program for LMFR Core Disruptive Accident Analysis – Version 1.B Model Summary and Program Description –", JNC TN9400 2001-003, 2000, 307p.

11) H. Yamano, et al.: " SIMMER-IV: A Three-Dimensional Computer Program for LMFR Core Disruptive Accident Analysis – Version 2.A Model Summary and Program Description –", JNC TN9400 2003-070, 2003, 333p.

12) W.R. Bohl, et al.: "AFDM: An Advanced Fluid Dynamics Model, Volume V: The Convective Transport Algorithm", LA-11692-MS, Vol. V, Los Alamos National Laboratory, 1990.

13) D. WIlhelm, et al.: "AFDM: An Advanced Fluid Dynamics Model, Volume II: Topologies, Flow Regimes and Interfacial Areas", LA-11692-MS, Vol. II, Los Alamos National Laboratory (September 1990).

14) Y. Tobita, et al.: "Interfacial Area Modeling for a Multiphase, Multicomponent FluidDynamics Code", Int. Conf on Multiphase Flows '91-Tsukuba, Tsukuba, Japan, Sept. 24-27, 1991.

15) M. Ishii: "Thermo-Fluid Dynamics Theory of Two-Phase Flow", Eyrolles, Paris (1975).

16) M. Ishii and N. Zuber: "Drag Coefficient and Relative Velocity in Bubbly, Droplet or Particulate Flows", AIChE J., 25, 843-855 (1979).

17) K. Morita, et al.: "Improved Modeling of Multicomponent Equations of State for a Multiphase Flow Code SIMMER-III", Int. Conf on Multiphase Flows '91-Tsukuba, Tsukuba, Japan, Sept. 24-27, 1991.

18) E. A. Fischer: "Fuel Equation of State Data for Use in Fast Reactor Accident Analysis", KfK-4889, Kernforschungs-zentrum Karlsruhe report (May 1992).

19) J. K. Fink and L. Leibowitz: Proc. 8th Symp. Thermophysical Properties, CONF-8106164-5, Guithersburg, Maryland, U.S.A., June 15-18, 1981.

20) E. A. Fischer: "Evaluation of the Uranium Equation of State Based on Recent Vapor Pressure Measurement", KfK-4084, Kernforschungs-zentrum Karlsruhe report (September 1987).

21) A. M. Tentner, et al.: "SAS4A LMFBR Whole Core Accident Analysis Code", Proc. Int. Top. Mtg. on Fast Reactor Safety, Knoxville, Tennessee, U.S.A., Apr. 21-25, 1985.

22) C. R. Bell, et al.: "Advances in the Mechnistic Assessment of Postdisassemnbry Energetics", Proc. Int. Mtg. on Fast Reactor Safety Technology, Seattle, Washington, U.S.A. Sept. 1979.

23) D. L. Basdekas, et al.: "A Qualification testing program plan for SIMMER", NUREG-0457, July 1978.

24) T. G. Theofanous and C. R. Bell: "An Assessment of CRBR Core Disruptive Accident Energetics", NUREG/CR-3224, LA-9716-MS (Mar. 1984).

25) B. E. Boyack, et al.: "TRAC-PF1 Developmental Assessment", NUREG/CR-3280, (July 1983).

26) D. P. Spalding, et al.: "Problem specification and collated solutions of the two-phase flow numerical benchmark experience 1986-7", DOE/EPRI Second Int. Workshop on Two-Phase Flow Fundamentals, Troy, New York, 16-20 March 1987.

Appendix: Summary Reports of Phase 1 SIMMER-III Code Assessment

This appendix contains all the summary reports contributed by the various authors. The original documents are reproduced in the same format and style without modifying their technical contents and the authors' conclusions, except for editorial changes. The input data listings and the FORTRAN modification listings for some of the test problems are not included, because they are applicable only to earely SIMMER-III versions.

The test problems are categorized into the five headings listed below. Thirty-four test problems have been achieved through international collaboration; the names of the contributing organizations are listed below in parentheses beside the abbreviated title of each test problem. Some of the research institusions have been re-organized or renamed since the original report was issued in 1996: PNC to JNC to JAEA, IPSN to IRSN, and FZK to KIT. The names of authors are shown in each summary report.

Category 1: Fluid convection algorithm

- Problem 1.1: Ideal gas shock tube (PNC)
- Problem 1.2: Two-phase shock tube (FZK)
- Problem 1.3: Oscillating manometer (IPSN)
- Problem 1.4: One-dimensional sedimentation (PNC)
- Problem 1.5: Two-dimensional sedimentation (PNC)
- Problem 1.6: One-dimensional sodium boiling (PNC)
- Problem 1.7: Liquid sloshing with particles (FZK)
- Problem 1.8: Water hammer (PNC)
- Problem 1.9: Impact of liquid slugs (FZK)
- Problem 1.10: Steam expulsion by subcooled water (PNC)
- Problem 1.11: Stability of one-dimensional bubble column (PNC)

Category 2: Interfacial area and momentum exchange models

- Problem 2.1: Zero-th dimensional pool flow (PNC)
- Problem 2.2: One-dimensional isothermal bubble column (CEA-G)
- Problem 2.3: Two-dimensional isothermal bubble column (CEA-G)
- Problem 2.4: Pressure drop in fully developed flow (CEA-G)
- Problem 2.5: Momentum exchange in pipe flow (PNC)
- Problem 2.6: Developing annular flow (PNC)

Category 3: Heat transfer

- Problem 3.1: Can-wall heat transfer (PNC)
- Problem 3.2: Structure axial heat transfer (PNC)
- Problem 3.3: Film boiling in sodium (PNC)

Category 4: Melting and freezing

Problem 4.1: Fuel freezing: GEYSER experiments (CEA-G)

Problem 4.2: Fuel freezing: SMPR experiments (CEA-G)

Problem 4.3: Freezing of hot melts in tubes: THEFIS (FZK)

Category 5: Vaporization and condensation

Problem 5.1: Condensation of steam on droplet (PNC)

Problem 5.2: Droplet evaporation (PNC)

Problem 5.3: Vapor bubble collapse (PNC)

Problem 5.4: Rapid fuel vaporization (FZK)

Problem 5.5: Boiling in a pipe (PNC)

Problem 5.6: Vapor condensation on structure (CEA-G)

Problem 5.7: Boiling pool with wall heat transfer (CEA-G)

Problem 5.8: Two-phase blowdown: Bartak's pipe (CEA-G)

Problem 5.9: Two-phase blowdown: Edwards' pipe (I) (CEA-G)

Problem 5.10: Two-phase blowdown: Edwards' pipe (2) (PNC)

Problem 5.11: Thermite injection into sodium: THINA (CEA-G)

Most of the above problems in fact involve several code models, but they are categorized in the most relevant category. For example, the Edwards' pipe two-phase blowdown problems (Problems 5.9 and 5.10) are placed in Category 5 because they involve rapid non-equilibrium water vaporization. However the rate of phase change is determined by transient evolution of interfacial areas and the long-term behavior is governed by fluid convection out of the pipe. Such inter-relationships between the test problems and models are summarized in Table 3-1.

The results of each test problems have been written as concise summary reports such that all the reports are compiled in this one document. To facilitate readers' understanding, each report is written in an identical pre-determined format. All the original contributions are included as they were written with minimal editorial change. This means all the positive and negative views by original authors are retained. Consequently some of them may be controversial and contradictory. A synthesis of results and conclusions is attempted in Chapter 4.

Problem 1.1: Ideal gas shock tube

"Ideal Gas Shock Tube Problem"

Satoru Kondo (PNC)

Outline of the Problem

A basic and the most studied benchmark problem of an ideal-gas shock tube is analyzed by a one-dimensional, single-component system with SIMMER-III to verify an adiabatic fluid convection model of the code. An analytical solution for this problem is available and is compared with the code prediction. An emphasis is on effectiveness of a higher-order differencing scheme implemented in the code.

1. Objectives of the Application

This is a very popular benchmark problem commonly exercised with a number of fluid dynamics codes. The objectives are: to confirm the validity of a fluid convection algorithm in a one-dimensional, single-component system; and especially to evaluate the higher-order differencing scheme in comparison with the former donor-cell differencing. Additionally this problem treats a pure gas flow, and hence the code capability of simulating a single-component gas flow is to be evaluated.

2. Description of the Problem

A straight cylinder containing ideal gas is initially divided into two zones by a diaphragm: Initially, gas is at rest at uniform temperature. The gas on the left of a diaphragm has higher pressure (and density) than one on the right. At t = 0, the diaphragm is removed to start the fluid motion. The shock front and the density discontinuity propagate to the right, while the rarefaction wave propagates to the left. The problem is simple but the resultant distributions of density, pressure and other state variables are rather complex. The accuracy of simulation depends on a numerical approach taken, such as a convection algorithm, a finite-differencing scheme, mesh cell sizes, time step sizes, etc.

3. Analytical Solution

An exact analytical solution for this problem is available in a text bool.[1)]

4. Understanding of Phenomena

In this simple adiabatic problem, without gravity nor wall friction, there is no uncertainty involved.

5. SIMMER-III Representation

5.1 Geometry, Initial and Boundary Conditions for a Reference Case

A 1-D axial mesh was used without gravity for simulating a cylinder of 2 m long. Initially, the lower half of the cylinder contains air at 10^6 Pa and the upper half at 10^5 Pa. The initial temperature is 300 K. So there is a factor of ten difference in initial pressure (and density). For the reference calculation (Case 1), 40 equal-sized axial noding was used ($\Delta z = 0.05$ m). The code option was higher-order differencing. A constant time step size of $\Delta t = 5\times10^{-6}$ s was used. The results are presented at 1.5 ms for the distributions of density, pressure, temperature and velocity.

No code modification was necessary.

5.2 Parametric Cases

Three parametric cases were run to examine the effects of mesh size and differencing schemes. The initial and boundary conditions stay the same. Finer noding with 80 axial mesh ($\Delta z = 0.025$ m) cells were used in Case 2. Cases 3 and 4 were respectively for 40 and 80 mesh cells, but a donor-cell differencing scheme was used this time.

6. Results

The initial densities in the two regions, as calculated from the specified pressure and temperature by the code, are 11.6 and 1.16 kg/m^3, respectively. The temperature distribution is uniform at 300 K and the initial velocity is zero.

The distributions of the four variables at 1.5 ms specified in Section 5.1 are shown in Figs. l(a) to l(d) for Case 1. The analytical solutions are also plotted as solid lines, while the code ·predictions are shown in dashed lines. As shown in these figures, SIMMER-III agrees fairly well with the analytical solution. The higher-order differencing is shown to reasonably control the numerical diffusion, indicating sharp edges and flat tops of the distributions. A much better agreement is obtained with finer noding in Case 2, for which the distributions of density, pressure, temperature and velocity are shown in Figs. 2(a) to 2(d), respectively.

The same results with the donor-cell differencing are shown for Cases 3 and 4 in Figs. 3 to 4. There is obvious interface smearing due to numerical diffusion especially in Case 3. Case 4 with finer noding improves the situation to some extent. Still the characteristics of sharp edges and flat tops are better simulated even in Case 1 with coarse noding.

7. Conclusion

SIMMER-III has been successfully applied to an ideal gas shock tube problem with excellent agreement with the analytical solution. A higher-order differencing scheme, a standard option of SIMMER-III, is shown to be very effective for mitigating the numerical diffusion which was sometimes intolerable in a conventional donor-cell (first-order) differencing method. There was no numerical instability problem in this one-dimensional simulation. It is encouraging that the code can suitably represent a high-velocity gas

flow as well as sonic and shock propagation. In the former SIMMER-II, any mesh cell has to contain a non-zero liquid mass, while SIMMER-III can treat a pure gas flow without code modification.

8. Recommendations for Model Improvement

None.

9. References

1) F. H. Harlow and A. A. Amsden: "Fluid Dynamics", A LASL Monograph, Los Alamos National Laboratory, LA-4700 (June 1971).

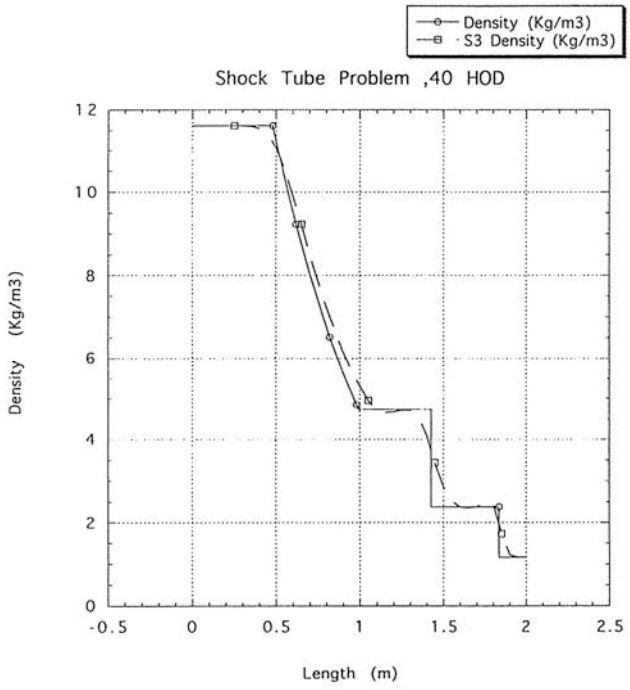

(a) Density

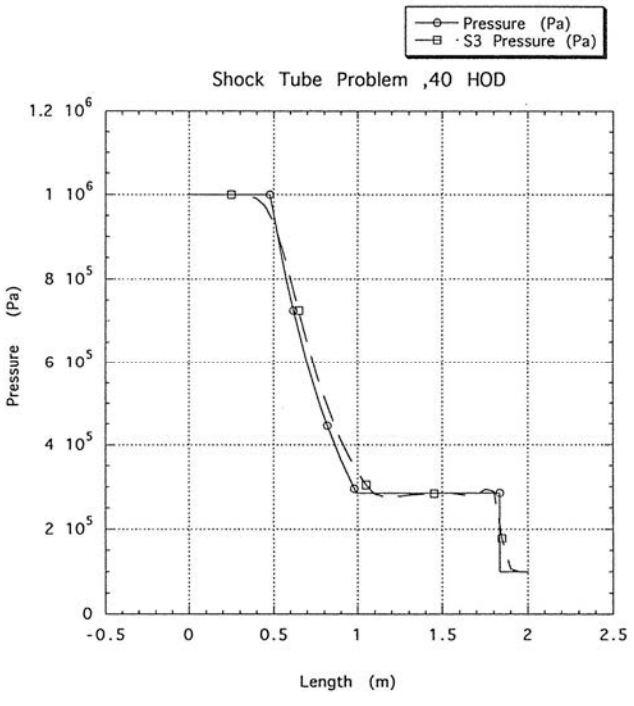

(b) Pressure

Fig. 1. Ideal gas shock tube problem with SIMMER-III (1/2)

(Case 1: 40 cells, higher-order differencing method)

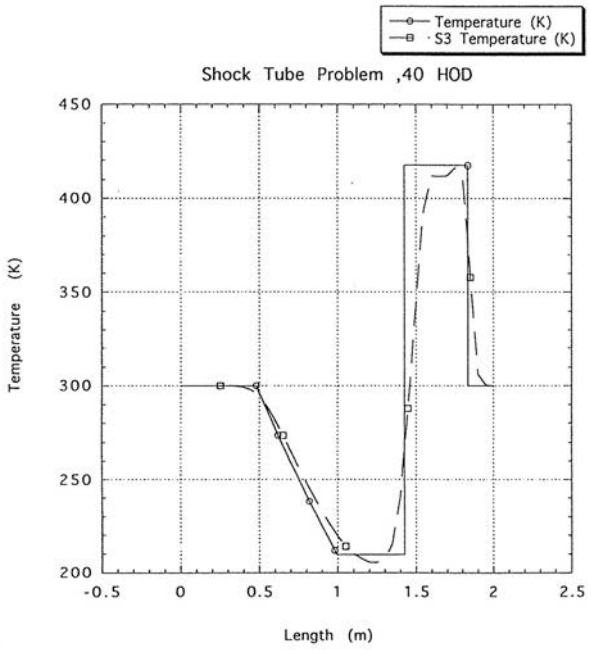

(c) Temperature

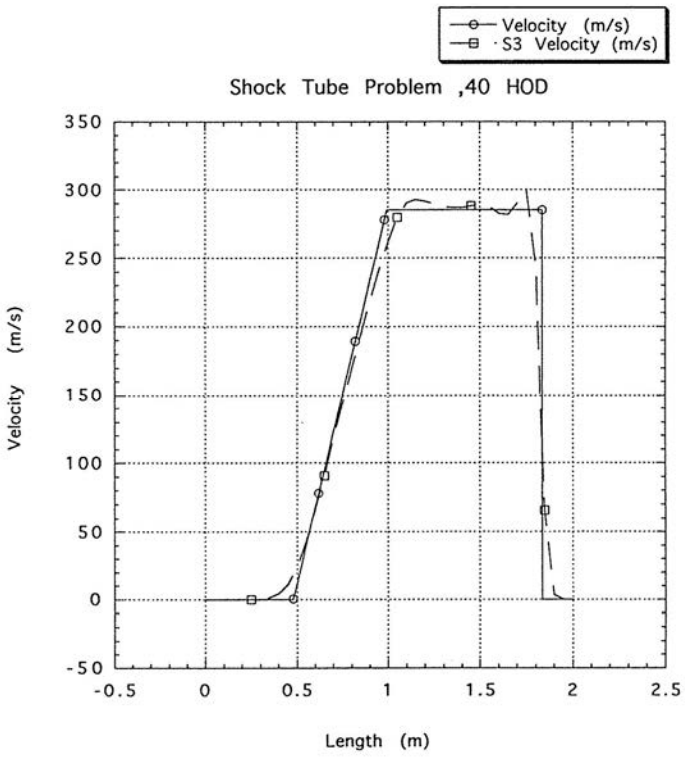

(d) Velocity

Fig. 1. Ideal gas shock tube problem with SIMMER-III (2/2)

(Case 1: 40 cells, higher-order differencing method)

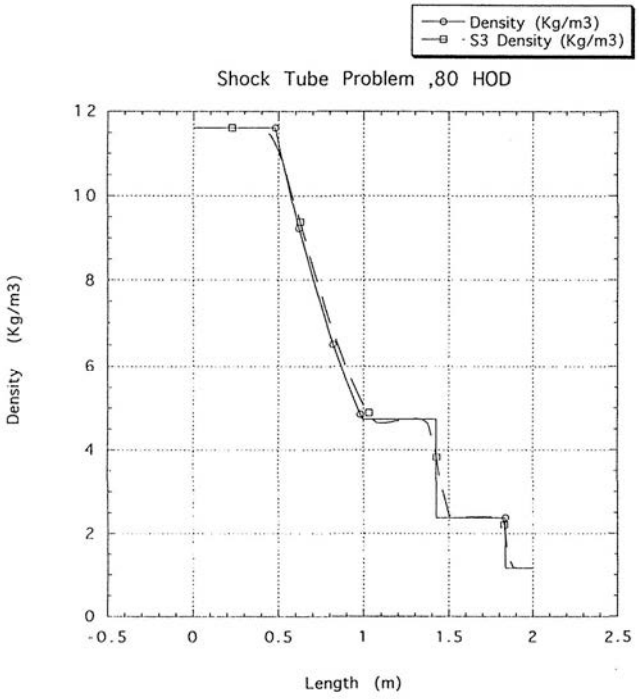

(a) Density

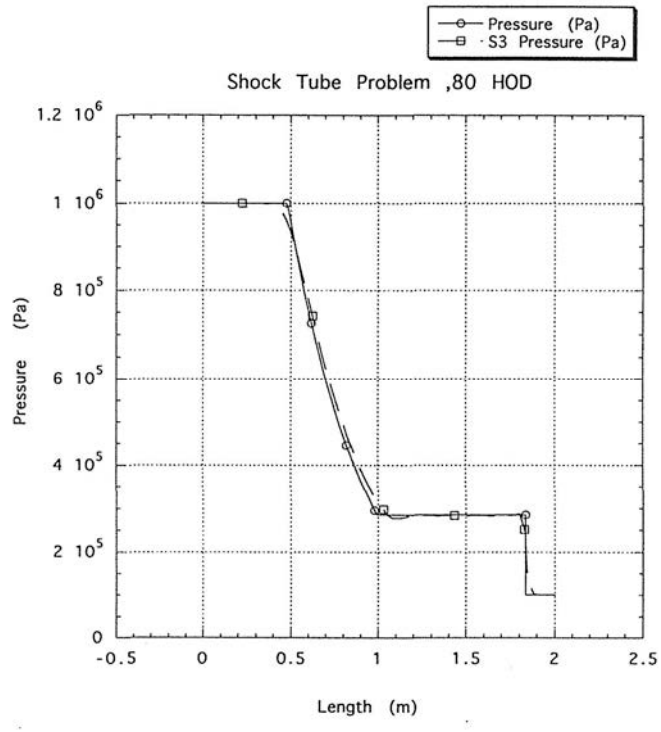

(b) Pressure

Fig. 2. Ideal gas shock tube problem with SIMMER-III (1/2)
(Case 2: 80 cells, higher-order differencing method)

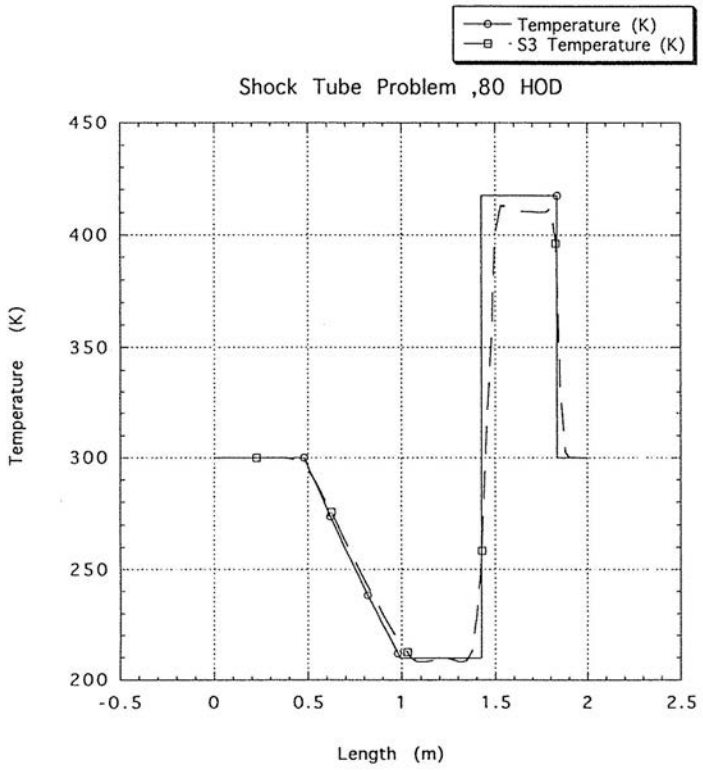

(c) Temperature

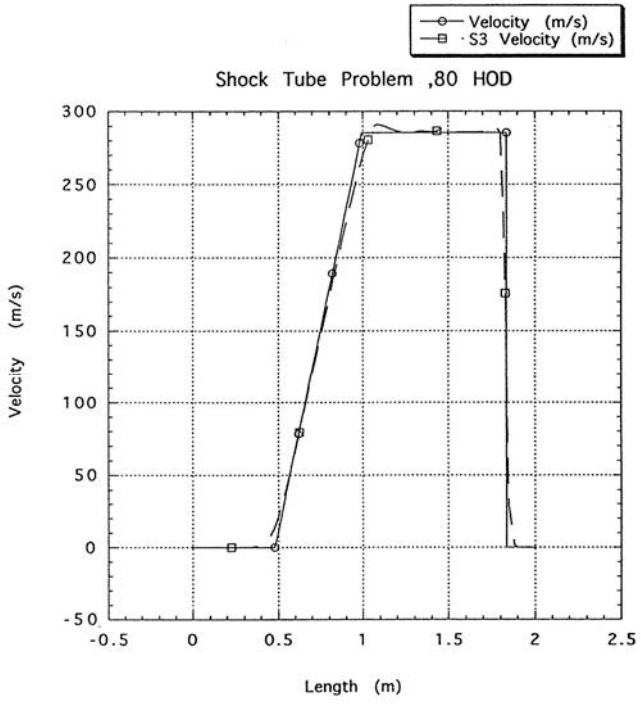

(d) Velocity

Fig. 2. Ideal gas shock tube problem with SIMMER-III (1/2)
(Case 2: 80 cells, higher-order differencing method)

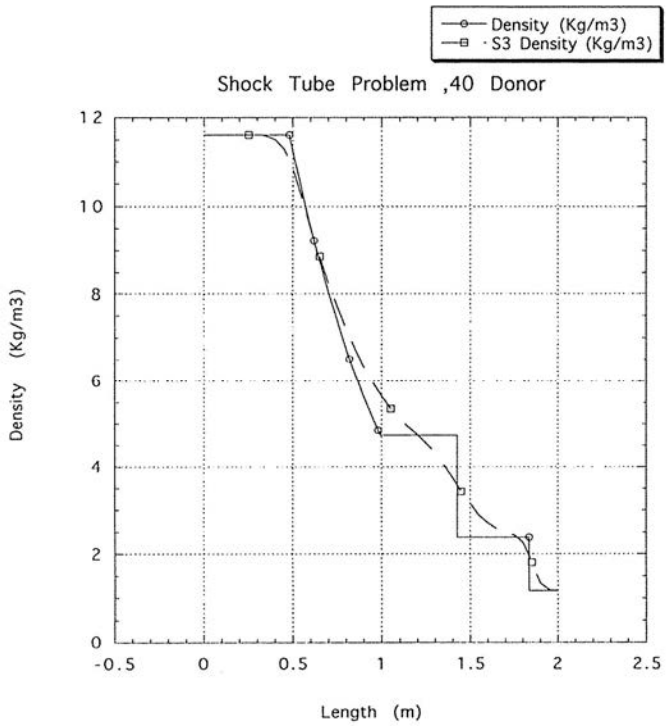

(a) Density

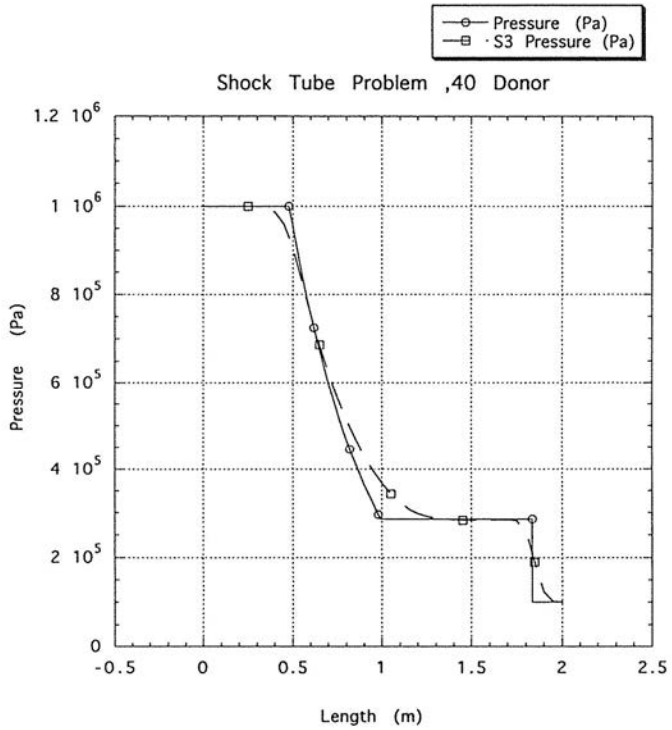

(b) Pressure

Fig. 3. Ideal gas shock tube problem with SIMMER-III (1/2)
(Case 3: 40 cells, donor-cell differencing method)

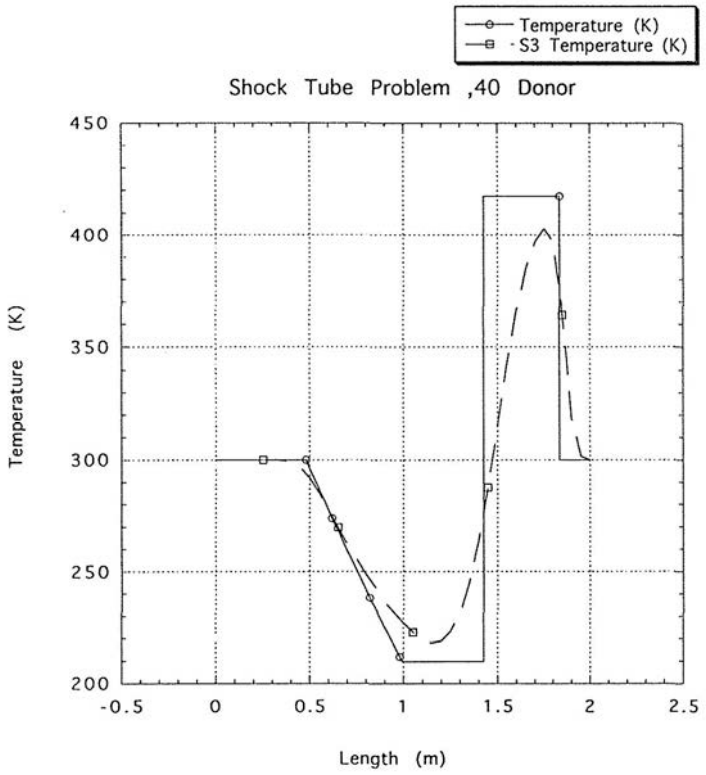

(c) Temperature

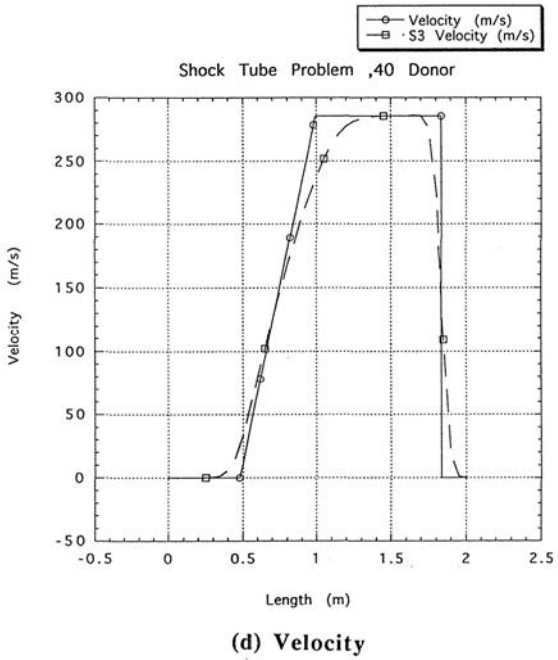

(d) Velocity

Fig. 3. Ideal gas shock tube problem with SIMMER-III (2/2)
(Case 3: 40 cells, donor-cell differencing method)

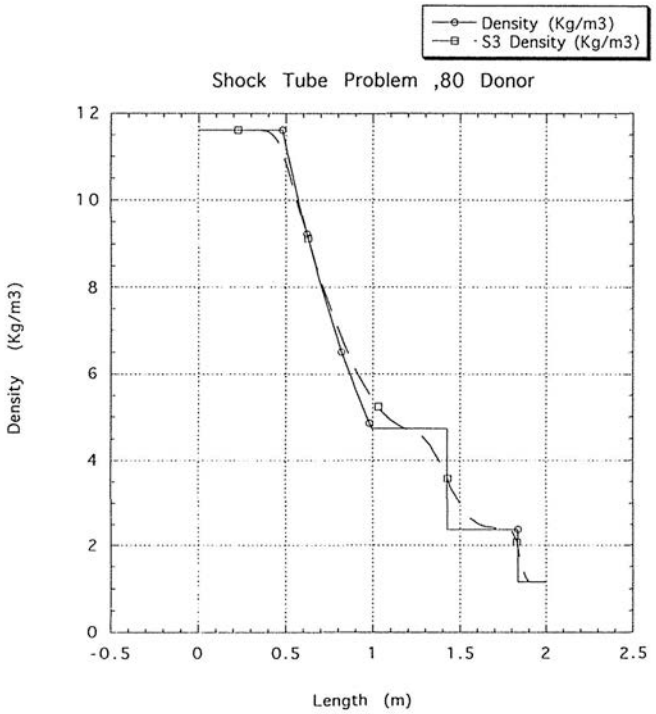

(a) Density

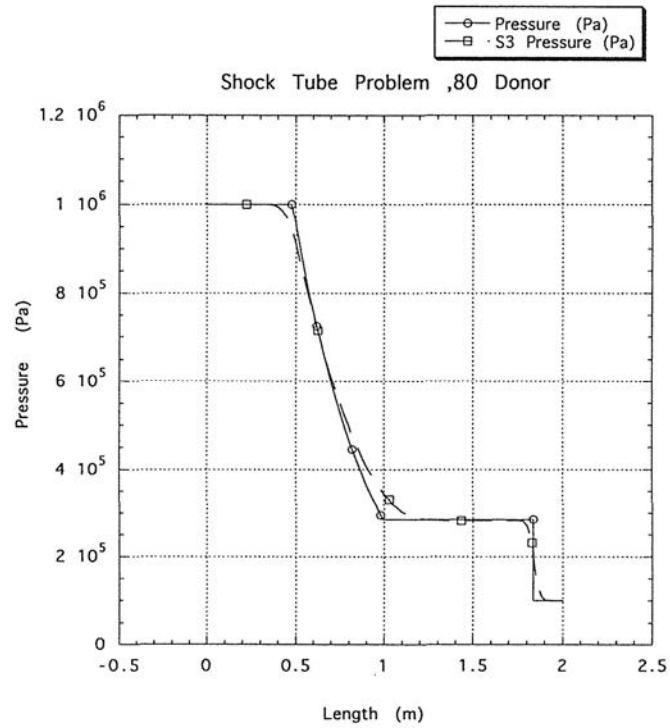

(b) Pressure

Fig. 4. Ideal gas shock tube problem with SIMMER-III (1/2)
(Case 4: 80 cells, donor-cell differencing method)

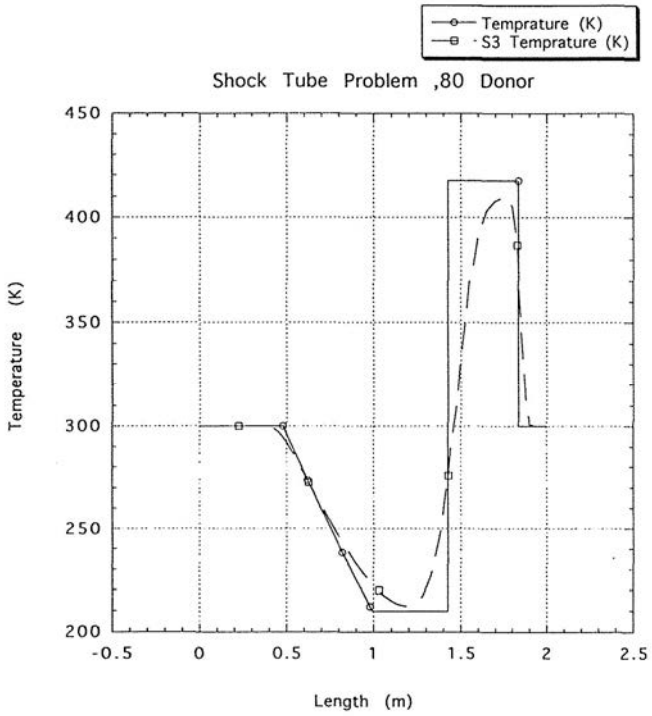

(c) Temperature

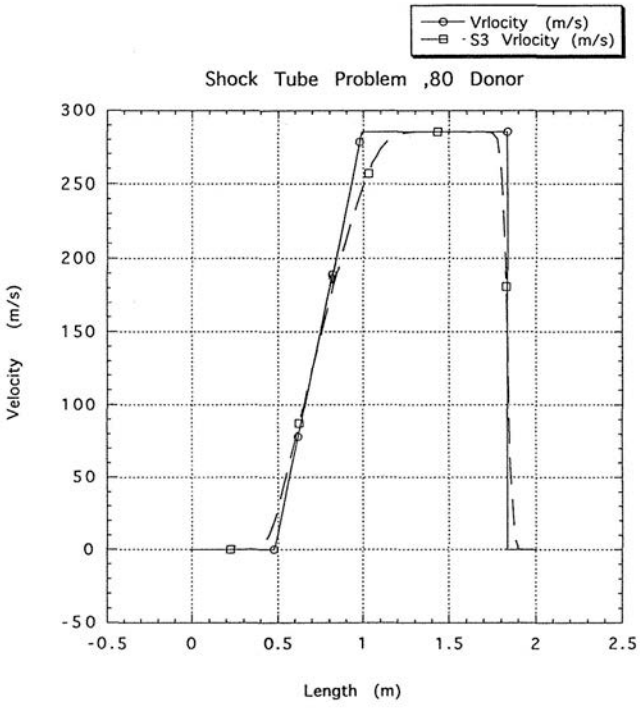

(d) Velocity

Fig. 4. Ideal gas shock tube problem with SIMMER-III (2/2)
(Case 4: 80 cells, donor-cell differencing method)

Problem 1.2: Two-phase shock tube

"Two-Phase Shock Tubes"

C.-D. Munz, W. Maschek, M. Goz, H. Jacobs, B. Stehle (FZK)

Outline of the Problem

A straight closed duct of uniform cross-section is divided into two equal parts by a diaphragm. On the left of the diaphragm, the duct contains compressed air; on the right, it contains atmospheric-pressure air, mingled with finely-divided liquid water. If the two-phase mixture is approximated by a single fluid and the gaswater mixture is considered to be homogeneous and to satisfy the equation of state of a perfect gas, an analytical solution of this shock-tube problem exists.

1. Objectives of the Application

This application concentrates on a verification of SIMMER-III applied to the simulation two-phase problems with strong pressure gradients.

2. Description of Exeperiments

A two-phase shock tube problem has been proposed by D. L. Youngs[1] as a numerical benchmark test for multiphase hydro-codes. The problem description is as follows: A straight closed duct of uniform cross-section is divided into two equal parts by a diaphragm. On the left of the diaphragm, the duct contains compressed air; on the right, it contains atmospheric-pressure air, mingled with finely-divided liquid water. The purpose of this problem is to test numerical methods for highly transient multicomponent compressible flow, predicting what happens when the diaphragm breaks.

Table 2.1. Two-phase shock tube problem.

rigid wall	Air high pressure: $p_l = 3\times10^5$ Pa normal density: $\rho_l = 1$ kg/m^3	Air 99% Water 1% normal pressure $p_r = 10^5$ Pa normal mixture density: $\rho_{water} = 1000$ kg/m^3	rigid wall
	1 m	1 m	

The overall length of the tube is 2 m, consisting of two 1 m long regions separated by a diaphragm. As boundary conditions impermeable walls are to be specified at both ends of the tube. Due to the left high pressure chamber of the shock tube, a shock wave to the right into the gas water mixture is generated, if the diaphragm breaks. The values of the physical variables are given in Table 2.1.

3. Analytical Solution

Under the assumption of no slip between water and gas, D. L. Youngs presented values for an approximate exact solution. He did not describe this approximation in detail. He only states that under the condition of no slip he solves the equations by the method of characteristics. The values of this approximation for the initial speed of the shock wave moving into the low pressure chamber and the conditions behind the shock wave are given in Table 3.1.

Table 3.1. Values of an approximate exact solution as given in Ref. 1).

shock speed:	$v_s = 172.1$ m/s
velocity behind shock:	$v_2 = 800.2$ m/s
pressure behind shock:	$p_2 = 2.517 \times 10^5$ Pa
gas density behind shock:	$\rho_2 = 1.874$ kg/m^3
water volume fraction behind shock:	$r_2 = 0.01874$

D. L. Young proposed to compare the numerical results of the codes with these approximate analytical results at time t = 3.0, 6.0, 9.0 and 12.0 ms. D. L. Young wrote that the method of characteristics may be used to find analytic solutions under the no slip condition. But, he did not explain this approximation and the method of solution. For such a shock tube problem usually the method of characteristics refuses to work without the introduction of additional information, e.g., the propagation rate of the shock wave. Then this shock wave can be tracked and the state before arid behind the shock wave can be calculated by the characteristic theory. In the following we try to get insight into the qualitative structure of the solution by considering the shock tube problem of a single fluid approximation.

Because of the relatively low mass fraction of water in the right part of the shock tube, the basic structure of the solution should be at least similar to the solution of a single fluid shock tube problem. We introduce such an approximation unter the assumption that no interaction between water and gas takes place and the multiphase flow is replaced by the flow of a homogeneous mixture. The structure of the solution of such a problem is the following: It consists of four constant states separated by three elementary waves. A shock wave travels to the right from the high into the low pressure region. A contact discontinuity follows the shock wave and moves with the fluid velocity. Here the density jumps, while the velocity and the pressure are constant across this line of discontinuity. Into the left high pressure region moves a rarefaction wave. This structure of the solution is sketched in Fig. 3.1.

If we use such a single fluid approximation to get an analytic solution we have to consider the following shock tube problem: Both parts of the shock tube are filled with gas. The water inside the right part of the shock tube yields an increase of the density only; i.e. the gas/water mixture is considered to be a homogeneous perfect gas. We assume that the equation of state is overall that of a perfect gas

$$p = (\gamma - 1)\rho\varepsilon \tag{3-1}$$

where ε is the specific internal energy and γ the constant adiabatic exponent (air: 1.4). The right and left values of the primitive variables are given in Table 3.2. In order to match the large density difference, the ideal gas approximation introduces a large difference in temperatures. The temperature of the left chamber of the shock tube is 1045 K, while in the right one it is T = 31.7 K.

The structure of the exact solution of this problem corresponds to that sketched in Fig. 3.1. This problem is the usual Riemann problem of gas dynamics and can be solved exactly in terms of the solution of a fixed point problem.[2] A fast iterative procedure for this Riemann problem has been proposed by Halter[3]. This iterative procedure has been used in our calculations.

Table 3.2. Single fluid shock tube problem.

Air	Air
$p_l = 3\times10^5$ Pa	$p_r = 10^5$ Pa
$\rho_l = 1$ kg/m^3	$\rho r = 10.99$ kg/m^3
$v_l = 0.0$ m/s	$v_r = 0.0$ m/s

Using this approximation we obtained the values in Table 3.3.

Table 3.3. Values of single fluid shock tube approximation with γ = 1.4.

shock speed:	$v_s = 172.1$ m/s
velocity behind shock:	$v_2 = 80.57$ m/s
pressure behind shock:	$p_2 = 2.515\times10^5$ Pa
gas density behind shock:	$\rho_2 = 1.84$ kg/m^3
water volume fraction behind shock:	$r_2 = 0.0189$

The values agree very well with the those of Young (Table 3.1). The computation times t = 3.0, 6.0, 9.0, and 12.0 ms as proposed by Youngs seem to be too large, if we consider these calculations. The velocity of the left boundary of the rarefaction wave is given by the sound velocity in the undisturbed state p_l, ρ_l, v_l This sound velocity is given by

$$c_l = \sqrt{\gamma p_l/\rho_l} \tag{3-2}$$

and has the value q = 650 m/s. Hence after the time t = 1.5 ms the rarefaction fan will reach the left wall. Here, the rarefaction wave is reflected, generating a wave which travels to the right and may disturb after some time the right going waves. Furthermore, after 6 ms the shock wave reaches the right wall and is re fleeted there. According to this simplified analytical solution a comparison between numerical results and this analytical solution should be performed within the time interval [0.0, 1.5] ms.

We solved the gas dynamic problem numerically with walls at both ends. We used here a so called high resolution scheme.[4] The numerical results are shown in Figs. 3.2, 3.3, and 3.4. These results at t = 1.5 ms coincide very well with the exact solutions of the Riemann problems. But at times t = 3.0 ms and t = 4.5 ms we see a strong influence on the pressure and velocity by the rarefaction wave reflected at the left wall. The total density of the mixture is only changed slightly. These results clearly show that the rarefaction wave reflected at the left wall influences the right going waves after some time. Hence the times for comparison proposed by Youngs should be reduced.

The solutions of these single fluid gas dynamical shock tube problems, of course, neglect any two phase effects and may give good approximations in special cases only. They can only show the following: If the two-phase solution.has a structure. as given in Fig. 3.1, then the single fluid approximation should give an estimation the right wave velocities. This is due to the fact that the propagation speed, e. g., of the shock wave, is determined by the integral conservation of mass, momentum and energy. If the two-phase mixture is homogeneous and the twophase effects do not generate another structure of the solutions, then the onefluid model will be a good approximation. If the two phase effects or effects generated by non-homogeneity of the mixture become relevant, these approximate solutions can only give an estimation of the average velocity but can not show details of the wave structure.

Additionally, we looked at another shock tube problem: the limit case of the two phase shock tube problem when the volume fraction of water tends to zero. The gas dynamic Riemann problem, considered here, is sketched in Table 3.4. The values of density and pressure coincide with the values of the two phase shock tube problem when the volume fraction of water tends to zero. The solution of this Riemann problem is sketched in Fig. 3.1. A shock wave travels to the right, followed by a contact surface, while a rarefaction wave moves into the high pressure region. The value of physical quantities obtained from the solution of this Riemann problem are given in Table 3.4. The solution at time t = 1.5 msec is given in Fig. 3.5.

Table 3.4. Gas dynamic shock tube problem.

Air	Air
$p = 3\times10^5$ Pa	$p = 10^5$ Pa
$\rho = 1$ kg/m^3	$\rho = 1$ kg/m^3
$v = 0.0$ m/s	$v = 0.0$ m/s

Table 3.5. Results of the gas dynamic shock tube approximation.

shock speed:	$v_s = 453.9$ m/s
velocity behind shock:	$v_2 = 201.44$ m/s
pressure behind shock:	$p_2 = 1.91\times10^5$ Pa
density behind shock:	$\rho_2 = 1.798$ kg/m^3

4. Understanding of Phenomena

The solution of the Rieman problems for homogeneous gas is well understood. But, the main question is, how accurate is that approximate model for the situation with real interphase exchange. The results in Chapter 6 show that the analytical solutions are rather poor for comparisons.

5. SIMMER-III Representation

5.1 Geometry, Initial and Boundary Conditions for a Reference Case

A 1-D mesh into the z-direction was used with a uniform grid of 100 zones in the space interval [0.0, 2.0]. The boundary conditions of a perfect were specified. No code modification was made.

6. Results

We started our comparison of the numerical results of SIMMER-III in the case of the pure gas dynamic shock tube problem. The space interval [0.0, 2.0] is discretized using 100 grid zones. In the two-dimensional SIMMER-III-Code we set IBM = 1 and JBM = 100. The constant of gravity is set to zero. In the exact solution, the maximum of the wave speed is at about 810 m/s. According to the CFL condition an appropriate time step for an explicit numerical scheme is then given by

$$\Delta t = 0.3\Delta x/810 = 0.741 \times 10^{-5} \ . \qquad (6\text{-}1)$$

The SIMMER-III-Code is a semi-implicit numerical scheme and hence the time step may be chosen larger than that given by (6.1). But the CFL-condition is a quite natural condition, if shock waves will be captured with a good resolution. It states that within one time step a wave can cross one-grid zone only and the numerical smearing introduced within on time step is limited by this spatial resolution. If the time step is increased, more dissipation will be introduced. Hence, to test the capability of the SIMMER-III-Code to resolve shock waves, the time step should be restricted by the CFLccondition. This is done in our calculation by setting DTMIN = DTMAX =0.741×10^{-5}.

Figures 6.1 and 6.2 show the results of SIMMER III for void fraction, pressure, velocity, and temperature at·time 1.5 ms. The small circles indicate the values of the numerical solution, while the solid line gives the exact solution. The results given by the first picture are produced using the usual time step calculation based on the velocity CFL-condition, but starting with the small value $\Delta t = 0.741 \times 10^{-5}$ to give the calculation the chance of a good initial resolution for the break-up of the discontinuity into the different waves. The results in Fig. 6.1 indicate a good approximation of the shock wave with some small wiggles behind it. The shock wave is captured within six grid zones. A relatively strong dissipation is observed at the left going rarefaction wave. This numerical smearing is strong and not expected for a second order accurate scheme. The small contact discontinuity is captured well within five grid zones as clearly visible at the temperature distribution. Only the small hump at the velocity distribution disturbs this

impression. If the time step is decreased to get a better resolution of the shock wave a lot of spurious oscillations are generated. This fact is clearly indicated in Fig. 6.2. The time step within the whole calculation has been fixed to 0.741×10^{-5}. Strong wiggles in the velocity and pressure distribution are shown in Fig. 6.2 behind the shock wave, which have been moved to the left up to the rarefaction wave.

The results for the two phase shock tube problem where the initial values are as given in Table 2.1 are shown in the Figs. 6.3 and 6.4. The first Figure shows those of the usual time step calculation, starting with the small time step 0.741×10^{-5}. Figure 6.4 shows results with the time step being fixed at this small value within the whole calculation. The differences between these pictures are relatively small. lnreasing the time step does not influence the results very much. One difference appears in the pressure plot. With small time steps, a steeper rise ofthe pressure in front of the compression wave becomes visible which may be interpreted as a shock wave running ahead. The figures indicate a large difference between the numerical solutions and the single-fluid approximations. There are of course two possibilities: the numerical results are bad or the single fluid approximations fail in this case.

We believe in the latter of these possibilities, which is motivated be the following considerations. Especially, Fig. 6.4 indicates that the fastest wave to the right is a shock wave propagating into the low pressure region. If we compare the velocity of this wave with the gas dynamic shock tube problem where the water volume fraction is set to zero (Table 3.5), we find that it is similar to that of the shock wave occuring in this problem. That means, within the two-phase shock tube problem the wave structure becomes more compli·cated: the single shock wave decouples into a pre-shock which moves with nearly the same velocity as in the pure gas. It becomes visible in Fig. 6.4 and is smeared out in the large time step calculation given in Fig. 6.3. Behind this pre-shock two-phase effects become important and smooth out the profile. The gas velocity of the two phase shock tube calculations are much higher than within the single fluid approximation and lie between this and the pure gas case. For comparison we·plot in Fig. 6.5 the numerical results of SIMM ER-III together with these two approximations.

The results given in the paper of Youngs[1)] are performed for different constants of a quadratic interphase friction law. For the values of this constant corresponding to low and intermediate interphase friction his results are much more similar to the single fluid approximation. This may be due to the fact, thatin these cases the interphase-friction law is not realistic. Unfortunately he does not show results for a value giving large velocity separation. Figure 6.6 shows the numerical results of SIMMER-III for the fluid and the gas velocity, which indicates that the velocity separation is large. This means, that the one-fluid approximation should not be a good candidate for comparison in this case. We remark that Kondo et al.[5)] performed calculation with the interphase friction law of Youngs and obtained a good agreement with the results of codes.

To get more clarity we applied another multifluid code to the two phase shock tube problem. At Kernforschungszentrum Karlsruhe (KfK), the IVA-KA code is being developed (in a first step) for describing

premixing of cerium melt relocating downwards into a water pool. It is a finite difference code and based on the code IVA3 that has originally been developed by Kolev.[6] In its present state, IVA-KA describes the individual but coupled motions of three fluids, i.e. a gas phase, liquid water, and some other material, i.e. cerium. The coupling between the fluids is due to assuming the same pressure in all three fields locally and due to exchange of momentum, energy, and mass. Thermal equilibrium between water and vapor is not assumed but is always being approached due to heat and mass transfer. The cerium can be liquid initially and freeze during the process (as particles) or it can consist of solid particles from the beginning.

Besides the usual conservation equations of mass, momentum, and energy (or entropy in the case of IVA-KA), IVA-KA solves additional conservation equations for the concentrations of "inert" components in all three fluids (e.g. noncondensable gas in the gas phase) and the particle number densities from which the sizes of discontinuous structures (bubbles, drops, and particles) can be determinded in connection with the corresponding volume fractions. Therefore such sizes depend on the history of the process. They are very important in calculating the ex change terms. The proper types of exchange terms are chosen on the basis of flow regimes assigned to each mesh cell and of the temperature conditions.

IVA-KA describes transient two or three-dimensional flow in cylindrical or in Cartesian coordinates. Complicated geometries can be simulated by a "porous body" approach, i.e. by excluding arbitrary volume fractions in any mesh cell from access by the fluid mixture and by assigning limited (possibly zero) permeabilities to cell boundaries. When IVA-KA is started with the same discretization parameters, it produces quite similar results as the SIMMER-III Code. IVA-KA uses first order donor-cell differencing but the numerical dissipation is not much stronger. The wave into the mixture is slower, but the overall structure of the numerical solutions is the same. The results are plotted in Fig. 6.6 and Fig. 6.7 in comparison with the single fluid approximations and the SIMMER-III results, respectively.

7. Conclusions

The numerical results of SIMMER-III for the pure gas dynamical shock tube problems are good except for spurious oscillations occuring at small time steps. The results for SIMMER-III for the two-phase shock tube problem agree very well with those of the multifluid code IVA-KA, but disagree with results of Young, which is thought to be due to the use of different friction laws. The numerical results and our considerations indicate that there is no reliable exact, numerical or experimental solution for the two-phase shock tube problem of Youngs under realistic conditions. Hence, we will look in the future for experimental results of two-phase shock tubes problems. For experiments the Youngs problem seems not to be a very favourable shock tube problem, because it is very difficult to get such a high volume fraction of water in experiments. To obtain the exact solution of the Riemann problem for a two-phase shock tube seems to be very complicated, which is due to the non-conservative form of the equations and the source terms.

Numerical results with a one-dimensional high resolution scheme for the multiphase flow equations including realistic interphase exchange terms would be very valuable, because they would allow to analyze the influences of the different terms and their numerical modelling.

8. Recommendations for Model Improvements

None.

9. References

1) G.F. Hewitt, J.M. Delhaye and N. Zuber: Multiphase Science and Technology, Volume 6, pp.653-662, Hemisphere Publishing Corporation, New York 1992.

2) T. Chang and L. Hsiao: The Riemann problem and Interaction of Waves in Gas Dynamics, Pitman monographs, United Kingdom 1989.

3) E. Halter: A fast solver for Riemann problems, Math. Meth. in the Appl. Science 7 (1983), pp. 101-107.

4) C.D. Munz and S. Hirmer: HYDSOL Version 2.0: Ein Programm zur numerischen Losung zweidimensionaler kompressibler Stromungen, internal report, KfK 1992.

5) Sa. Kondo, Y. Tobita, K. Morita und N. Shirakawa: SIMMER-III: An advanced computer program for LMFBR severe accident analysis, Int. Conf. on Design and Safety of Advanced Nuclear Power Plants, Tokyo 1992.

6) N.I. Kolev: IVA3: A transient 3D, three phase three-component flow analyzer, Proc. Int. Mtg. on Safety of Thermal Reactors, Portland, OR, 1991, pp. 171-180.

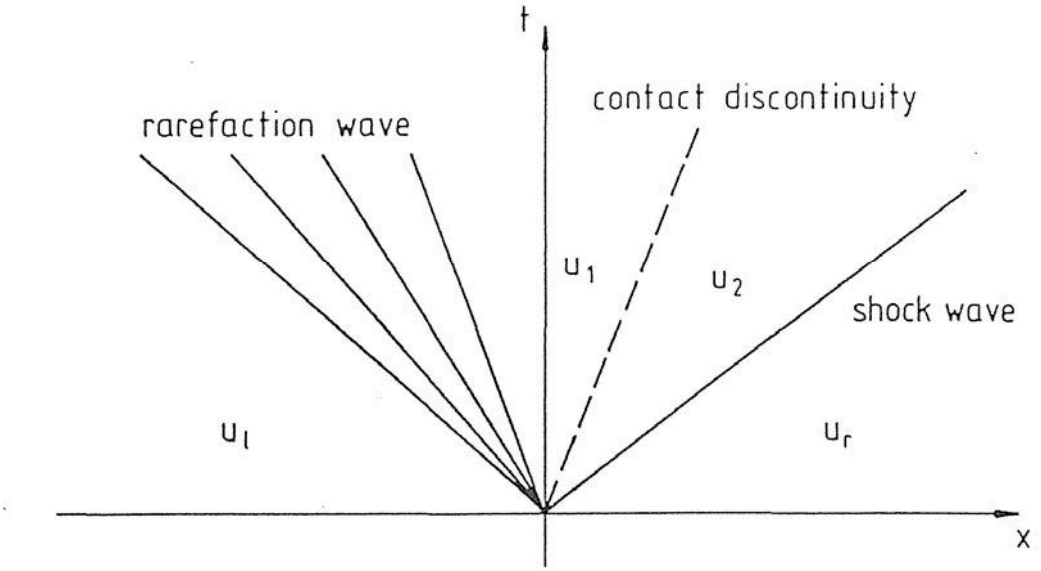

Fig. 3.1. Single fluid shock tube solution in the (x, t)-plane.

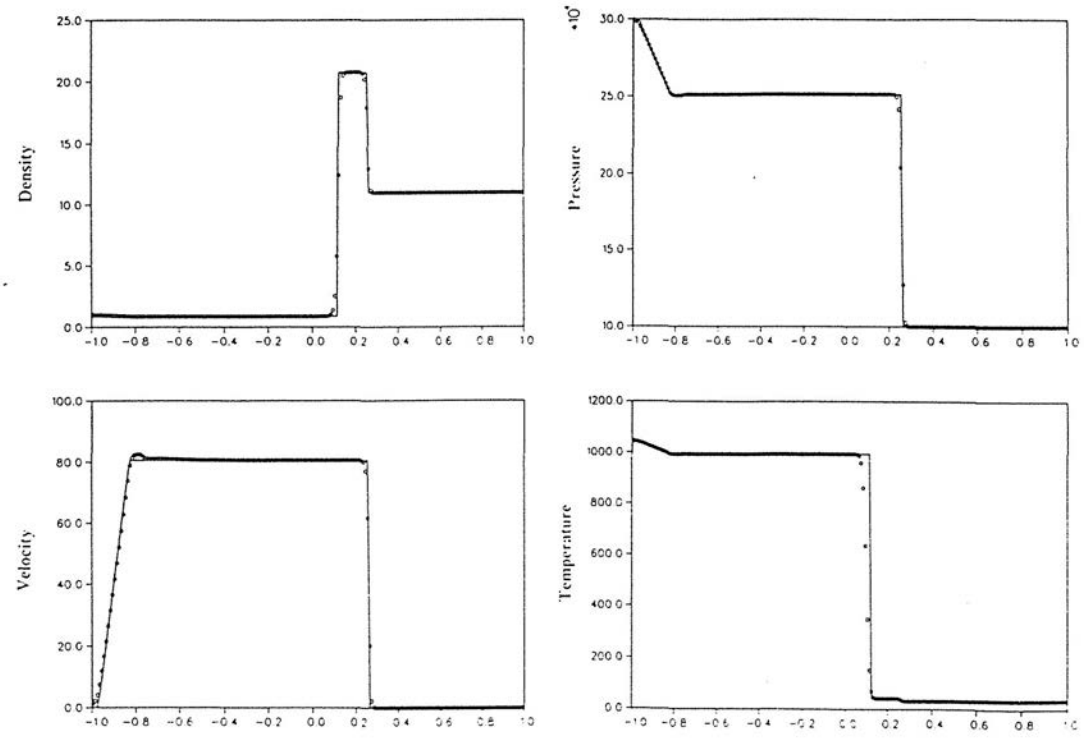

Fig. 3.2. Numerical solution with constant γ at t = 1.5 ms.

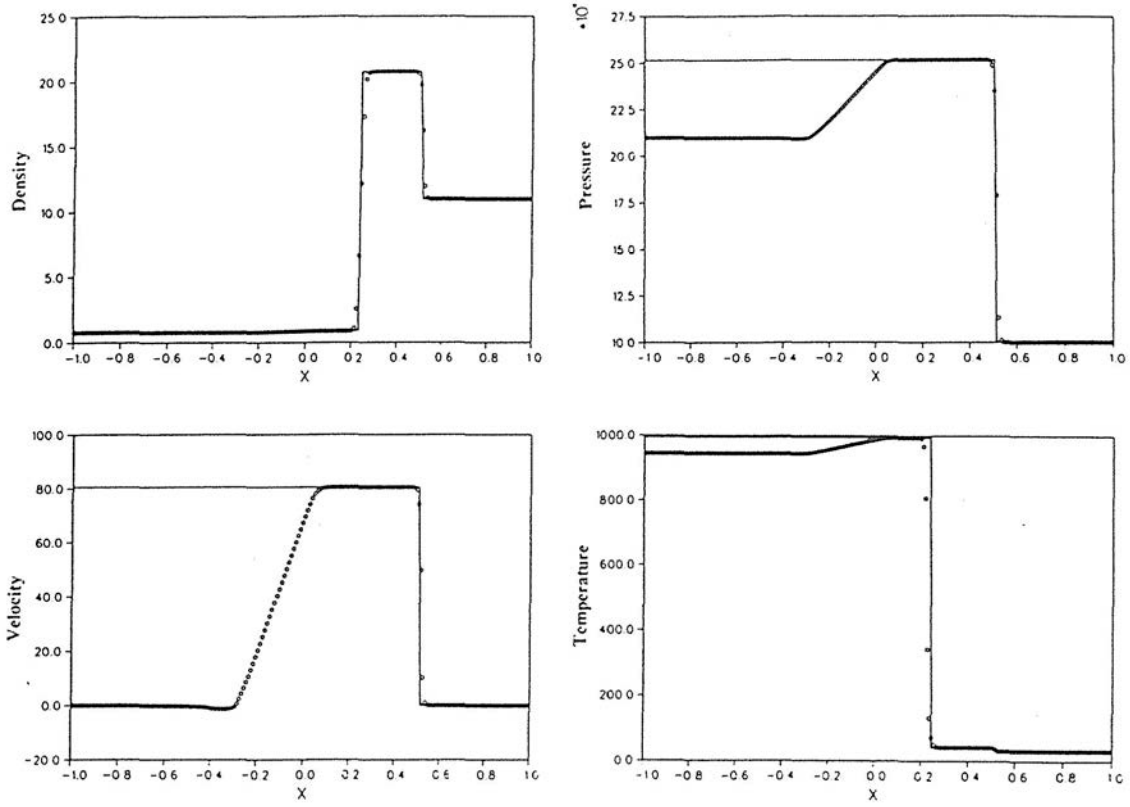

Fig. 3.3. Numerical solution with constant γ at t = 3.0 ms.

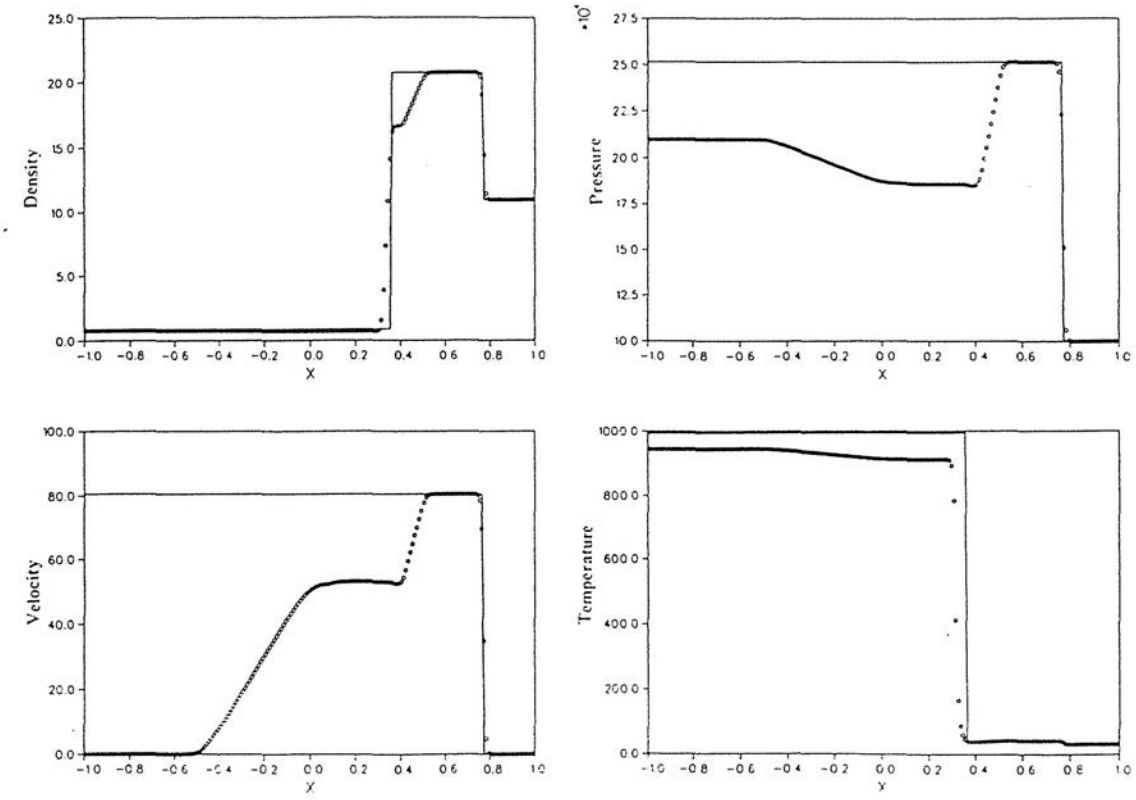

Fig. 3.4. Numerical solution with constant γ at t = 4.5 ms.

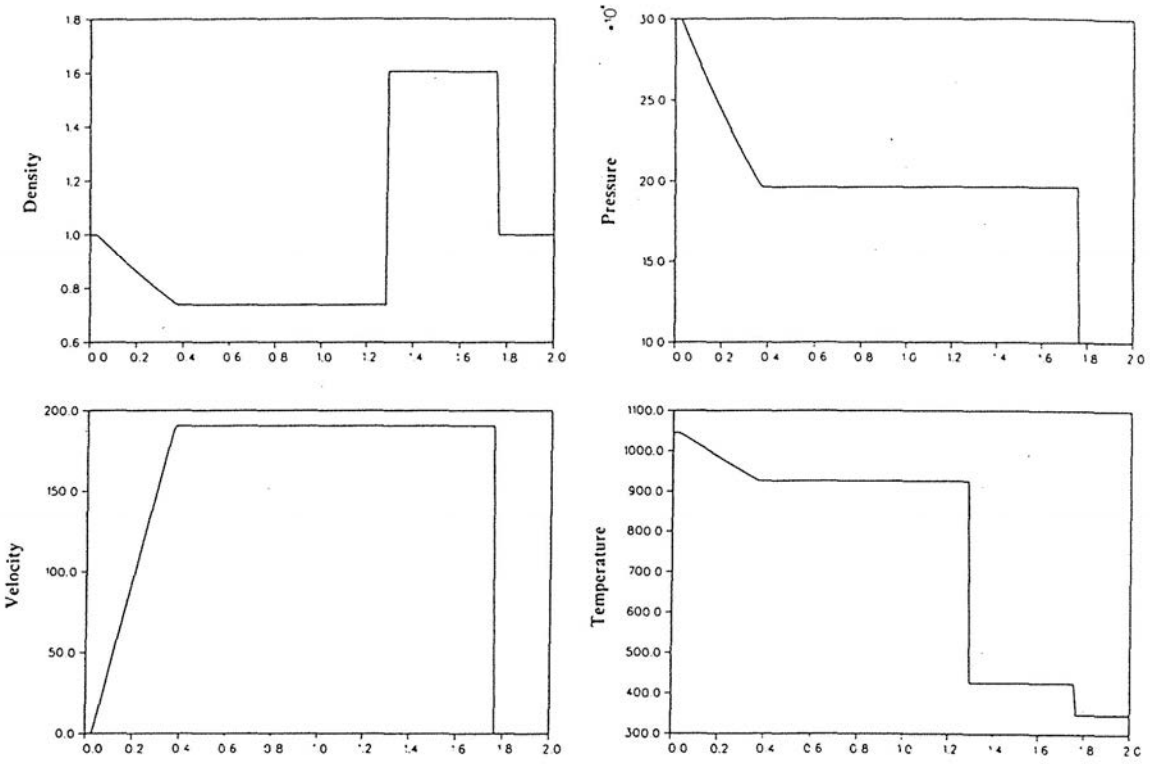

Fig. 3.5 Exact solution of the gas dynamic shock tube problem at t = 1.5 ms.

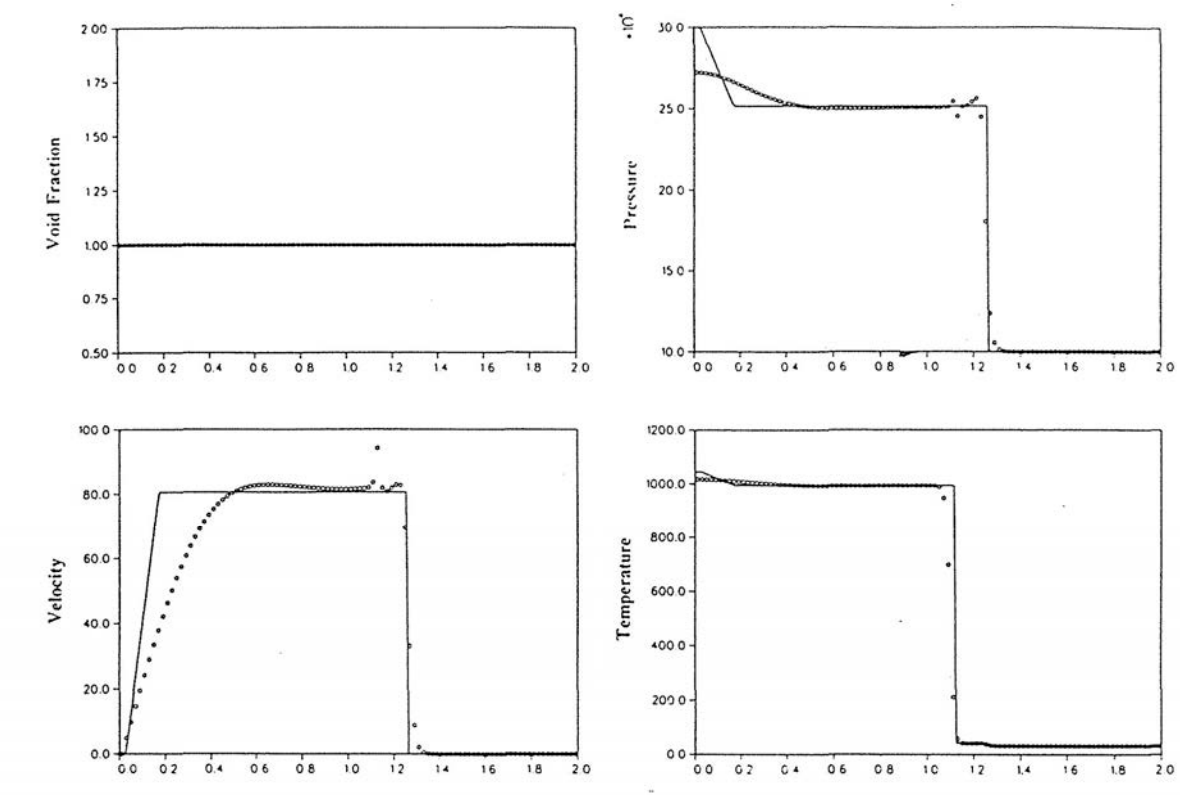

Fig. 6.1. SIMMER-III results for single fluid approximation.

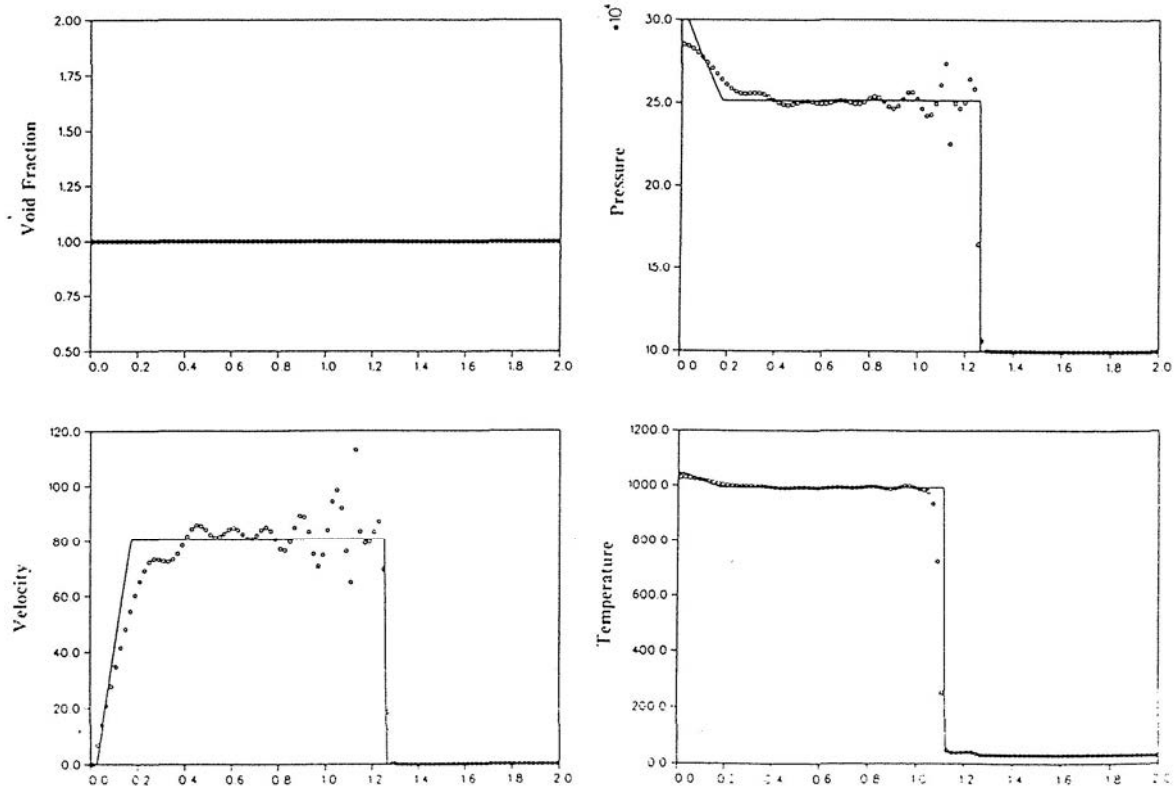

Fig. 6.2 SIMMER-III results for single fluid approximation; small time steps.

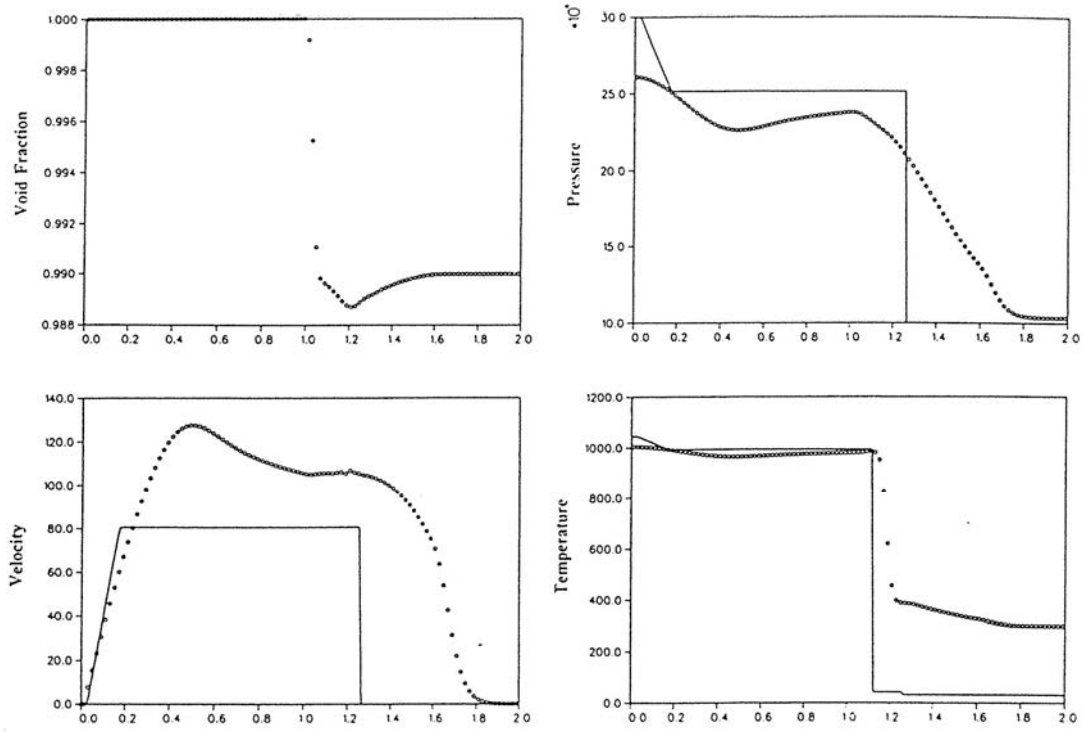

Fig. 6.3. SIMMER-III results for two phase shock tube problem in comparison with single fluid approximation at time 1.5 ms.

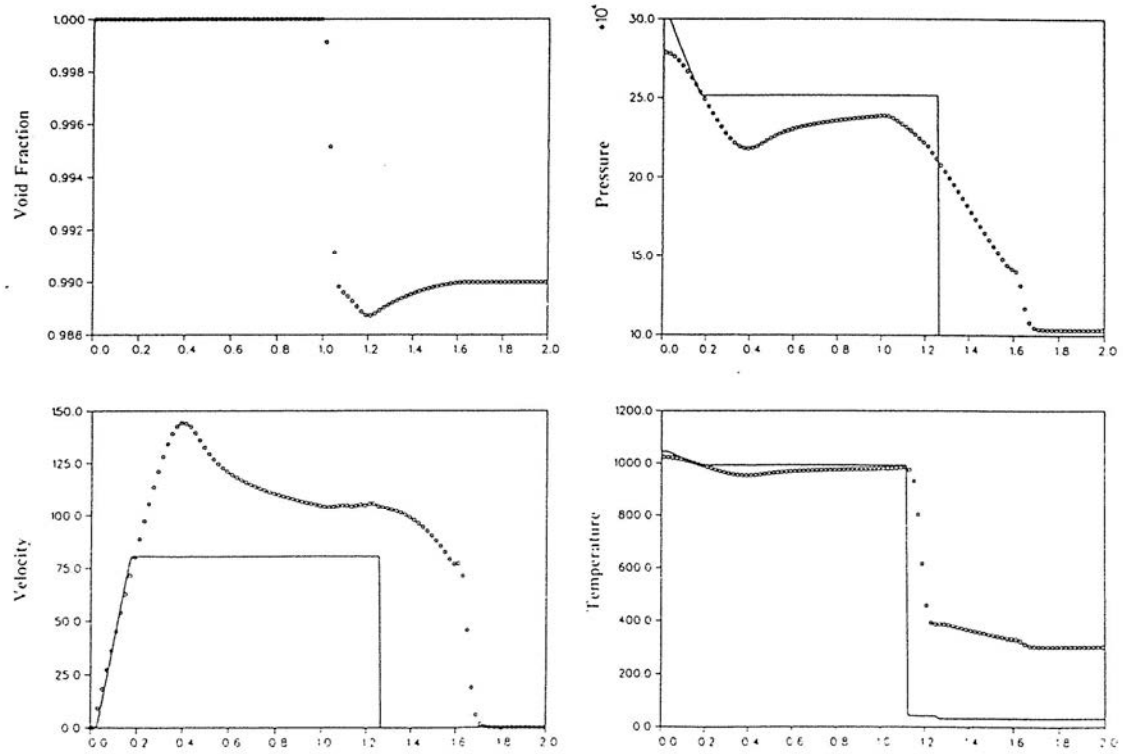

Fig. 6.4. SIMMER-III results for twp phase shock tube problem in comparison with single fluid approximation at time 1.5 ms, small time steps.

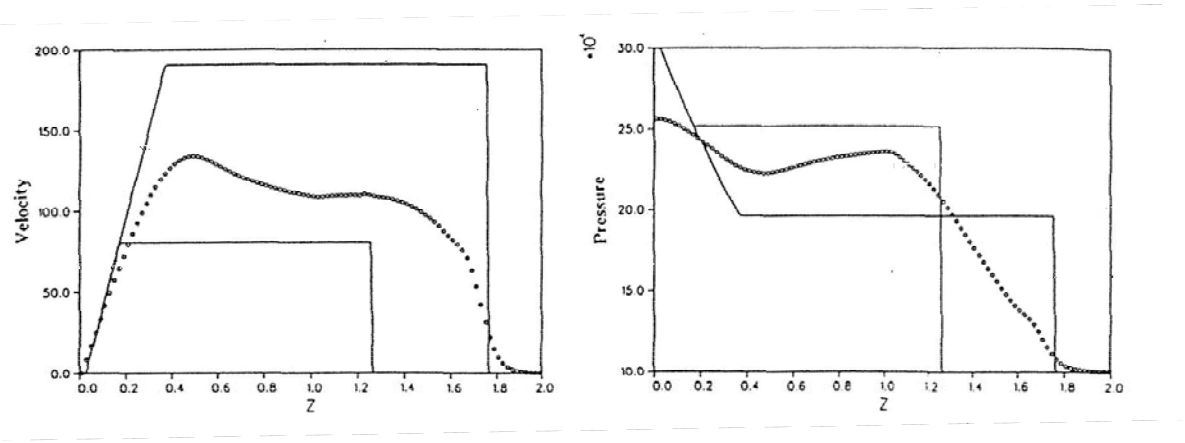

Fig. 6.5. Comparison of SIMMER-III Results (ooo) with single-fluid approximation (---) and pure gas solution (---) at time t = 1.5 ms.

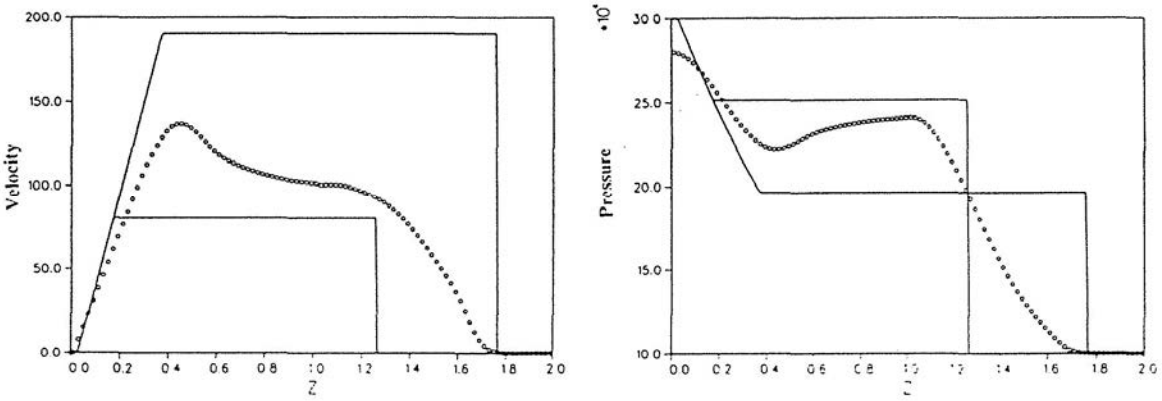

Fig. 6.6. IVA-KA results for the two phase shock tube problem in comparison with single fluid approximations at time 1.5 ms.

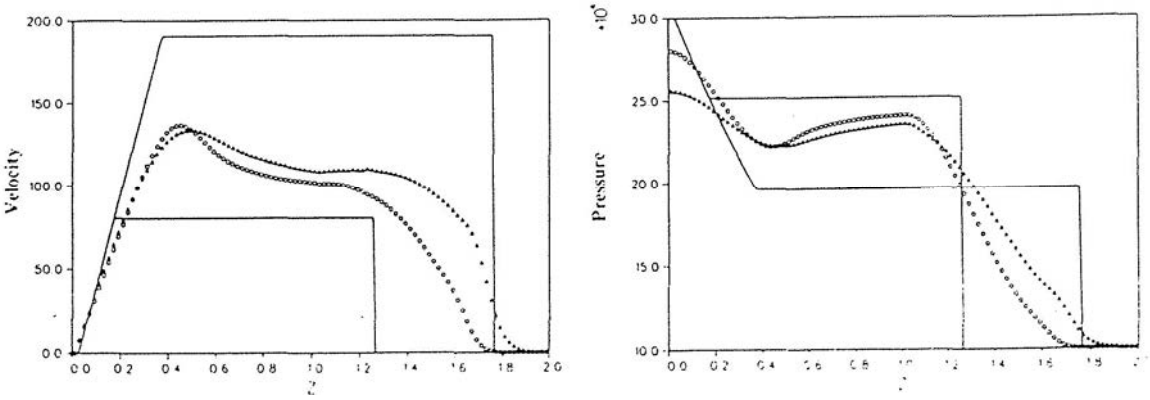

Fig. 6.7. Comparison of IVA-KA (■■■) and SIMMER Ill (ΔΔΔ) results.

Problem 1.3: Oscillating manometer

"Oscillating Manometer in 1D and 2D"

Thierry Jeanne (IPSN)

Outline of the Case

The problem consists of a « U » tube manometer which is connected at the top, so that a closed system is formed. The system initially contains gas and liquid with the liquid forming equal collapsed levels in each arms of the manometer, further all parts of the fluid system have a uniform velocity, but zero acceleration. The initial velocity is specified to be large enough to cause the vapor-liquid interface to cross node boundaries. The system will oscillate until damped by numerical dissipation.

1. Objectives of the Application

The objectives ofthis problem are:

- to test the ability of the numerical solution method to preserve system mass, which is a constant and to compare the calculated parameters (velocity, period, ...) with analytical results as well as those of the other implicit codes,
- to model the period of oscillations, which is analytically known,
- to evaluate the capability of the numerical discretization scheme to retain the gas-liquid interface.

2. Benchmark problem

For this benchmark problem [1], the fluid motions are simulated by water and air under the following initial conditions (Fig. 1):

- isothermal throughout at 50°C temperature,
- pressure at the interfaces between the vapor and the liquid equal to 1.013×10^5 Pa,
- length of the manometer: 20 m (10 m for each arm), and diameter: l m,
- initial position of the liquid-vapor interface : 5.0 m above the bottom of each manometer leg,
- all fluid initially has a velocity V_0 of 2.1 m/s,
- the two legs are superposed but for one leg, the gravity is negative.

The comparison of the SIMMER-III calculation with the other implicit codes, will be performed on the maxima and minima values of:

- the mass flow rate at the bottom of the manometer,
- the total amount of liquid in the right and left legs,
- and on the time at which they occur.

The calculations must be made with a nominal time-step equal to 0.025 s in order to facilitate the comparison of results. The behaviour of the oscillating manometer is simulated for 20 seconds.

3. Analytical solution

For the presentation of the analytical solution, we use the following notation:

- L: the length of the liquid column (10 m),
- x : the liquid level in the right leg of the manometer relative to the initial position of the liquid.

Without wall friction, the oscillating motion of a liquid in the « U » tube as modelled obeys the following equation (if the change of direction at the bottom is smooth and does not introduce a pressure loss):

$$\frac{d^2x}{dt^2} + \frac{2gx}{L} = 0$$

With the following initial conditions:

$$\begin{cases} t = 0 \\ x = 0 \\ dx/dt = V_0 \end{cases}$$

The solution of this equation is:

$$\mathrm{x} = V_0 \sqrt{\frac{L}{2g}} \sin\left(\sqrt{\frac{2g}{L}} t\right)$$

The liquid velocity is:

$$V = \frac{dx}{dt} = V_0 \cos\left(\sqrt{\frac{2g}{L}} t\right).$$

4. Understanding of phenomena

The oscillating manometer is a simple benchmarck, which presents an analytical solution. The main interest of this test case is to show the numerical diffusion effect on the mass transfer between the cells, during the liquid oscillating motion.

As the numerical diffusion depends on the resolution method, to validate SIMMER-III in lD, we will only compare the results with those obtained with other implicite formulation codes (CATHARE [ISPRA], CATHARE [CENG], PHOENICS, THERF), and will show that we get similar results. The results of each code are plotted on Figs. 2 and 3.

5. SIMMER-III Representation

5.1 Geometry, initial and boundary conditions for the reference case

A 1D mesh is used including two similar columns which are coupled at the top and the bottom. The mesh scheme, geometry and initial conditions are illustrated in Fig. 1. Thus, the problem is a closed and adiabatic system, the thermal boundary condition is a zero heat flux at the wall. The friction between the

liquid and the wall is not taken into account. A higher order differencing method is used in the reference case.

As suggested in this benchmark problem[1)], we imposed the nominal time step to 0.025 s in order to facilitate comparaison of results between the different implicite codes listed previously.

5.2 Code modifications

To perform the 1D calculations, the code version includes some modifications which allow the coupling of the top and of the bottom of the two legs of the manometer as illustrated in Fig. 1. The modifications concern the subroutines « VITER; VITERP and WORK » to do the system at the boundary conditions, and to simulate the gravity direction change applied to the fluid motion passing from one leg of the manometer to the other leg.

5.3 Parametric cases

In 1D, the parametric calculation is based on the donor cell numerical method (first order differencing scheme) to solve the mass, momentum and energy equations.

We completed this study by a partial 2D geometry analysis with a simple meshing [I=l,2; J=l,10] which is represented in Fig. 4. The transverse liquid motion is avoided by the use of the code option « virtual wall » between the cells of the two columns at the axial position [J=2,9]. With these conditions, the connection between the two legs is applied at the bottom and the top of the system and allows respectively the liquid and the gas motions during the transient calculations.

In this parametric case, as in 1D geometry, we compare the SIMMER-III solution methods using the higher order differencing scheme with the donor cell differencing scheme.

6. Results and discussion

In general, we noticed on every calculation result, a correct reproduction of the period of the phenomena, with a decrease of the oscillation amplitude due to diffusion process which differs according with the use of 1D or 2D scheme. A comparison of the reference test case (higher order differencing method in 1D) with the other implicit codes formulation shows that the transient behavior is similar as recalled in Figs. 2 and 3.

6.1 One dimension calculations

In the 1D calculations, we cannot impose the time step to 0.025 s as it is suggested in this benchmark problem, and we observed that all the calculations are controlled by an optimum pressure iteration criterion.

We found that in the reference case, the diffusion is smaller than when using the donor cell method. This behavior can be seen in Figs. 5 and 6 where is plotted the liquid volume fraction distribution in the cell

at the maxima and minima values of the calculated liquid mass in the two legs of the manometer during the transient.

In the reference case, the mass distribution covers twelve meshes, with a full liquid mesh distribution except for the two meshes on each part of the liquid column. Whereas in the other case, the mass repartition covers twelve meshes at the beginning of the transient and thirteen meshes after 5.6 s, showing a parabolic distribution.

As far as the period of the phenomena is concerned, we can notice on Figs. 7 and 8 (extremum values are recalled in Tables 1 and 2), that the higher order reference case is in a very good agreement with the analytic solution. For the donor cell parametric case the results are correct but we can show a small increase of the period during the transient.

These results can be explained by the diffusion effect due to the liquid represention in the cell by droplets. In fact, for a mesh which is voiding, the code does not calculate its free liquid surface evolution but assumes that the liquid is represented by a droplet uniform distribution. With this condition the hydrostatic pressure inside a mesh is reduced inversely to the liquid mass (Figs. 9 and 10) and the viscosity force between droplets depends on the cell liquid volume fraction. When the liquid volume fraction decreases below a characteristic value, the viscosity forces are being to be neglected and the droplet will be mainly submitted to the gravity force. This effect causes an acceleration of the liquid until the voiding of the cell, which involves an increase velocity above the initial value V_0 (maximum of the velocity in the analytic solution).

In the two test cases, we observe this behaviour when the liquid volume fraction decreases below 0.1 (Figs. 11, 12, 14 and 15). With the higher order method we take into account the acceleration effect and we get for cells number (1,16) and (1,17) larger liquid velocity than with the donor cell method. The numerical method effect causes the cell voiding more quickly in the reference case. If we compare the mass quantity in the left and right legs of the manometer, we can observe in Figs. 5 and 6 for the two calculations, that the two first meshes in the direction of the liquid motion are every time fuller than the two last meshes. This effect explains that on Fig. 7, for the higher order test case, the total liquid mass in the left leg, when compared with the analytic solution, shows during the transient a larger discrepancy at the maximum values than those obtained at the minimum values. However, in the donor cell parametric case, as the diffusion is more important and involved a parabolic liquid distribution, this effect cannot be observed and the liquid mass amplitude decrease shows a regular behaviour at the successive maximum and minimum positions.

During the transient calculation of the reference test case, we can also observe, when the velocity reaches its extremum values (Fig. 11), that the velocity of the cell (l,16), determined on the interface between the cells (1,16) and (1,17), has an abnormal oscillating periodic behavior. However, we can notice that this abnormal velocity variation appears when the cells (1,16) and (1,17) are nearly empty, and must be probably linked to the lack of pressure iteration stability.

Consequently as the cell voiding is slower in the donor cell test case, the minimum liquid positions in each leg of the manometer are obtained later, and explain a small increase of the period during the transient (Figs. 7 and 8). For the higher order test case as the velocities are greater, the liquid mass in the upper cells is less important and this effect on the minimum position is less important. This point explains that we do not observe a variation of the period in the reference calculation.

If we look at the cell pressures during the transient in the left leg of the manometer in the reference case (Fig. 9) we can observe at 2.16235 s on cells full of water, some higher pressure peaks which decrease from the bottom cell to the top cell. These pressure peaks appear when we get the maximum velocity at the bottom of the manometer, the interface between the cells (1,10) and (1,11). As at this interface the maximum velocity is obtained just before it is obtained in the other cells, when the velocity begins to decrease the quantity of liquid mass which enters is more important than the quantity which gets out. This behaviour causes a compression of the full liquid cell (1,10), and involves a pressure peak. This compressive effect is transferred to the upper cells full of water. In the donor parametric test case, as the diffusion is more important with a parabolic distribution, the velocity decrease at the bottom of the manometer does not involve the compression of cells full of water.

Another consequence of the numerical diffusion effect is that during half a period when the liquid passes from one leg to the other, the meshes which are not totally full, have a coherent behaviour (Figs. 12 and 14). However when the liquid motion is inversed, these meshes have an incoherent behaviour with regard to the main part of the liquid (Figs. 11 and 13), and causes a loss of momentum.

6.2 Two dimensions calculations

In the 2D calculations, the time step as it is suggested in this benchmark problem, is respected and imposed to 0.0025 s.

In these calculations, we observed a larger decrease of the amplitude than in the 1D calculations (Figs. 14 and 16). This behaviour is due to the cumulative effects of the numerical diffusion and of the modification of the direction of the liquid motion at the bottom of the manometer. As the numerical diffusion behaviour is similar to the 1D test cases, we will focus in this second part on the velocity direction change effect.

The 2D geometrical representation involves to the liquid motion a direction change at the bottom of the manometer. This mesh representation causes a loss of momentum by a velocity reduction determined by the velocity continuity equation in the mesh cell center. Initially, this reduction is equal to « $V_0/\sqrt{2}$ » as shown in Fig. 17. On the mass flow rate results at the bottom of the manometer (Fig. 8) we added the function linked to the decrease of the mass flow rate determined at the maxima and the minima values, where we applied successively the previous reduction:

$$\begin{cases} W_0 = V_0 \\ W_{kT/2} = \left(\frac{-1}{\sqrt{2}}\right)^k W_{(k-1)T/2} \\ k \in N \end{cases}$$

With these conditions, on Fig. 8, we observe on the first minimum value a good agreement with the decreasing function by direction change, but for the other minima and maxima values the amplitudes calculated by the higher order and by the donnor cell test cases are larger than those obtained with this decreasing function. This behaviour is explained by the initial condition of the problem. In fact, at the beginning of the calculation the loss of momentum is applied to the liquid mass which passes from the right leg to the left leg and does not correspond to the initial mass contained in the left leg. The potential energy accumulated during the transient at the liquid maxima positions in the two SIMMER-III calculations are more important than those obtained by the decreasing function which considers a loss of momentum applied to the whole liquid columns at each liquid motion direction change.

As in the 1D analysis, we observe in Figs. 7 and 8 respectively for the liquid mass variations in the left leg and for the mass flow rate at the bottom of the manometer (extremum values are recalled in Tables 3 and 4), that the numerical diffusion which affects the amplitude decrease during the transient is larger in the donnor cell test case than in the higher order test case.

Concerning the period we observe a good agreement with the analytic solution. However we notice during the transient a small increase of the period of the same order in the two calculations when compared with the analytic solution. But if we compare it to the 1D donor cell test case, we can observe that this increase is less important. This behavior is due to the loss of momentum due to the direction change which causes less liquid diffusion between the cells.

By comparison with the 1D test case, as the mass variation in each leg of the manometer is less important by lost of momentum due to the direction change, a reduced number of cells are affected by the water voiding or filling and a better stability of the pressure iterations is obtained.

Remark: as in this case, there is a sudden change of direction at the bottom, a physical pressure loss exists and corresponds to the kinetic energy, which is equal to « $k\rho v^2$ » with « k » close to « 2 » (double bend). This term should have been considered in the analytic equation and would have introduced a damping effect. This could explain the damping observed in SIMMER-III.

7. Conclusions

The manometer benchmarck problem as calculated with the SIMMER-III code, shows a satisfactory behaviour similar to the other implicit code results. Using the higher order differencing method (reference case) we get less numerical diffusion than when using the 1D donor cell method (parametric case) which leads for the liquid motion to a parabolic distribution form.

We also observe when using the donor cell method that we get a small increase of the period due to the difficulty to void the cell, which causes a delay to get the minimum position of the liquid in each leg of the manometer. This effect does not appear in the reference case as the acceleration is taken into account to calculate the velocity variation which induces a faster cell voiding. Except these small discrepancies, these two calculations show that the total mass variation in each leg and the mass flow rate at the bottom of the manometer are very consistent.

With regard to the 2D calculations, the scheme used is limited to two axial columns with one horizontal mesh which causes to the liquid motion an orthogonal direction change at the bottom of the manometer. We show that this geometrical representation causes a loss of momentum during the transient at each inversion of liquid motion. The amplitude of the total mass variation in each leg and the mass flow rate at the bottom of the manometer decrease faster when compared with the 1D results. We can also observe that after a few oscillations the variation of the extremum values of the liquid mass in one leg shows a better behaviour when using the higher order numerical method than when using the donor cell method.

This study could be improved by adding more parametric test cases which could take into account the effect of:

- different initial liquid position in each leg with a zero initial liquid velocity (in 1D or 2D),
- direction change at the bottom of the manometer based on a refined discretization which can lead to reduce the loss of momentum.

8. Recommendations for model improvements

Taking into account the results of this benchmark, the behaviour of the SIMMER-III code is coherent with regard to the other implicit codes (CATHARE, PHOENICS and THERF).

9. Reference

1) G. F Hewitt, J.M. Delhaye, N. Zuber: Numerical Benchmark Test n° 2.2, Problem devised by V. H. Ramsom, Multiphase Science and Technology, Volume 6.

Tables 1 – 4: Maxima and minima liquid mass (kg) in each leg of the manometer, and mass flow rate (kg/s) at the bottom of the manometer for each calculation

Table 1. 1D SIMMER-III test case usmg the higher order numerical method.

Time	Mass in left leg	Mass in righ leg	Time	Mass flow rate at the bottom
0.00000	4913.740	4913.740	0.00000	2063.816
1.08195	6235.947	3591.283	2.16235	-1810.782
3.37880	3628.656	6198.511	4.46353	1727.276
5.67952	6112.225	3714.929	6.89614	-1654.915
7.84368	3711.685	6115.446	8.92429	1564.343
10.14058	5946.179	3880.939	11.3540	-1497.721
12.29778	3789.372	6037.733	13.3801	1411.267
14.59620	5806.161	4020.933	15.8155	-1337.785
16.75988	3889.892	5937.195	17.8339	1238.820
19.05431	5680.269	4146.798		

Table 2. 1D SIMMER-III test case using the donor cell numerical method.

Time	Mass in left leg	Mass in righ leg	Time	Mass flow rate at the bottom
0.00000	4913.740	4913.740	0.00000	2063.82
1.08247	6196.458	3630.731	2.30182	-1768.59
3.38336	3703.418	6123.613	4.46225	1604.27
5.67709	6038.060	3788.905	6.75994	-1519.84
7.98088	3867.211	5959.698	9.05609	1402.00
10.27056	5878.717	3948.143	11.49188	-1279.29
12.57901	4022.062	5804.751	13.64959	1161.16
14.86908	5734.077	4092.701	15.95176	-1064.89
17.29932	4153.281	5673.458	18.38249	987.261
19.60066	5620.021	4206.502		

Table 3. 2D SIMMER-III test case using the higher order numerical method.

Time	Mass in left leg	Mass in righ leg	Time	Mass flow rate at the bottom
0.00000	4913.740	4913.740	0.00000	2063.816
1.10000	6103.109	3724.172	2.05000	-1402.784
3.25000	4081.603	5745.588	4.32500	970.650
5.55000	5531.658	4295.492	6.77500	-743.016
7.85000	4415.985	5411.145	9.07500	620.958
10.15000	5341.219	4485.898	11.37500	-548.720
12.45000	4528.745	5298.364	13.65000	504.778
14.75000	5271.474	4555.629	15.95000	-476.796
17.05000	4572.805	5254.294	18.52500	458.685
19.32500	5243.974	4583.121		

Table 4. 2D SIMMER-III test case using the donor cell numerical method.

Time	Mass in left leg	Mass in righ leg	Time	Mass flow rate at the bottom
0.00000	4913.740	4913.740	0.00000	2063.816
1.10000	6083.748	3743.454	2.05000	-1371.101
3.40000	4084.553	5742.539	4.47500	1039.590
5.70000	5538.276	4288.758	6.77500	-790.725
7.97500	4445.467	5381.531	9.07500	593.995
10.27500	5255.190	4571.783	11.37500	-431.891
12.57450	4668.086	5158.864	13.65000	312.849
14.75000	5093.340	4733.595	15.82500	-225.636
16.90000	4777.386	5049.541	18.25000	176.410
19.32500	5035.528	4791.399		

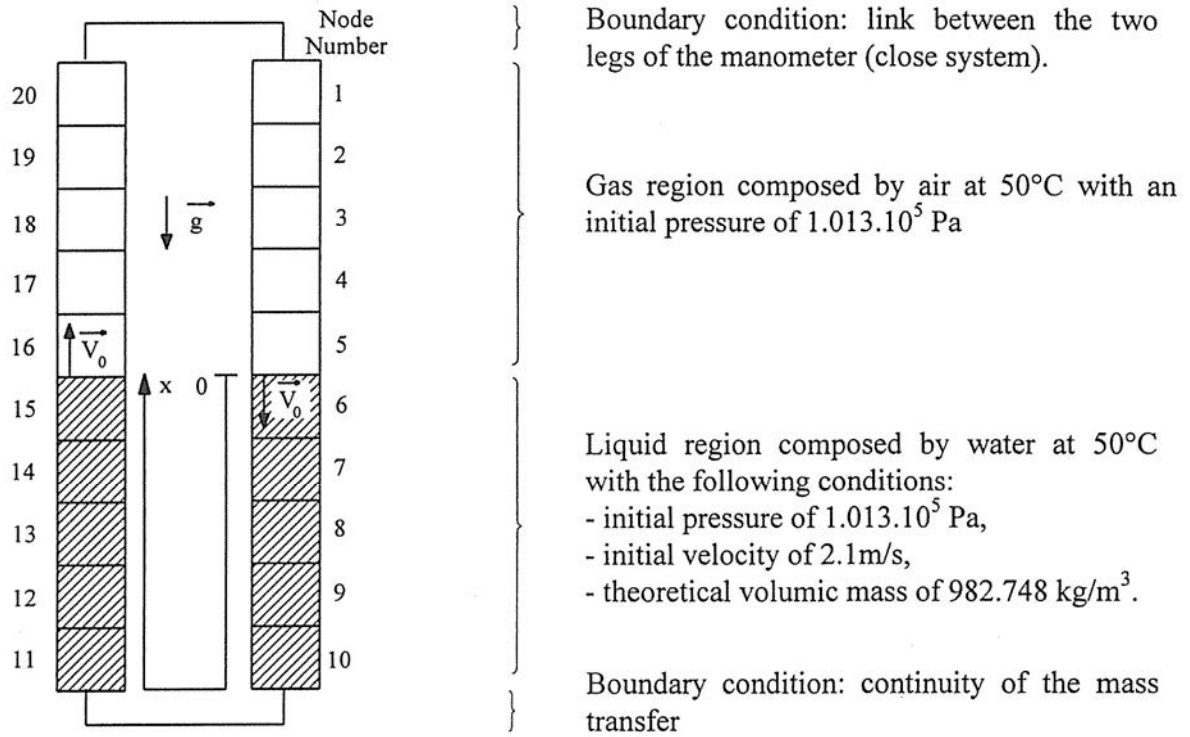

Fig. 1. 1D geometrical mesh cell representation.

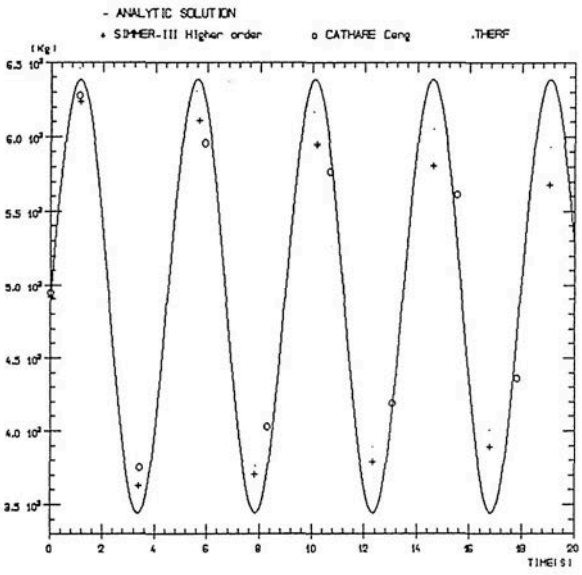

Fig. 2. the implicit formulation codes results concerning the maxima and minima value of the mass in the left leg of the manometer.

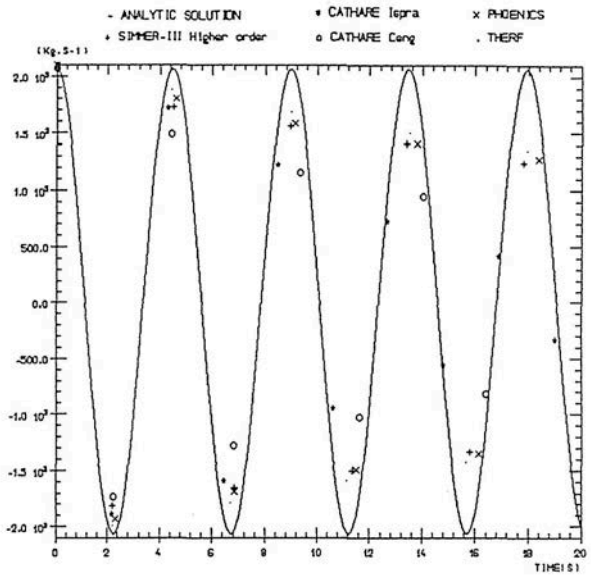

Fig. 3. the implicit formulation codes results concerning the maxima and minima values of the mass flow rate at the bottom of the manometer.

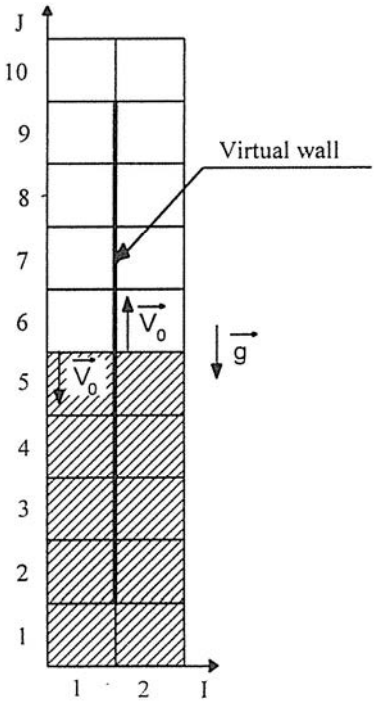

The description and the thermal hydraulic caracteristics of the physical regions are similar to those in the figure 1
The « virtual wall » conditions is used to suppress the radial fluid motion

Fig. 4. 2D geometrical mesh cell representation.

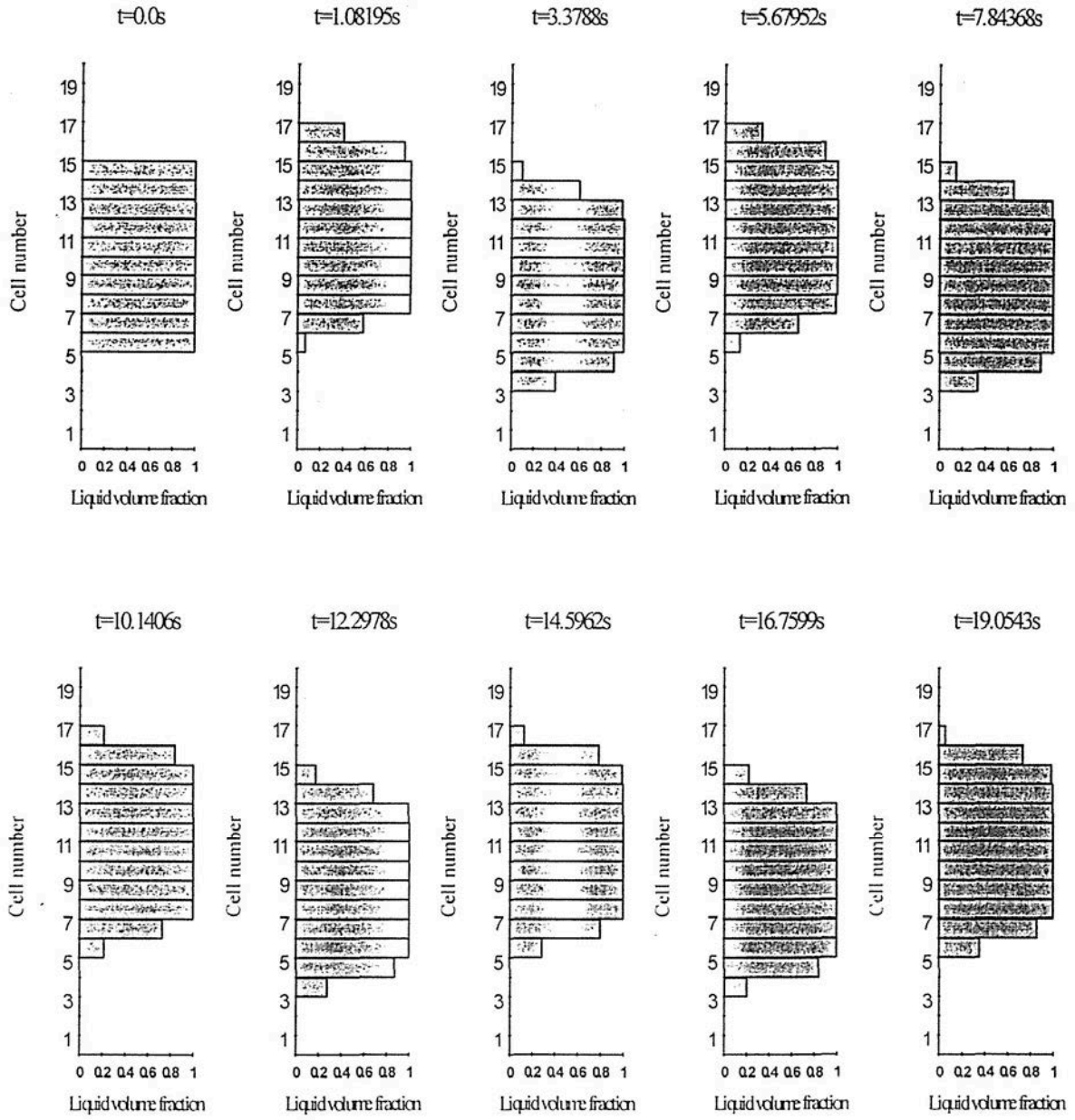

Fig. 5. Liquid volume fraction distribution at the maximum and minimum liquid mass in one leg. (1D reference case with the higher order numerical method)

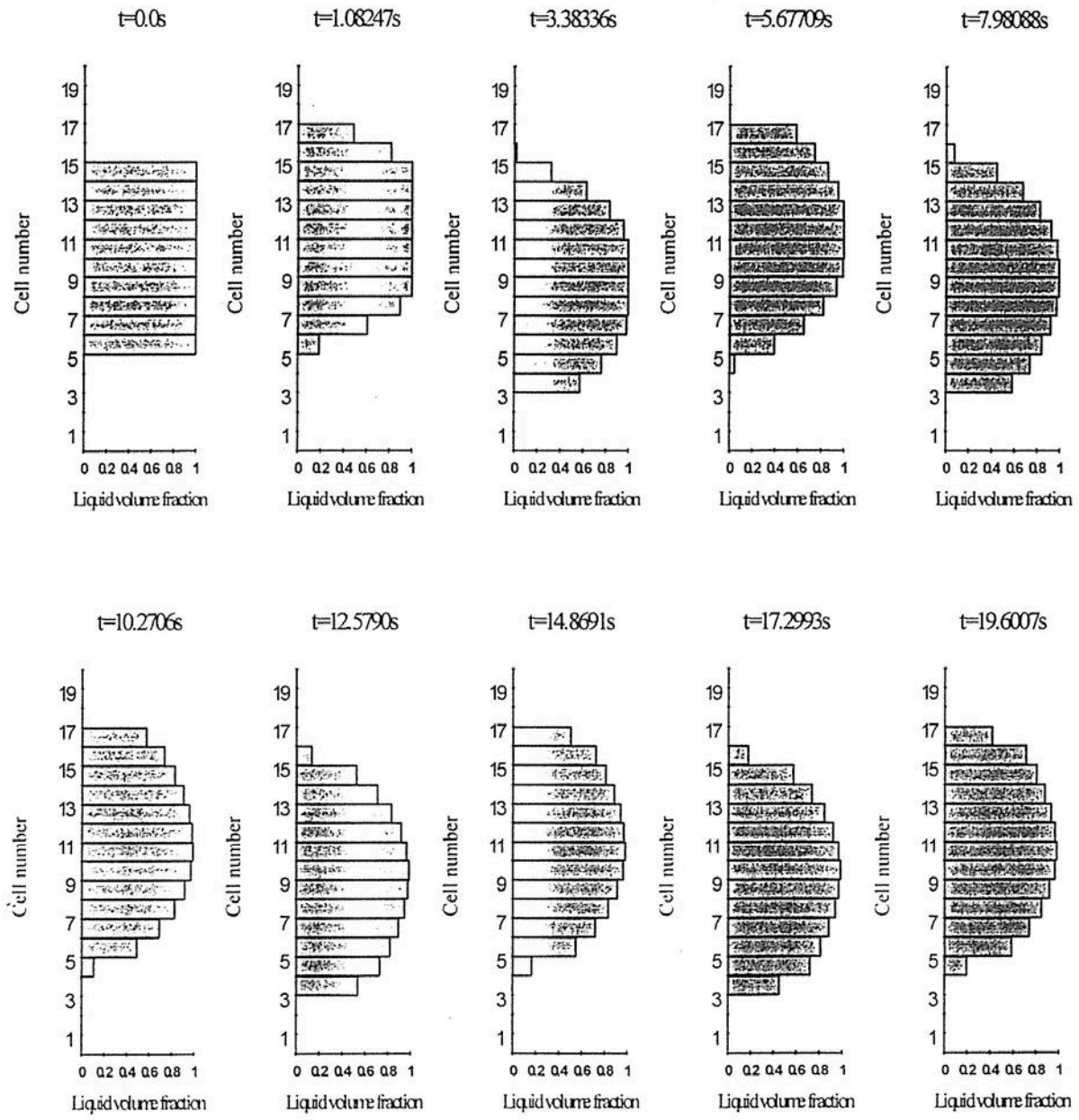

Fig. 6. Liquid volume fraction distribution at the maximum and minimum liquid mass in one leg. (1D parametric case with the donor cell numerical method)

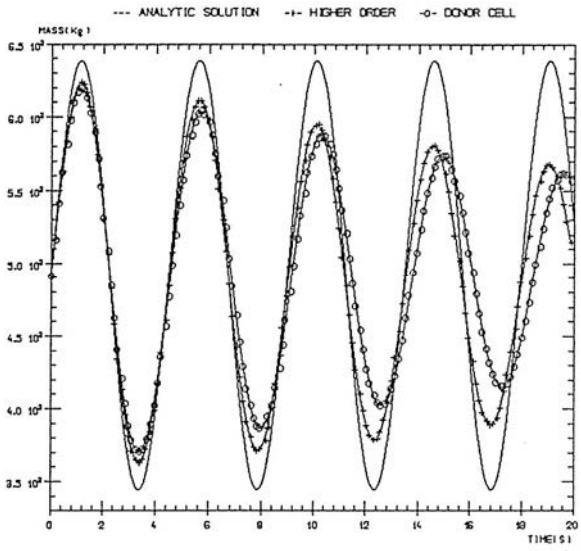

Fig. 7. 1D SIMMER-III results: liquid mass in the left leg of the manometer.

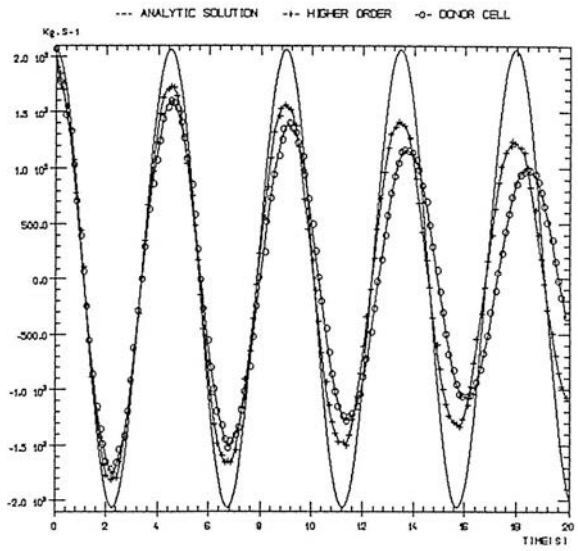

Fig. 8. 1D SIMMER-III results: mass flow rate at the bottom of the manometer.

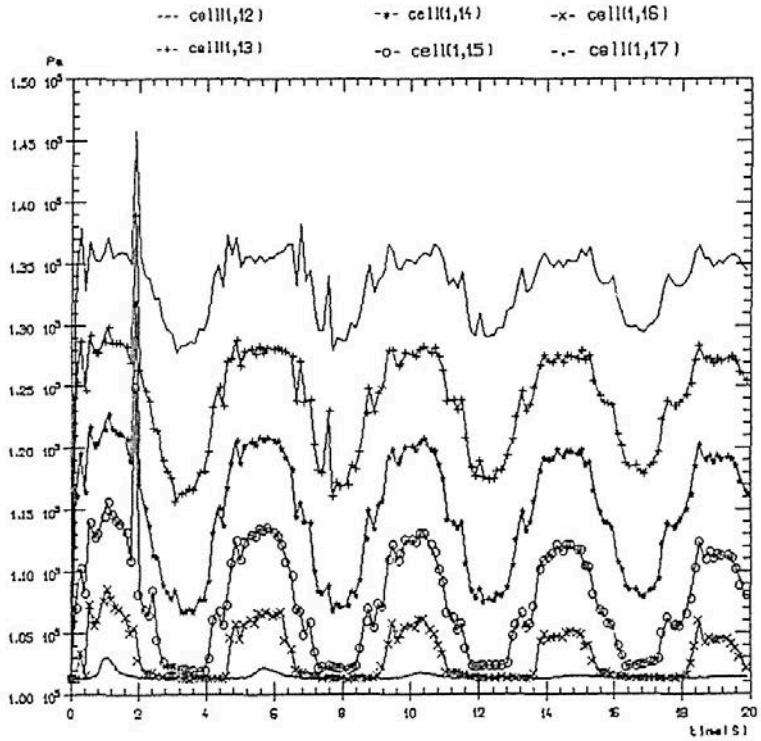

Fig. 9. 1D SIMMER-III results using the higher order numerical method showing the transient pressure of characteristic meshes.

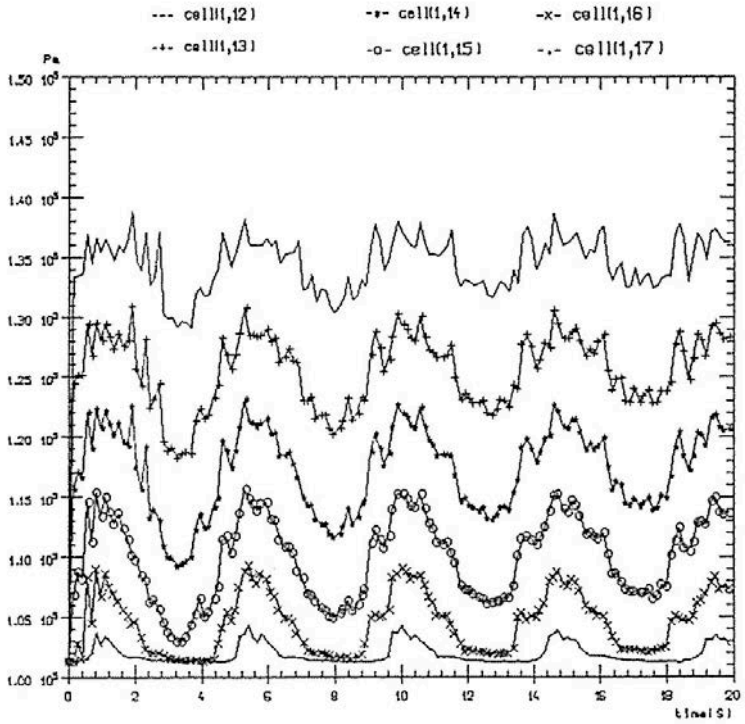

Fig. 10. 1D SIMMER-III results using the donor cell numerical method showing the pressure evolution of characteristic meshes.

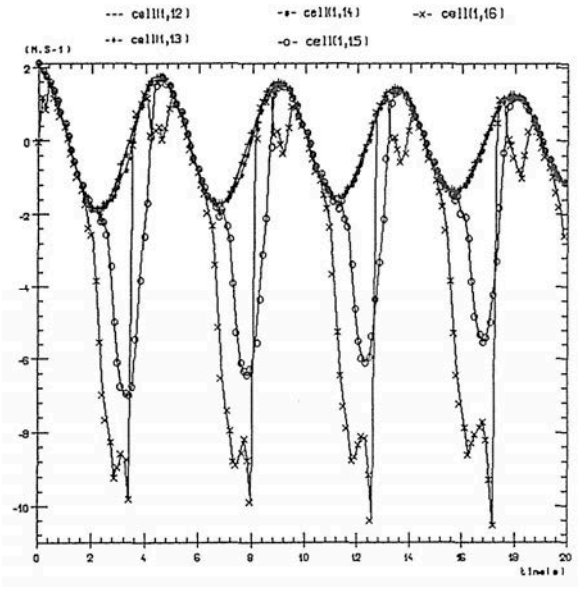

Fig. 11. 1D SIMMER-III results using the higher numerical method showing the velocity evolution of characteristic meshes.

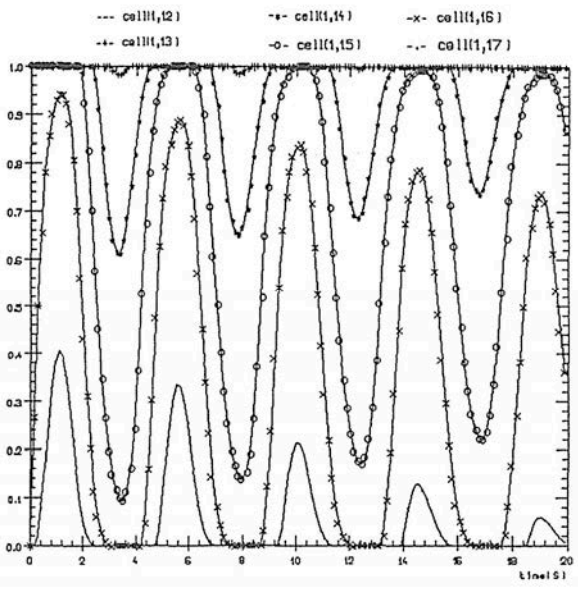

Fig. 12. 1D SIMMER-III results using the higher numerical method showing the evolusion of the liquid volume fraction of characteristic meshes.

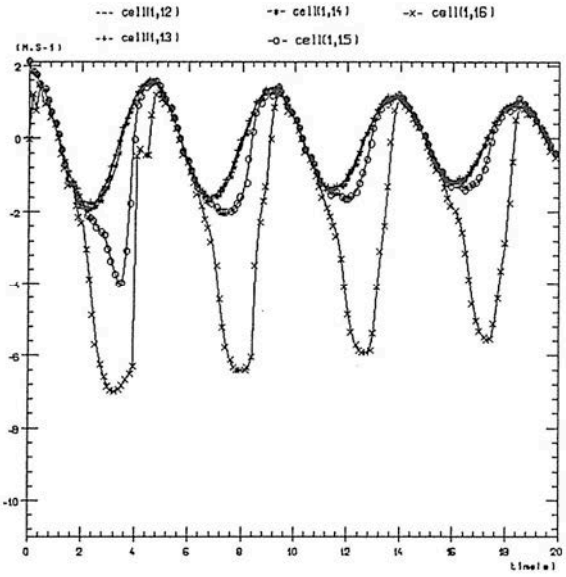

Fig. 13. 1D SIMMER-III results using the donor cell numerical method showing the velocity evolution of characteristic meshes.

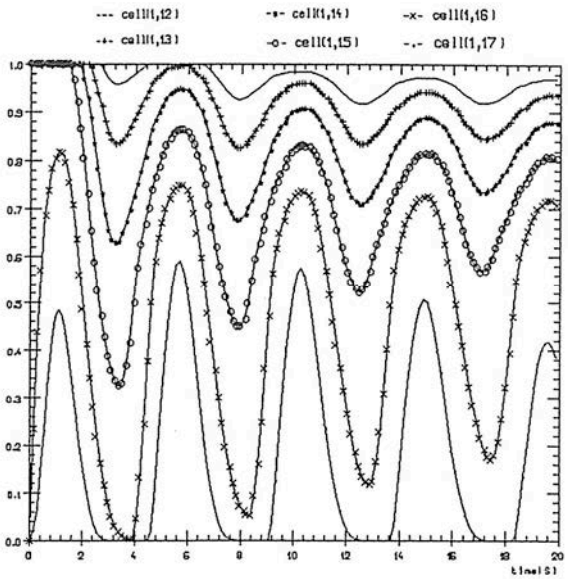

Fig. 14. 1D SIMMER-III results using the donor cell numerical method showing the evvolution of th liquid volume fraction of characteristic meshes.

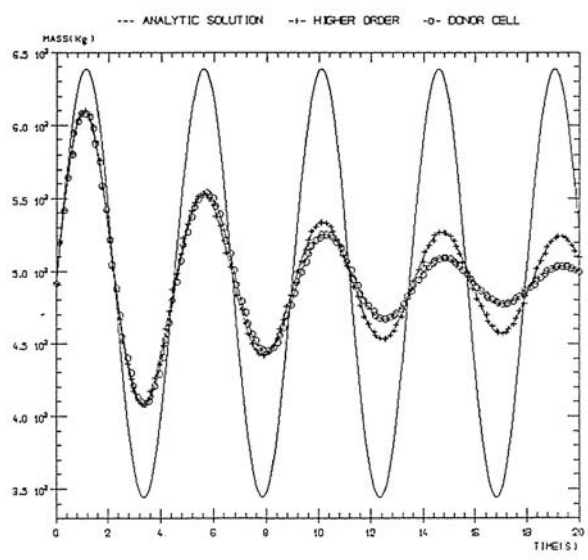

Fig. 15. 2D SIMMER-III results: liquid mass in the left leg of the manometer.

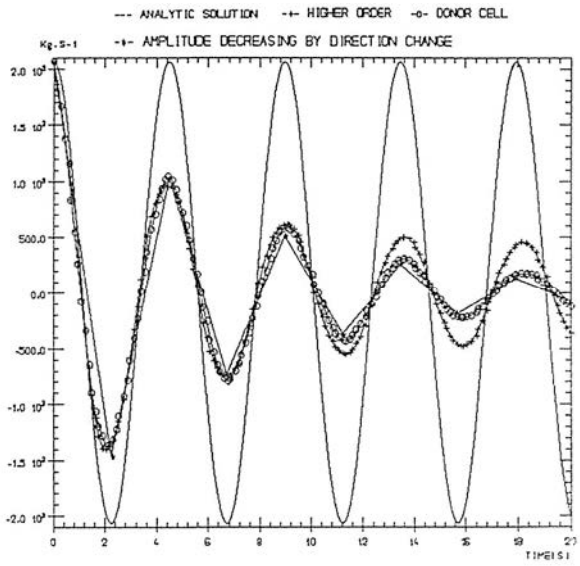

Fig. 16. 2D SIMMER-III results: mass flow rate at the bottom of the manometer.

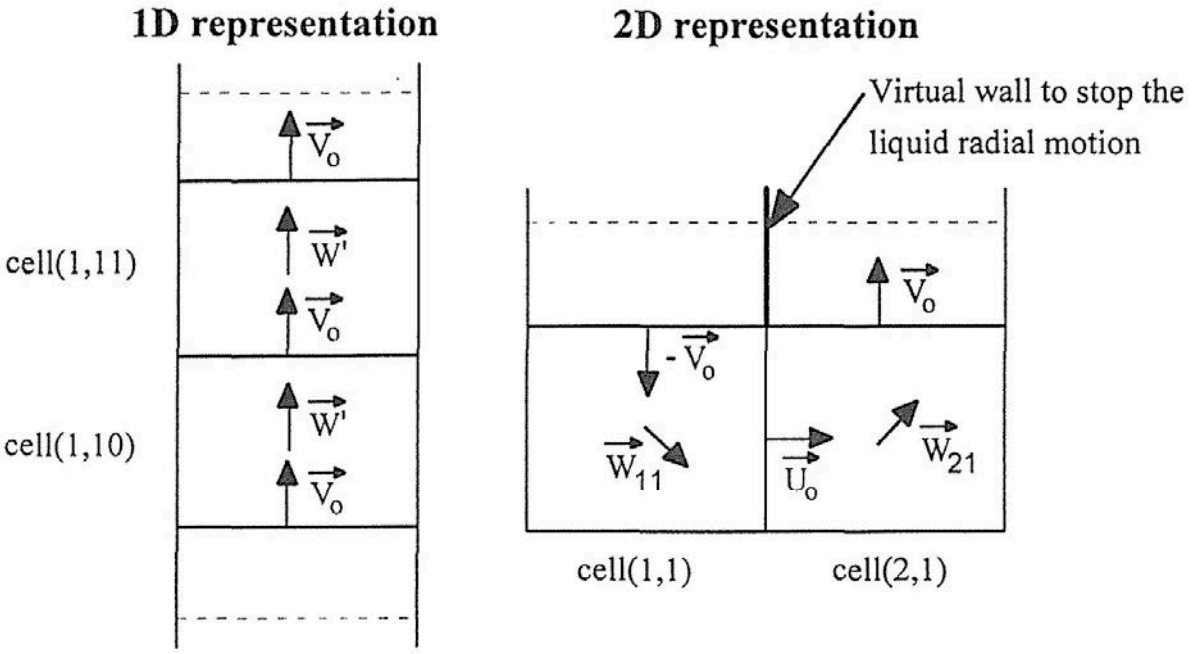

$$\vec{W} = \vec{V}_0$$

$$\begin{cases} U_0 = V_0 \\ \vec{W}_{11} = \dfrac{\vec{U}_0 - \vec{V}_0}{2} \\ W_{11} = W_{21} = \dfrac{V_0}{\sqrt{2}} \end{cases}$$

Fig. 17. Initial equivalent velocity in the cell center at the bottom of the manometer in the 1D and 2D geometrical representation.

Problem 1.4: One-dimensional sedimentation

"One-Dimensional Sedimentation Problem"

Satoru Kondo (PNC)

Outline of the Case

This problem was taken from the DOE/EPRI benchmark problems for two-phase flow codes. A transient behavior of gravity-driven inter-penetration and separation (sedimentation) of the two liquid components having different densities is examined in one dimension. An emphasis is on the numerical method for fluid convection, such as the spatial differencing scheme, the effect of inter-phasic friction and mesh sizes. The results are compared with the analytical solutions and other benchmarked codes.

1. Objectives of the Application

This problem was taken from Problem 2.4 of the DOE/EPRI benchmark problems for twophase flow codes.[1)] The problem was devised by D. L. Youngs together with a similar but different benchmark problem in two dimension. A transient behavior of gravity-driven interpenetration and separation (sedimentation) of the two liquid components having different densities is examined in one dimension. The objective of the problem is to validate the numerical algorithm of treating this behavior with and without inter-field momentum coupling.

The specific objectives of SIMMER-III application are: to verify the code capability of modeling a two-component, two-field, liquid/liquid system; and to provide basis understanding of simulating a fuel-steel molten pool during an LMFR CDA which potentially undergoes gravity driven sedimentation. The results are compared with the analytical solutions and other benchmarked codes.[2)]

2. Description of the Problem

Although the detailed description of the problem is available,[2)] it is briefly explained here. In this one-dimensional problem, a heavy phase (fluid 1) is placed above a light phase (fluid 2), as shown in Fig. 1. Both the fluids are initially at rest. Each zone has an axial length of 1 m. Due to gravity and buoyancy, the two fluids inter-penetrate each other and overturn to a final re-separated state. The two fluids are specified to have densities of $\rho_1 = 1.0$ and $\rho_2 = 0.999$, respectively. The rate of the inter-penetration and sedimentation depends on the gravity acceleration and inter-phase friction. The gravity is specified to be determined such that:

$$\frac{2(\rho_1 - \rho_2)}{(\rho_1 - \rho_2)} g = 1.0$$

The inter-phase friction is represented by a linear function of a velocity difference as:

$$F = C_f(\alpha_1\rho_1 - \alpha_2\rho_2)\alpha_1\alpha_2(v_1 - v_2)$$

Depending on the value of C_f, the following three cases are proposed to be run.

Case 1: $C_f = 1.0 \times 10^3$ (high friction, up to 4000 s)

Case 2: $C_f = 2.0$ (low friction, up to 10 s)

Case 3: $C_f = 0.0$ (no friction, up to 4 s)

Actually Case 1 was not run with SIMMER-III this time, because of a very long simulation time proposed. The behaviors with and without friction are well represented and reasonably examined by Cases 2 and 3.

3. Analytical Solution

An analytical solution for this problem is available and documented in detail.[2)] It will be compared with the SIMMER-III results. Also discussed are the results of other computer codes benchmarked, DLY, PHOENICS, MINCS and ATHENA. In this chapter, additional theoretical consideration is made on a physical mechanism of gravity-induced phase interchange. Consider the momentum equations for initially stagnant two components with no mass transfer.

$$\frac{d\bar{\rho}_1 v_1}{dt} = -\alpha_1\frac{dP}{dz} + F + \bar{\rho}_1 g$$

$$\frac{d\bar{\rho}_2 v_2}{dt} = -\alpha_2\frac{dP}{dz} + F + \bar{\rho}_2 g$$

From the continuity, $v_1 = -v_2 \equiv v$. If we assume the fluids are incompressible and uniformly mixed with their volume fractions of 0.5, then the above equations are reduced to:

$$\rho_1\frac{dv}{dt} = -\frac{dP}{dz} + 2F + \rho_1 g$$

$$\rho_2\frac{dv}{dt} = -\frac{dP}{dz} + 2F + \rho_2 g$$

By subtracting, the resultant acceleration for each phase is

$$\frac{dv}{dt} = -\frac{(\rho_1 - \rho_2)}{(\rho_1 + \rho_2)}g$$

The net acceleration for a relative inter-penetration motion is

$$\frac{d\Delta v}{dt} = -\frac{2(\rho_1 - \rho_2)}{(\rho_1 + \rho_2)}g$$

This is the acceleration which actually drives an entire behavior of interchange motion of two phases. The right hand side of this equation is the same as one appearing in the problem definition in Chapter 2. By specification, the net acceleration has to be set to 1. 0. It is noted absolute values of the densities can be arbitrarily specified, but the gravity acceleration has to be determined so as to obtain the acceleration of 1.0.

4. Understanding of Phenomena

In this an adiabatic problem, with inter-phase friction being specified by problem definition, there is no uncertainty involved. Thus the analytical solution is available.

5. SIMMER-III Representation

5.1 Geometry, Initial and Boundary Conditions for a Reference Case

A 1-D axial mesh was used for representing a cylinder of 2 m long with rigid boundary conditions. Wall friction was not considered. Initially, the lower half of the cylinder contains a light fluid represented by the liquid steel component and the upper half a heavy fluid represented by the liquid fuel component. A preliminary calculation with specified conditions was not successful. The densities and their difference are very small and the resultant gravity acceleration becomes extremely large (g = 999.5 m/s^2). This caused difficulty for the pressure iteration to converge. Based on the theoretical consideration in Chapter 3, therefore, it was decided to use the nominal densities of liquid fuel and steel:

$$\rho_1 = 9189.99 \ (\mathrm{kg/m^3})$$

$$\rho_2 = 7101.1 \ (\mathrm{kg/m^3})$$

The resultant value of gravity, determined so as to set the net acceleration to 1.0 m/s^2, is

$$g = -3.83717 \ (\mathrm{m/s^2}) \ .$$

For the reference calculation (Case 2 with low inter-phase friction) used a donor-cell differencing method, with 20 equal-sized axial noding (Δz = 0.1 m). The results for the distribution of light phase (steel) are presented at every 2 s and compared to the analytical solution. Two parametric calculations were performed for Case 2 with the same axial noding using the higher-order differencing method and with finer axial noding (80 mesh cells) using the donor-cell differencing. Similarly three cases were run for Case 3 with no friction. Case 1 was not run because of the reason mentioned already.

5.2 Code Modifications

A special correction was necessary to model a specified momentum exchange function. This was done by directly changing the function coefficients, AQQ and BQQ, in the subroutines VITER and VITERP. The subroutine MXF itself was untouched. The code options NOMF and NOVC were used.

5. 3 Parametric Cases

Three parametric cases were run to examine the effects of mesh size and differencing schemes. The initial and boundary conditions stay the same. Finer noding with 80 axial mesh (Δz = 0. 025 m) cells were

used in Case 2. Cases 3 and 4 were respectively for 40 and 80 mesh cells, but a donor-cell differencing scheme was used this time.

6. Results

The reference case result shows reasonable agreement with the analytical solution (see Fig. 2). The code has proved to be simulating a sequence of fluid inter-penetration and final separation (sedimentation). However, in this donor-cell differencing, the interface smearing becomes apparent with time due to numerical diffusion. The parametric case with the higher-order differencing did not improve the situation largely in this coarse-mesh simulation. As shown in Fig. 3, the case still indicated reduced numerical diffusion in a later stage of simulation. An excellent agreement was obtained with finer noding as shown in Fig. 4. For the three cases run, no numerical problem was observed. The results of other codes benchmarked are shown in Fig. 5. It is concluded that the performance of SIMMER-III is almost comparable to them. It is also concluded that the initial setup of material densities and gravity was acceptable. Case 2 was a simulation with realistic magnitude of friction coefficient, and the fuel and steel separation in a 1-m scale occurred in less than 10 s. With the nominal value of gravity, this process may be further accelerated. Still the gravity- and buoyancy-induced separation process proceeds in the order of several seconds. Thus SIMMER-III was confirmed to be applicable to assessing such a phase separation process.

Case 3 is for the same problem with no inter-phase friction. This case seemed simpler than Case 2 with friction, but later turned out to be more difficult from the numerical point of view. The results of the reference case is shown in Fig. 6. The comparison with the analytical solution is reasonable but there obviously is a large effect of interface smearing due to numerical diffusion. The case with higher-order differencing, shown in Fig. 7, reduces the numerical diffusion to some extent. More important result obtained was the development of instability beyond 2 s. The case with finer noding further reduces numerical smearing, but similar or even larger instability development was observed (see Fig. 8). The results of other codes benchmarked are shown in Fig. 9. In general, agreement with the analytical solution was worse than Case 2. Instability development similar to SIMMER-III was also observed in some codes.

Although not discussed in detail, some code (such as MINCS) succeeded to eliminate the numerical problem even with employing finer noding. From these observations, it was found that even though excessive numerical diffusion is undesirable from the accuracy point of view, it has a merit to stabilize the numerical simulation. In other words, the numerical diffusion can damp numerical disturbances to grow to instability. This case with no friction is unrealistic physically, and real multi-phase situations of SIMMER-III application always involve momentum coupling, like in Case 2. This means that the code is sufficiently stable without generating numerical problems. It is still noted, however, that an application of standard SIMMER-III (higher-order differencing) to a finer noding simulation, with no or extremely small friction, tends to become unstable.

7. Conclusions

SIMMER-III has been successfully applied to a one-dimensional sedimentation problem, in which two fluids having different densities inter-penetrate and separate due to gravity. The calculated results compare well with the analytical solutions and other code predictions. Thus it is concluded that SIMMER-III is comparable to other existing state-of-the-art codes. As expected, better results are obtained with the higher-order differencing method or employing finer noding because of reduced numerical diffusion. However, in the cases with mitigated numerical diffusion (no numerical damping effect), calculations tend to become unstable if there is no or extremely small friction.

This benchmark problem has confirmed the validity of the basic multi-phase flow convection algorithm and numerical solution method. Together with the two-dimensional sedimentation problem reported with this report, a reasonable first step was reached in simulating a twocomponent system, especially a fuel/steel pool behavior during an LMFR CDA.

8. Recommendations for Model Improvement

None.

9. References

1) G. F. Hewitt, et al.: "Multiphase Science and Technology, Volume 3", Hemisphere Publishing Corporation (1987).

2) D. P. Spolding e al.: "Problem specifications and collated solutions of the two-phase flow numerical-benchmark experience 1986-7", DOE/EPRI Second Int. Workshop on Two-Phase Flow Fundamentals, Troy, New York, 16-20 March, 1987.

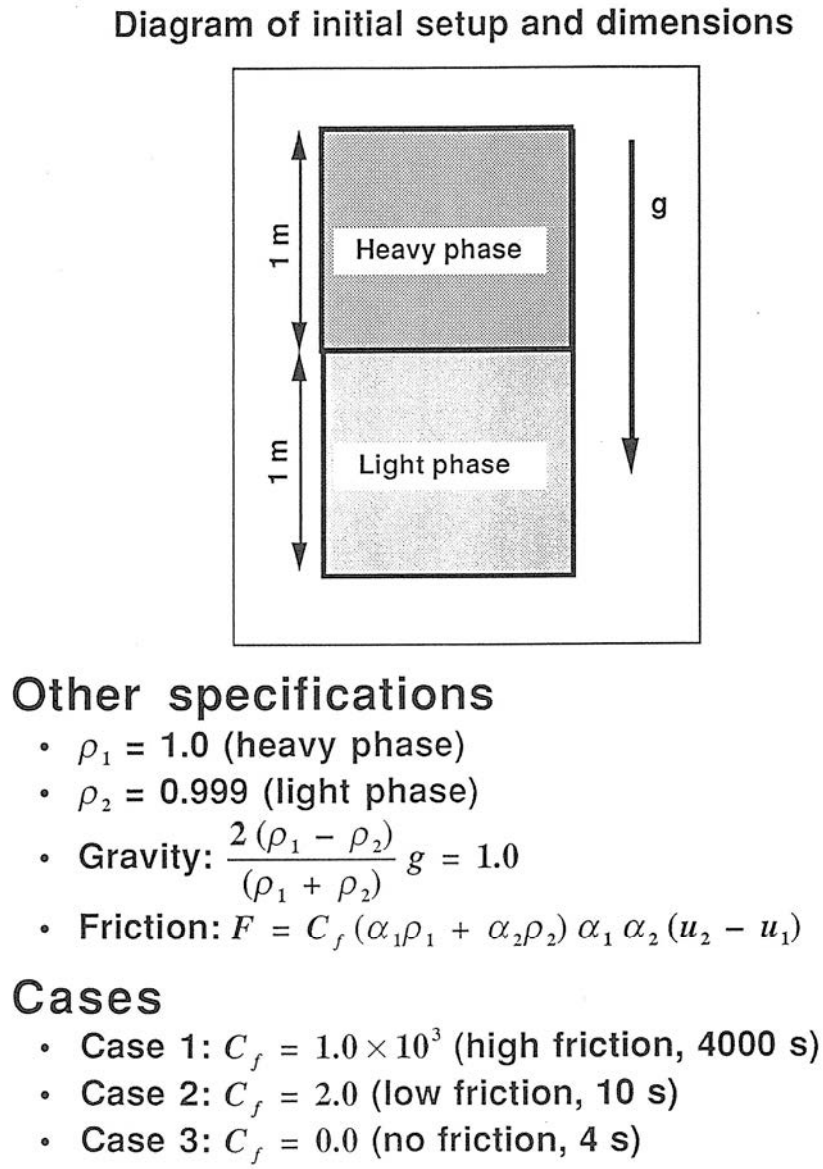

Fig. 1. Geometry and conditions for one-dimensional sedimentation problem with SIMMER-III.

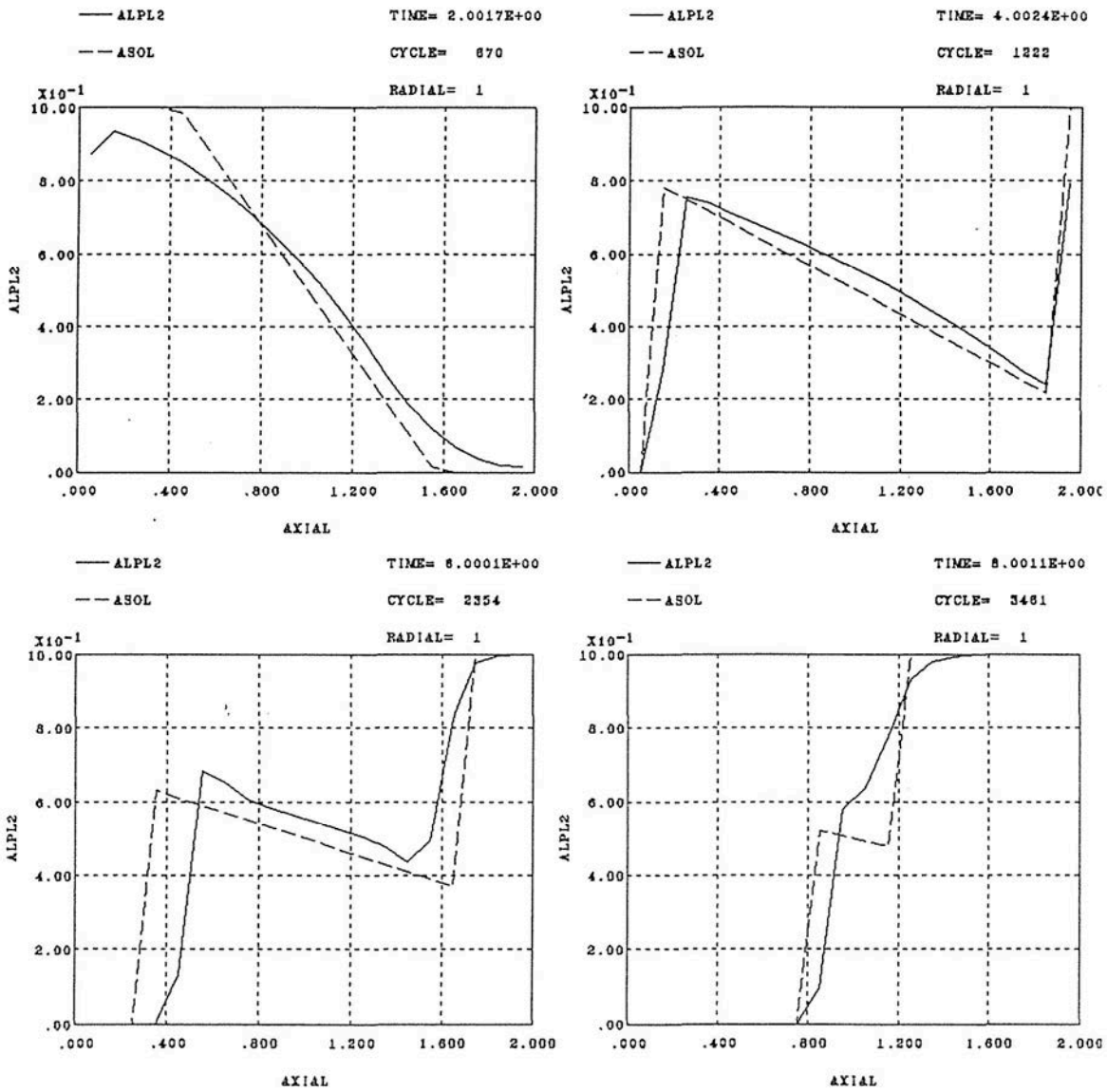

Fig. 2. One-dimensional sedimentation problem with SIMMER-III.
(Case 2: low friction, 20 cells, donor-cell differencing)

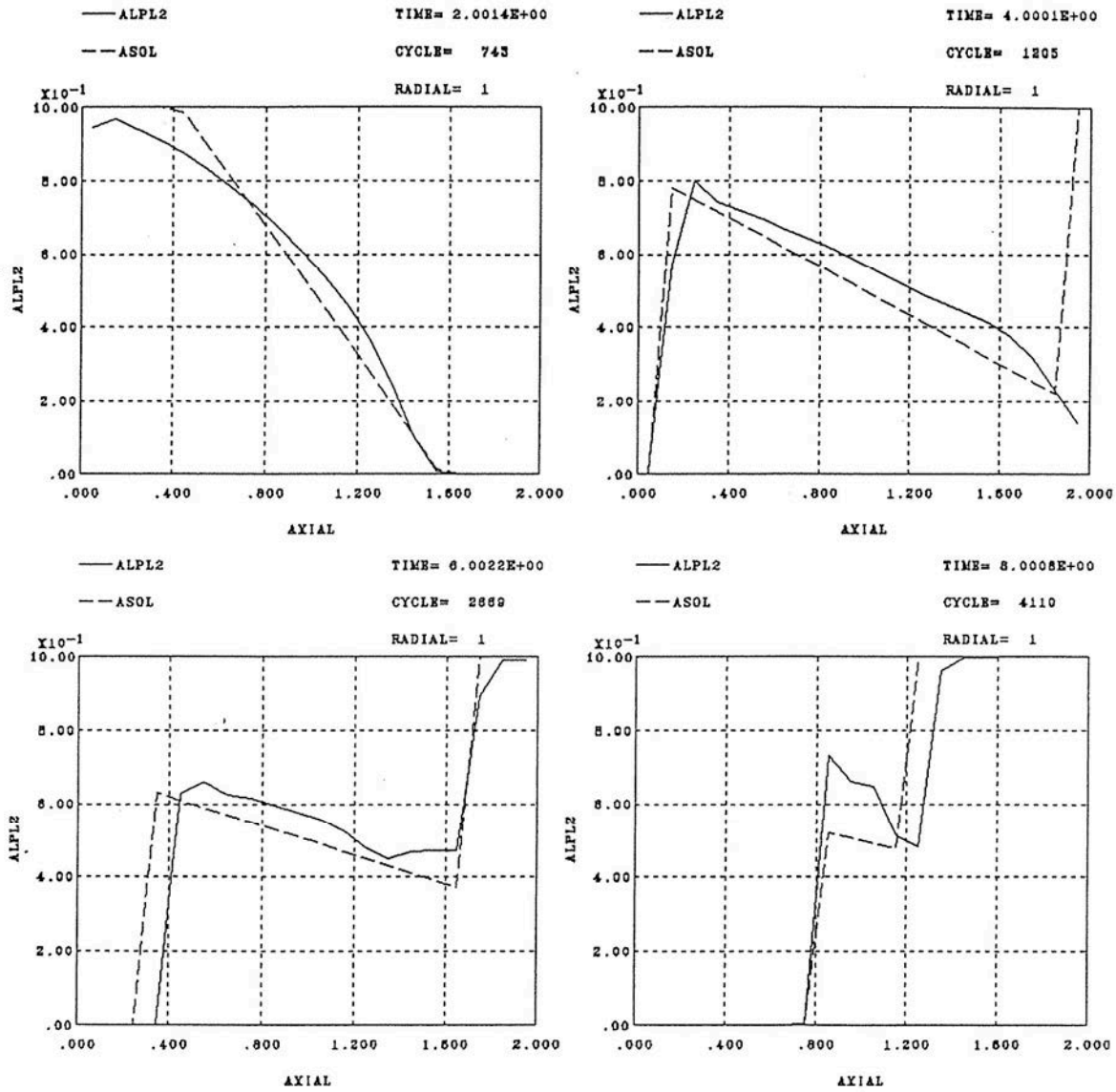

Fig. 3. One-dimensional sedimentation problem with SIMMER-III.
(Case 2: low friction, 20 cells, higher-order differencing)

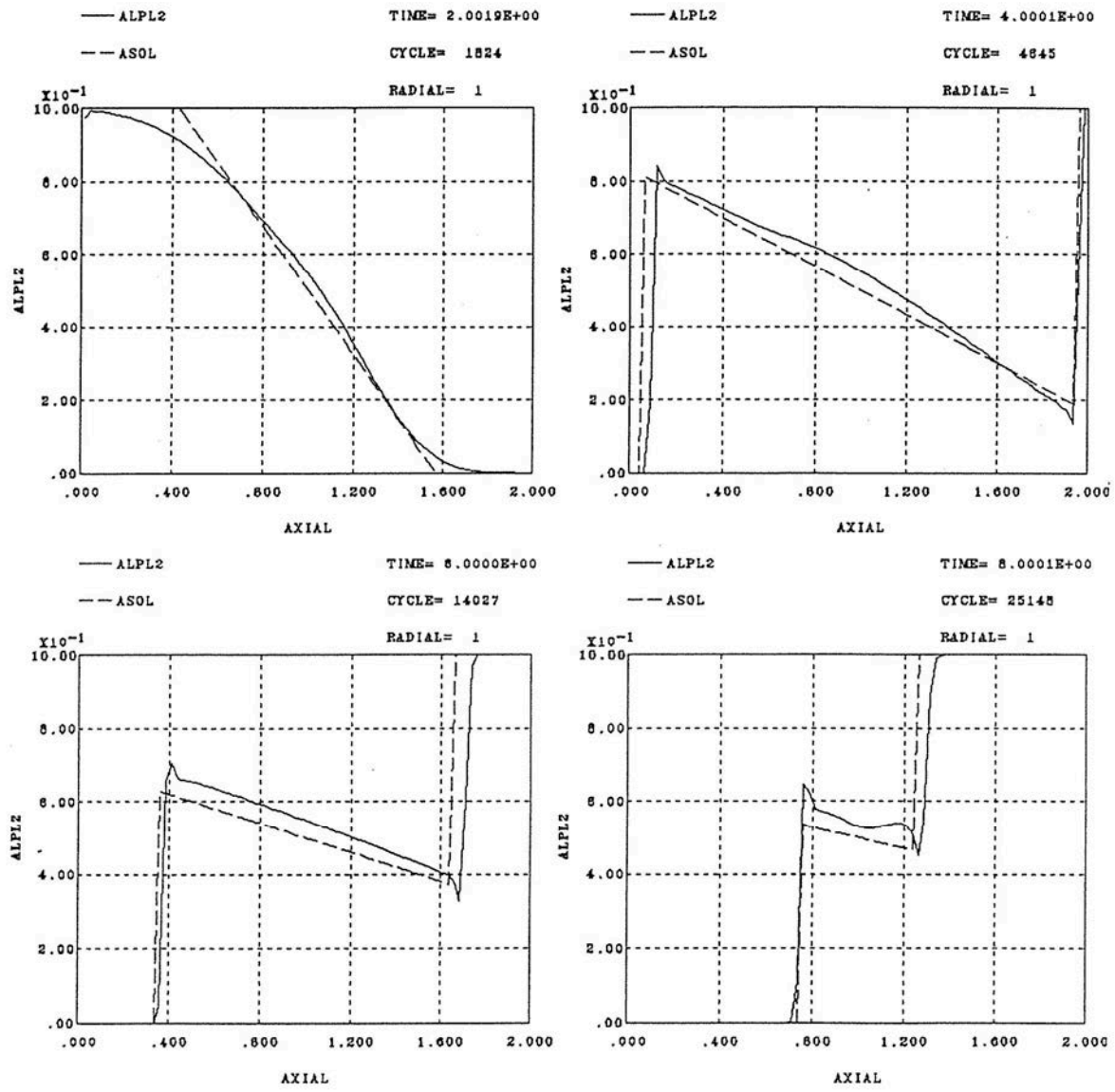

Fig. 4. One-dimensional sedimentation problem with SIMMER-III.

(Case 2: low friction, 80 cells, donor-cell differencing)

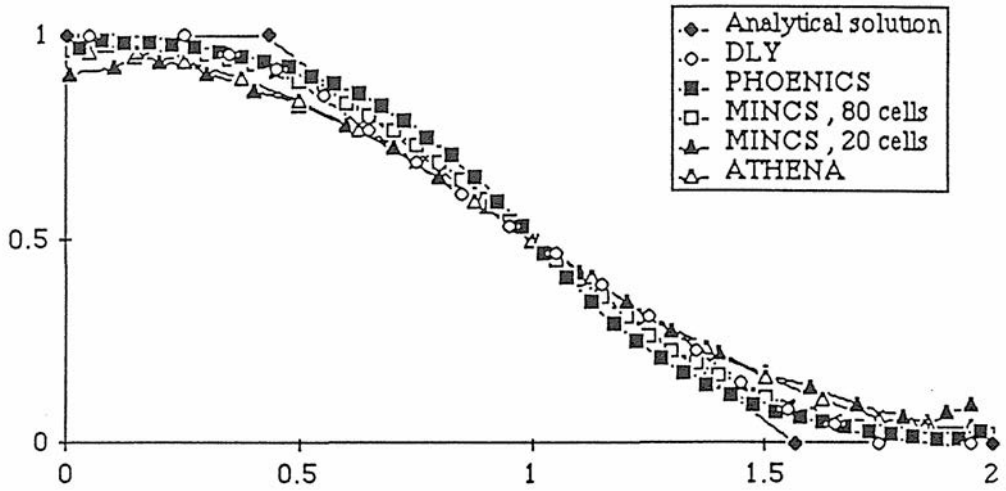

plot of volume fraction of the dense phase vs. distance.
for time = 2 s. Case 2.

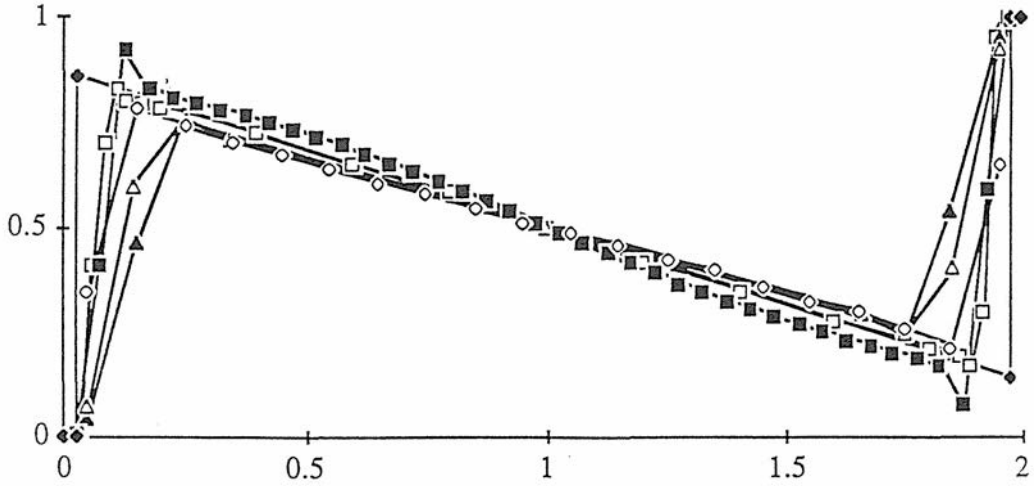

plot of volume fraction of the dense phase vs. distance.
for time = 4 s. Case 2. Symbols as shown above.

Fig. 5. One-dimensional sedimentation problem with other benchmarked codes.[2)]
(Case 2: low friction)

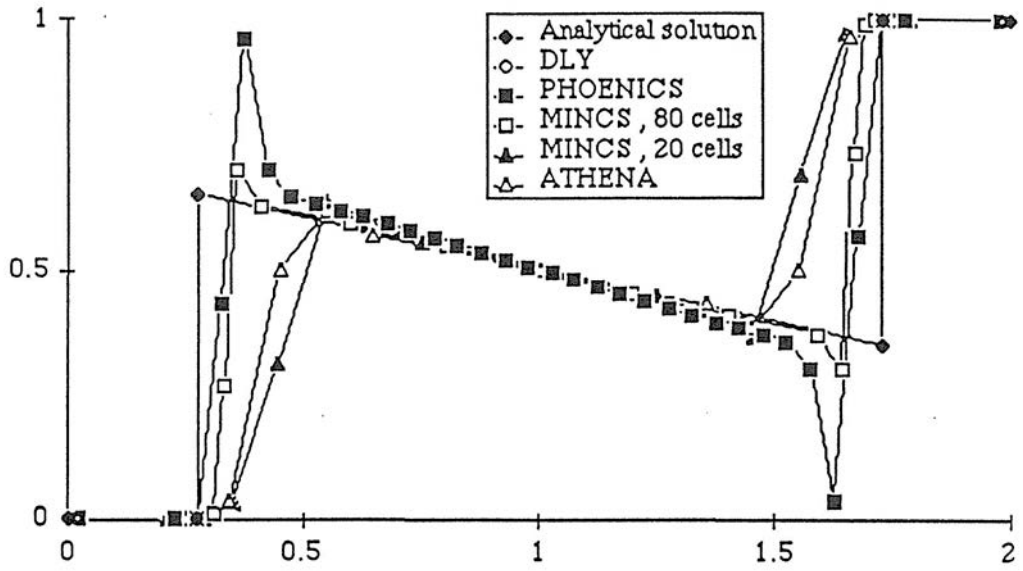

plot of volume fraction of the dense phase vs. distance. for time = 6 s. Case 2.

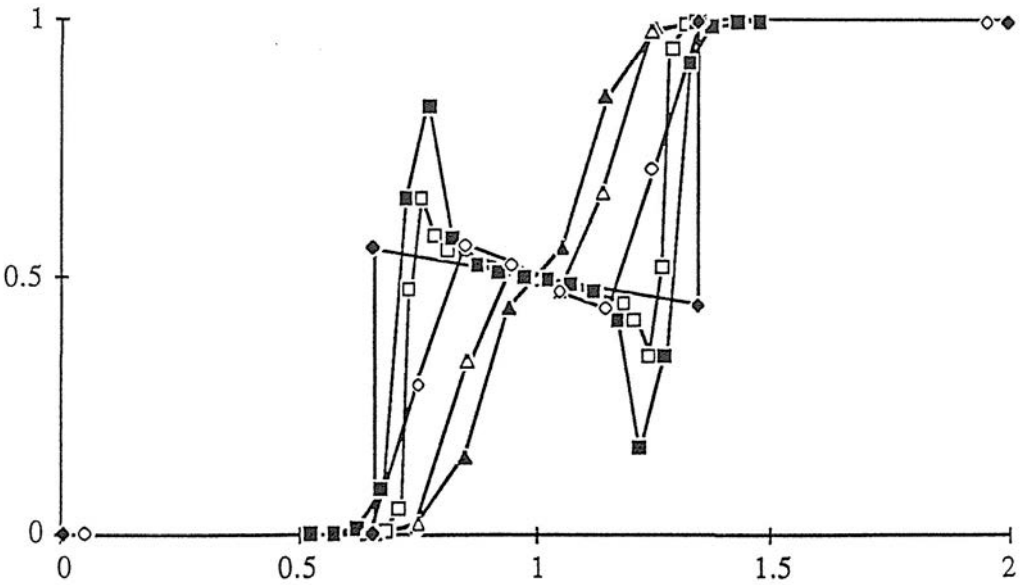

plot of volume fraction of the dense phase vs. distance. for time = 8 s. Case 2. Symbols as shown above.

Fig. 6. One-dimensional sedimentation problem with SIMMER-III. (Case 3: no friction, 20 cells, donor-cell differencing)

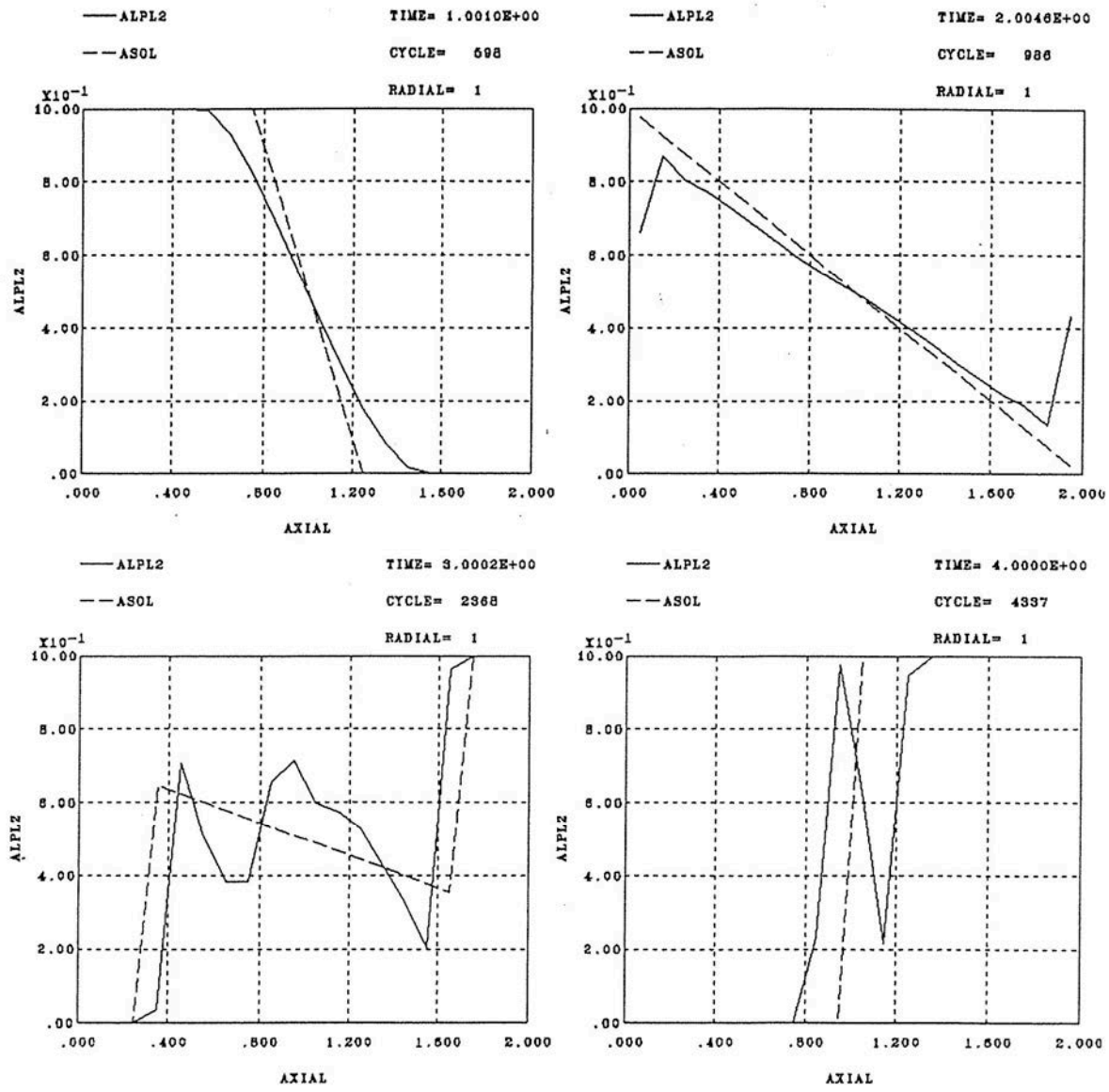

Fig. 7. One-dimensional sedimentation problem with SIMMER-III.
(Case 3: no friction, 20 cells, higher-order differencing)

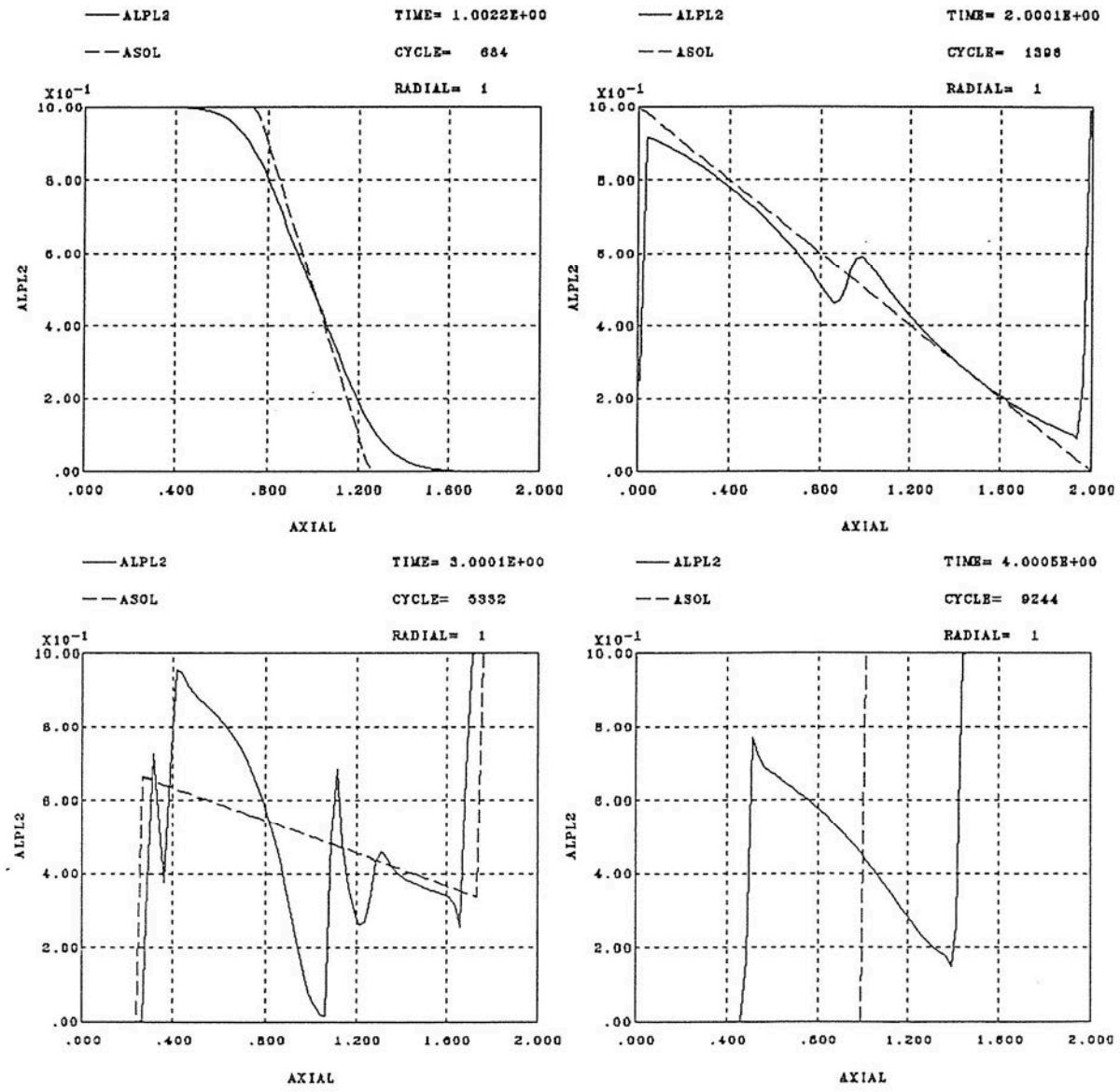

Fig. 8. One-dimensional sedimentation problem with SIMMER-III.
(Case 2: low friction, 80 cells, donor-cell differencing)

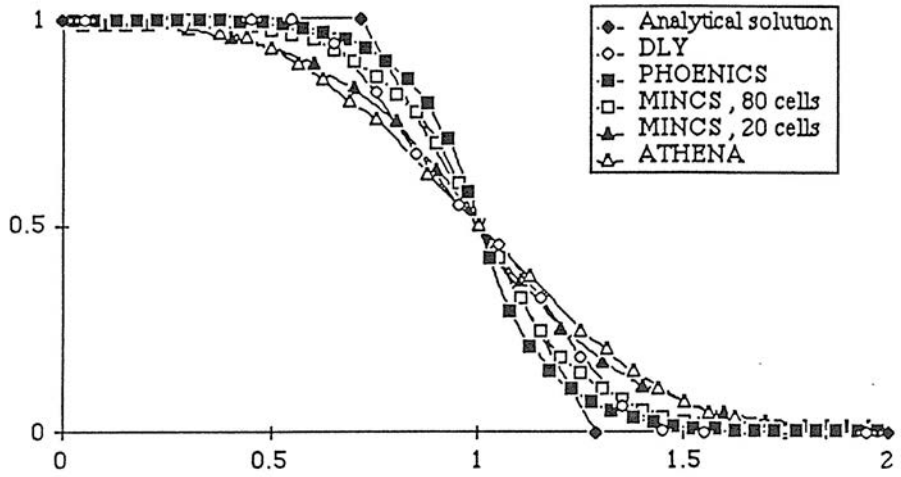

plot of volume fraction of the dense phase vs. distance.
for time = 1 s. Case 3.

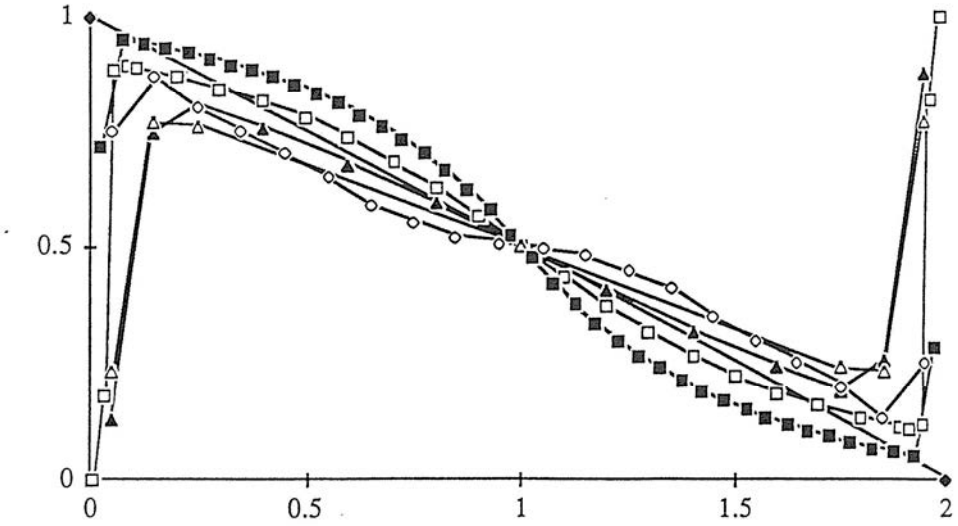

plot of volume fraction of the dense phase vs. distance.
for time = 2 s . Case 3. Symbols as shown above.

Fig. 9. One-dimensional sedimentation problem with other benchmarked codes.[2)](1/2)

(Case 3: low friction)

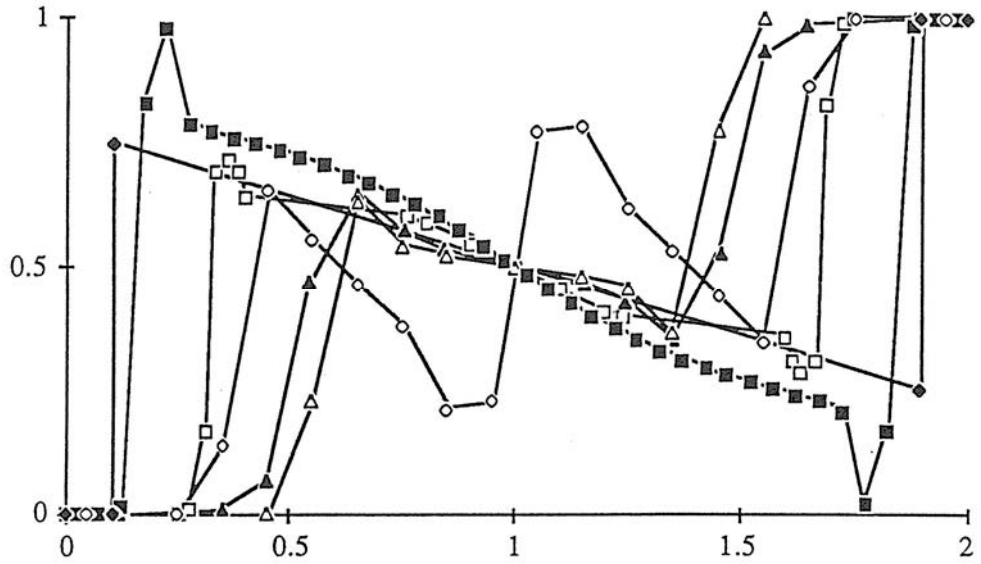

plot of volume fraction of the dense phase vs. distance.
for time = 3 s . Case 3. Symbols as shown below.

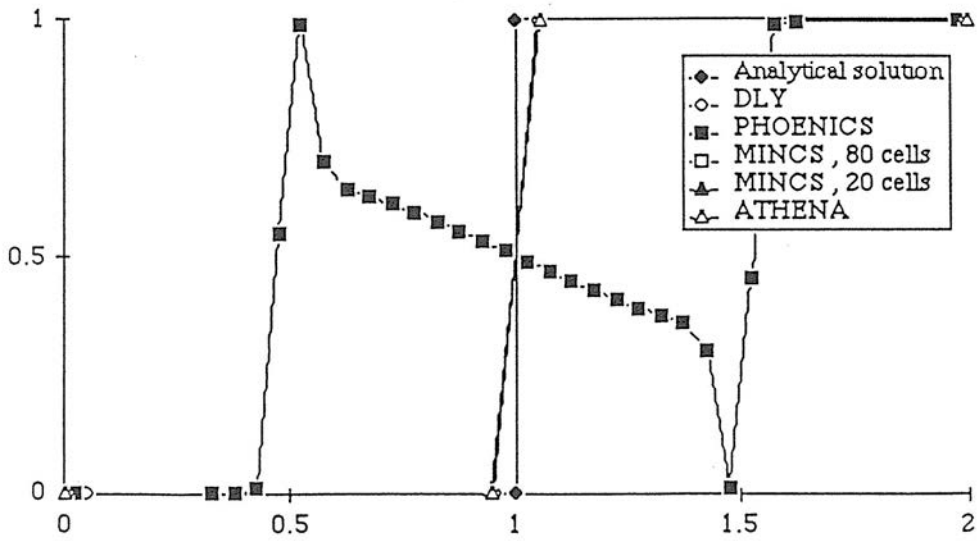

plot of volume fraction of the dense phase vs. distance.

for time = 4s . Case 3.

Fig. 9. One-dimensional sedimentation problem with other benchmarked codes.[2)] (2/2)
(Case 3: low friction)

Problem 1.5: Two-dimensional sedimentation

"Two-Dimensional Sedimentation Problem"

Satoru Kondo (PNC)

Outline of the Case

This problem was taken from the DOE/EPRI benchmark problems for two-phase flow codes. A transient behavior of a large-scale, gravity-driven, overturning motion of the two liquid components having different densities is examined in a two-dimensional tilted geometry. An emphasis is on the numerical method for fluid convection, such as the spatial differencing scheme, the effect of inter-phasic friction and mesh sizes. No analytical solution is available and the results are compared with other benchmarked codes.

1. Objectives of the Application

This problem was taken from Problem 4.1 of the DOE/EPRI benchmark problems for two-phase flow codes.[1)] The problem was devised by D. L. Youngs together with a similar but different benchmark problem in one dimension. A transient behavior of gravity-driven overturning motion of the two liquid components having different densities is examined in a two-dimensional tilted geometry. The objective of the problem is to validate the numerical algorithm of treating this behavior with and without inter-field momentum coupling. The specific objectives of SIMMER-III application are: to verify the code capability of modeling a two-component, two-field, liquid/liquid system; and to provide basis understanding of simulating a fuel-steel molten pool during an LMFR CDA which potentially undergoes gravity-driven sedimentation. No analytical solution is available and the results are compared with the other benchmarked codes.[2)]

Because of the similarity of the problems and fundamental physical mechanisms, an accompanying problem in one dimension should also be referred to.

2. Description of the Problem

Although the detailed description of the problem is available,[2)] it is briefly explained here. In this two-dimensional problem, a heavy phase (fluid 1) is placed above a light phase (fluid 2), as shown in Fig. 1. The entire system is tilted (inclined) by 10 degrees from the direction of gravity, as shown in the figure. Both the fluids are initially at rest. Each zone has a vertical length of 1 m with a horizontal length of 1.5 m. Due to gravity and buoyancy that drive the fluid motion and the specified tilted geometry, the two fluids start to undergo a large-scale overtuning motion. Namely, the heavy fluid flows down along the right boundary, while the light fluid flows up along the left boundary. The two fluids are specified to have densities of $\rho_1 = 1.0$ and $\rho_2 = 0.999$, respectively. The rate of the inter-penetration and sedimentation depends on the gravity acceleration and inter-phase friction. The gravity is specified to be determined such that:

$$\frac{2(\rho_1 - \rho_2)}{(\rho_1 - \rho_2)} g = 1.0$$

The inter-phase friction is represented by a linear function of a velocity difference as:

$$F = C_f(\alpha_1\rho_1 - \alpha_2\rho_2)\alpha_1\alpha_2(v_1 - v_2)$$

Depending on the value of C_f, the following two cases are proposed to be run.

Case 1: $C_f = 1.0 \times 10^3$ (high friction)

Case 2: $C_f = 2.0$ (low friction)

3. Analytical Solution

No analytical solution for this problem is available. SIMMER-III results are compared with other computer codes benchmarked, PHOENICS and PHOENICS VL, and documented in Ref. 2). The latter code is a version of PHOENICS modified at AEE, Harwell, UK. Only the Case 2 result was presented by PHOENICS VL.

Similar to the one-dimensional problem, a driving force for overturning motion is characterized by the net (relative) acceleration driven by the density difference.

$$\frac{d\Delta v}{dt} = -\frac{2(\rho_1 - \rho_2)}{(\rho_1 + \rho_2)} g$$

This is the acceleration which actually drives an entire behavior of interchange motion of two phases. The right hand side of this equation is the same as one appearing in the problem definition in Chapter 2. By specification, the net acceleration has to be set to 1.0. It is noted absolute values of the densities can be arbitrarily specified, but the gravity acceleration has to be determined so as to obtain the acceleration of 1.0.

Treating an inclined geometry in an X-Y coordinate system with SIMMER-III is straightforward; only the gravity term has to be divided into X and Y directions. This is done by modifying the momentume equations as:

$$\frac{\partial \bar{\rho}_M u_q}{dt} + \Delta \cdot \left(\bar{\rho}_M {u_q}^2\right) = -\alpha_M \frac{dP}{dx} + F_i + \bar{\rho}_M g \sin\theta$$

$$\frac{\partial \bar{\rho}_M v_q}{dt} + \Delta \cdot \left(\bar{\rho}_M {v_q}^2\right) = -\alpha_M \frac{dP}{dy} + F_j + \bar{\rho}_M g \cos\theta \quad .$$

4. Understanding of Phenomena

In this an adiabatic problem, with inter-phase friction being specified by problem definition, there is no uncertainty involved. However there is no analytical solution is available and only a limited application was acutally made with other codes, because a difficulty of applying the code to a two-dimensional tilted geometry. The comparison of the two code versions of PHOENICS tended not to agree with each other. Thus there is no solid basis to validate or justify the results.

5. SIMMER-III Representation

5.1 Geometry, Initial and Boundary Conditions for a Reference Case

A 2-D X-Y coordinate was used for representing a rectangle of 2 m long and 1.5 m wide with rigid boundary conditions. Wall friction was not considered. Initially, the lower half of the system contains a light fluid represented by the liquid steel component and the upper half a heavy fluid represented by the liquid fuel component. This mesh system is tilted by 10 degrees clockwise relative to the direction of gravity.

Based on the theoretical consideration in Chapter 3 of the 1-D problem report, it was decided to use the same nominal densities of liquid fuel and steel.

$$\rho_1 = 9189.99 \ (\mathrm{kg/m^3})$$

$$\rho_2 = 7101.1 \ (\mathrm{kg/m^3})$$

The resultant value of gravity, determined so as to set the net acceleration to 1.0 m/s^2, is

$$g = -3.83717 \ (\mathrm{m/s^2})$$

All the calculations were done with equal-sized, 15 by 20 mesh cells in an X-Y coordinate system ($\Delta x = \Delta y = 0.1$ m). The reference case of this study is Case 2 simulation with the higher-order differencing method. The distributions of light phase (steel) valume fraction are presented at selected time points of over-turning motion. Case 2 was also run with the donor-cell differencing method for comparison.

Similarly Case 1 was run for the two cases with higher-order and donor-cell differencing methods.

5.2 Code Modifications

A special correction was necessary for this test problem to model a specified momentum exchange function. This was done by directly changing the function coefficients, AQQ and BQQ, in the subroutines VITER and VITERP. The subroutine MXF itself was untouched. Also necessary was a special correction to treat a tilted geometry; this was done by modifying the gravity terms in the subroutines VITER and VITERP.

The code options NOMF and NOVC were used.

5.3 Parametric Cases

See Section 5.1.

6. Results

The results of the two calculations for Case 2 using SIMMER-III with and without higher-order differencing are shown in Fig. 2. The Case 2 simulations with PHOENICS and PHOENICS VL are shown in Fig. 3. By comparing these figures, it is found that the SIMMER-III result with the donor-cell differencing agreed excellently with the PHOENICS VL result. Obviously the original PHOENICS overestimated the rate of overturning. We cannot evaluate the validity of PHOENICS in detail due to lack of information. A larger time step size (Δt= 0.2 s) might be a cause of a faster motion. However additional SIMMER-III calculations with larger time stepsizes (up to 0.01 s) did not change the result. Anyway, if we assume the VL version should calculate the problem more reasonably, then the present SIMMER-III simulation could be regarded as plausible. The standard case with higher-order differencing does not change the motion but shows finger-like shapes in material distribution. This may mean that better resolution of interfaces is calculated in this case by reducing the numerical diffusion. A broad and smeared interface between the two fluids is not due to numerical diffusion. An assumption of low friction in Case 2 allows more inter-phase penetration than Case 1 (high friction).

The results for Case 1 with SIMMER-III are shown in Fig. 4. For Case 1, the result is available only with PHOENICS as shown in Fig. 5. Similarly to Case 2, PHOENICS predicted much faster fluid overturning than SIMMER-III. If the previous assumption that the consistent results of SIMMER-III and PHOENICS VL are valid, we argue that SIMMER-III calculations are plausible. We cannot be conclusive since no result is available and hence no direct comparison possible. At least we can argue that, if Case 2 simulation is reliable, the Case 1 result is also reasonable. This is becasue the case with high friction has less uncertainty due to limited inter-phase smearing. Actually a sharper interface is predicted in Case 1 because of difficulty on fluid inter-penetration in a short time. An even sharper interface is predicted with higher-order differencing, due to reduced numerical diffusion.

The discussions written in Ref. 2) are very interesting to note here. Spalding mentioned that no codes (such as PHOENICS VL) were satisfying for this problem. Especially the result for the case with high friction (Case 1) was curious. This is true in that the original figures of Ref. 2) contradict in such a way that inter-phase smearing looks less in a low friction case. The present author judged the case numbers in the original report[2] were simply wrong.

Additional general discussions are summarized. Even though the basic mechanism of driving a sedimentation process is the same, phenomena and their time scales are different between 1-D and 2-D problems. In a 1-D problem, the sedimentation is dominated by inter-penetration under the driving force provided by gravity and the inter-phase friction acting against it. For a 2-D problem, on the other hand, the sedimentation process is governed by a global over-turning motion. This is especially true with a inclined geometry as specified in this problem.

7. Conclusions

SIMMER-III has been successfully applied to a two-dimensional sedimentation problem, in which two fluids having different densities undergo a global over-turning motion driven by gravity. Since there is no analytical solution nor direct experimental data available, there is no solid basis of SIMMER-III validation. The two previous codes benchmarked, PHOENICS and PHOENICS VL, disagreed with each other. The SIMMER-III prediciton agreed almost with the PHOENICS VL result. If we assume the modified version (VL) is more appropriate than the original PHOENICS, we can argue that SIMMER-III results are plausible. At least, SIMMER-III is comparable to PHOENICS VL.

This benchmark problem has confirmed the validity of the basic multi-phase flow convection algorithm and numerical solution method. Together with the one-dimensional sedimentation problem reported with this report, a reasonable first step was reached in simulating a two-component system, especially a fuel/steel pool behavior during an LMFR CDA.

8. Recommendations for Model Improvement

No model improvements for SIMMER-III are recommended on the basis of these results. It was later decided to include the q terms in the momentum equations of standard SIMMER-III (Version 2.A and later). It was later pointed out that additional change was necessary to the pressure-volume work terms as well. This also has been included.

9. References

1) G. F. Hewitt, et al.: “Multiphase Science and Technology, Volume 3”, Hemisphere Publishing Corporation (1987).

2) D. P. Spolding et al.: “Problem specification and collated solutions of the two-phase flow numerical-benchmark experience 1986-7”, DOE/EPRI Second Int. Workshop on Two-Phase Flow Fundamentals, Troy, New York, 16-20 March, 1987.

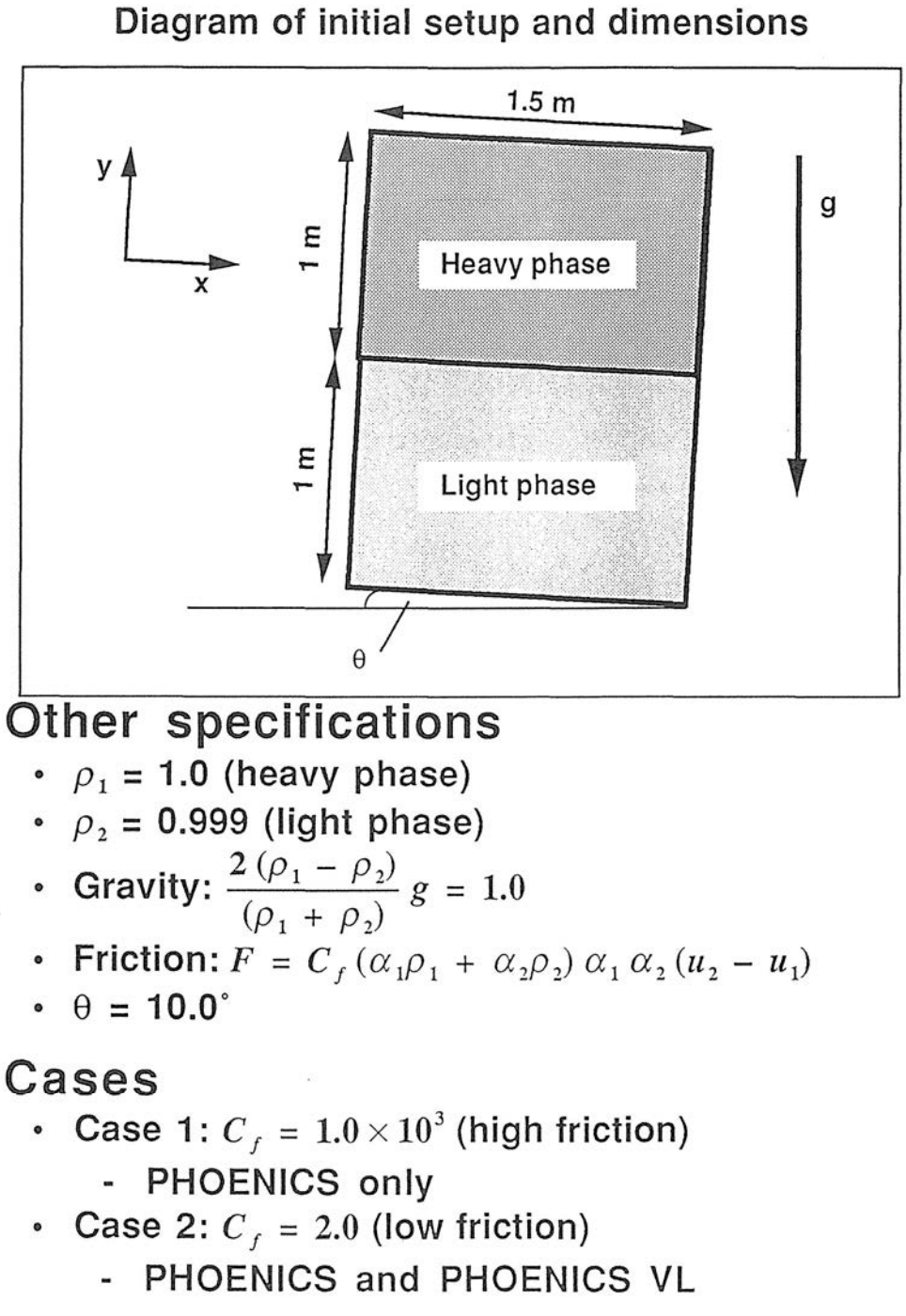

Fig. 1. Geometry and conditions for two-dimensional sedimentation problem in a tilted coordinate with SIMMER-III.

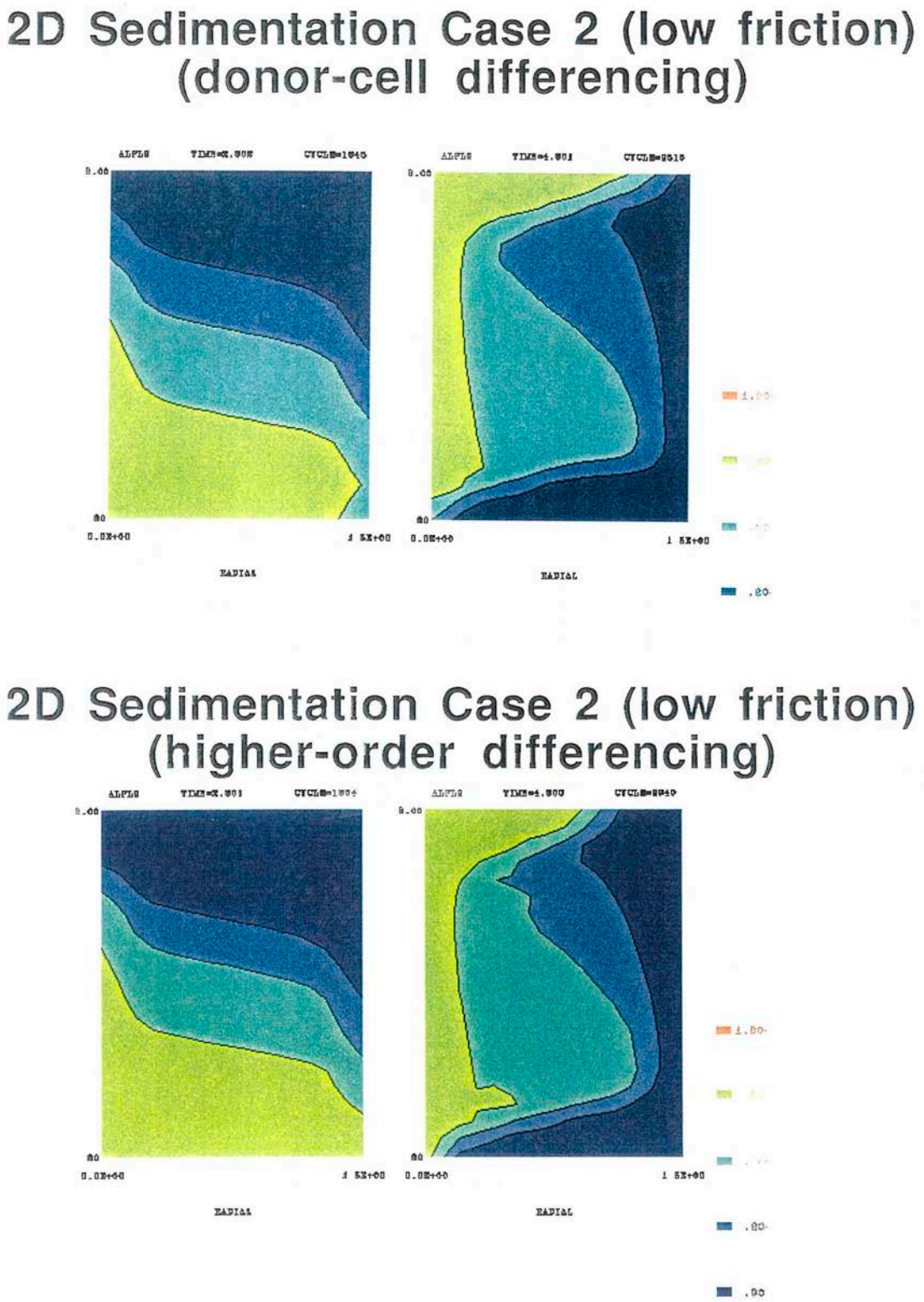

Fig. 2. Two-dimensional sedimentation problem with SIMMER-III.

(Case 2: low friction)

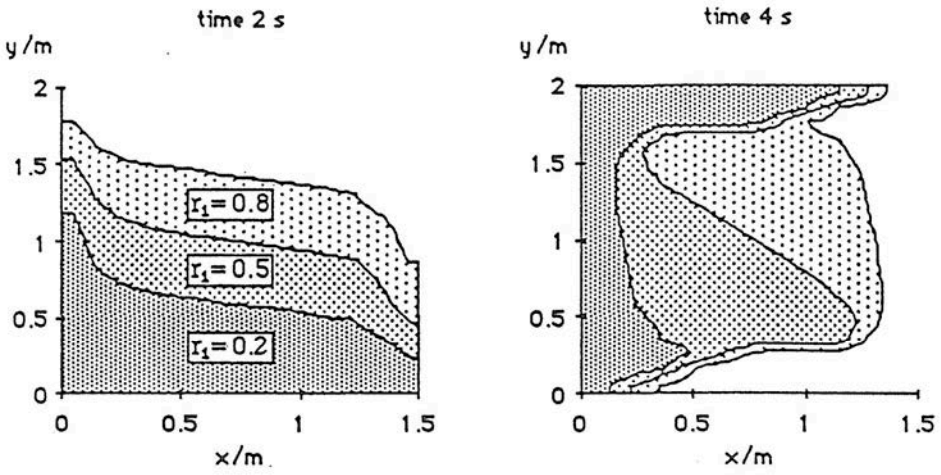

PHOENICS VL results, contour plot of volume fraction.

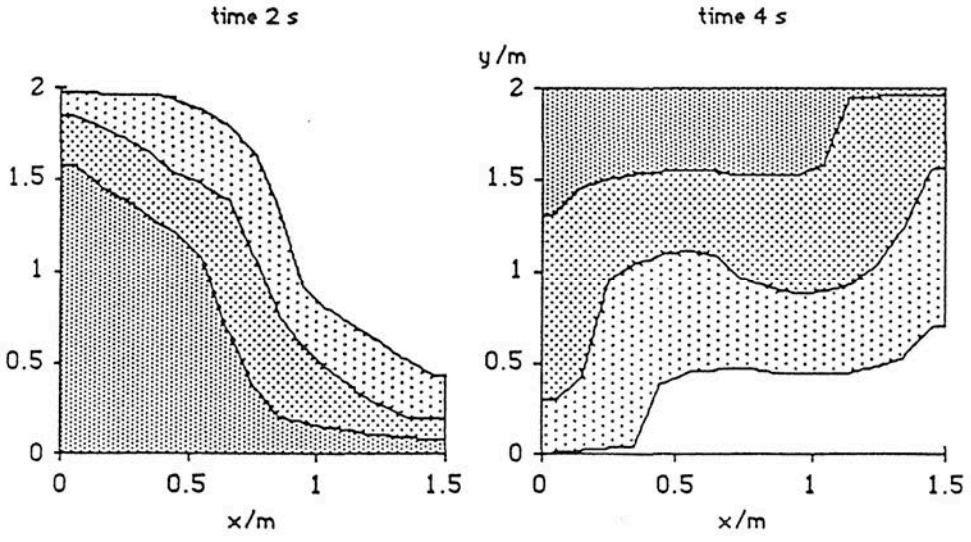

PHOENICS results. Contour plot of volume fraction.

Fig. 3. Two-dimensional sedimentation problem with other benchmarked codes.[2)]

(Case 2: low friction)

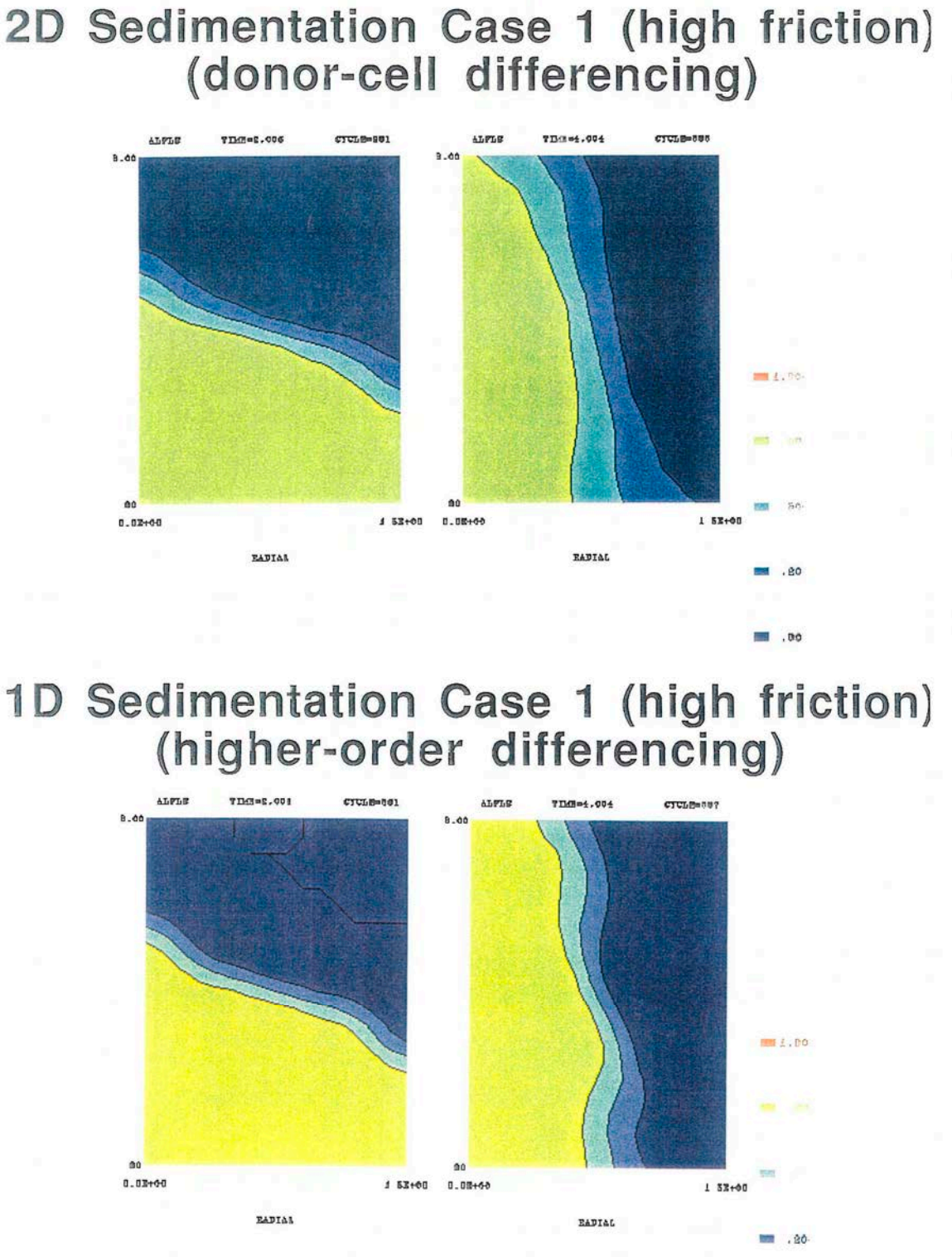

Fig. 4. Two-dimensional sedimentation problem with SIMMER-III.

(Case 1: high friction)

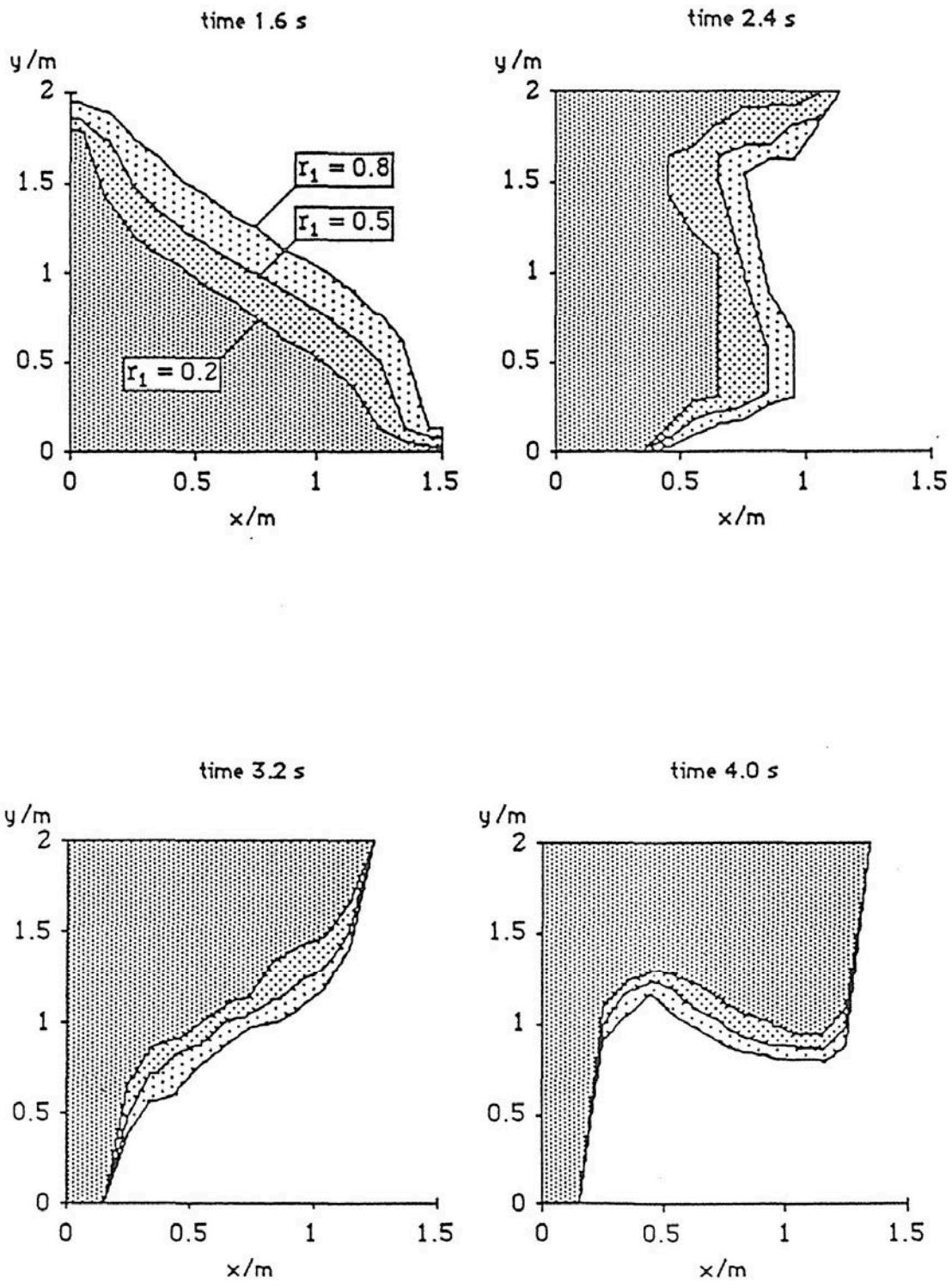

Fig. 5. Two-dimensional sedimentation problem with other benchmarked codes.[2)]

(Case 1: high friction)

Problem 1.6: One-dimensional sodium boiling

"One-Dimensional Sodium Boiling"

Satoru Kondo (PNC)

Outline of the Case

This is a small test problem to simulate the expulsion of initially superheated sodium in one-dimension. No comparison is made with analytical solution or experimental data. Instead, the problem is to simply simulate the progression of sodium boiling, including nucleation and incipient boiling starting from superheated single-phase liquid sodium, rapid vaporization and void growth and the resultant sodium slug expulsion. Thus the simulation is rather integral covering the models for interfacial areas, vaporization and condensation, and fluid convection.

A special emphasis is on investigating the effect of decoupling intra-cell transfer from inter-cell convection in the four-step algorithm employed in SIMMER-III. The cause of the decoupling effect and the resultant time-step-size sensitivity are studied with recommendation on time step selection.

1. Objectives of the Application

This is a small test problem to simulate the expulsion of initially superheated sodium in one dimension. No comparison is made with analytical solution or experimental data. Instead, the problem is to simply simulate the progression of sodium boiling, including nucleation and incipient boiling starting from superheated single-phase liquid sodium, rapid vaporization and void growth and the resultant sodium slug expulsion. Thus the first objective is to confirm that SIMMER-III can simulate an overall behavior of sodium boiling, covering the models for interfacial areas, vaporization and condensation, and fluid convection. The second and more important objective of the problem is to investigate the effect of decoupling intra-cell transfer from inter-cell convection in the four-step algorithm employed in SIMMER-III. The cause of the decoupling effect and the resultant time-step-size sensitivity are studied with recommendation on time step selection.

2. Description of the Problem

A schematic of the computational setup is depicted in Fig. 1. The lower one third of a vertical pipe of 1. 5 m in length is filled with liquid sodium initially at rest. The lower 0. 25 m of the sodium column is superheated to 1400 K, while the upper sodium temperature is 1150 K, which is slightly below the saturation temperature at the initial system pressure of 0.1 MPa. With the large superheat of about 250 K, an incipient boiling behavior is very violent. Rapid vaporization and the resultant void growth accelerate the upper sodium slug in a short time.

Only an initial short time period is calculated up to the initial several milliseconds.

3. Analytical Solution

None.

4. Understanding of Phenomena

Simulation of sodium boiling itself is known to be difficult, because of large liquid-to-vapor density ratio. This means rapid rate of bubble growth results in rapid slug expulsion. A large incipient boiling superheat causes much faster vaporization due to highly non-equilibrium initial condition. Also the phase transition from single to two phase sometimes generated numerical problems in the previous codes. With this test problem the code capability of simulating a sequence of sodium boiling is confirmed. With this simulation, the code must be shown to be sufficiently robust numerically under such a highly transient condition.

In the basic fluid-dynamics algorithm based on the four step method, intra-cell heat and mass transfer is calculated in Step 1, independent of fluid convection in Steps 2–4. This means the mass conservation in Step 1 omits the convection term, whilst one in Step 2 eliminates the source terms. This method was employed for the two main reasons. First, in a multi-component system of SIMMER-III, it was not considered practical to include all the transfer processes into a fluid-convection algorithm (pressure iteration). Second, Step 1 operations of local heat and mass transfer are sufficiently complex and subject to future elaboration. Thus it was recommended to modularized Step 1 for future possible replacement with an improved model. The influence of source term decoupling in SIMMER-III under various conditions must be assessed in order to confirm associated errors are tolerable for major application areas of the code or to recommend a remedy to minimize the errors.

It is generally understood that the effect of source-term decoupling is tolerable when either intracell mass transfer or inter-cell transfer is dominant. However the effect may become intolerable when the rate of intra-cell mass transfer is large enough to compete with fluid convection. This is especially true under the condition of rapid vaporization or condensation. Therefore, this concern can be suitably studied by this test problem, in which rapid sodium vaporization (intracell transfer) and expulsion (convection) occur simultaneously.

The source-term decoupling may possibly introduce sensitivity to time step sizes. A mechanism of this is explained as follows for the case of rapid vaporization relevant to this test problem. In Step 1, the rate of sodium vaporization is calculated based on the beginning-of-time-step conditions and the end-of-time-step states are updated. In this case cell pressure resulting from vaporization is calculated. This pressure buildup is relieved by fluid convection out of the cell calculated in Steps 2–4. If the fluid convection is calculated simultaneously with vaporization, pressure relief by convection allows more sodium to vaporize. This means the current four-step algorithm with source-term decoupling tends to underestimate the rate of

vaporization. More importantly this effect can be very sensitive to time step sizes. The questions therefore are: whether such effect is tolerable, what is an appropriate time step control to mitigate this sensitivity, and whether there is a remedy to improve this situation.

5. SIMMER-III Representation

5.1 Geometry, Initial and Boundary Conditions for a Reference Case

As shown in Fig. 1, a 1-D axial mesh was used for representing a cylinder of 1.5 m long with rigid boundary conditions. The axial noding for SIMMER-III calculations is also indicated as well. No wall friction nor heat loss was considered. All the calculations were performed with the same initial and boundary conditions. Only the time step size and its control were varied. The reference case used a constant time step size of L'.t = 10-s (s). The result is presented only by pressure evolution at the fourth axial cell from the bottom. As described in the previous chapter, the influence of source-term decoupling is best examined by monitoring the end-of-Step 1 pressure. Thus the intermediate pressure, at the end of Step 1, is compared with the end-of-Step 4 (end-of-time-step) pressure.

Standard EOS and model parameters defaulted in SIMMER-III are used in this test problem.

5.2 Code Modifications

No model change was necessary to run this problem. To monitor and output the end-of-Step 1 pressure, a correction was inserted to transfer a Step 1 variable over to Steps 2–4. Also this study has proposed an additional time step control based on a ratio of Step 1 and Step 4 pressures. These code modifications have already been included in a later SIMMER-III version.

5.3 Parametric Cases

Several parametric cases were run for this problem to examine the effects of time step sizes: constant time step sizes of 10^{-3}, 10^{-4} , 10^{-5} and 10^{-6}, and a standard variable time step control (between 10^{-2} and 10^{-8}). An additional time step control to restrict a ratio of the end-of-Step 1 pressure to the end-of-Step 4 pressure was also tested and compared.

6. Results

It was shown that SIMMER-III could simulate an entire sequence of sodium boiling and expulsion, starting from a highly superheated single-phase liquid condition. No numerical problem nor instability was observed. This means the numerical method of the code is robust against severe calculational conditions. Although we cannot argue the validity of the simulation in this problem, it is encouraging that SIMMER-III is shown to be applicable to an analysis of rapid sodium boiling.

The results of initial pressure evolution due to rapid vaporization are compared in Figs. 2 to 5, among the cases with different time step sizes from l0^{-3} to 10^{-6} s. The solid lines represent actual ·pressure histories

at the end of each cycle, whilst the dashed lines show intermediate pressure at the end of Step 1. A large difference between the pressures indicates the influence of source term decoupling is large. It is indicated in the figure that almost perfect agreement between the two was observed with $\Delta t = 10^{-5}$ and 10^{-6}. This means the influence of source-term decoupling is negligible for this problem with the minimum time step of 10^{-5} or less. With increasing the time step size, the difference between the two pressures becomes larger. This results in underestimated rate of sodium vaporization. With $\Delta t = 10^{-4}$, the calculated pressure evolution seems still acceptable. However the result with $\Delta t = 10^{-3}$ is intolerable, indicating retarded boiling progression. This is an obvious effect of source-term decoupling that large pressure buildup with a larger time step is not relieved until the end of a convection calculation; this in mrn results in underestimation of vaporization rate.

The calculated result with variable time step sizes did not work very well. Since SIMMER-III does not control time step sizes based on phase transition rate, automatically determined time step sizes stay around 10^{-3} or even less. Thus an unacceptable result was obtained, similar to the 10^{-3} case. This does not mean the standard variable time step control in. SIMMER-III is inappropriate. Instead, it might be recommended that the minimum time step size allowed be restricted to 104 at least or even smaller (if better resolution is required).

As noted previously, an additional time step control was developed to restrict the ratio of pressure difference between Steps 1 and 4. The result without specifying the minimum time step size is shown in Fig. 6. It is indicated that the problematic pressure difference with standard time step control is mitigated, but that the pressure evolution shows a non-smooth, wavy behavior. This was caused by the on and off nature of this time step control. Therefore it is currently recommended that the standard time step control be used with specifying the minimum size depending on the problem, 10^{-4} at least for case involving rapid vaporization. A stricter control might be necessary for such cases with much faster phase transitions as vapor condensation in highly subcooled liquid or energetic fuel-coolant interactions.

7. Conclusions

Although we cannot argue the validity of the simulation directly from this problem, it is encouraging that SIMMER-III is shown to be applicable to an analysis of the entire sequence of sodium boiling including rapid vaporization and expulsion.

Appropriateness and possible limitation of the four-step algorithm were addressed in detail using this problem. A fundamental cause of introducing time-step-size sensitivity has been identified for the case that a rapid mass transfer rate of vaporization competes with fluid convection. As the result of the calculations, it is recommended that the standard time step control be used with specifying the minimum size depending on the problem, 10^{-4} at least for case involving rapid vaporization. A stricter control might be necessary for such cases with much faster phase transitions as vapor condensation in highly subcooled liquid or energetic fuel-coolant interactions. It must be noted that, with larger time step sizes, such as 10^{-3} or larger, the current

SIMMER-III tends to underestimate the rate of vaporization or condensation. Hence an appropriate time step control should be considered depending on a problem, especially when a large rate of phase transition.

A remedy to directly mitigate the source-term decoupling has been later developed at PNC and is being tested. This effort is expected to eliminate the concern discussed in this test problem. However, there still remains fundamental limitations on time step size because of assumed linearization in temporal discretization of the basic equations.

8. Recommendations for Model Improvement

None, except for continuing study on the remedy for mitigating source-term decoupling.

9. References

None.

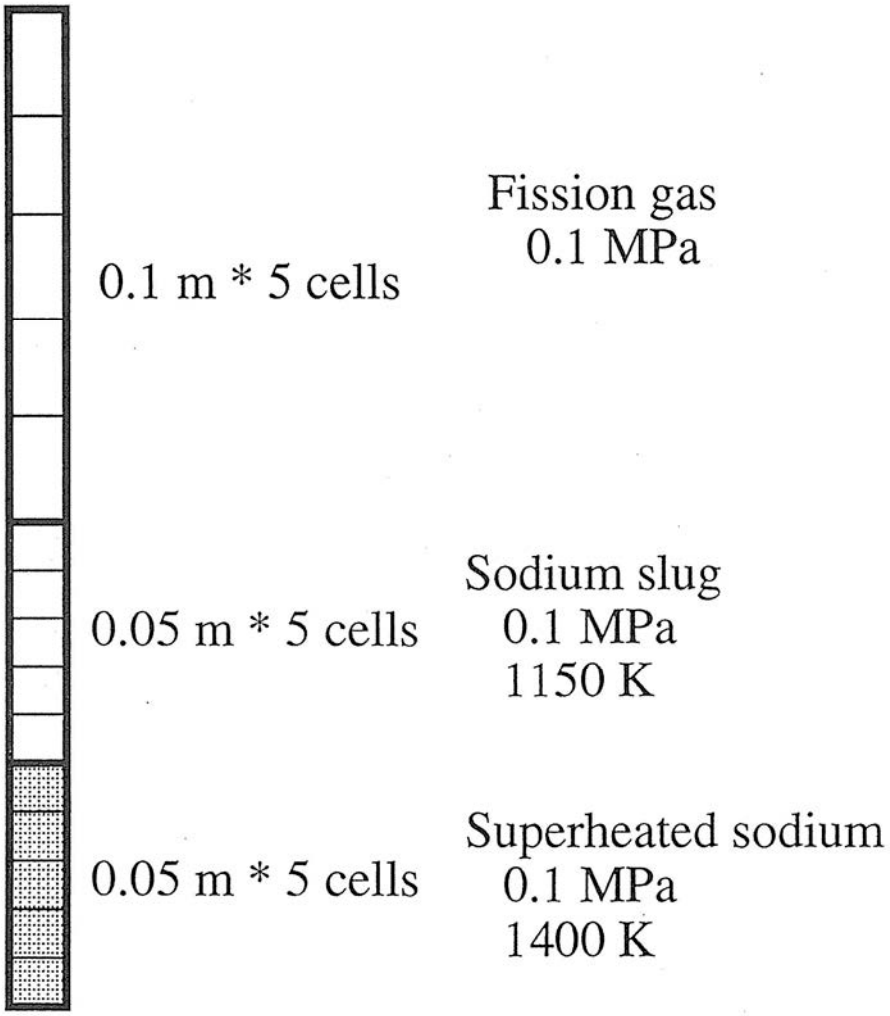

Fig. 1. Computational setup for one-dimensional sodium boiling analysis with SIMMER-III.

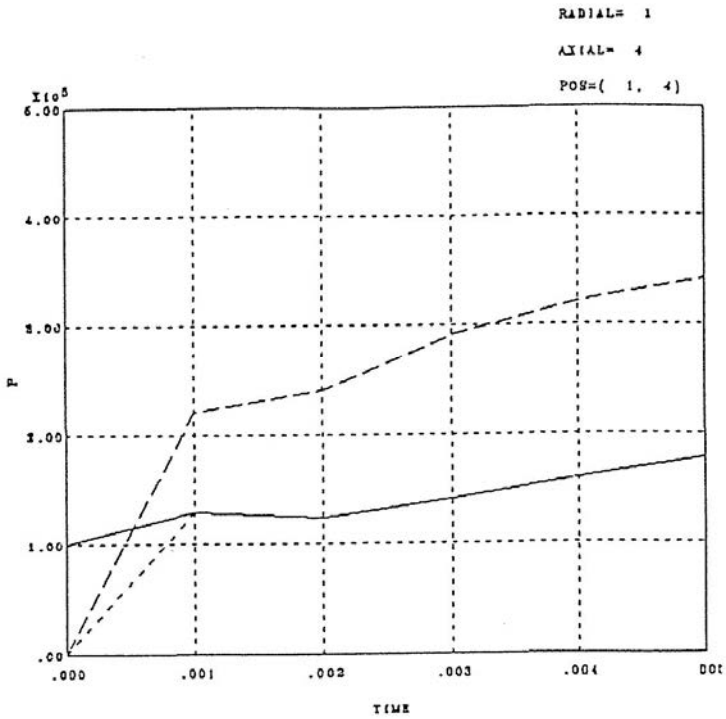

Fig. 2. Calculated early pressure evolution after boiling onset: $\Delta t = 10^{-3}$ (solid line: end of time step, dached line: end of STEP 1).

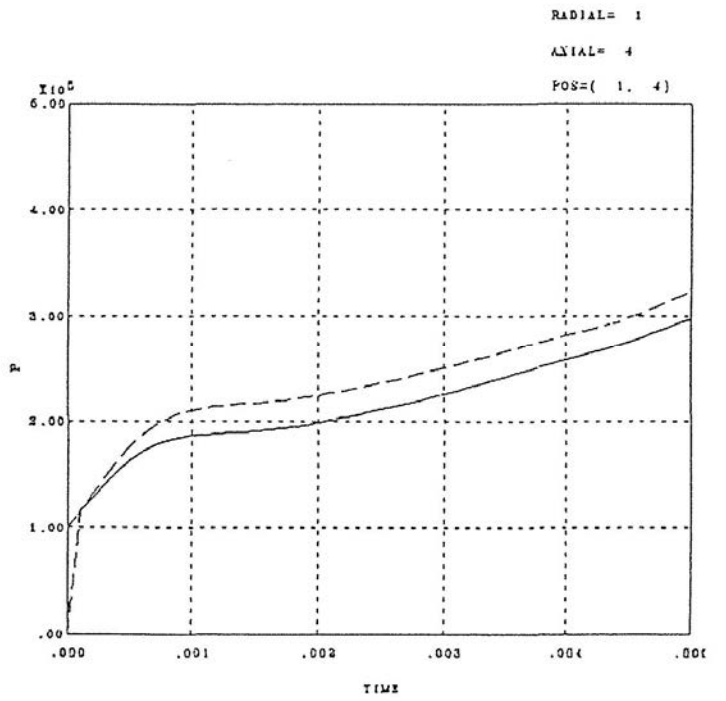

Fig. 3. Calculated early pressure evolution after boiling onset: $\Delta t = 10^{-4}$ (solid line: end of time step, dached line: end of STEP1).

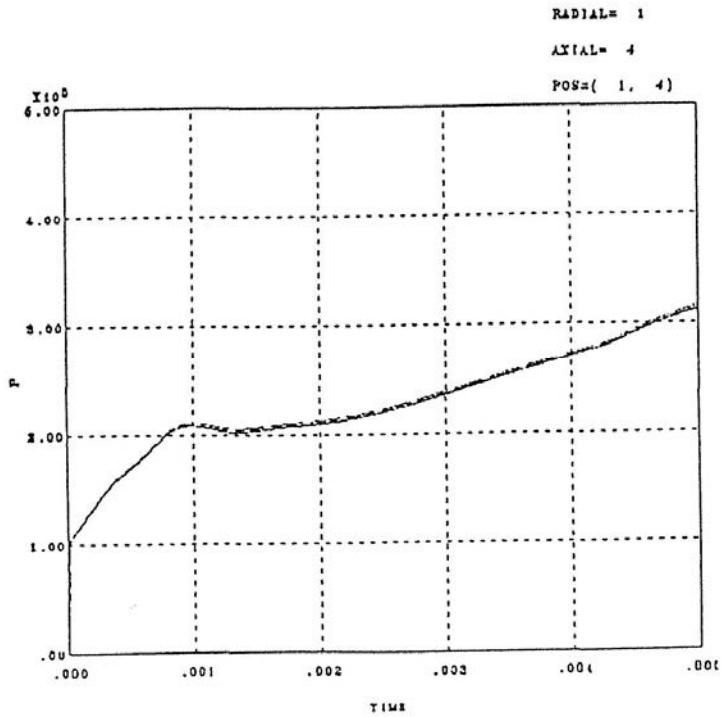

Fig. 4. Calculated early pressure evolution after boiling onset: $\Delta t = 10^{-5}$ (solid line: end of time step, dached line: end of STEP1).

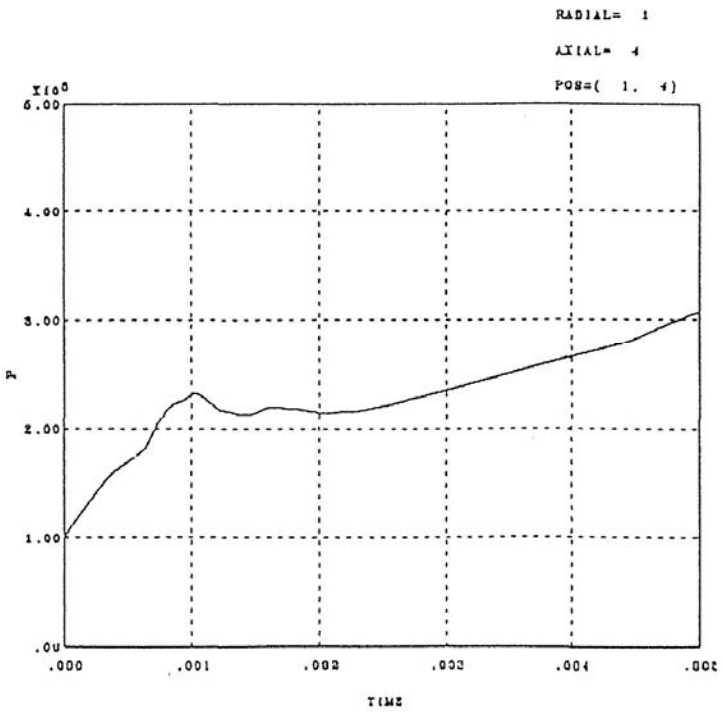

Fig. 5. Calculated early pressure evolution after boiling onset: $\Delta t = 10^{-6}$ (solid line: end of time step, dached line: end of STEP1).

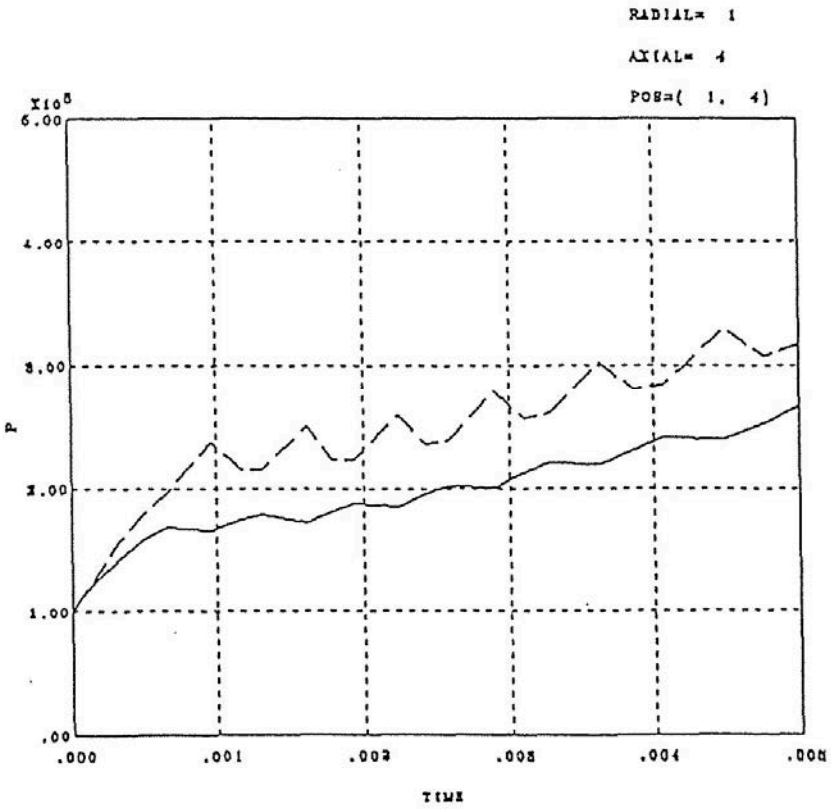

Fig. 6. Calculated early pressure evolution after boiling onset: with additional time step control (solid line: end of time step, dached line: end of STEP1).

Problem 1.7: Liquid sloshing with particles

"Liquid Sloshing Motion Including Particles"

W. Maschek, E. Hesselschwerdt, C.-D. Munz, S. Kleinheins (FZK)

Outline of Case

In the framework of the SIMMER-III code assessment liquid sloshing processes are simulated and compared with experiments. Such liquid sloshing phenomena can play an important role in core disruptive accidents. The SIMMER-III code should therefore be capable to describe sloshing processes with good accuracy. The calculations presented are compared with experiments in which particles are embedded into the flow.

1. Objectives of the Application

Liquid sloshing motions play an important role in core disruptive accident simulations of liquid metal reactors. Under pessimistic assumptions analyses show that the reactor core melts and a large whole core liquid fuel pool confined by blockages (frozen fuel and blanket structures) can be formed in the so-called transition phase.[1)] A local fuel compaction may trigger a mild nuclear excursion in this pool. The following energy deposition leads to a pressure build-up in the core center which pushes the liquid fuel towards the pool periphery. Driven by gravity the fuel sloshes back towards the pool center and piles up in a neutronically critical or even supercritical configuration. This "centralized sloshing"[2), 3), 4)] can lead to energetic nuclear power excursions and the conditions and phenomena of these processes have therefore been studied extensively.

The simulation of sloshing motions provides an excellent test for the fluiddynamic module of codes like SIMMER-III. Such a code must be able to describe sloshing with good accuracy. During the sloshing process smooth liquid surfaces may change and will break-up and smooth wave packages transform into sharp liquid peaks. SIMMER-III is a multiphase phase code with no specific tracking of the free fluid surface. SIMMER-III is based on volume and time averaged equations. By this and the inherent numerical diffusion of the code the free surface of the moving liquid is smeared out to a certain extent. This represents a general difficulty in describing sloshing phenomena by numerical calculations. As could be shown in Refs. 3) and 5) higher order differencing (2nd order) as generally used in SIMMER-III is a necessity when describing liquid sloshing motions. The code calculations were compared with experiments[6)] in which different types of sloshing motions were investigated. The above analyses concentrated on sloshing of pure liquids. Some experiments were also performed with particles mixed into the flow mainly to investigate their damping influence.[6)] Another question was if particles of a specific density and size would be seperated from the liquid during a sloshing process.

In the following two different sets of calculations are performed. At first a water step problem is run with no particles. This example was chosen to get started with a simpler two field (liquid-gas) simulation and also because the recalculation of this case with AFDM[7] showed some deficiencies.[5] Second a dam break problem with a ring of particles in some distance from the water column was tested.[6]

2. Description of Experiments

Two typical sloshing problems from the experimental series in Ref. 6) are investigated in this exercise (Table 2.1 and Fig. 2.1). In the first case (case SA-D1X-3 in Ref. 6)) a cylindrical container is divided into two concentric parts by a cylindrical diaphragm. The inner cylinder contains water of a certain height, the outer cylinder contains water at a lower level. An (r,z) diagram of this situation is shown in Fig. 2.2.

In the second case (case SE-D1P-1 in Ref. 6)) no liquid was in the outer container (dam-break problem), but a ring of particles was placed around the central water column at a certain distance (see Fig 2.3). The particles (Specification: Acryl P210D) have a density of 1.13 g/cm^3. The shape of the particles is cylindrical with a diameter of 2.5 mm and a height of 3 mm.

3. Analytical Solution

Analytical solutions are available for the outward sloshing phase when the water-depth is small (shallow water theory[8]). For the total sloshing process no analytical solutions are available.

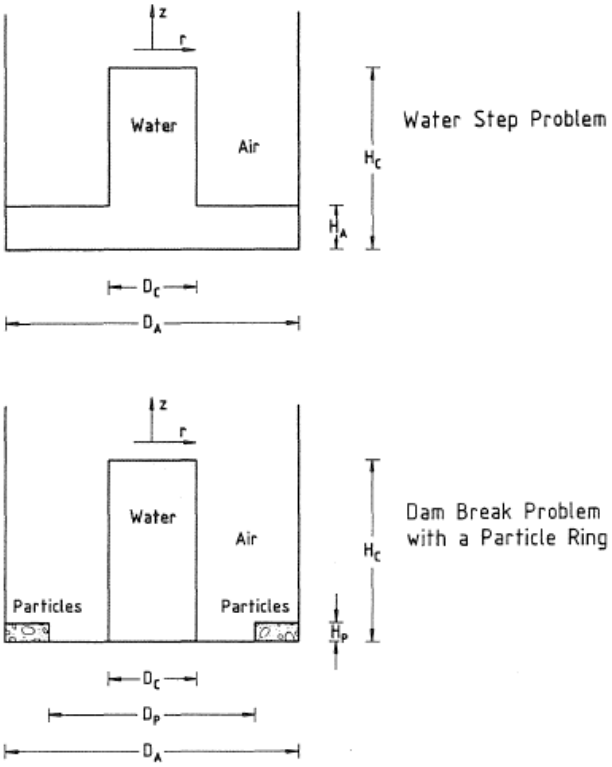

Fig. 2.1. The two sloshing problems investigated.

Table 2.1. Experimental results for the water step problem and for dam break problems with particles in the flow.

SLOSHING TEST CLASSIFICATION:		SA – Water step								
Experimental series signature	Diameter of central water cylinder [cm]	Height of water [cm]		Type of obstacles/ disturbance	Slosh at ourter wall		Slosh at pool center			
		Inner cylinder	Outer cylinder		Time max. height at wall [s]	Max. height at wall [s]	Time of first peak [s]	Height of first peak [cm]	Time of second peak [s]	Height of second peak [cm]
D1X-3	11	20	5	-	0.35±0.02	11.0±1	0.52±0.04	15.0±3	1.24±0.04	50±5

SLOSHING TEST CLASSIFICATION:		SE – Dam break								
Experimental series signature	Diameter of central water cylinder [cm]	Height of water [cm]		Type of obstacles/ disturbance: particles		Slosh at ourter wall			Slosh at pool center	
		Inner cylinder	Outer cylinder	Particle height in central cylinder [cm]	Particle height in outer cylinder [cm]	Arrival time at wall [s]	Time of max. height [s]	Max. height liquid/ particles [cm]	Time of max. height [s]	Max. height [cm]
D1O-1	11	20	-	-	1	28.0±0.02	0.40±0.02	10/8±1	0.80±0.04	25±5

4. Understanding of Phenomena

4.1 The Water Step Problem

The water step problem represents an oscillating system by the interaction of the central water column with the outer water ring. Under specific mass combinations as in experiment SA-D1X-3 (Mcolumn: Mring = 1:3.75)[6] the interaction of deep water waves with surface waves (layers of water which move on different time scales and in different directions) creates the complicated sloshing pattern as seen in Fig. 2.2. Generally from fluid dynamics theory[8] one can interfere that most of the damping in this oscillating system is related to surface waves. The kinetic energy is mostly stored in these wave packages. In the water step system with deep water areas the damping is much less than in a system with shallow water and several oscillating sloshing cycles can be observed. In the experiments the water of the central water column was colored dark to observe the detailed liquid motion. After release of the water column a surface wave and a deep water wave are created which move outwards. The deep water wave moves faster and pushes the clear water ring upwards at the container walls. The clear water of the outer ring is pushed upwards at the outer container walls. The dark water does not reach the outer container and stays at the pool bottom. In sloshing back the clear water compresses the dark water and pushes it upwards in the pool center. A dark water hump is formed. The dark water hump collapses in a broad roll and triggers an outward motion in the deep water but also a surface wave travels outward. The clear water is again pushed upwards the outer container walls and again compresses the central dark water which has spread out below the surface. The high water peak which has also been observed in the dam break problem experiments [6] emerges. The high sloshing peak thus appears in the second sloshing cycle. Both the water hump and the high water peak consist of the dark water.

4.2 The Dam Break Problem with a Particle Ring

The influence of particles on the sloshing process was investigated in a series of experiments.[6] The main interest was in the damping effect of these particles on the sloshing motion. Another issue to investigate was if particles of a specific size and density have a trend to seperate from the liquid or stay intimately mixed. If a separation would take place the assumptions of SIMMER-III to put the heavy particles into the same velocity field as the liquid fuel would be questionable.

For the experiments a special size and particle density was chosen. The particles had an approx. 10% higher density than the liquid. This density increase would be similar for solid fuel particles in accident simulations. In the first experiment the particles were positioned in a ring around the central water column. The particle ring started at a radius of R = 14.5 cm in experiment SE-D1P-1 (Fig. 2.3). The particle bed height was 1 cm.

As can be seen from the experiment the liquid piles up when it hits the particle area and pushes them upwards the container walls while some mixing with the flow takes place. The pure water slightly passes

the particles at the wall but generally the particles remain mixed into the flow which can be clearly seen in the centralized back-slosh. Due to the particles in the flow no symmetric and straight sloshing peak can be built up, but a cloud of liquid/gas/particles emerges. The coherence of liquid motion is destroyed by the particles and the central sloshing peak is damped.

5. SIMMER-III Representation

Two cases are given, a water-step problem and a dam-break problem including particles in the flow.

5.1 Geometry, Initial and Boundary conditions

The essential values to be compared with the experiment are the sloshing heights and arrival times of the liquid at the outer container wall and the liquid peak after convergence of the water at the center. For the simulation of the water-step problem with SIMMER-III, a 2-D mesh of 24 × 30 mesh points was chosen. The higher order differencing option was used. All other input values (e. g. concerning momentum exchange) were chosen as the defaulted ones in SIMMER- III. As we have an isothermal problem no heat and mass transfer takes place. The fluiddynamics parts of the code, the interfacial area model and the momentum exchange model are tested in these calculations. For the dam-break problem including particles a mesh of 25 × 30 cells has been used.

To test the SIMMER-III assumption concerning the distribution of particles on the momentums field for heavy and light components the solid particles where put into the liquid fuel field. This would also be the case with fuel particles in accident simulations.

For the SIMMER-III simulation (case D1P-1) the choice of the mesh leads to some problems. For a good simulation with low numerical damping a rather fine mesh is optimal. On the other side the size of the particles (max. dimension = 3 mm) defines a lower limit for the mesh size as an ensemble of particles should exist in a mesh. for the present calculation the smallest dimension of the axial mesh is chosen as 5 mm.

In the input the maximum packing fraction for defining the particle viscosity was defined as 0.7 and the multiplier of the drag coefficient CCD was set to 1.0.[9] Again, no friction of the fluid and the particles at the pool bottom is modelled within the code framework.

No code modification was made.

6. Results

6.1 Water-step Problem

In Fig. 6.1 and Table 6.1 the results of the SIMMER-III calculation (case D1X-3) are displayed. The comparison between the experimental values and the calculations shows good agreement in the phase when the central water column collapses up to the time when the maximum water height is reached at the outer

wall. First the outgoing wave typical for the two-dimensional waterstep problem is nicely simulated. In the experiment a first central slosh results in a water-hump at the center without any sharp liquid peak. In the SIMMER-III simulation the water hump is also visible but an additional water peak exists above the hump. The maximum height of this narrow liquid peak is given in Table 6.1.

Table 6.1 Comparison of experimental and calculational results for the waterstep problem D1X-3.

SA D1X-3	Slosh at outer wall		Slosh at pool center			
	Time max. height at wall [s]	Max. height at wall [cm]	Time of first peak [s]	Height of first peak [cm]	Time of second peak [s]	Height of second peak [cm]
Experiment	0.36±0.02	11.0±1	0.62±0.04	15.0±3	1.24±0.04	50.0±5
Calculation	0.35	12.0	0.58	21.0	1.24	36

In the experiment no central spike occurs in the first in-slosh for the specific mass ratio of 1:3.75 (SA-D1X-3) for the water column to the outer pool. In experiments with other mass ratios a central spike however emerges.[6] This shows that a delicate balance of moving masses and forces creates the hump - a feature which is not covered by the code simulation. The difference between experiment and simulation m·ay result from a lack of two modelling features. From the experiment with differently coloured water it can be seen that the different fluids from the central column and the surrounding pool move as independent layers with partial surface mixing. In SIMMER-III there does not exist a model for momentum exchange between the calculational cells. The lack of such a model influences the results of this sloshing calculation. Additionally no friction at the pool bottom is simulated. After a second outward slosh a narrow peak emerges in the experiment which reaches a large height of 50 cm. Though the overall timing in the calculation is quite good the central peak is only 36 cm high and underestimates the experimental value. It is important to note that the essential mass distributions as a function of time are calculated with sufficient accuracy. Based on the calculations performed one can deduce that SIMMER-III simulates the water-step problem with reasonable accuracy when the essential mass distributions and the timing of motion are regarded. The details of the simulation could however be improved by introducing models for intercell momentum exchange and friction at the bottom walls.

6.2 Dam-Break Problem with a Particle Ring

As can be seen in Table 6.2 and Fig. 6.2 in the calculations the outward moving liquid pushes the particle ring towards the outer container wall. The particle bed at the bottom is penetrated partly by the fluid. When the liquid sloshes up the container walls, the particles are in front of the water wave. The main liquid mass remains however below the liquid particle accumulation. A thin particle layer is pushed much further up than in the experiment. After flow reversal the liquid and particles are fully mixed and reassemble at the center of the container.

Table 6.2 Comparison of experimental and calculational results for the dam break problem with particles D1P-1.

SA D1P-1	Slosh at outer wall			Slosh at pool center	
	Arrival time at wall [s]	Time of max. height [s]	Max. height liquid/ particles [cm]	Time of max. height [s]	Max. height [cm]
Experiment	0.28±0.02	0.40±0.02	10/8±1	0.80±0.04	25±5
Calculation	0.25	0.40	10/17	0.80	27.0

From the simulation and the experiments it can be observed that the liquid mixes with the particle bed and the particles of the specific size also remain intimately mixed in the flow. Thus the assumption of putting fuel particles into the liquid fuel field is a reasonable choice. The simulation of sloshing with a particle ring is quite satisfactory. The impact of the liquid on the particle bed, its acceleration, and the mixing of the liquid and the particles is simulated adequately. The calculated main mass distribution of the liquid agrees with the experiment. The sloshing height at the wall is overestimated for the particles. Again, no bottom friction of the particle field is simulated by SIMMER-III. The central inward slosh is overestimated in its size compared to the experiment in which the central slosh produces a broad liquid peak which is broken up in drops and particles. This is not surprising as in the twodimensional code framework the symmetry of the converging waves is preserved and the emerging instabilities are not simulated. Thus in the simulation a high central sloshing peak emerges. In comparison to the sloshing motion without particles the damping effect of particles is clearly visible in the sloshing heights achieved.

For completeness a SIMMER-III simulation (case D1) of the experiment has been performed using first order donor cell differencing for the momentum equations. The results are displayed in Fig. 6.3. As can be clearly seen the mass distributions are not adequately calculated. A strong smearing of the wave packages can be observed. The use of the first order donor cell differencing leads to incorrect results.

7. Conclusions

In summary the following conclusions can be drawn from the recalculation of the sloshing experiments with and without particles in the flow:

1) The essential features of the sloshing process are well captured by the SIMMER-III code. The essential mass distributions and velocities of the water waves are recalculated by the code.

2) The calculation of some details of the sloshing process when liquid shear flows occur in the liquid pool and dominate the behaviour are beyond the capability of the code. The main reasons for this are:

   - no intercell momentum exchange is simulated

   - no friction at the pool bottom is simulated

3) The instabilities of the converging water waves during the in-slosh cannot be simulated within the twodimensional framework of the SIMMER-III code. A tendency exists to overestimate central sloshing heights and the central mass accumulation.

4) The interaction of the liquid and particles can be calculated with good accuracy in the sloshing simulations. Both the particle mass distributions and the intermixing of liquid and particles can be represented by the code. The assumption of putting the solid fuel particles into the liquid fuel field seems to be justified on the basis of the experiments performed.

5) Comparative calculations show that application of second order differencing is essential for simulating the sloshing processes (with and without particles). Excessive numerical damping and diffusion discredit the first order donor cell differencing approach.

8. Recommendations

The inclusion of friction at the bottom cells and intercell momentum exchange would further improve the capability of the code.

9. References

1) W. Maschek, E. A. Fischer and M. W. Asprey: Transition Phase and Recriticality Analyses for a SNR-Type Homogeneous Core with the SIMMER-II Code, Proc. Int. Topi. Mtg. Liquid Metal Fast Breeder Reactor Safety and Related Design and Operational Aspects, Lyons, France, July 19-23, 1982, Vol. Ill, p. 357, European Nuclear Society (1982).

2) W. Maschek, C. D. Munz and L. Meyer: An Assessment of Liquid Sloshing Phenomena in Pools Based on AFDM/SIMMER Code Calculations and Experiments, Proc. 1990 Int. Fast Reactor Safety Mtg., Snowbird, Utah, August 12-16, 1990, Vol. IV, p. 395, American Nuclear Society (1990).

3) W. Maschek, C. D. Munz, L. Meyer: Investigations of Sloshing Fluid Motions in Pools related to Recriticalities in Liquid-Metal Fast Breeder Reactor Core Meltdown Accidents, Nucl. Techn. 98, pp. 27-43 (1992).

4) Sa. Kondo, Y. Tobita, K. Morita, N. Shirakawa: SIMMER-III: An Advanced Computer Program for LMFBR Severe Accident Analysis, ANP'92, Vol. IV, 40-5, Tokyo, Oct. 1992.

5) C. D. Munz, W. Maschek: Comparison of Results of Two-Phase Fluid Dynamics Codes on Sloshing Experiments KfK 5091 (1992).

6) W. Maschek, A. Roth, M. Kirstahler, L. Meyer: Simulation Experiments for Centralized Liquid Sloshing Motions KfK 5090 (1992).

7) W. R. Bohl, D. Wilhelm, J. Berthier and F. R. Parker: -The AFDM Program: Scope and Significance, Proc. 1990 Int. Fast Reactor Safety Mtg., Snowbird, Utah, August 12-16, 1990, Vol. II, p. 155, American Nuclear Society (1990).

8) J. J. Stoker: Water waves lnterscience Publishers, New York, (1957).

9) M. Ishii, K. Mishima: Study of Two-Fluid Model and lnterfacial Area NUREG/CR-1873 (1980).

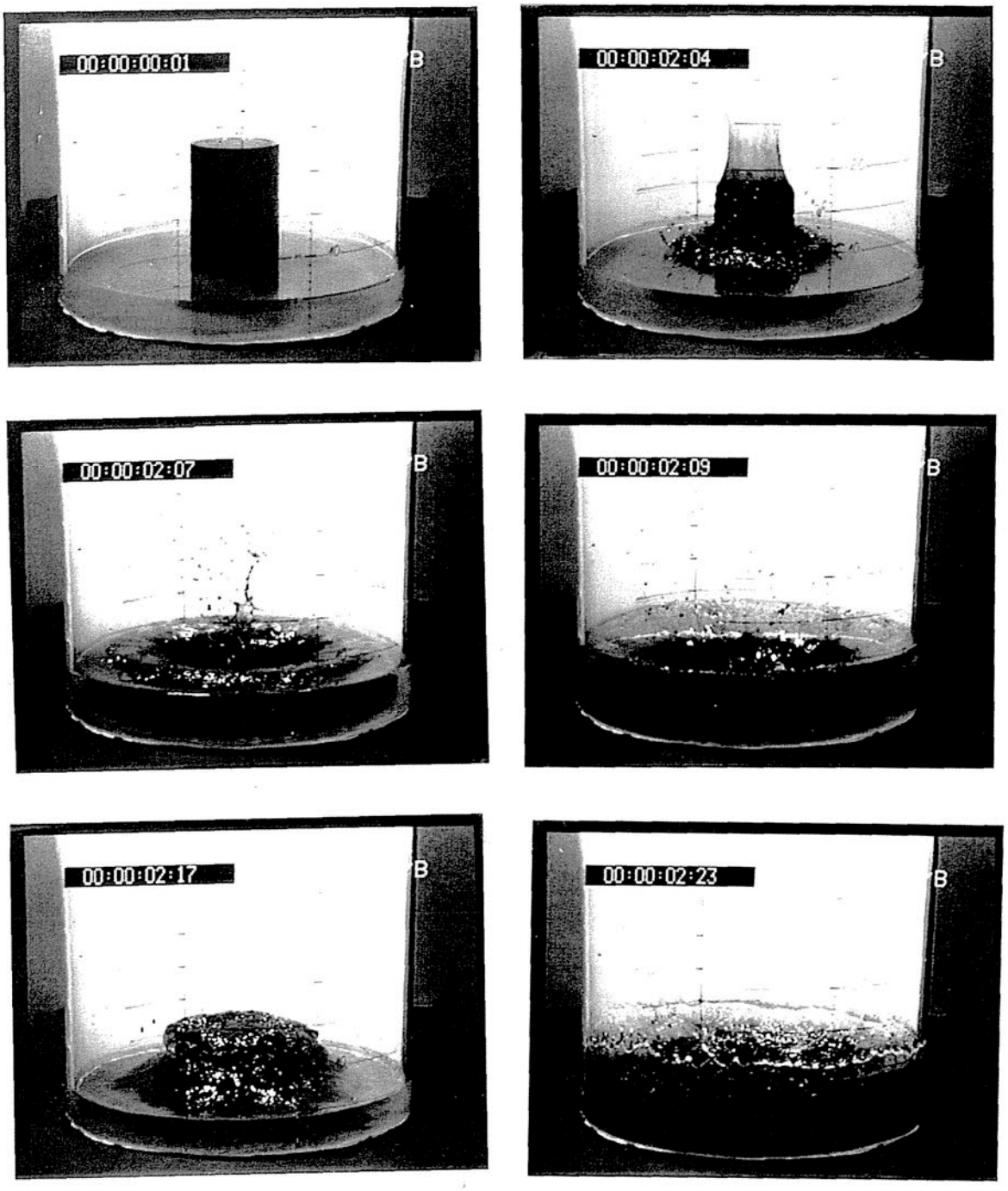

Fig. 2.2. Sloshing motions seen in a typical water step problem (1/2).

Note: The numbers in the left upper window refer to video frames.

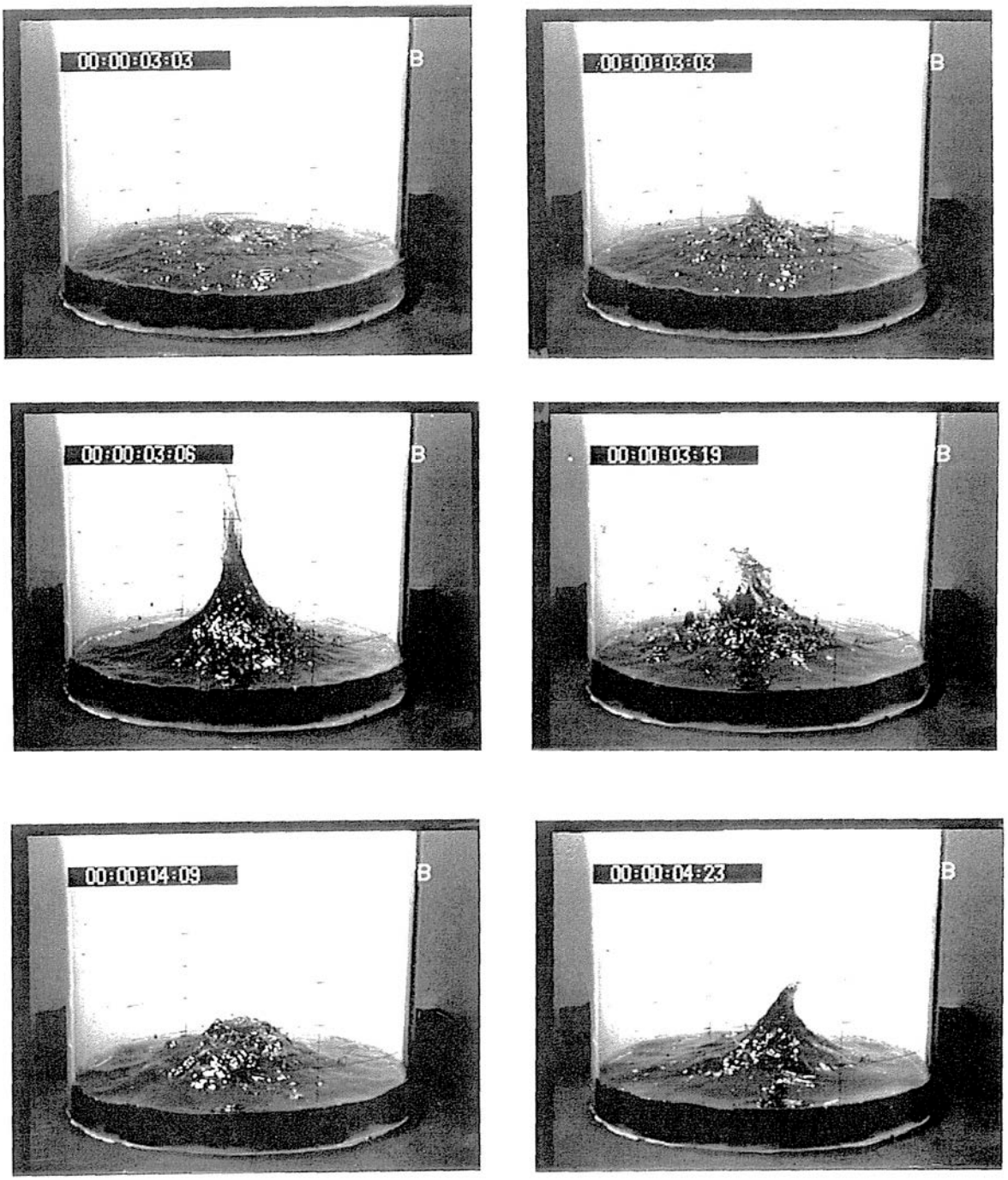

Fig. 2.2. Sloshing motions seen in a typical water step problem (2/2).

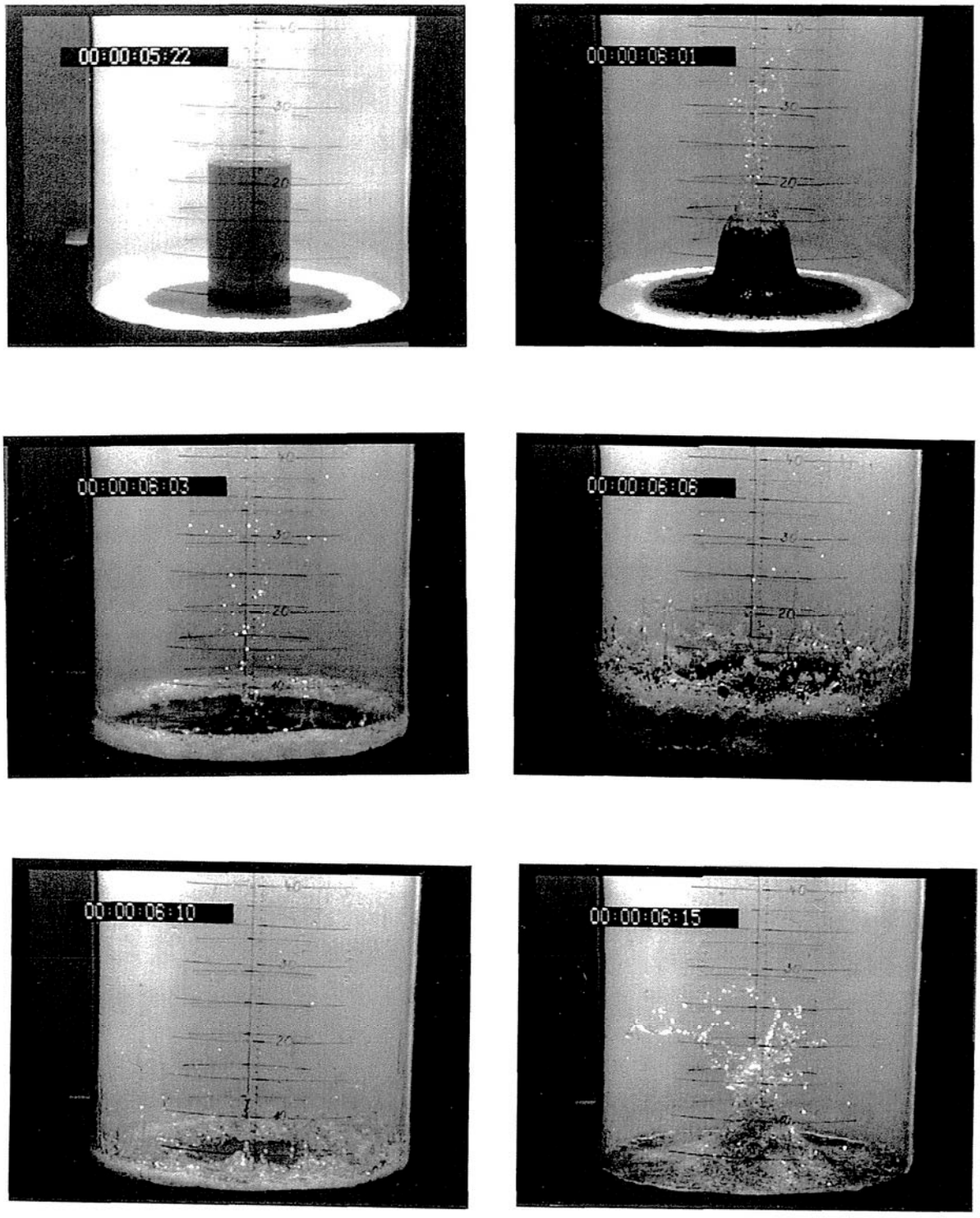

Fig. 2.3. Dam break problem SE-D1P-1 with particles in the flow.

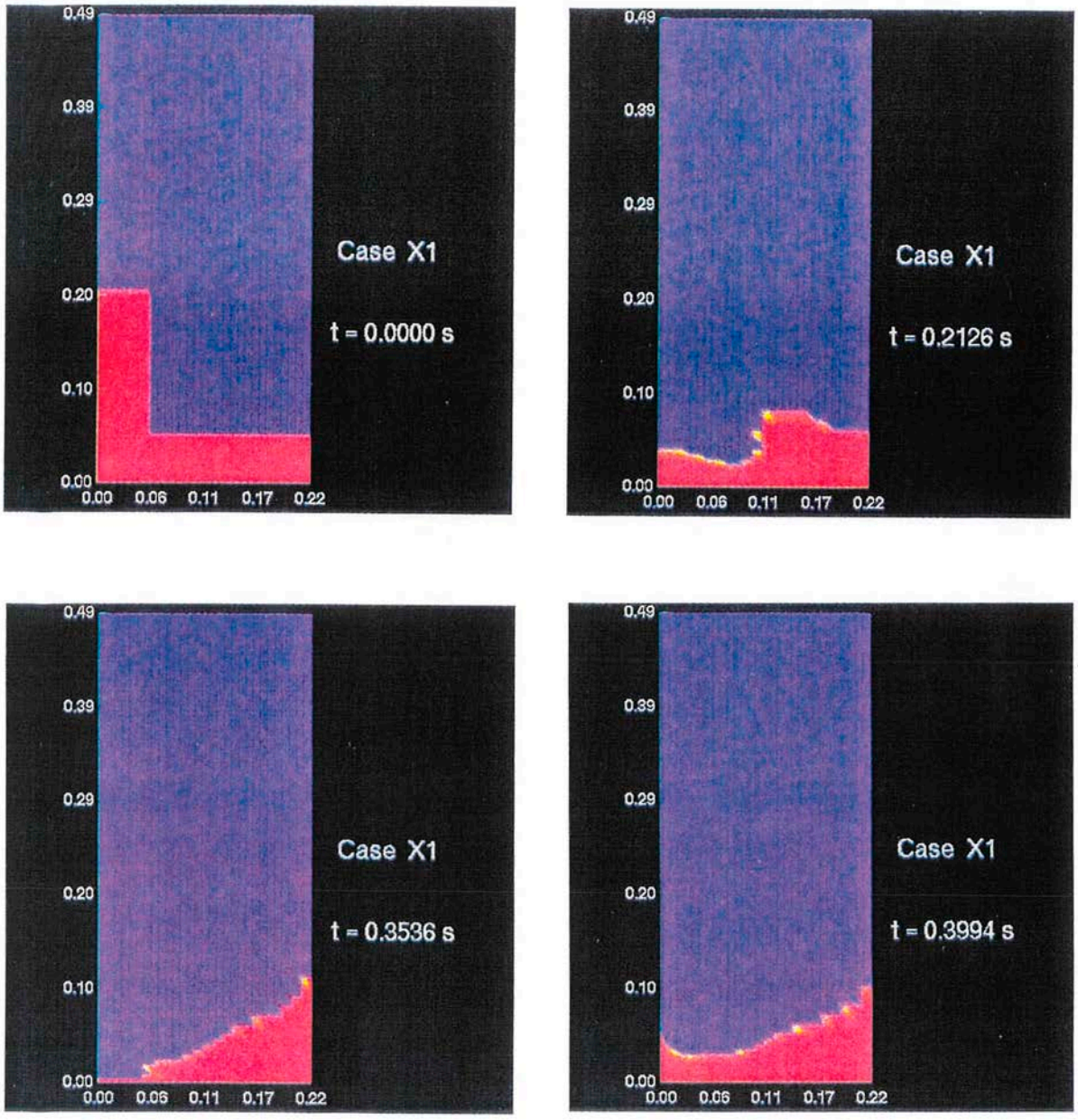

Fig. 6.1. Simulation of the water-step problem with SIMMER-III (1/2).

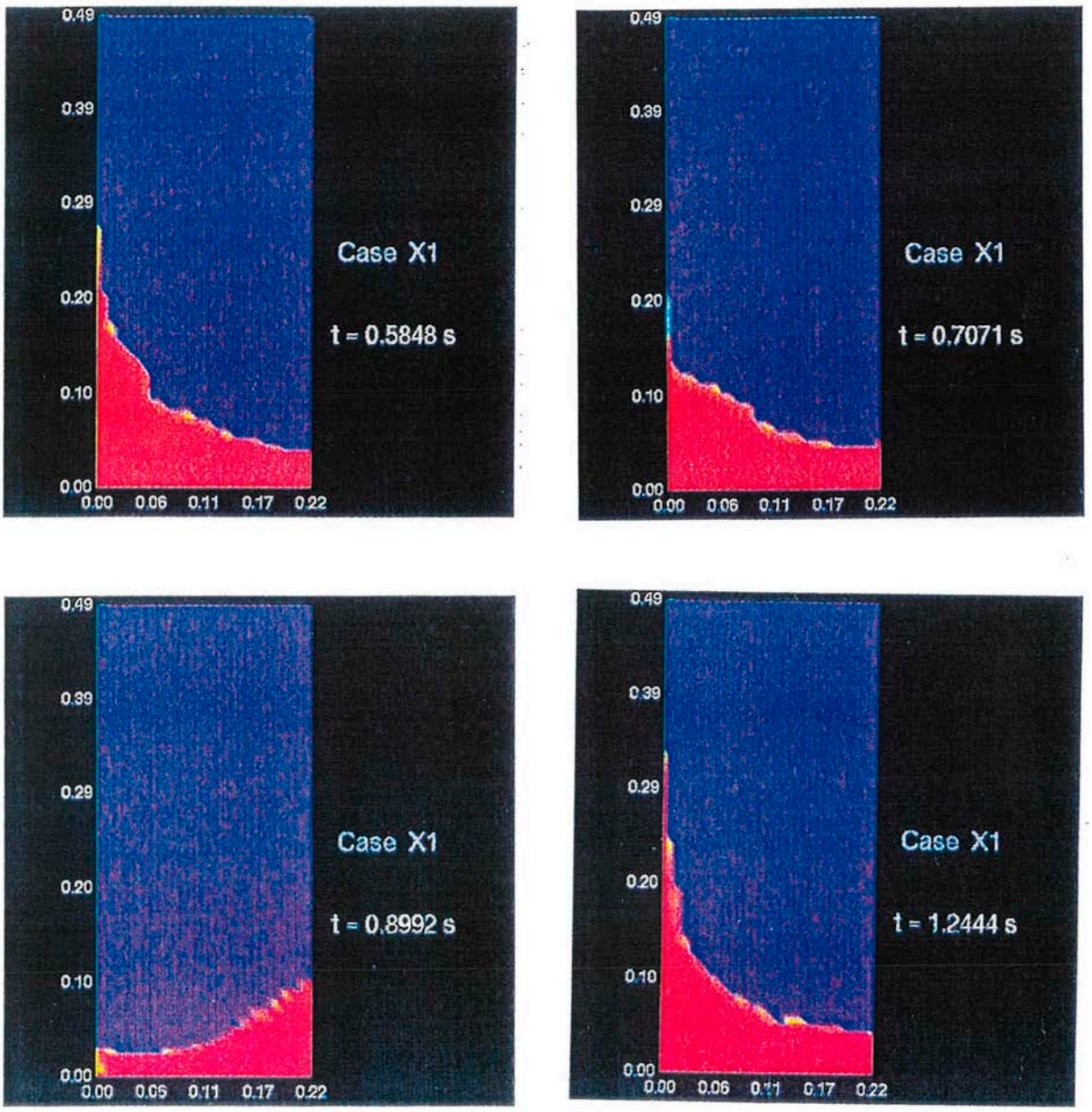

Fig. 6.1. Simulation of the water-step problem with SIMMER-III (2/2).

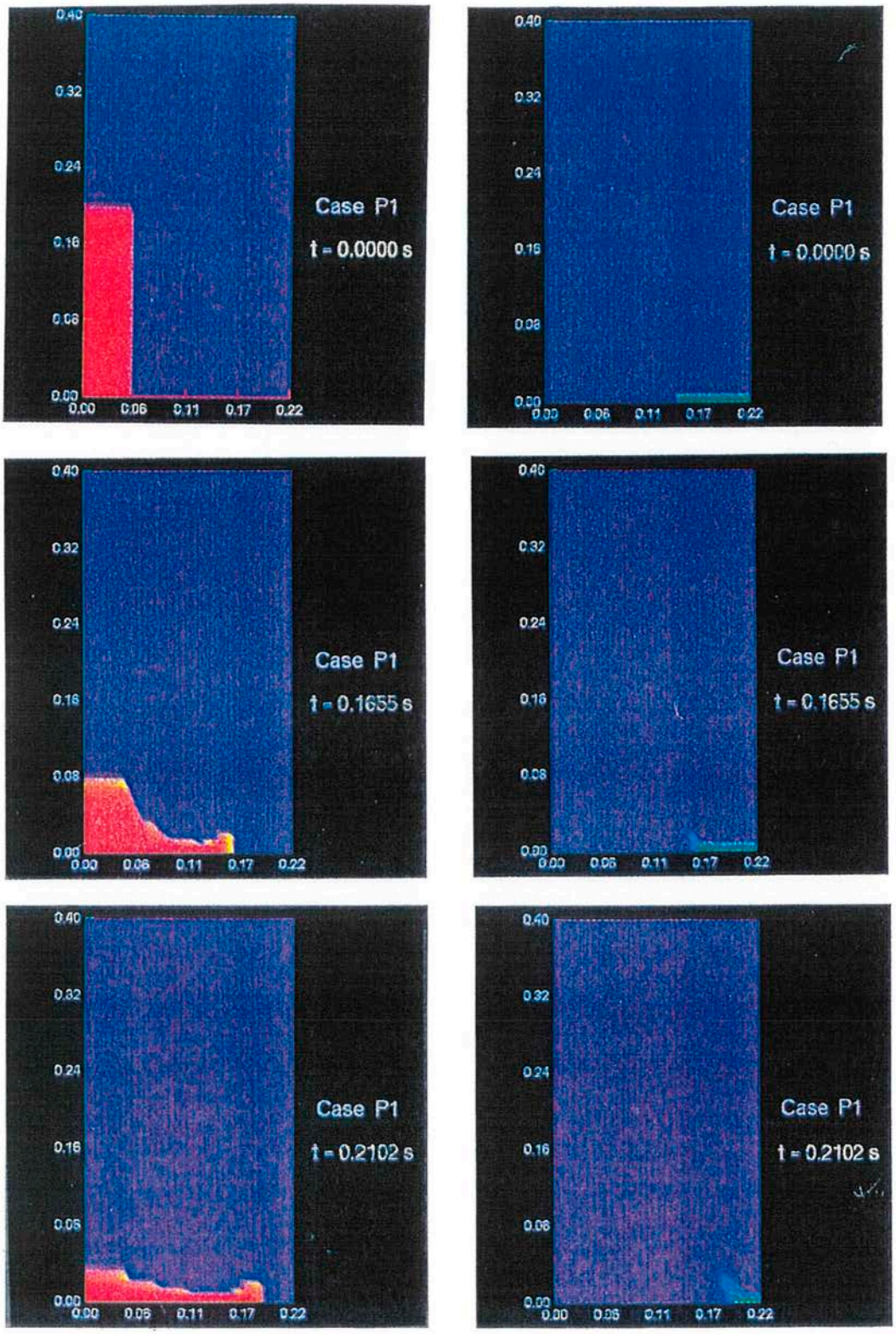

Fig. 6.2. Numerical simulation of the dam break problem SE-D1P-1 with SIMMER-III (second order differencing option) (1/3).

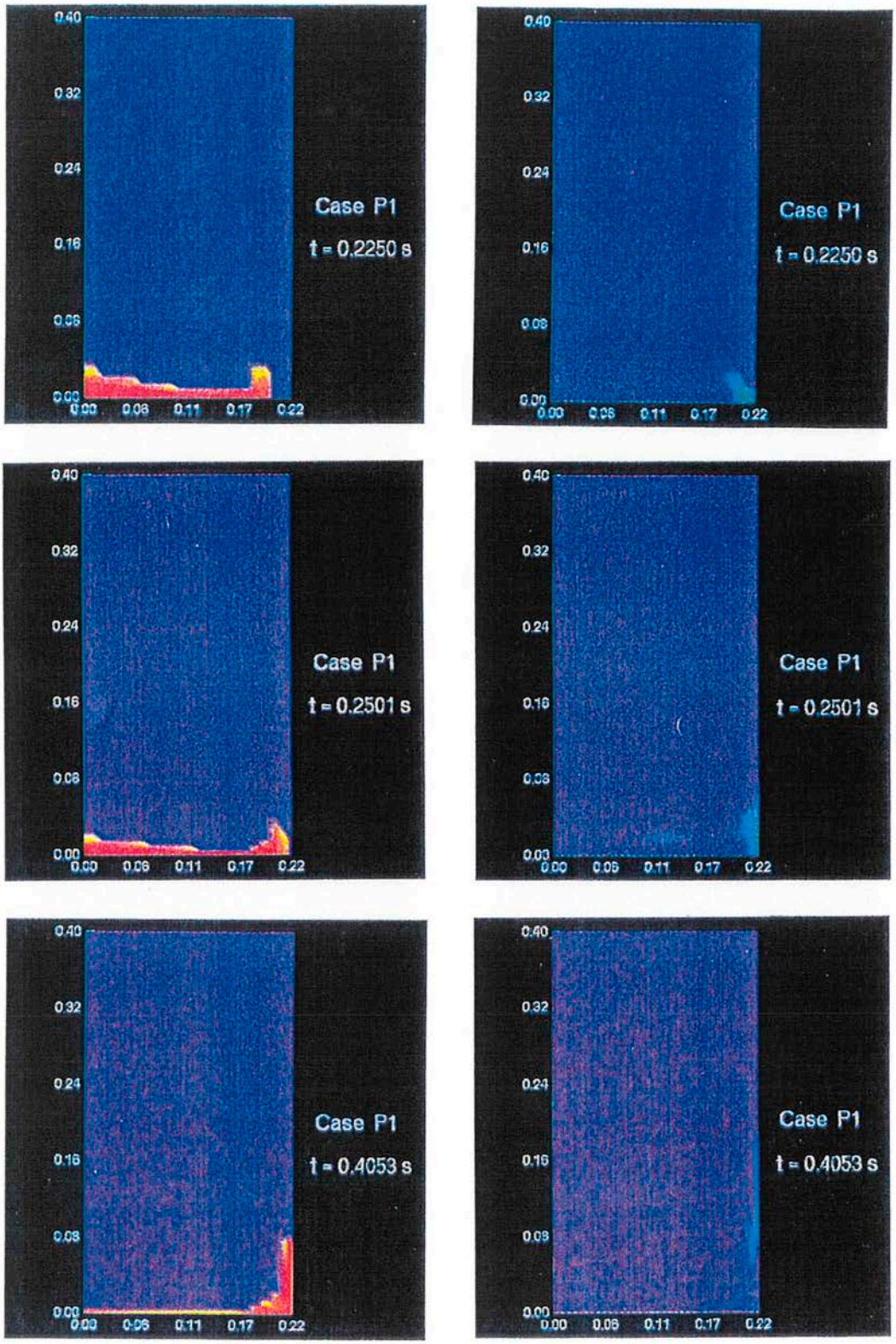

Fig. 6.2. Numerical simulation of the dam break problem SE-D1P-1 with SIMMER-III (second order differencing option) (2/3).

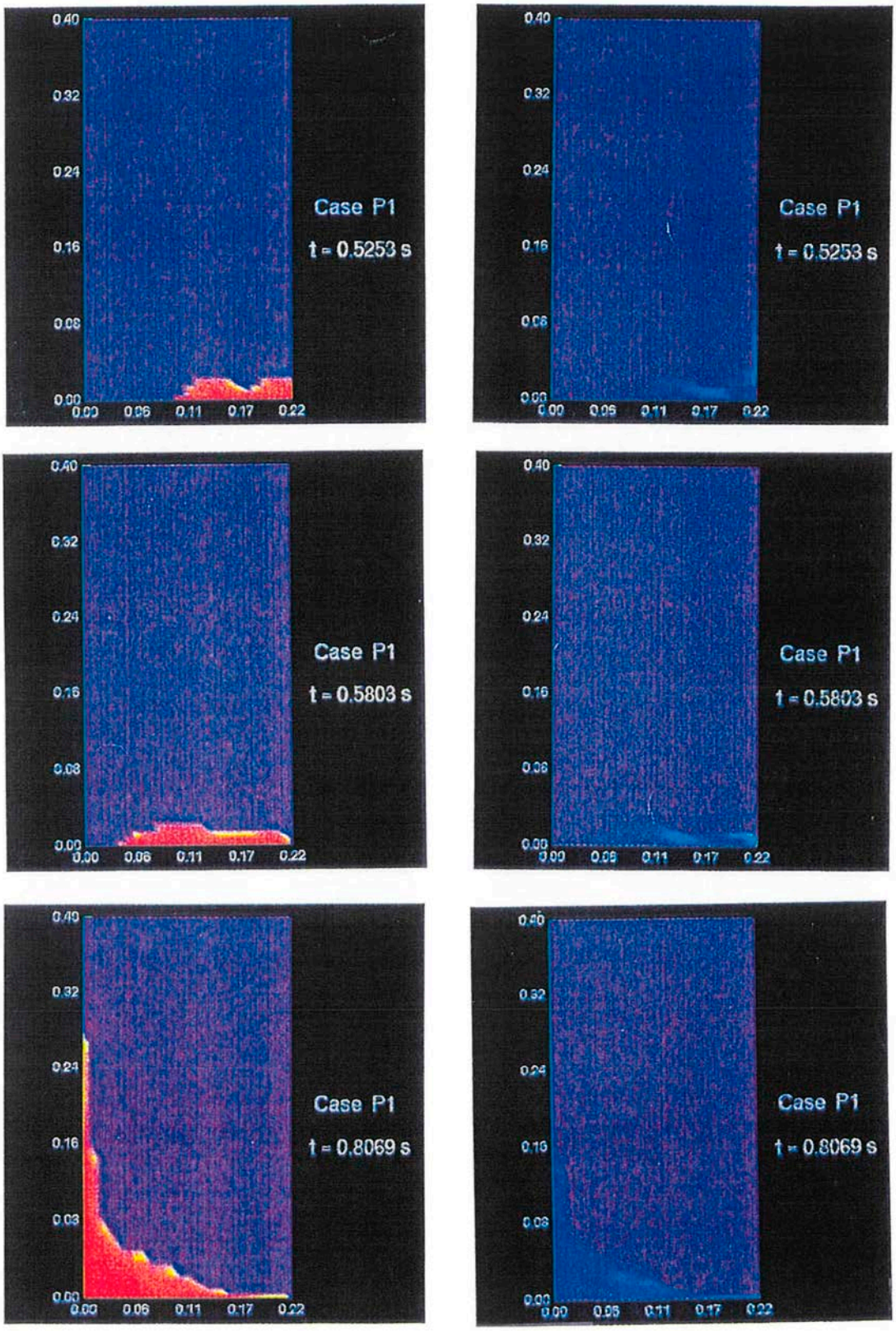

Fig. 6.2. Numerical simulation of the dam break problem SE-D1P-1 with SIMMER-III (second order differencing option) (3/3).

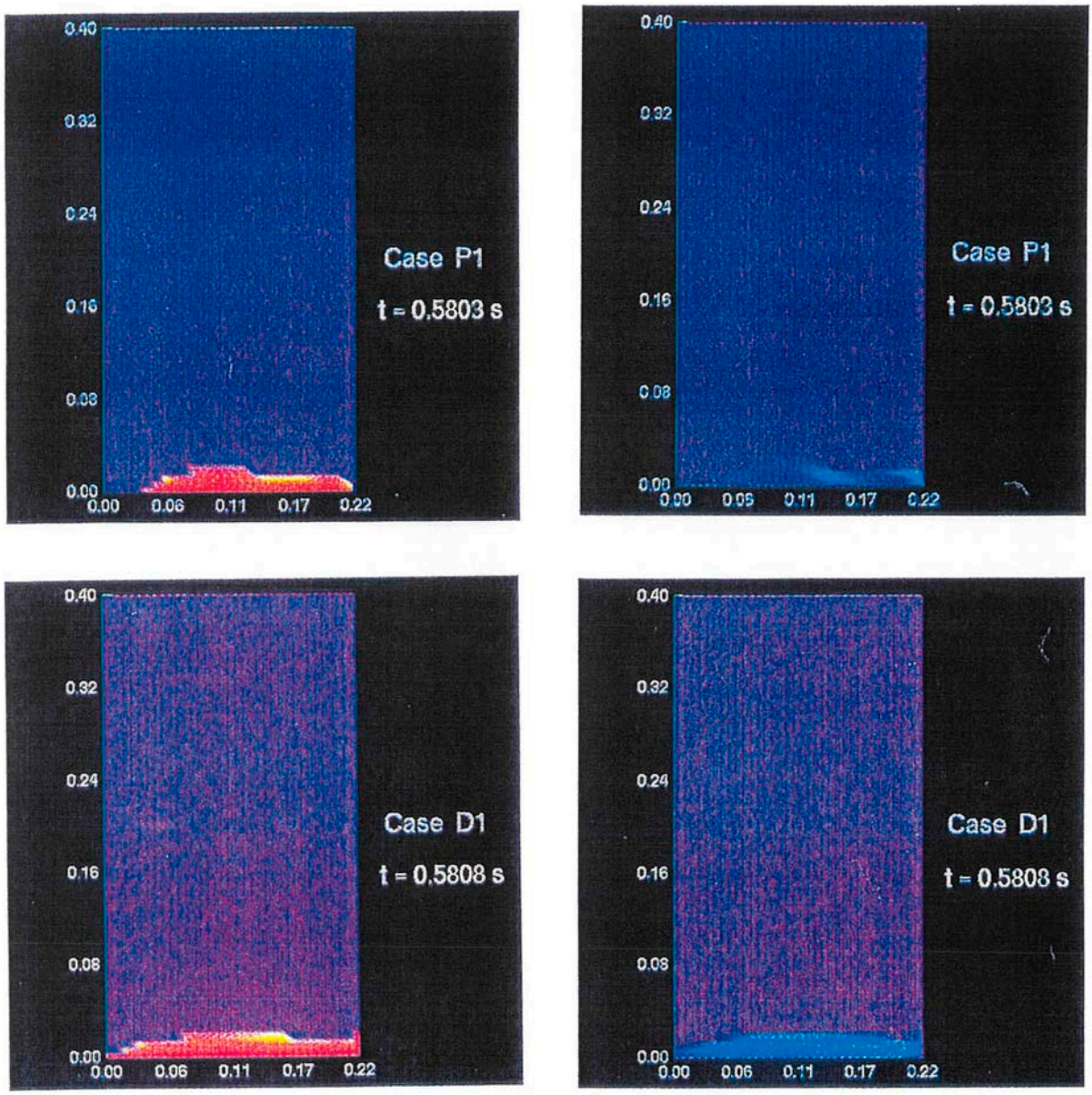

Fig. 6.3. Comparison of the wave package smearing in the numerical simulations of the dam break problem SE-D1P-1 with SIMMER-III.

Second order differencing option (above - case P1)

First order differencing option (below - case D1)

Problem 1.8: Water hammer

"Water Hammer Problem"

Koji Morita (PNC)

Outline of the Case

Pressure rise in a pipe caused by a sudden change in the rate of flow or stoppage of flow in the pipe is known as water hammer. For sudden flow stoppage, the pressure rise due to the deceleration of a compressible fluid in a non-expandable pipe is finite; the fluid in the line behaves as a "plug" and the pressure rise is that corresponding to the inertia effects of this plug. A finite maximum pressure rise is determined by the expending of a part of the kinetic energy of the moving fluid in compressing the fluid.

1. Objectives of the Application

The objective of this problem is to test the SIMMER-III (S-III) fluid dynamics modeling for compressible flows. Characteristics of the water hammer can be related to the velocity of wave propagation in a fluid. In a non-expandable pip, the pressure wave propagates through the compression of the fluid, and hence with the velocity of sound in the fluid. These features tests the wave propagation characteristic and the ability of the numerical solution method of the fluid dynamics coupled with the EOS model that provides the fluid compressibility.

2. Description of the Benchmark Problem

The problem consists of a horizontal pipe, in which a liquid column moving toward the closed end of the pipe. The liquid column initially has a uniform velocity and then is suddenly stopped when the top of the moving column arrives at the closed end. For the sudden stoppage, a finite pressure rise occurs due to the expending of a part of the kinetic energy of the moving fluid in compressing the fluid.

3. Analytical Solution

The equation for maximum pressure or head rise produced by a sudden flow change can be derived from Newton's second law, relating force to the rate of change of momentum, utilizing the velocity of the pressure waves, which are set owing to the inertia of the fluid in the line. The resulting equation is referred to as the Joukowsky or water-hammer equation[1)]:

$$\Delta p = \rho a \Delta V \tag{1}$$

where a = velocity of wave propagation [m/s]; Δp = maximum head rise [Pa]; ΔV = change in velocity [m/s]; ρ = fluid density [kg/m^3]. Neglecting the pipe expansion, the velocity of wave propagation can be replaced with the velocity of sound in the fluid, c. The maximum head rise given by Eq. (1) can also be

developed if the flow is changed within the time it takes the pressure wave to travel from the point of stoppage to the end of the pipe or to the location of total wave reflection an return; that is, within one period as given by

$$\tau = 2L/c \qquad (2)$$

where τ = pipe period [s]; L = length of fluid column [m].

4. Understanding of Phenomena

The phenomena addressed in the problem are well understood.

5. SIMMER-III Representation

5.1. Geometry, Initial and Boundary Conditions for a Reference Case

The horizontal pipe 5 cm in diameter and 55 cm in length is closed at one end and is opened at the other. In the pipe, initially, the side of the closed end is filled with a liquid sodium column L = 50 cm and the other side is with a saturated sodium vapor. All fluid is isothermal at 700 K, initially moving toward the closed end with a uniform velocity of Vi= 1.0 m/s. An adiabatic, free slip and rigid wall boundary condition is imposed on the pipe wall. At the closed end, the velocity is forced to equal zero. The open end is exposed to a saturated sodium vapor at 700 K with a continuous inflow/outflow boundary condition. One dimensional analysis is performed with a uniform axial mesh size Δz= 5.0 cm. The calculation starts at a time just the top of the moving column arrives at the closed end, that is, a sudden flow stoppage occurs: $\Delta V = Vi$. The schematic and nodalization diagram for the reference case (Case 1) is shown in Fig. 1 .

5.2. Code Modifications

None.

5.3. Parametric Cases

To estimate the influence of change in velocity on the water hammer, two different initial velocities of the liquid column were specified. The influence of numerical specifications using smaller time step and axial mesh size were also investigated for three different initial velocities. The initial conditions and numerical specifications used in the calculations are shown in Table 1.

6. Results

The S-III results and the analytical solutions are summarized in Table 2. To obtain the analytical solutions, sodium properties at 700 K, ρ =841 kg/m^3 and c =2390 m/s, were used. The S-III results show good agreement with the analytical solutions on the maximum pressure rise and the pipe period. In comparison with Fig. 2-1, Fig. 2-2 shows that the smaller numerical specifications give more accurate time integration because numerical diffusion is decreased.

7. Conclusions

The S-III fluid dynamics modeling for compressible flows well simulates the characteristics of the water hammer. This means that the numerical solution method of fluid dynamics is consistent with the EOS modeling.

8. Recommendations for Model Improvement

None.

9. References

1) J. H. Perry et al.: Chemical Engineers' Handbook, Fourth Edition, pp. 5-55, McGrawHill, New York (1963).

Table 1. Initial conditions and numerical specifications for the problem.

	Initial velocity : Vi (m/s)	Maximum time step : Δt (s)	Axial mesh : Δz (cm)
Case 1	1	1.0×10^{-5}	5.0
Case 2	5		
Case 3	20		
Case 1 X	1	1.0×10^{-6}	1.25
Case 2 X	5		
Case 3 X	20		

Table 2. S-III results compared with analytical solutions.

	Maximum head rise : Δp (MPa)		Pipe period : τ (ms)	
	S-III	Analytical	S-III	Analytical
Case 1 (Vi = 1 m/s)	2.02	2.01	0.404	0.418
Case 2 (Vi = 5 m/s)	10.1	10.0	0.401	
Case 3 (Vi = 20 m/s)	41.1	40.2	0.398	
Case 1 X (Vi = 1 m/s)	2.02	2.01	0.415	0.418
Case 2 X (Vi = 5 m/s)	10.1	10.0	0.413	
Case 3 X (Vi = 20 m/s)	41.1	40.2	0.409	

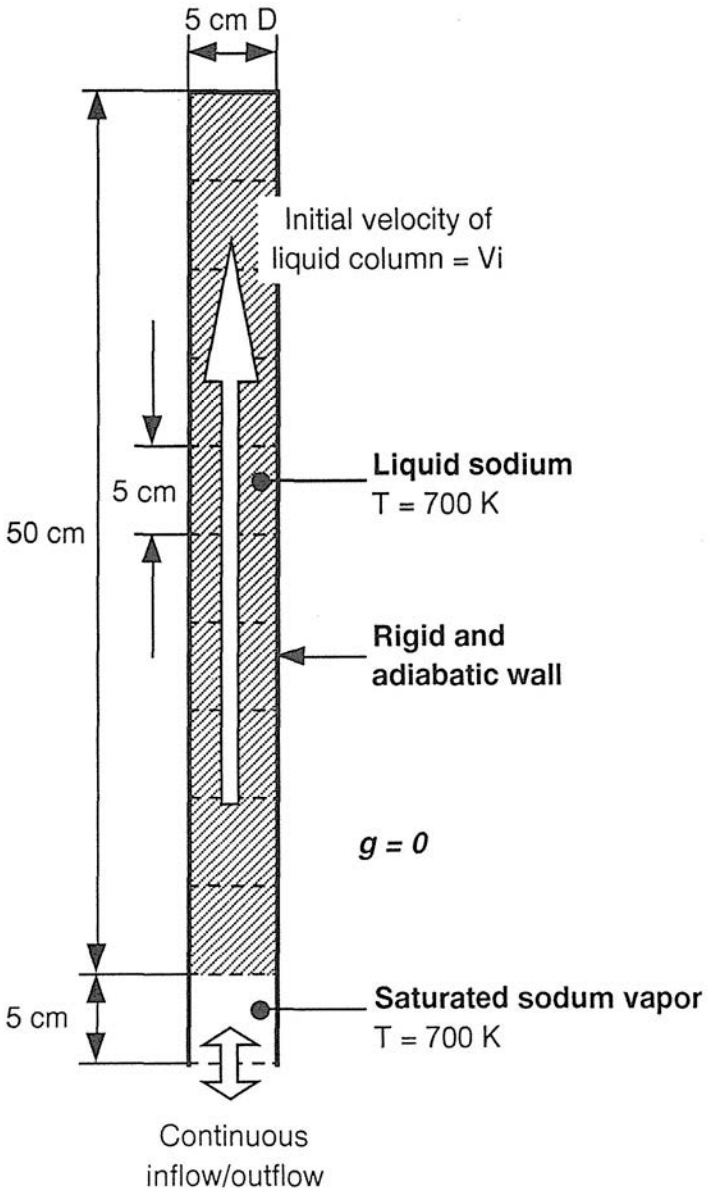

Fig. 1. Schematic and nodalization diagram for Case 1.

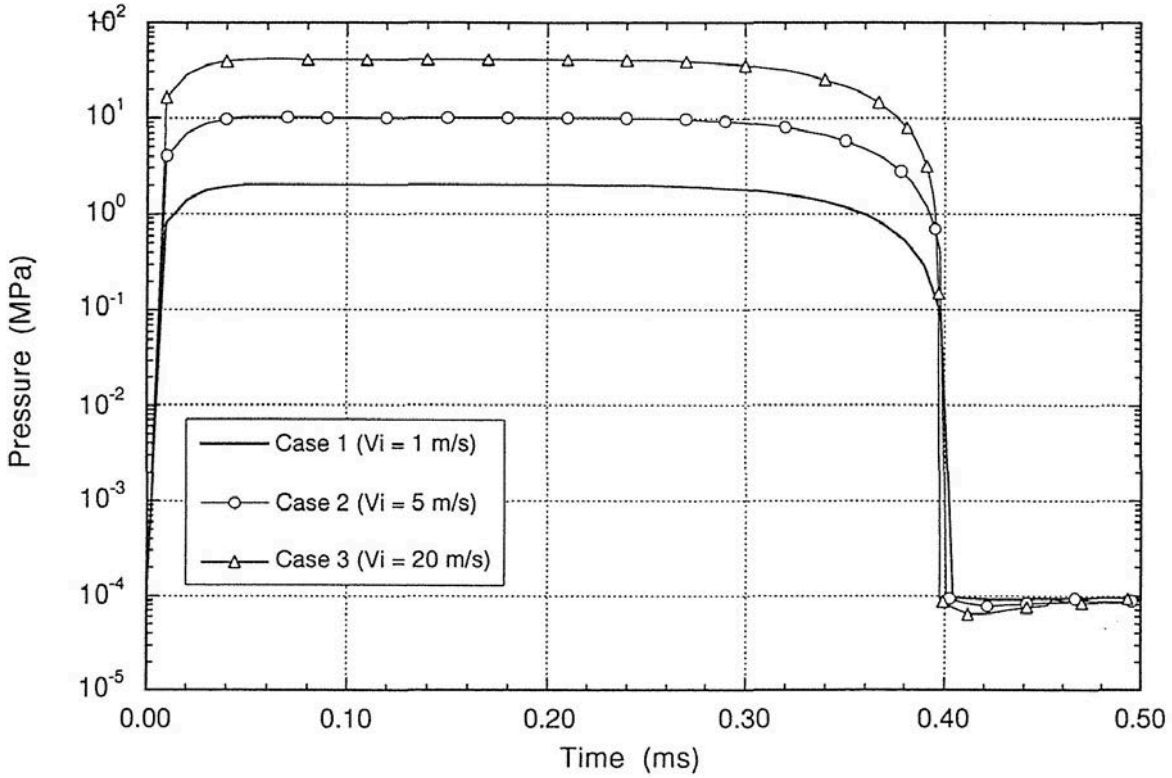

Fig. 2-1. Sodium vapor pressures at the top cell ($\Delta t = 1.0\times10^{-5}$ s, Δz =5.0 cm).

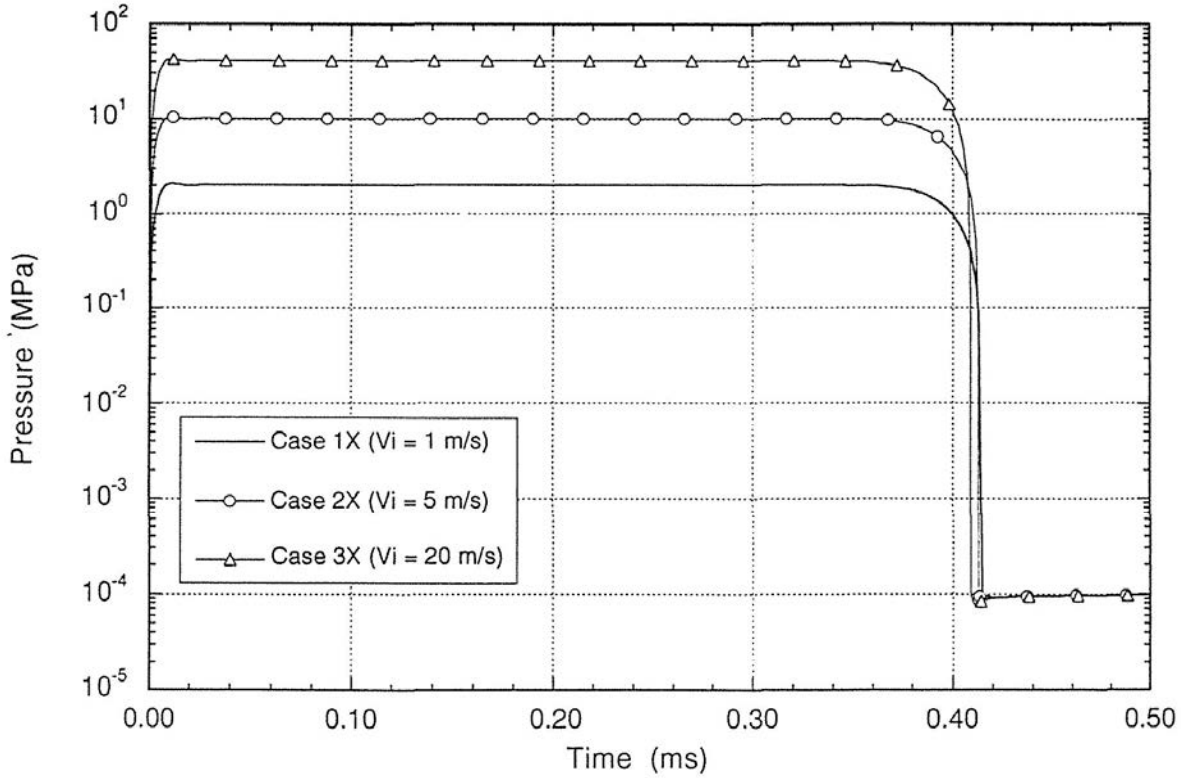

Fig. 2-2. Sodium vapor pressures at the top cell ($\Delta t = 1.0\times10^{-6}$ s, Δz=1.25 cm).

Problem 1.9: Impact of liquid slugs

"Impact of Liquid Slugs on Rigid Surfaces"

W. Maschek, G. Arnecke, S. Kleinheins, M. Flad (FZK)

Outline of the Case

The purpose of this application of SIMMER-III is the simulation of continuous liquid slugs moving through gas/air and their impact behavior on rigid surfaces. In the case of a vapor explosion in the vessel of a PWR a molten cerium slug might be accelerated upwards which then impinges on the upper vessel structure. This phenomenon is described with codes like PLEXUS. In the present application of SIMMER-III some specific calculations of PLEXUS are recalculated and corns pared with SIMMER-III results. The simulation of a falling liquid slug through air driven by gravity or pressure is of interest as in SIMMER-III no free fluid surface with its related instabilities is modelled.

1. Objectives of the Application

This application of SIMMER-III should investigate the motion of liquid slugs in air, the impact behavior of these slugs on rigid surfaces and obstacles and the momentum transfer during impact. In addition, the modelling of virtual walls in SIMMER-III is tested. The results can also serve as a check for results of the PLEXUS code[1)] for the specific case of slug impact on a rigid surface. In PLEXUS the fuel slug is modelled by an ensemble of small compressible spheres (particles). With decreasing sphere-radius the PLEXUS model should converge against the continuum model of fluids, which is however not fulfilled. When the particle slug impacts on a rigid surface the whole slug disintegrates and disperses (Fig. 1.1). SIMMER-III shows a different behavior with the fluid slug flowing and spreading after impact on a rigid wall or an obstacle. The comparison with experiments and other code calculations back the SIMMER-III results. The momentum transfer calculated by SIMMER-III is less than the one calculated by PLEXUS. The motion of the falling liquid slug through air driven by gravity or pressure is of interest as no free fluid surface is modelled in SIMMER-III with its related Taylor or Helmholtz instabilities.

2. Description of Experiments

Two types of experiments are needed for comparison with the calculations. Firstly, experimental information about falling slugs through air is necessary and secondly, experiments on the impact of liquids on a rigid surface or an obstacle is needed.

In Ref. 2) a liquid slug is released from a container and falls approximately as a cylinder towards a lower water surface. Surface disturbances of various wavelengths can be observed. The lower slug surface shows some 'mushrooming'. For the impact phenomena of liquid slugs, in literature, experiments

with impinging solids (projectiles) and liquid jets on rigid surfaces are reported. Experiments for soft pellets are e.g. reported in.[3] A pellet of rocket propellant is accelerated towards a rigid surface and is deformed. The generated shock wave finally ignites the pellet and destroys it. Before this, the pellet is deformed and shows a flowlike behavior (Fig.2.1). The numerical simulation of the deformation and flowing process is simulated with the SALE[4] and HELP[5] code (fluiddynamic codes). The pellet is simulated as a nonviscous, compressible fluid. The results of the simulation compared to experiment are described as excellent.

In Ref. 6) the results of impact phenomena of water drops on rigid structures are displayed (Fig. 2.2). The impact velocity is approx. 150 m/s. Compressible and incompressible code calculations are used for the simulation. The results show the typical deformation and flowing process. Additional experimental and theoretical information can also be gained.[7), 8)] No disintegration process of the bulk slug is observed in all these analyses and experiments.

3. Analytical Solution

Analytical solution for impact processes of a liquid on a rigid surface based on continuum-theoretical approaches imply a flow redistribution at impact and no disintegration of the slugs.[9)]

4. Understanding of Phenomena

Experimental information on the impact of liquid droplets and slugs is available.

5. SIMMER-III Representation

Three different cases have been analyzed with liquid slugs accelerated either by gravity or vapor pressure and finally hitting a rigid surface or a rigid target. The liquid slugs analyzed had a height to diameter ratio of 0.42. An additional case with a long liquid slug with a H/D ratio of 16.7 has been investigated to further study the liquid/gas flow phenomena and surface phenomena modelled by SIMMER-III. The different cases are displayed in Table 5.1 and the geometrical arrangements are schematically displayed in Fig. 5.1.

5.1 Geometry, Initial and Boundary Conditions

A 2-D mesh with (50×100 cells) has been used for the calculations. In the gravity driven cases the liquid water slug is used. The initial conditions for the pressure driven slugs are, that a hot two phase fuel region with 5 MPa is layered above and accelerates a cold liquid fuel slug. The slug moves within a tube modelled by virtual walls. In the case J2 the obstacle has both been modelled by virtual walls and a solid structure (structure model).

5.2 Parametric Cases

See Table 5.1.

6. Results

Case S1

In case S1 (Fig. 5.2) the liquid water slug drops onto the horizontal surface with a velocity of 6.2 m/s. The peak pressures obtained are 3.2×10^5 Pa, far below acoustic pressures. (Note the ambient pressure in Fig. 5.3, which is modelled to obtain similar conditions to the cases J1 and J2.) For the calculation the 2nd order numerical scheme has been used. The pressure distribution is given in Fig. 5.3.

The momentum transfer is determined by fluid forces and at the maximum about 60 percent of the initial momentum (evaluation of momentum at central impact location) is imparted in $\Delta t = h_{slug}/v_{slug}$. This magnitude of momentum transfer is backed by experiments.[10] After impact, the liquid slug spreads and flows along the surface. An additional calculation with a first order scheme (case S1D) shows a strong numerical smearing and damping. The impact pressures and the momentum transfer are reduced by a factor of 2. Thus the application of the first order method gives inadequate results.

In Fig. 5.2 one can observe some surface perturbations at the lower and radial outer surface. They are not related to a Taylor or Kelvin-Helmholtz instability as in SIMMER-III no free surface of the liquid slug is modelled (see case S2).

Case J1

In case J1 a liquid fuel slug is accelerated by a high temperature two phase fuel cushion. The liquid slug moves between virtual walls and impacts the lower boundary with v~33 m/s (Fig. 5.4). The peak pressure in the central impact location (point of momentum evaluation) goes up to 7×10^8 Pa (Fig. 5.5). After impact the reflected pressure wave leads to some cavitation processes. The momentum transfer is dominated by shock waves and about 85% of the initial momentum is transferred in the first pressure peak ($\Delta t = h_{slug}/c_{sound}$). Again the slug starts a flowing process after impact.

Case J2

In case J2 the pressure accelerated fuel slug hits an obstacle before impinging on the lower rigid surface (Fig. 5.6). The peak velocities obtained are 32 m/s and the peak pressures are 6×10^8 Pa (Fig. 5.7). After the impact the flowing processes around the obstacle can be identified which finally turns into a drippling process when the pressure is reliefed. About 70% of the initial momentum is transferred in the first pressure peak.

The obstacle was modelled both by the ordinary structure model and by virtual walls. Problems occurred with the virtual wall model when the slug impacted on the horizontal wall. The timesteps became increasingly small and levelled of at 10^{-8} s (condition OPTPIT, number of pressure iteration limit exceeded).

Case S2

In case S2 the falling of a long cylindrical slug is modelled to investigate the liquid/gas interaction at the slug surface. The results are compared qualitatively to the experimental result from Ref. 2). Three calculations have been performed with a variation of the drag coefficients CDD (10^{-4}, 1, 10^{4}) displayed in Fig. 5.8, and Fig. 5.9. It can be seen from the results that the bulging out of the liquid is strongly controlled by the drag coefficient CDD and can be suppressed by a large CDD value. For a good adjustment of the CDD values further experimental results seem to be necessary.

7. Conclusions

SIMMER-III is able both to describe the movement of liquid slugs through gas and the impact of such slugs on rigid structures. The results of other codes and experimental results back the SIMMER-III impact calculations. When using a first order numerical scheme, strong numerical diffusion effects can be observed and the impact pressues and the momentum transfer is underestimated.

8. Recommendations

To better simulate surface instabilities of liquid slugs a modelling of free surfaces is required. Similar techniques as realized in SOLA-VOF[11] could be used but seem to be difficult to implement in the environment of a multiphase, multicomponent, multifield code. Simple experiments with falling slugs could provide better data for the simulation of surface effects.

9. References

1) H. Bung, P. Galon, M. Lepareux, A. Combescure: A New Method for the Treatment of Impact and Penetration Problems. SMIRT 12, (1993), Paper 802/1.

2) H.N. Oguz, A. Prosperetti, A. Kolaini: Air Entrainment of a Falling Water Mass, J. Fluid Mech., Vol. 294,181 (1995).

3) Robert R. Karpp: A Model for Computing Late Detonations Initiated in Propellants by Impact LA 10270-MS (1984).

4) L.J. Hageman, D.E. Wilkins, R.T. Sedgwik, and J.L. Waddell: HELP: A Multi-Material Eulerian Program for Compressible Fluid and Elastic-Plastic Flows in Two Space Dimensions and Time, Systems, Science and Software report SSS-R-75-2654 (1975).

5) A.A. Amsden, H.M. Ruppel, and C.W. Hirt: SALE: A Simplified ALE Computer Program for Fluid Flow at All Speeds, Los Alamos Scientifc Laboratory Report LA-8095 (1980).

6) N. Nishikawa, S. Amatatu, T. Suzuki: Simulation of Impact Phenomena by Impinging Droplets Comp. Fluid Dynamics, 569, G. de Vahl Davis and C. Fletcher (Ed.) Elsevier Science Publishers B.V. (North-Holland) (1988).

7) J.B.G.Hwang, F.G. Hammitt: High-Speed Impact Between Curved Liquid Surface and Rigid Flat Surface, Trans. of the ASME, Journal of Fluids Engineering, Vol.99, No.2, pp.396-404, (1977).

8) C. Mundo, M. Sommerfeld, C. Tropea: Droplet-Wall Collisions: Experimental Studies of the Deformation and Breakup Process, Int. J. Multiphase Flow, Vol. 21, No.2, pp.151-173 (1995).

9) B. Goeller: 1995 (Internal FZK report).

10) Th. Stach: 1995 (Internal FZK report).

11) B.D. Nichols, C.W. Hirt, R.S. Hotchkiss: SOLA-VOF: A Solution Algorithm for Transient Fluid Flow with Multiple Free Boundaries LA-8355 (1980)

12) L.A. Glenn: On the Dynamics of Hypervelocity Liquid Jet Impact on a Flat Surface, Journal of Appl. and Physics (ZAMP), Vol. 25, No.3, pp.383-398, (1974).

Table 5.1. SIMMER-III calculational cases.

Case	Acceleration	Fall-distance (cm) Pressure (MPa)	Geometry H/D ratio	Impact conditions
S1	gravitaion	200	0.42	surface
J1	pressure	5	0.42	surface
J2	pressure	5	0.38	obstacle
S2	gravitation	580	16.7	surface

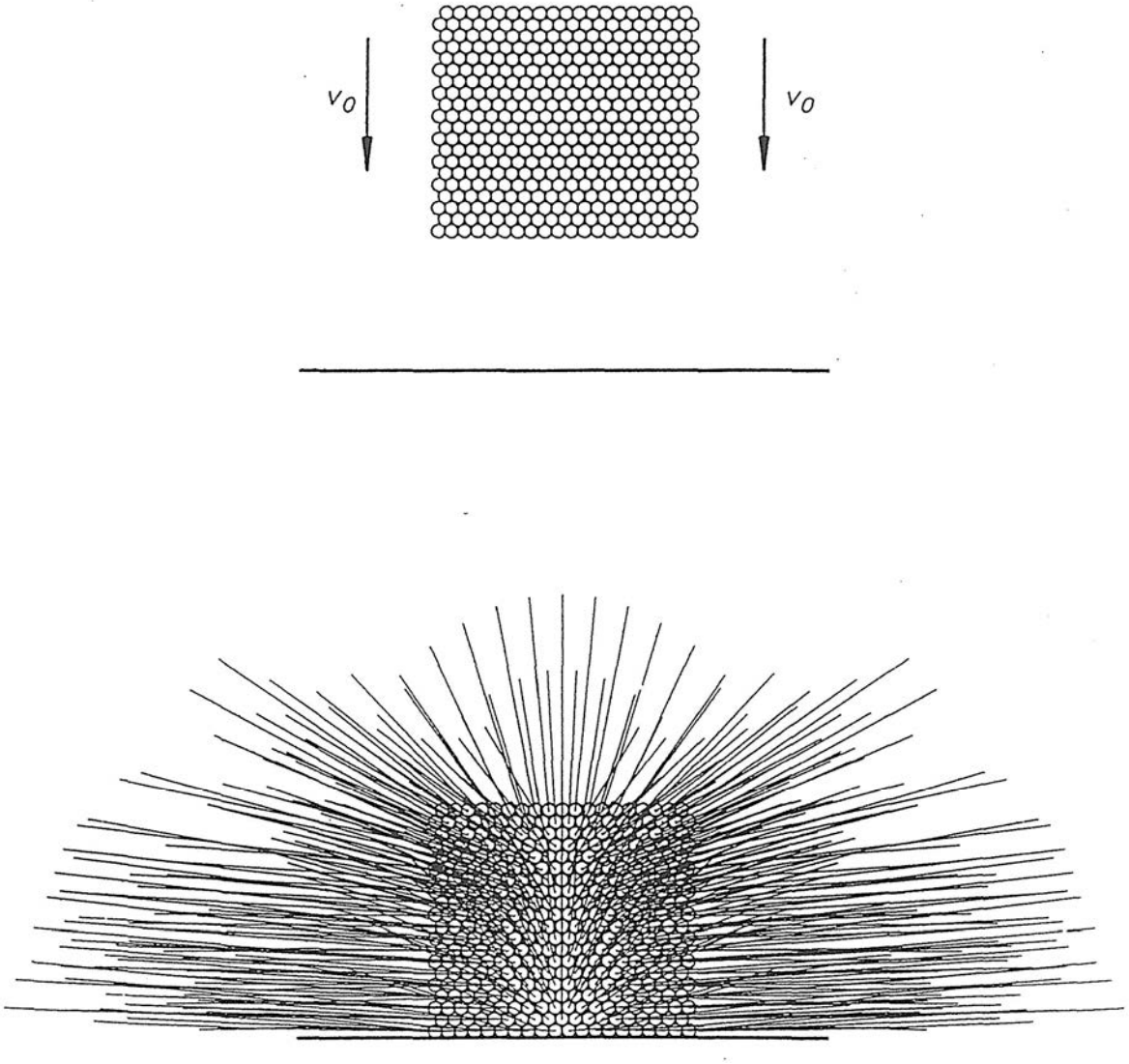

Fig. 1.1. Impact of a plane compressible water slug on a rigid surface simulated by PLEXUS.

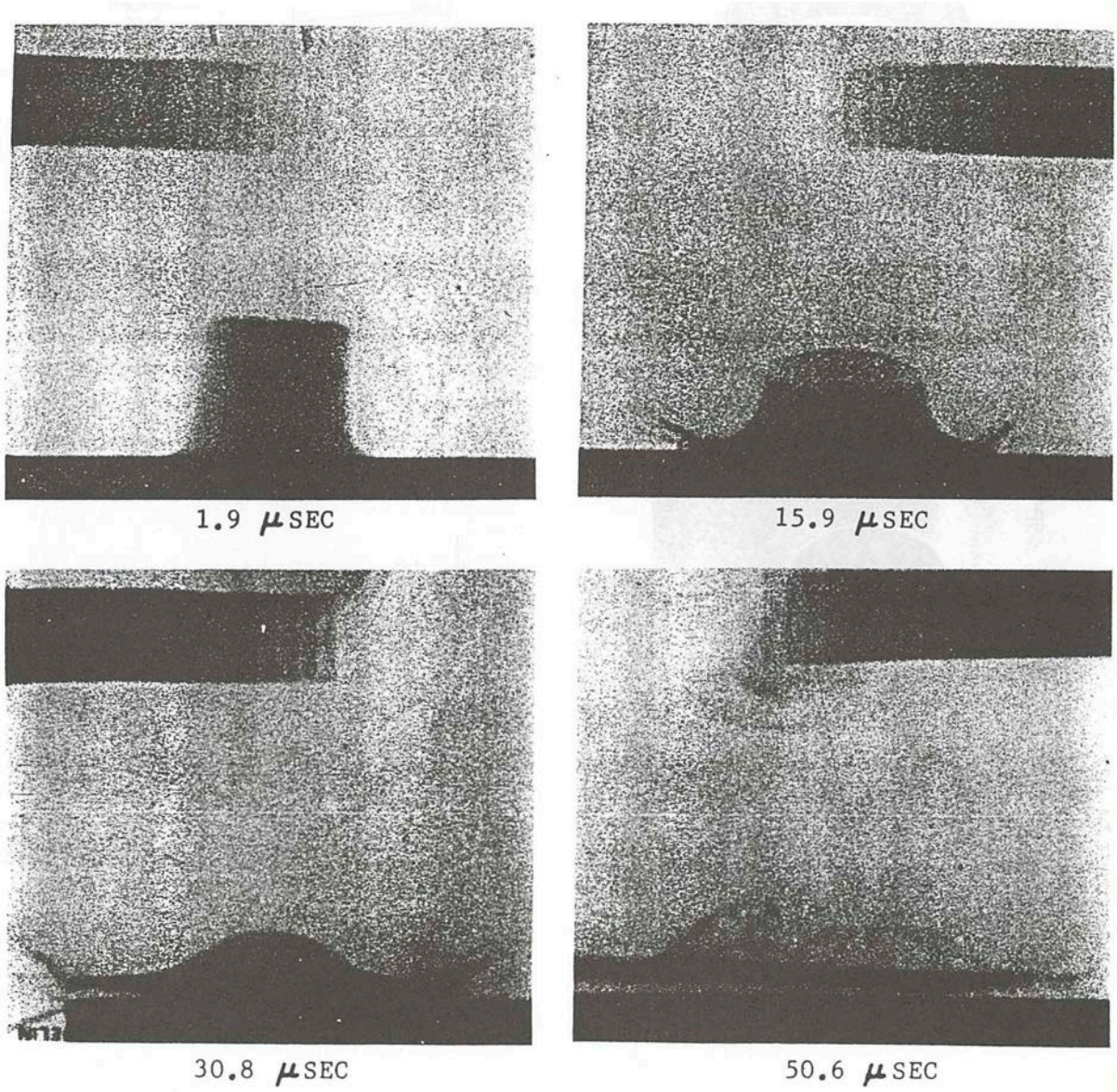

Fig. 2.1. Radiograph of pellet impact on a rigid surface.

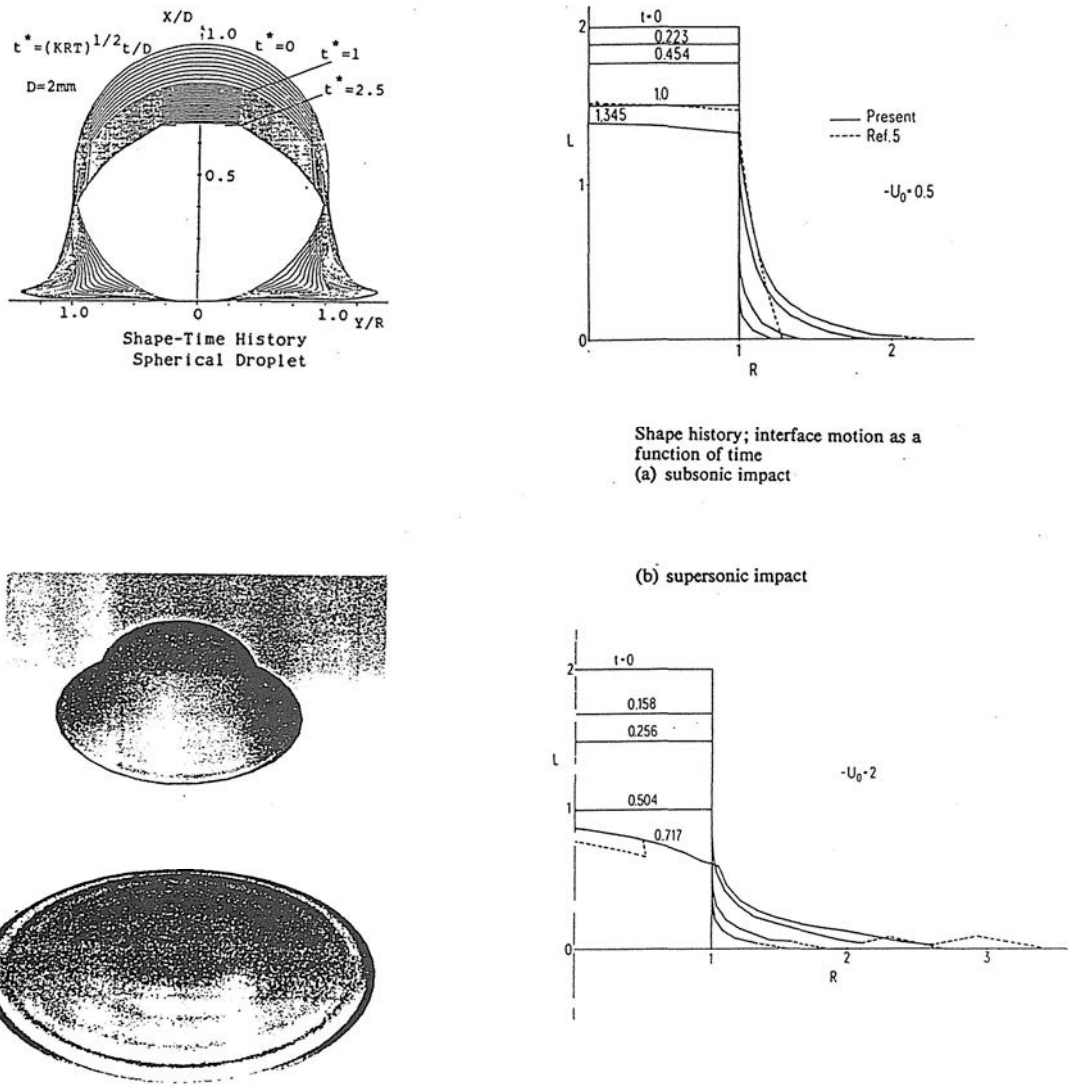

Fig. 2.2. Shape-time history of a sperical droplet [6] and a liquid slug [12] impacting on a rigid surface.

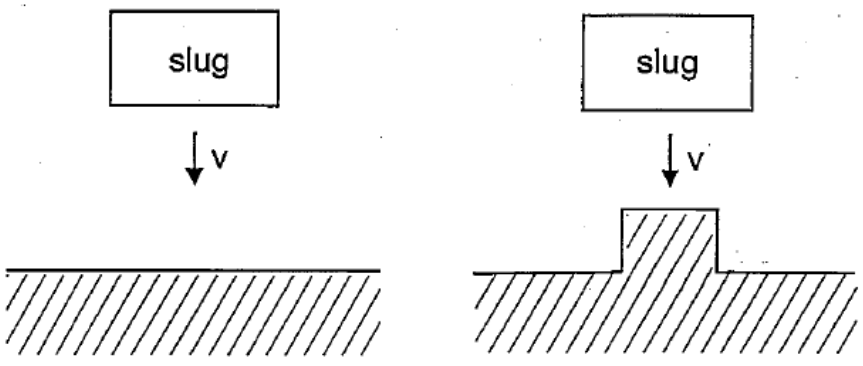

Fig. 5.1. Geometrial arrangement of liquid slug impact-structure.

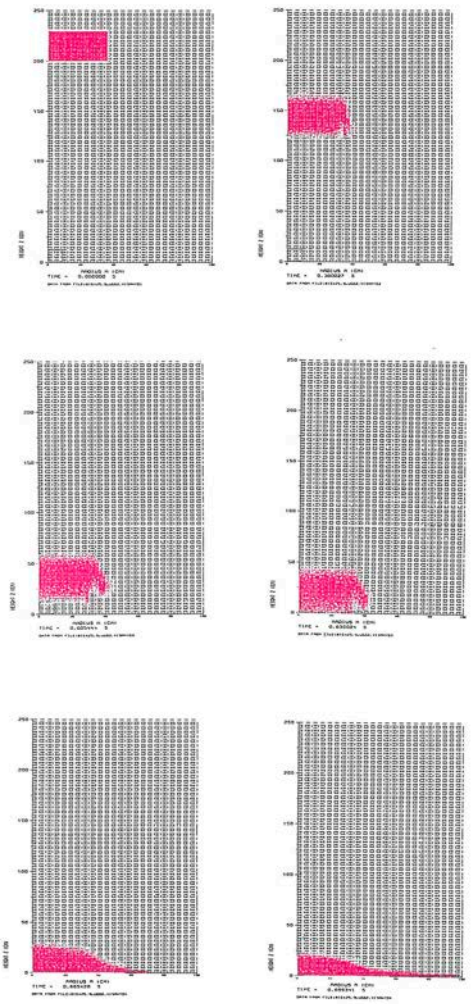

Fig. 5.2. Motion and impact of liquid slug (case S1).

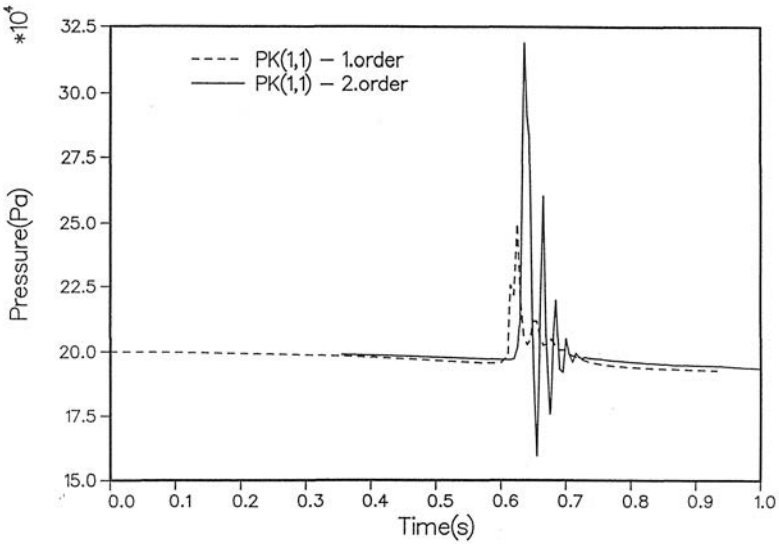

Fig. 5.3. Pressure trace of cases S1 (second order numerial scheme) and S1D (first order).

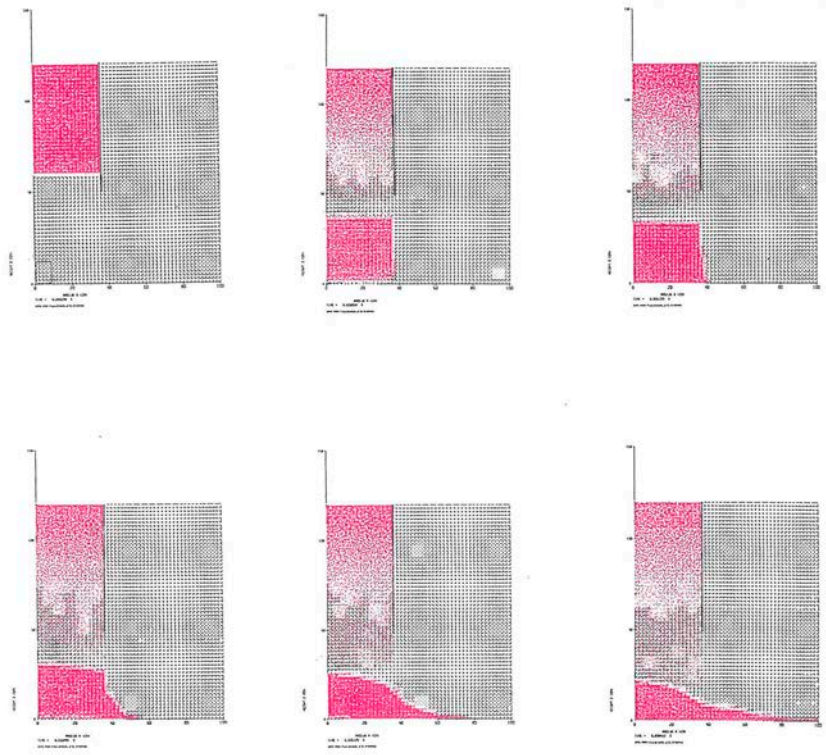

Fig. 5.4. Motion and impact of a liquid slug (case J1).

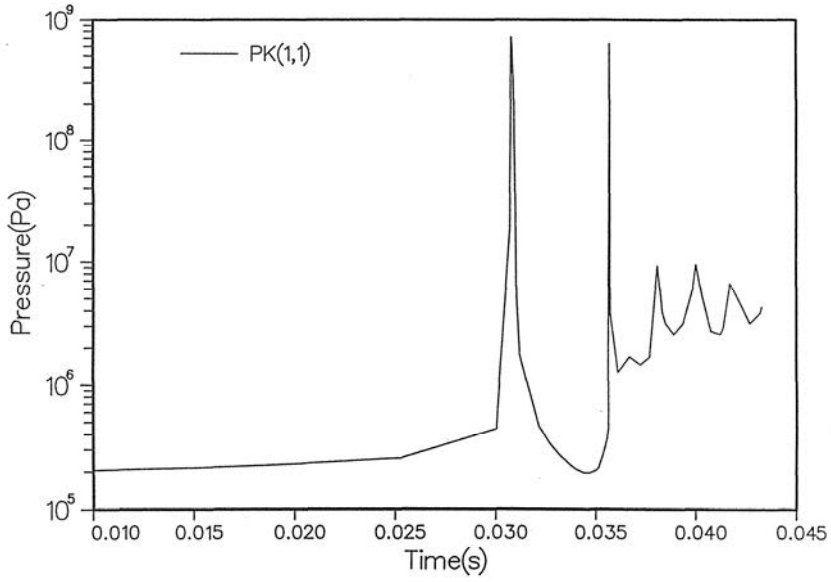

Fig. 5.5. Pressure trace of case J1.

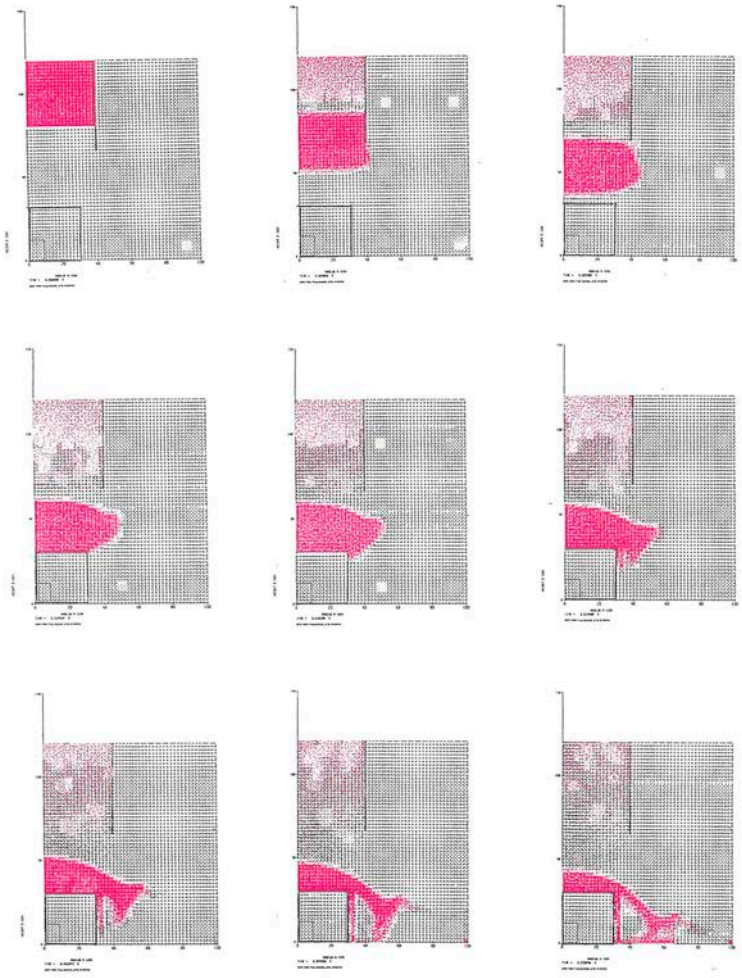

Fig. 5.6. Motion and impact of a liquid slug on an obstacle (case J2).

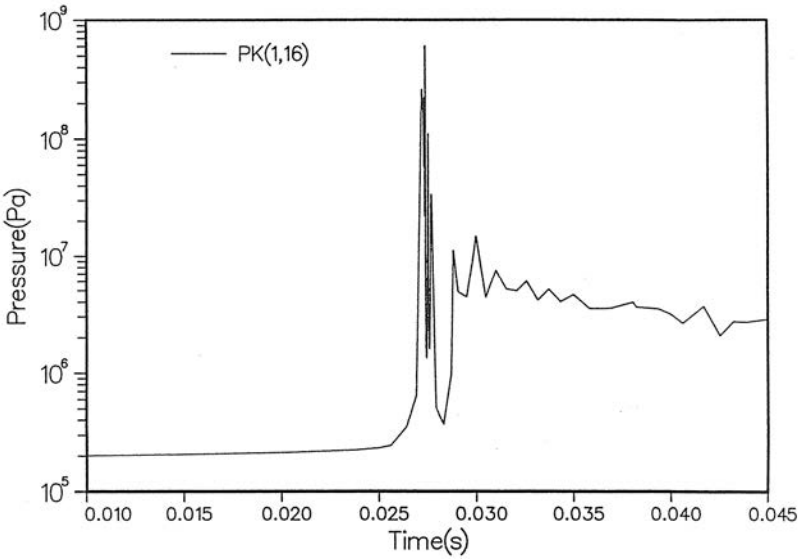

Fig. 5.7. Pressure trace of case J2.

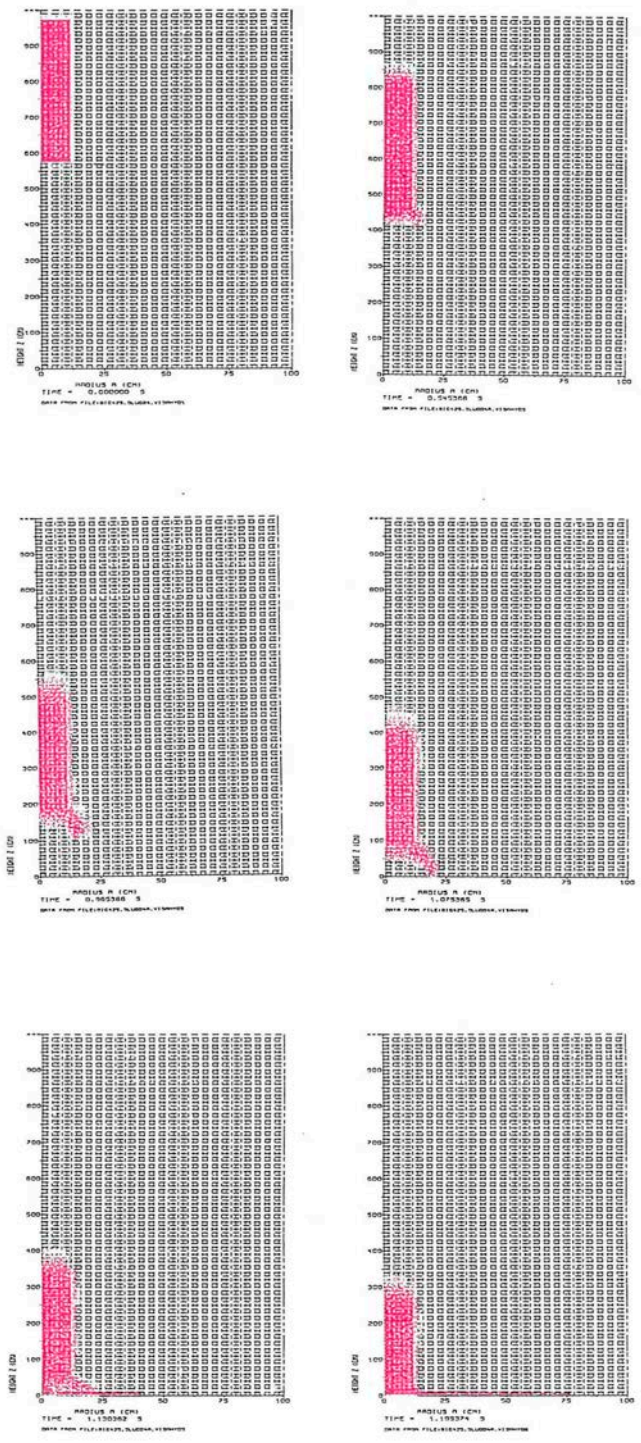

Fig. 5.8. Motion and impact of liquid slug (case S2).

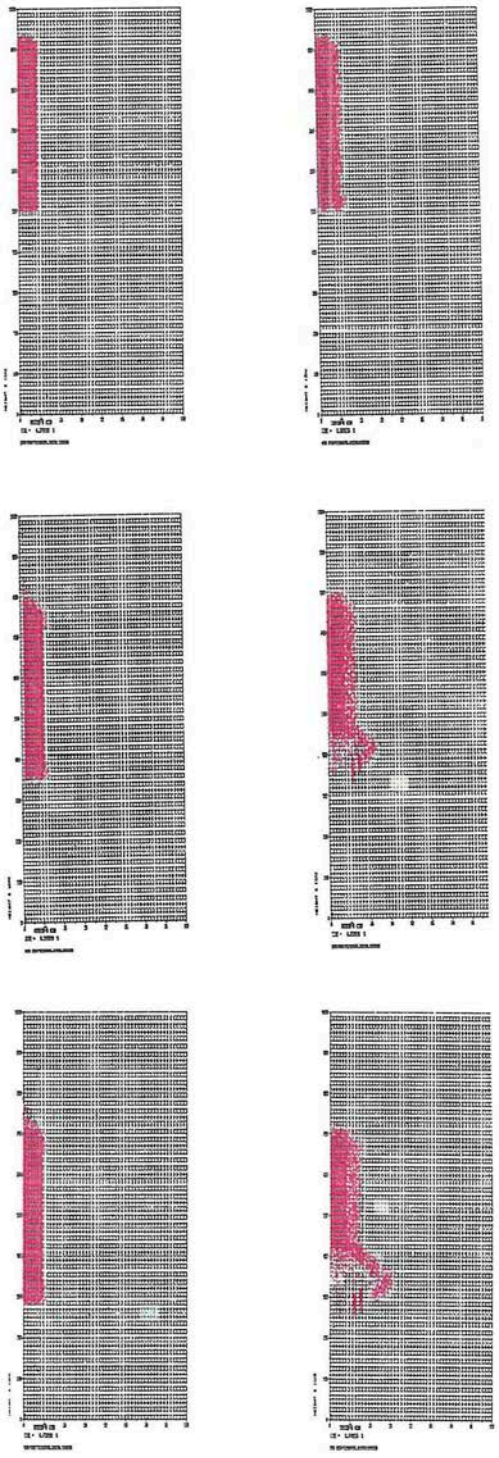

Fig. 5.9. Influence of the CDD drag parameter on surface instabilities of the slug (caseS2) - CDD=10^4 and CDD=10^{-4}.

Problem 1.10: Steam expulsion by subcooled water

"Expulsion of Steam by Sub-cooled Water"

Koji Morita (PNC)

Outline of the Case

The problem is one of the numerical benchmark problems proposed by the Workshop on Two-Phase Flow Fundamentals.[1] This one-dimensional transient problem is to investigate the so-called water packing. Spurious pressure spikes due to the water packing are often calculated numerically when a surface of the water crosses a finite-difference cell edges. This water packing is a common problem for multi-fluid model codes which use fixed node discretization schemes.

1. Objectives of the Application

The problem is formulated to test numerical solution methods for anomalous numerical behavior that is characteristic of fixed node discretization schemes.

2. Description of the Benchmark Problem

The problem consists of a constant volume injection rate of subcooled water into a vertical tube initially filled with superheated steam and connected at the top to a constant pressure source of superheated steam. As the subcooled water is injected, condensation begins causing vapor to move toward the liquid at high velocities and the superheated steam is drawn into the tube. Numerically, the process proceeds normally until a Eulerian computational mesh cell fills with liquid at which time a large fictious pressure spike occurs. This spiking is called "water packing".

3. Analytical Solution

The problem does not have an exact analytical solution. A filling time of the tube is estimated to be less than 6.0 s after the beginning of water injection as a result of condensation.[1]

4. Understanding of Phenomena

The phenomena addressed in the problem can be considered well understood. According to Ref. 2), the pressure spikes due to water packing are caused when the free falling liquid above the surface is forced to change its direction upward as soon as the surface of water crosses cells. The water packing is judged to be common problem for multi-phase model codes which adopt momentum equations of non-conservative form.

5. SIMMER-III Representation

5.1. Geometry, Initial and Boundary Conditions for a Reference Case

The reference calculation was performed using the following specifications:

a. The problem consists of a vertical tube 1.0 m diameter and 3.0 m height with.a constant velocity input at the bottom of the tube and a constant pressure reservoir of superheated steam at the top. A uniform spatial discretization consisting of ten equal intervals 0.3 m length is used. A schematic of the system is shown in Fig. 1.

b. The initial ·condition in the tube are: superheated steam at a constant pressure and temperature equal to 0.4· MPa and 163.0, respectively. The injected water is subcooled at a pressure and temperature equal to 0.4 MPa and 50.0 ℃, respectively. The steam reservoir is superheated and held constant at pressure and temperature equal to 0.4 MPa and 163.0 ℃, respectively. The problem is initialized by allowing hydrostatic gradients to form for a period of 2.0 s before injection of the subcooled water.

c. The boundary conditions for this problem consist of specifying the inflow velocity of the subcooled water as a function of time and the conditions of the constant pressure reservoir at the top. A null inflow velocity is specified for the first 2. 0 s of the transient to establish the stagnant condition in the tube. Thereafter, the inflow velocity of the subcooled water is specified to be 0.5 m/s at a constant pressure and temperature equal to 0.4 MPa and 163.0 ℃, respectively. A constant pressure and temperature equal to 0.4 MPa and 163. 0 ℃ respectively are specified for the steam reservoir at the top of the tube. The walls of the tube are specified to be rigid and adiabatic.

d. The thermodynamic properties of water were calculated using the simplified analytic EOS[3)] instead of the S-III standard AEOS for water. The parameters were determined based on the properties at 323.15 K.[4)] This is because the temperature change in the problem is not large and the SAEOS may give more exact properties over a narrow temperature range rather than the standard AEOS.

e. The calculation was performed without condensation to eliminate a difficulty related to the phase transition. In addition, no change of IFA due to IFA source terms was allowed to eliminate the dependence of MXF between continuous and discontinuous phases on the IFA source term modeling.

f. The calculation was performed using a constant time step of 50 ms until the tube is filled with the water.

5.2. Code Modifications

The standard S-III was used for calculations except for the treatment of momentum-exchange coefficients **(**MXCs). The code was modified so that the input multipliers of MXCs between continuous and discontinuous phases become effective for both two terms defining a MXC. Note that this modification was used only for a parametric calculation, reduced MXC case.

5.3. Parametric Cases

To estimate the influence of the momentum coupling and the phase transition on the water packing, the reference calculation was repeated under the different conditions. The MXCs between the continuous and discontinuous phases were reduced by factor 10^{-2} than those used in the reference case and the reference case was recalculated with condensation.

6. Results

The calculated results of pressure, void fraction and liquid velocity are shown for the reference case, the reduced MXCs case, and the case with condensation in Figs. 2, 3, and 4, respectively. In the reference case and the reduced MXC case, pressure spikes are calculated and these propagate from bottom to top of the tube. As water flows into a cells, the liquid is forced to drop by gravitational force just before the cell is filled with liquid. The liquid velocity at the top edge of the cell begins to decrease and then reaches a negative value. This negative liquid velocity is forced to change its direction upward as soon as the upper cell starts to fill with liquid and the pressure spike is generated at the moment. The positive velocity after the cell is filled with liquid is corresponding to the water injection velocity. In the reduced MXCs case, more spurious pressure spikes are calculated than those in the reference case. According to the discussion in Ref. 2), the height of a pressure spike is determined by the time derivative of the liquid velocity at the time when the cell is filled with liquid. Therefore, pressure spikes in the reduced MXCs case are enhanced by the larger rate of liquid velocity change from negative to positive due to the smaller momentum coupling between liquid and vapor. On the other hand, in the case with condensation each cell fills with liquid faster and pressure spikes are considerably relaxed in comparison with the cases without condensation. This is because the condensation causes the vapor to move toward the water surface and then this produces the larger momentum coupling between liquid and vapor. As the.results, the rate of liquid velocity change from negative to positive is forced to decrease so that the pressure spikes are relaxed.

7. Conclusions

The following conclusions were obtained from this assessment study:

a. The water packing is a common problem for multi-fluid model codes using a staggered mesh system when a surface of water crosses a finite-difference cell edge and hence the S-III fluid-dynamics model causes the water packing.

b. Pressure spikes caused by the water packing are sensitive to the momentum coupling between . vapor and liquid. This means that the magnitude of pressure spikes are phase transition rates.

c. Although the water packing involves several nonphysical behavior of pressure and velocity, the effects on the bulk-fluid movement is not so significant. This fact can be seen from the void fraction histories in the three cases performed.

8. Recommendations for Model Improvement

Several numerical technique has been developed to scale down pressure spikes due to water packing for two-fluid model codes.[2), 3), 4), 5)] The most successful approach seems to be a method proposed by Abe et al.,[2)] in which a correction factor is introduced into the convective term, the differential term and the gravity term of the momentum equation.

9. References

1) D. B. Spolding et al.: Problem specification and collated solutions of the two-phase numerical-benchmark experience 1986-7, DOE/EPRI Second International Workshop on Two-Phase Flow Fundamentals, 16-20 March, 1987, Troy, New York.

2) Y. Abe et al.: Elimination of Numerical Pressure Spikes Induced by Two-Fluid Model, J. Nucl. Sci. Tech., Vol.30, No.12, pp. 1214-1224 (1993).

3) Los Alamos National Laboratory: TRAC-PF1/MOD1: An advanced best estimate computer program for pressurized water reactor thermal-hydraulic analysis, NUREG/CR-3858, LA-10157-MS (1986).

4) W. L. Weaber et al.: TRAC-BF1 manual, extension to TRAC-BF1/MOD1, NUREG/CR-4391, EGG-2471 (1986).

5) V. H. Ranson et al.: RELAP5/MOD2 Code Manual, NUREG/CR-4312, EGG-2396 (1985).

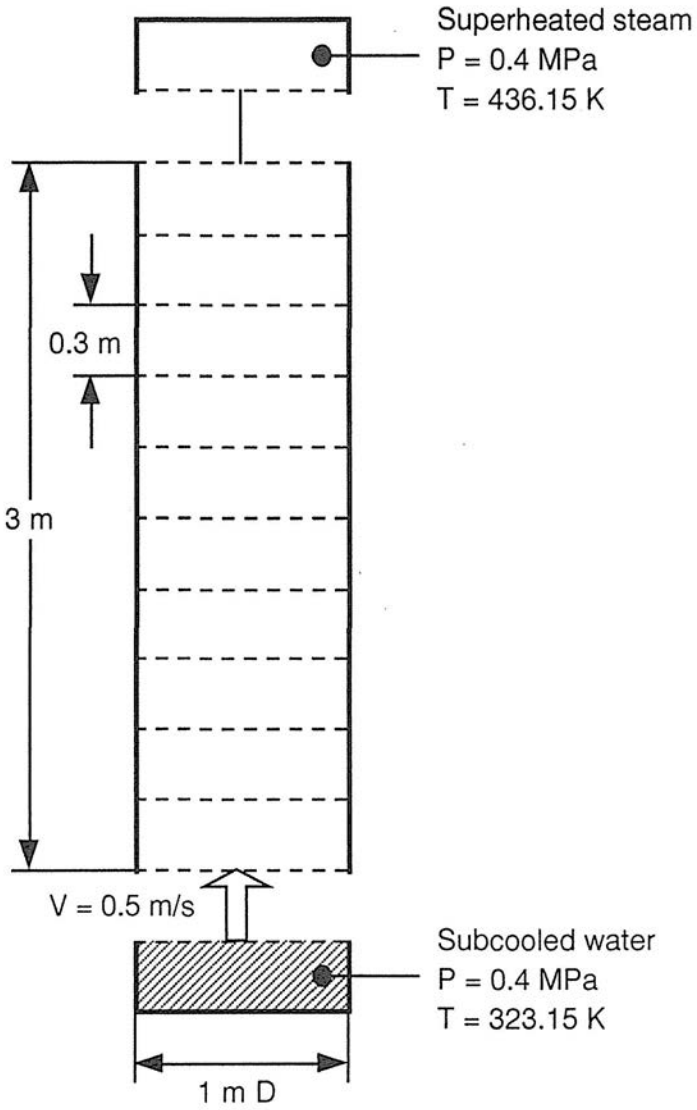

Fig. 1. Schematic and nodalization diagram for the problem.

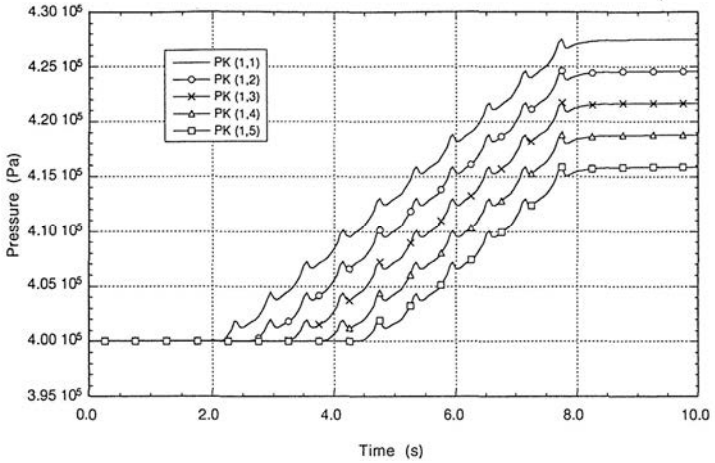

Fig. 2-1. Pressure for the first 5 cells (reference).

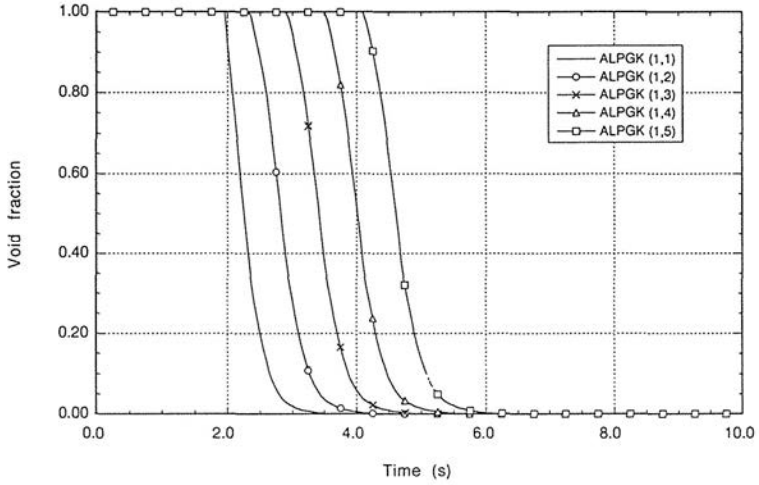

Fig. 2-2. Void fraction for the first 5 cells (reference).

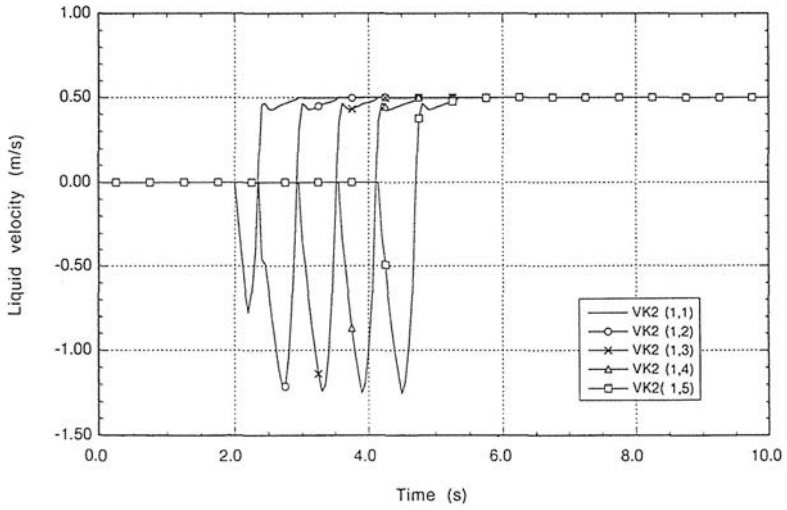

Fig. 2-3. Liquid velocity for the first 5 cells (reference).

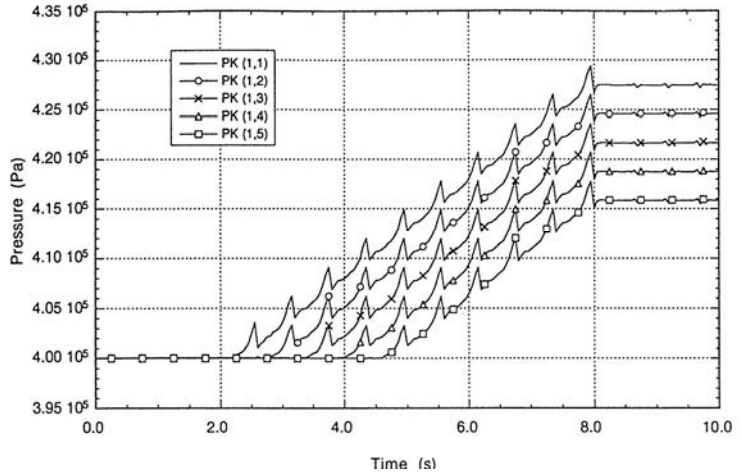

Fig. 3-1. Pressure for the first 5 cells (with reduced MXCs).

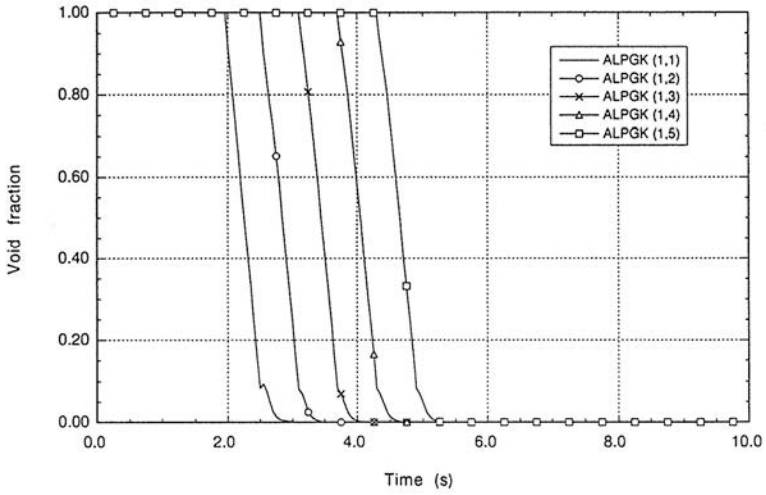

Fig. 3-2. Void fraction for the first 5 cells (with reduced MXCs).

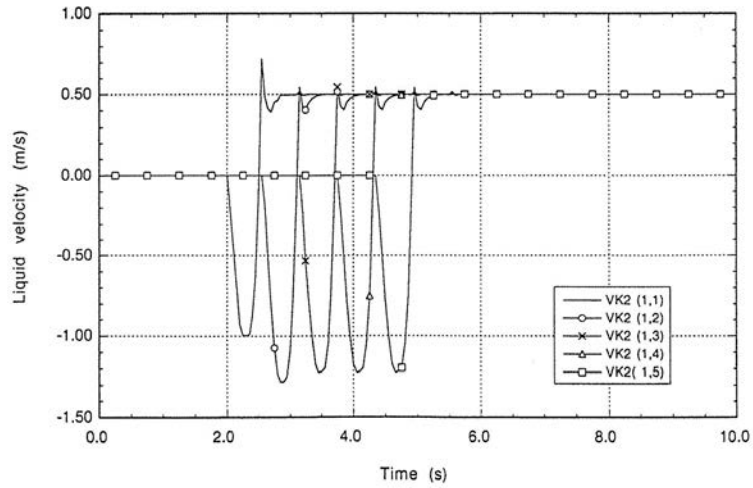

Fig. 3-3. Liquid velocity for the first 5 cells (with reduced MXCs).

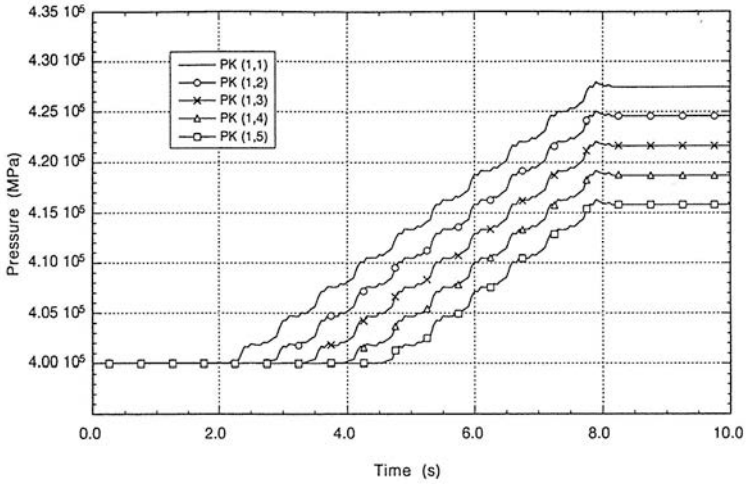

Fig. 4-1. Pressure for the first 5 cells (with condensation).

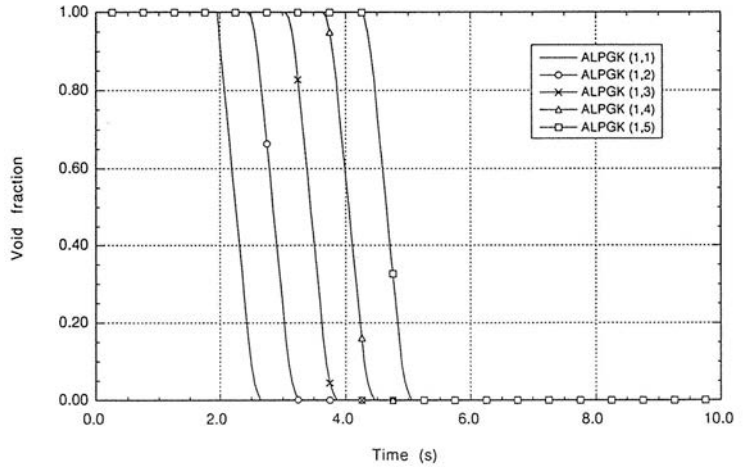

Fig. 4-2. Void fraction for the first 5 cells (with condensation).

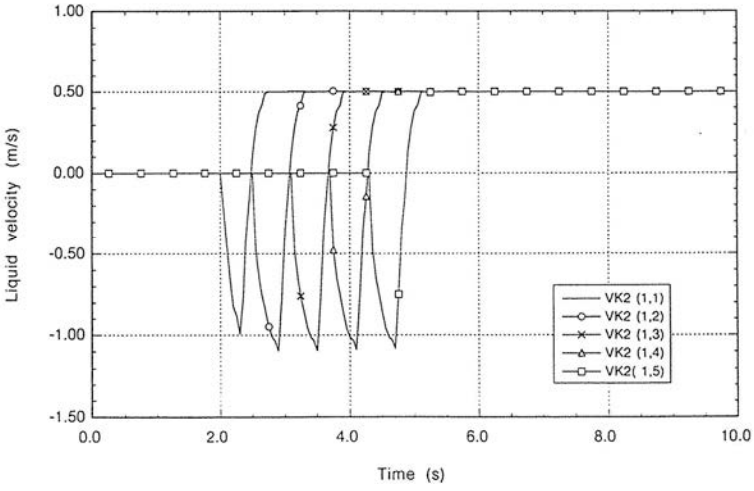

Fig. 4-3. Liquid velocity for the first 5 cells (with condensation).

Problem 1.11: Stability of one-dimensional bubble column

"Stability of a One-Dimensional Bubble Column"

E. A. Fischer (PNC)

Outline of the Case

The stability behavior of the SIMMER-III two-phase equations in one dimension is examined, using a bubble column as an example. The emphasis is on the properties of the solutions (stable or oscillating), for different void fractions, rather than on comparison with experiment, though experimental data are available from many authors.

1. Objectives of the Application

Instabilities in two-phase flow simulations were observed and dicussed frequently in the literature.[1), 2)] The present application concentrates on the SIMMER-III formulation of the two-fluid equations in one dimension, and on the stability of their solutions. It is known that these equations without a virtual mass term, have two complex characteristics, so that the initial value ·problem is ill posed. The properties of the SIMMER-III equations, which are determined by the virtual mass term, themomentum exchange model, and the interfacial area model, will be studied.

2. Description of the Experiment

Experimental data on bubble column are available in the literature, see e.g. Ref. 3). However, the purpose of the present application is to study the properties of the solutions, rather than to carry out a quantitative comparison with experiment. As a qualitative information, the fact that bubble column experiments show oscillatory behavior is used.

3. Analytical Solution

The one-dimensional bubble column problem has an approximate analytical steady-state solution, if the hydrostatic pressure gradient over the column height is neglected. This is, however, suitable only for rough semi-quantitative estimates. On the other hand, the stability of the steady state solution against small-amplitude oscillations can be examined by analytical methods, using a linear stability analysis.

4. Understanding of Phenomena

The SIMMER-III numerical results in one dimension show that the problem is well posed, and the results are compatible with the linear stability analysis. It is, therefore, believed that the properties of the SIMMER-III two-fluid equations, with virtual mass terms, are understood in principle. It should be

mentioned here that the more realistic two-dimensional case is much more difficult, and certainly requires a more extensive effort than has been put into the present work.

5. SIMMER-III Representation

5.1 Geometry, Initial and Boundary Conditions for a Reference Case

A 1-D mesh was used, with 10 cells of length 0.15 m in axial direction. The materials were water and fission gas. An estimated steady-state value was used as the initial value for the water volume fraction. The cells also contained a small amount of structure. At the bottom of the column, gas is injected at a given velocity, constant in time. A constant pressure boundary condition was applied at the top. The results of two cases are presented, with gas velocities equal to 0.35 m/s, and 0.80 m/s.

5.2 Code Modifications

None. To find the time-averaged values of the variables in the oscillating solution, a post-processing routine BF-TAV was used.

5.3 Parametric Cases

In addition to the two cases mentioned, with inlet velocities 0.35 and 0.8 m/s, some cases with low void fraction (< 0.3) were run. They showed stable behavior, as expected. However, as the gas velocity from the Ishii correlation[4] shows very little dependence on the void fraction in this range, it is probably not a suitable quantity to characterize the configuration of the bubble column.

6. Results

The two reference cases run, with gas velocities 0.35 and 0.8 *mis,* span about the range of the transition flow regime of SIMMER-III. The first case is at the lower end, and leads to a constant state. The three relevant variables, void fraction, gas and liquid velocities, are shown in Fig. 1, and confirm the constant state. The void fraction increases slightly for the higher cells, because the hydrostatic pressure decreases, and the bubble volume increases. The average is 0.402, which is close to the zero dimensional value. The second application, with the higher gas velocity, leads to an oscillating solution, as shown in Fig. 2. The oscillations of all the three variables are nonlinear. The amplitude is lowest in cell 2, and increases with higher cell numbers. The average void fraction, 0.557, is slightly higher than the zero dimensional value, 0.548. The data are qualitatively compatible with the results of a linear stability analysis, but SIMMER-III predicts lower oscillation frequencies.

7. Conclusions

SIMMER-III has been successfully applied to a one-dimensional bubble column problem, in the transition flow regime. No numerical difficulties were incurred, showing tha the problem is well posed. The results show that the transition from constant state solution to oscillatory solution occurs in the transition

flow regime. This is consistent with the linear stability analysis performed by the author. However, the different frequencies are, at present, not understood.

8. Recommendations for Model Improvement

None.

9. References

1) H. C. No and M. S. Kazimi: Effects of Virtual Mass on the Mathematical Characteristics and Numerical Stability of the Two-Fluid Model, Nucl. Sci. Eng., Vol.89, pp.197-206 (1985).

2) A. V. Jones and A. Prosperetti: On the suitability of first-order differential models for two-phase flow prediction, Int. J. Multiphase Flow, Vol.11, pp.133-148 (1985).

3) S. C. Saxena and N. S. Rao: Heat transfer and gas holdup in a two-phase bubble column: Air-water system — Review and new data, Exp. Thermal Fluid Science, Vol.4, pp.139 -151 (1991).

4) M. Ishii and N. Zuber: Drag Coefficient and Relative Velocity in Bubbly, Droplet or Particulate Flows, AIChE Journal, Vol.25, No 5, p. 843-855 (1979).

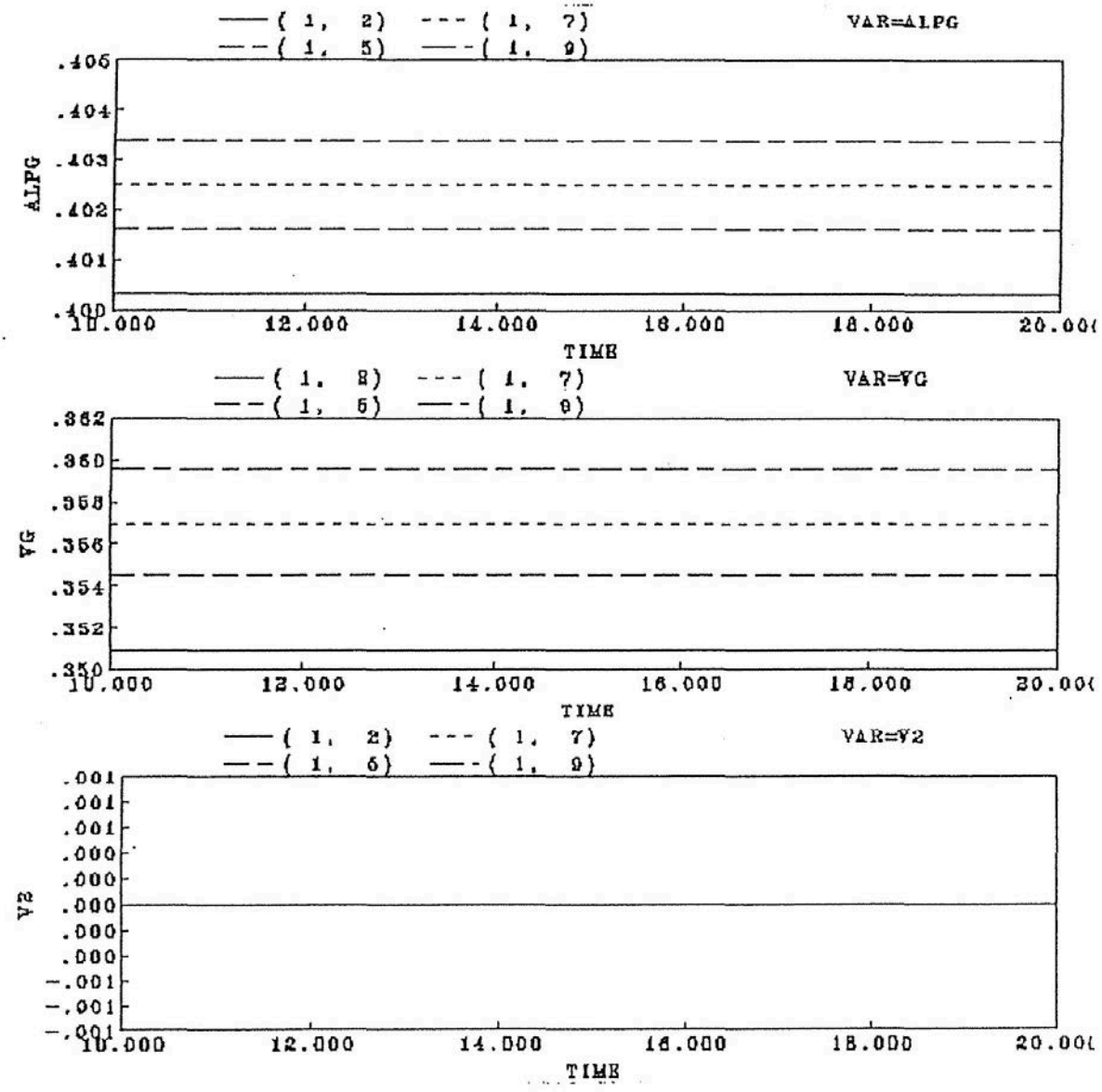

Fig. 1. Void fraction, gas and liquid velocities in 1-D bubble-column simulation with SIMMER-III. (Case 1: gas velosity = 0.35 m/s)

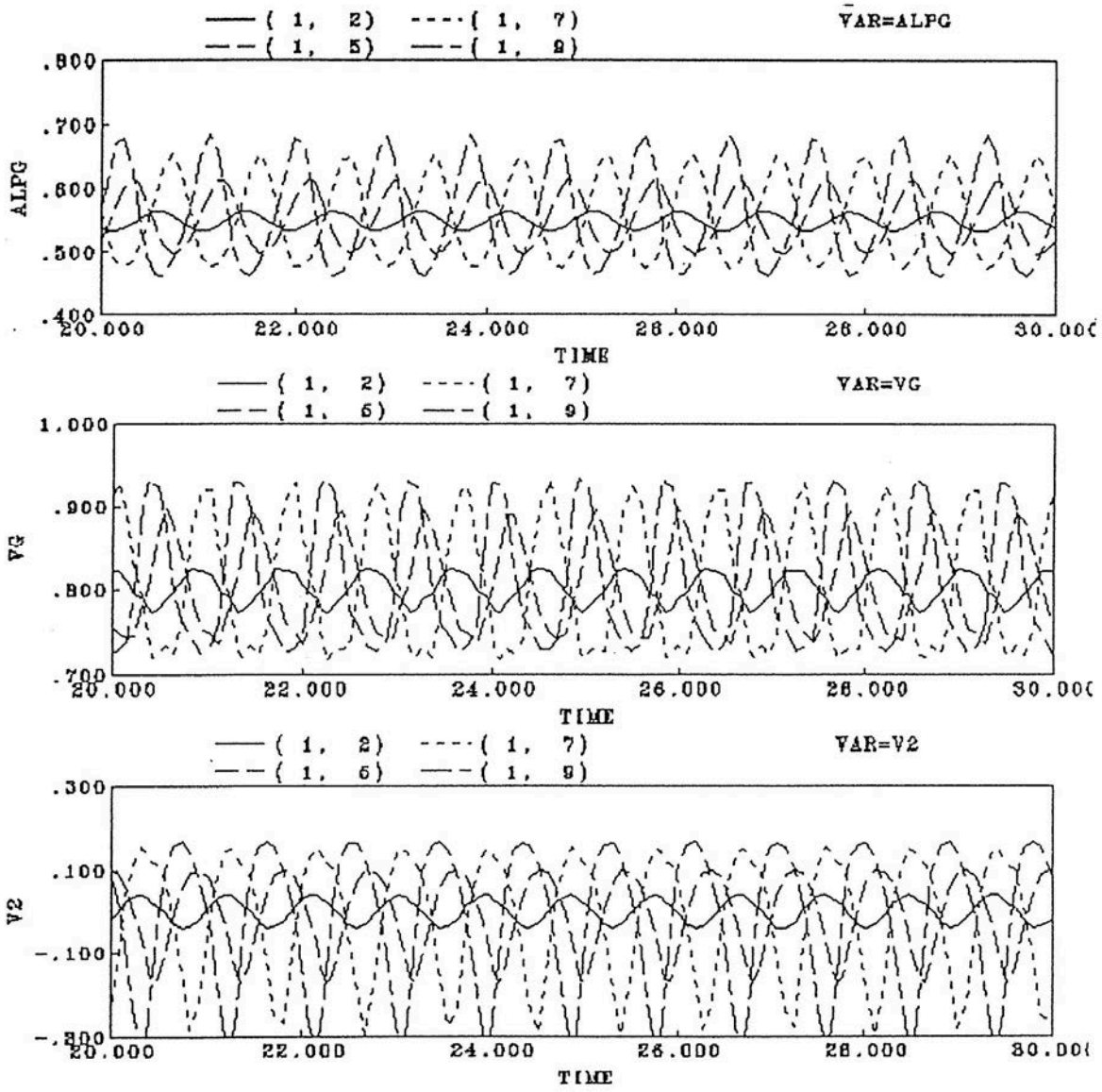

Fig. 2. Void fraction, gas and liquid velocities in 1-D bubble-column simulation with SIMMER-III. (Case 2: gas velosity = 0.8 m/s)

Problem 2.1: Zero-th dimensional pool flow

"Momentum Exchange in Pool Flow"

Yoshiharu TOBITA (PNC)

Outline of the Case

The vapor-liquid and liquid-liquid interphase friction model is tested in an ideal 0-dimentional system. The relationships between volumetric fraction and flux are compared with some experiments including air-water[1), 2)], steam-water[3)], and water-mercury[4)] system.

1. Objectives of the Application

This application concentrates on a verification of the interfacial area and momentum exchange function model in SIMMER-III without the effect of convection algorithm. The application does not provide a test of multi-dimensional effect in a pool geometry such as void fraction distribution and internal flow circulation in a pool.

2. Description of the Experiment

The experimental data from several experiments are compiled in Refs. 1) – 4). All experiments were performed in batch operation condition in which the velocity of continuous fluids becomes zero after the integration for all test section. All experiments reported the volumetric fluxes (superficial velocities) as the functions of volumetric fractions with averaging over the entire test section.

3. Analytical Solution

No analytical solution is available. However, Ishii, et al.[1)] proposed a semi-empirical correlation of interphase friction which is applicable for wide range of volumetric fraction and combination of materials and SIMMER-III uses this formulation. Therefore, the calculated results were compared with this correlation to check the validity of programming.

4. Understanding of Phenomena

In the bubbly flow regime, the air velocity plotted in Fig. 1 and Fig. 2 show relatively good agreements among the experiments and semi-empirical correlation as far as the flow situation remains 1-dimensional, i.e. the flow circulation in a pool is negligible as shown in Fig.3. Therefore, the phenomena are considered well understood in this situation. On the other hand, the experimental data show rather wide scattering for the void fraction above 30% in Fig. 1 and Fig.2. Two explanations are possible for this scattering. The one is the dependency of bubbly-chum transition criterion on the pool geometry and the way of gas injection. For example, Orth observed the void fraction at bubbly-chum transition to vary from 0.3 to 0.6 depending on

the pool depth as shown in Fig. 2. The another mechanism is the existence of circulation pattern in a pool as was discussed by Wilhelm[5] and observed experimentally in Ref. 6). The continuous phase may form circulating pattern in a pool depending on the way of gas injection, geometric shape of the pool, and void fraction. This will certainly affects the averaged gas velocity in pool. In order to clarify this multidimensional effects on the relationship between the averaged void fraction and vapor velocity, more detailed study on the flow structure in the pool, including the effect of turbulence, will be needed in the future. At the moment, any physical model which describes these phenomena satisfactory is not available and our understanding in this flow situation is limited.

In the volumetric heated steam-water experiments, the experimental data scatters rather widely as shown in Fig.4. Farahat's experiments should be excepted from this discussion because foamy flow was formed even with very high void fraction due to the addition of electrolyte to water. The important point to note in the other experiments is the void fraction distribution along the pool depth. The vapor velocity was measured at the surface of the boiling pool where the void fraction is much greater than the averaged void fraction over the pool in these experiments. Therefore, the reported void fraction is smaller than the local void fraction which corresponds to the reported vapor velocity. This effect will be especially important in a low void fraction region.

5. SIMMER-III Representation

5.1. Geometry, Initial and Boundary Conditions for a Reference Case

A 0-dimentional system, i.e. one mesh system, was used just to provide a set of experimental condition to SIMMER-III subroutines which calculate interfacial area (IFA) and momentum exchange functions (MXF).

5.2. Code Modifications

In order to concentrate on the verification of IFA and MXF models, ad-hoc modification was made to neglect the convection term in momentum equation. The momentum equation without convection term reads

$$\frac{\partial \bar{\rho}_q \vec{v}_q}{\partial t} = -\alpha_q \nabla p + \bar{\rho}_q \vec{g} - K_{qS}\vec{v}_q - K_{qq'}\vec{v}_{qq'} - \theta_{L,G}\alpha_G VM\left(\frac{\partial \vec{v}_G}{\partial t} - \alpha_{q1,eff}\frac{\partial \vec{v}_{q1}}{\partial t} - \alpha_{q2,eff}\frac{\partial \vec{v}_{q2}}{\partial t}\right). \quad (1)$$

Finite differencing with respect to time gives, for the $q1$ component as example,

$$\left(\frac{\bar{\rho}_{q1}}{\Delta t} + K_{q1,S} + K_{q1,q2} + K_{q1,q3} - \frac{\theta_{L,G}\alpha_{q1,eff}\alpha_G VM}{\Delta t}\right) v_{q1}^{n+1} \quad (2)$$

$$-\left(K_{q1,q2}+\frac{\theta_{L,G}\alpha_{q2,eff}\alpha_G VM}{\Delta t}\right)v_{q2}^{n+1}-\left(K_{q1,q3}+\frac{\theta_{L,G}\alpha_{q3,eff}\alpha_G VM}{\Delta t}\right)v_{q3}^{n+1}$$

$$=\left(\frac{\bar{\rho}_{q1}}{\Delta t}-\frac{\theta_{L,G}\alpha_{q1,eff}\alpha_G VM}{\Delta t}\right)v_{q1}^{n}-\frac{\theta_{L,G}\alpha_{q2,eff}\alpha_G VM}{\Delta t}v_{q3}^{n}-\frac{\theta_{L,G}\alpha_{q3,eff}\alpha_G VM}{\Delta t}v_{q3}^{n}.$$

Equation (2) consists of three linear equation for the updated velocities v_q^{n+1}. Ad-hoc subroutines and modifications were made to solve Eq. (2) and update the velocities until steady state is obtained.

5.3. Parametric Cases

The volume fraction of lighter phases was varied from 0.1 to 0.9.

6. Results

6.1. Air-water experiments

In the air-water system, SIMMER-III results show fairly good agreement with experiments and Ishii's correlation as long as the void fraction is less than 25% as shown in Figs. 1 and 2. Therefore, the basic validity of SIMMER-III IFA and MXF models in bubbly flow is confirmed. This means also that SIMMER-III calculates the local velocity difference between vapor and liquid correctly even in a multi-dimensional pool with internal circulation if the flow remains bubbly flow. When the void fraction exceeds 30%, the experimental data show rather wide scattering as was discussed in section 4. In spite of the limitation of this application that the effect of internal circulation in pool was not taken into account, SIMMER-III results fell on the center part of the scattering data points in Figs. 1 and 2. In SIMMER-III modeling, the transition from bubbly to churn flow is presumed to occur at void fraction of 30% following the recommendation by Ishii and Zuber[7] and shows agreement with the Orth's data in the pool with initial depth greater than 29.7 cm. However, the void fraction at bubbly-churn transition becomes higher than 30% in the pool with its initial pool depth smaller than 20 cm. This is because enough time is not given for bubble to coalescence and produce churn flow if the pool depth is small. Though the inclusion of this kind of time dependency in flow regime transition is desirable to analyze the pool boiling behavior in a general manner, the constant criterion of 30% is enough for reactor application because the pool depth in transition phase is greater than several 10 cm which is enough to cause bubbly-chum transition at void fraction of around 30%.

Concerning the IFA modeling, the equilibrium .radius and time constants by fluid-dynamic breakup and turbulent breakup models are plotted in Fig.4. Since this calculation was performed until steady state condition was achieved, the turbulent breakup becomes dominant in this case. The predicted bubble radius correspond to the results in a 1-dimentional analysis by Wilhelm[5] as plotted in Fig. 5.

6.2. Steam-water experiments

The void fraction measured in steam-water experiments[3] shown in Fig. 6 are smaller than SIMMER-III results for the same vapor velocity. This is because the vapor velocity was measured at the pool surface where the void fraction is much greater than the pool averaged void fraction as was discussed in Section 4. Apparently, 1-dimentional or 2-dimentional calculation is required to take into account the effect of this spatial void fraction distribution but they are beyond the scope of this study, which is to check the IFA and MXF modeling without the effect of convection.

6.3. Water-mercury experiment

The calculation for mercury-water experiment by Kutateladze[4)] was performed to check the validity of liquid-liquid IFA and MXF models in SIMMER-III. The calculated water velocity is plotted in Fig. 7 together with the experiment data. Again, the SIMMER-III result shows relatively good agreement with the experiment for the volumetric fraction of water less than 30%. For the volumetric fraction of water larger than 30%, SIMMER-III overestimates the water velocity.

7. Conclusions

In summary the following conclusions can be drawn from the 0-dimentional calculation of pool flow experiments.

1) SIMMER-III has been successfully used to simulate the gas velocity in air-water bubbly flow and water velocity in water-mercury system where the volumetric fractions of dispersed phases are less than 25% and 30%, respectively.

2) In the situation that the spatial distribution of void fraction or the internal circulation in a pool become important, the scattering of experimental data is large and clear comparison with SIMMER-III results becomes difficult.

3) Orth's experiment showed that the bubbly-churn transition is dependent on the time duration of the bubble staying in pool. Though the inclusion of time dependency in flow regime transition is desirable to analyze the pool boiling behavior in a general manner, the constant criterion of 30% is judged to be appropriate for reactor application because the pool depth in transition phase is enough deep to form churn turbulent flow at void fraction around 30% to 40%.

4) SIMMER-III reproduced water velocity in the water-mercury experiments by Kutateladze for the volumetric fraction of water less than 40%. However, SIMMER-III predicted higher water velocity in the transition region from mercury-continuous to water-continuous flow. The cause of this discrepancy is not clarified for the moment.

8. Recommendations for Model Improvement

The inclusion of time dependency of bubble-chum transition is desirable to enhance the applicability of this code to the general pool flow situation. More elaborated 1-dimensional or 2-dimentional analysis is necessary to study the effect of void fraction distribution and internal circulation in pool.

9. References

1) M. Ishii and N. Zuber: "Drag coefficient and Relative Velocity in Bubble, Droplet, or Particle Flows", AIChE Journal, Vol.25, No.5, pp.843-855, Sept. 1979.

2) K. W. ORTH, et al.: "Hydrodynamic Aspects of Volume Boiling", ANURAS 80-6 (Mar. 1980).

3) T. Ginsberg, et al.: "Flow Behavior of Volume-Heated Boiling Pools: Implications with Respect to Transition Phase Accident Conditions", Nuclear Technology, Vol.46, pp.391-398. (Dec. 1979).

4) S. S. Kutateladze and V. N. Moskvicheva, "Hydrodynamics of a Two-Component Layer as Related to the Theory of Crises in the Process of Boiling", Zhurnal Tekhnicheskoi Fiziki, Vol.29, No.9, pp.1135-1139. (Sept. 1959).

5) D. Wilhelm: "Assessment of SIMMER-III Performance on Pool and Depressurization Experiments", STR/LML/95-315, (May 1995).

6) H.A. Jacobsen, et al.: "On the prediction of local flow structures in internal loop and bubble column reactors using a two-fluid model", Computers and Chemical Engineering, Vol.17, pp.S531-S536, 1993.

7) M. Ishii and K. Mishima: "Two-fluid model and hydrodynamic constitutive relations", Nucl. Eng. Design, Vol.82, Issues 2-3, pp.107-126 (1986).

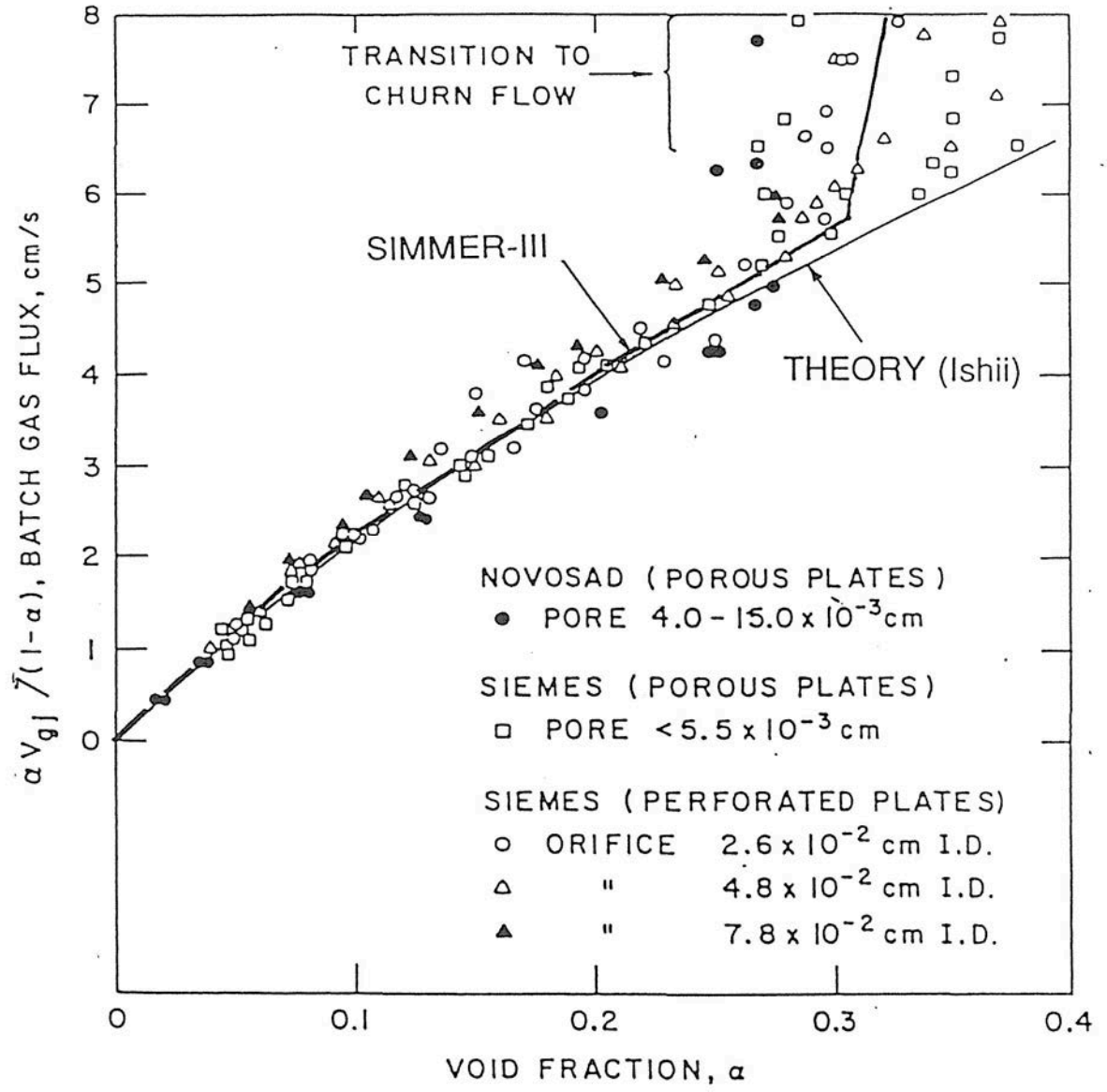

Fig. 1. Calculated gas flux under batch operation compared with air-water experimental data.

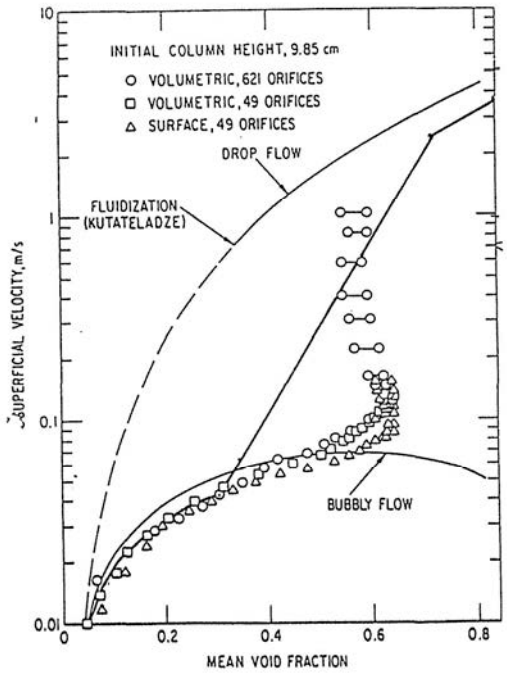

Fig. 2-1 Initial pool height = 9.85cm

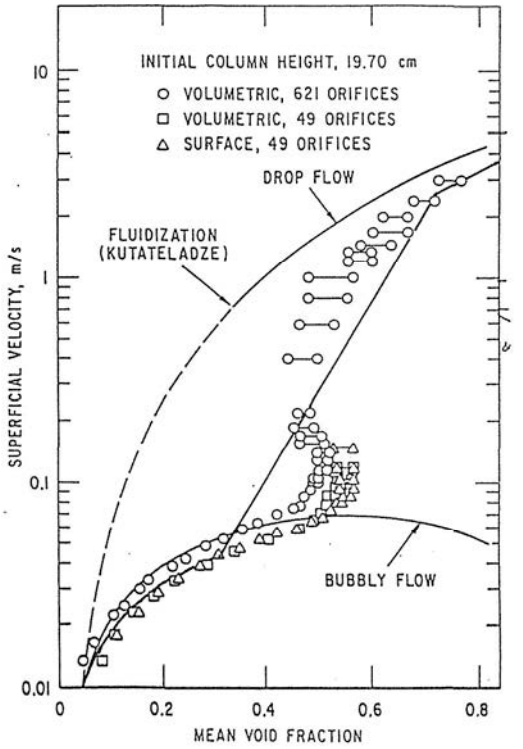

Fig. 2-2 Initial pool height = 19.7cm

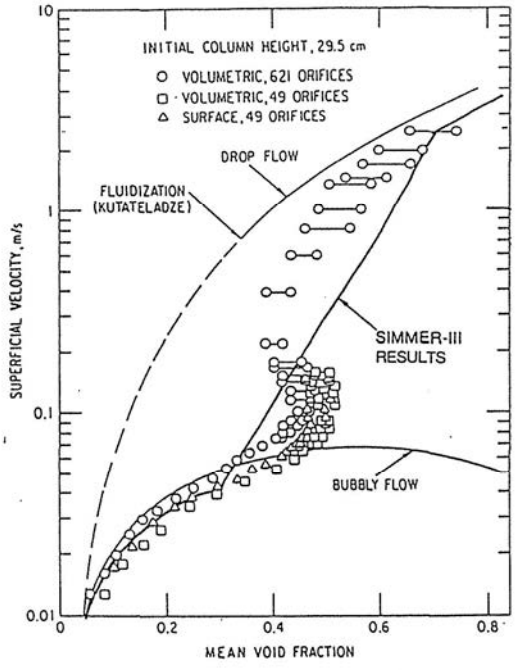

Fig. 2-3 Initial pool height = 29.5cm

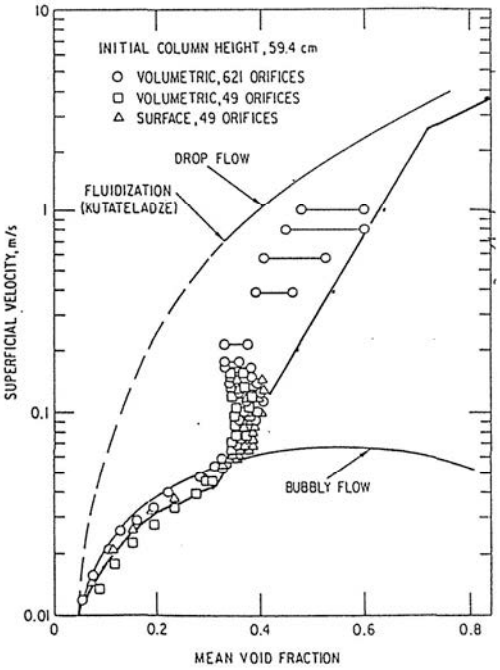

Fig. 2-4 Initial pool height = 59.4cm

Fig. 2. Superficial velocity versus mean void fraction in Orth's experiment compared with calculation.

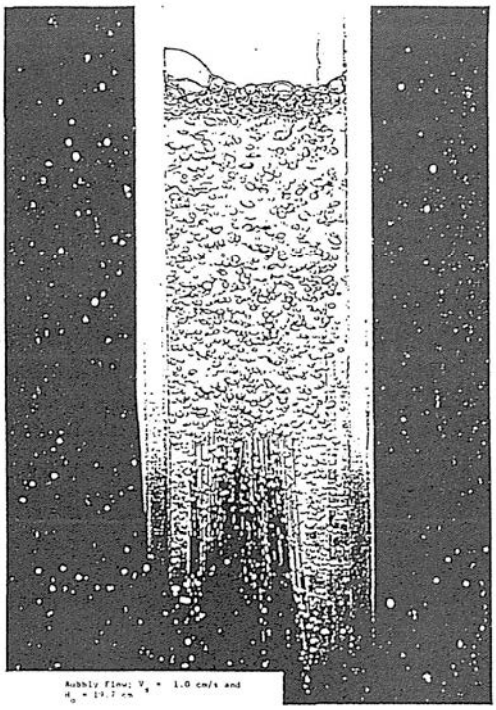

Fig. 3-1 Bubbly flow; V_s=1.0cm/s and H_0=19.7cm

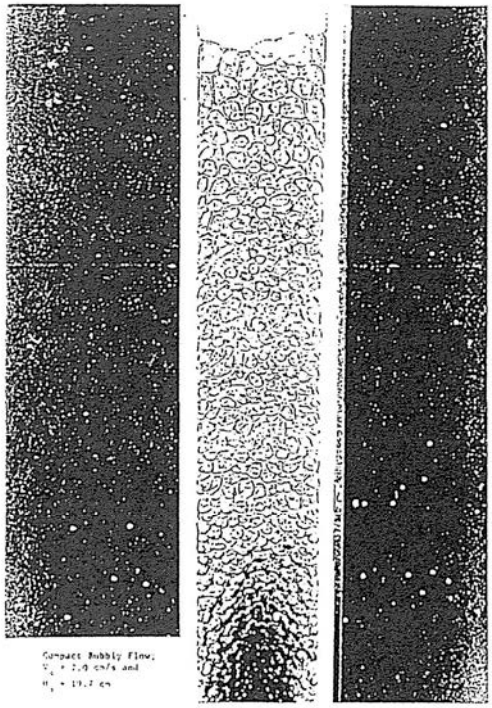

Fig. 3-2 Foamy flow; V_s=7.0cm/s and H_0=19.7cm

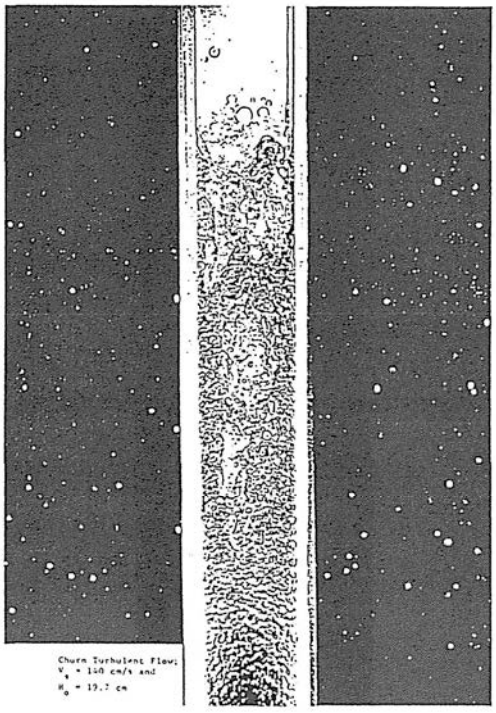

Fig. 3-3 Churn turbulent flow; V_s=140.0cm/s and H_0=19.7cm

Fig. 3. Flow pattern observed in Orth's experiment.

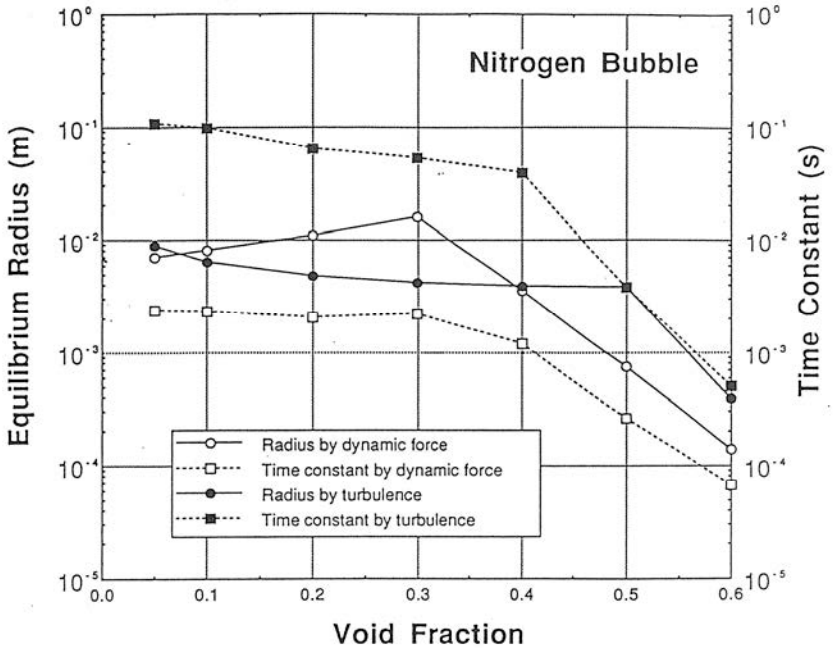

Fig. 4. Comparison of equilibrium fadii and time constants between dynamic force and buoyancy driven turbulence in N_2-water system.

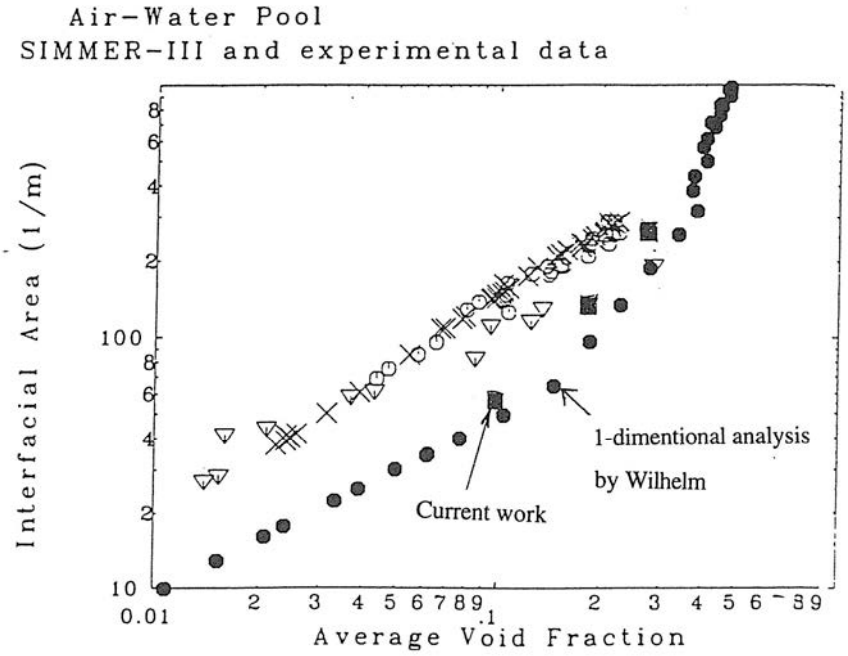

Fig. 5. Interfacial surface areas over void fractions averaged over the entire bubble column.

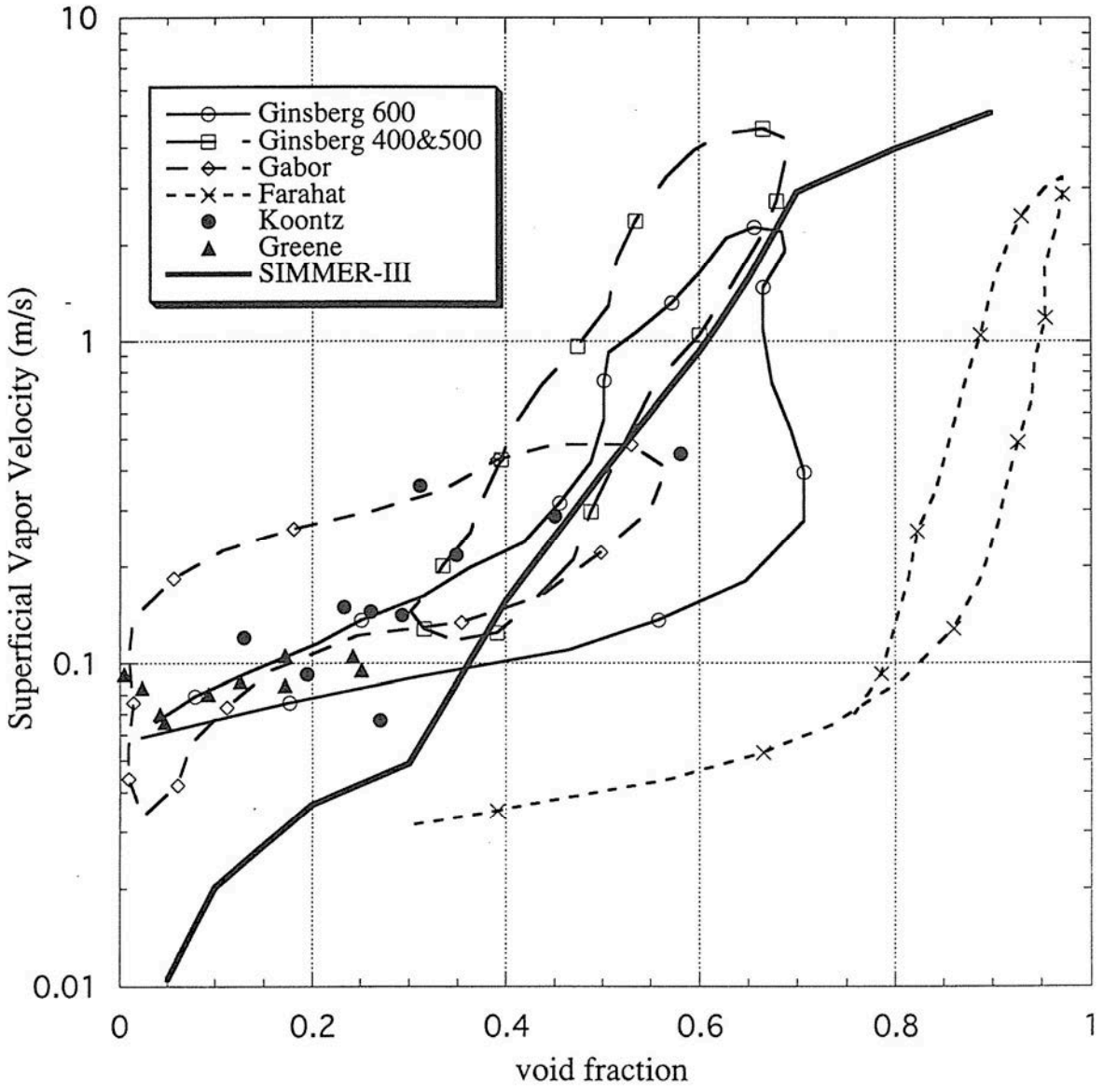

Fig. 6. Calculated steam flux in volumetrically heated boiling pool with experimental data.

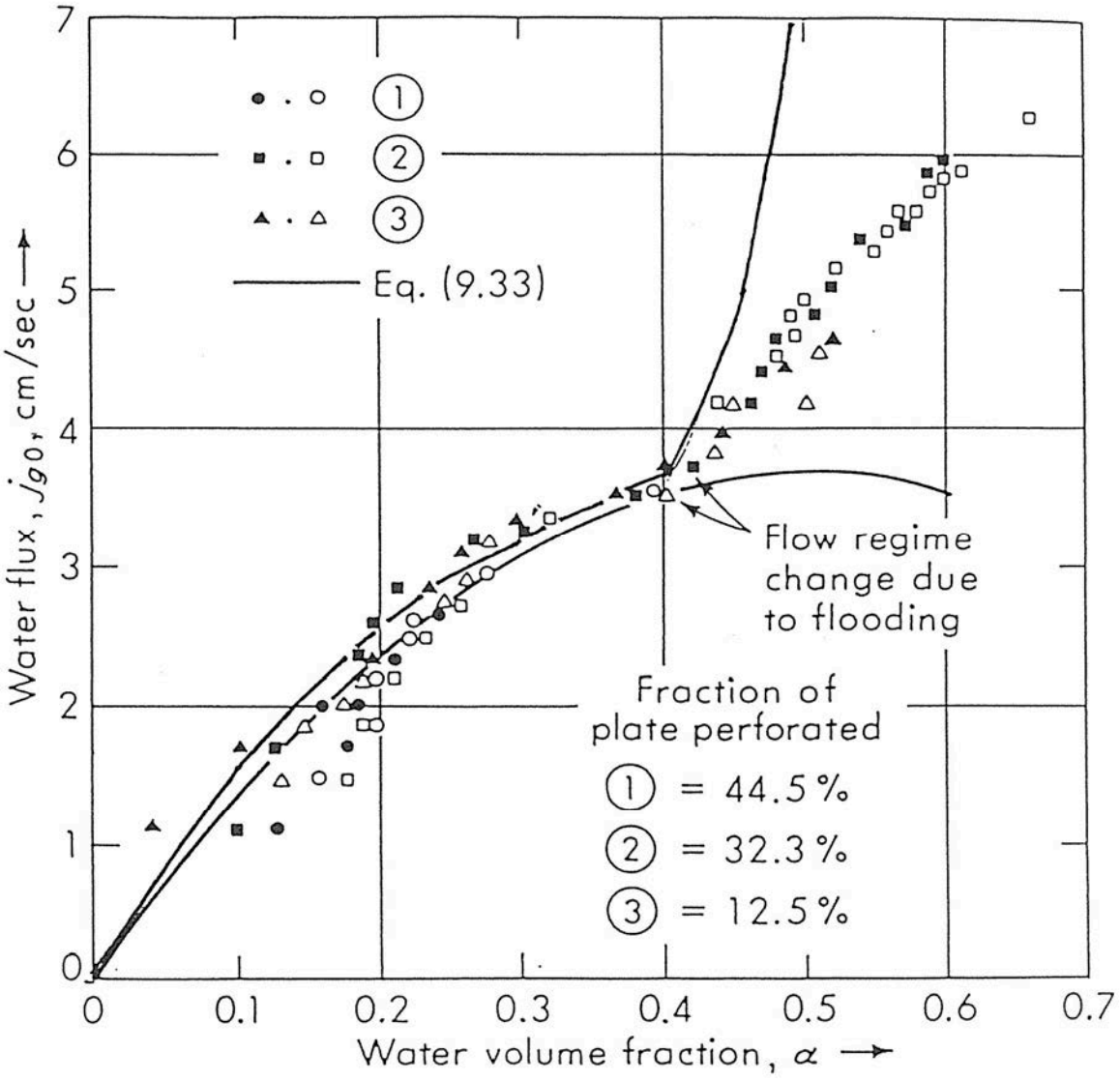

Fig. 7. Calculated water flux in mercury pool compared with experimental data.

Problem 2.2: One-dimensional isothermal bubble column

"Isothermal Flow in Bubble Columns (1-D)"

Dirk Wilhelm and Fabien Boulanger (CEA-G)

Outline of the Case

Gas is injected at the bottom of a liquid column. An isothennal flow is considered. To analyze the volume averages measured in experiments, a 1-D representation is proposed. This is a first and basic test of the interfacial areas and friction factors as function of the void fraction.

1. Objectives of the Application

The objective is to test the interfacial areas and friction factors models on a basic case. For this, a 1-D calculation of a bubble column is used. It can give valuable infonnations, even if a 2-D approach is known to be necessary.

2. Description of the Experiment

There is a wealth of information about bubble columns because of the specific interest of the chemical industry. The most appropriate data for studying transition phase problems come from chemical batch reactors because these operate such that the net throughput of the continuous phase is zero. Most references give the superficial gas velocities as functions of the void fraction or hold-up, all values being averaged over the entire test reactor.[1), 2), 3), 4)] While chemical engineers claim the importance of knowing the interfacial surface areas in bubble columns, the literature is less abundant because of the difficulty to measure the areas, especially at elevated void fractions.

This report refers to three papers which have published similar results of interfaclal surface areas over void fractions, averaged over the entire test reactor. [5), 6). 7)]

3. SIMMER-III Representation

3.1 Geometry, Initial and Boundary conditions

A 1-D mesh was used (15 cells). Gas was injected in the bottom cell. A water pool was defined in the 11 next cells and a cover gas zone was defined in the last 3 cells. Atmospheric pressure and room temperature was used.

3.2 Code Modifications

None.

3.3 Parametric Cases

A wide range of inlet void fraction is considered.

4. Results

The result are being compared in Fig.1 and Fig.2 to the data given by the references above. Fig.1 shows a good agreement between SIMMER-III superficial gas velocities and experiments for low void fractions, and an increasing discrepancy for high void fractions. Fig.2 shows SIMMER-III interfacial areas compared to experiments with a good representation of the increase of areas with void fraction up to 30% void. Above 30%, there are no more experimental data, but SIMMER-III values increase drastically. At the same time, the calculated superficial velocities increase as well indicating that the potential increase in coupling between the phases through higher areas must be overcompensated by a very large decrease in interfacial friction factors. This decrease may be larger than the Ishii-Zuber proposals for the drag coefficients.[1)] At void fractions larger than 50%, the experimental gas velocities are larger than the value calculated by SIMMER-III (0.5 m/s). The reason may be found in the detailed analysis of bubble columns because for this purpose, it is necessary *to* study the distribution of phases and their velocities. Therefore, the one-dimensional exercise can give only a very rough picture of the behaviour of a two-phase pool with elevated void fractions.

In Ref. 8), the slip velocities are about 0.15 m/s for superficial gas velocities below 0.05 m/s, and around 0.5 m/s for superficial velocities larger than 0.2 m/s with the tendency of reaching an upper limit around this value. Ii is therefore the velocity of the continuous phase that contributes the essential part to the increase of the superficial velocities of Fig.1 for void fractions above 30%. The continuous phase is predicted to stay calm in the so-called homogeneous twophase flow at low void fractions (lower than 20%). However, recirculation has also been seen for homogeneous flow. Not only is this mechanism decisive, but also it contributes to the way the phases are distributed within the pool. Fig.3 shows the local axial velocities of [9] for an air-water bubble column. It shows the recirculating water velocities with upwards directions in the pool center, and downwards directions close to the wall. The maximum slip velocities are around 0.6 m/s in regions where the void fraction is about 30%, whereas the maximum void is at 40%. The distribution of the void, and by that the average voidover the entire pool is influenced by the recirculation of the continuous phase.

Additionally, Fig.1 experimental data show larger deviations from experiment to experiment at high void fractions. This is not only due to the way the bubbles are generated, but also because this indicates additional mechanism that depend on the size of the pools. These phenomena are related to the production of large bubbles in the center of the pool.[10)] These are bubbles that are likely not to be produced by mere coalescence, but by agglomeration of many smaller bubbles. The development of bubble agglomerations is dependent upon the free cross section of the pool. In any case, the effect is that the apparent contact area

with the continuous phase is reduced, and that the slip velocity is increased beyond the values for clusters of separated bubbles. The SIMMER-III values for interfacial areas (Fig. 2) show the opposite behaviour.

5. Conclusions

The models for the steady state of interfacial areas and friction factors looks reasonable for low void fraction. But for void fraction higher than 30% they are questionable. A 2-D calculation has also been performed as reported in Problem 2.3.

6. Recommendations for Model Improvement

There is a need to revise the models for the steady state of interfacial areas and friction factors. It can be suggested to replace interpolation procedures without physical mesaning by standard constitutive equations of the literature. A more-detailed discussion can be found in Ref. 11).

7. References

1) M. Ishii, N. Zuber: Drag Coefficient and Relative Velocity in Bubbly, Droplet, or Particulate Flows, AIChE Journal, Vol. 25, No. 5, pp. 843-855, 1979.

2) S.C. Saxena, N.S. Rao: Heat Transfer and Gas Holdup in a Two-Phase Bubble Column: Air-Water System - Review and New Data, Exp.Thermal Fluid Science, Vol. 4, No.2, pp. 139-151, 1991.

3) R. Nottenkiimper, A. Steiff, P.M. Weinspach: Experimental Investigation of Hydrodynamics of Bubble Columns, Ger. Chem. Eng., No.6, pp. 147-155, 1983.

4) N. Zuber, J.A. Findlay: Average Volumetric Concentration in Two-Phase Flow Systems, Journal of Heat Transfer, pp.453-468, 1965.

5) S.T. Revankar, M. Ishii: Local Interfacial Area Measurement in Bubbly Flow, Int. J. Heat Mass Transfer, Vol. 35, No. 4, pp.913 -925, 1992.

6) G. Kocamustafaogulari, Z. Wang: An Experimental Study on Local Interfacial Parameters in a Horizontal Bubbly Two-Phase Flow, Int. J. Multiphase Flow, Vol. 17, No. 5, pp. 553-572, 1991.

7) I. Kataoka, A. Serizawa: Interfacial Area Concentration in Bubbly Flow, Nucl. Eng. and Design, No. 120, pp. 163-180, 1990.

8) K. Ueyama, T. Miyauchi: Properties of Recirculating Turbulent Two Phase Flow in Gas Bubble Columns, AIChE Journal, Vol.25, No. 2, pp. 258-266, 1979.

9) H.A. Jacobsen, H.F. Svendson, K.W. Hjarbo: On the prediction oflocal flow structures in internal loop and bubble column reactors using a two-fluid model, Computers and Chemical Engineering, Vol.17, pp. S531-S536, 1993.

10) H. Wezorke, A. Steiff, P.M. Weinspach: Zurn Einfluss von Grossblasen in Blasensaeulenreaktoren, Chemie-Ingenieur-Technik, Vol.60, No.11, pp. 918-919, 1988.

11) D. Wilhelm: Assessment of Simmer3 performance on pool and depressurimtion experiments. Report CEA/DRN/STR/LML/95-315, chap.8, CEA-Grenoble, 1995.

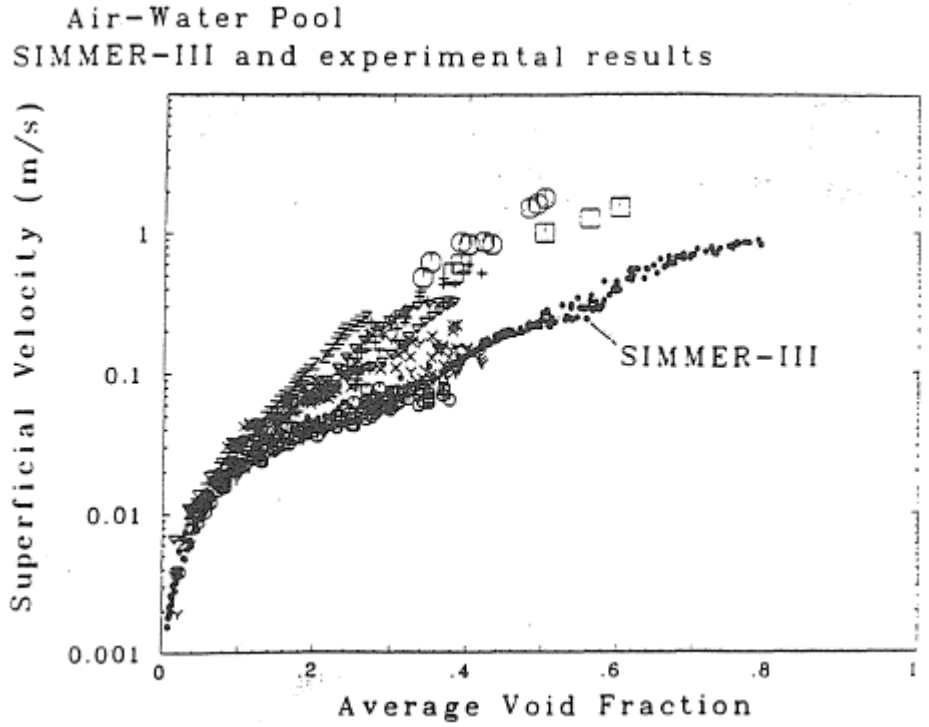

Fig. 1. Superficial velocities over void fractions averaged over the entire bubble column.

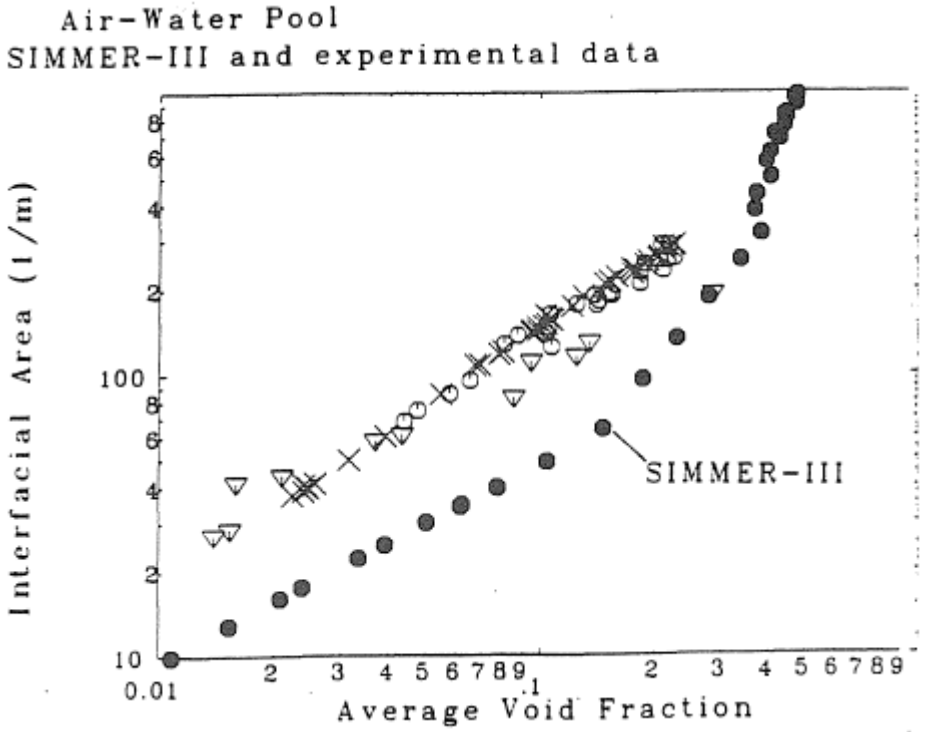

Fig. 2. Interfacial surface areas over void fractions averaged over the entire bubble column or pipe.

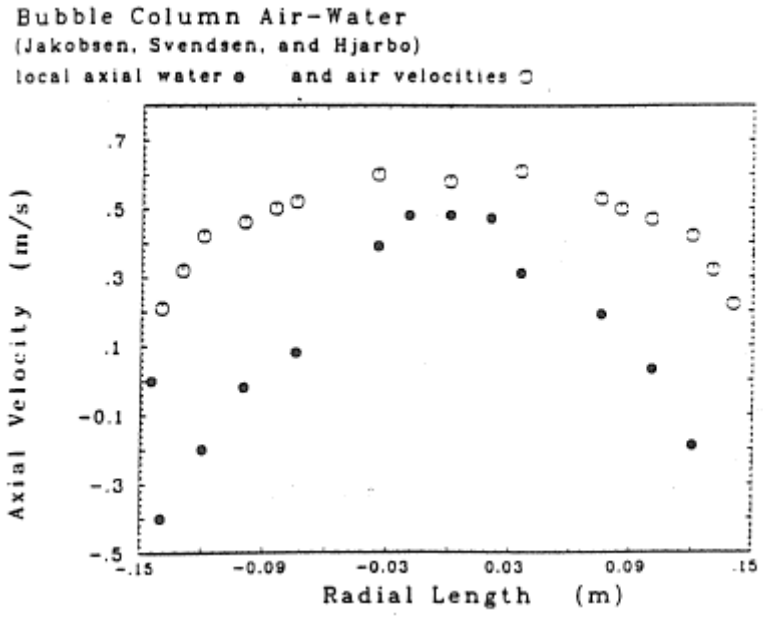

Fig. 3. Local axial velocities over the cross section of a bubble column.

Problem 2.3: Two-dimensional isothermal bubble column

"Isothermal Flow In Bubble Columns (2-D)"

Dirk Wilhelm and Fabien Boulanger (CEA-G)

Outline of the case

Gas is injected at the bottom of a liquid column. An isothennal flow is considered. A two-dimensional calculation is performed in order to test the pool dynamics.

1. Objectives of the application

SIMMER-III Version 1 G is used to repeat a two-dimensional calculation of a bubble colwnn that was already perfonned with version 1.A as reported in Problem 2.2. The introduction of a lateral wall facilitates the development of the backmixing processes of the continuous phase. The objective is to test the pool dynamics in a basic isothermal flow configuration.

2. Description of the experiment

There is a wealth of information about bubble columns because of the specific interest of the chemical industry. References can be found in Problem 2.2. A gas flow is injected at the bottom of an initially stagnant water pool. The final flow is characterized by:

- an ascending gas-water mixture at the column center with low slip between phases
- a descending water flow combined to a slow ascending gas flow at the lateral walls (large slip).

3. Analytical solution

There is no analytical solution.

The state-of-the-art methods for describing the hydrodynamics of bubble columns is characterized by the use of turbulence models. Considering k-ε models, a multitude of proposals for modeling the two parameters in twophase flow are available.[1)] Moreover, results of simpler mixing length calculations have been presented that seem to match experimental results better.[2)] However, the implementation of such complex models is still not available in industrial multiphase reactor codes.

A calculation similar to the present one has been perfonned with the MC3D code.[3)] This code like SIMMER-III does not include turbulence model. However, MC3D is basically three-dimensional so the boundary conditions of that code are different to those of SIMMER-III. The results calculated show a recirculation of water in the wrong sense. Above all, this sense may not be stable. Similar results have

been obtained with the off-the-shelf version of the AFDM code. This outlines the difficulties for a code to compute such a flow.

4. Understanding of phenomena

The proper calculation of the redistribution of phases in bubble columns will have a profound effect on the values averaged over the whole pool. It is necessary for a code to perform well on such a case to be able to compute a reactor transition phase.

5. SIMMER-III Representation

5.1 Geometry, Initial and Boundary conditions

A 2-D mesh was used, as illustrated in Fig. 1. The initial water column extends up to 0.45 m. A flow of air was specified to be constant at the lower boundary, representing the air mass flow through a sieve plate. Atmospheric pressure and room temperature was used. The wall volume fraction in the boundaty cells was 10%, the surface area was 30 m^2/m^3.

6. Results

The first 10 seconds are characterized by some internal void oscillations within the pool, but a rather stable pool surface. After, the velocity distribution shows downward gas velocities in the pool center and at the wall, and upward velocities in the annulus around the center (Fig. 2). Fig. 3 shows the water velocities. This flow is not correct, as the gas and the water are known to rise in the center of the pool and flow down in the outer region. Here, the recirculation is in the wrong sense.

Fig. 4 shows the axial void distribution at a radius of 0.063 mat different times. It is apparent that the void distribution does not reflect the physics of the bubble column, as can be seen in Fig. 5.

7. Conclusions

The results show that there is a need to qualitatively improve the pool modeling before embarking on the much more difficult task to quantitatively predict the void and the velocities. Similar results obtained with MC3D and AFDM code show that the task is not an easy one.

8. Recommendations for Model Improvement

From the state-of-the-art, one must consider the introduction of a turbulence model into SIMMER-III. The implementation of such methods into SIMMER-III is limited to be done in an explicit way, the stability of which is questionable. Since these problems are known since 1989, it may be time to start a research program.

9. References

1) H.A. Jacobsen, H.F. Svendson, K.W. Hjarbo: On the prediction of local flow structures in internal loop and bubble column reactors sing a two-fluid model, Computers and Chemical Engineering, Vol.17, pp. S531-S536, 1993

2) M. Lance: Les ecoulements a bulles dans les reacteurs chimiques, Reunion GREDIC sur les ecoulements diphasiques, 26 janvier 1995, CEA-Grenoble

3) M. Valette: Private communication, CEA-Grenoble, Sept. 1994

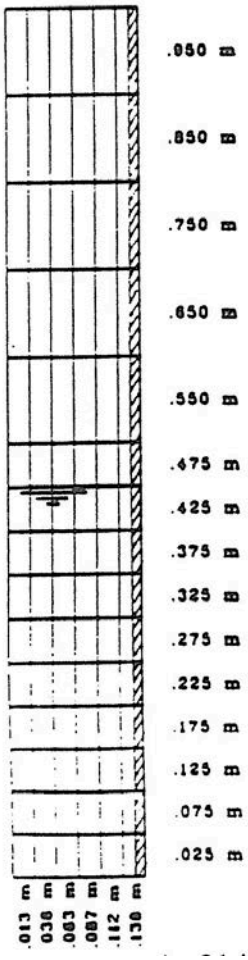

Fig. 1. Mesh cell set of a 2-D bubble column.

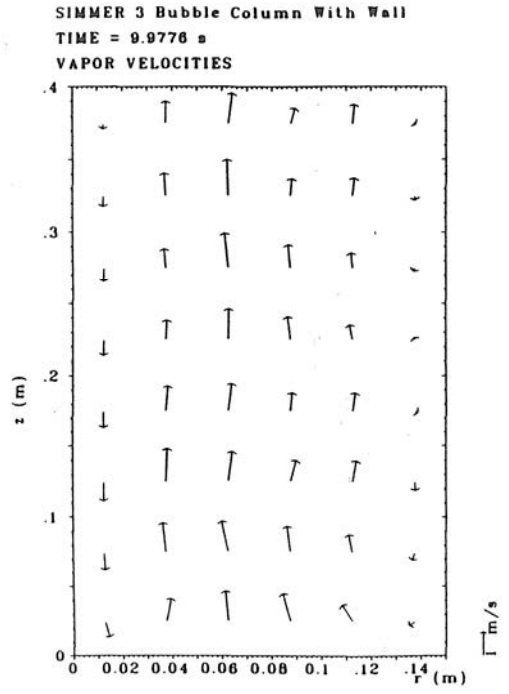

Fig. 2. Air velocities in the liquid section of a bubble column.

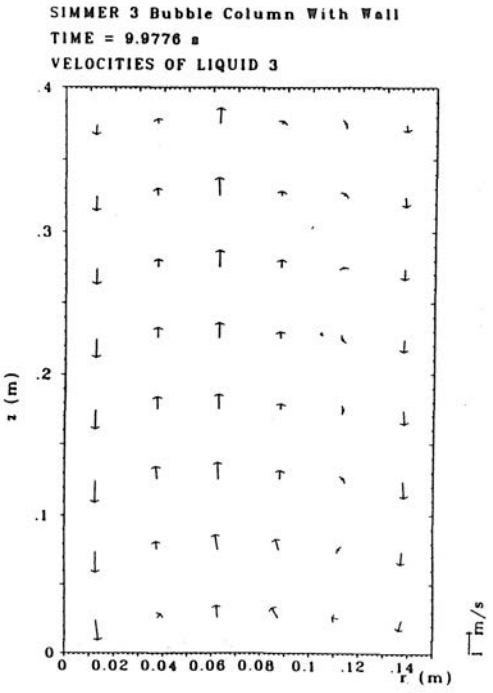

Fig. 3. Water velocities in the liquid section of a bubble column.

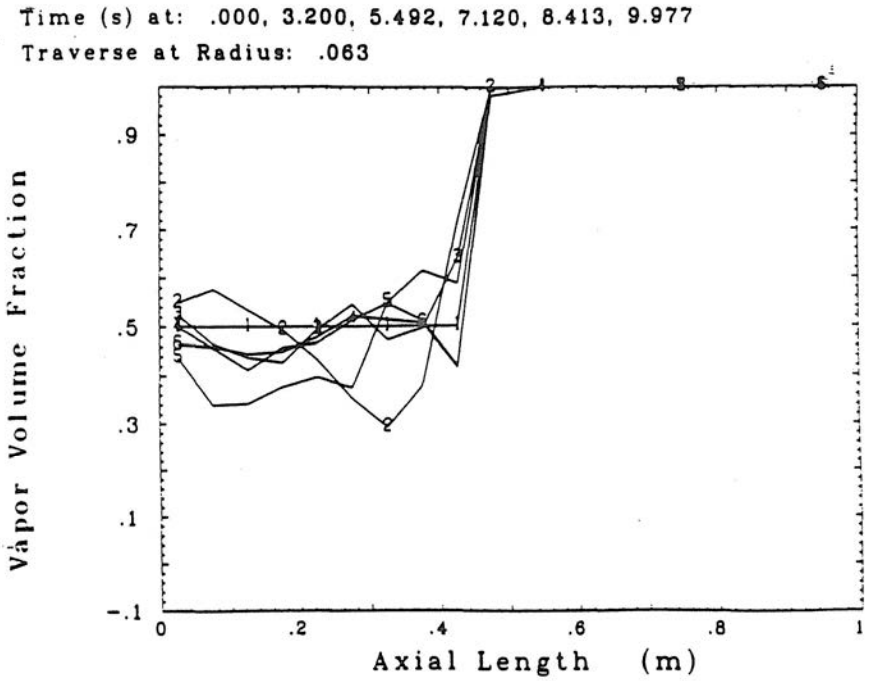

Fig. 4. Void profiles along the middle of a bubble column.

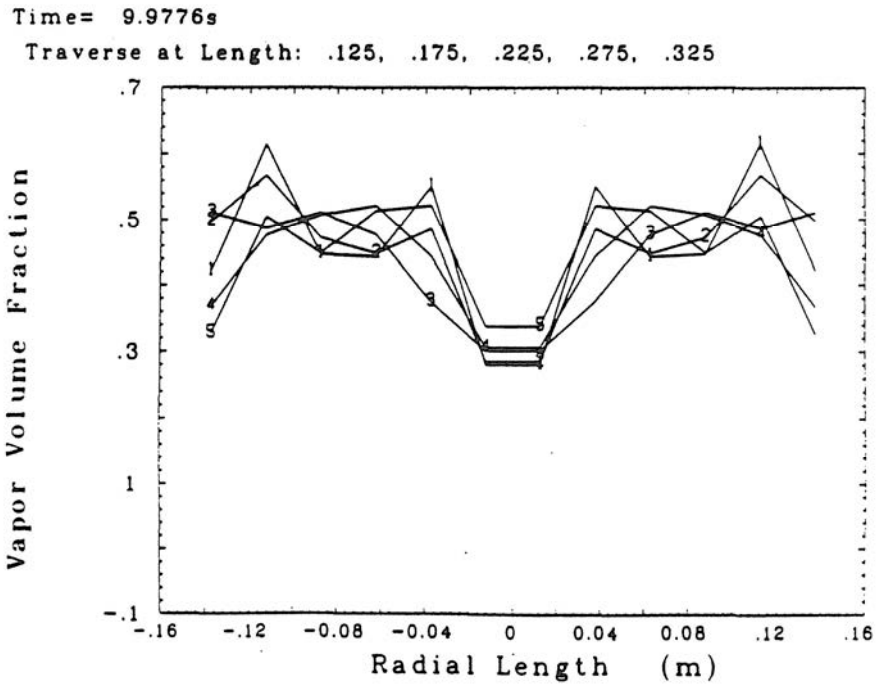

Fig. 5. Void profiles at different horizontal cuts of a bubble column.

Problem 2.4: Pressure drop in fully developed flow

"Pressure Drop and Entrained Fraction in a Fully Developed Flow"

Simone Vandroux-Koenig and Fabien Boulanger (CEA-G)

Outline of the case

On the LOTUS rig, a two phase air-water flow is established in a long vertical tube. The liquid flowrate is constant, a large range of gas flowrates is available. The two-phase pressure drop is measured. In case of annular flow, the liquid film flowrate in the tube is also measured. Those experiments allows to test the SIMMER-III (S-III) description of flow regime transitions and the MXF.

1. Objectives of the application

The LOTUS experiment provides a good test for the different channel flow regimes and for the momentum exchange coefficients used in S-III.

2. Description of the Experiment

It has been performed on the LOTUS rig at Harwell.[1), 2), 3)] Air and water are introduced from the bottom of a straight 23 m long and 31.8 mm internal diameter vertical copper pipe. The liquid is injected through a porous wall section. The outlet pressure is maintained at 239 kPa, and the liquid mass flux is constant: 297.1 kg m^{-2} s^{-1}. The air flow-rate is varied in a wide range, from slug flow to annular dispersed flow. For the injection, only fluid mass fluxes are measured. Inlet pressure, volume fractions and velocities are not reported.

The two-phase pressure drop and the entrainment fraction are measured at the end of the pipe (18 m from the injection, i.e. 570 tube diameters so the flow is fully developed). The liquid film flowrate is measured by extracting the film through a porous wall section. The experimental data for pressure gradient and for the superficial mass flux in the liquid film m_{LF} (i.e. the mass rate of flow divided by the cross sectional area of the channel) are given in Table 1.

3. Analytical solution

Fully developed two phase flow is a basic test for every multiphase code. However due to the complexity and number of the flow encountered, no global analytical solution is possible.

4. Understanding of phenomena

The film flowrate is represented as a function of air mass flux in Fig. 1 for different inlet liquid mass flows. It shows that with increasing gas flowrate, there is initially a very rapid reduction in film flowrate,

particularly at high total liquid flowrates. It then seems to reach an asymptotic value of about 12 kg m^{-2} s^{-1}. This value corresponds to a film thickness under which no entrainment can occur.

The two-phase pressure drop is represented as a function of air mass flux in Fig. 2. The pressure gradient curve demonstrates local maxima and minima at different gas flowrates. The existence of local minima and maxima in the curve is well known in the lower gas flowrate region. It is associated with the existence of a variety of flow regimes, including slug flow, chum flow and chum annular flow.

For high gas flowrates however, here about 100 kg m^{-2} s^{-1}, in the annular flow region, this particular trend was observed for the first time by Owen.[1), 2), 3)] Basically, two competing processes, which occur as the gas flow increases in annular flow, can be recognized:

- a tendency to increase the interfacial shear stress as the gas flow increases,
- as the gas flow increases, the amount of liquid in the film and the thickness of the film decreases rapidly, and this causes a reduction in wave activity on the interface, and a consequent reduction in interfacial friction factor.

The region in which the pressure gradient is decreasing with increasing gas fiowrate is one in which the second of these two processes becomes dominant. At last, when most of the film has been entrained away and a «micro film» is left, the first process becomes dominant, and the pressure drop increases again. Standard empirical pressure drop correlations fail to reproduce this trend.

5. SIMMER-III Representation

5.1 Geometry, Initial and Boundary conditions

A 1-D axisymmetrical mesh was used. The tube is represented from the bottom injection to the top measurement devices (19.4 m). It includes a right canwall to be able to calculate frictional pressure drop. Its external diameter is set to 36 mm.

The outlet pressure and the entry temperature of the fluids (293 K) are imposed. The inlet boundary conditions (pressure, volume fractions and velocities) have to be calculated in an iterative way[4)]:

- an inlet pressure is guessed
- volume fractions and velocities are estimated using standard correlations (no slip)
- resulting Sill inlet mass fluxes are compared to the data, and pressure adjusted accordingly
- The steel structure minimum temperature had to be lowered to 293 K (PTS(2) in &XEOS).

5.2 Code modifications

A serious bug in the interfacial area modeling (between liquid and vapor) was fixed. The impact was checked on run 23 and 35 (§6) but was found to be of second order.

5.3 Parametric cases

Various inlet gas flowrate have been considered.

6. Results

Some experiments are chosen among the experimental runs listed in Table 1. A comparison of the calculated and experimental film flowrate can be found in Fig. 3. It is highly overestimated. A comparison of the experimental and calculated total pressure gradient can be found in Fig. 4. The results are rather good compared to those obtained by other codes.[1), 4)] However, the· local minimum and maximum in the annular flow regime are not reproduced.

The expansion is adiabatic. This causes a very sharp decrease of the gas temperature along the tube. The higher the gas flux is, the more significant this decrease is (even below 273 K). It can even cause the program failure. Unfortunately, no experimental data on temperatures were available. For this reason, two new computations were tested: first an isothermal flow (constant gas temperature), second a calculation with heat transfer model activated. The conclusion is the change in pressure drop is low (about 7%) and the general behavior unchanged. So. the study is restrained to the adiabatic case.

For·annular flow configurations (run 30 to 42), the code behaves in a satisfactory way. The run 35 is detailed as a representative one. As soon as the chum/annular transition is reached (run 23), severe oscillations and unphysical results make it difficult to carry on the calculation. The results of this run are also presented.

6.1 Annular flow: run 35

A steady state is reached in about 2 seconds, after the water reached the outlet and some oscillations. Results are discussed at time 3 s.

Figure 5 represents the temperature in the tube. It drops very regularly along the tube. Figure 6 represents the radial cut of the pressure along the tube. The pressure drop is constant. Figure 7 .shows the water velocity. It remains very close.from the gas velocity. The reason for this is that, in the code, the liquid droplets and the liquid film are affected the same velocity. The droplets are entrained in the gas flux, with velocities close to the gas velocity, and thus the liquid film has a non-realistic velocity. It would be necessary, either to reconsider this choice of affected velocities, or to modify consequently the momentum exchange function between droplets and vapor. This confirms the conclusions of Suh's study.[5)] The velocity increase along the tube is due to a corresponding decrease of water volume fraction.

A parametric study was performed on this run:

- entry conditions

A calculation was performed considering a slip between air and water at the inlet boundary condition, using the Wallis correlation. This corresponds to a inlet superficial liquid velocity of 3.95 m/s and an air one of 25.41 m/s. The water velocities very quickly reach the air velocity, due to the wrong evaluation of the momentum exchange function between droplets and gas. The pressure and temperature are similar to the no slip initial calculation. This justifies that, as long as the momentum exchange function is not improved, it is not really necessary to have more precise entry conditions. The no slip results are therefore representative of the code comportment.

- heat and mass transfer

The observed sharp decrease of gas temperature seemed too significant. Lacking experimental data, the influence of temperatures on pressure drop needs to be checked. A first calculation supposed the gas temperature to be constant, equal to 293 K. The pressure and water velocity results are similar to the standard ones, being a little higher though. For instance, the pressure drop is increased of 7%.

A second calculation is made using the HMT (options NOMF, NOVC off) and a thicker pipe wall. The results are very similar to the previous ones, apart from the initial transient which is not good. These calculations show that the HMT model for the gas expansion increases the pressure drop of about 7%. The general behaviour in the tube is not affected.

6.2 Churn/annular flow transition: run 23

During the calculation of run 23, there are changes of flow regime in the pipe. This leads to a very strange behaviour of the calculation, and to significant oscillations. This can cause the calculation failure. For instance, Fig. 8 shows the pressure as a function of time, at different locations. No steady state seems to be reached, and the oscillations seem to go on. Figure 9 represents the water velocity along the tube, at different times. It clearly shows non physical behavior, with very sharp and sudden velocity changes along the tube. The water volume fraction follows the same trend.

Two things were tried to improve the results:

- try and force the flow regime to remain annular (imposing IRGMK=3 in subroutine IFARG). But this made the calculation fail even earlier.
- activate the HMT. Apart from a strange initial transient as with run 35 (§6.1), after about 8 seconds of calculation, the oscillations become much smaller and very regular. The pressure drop is also oscillating. It is therefore not possible to obtain a precise value of the pressure drop. Again, the comportment of the water velocity and volume fraction along the tube seems neither very realistic nor very physical.

Calculations with smaller gas flowrates, Table 1, give similar results as run 23 (failure due to severe instabilities).

6.3 Discussion

In the annular flow region, the calculated film flowrate (Fig. 3) is in bad agreement with the experimental values. Droplet entrainment is highly underevaluated in the calculation (Sill uses the Ishii-Mishima correlation). The decrease of the flowrate with inereasing air mass flux is not reproduced. In fact, the wave activity in the film is not modeled in S-III, turbulence in the boundary layer is not taken into account. This can partly explain the bad results obtained.

As the wave activity is not taken into account, the reduction in interfacial friction factor corresponding to the reduction of wave activity on the interface, due to the decrease of the film thickness can not be represented.

Clearly, the current MXF for the annular flow should be improved:

- Momentum coupling of the liquid and the vapor. In S-III, the vapor field is too strongly connected with liquid field, because the liquid droplets and film have the same velocity field. In the real situation, the droplet moves faster than the liquid fi1m because of its strong coupling with the vapor. To solve this problem, the momentum transfer by the entrainment and deposition of droplets should be modeled.
- The MXF between the liquid film and the gas core is too small in pure annular flows. In S-III, the surface of the liquid film is supposed to be smooth, there is no modeling of a wave formation on the film. This leads to an under estimation of the interfacial area, and thus of the MXF. The wave formation should therefore be modeled.
- The MXF between the liquid film and the structure is also underetimated, because the turbulent enhancement in the liquid film by the vapor flow is not modeled. The parametric study by Dr. Suh [5] came to the same conclusion. Additionally, it provides an order of magnitude of the MXF correction factors necessary to reproduce an annular flow.

7. Conclusions

A proper calculation is only possible in the annular flow region. As soon as the churn/annular transition is reached, very significant oscillations make it difficult to carry on the calculation. This is very restrictive. The transition between the different flow regimes should be studied in order to suppress these instabilities.

In annular flow, the pressure drop results are rather good. But the calculated exchanges between gas and liquid film are wrong, droplet entrainment is highly underevaluated. The results are explained by inaccuracies in the MXF.

Further work on the MXF models should be done in order to improve the results. Moreover, the transition made between the different flow regimes should be improved.

8. Recommendations for Model Improvement

The approach used in other codes have been looked at. For instance, the CA1HARE code can provide guidelines to improve S-III's MXF. It is detailed in Ref. 4).

9. References

1) G. F. Hewitt, et al.: Multiphase Science and Technology, volume 4, pp. 145-154 and volume 6, pp. 5-13 (1987).

2) D.G. Owen, G,F. Hewitt: Data and analysis of pressure gradient and liquid entrainment in vertical Annular gas-liquid flow. European two-phase flow group meeting, Marchwood, Eng. LAB., 4-7 June 1985.

3) D.G. Owen, G.F. Hewitt, T.R. Bott: Equilibrium annular flows at high mass fluxes; data and interpretation. Physico chemical Hydrodynamics, vol. 6, n 1/2, pp 115-131, 1985.

4) S. Vandroux-Koenig: Pressure drop and entrained fraction in a fully developed flow- Simmer m calculations. Report CEAfDRN/DTP/STRfLML/94-293, March 1995.

5) N.D. Suh, Y. Tobita: private communication.

Table 1. Ecxperimental data in LOTUS

$$m_{LF} = 297.1\ \mathrm{kg \cdot m^{-2} s^{-1}}$$

Run No.	Air mass flux $\dot{m}_G$ kg/m²s	Estimated uncertainty in $\dot{m}_G$ ± %	Observed flow regime	Pressure gradient (dp/dz) Pa/m	Estimated Uncertainty in (dp/dz) ± %	Mass flow rate in film divided by channel cross section $\dot{m}_{LF}$ kg/m²s	Estimated uncertainty in $\dot{m}_{LF}$ ± %
1	2.96	50.0	Bubble	9489.0	0.3	-	-
2	4.41	25.0	Bubble	9489.0	0.3	-	-
3	5.64	25.0	Bubble	8851.0	0.6	-	-
4	6.56	12.5	Slug	3388.0	2.3	-	-
5	7.53	10.0	Slug	3217.0	3.9	-	-
6	8.50	8.4	Slug	2876.0	8.5	-	-
7	8.63	8.4	Slug	2754.0	8.9	-	-
8	8.80	8.4	Slug	2632.0	9.3	-	-
9	8.95	8.4	Slug/churn	2656.0	9.3	-	-
10	9.09	8.4	Slug/churn	2559.0	9.6	-	-
11	9.23	8.4	Slug/churn	2486.0	9.9	-	-
12	9.42	8.4	Slug/churn	2486.0	9.9	-	-
13	14.28	3.0	Slug/churn	2510.0	9.8	-	-
14	14.54	3.0	Churn	2632.0	9.3	-	-
15	15.17	2.8	Churn	2632.0	9.3	-	-
16	15.56	2.7	Churn	2608.0	9.4	-	-
17	16.18	2.6	Churn	2608.0	9.4	-	-
18	16.95	2.5	Churn	2754.0	8.9	-	-
19	17.00	2.6	Churn	2705.0	9.1	-	-
20	17.29	2.6	Churn	2754.0	7.2	-	-
21	16.91	2.0	Churn	2778.0	7.1	-	-
22	18.89	1.8	Churn/annular	2730.0	4.6	-	-
23	20.49	1.7	Churn/annular	2656.0	4.7	-	-
24	21.35	1.7	Churn/annular	2681.0	4.7	-	-
25	23.39	1.6	Churn/annular	2681.0	4.7	-	-
26	24.90	1.5	Churn/annular	2681.0	4.7	-	-
27	24.80	1.6	Churn/annular	2681.0	4.7	-	-
28	25.48	1.5	Churn/annular	2754.0	4.5	-	-
29	27.65	2.0	Churn/annular	2803.0	4.5	-	-
30	29.59	1.9	Churn/annular	2876.0	4.4	-	-
31	33.91	1.4	Churn/annular	2900.0	2.7	-	-
32	38.24	1.3	Churn/annular	3022.0	2.6	-	-
33	50.72	1.5	Annular	3629.0	1.9	-	-
34	80.80	2.0	Annular	4363.0	1.2	125	5.0
35	86.59	1.9	Annular	4485.0	1.2	110	4.5
36	95.71	1.7	Annular	4582.0	1.2	83	6.0
37	102.85	1.3	Annular	4631.0	1.1	70	6.0
38	113.11	1.3	Annular	4655.0	1.1	50	6.0
39	129.74	1.2	Annular	4704.0	1.1	35	6.0
40	144.17	1.2	Annular	4972.0	1.0	26	4.0
41	157.06	1.2	Annular	5362.0	1.0	23	2.5
42	161.60	1.2	Annular	5603.0	0.9	22	2.0

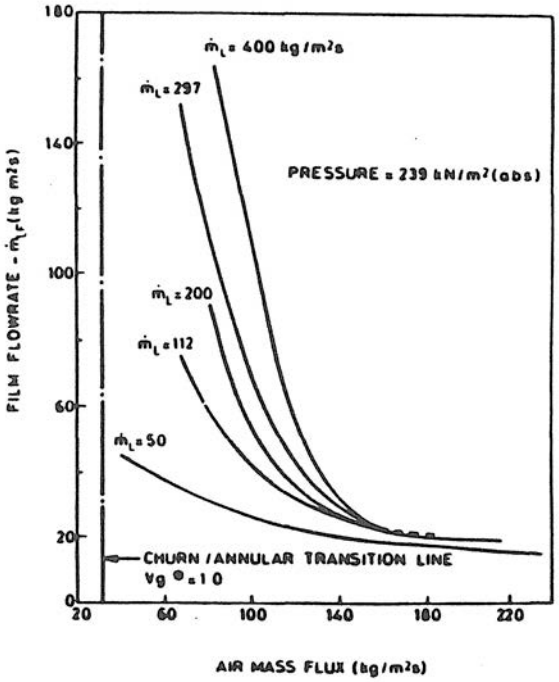

Fig. 1. Film flowrate plotted as a function of air mass flux.

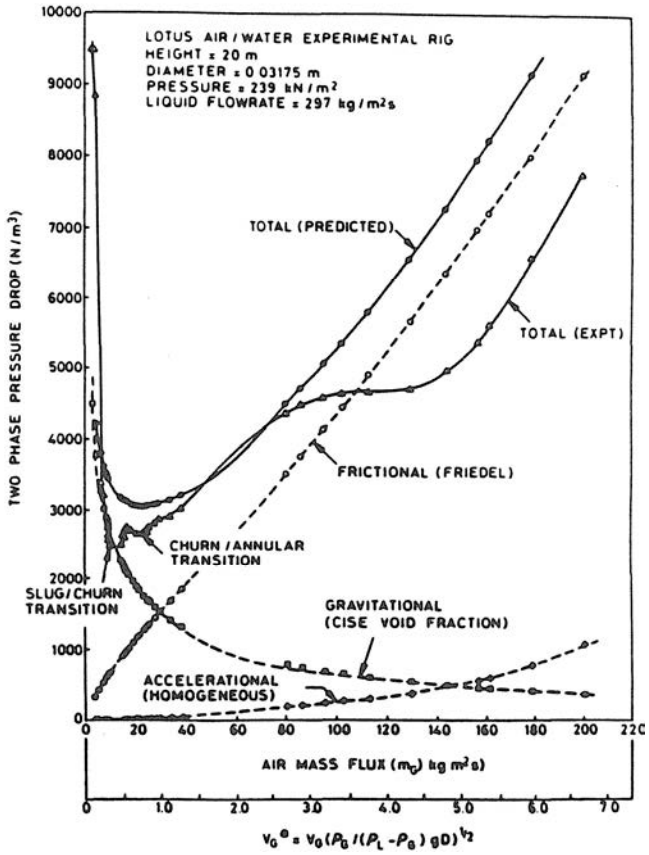

Fig. 2. Variation of total pressure gradient with air mass flux.

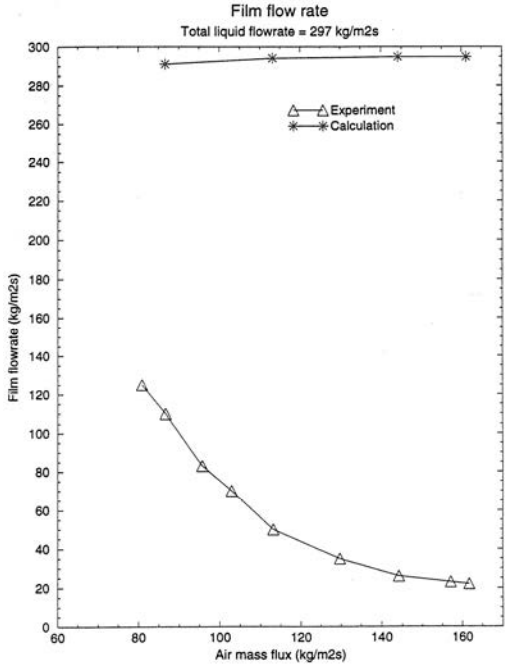

Fig. 3. Film flowrate: comparison between experiment and calculation.

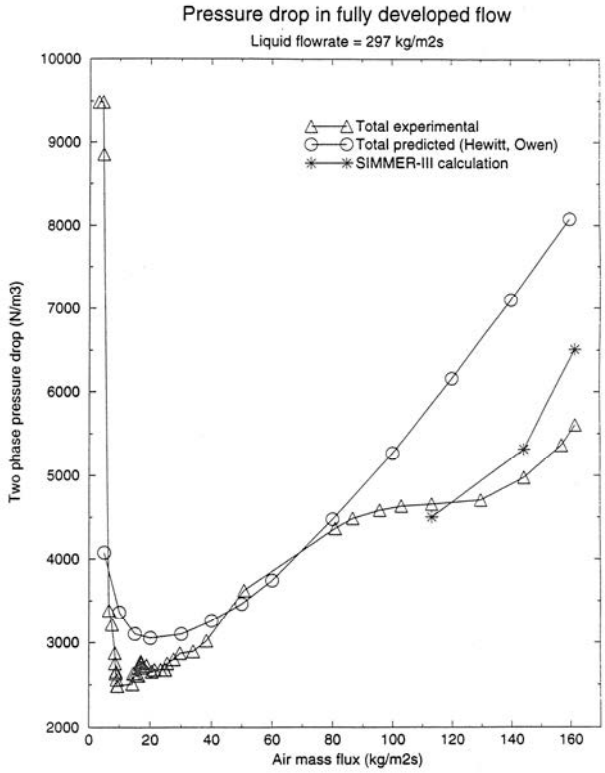

Fig. 4. Total pressure gradient: comparison between experiment and calculation.

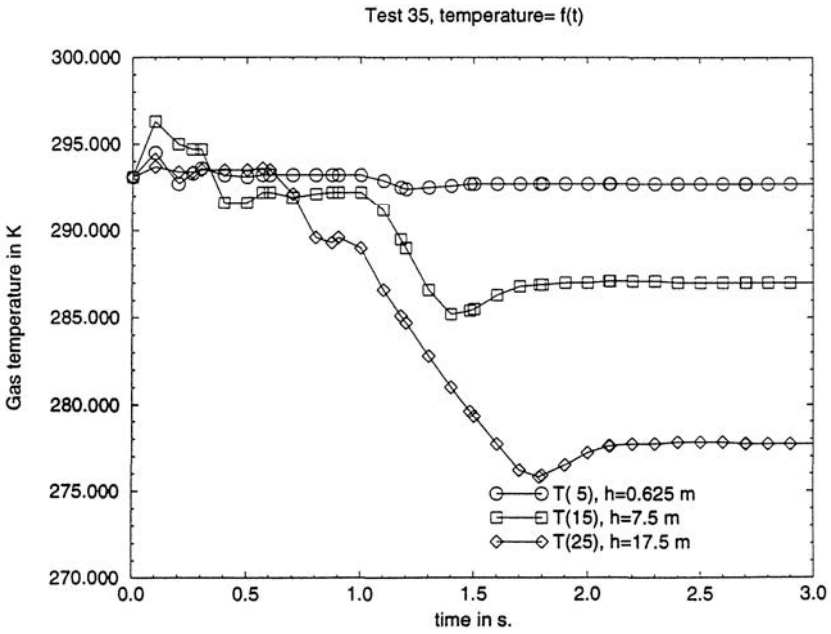

Fig. 5. Run 35: gas temperature as a function of time.

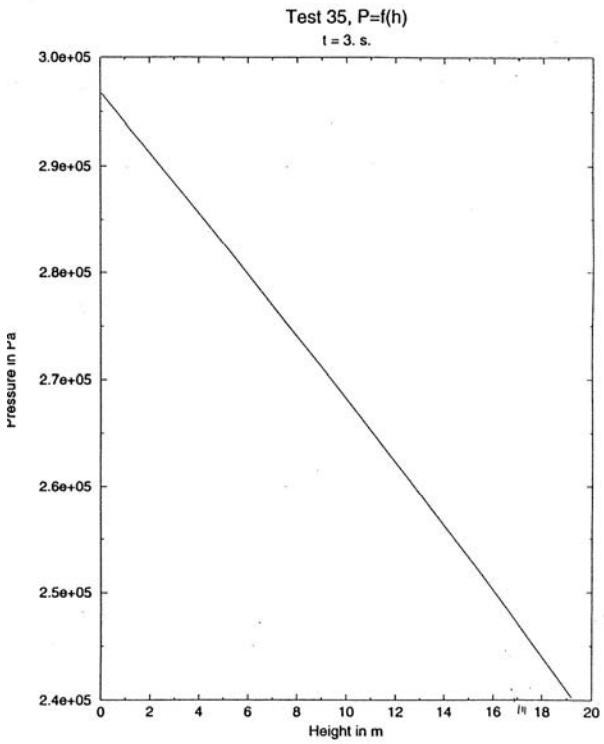

Fig. 6. Run 35: radial cross section of the pressure t=3 s.

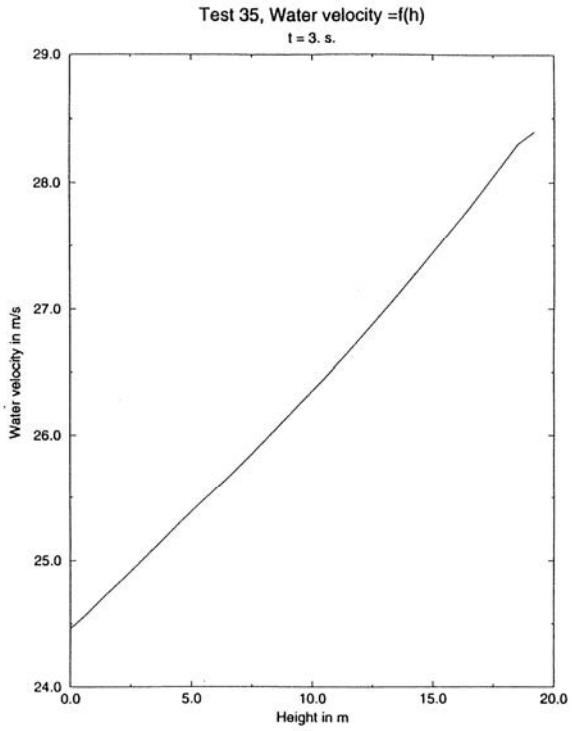

Fig. 7. Run 35: radial cross section of water velocity at t = 3 s.

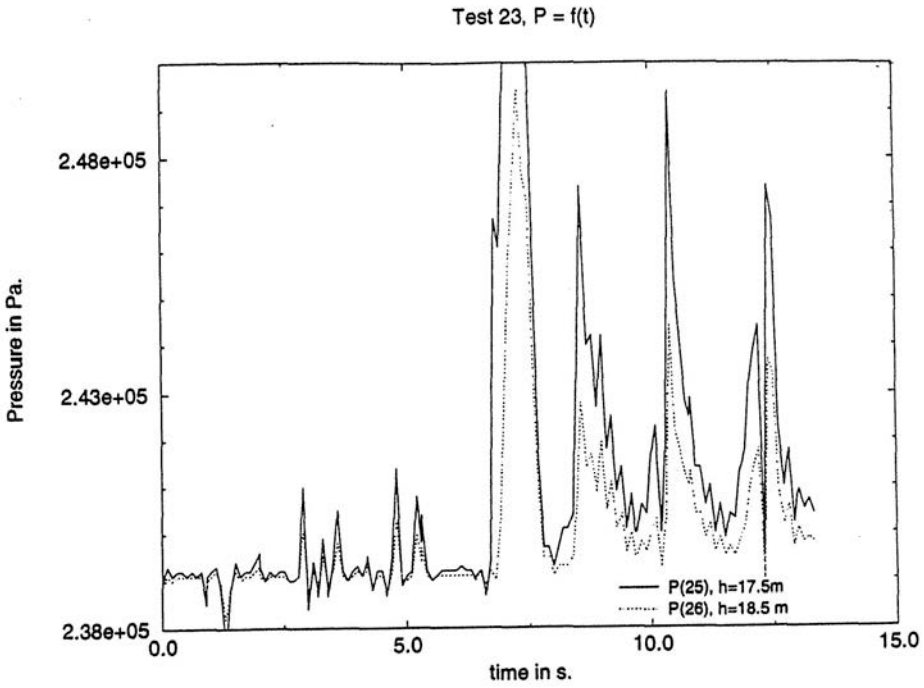

Fig. 8. Run 23: pressure as a function of time.

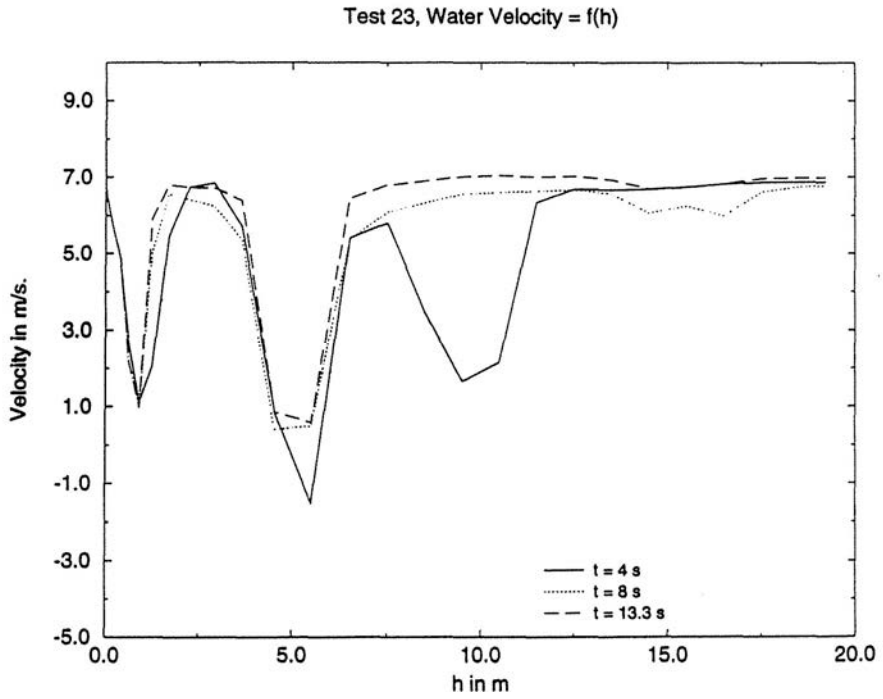

Fig. 9. Run 23: radial cross section of water velocity at different times.

Problem 2.5: Momentum exchange in pipe flow

"Momentum Exchange in Pipe Flow"

Yoshihara TOBITA (PNC)

Outline of the Case

The pressure drop in two-phase flow in a single straight pipe is compared with the experimental data taken from Ref. 1). The flow regime covers bubbly, slug, and pure annular flow. The original SIMMER-III model turned out to underestimate the pressure drop in bubbly flow and overestimate it in annular flow. This is because SIMMER-III does not take into account the effect of turbulence enhancement in a liquid film due to the vapor flow which has a higher velocity than liquid.

1. Objectives of the Application

The objective of this study is to check the applicability of the formulation of fluid-structure momentum exchange function in SIMMER-III and propose a model improvement if necessary. The flow regime examined is bubble, slug, and annular flow.

2. Description of the Experimenf

The experimental data are taken from Inoue's experiment of upward cocurrent air-water two-phase flow in a vertical pipe.[1)] In this experiment, the pressure dtop in a vertical pipe of 2 m long and entrance section of 50 cm long was measured. The inner diameter of the pipe ranged from 5 mm to 29.5 mm and.the flow regime ranged from bubbly flow to annular flow. The air was supplied through porous metal block at the bottom of the test section and the diameter of the bubbles were well controlled in the range of 3 to 4 mm. The range of liquid flow rate was 0 – 0.5 liter/s and the vapor flow rate 0 – 0.8 liter/s. The measured pressure drops are plotted in Figs. 1 – 6, in which the vertical axis is two-phase pressure loss multiplier and the horizontal axis is gas quality. The numerical values in brackets is the superficial velocities of water.

3. Analytical Solution

Analytical solution is not available. However, the Lockhart-Martinelli (L-M) correlation is used to predict the two-phase pressure drop in many two-phase flow codes.

4. Understanding of Phenomena

The general trend of the two-phase pressure drop is represented by the L-M correlation. However, experimental data showed a large discrepancy from this correlation depending on the flow situation. One cause of this discrepancy is the effect of turbulent enhancement in liquid phase by the presence of the gas phase. Because the L-M correlation is based on the separated flow model, it does not take into account the

effect of gas-liquid interaction. In order to adopt this mechanism into the pressure drop prediction, some models and semi-empirical correlation were proposed in the literature. After comparative assessment of these correlations, the model proposed by Ueda[2] is employed in SIMMER-III modeling. A brief description of this model is given in Appendix to this summary report.

5. SIMMER-III Representation

5.1. Geometry, Initial and Boundary Conditions for a Reference Case

A 0-dimensional system, i.e. one mesh cell, was used just to provide a set of experimental condition to SIMMER-III subroutines which calculate interfacial area (IFA) and momenmm exchange functions (MXF).

5.2. Code Modifications

The objective of this study is to investigate the pressure drop characteristics of SIMMER-III modeling in two-phase flow in a pipe from the bubbly flow regime to the annular flow regime. The pressure drop in these flow situation is dominated mainly by the liquid-structure momentum exchange. On the other hand, previous experience in annular flow analysis (see Problem 2.6 "Developing Annular Flow") showed that the SIMMER-III prediction of the liquid film-vapor momentum coupling is not satisfactory. These factors let this study concentrate on the liquid-structure momentum exchange process.

An ad-hoc modification was made to neglect the convection term in momentum equation as was done in Problem 2.1 "Zero-th dimensional pool flow". Inoue reported the pressure drop for liquid superficial velocity and gas quality. The average void fraction is calculated using the well-known CISE correlation.[3] The gas velocity is then obtained from void fraction and gas quality and the SIMMER-III model calculate the momentum exchange function using these quantities. Assuming that the momentum transferred from gas phase to liquid phase is much smaller than that from the structure in a two-phase flow in a pipe, the liquid velocity is calculated by the following equation:

$$K_{ls} v_l + \alpha_l \nabla p - \bar{\rho}_l g = 0 \qquad (1)$$

Because the momentum exchange function K_{ls}, is a linear function of v_l, Eq. (1) becomes a quadratic equation to be solved for v_l. This procedure is iterated by controlling the pressure loss until the calculated liquid velocity becomes equal to the experimental condition.

5.3. Parametric Cases

After having performed some preliminary calculations, we found that the present SIMMER-III model cannot reproduce the pressure loss characteristics in two-phase flow. It is unable to simulate the pressure loss increase in the low gas quality region, but also underestimates the pressure drop prediction by L-M correlation in high gas quality region. Part of this discrepancy can be attributed to the lack of the modeling

of turbulence enhancement in the liquid phase due to the relative motion of gas phase. In order to adopt this mechanism into the pressure drop prediction the model proposed by Ueda[2)] is employed in SIMMER-III modeling after a comparative assessment of available models. The effect of this model is depicted by comparing with the results by original SIMMER-III model.

6. Results

The calculated two-phase pressure multipliers by the original SIMMER-III model are plotted against the gas quality for the pipe diameter of 28.8 mm and 5 mm in Figs. 1 and 2, respectively. In these figures, the dots represent the experimental data and the numerical values in brackets is the superficial velocity of water. The prediction by L-M correlation is also plotted in these figures. The results by SIMMER-III model with Ueda's model are plotted in Figs. 3 – 6 for the pipe diameter of 28.8 mm, 19 mm, 9 mm and 5 mm.

As was discussed in section 2, the general trend of two-phase pressure drop can be represented by L-M correlation. However, neither L-M correlation nor the original SIMMER-III model can reproduce the pressure loss increase in low gas quality and low liquid velocity condition. In addition, the original SIMMER-III model also underestimates the pressure drop in high gas quality region compared with L-M correlation. This discrepancy is thought to stem from the lack of the turbulence enhancement effect in liquid phase by the relative motion of gas. This result required the improvement of liquid-structure momentum exchange function and Ueda's model was implemented to SIMMER-III.

The predicted pressure loss by SIMMER-III with Ueda's model reproduces the general pressure loss behavior very well from the bubbly flow regime to annular flow regime. The pressure loss in the low gas quality and low liquid velocity region is also traced by SIMMERIII well.

7. Conclusions

If appropriate correlations for the turbulence enhancement in liquid phase are used, SIMMER-III can successfully simulate pressure loss characteristics in a pipe with different radius from 5 mm to 28.8 mm and in a wide range of flow regimes from bubbly flow to annular flow.

8. Recommendations for Model Improvement

Based on the results of this study, model improvements on the liquid-structure momentum exchange function are proposed and have already been implemented in Version 2.A.

9. References

1) A. Inoue and S. Aoki: "Basic study on the pressure drop in two-phase flow in a pipe", Transaction of the JSME (in Japanese), Vol.32, No.238, pp.940 - 947, 1966.

2) T. Ueda: "On the upward flow of gas-liquid mixture in a pipe", Transaction of the JSME (in Japanese), Vol.33, No.248, pp.601 - 625, 1967.

3) A. Premoli, et al.: "An empirical correlation for evaluating two-phase mixture density under adiabatic conditions", European Two-Phase Flow Group Meeting, Milan, 1970.

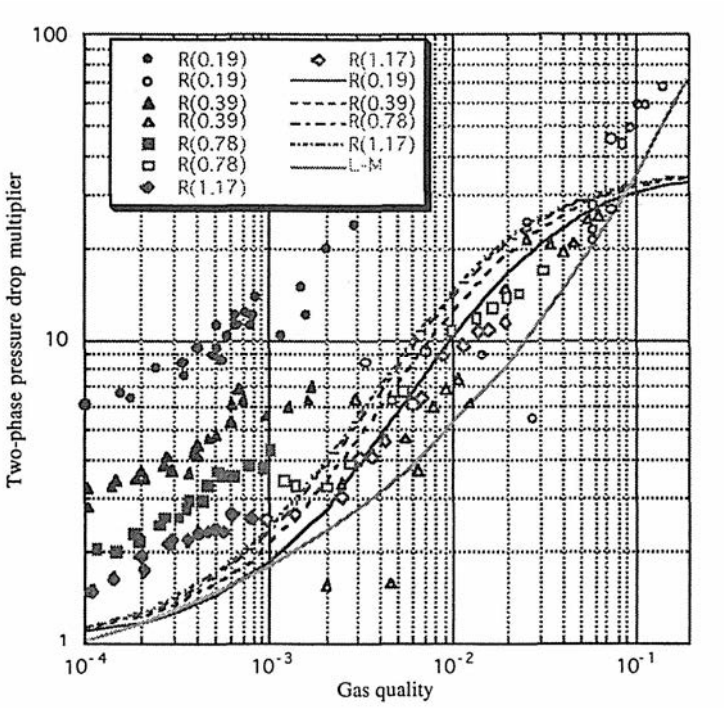

Fig. 1. Two-phase pressure loss in a pipe with its diameter of 28.8 mm. (original SIMMER-III model)

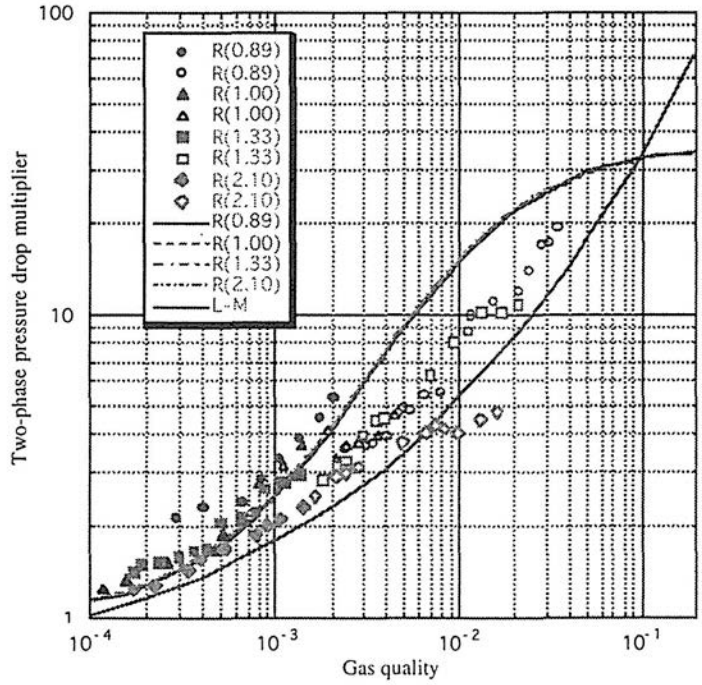

Fig. 2. Two-phase pressure loss in a pipe with its diameter of 5 mm. (original SIMMER-III model)

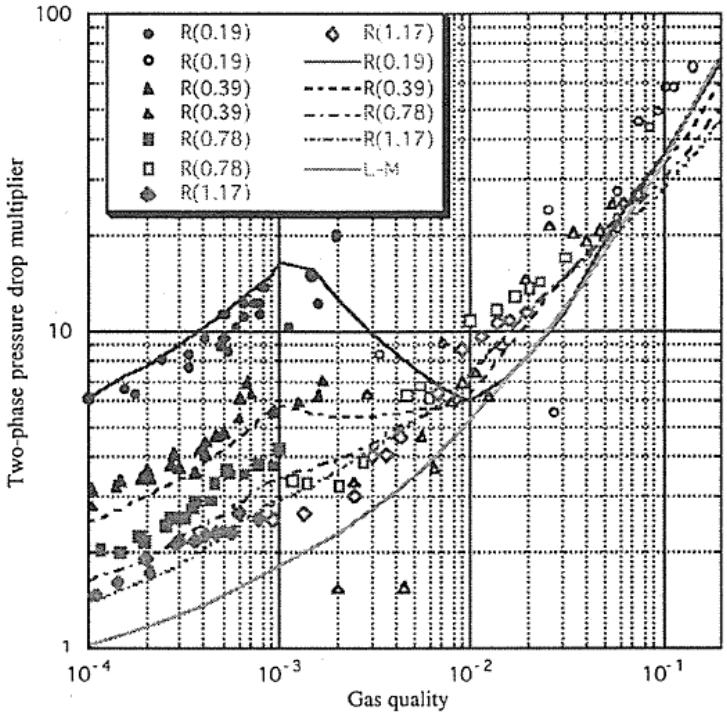

Fig. 3. Two-phase pressure loss in a pipe with its diameter of 28.8 mm. (SIMMER-III with Ueda's model)

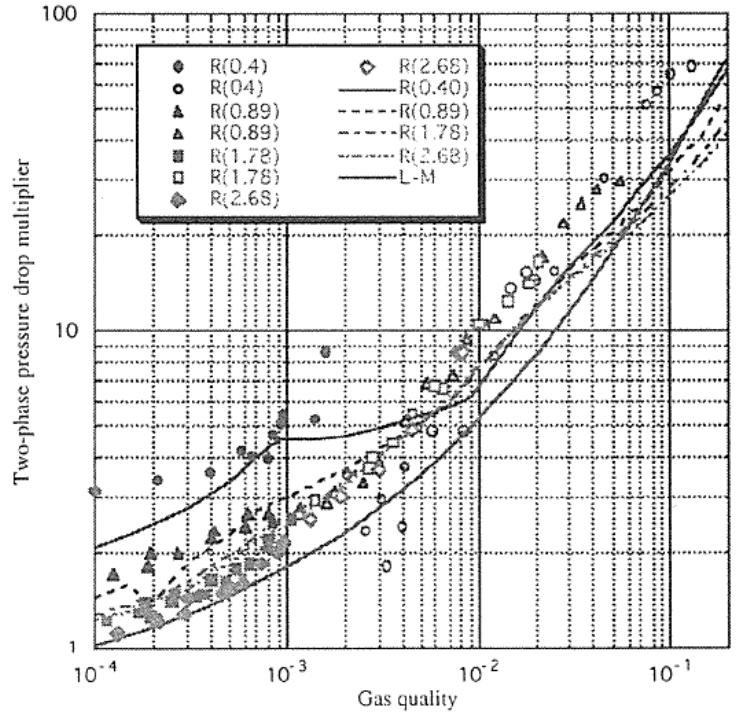

Fig. 4. Two-phase pressure loss in a pipe with its diameter of 19 mm. (SIMMER-III with Ueda's model)

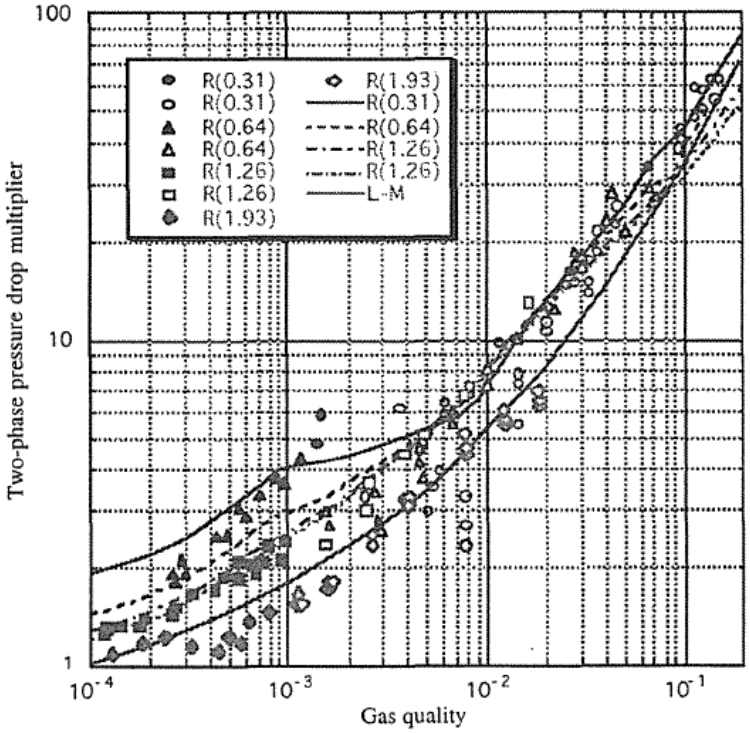

Fig. 5. Two-phase pressure loss in a pipe with its diameter of 9 mm.
(SIMMER-III with Ueda's model)

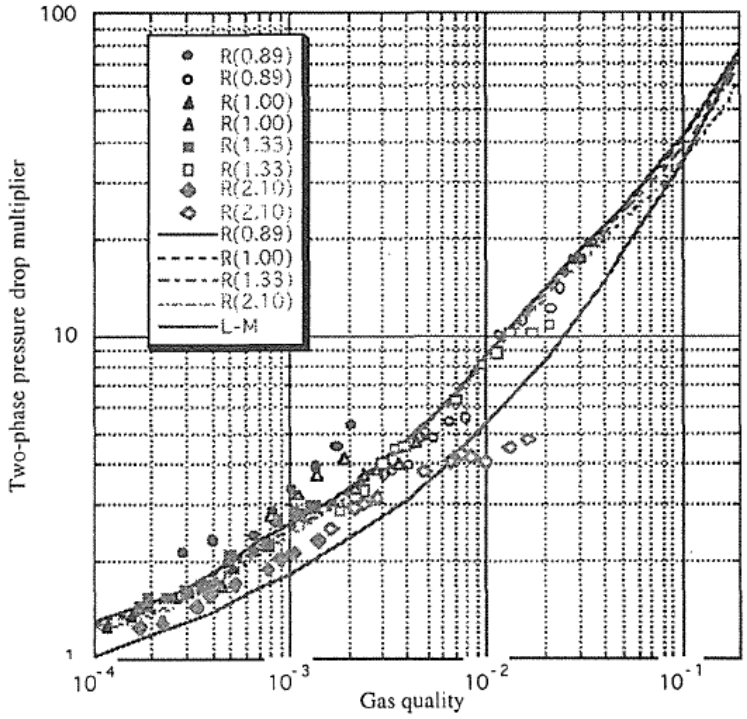

Fig. 6. Two-phase pressure loss in a pipe with its diameter of 5 mm.
(SIMMER-III with Ueda's model)

Appendix to Problem 2.5: Brief description of Ueda's model

The relationship between the pressure drop and the shear stress at the wall is given by

$$\frac{\Delta P}{\Delta L} = \frac{2}{r}\tau$$

since

$$\pi r^2 \Delta P = 2\pi r \tau_0 \Delta L$$

The pressure balance in the vapor core in annular flow yields

$$\frac{\Delta P}{\Delta L} = \rho_g g + \frac{2}{r_i}\tau_i \tag{1}$$

If we define τ_0 as the share force at wall surface, the following equations hold:

$$\tau_0 = \frac{r_0}{2}\left(\frac{\Delta P}{\Delta L}\right)_{TP}$$

$$\frac{\Delta P}{\Delta L} = \alpha\rho_g g + (1-\alpha)\rho_l g + \left(\frac{\Delta P}{\Delta L}\right)_{TP}$$

and

$$\frac{\Delta P}{\Delta L} = \left(\frac{r_i}{r_0}\right)^2 \rho_g g + \left[1 - \left(\frac{r_i}{r_0}\right)^2\right]\rho_l g + \frac{2}{r_0}\tau_0 \tag{2}$$

Let τ the shear stress at arbitrary location, the force balance in the liquid film,

$$\frac{\Delta P}{\Delta L} = \left(\frac{r_i}{r}\right)^2 \rho_g g + \left[1 - \left(\frac{r_i}{r}\right)^2\right]\rho_l g + \frac{2}{r}\tau$$

results in

$$\tau = \frac{r}{r_0}\tau_0 + \frac{r}{2}(\rho_\ell - \rho_g)g\left[\left(\frac{r_i}{r}\right)^2 - \left(\frac{r_i}{r_0}\right)^2\right] = \tau_0 + \varphi y + \frac{\Delta\rho g\alpha}{2}\left(\frac{{r_0}^2}{r} - 2r_0 + r\right) \tag{3}$$

The definition of the shear stress is expressed as

$$\tau = \rho_l \nu_l \frac{du}{dr} \tag{4}$$

wherev, ν_ℓ is the kinematic viscosity in the laminar layer. The integration of Eq. (4) from the wall surface ($y = 0,\ r = r_0$) to the boundary of laminar layer ($r_\delta \le r \le r_0$) gives the velocity at the laminar boundary.

$$u_\delta = \frac{1}{\rho_l \nu_l}\left[\tau_0\delta + \frac{\varphi}{2}\delta^2 - \frac{\Delta\rho g\alpha}{2}\left({r_0}^2 \log\frac{r_0 - \delta}{r_0} + r_0\delta + \frac{1}{2}\delta^2\right)\right] \tag{5}$$

where

$$\varphi = \Delta\rho g\alpha - \frac{\tau_0}{r_0}$$

Here we start from the single phase flow. The wall share stress is given by

$$\tau_0 = \frac{1}{2} C_D \rho_l {u_m}^2 \tag{6}$$

where u_m is the average velocity of liquids. In the single phase flow, the void fraction is zero ($\alpha = 0$) and Eq. (5) becomes

$$u_\delta = \frac{1}{\rho_l \nu_l}\left[\tau_0 \delta - \frac{\tau_0}{2r_0}\delta^2\right]$$

Neglecting the second term and substituting Eq. (6), we get

$$u_\delta = \frac{\delta C_D {u_m}^2}{2\nu_l} \tag{7}$$

In the developed turbulent flow in single component flow, the thickness of the laminar boundary layer is given by the following non-dimensional length,

$$\delta^+ = \sqrt{\frac{\tau_0}{\rho}}\frac{\delta}{\nu} = K$$

The non-dimensional velocity at this thickness is defined as

$${u_\delta}^+ = u_\delta \Big/ \sqrt{\frac{\tau_0}{\rho}}$$

then ${u_\delta}^+ = \delta^+$.

$${u_\delta}^+ \delta^+ = \frac{u_\delta \delta}{\nu} = K^2$$

The generalized flow distribution gives K = 5 , the assumption of two regimes gives K = 12. The flow situation in two-phase flow will be different from that in single phase flow, the value of K should be between 5 and 12. Therefore, K = 7 is assumed here. Then, this equation becomes as follows:

$$\delta = 50\frac{\nu_l}{u_\delta} \tag{8}$$

Substituting Eq. (8) into Eq. (7), the velocity at the laminar boundary layer is given as the function of the mean velocity u_m,

$$u_\delta = \sqrt{25C_D}u_m \tag{9}$$

In two-phase flow, the flow condition is different from single phase flow, and the equation does not hold with its original form. However, the introduction of additional correction term is assumed to give the appropriate effective mean velocity for two-phase flow.

In an upward annular flow, the gas velocity is greater than the liquid velocity and this veiocity difference will enhance the turbulence in the liquid film and hence increases u_δ. This effect is expressed by the following term,

$$\Delta u_{\ell 1} = C_1 {Re_s}^{C_2} u_s \tag{10}$$

where u_s is the slip velocity, $Re_s = u_s 2y_i/\nu_\ell$, and y_i is the liquid film thickness.

The velocity increase in the turbulence layer in two-phase flow should be greater than that of single phase flow. This mechanism lowers the effective mean velocity. Assuming that the eddy diffusivity is proportional to the distance from the wall and the characteristic velocity u_{ed}, which corresponds to the intensity of the turbulence, this effect is expressed by

$$\Delta u_{\ell 2} = C_3 Fr_{ed} u_{ed} \tag{11}$$

where

$$Fr_{ed} = \frac{g\alpha 2y_i}{{u_s}^2}$$

$$u_{ed} = j_g + j_l$$

Eventually, the effective mean velocity is given as follow,

$$u_m^* = u_l + \Delta u_{l1} - \Delta u_{l2} \tag{12}$$

The experimental data gave the relation between $u_m^* u$: and $u_\delta u$, as

$$u_\delta = \frac{1.10}{{Re_m}^{1/8}} u_m^* \tag{13}$$

In the case of bubbly flow, the relative motion of bubbles promote the turbulence in liquid and then increases u_δ. This effect is expressed by the following correction term.

$$\Delta u_{\ell 3} = C_4 {Fr_s}^{C_5} {u_s}^{C_6} \tag{14}$$

where

$$Fr_s = \frac{g\alpha 2y_i}{{u_s}^2}$$

$$u_{ed} = j_g + j_l$$

At the limit of $\alpha \to 0$, the velocity at the laminar boundary layer should reduce to Eq. (9). Therefore, the following equation is used for bubbly flow,

$$u_\delta = \sqrt{25 C_D} u_m^* \tag{15}$$

Substituting eq. (8) into eq. (5) and rearranging, we get

$$\tau_{TP} = \frac{\left[\frac{\rho_l {u_\delta}^2}{50} - \frac{50\nu_l}{2u_\delta}\rho_l g\alpha\right]}{\left(1 - \frac{50\nu_l}{D_h u_\delta}\right)} \tag{16}$$

The ratio of τ_{TP} to τ_0 gives the pressure drop multiplication factor R in two-phase flow.

SIMMER-III explicitly represents the bubbly and annular flow regimes, whilst the intermediate regime (slug flow regime) is modeled by a transition flow where a mesh cell is treated as a combination of a bubbly and annular regions. The ratio of the bubble flow region which occupies the structure surface is modeled as the ratio of the interface area of the liquid slug F_{slug} contacting to the structure surface. The multipliers in the bubbly flow region and annular flow region are then averaged logarithmically to obtain the overall multiplier as follows.

$$R = {R_{bubbly}}^{F_{slug}} {R_{annular}}^{1-F_{slug}} \tag{17}$$

Finally, the coefficients in Eqs. (10), (11) and (15) have been determined through a trial-and-error procedure to obtain best agreement with the experimental data as:

$$\begin{aligned} C_1 &= 0.75 \\ C_2 &= -0.25 \\ C_3 &= -12.0 \\ C_4 &= 2.3 \\ C_5 &= 0.3 \\ C_6 &= 1.8 \end{aligned} \tag{18}$$

Problem 2.6: Developing annular flow

"Developing Annular Flow"

Yoshiharu TOBITA (PNC)

Outline of the Case

The cases analyzed here are the steady-state experiments performed in LOTUS test facility by Hewitt.[1] The experiments concern the pressure drop and average flow rate of air and water in a two-phase system in fully developed pure annular flow and developing annular-dispersed flow.

1. Objectives of the Application

This application is aiming at testing the pressure drop characteristics and the momentum coupling between air and water in annular flow regime both in fully-developed pure annular flow and developing annular-dispersed flow. The former application was intended to check the validity of the momentum coupling between core air flow and liquid film, and the momentum coupling between liquid film and structure. The latter application was performed to check the modeling of droplet entrainment and momentum exchange between vapor and liquid which consists of entrained droplets and liquid film on the structure surface.

2. Description of the Problem

2-1) Fully developed annular flow

Experimental data to simulate were obtained from points in Fig. 1 (Fig. 11.17b of the well-known Wallis' text book[2]). Unfortunately, detailed descriptions of the experiments were not given in the book, so we were forced to read values of data points from the graph. Detailed information on the experiments can be found in Ref. 1).

From the points in the Fig. 1, we read numerical values of dimensionless gas and liquid volumetric flux rates J_g^* and J_f^*, dimensionless pressure drop ΔP^* and inner diameter of tube for each point in the figure. Here the parameters are non-dimensionalized as follows.

$$J_g^* = J_g \rho_g{}^{1/2} \left[gD\left(\rho_f - \rho_g\right) \right]^{1/2} \tag{1}$$

$$J_f^* = J_f \rho_f{}^{1/2} \left[gD\left(\rho_f - \rho_g\right) \right]^{1/2} \tag{2}$$

$$\Delta P^* = \left(\frac{dP}{dz} - \rho_g g \right) / g\left(\rho_f - \rho_g\right) \tag{3}$$

Once we have J_g^* and J_f^*, we can calculate the void fraction α for the corresponding system using the following correlation.

$$\frac{J_g^*}{1-2.85(1-\alpha)} - \frac{J_f^*}{2.85(1-\alpha)} = 0.775 \quad (4)$$

This correlation, presented in Ref. l), is valid for co-current upward annular flows only. Among the data points in the Fig. 1, we take only those data with J_g^* and ΔP^* less than 1 and 0.2, respectively, because these points represent annular flows where entrainment fraction is almost zero.

2-2) Developing annular flow

The experiment is that of DOE/EPRI #3 "Developing Annular Flow". The flow tube was made from sections of 31.75 mm bore commercial acrylic resin (Perspex/Plexiglass) pipe which had been straightened and annealed. This flow tube was mounted in clamps and was made vertical and straight to within about 1.5 mm over the tube length (which could be of the order of 7 ~ 8 m including inlet and outlet sections). A vertical calming length of over 2 m was introduced between the air inlet pipe and the water injector to allow the setting up of a relatively swirl-free air stream at the point of injection, with a velocity profile near to that for equilibrium smooth pipe turbulent flow.

A porous wall injector was employed in the experiments. The dimension and configuration of this device is illustrated in Fig. 2. The injector was constructed from acrylic resin and a porous bronze sinter tube. Liquid is introduced evenly around the circumference and its rate is not influenced appreciably by the flow pressure fluctuations. The flow rates were fixed to 0.126 kg/s of water and 0.063 kg/s of air. The mean pressure in the channel was around 170 kPa and the fluids were at temperatures close to ambient which had a mean value of 19 ℃ over the course of the experiments with a standard deviation of 1.8 ℃.

The air input flows were measured using a standard orifice and the water input flows using calibrated rotarneters. The estimated accuracy for the air flow measurement is better than 1% and that for the water flow measurement better than 2%.

The pressure gradient was measured using an inverted water manometer and the estimated accuracy is of the order of 5%. Liquid film thickness was measured using flush conductance probes. The precision of the measurement is probably around 5% while the accuracy might be expected to be 3 – 5% lower than the actual value. Local liquid mass flux, impact pressure velocity are measured using a sampling probe. The accuracy of the liquid flow measured is of the order of 2%. The accuracy of the impact pressure measurement was estimated to be around 0.02%.

The entrained liquid fraction was obtained by integrating the liquid mass flux profile over a central cylinder of 26.67 mm in diameter. The standard deviation of the integral fraction entrained was estimated to be of the order of 3%. For each given distance from the injector, up to 10 separate traverses were made, carried out at various angles. Averaged parameters from these traverses, and average values of film

thickness and pressure gradient at the same distance were taken and the data are given in Table 1. To illustrate the development of respective profiles, the results from three typical traverses were presented in Table 2, giving data for impact pressure, water mass flux and local velocity.

3. Analytical Solution

No analytical solutions are available.

4. Understanding of Phenomena

Many experimental and theoretical studies were done in the past and basic mechanisms involved in these phenomena are understood. However, the pressure drop correlations proposed so far employ integral formulations which give the overall two-phase pressur drop for given flow rates. The microscopic phenomena such as the momentum coupling between vapor core and liquid film, momentum exchange between liquid film and wall are not fully understood for all the flow regimes. Therefore, the reproduction of the complex pressure drop observed in fully developed two-phase flow with single modeling framework still remains as a big challenge for the modelers.[6)]

The rate of droplet entrainment from the liquid film in annular flow is well understood experimentally and theoretically. The pressure drop characteristics in dispersed annular flow are well reproduced by three velocity model which treats the velocity of droplets and liquid film independently. However, this treatment is not possible in SIMMER-III, which assigns same velocity to droplet and liquid of the same material component and hence the development of a remedy to accommodate this problem will require further investigation.

5. SIMMER-III Representation

5.1 Geometry, Initial and Boundary Conditions for a Reference Case

5.1.1 Fully developed annular flow

The simulation can be performed by either one of two ways. The first one is to calculate pressure drop by giving volumetric flux rates for each phase as inputs. The second one is to calculate volumetric flux rates by imposing the given pressure drop as input boundary conditions. Since we could not give velocity boundary condition as input with SIMMER-III version used in this study, we adopted the second way of calculation. The system is one-dimensional in the sense that we neglect all radial distributions of the parameters. The pressure at the bottom and top boundaries are kept constant in such a way that a constant pressure gradient of experimental value was imposed on the system. If the calculation reaches a steady-state solution with this boundary condition, then we compared the void fraction and the flow velocity for each phase with the experimental values. The experimental conditions we have chosen correspond to system where SIMMER-III predicts the entrainment rate to be zero. So the momentum exchange between droplet and gas does not exist, and the only friction mechanism for gas flow is its momentum exchange with

liquid film. Thus by comparing the calculated gas velocity with that of experimental value, we can evaluate the appropriateness of momentum exchange coefficient between liquid film and air.

5.1.2 Developing annular flow

The system to simulate is a pipe of 6 meter long with its diameter of 31.75 mm. The real system has a two-dimensional velocity distribution and the input flow rates of water and air are kept constant at the same time during the experiment. For the numerical calculation, we assume one-dimensional system and neglect radial velocity distribution. Also constant pressure gradient is imposed as boundary condition. This one-dimensional system with its pressure boundary condition only seems to be too simplified compared to that of real experiments. But doing this way we expect to be able to check the modeling qualitatively.

5.2 Code Modifications

None.

5.3 Parametric Cases

5.3.1 Fully developed annular flow

After having performed some preliminary calculations, we found that the present SIMMER-III model is far from satisfaction underestimating the liquid-vapor momentum coupling. The calculation did not even reach a steady-state showing oscillatory behavior. On the other hand, when we multiply the liquid-vapor momentum exchange function by some factor, it was possible to get reasonable steady state condition. This experience led us to the conclusion that the only way of doing this simulation is to find a correlation of multiplication factor to the momentum exchange function. Thus we have tried to find some multiplication factors by trial and error which make the calculation reach reasonable steady-state solution. After gathering data of these multiplication factors for different annular flow conditions, we tried to formulate an empirical correlation of multiplication factor.

6. Results

6.1 Fully developed annular flow

Table 3-A shows numerical values of experimental data used in deriving a functional relationship of multiplication factor. These three data points represent most effectively the available range of experiments in Fig. 1.

Table 3-B shows the simulation results corresponding to the experiments. Here the factor means that we should multiply liquid-vapor momentum coupling by that factor to arrive to any reasonable solution.

As is clear from the data of Table 3-B, we obtain quite correct values of gas velocity v_g and void fraction α if liquid-vapor momentum exchange coefficient could have correct values. The errors against

the experimental values are less than 1% for velocity *v,* and around 2% for void fraction α. Since the void fraction calculated by the correlation in Eq. (4) already has around 3% of error, we can accept the calculated values as reasonable.

Meanwhile the calculated liquid velocity v_f cannot be compared directly with the experimental data. This is because even if the correct momentum quantities are transfered to the liquid film from air flow through the air-water interface, there is another friction mechanism for the liquid film acting between the structure and liquid. The model of SIMMER-III for this structure-liquid interaction is based on Reynolds number and contact area, but the apparent inability of the code to reproduce reasonable liquid film velocity implies that this model should be reevaluated. Since our present interests are the interaction between liquid and gas flow, we will not pay much attention to the liquid film flow rate.

Now with the above information, we can try to formulate the functional relations of multiplication factor. From Table 3-A we can see that the difference of dimensionless volumetric flow rates between phases $J_g^* - J_f^*$ shows most regular functional relationship with the multiplication factor. Choosing this as one parameter seems physically reasonable.

The other one parameter we choose is J_g^*. In fact we have other candidates of parameters like α or pressure drop gradient, but some trial and errors show that J_g^* is the best choice. Using parameters $J_g^* - J_f^*$ and J_g^*, we derive the following correlation based on the data of Table 3-B.

$$F_{ac} = \mathrm{A}\left(J_g^* - J_f^*\right)^B {J_g^*}^C \tag{5}$$

where A= 10.136, B = -0.7594, and C = -1.2278.

The validity of the empirical correlation (5) has been tested by applying this correlation to other experimental data points. We have checked with 4 different data points. It must be stressed that these 7 experimental data (3 have been used to derive the correlation (5) and 4 have been used to test it) are uniformly distributed in the area (which contains available data for our purpose) and covers all the typical data in that area.

The results of this checking is shown in Table 4. For example take an example of test #2. We have experimental values of J_g^* and J_f^*, thus we calculate from the correlation (5) that the multiplication factor should be 28.8. So we multiply the liquid-vapor momentum exchange function by 28.8 and run the code. This calculation gives us a gas velocity of 10.3 and void fraction of 0.864 which compares well with the corresponding experimental values. All the 4 test results show that the errors are within 10%.

6.2 Developing annular flow

As we can expect from the results in the previous fully developed annular flow analysis, we need the liquid-vapor momentum exchange function multiplied by some factor which will make the solution reasonable. Also in the case of fully developed annular flow, the equilibrium entrainment volume fraction

is around 0.5. These facts enable us to assume the momentum exchange between droplet and gas will be more dominant than the liquid film-gas interaction. For these reasons we will neglect effects of liquid film-gas interaction and concentrate only on the droplet-gas interaction. This means that we put to zero the gas-liquid film momentum exchange and multiply the droplet-gas momentum exchange function by some factor in the calculation. By repeating many similar simulations we found that to arrive to a solution we should multiply the droplet-gas momentum exchange function by 8.0×10^{-4}. The structure-liquid interaction term is also multiplied by 4. Multiplying with these factors, we have tried to match the gas and liquid flow rates with the experimental values.

To do more realistic simulation, it is necessary to provide constant gas and liquid flow rates as input condition. But this being impossible in SIMMER-III version l.B, we should be very careful in interpreting the simulation results. The fraction of entrained liquid in Fig. 3 shows that until the pipe length 2 ~ 3 m, the discrepancy between the measured and simulation values are very large. This gap can be easily attributed to the fact the present liquid entrainment models do not take into account the entrance effect. Actually this entrance effect is very prominent in two-phase flow and a rough calculation shows that the entrance length is about 9 m for this system while the system length is 6 m.

Comparison of film thickness shows that the simulation results produce thinner film thickness. Though it cannot be said whether the value itself is satisfactory or not, we can at least understand why this happens. The entrainment rate is a function of gas velocity and in the experimental condition, the gas velocity has a radial distribution, with larger velocity at the center than at the wall side. Thus when we match the measured and calculational mass flow rates of gas during the simulation, we have larger gas velocity than the experiment at the liquid/gas interface. The relative velocity being larger than the experiment, we have larger entrainment fraction and thinner liquid film thickness than the measured value. Thus the results are at least qualitatively correct.

7. Conclusions

We have evaluated the momentum-exchange functions adopted in SIMMER-III code. From this evaluation, we could have the following conclusions.

1. To be able to perform more realistic simulations we should give constant input inflow of gas and liquid as boundary conditions. The boundary condition input algorithms should be ameliorated to be able to allow this kind of input condition.

2. In the present code, the same liquid film velocity is assigned to the liquid droplets. Algorithm should be modified such that the different velocity might be assigned to the liquid drqplets.

3. The proposed empirical correlation of multiplication factor will give reasonable results when applied within the valid range of parameters.

8. Recommendations for Model Improvement

Model improvement on the gas-liquid film, liquid film-structure, and droplets-gas. momentum exchange functions are recommended.

9. References

1) D. B. Spalding et al.: "Problem specification and collated solutions of the two-phase numerical-benchmark experience 1986-7", DOE/EPRI Second International Workshop on Two-Phase Flow Fundamentals, 16-20 March, 1987, Troy, New York.

2) G. B. Wallis: "One-dimensional two-phase flow", McGraw-Hill, N.Y., 1969.

3) Y. Tobita et al.: "Interfacial area modeling for a multiphase, multi-component fluid dynamics code", Int. Cong. on Multiphase Flows, Tsukuba, 1991.

4) M. Ishii and K. Mishima: "Liquid transfer and entrainment correlation for droplet-annular flow", Proc. of 7th Int. Heat Transfers. Conf., Munchen, CONF-82901-7, 1982

5) I. Kataoka and M. Ishii: "EntrainmentRateinannulartwo-phaseflow", ANL/RAS/LWR 82-1, Feb. 1982.

6) G. F. Hewitt and, N. S. Hall-Taylor: "AnnularTwo-PhaseFlow", Pergamon Press, 1970.

Table 1 Typical averaging probe data: Porous wall injection

Typical traversing probe data: Porous wall injection

Run number	39			55			10*		
Distance from top of injector m	0.1524			2.9210			5.3086		
Local static pressure kPa	186.9			170.4			162.0		
Ambient temperature °C	20.0			22.8			25.0		
Pressure gradient kPa/m	6.54			5.03			4.79		
Film thickness mm	0.424			0.312			0.312		
Data from traversing probe at y/D of:	Impact pressure KPa	Water mass flux kg/m²s	Local velocity m/s	Impact pressure kPa	Water mass flux kg/m²s	Local velocity m/s	Impact pressure kPa	Water mass flux kg/m²s	Local velocity m/s
0.082	1.079	61.3	20.3	2.412	85.0	27.0	2.216	76.4	32.1
0.122	1.392	30.7	29.2	3.000	91.4	35.4	3.472	89.2	41.3
0.162	1.755	21.2	35.3	3.707	99.8	42.0	4.795	105	48.6
0.241	2.511	11.9	44.9	4.678	102	50.0	6.845	122	58.4
0.321	3.138	18.7	49.1	5.972	97.8	56.4	8.296	132	64.8
0.401	3.491	5.45	54.8	6.776	97.8	61.4	9.375	138	69.3
0.486	3.609	4.76	55.9	7.247	97.8	63.2	9.904	138	71.9
0.496	3.579	5.11	55.6	7.404	97.8	61.4	9.904	138	71.8
0.560	3.569	5.29	55.5	7.404	98.9	64.3	9.904	140	71.6
0.639	3.422	6.31	54.1	7.110	99.4	63.1	9.463	139	69.6
0.719	3.001	9.38	49.9	5.972	91.4	58.9	8.365	134	64.9
0.799	2.265	15.1	41.8	5.207	81.9	52.5	6.698	123	57.6
0.838	1.883	19.8	36.9	4.227	78.5	49.1	5.766	113	53.6
0.878	1.491	29.0	30.7	3.619	70.1	43.8	4.472	97.6	47.4
0.910	1.255	49.5	24.3	3.109	70.1	39.9	3.305	84.5	40.7
0.926	1.157	86.9	18.2	2.667	76.5	33.7	2.893	77.6	38.3
0.942	1.294	211	11.2	2.265	353	27.1	2.491	76.5	34.8
0.950	1.461	347	8.32	2.069	446	20.9	2.373	85.9	32.1
0.958	1.971	541	7.56	1.991	480	17.5	2.363	118	27.4
0.970	2.334	790	6.46	2.030	503	13.3	2.354	195	19.9
Total integrated air mass flow kg/s (Input flow - 0.0630 kg/s)	0.0528			0.0607			0.0683		
Integrated fraction of total liquid flow in central 26.67 mm diameter cylinder	0.0843			0.420			0.521		

Table 2. Data for average parameters: Air-water annular flow experiments.

Data for average parameters: Air-water annular flow experiments

I : Porous wall injector					
Distance from top of injector section m	Ambient temperature °C	Local static pressure kPa	Pressure gradient kPa/m	Film thickness mm	Liquid flow fraction in central 26.67 mm cylinder
0.1524	19.4	184.7	6.54	0.423	0.094
0.6096	18.3	181.8	6.02	0.361	0.203
1.0668	17.5	180.7	5.65	0.335	0.262
1.5240	15.0	176.4	5.41	0.323	0.319
1.9812	18.9	173.1	5.24	0.319	0.358
2.4638	21.9	172.5	5.10	0.315	0.382
2.9210	21.1	170.8	5.03	0.312	0.415
3.4290	20.5	169.6	5.03	0.312	0.444
3.8354	20.0	166.3	4.99	0.312	0.466
4.3942	20.4	164.9	4.96	0.312	0.480
4.8514	20.9	163.6	4.93	0.312	0.505
5.3086	22.6	161.7	4.79	0.312	0.523

Table 3 Annular flow

A. Experimental Data

	#1	#2	#3
$J_g^* - J_f^*$	0.375	0.487	0.775
J_g^*	0.5	0.5	0.9
$-d_p/dz$ N/m^3	1868	1290	1351
I. D m	0.0254	0.0254	0.0254
V_g m/sec	8.55	8.10	13.96
V_f m/sec	0.35	0.048	0.65
α_G	0.82	0.87	0.9
B. SIMULATION RESULTS			
multiplication factor	50	41	14
V_g m/sec	8.56	8.11	13.9
error	0.11	0.12	0.43
V_f m/sec	0.55	0.5	0.54
α	0.83	0.89	0.89
error %	1.2	2.3	1.1

Table 4. Tests of multiplication factor.

Check #1

	V_g	V_f	α	J_g^*	J_f^*	-dP/dz, N/m^3	I. D inch
Exp.	8.87	0.086	0.87	0.635	0.026	1115.6	3/4
Simul.	8.13	0.32	0.91				
Error %	8.3		4.6			multiplication factor = 25.8	

Check #2

	V_g	V_f	α	J_g^*	J_f^*	-dP/dz, N/m^3	I. D inch
Exp.	10.52	0.44	0.857	0.64	0.125	1515	1
Simul.	10.3	0.544	0.864				
Error %	2		0.8			multiplication factor = 28.8	

Check #3

	V_g	V_f	α	J_g^*	J_f^*	-dP/dz, N/m^3	I. D inch
Exp.	9.0	0.062	0.9	0.57	0.013	1017	1
Simul.	8.5	0.46	0.914				
Error %	5.6		1.6			multiplication factor = 31.3	

Check #4

	V_g	V_f	α	J_g^*	J_f^*	-dP/dz, N/m^3	I. D inch
Exp.	6.43	0.0685	0.84	0.44	0.026	1483	3/4
Simul.	6.54	0.428	0.87				
Error %	1.7		3.6			multiplication factor = 53.7	

Table 5. Simulation results of developing annular flow.

position	ΔP	P_i kPa	E_R	$\dot{m}_{air}$	$\dot{m}_{liq}$ kg/sec	δ mm
0.5m	4.28	186.68	0.949	0.0565	0.149	0.26
1.5m	4.47	182.34	0.941	0.575	0.149	0.255
2.5m	4.56	177.83	0.507	0.059	0.149	0.24
3.5m	4.65	173.23	0.523	0.061	0.149	0.22
4.5m	4.75	168.53	0.541	0.063	0.149	0.22
5.5m	4.89	163.72	0.561	0.064	0.149	0.22

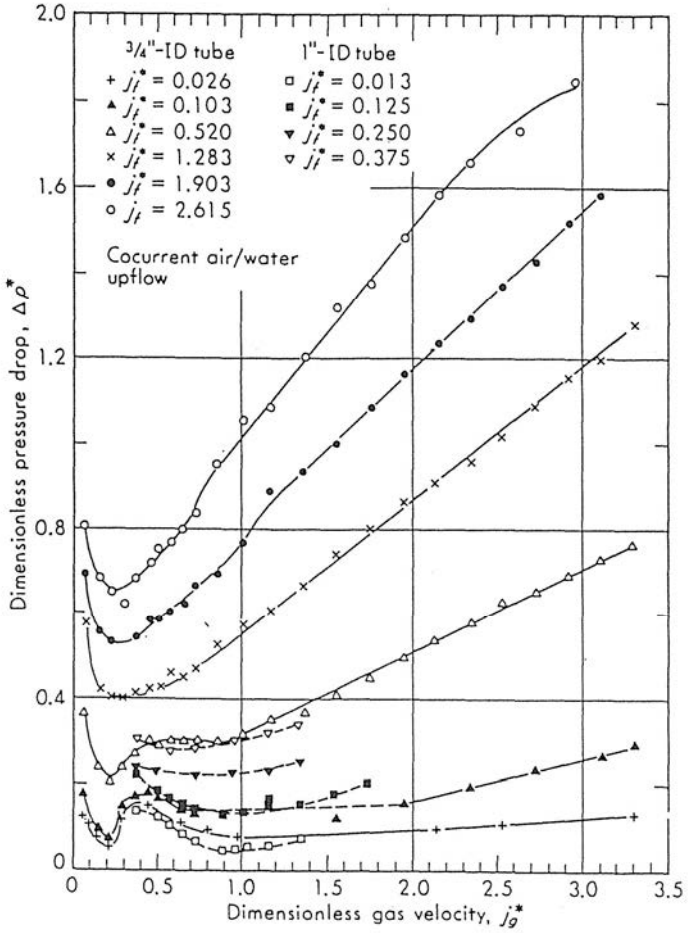

Fig. 1. Pressure drop as a function of air velocity at constant water rates, upward annular flow.

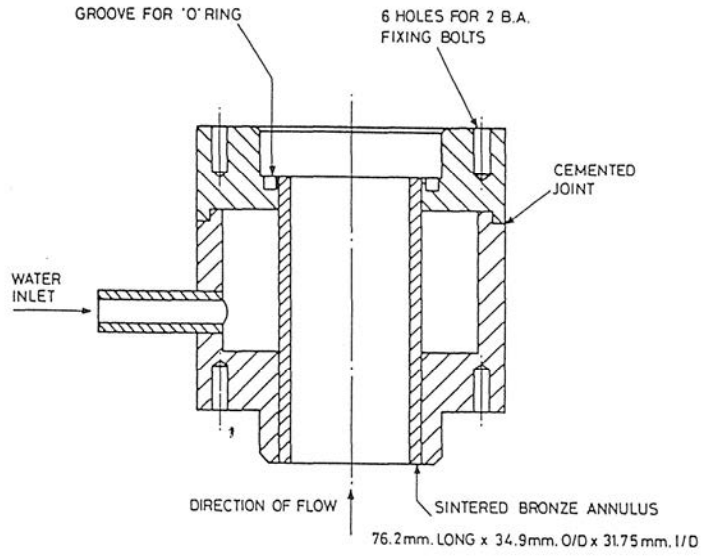

Fig. 2. Porous wall injection device.

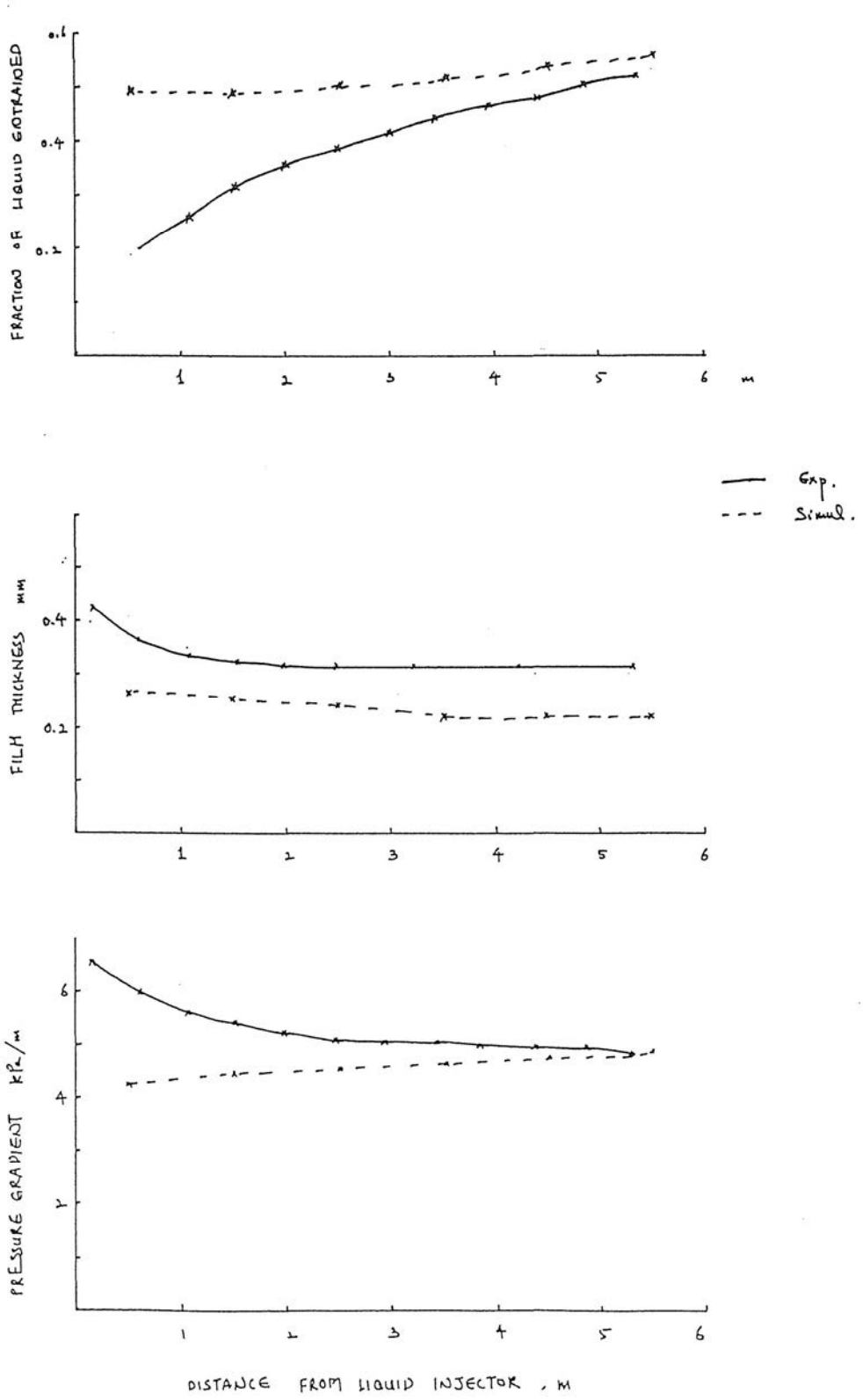

Fig. 3. Comparison of developing annular flow simulation results.

Problem 3.1: Can-wall heat transfer

"Verification of SIMMER-III Can Wall Heat Conduction Calculation"

Kenji Kamiyama (PNC)

Outline of the Case

The can wall treated in the SIMMER-III (S-III) code has two temperature nodes: the surface node and the interior node. The thickness of the can wall surface node is determined by a thermal penetration distance based on an input thermal time constant. Since the heat transfer coefficient of the can wall surface node is determined by thermal penetration distance, heat transfer to the can wall strongly depends on the thermal time constant. Therefore the S-III heat conduction model of the can wall, and the effect of the thermal time constant, are examined by comparing S-III results with results from a generalized heat conduction code, TAC-2D, for well-defined benchmark problems.

1. Objectives of the Application

The present application concentrates on the verification of S-III two-node heat conduction model and the estimation of the thermal time constant by comparing S-III results with TAC-2D calculations for a well-defined geometry.

2. Description of benchmark problems

Two problems were defined. In the first problem a constant heat flux was assigned to the can wall surface in order to verify the heat conduction calculation inside the can-wall. In the second problem a high temperature material was placed on the can wall in order to examine the effect of the thermal time constant on heat transfer to the can wall. The geometry is shown in Fig. 1.

3. Analytical Solution

TAC-2D is a code for calculating steady-state and transient temperatures in two-dimensional problems by the finite difference method, so it should solve the benchmark problems accurately. For the second problem, it is important to get the accurate solution of the temperature decrease of the high temperature material. Therefore, in TAC-2D, 15 temperature nodes were set inside the can wall.

4. Understanding of Phenomena

It is believed that results calculated by TAC-2D can be regarded as accurate solutions.

5. SIMMER-III Representation

5.1 Geometry, Initial and Boundary Conditions for a Reference Case

One mesh cell was used with closed boundary condition. The higher temperature material was represented by the fuel crust. The geometric model and the initial conditions for this calculations are shown in Fig. 1.

Constant EOS and TPP parameters were used so as to eliminate the temperature dependence of properties, and the same thermophysical data and geometry was given to TAC-2D. In the first benchmark problem, an extremely large heat capacity was assigned to the fuel crust, in order to keep its temperature constant.

5.2 Parametric Cases

In each benchmark ploblem, three cases were calculated, using three different values of the thermal time constant of the can wall, TAUST(2). Values of the thermal time constant used, and the thickness of the can wall surface node for each case, are presented in Table 1. In the first benchmark ploblem, three cases should give the same result as the TAC-2D calculation. In the second benchmark ploblem the three cases were set the same way as the first problem but the results should differ.

6. Results

For the first benchmark problem S-III calculations are compared with TAC-2D results in Figs. 2, 3 and 4 for each value of the thermal time constants. The figures show that S-III exactly reproduces evolution of temperature calculated in TAC-2D for each value of the thermal time constant.

For the second benchmark problem the S-III calculations are compared with the accurate solution in Figs. 5 and 6. Figure 5 shows the short time scale temperature history and Fig. 6 the long time scale history. Case 1 is close to the accurate solution for only 10 ms, but after this time, it diverges from the accurate solution. Case 2 is close to the accurate solution for 100 ms before diverging. Case 3 seems the closest result on the long time scale, although it underestimates the short time scale heat transfer.

7. Conclusions

S-III calculates heat conduction inside the can wall correctly. However, the default value of thermal time constant (one millisecond) is rather small and is most appropriate for calculating phenomena which might occur on a time scale of milliseconds or less.

8. Recommendations for Model Improvement

There are no recommendations for model improvement. The thermal time constant should be set by the code user to a value corresponding to the time scale of the phenomenon to be calculated.

9. References

None

Table 1. The thermal time constant and the thickness of the structure in each case.

Case	TAUST(2)	2δ
1	$1.00X10^{-3}$	$0.2477X10^{-3}$
2	$1.00X10^{-2}$	$0.7833X10^{-3}$
3	$5.00X10^{-2}$	$1.7515X10^{-3}$

(Unit : m)

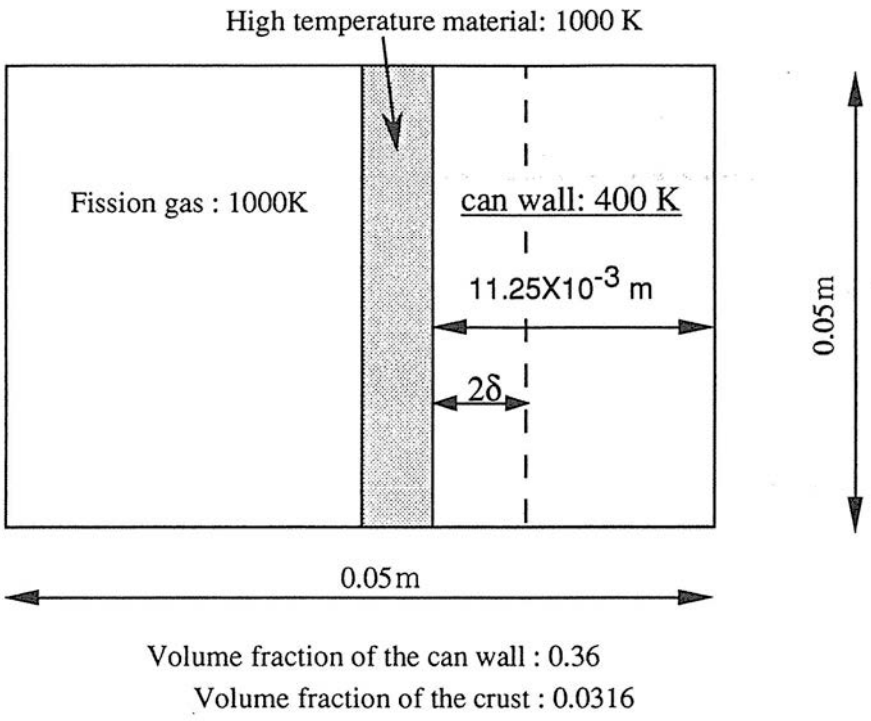

Fig. 1. Geometric model for can wall heat conduction problem.

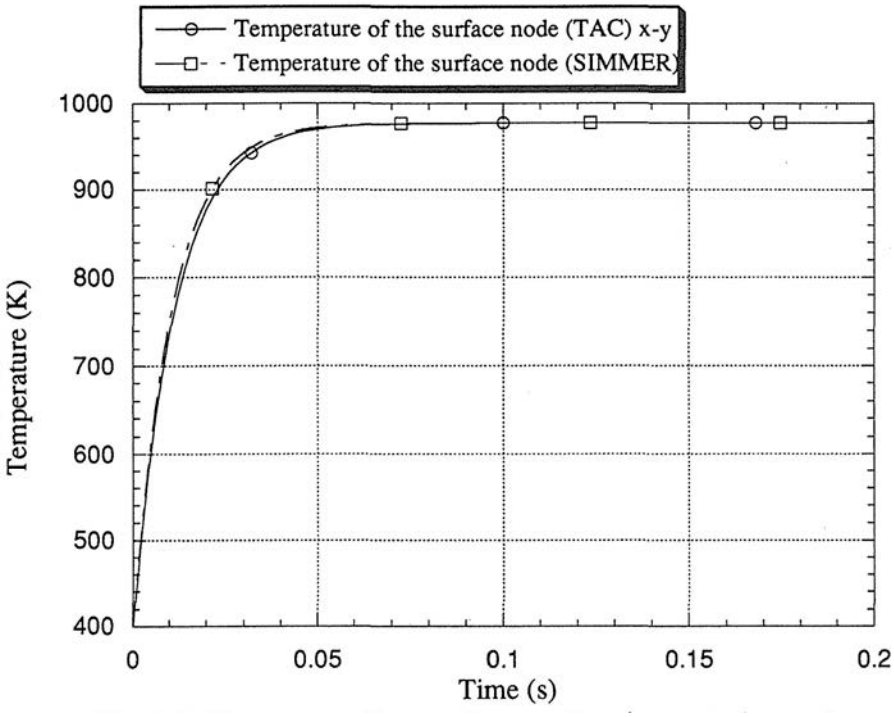

Fig. 2-1. Temperature history of can wall surface node in case 1.

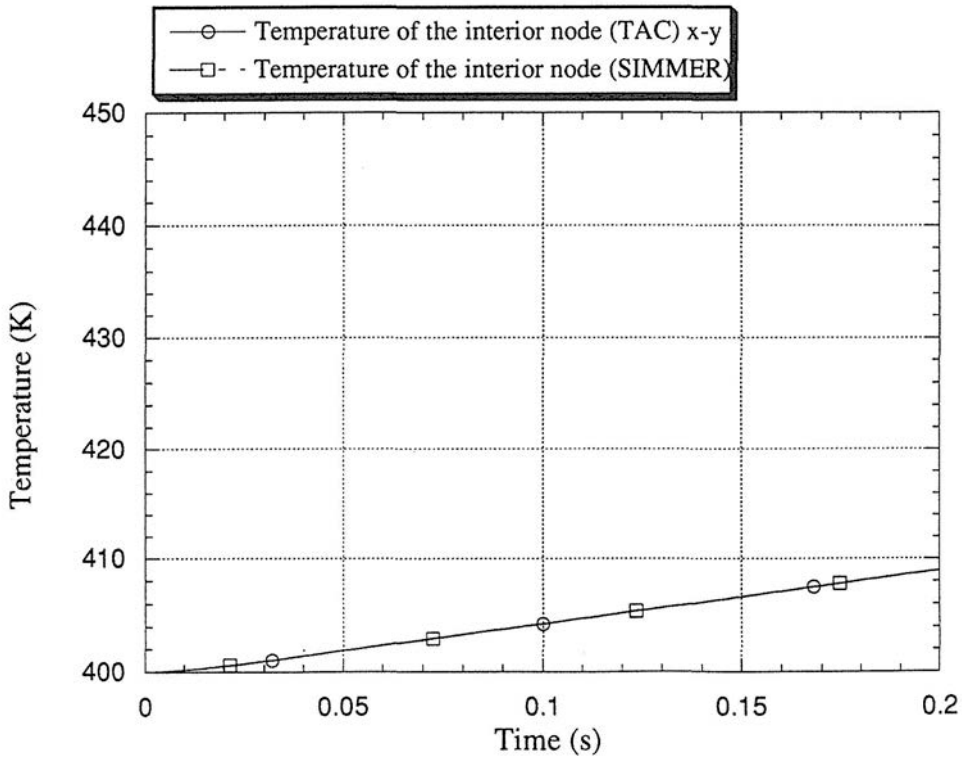

Fig. 2-2. Temperature history of can wall interior node in case 1.

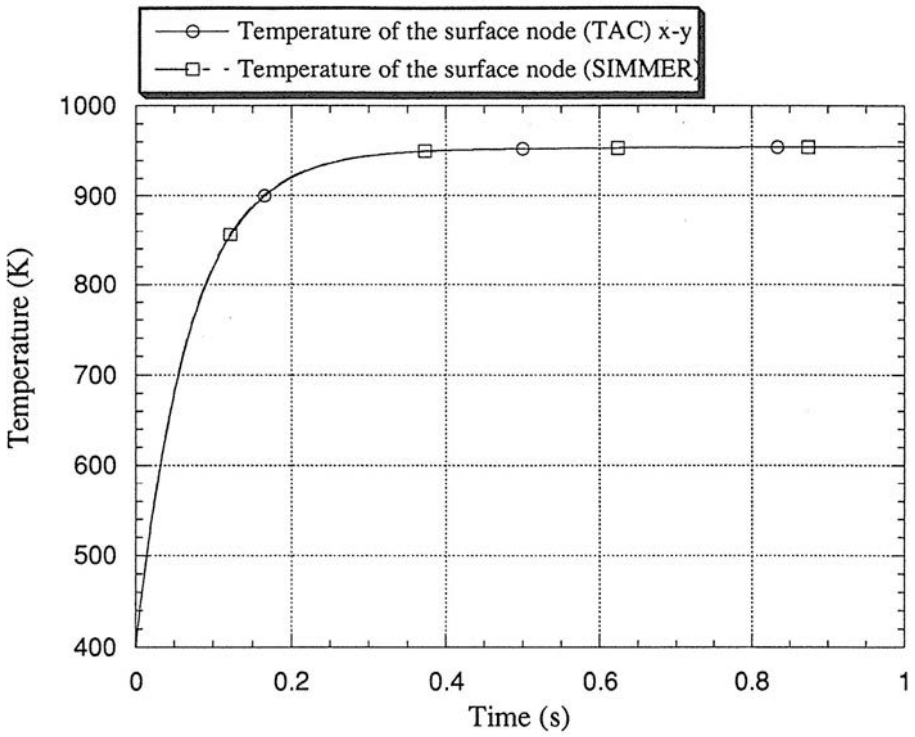

Fig. 3-1. Temperature history of can wall surface node in case 2.

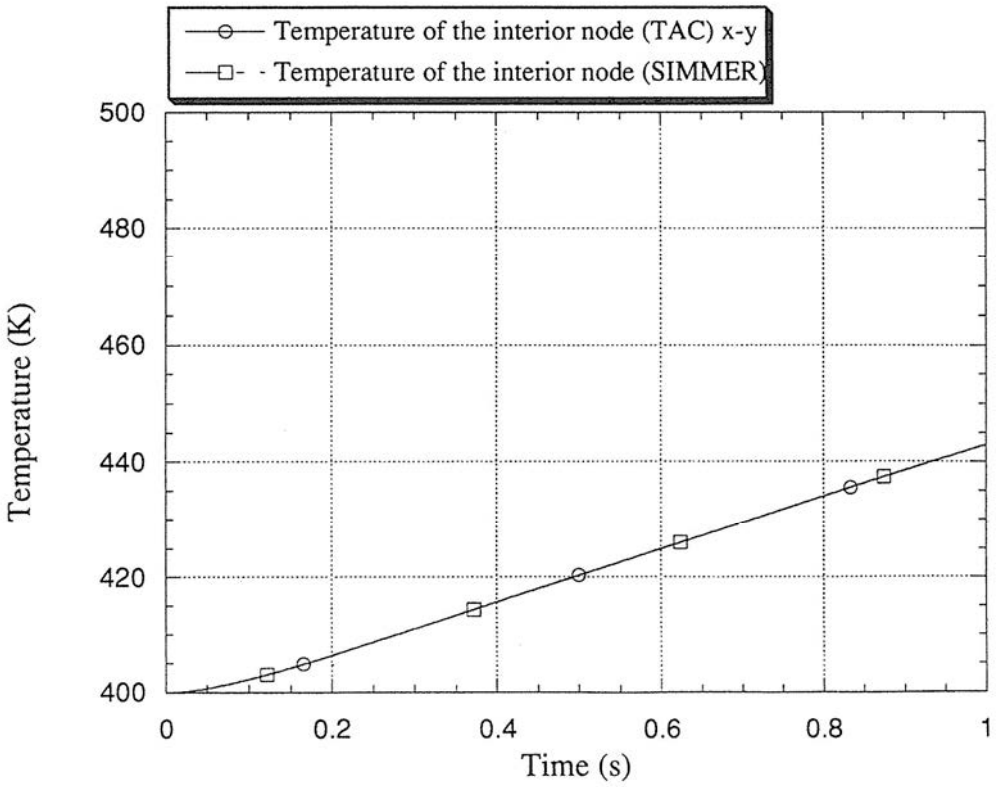

Fig. 3-2. Temperature history of can wall interior node in case 2.

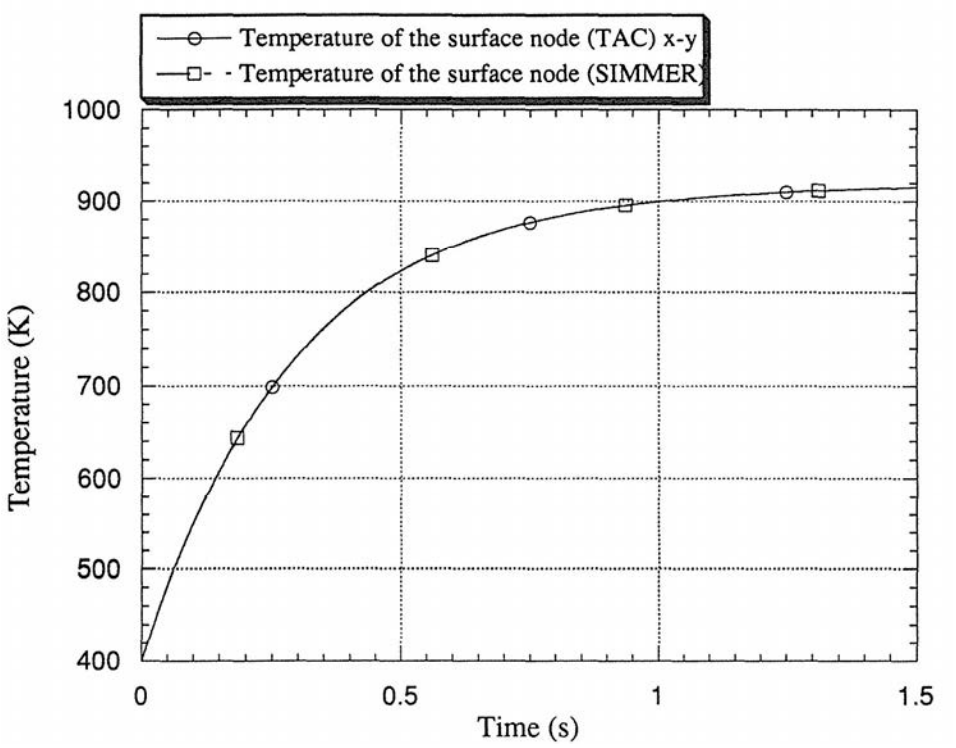

Fig. 4-1. Temperature history of can wall surface node in case 3.

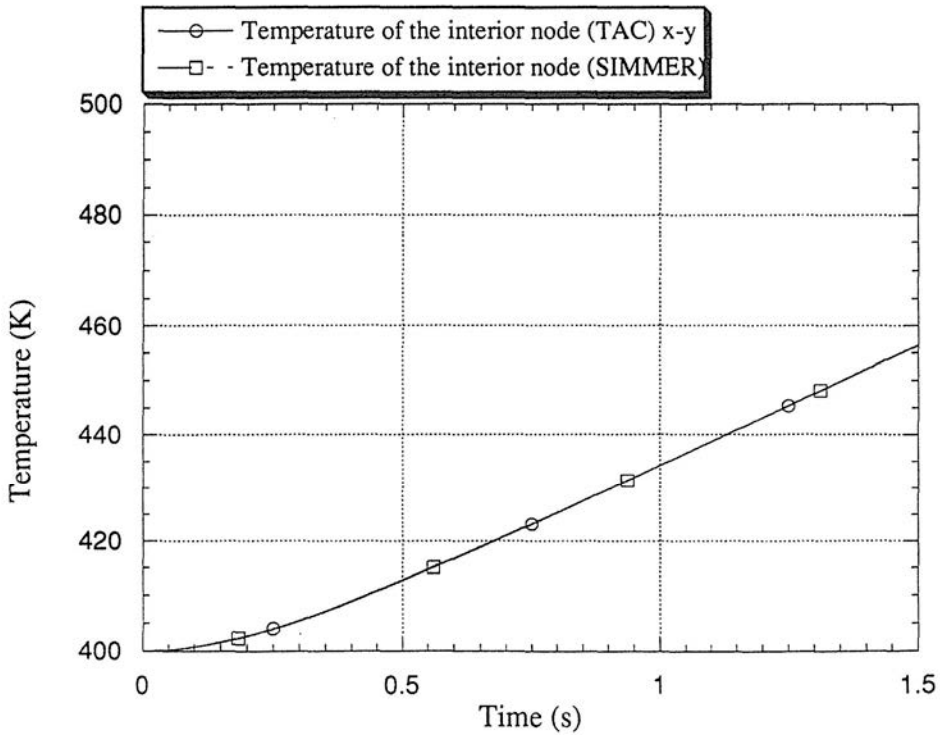

Fig. 4-2. Temperature history of can wall interior node in case 3.

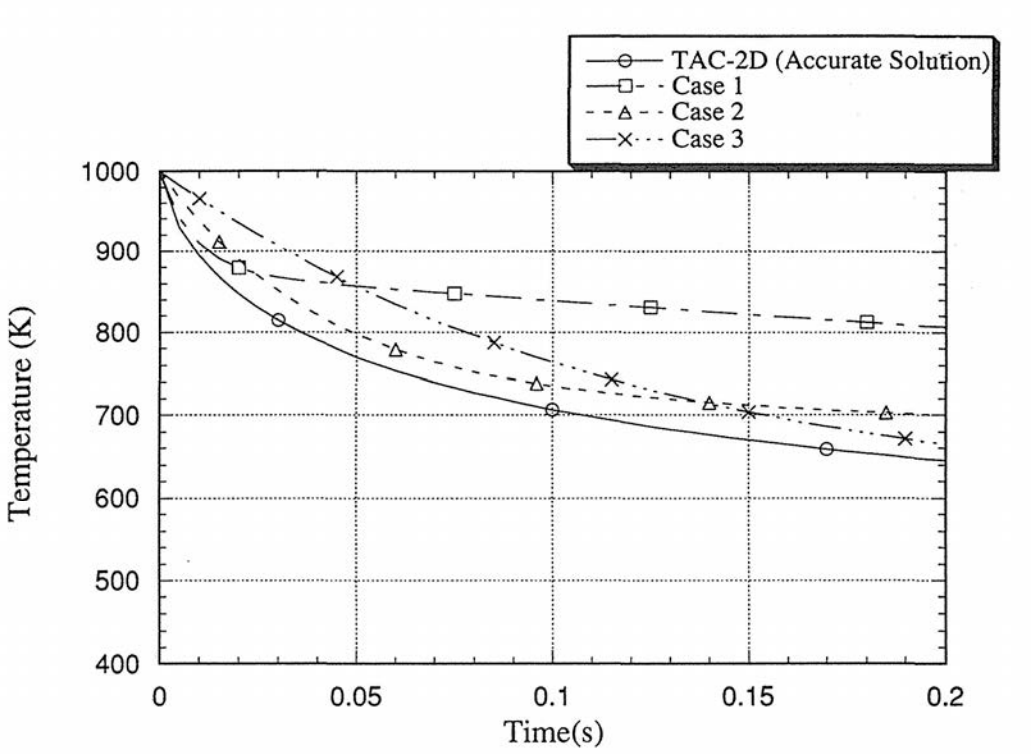

Fig. 5. The temperature history of the high temperature material (until 0.2 s).

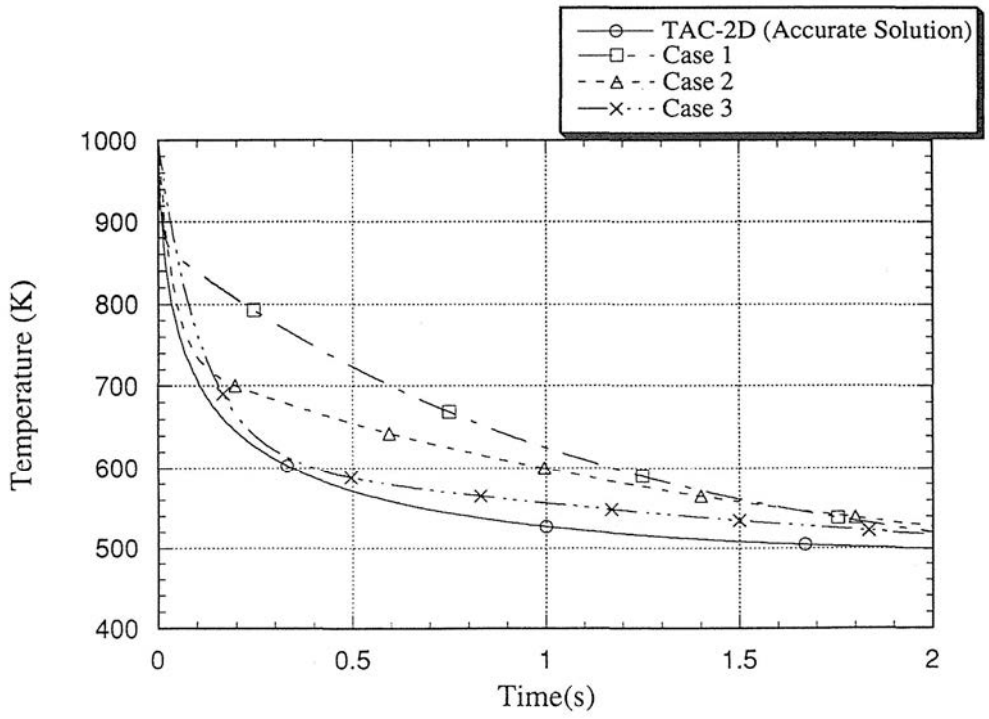

Fig. 6. The temperature history of the high temperature material (until 2.0 s).

Problem 3.2: Structure axial heat transfer

"Structure axial heat transfer"

Yoshiharu TOBITA (PNC)

Outline of the Case

The temperature at the edge of an infinite slab is suddenly raised to 1000 K from the initial temperature of 500 K. The transient temperature distribution calculated by SIMMER-III is compared with the theoretical solution.

1. Objectives of the Application

This application aims to validate the inter-cell heat transfer model in structure component. The inter-cell heat transfer models for liquid and vapor component are programmed in the same manner with the model for structure field, the verification of basic model and programming for overall inter-cell heat transfer model can be checked with this application.

2. Description of the Experiment

An infinite slab made of stainless steel with its length of 0.l m is set to the initial uniform temperature of 500 K. The temperature of the edge of this slab is suddenlyy raised to 1000 K and kept constant afterwards. The transient temperature distribution develops from this edge into the slab as time passes.

3. Analytical Solution

The slab length of 0.1 m can be regarded as infinite for the thermal property of steel up to 100 s and an analytical solution exists for the infinite slab. This is well approximated by the following quadratic equation,

$$\frac{T - T_0}{T_s - T_0}\Delta P^* = \left(\frac{\chi}{\sqrt{3\alpha t}}\right) - \frac{1}{4}\left(\frac{\chi}{\sqrt{3\alpha t}}\right)^2$$

where T is the temperature at the location χ, $T_0$is the initial temperature of the slab, T_s is the surface temperature, and α is the temperature diffusivity.

4. Understanding of Phenomena

The phenomena is well understood.

5. SIMMER-III Representation

5.1. Geometry, Initial and Boundary Conditions for a Reference Case

A 0-dimentional system, i.e. one mesh system, was used just to provide a set of experimental condition to SIMMER-III subroutines which calculate interfacial area (IFA) and momentum exchange functions (MXF). For the axial heat transfer tested in this test problem, a new inter-cell heat transfer model has been implemented in SIMMER-III and is later made available after Version 2.

6. Results

The transient of temperature distribution is plotted with the theoretical solution for t = 20 s, 60 s, and 100 s in Fig. 1. The code prediction agrees well with the theory.

7. Conclusions

The structure axial heat transfer model was validated by the comparison with theoretical solution.

8. Recommendations for Model Improvement

None.

9. References

None.

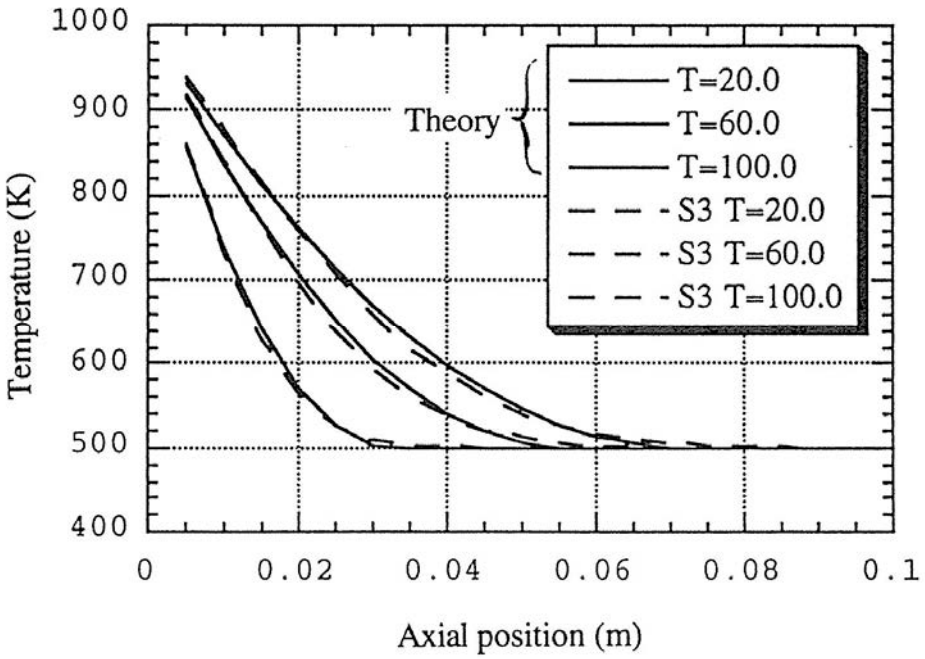

Fig. 1. Transient of temperature distribution.

Problem 3.3: Film boiling in sodium

"Film Boiling on a Metal Sphere in Liquid Sodium"

Dayid Brear (PNC)

Outline of the Case

A hot, stationary tantalum sphere was quenched in a pool of subcooled liquid sodium. The transient surface temperature of the sphere and the boiling heat fluxes, in particular film boiling heat fluxes, were recorded as the sphere cooled. The process was repeated for a further four degrees of sodium subcooling.

1. Objectives of the Application

To validate and calibrate the SIMMER-III film boiling model in a well-defined geometry and under controlled conditions. ·

2. Description of the Experiment

The experimental conditions and the results are described in Refs. 1), 2). A hot tantalum sphere was immersed in liquid sodium at atmospheric pressure. The diameter of the sphere ranged from 1.27 to 2.54 cm, though most results were obtained using a 2.54 cm diameter sphere. The initial temperature of the sphere ranged from 1800 K to 2630 K. The main experimental parameter was the sodium subcooling, which varied between 6.4 K and 31.4 K in the experimental Runs in which film boiling was observed (the sodium saturation pressure at atmospheric pressure is 1155 K).

For each experimental Run the transient surface temperature of the sphere was recorded as the sphere cooled down. The transient heat fluxes were estimated by solving the heat conduction equation in the sphere, which enabled boiling curves to be constructed. The minimum film boiling. temperature and minimum heat flux were then deduced from the boiling curve obtained in each Run.

3. Analytical Solution

There are no analytical solutions for the problem, although the authors of Refs. 1), 2) developed an empirical correlation based on the experimental results.

4. Understanding of Phenomena

These experiments seem to be the only measurement of film boiling around spheres in liquid sodium. Nevertheless the boiling curves obtained during different experimental Runs under similar initial conditions are consistent, indicating that the results are reproducible. Furthermore the boiling curve, and the parametric dependence of film boiling heat fluxes, are qualitatively similar to results obtained for water. The experimental results seem to be reliable.

5. SIMMER-III Representation

5.1 Geometry, Initial and Boundary Conditions for a Reference Case

A single-cell calculation was performed. The solid sphere was represented by a single droplet of liquid energy component 1, since film boiling is calculated in SIMMER-III only for liquid-liquid contact. The sodium was represented, as usual, by liquid energy component 3.

The EOS properties of liquid energy component 1 were specified so as to avoid freezing or vaporization of liquid 1 during the transient. Liquid 1 was also assigned a high thermal conductivity to ensure that the "sphere" wall temperature could be equated to the bulk temperature of liquid 1. The liquid sodium coolant was assigned default EOS properties.

5.2 Code Modifications

An ad-hoc correction was introduced into subroutine STEP1 to collect all of liquid energy component 1 in the cell into a single droplet (to represent the sphere).

5.3 Parametric Cases

For each sodium subcooling a parametric calculation was performed as well as a.base case calculation. The base case calculations used default input parameters. The parametric cases differ from the base case calculations by:

(a) using alternative input data: CMFB (which determines the saturated minimum film boiling temperature) was changed from 0.55 to 0.5 and FILMIN (which determines the dependence of minimum film boiling temperature on subcooling) was changed from 1.4×10^{-4} to 4×10^{-5}, and

(b) a coding modification: the liquid-side heat transfer Nusselt number was multiplied by a factor of 2.

The reason for making the parametric calculations is discussed in Section 6.

6. Results

The calculated and measured heat transfer coefficients during film boiling are shown in Figs. 1 (a) to 1 (e) for five degrees of sodium subcooling. The base case calculation generally underestimates the measured HTCs, and the discrepancy increases with subcooling. The parametric calculations are in better agreement with the experimental results because heat transfer in the subcooled liquid is enhanced by a factor of 2.

The calculated and measured minimum film boiling temperatures are plotted in Fig. 1 (f) as a function of sodium subcooling. The base case calculation tends to overestimate the minimum film boiling temperature at all subcoolings. The results of the parametric calculations are in better agreement with the data due to the modifications to the input data described in Section 5.3. Note that the measured dependence

of the minimum film boiling temperature on sodium subcooling is very uncertain due to the scatter in the experimental data. However it is notable that film boiling was not observed for spheres immersed in sodium with subcoolings of 42 K and higher.

A representative experimental boiling curve is shown in Fig. 2. The heat fluxes in the film boiling regime, and around the minimum film boiling temperature, are reproduced by SIMMER-III fairly well (though slightly underestimated as noted above). In particular the calculated film boiling heat fluxes are an order of magnitude less than what would be predicted without a film boiling model. The high heat fluxes in the nucleate boiling regime are not reproduced, but this is not surprising because there is no attempt to simulate nucleate boiling for the liquid droplet-liquid interactions·modellled by SIMMER-III.

Note that there is a sharp change in the heat fluxes calculated by SIMMER-III in Fig. 2. This is a minor error in the interpolation procedure between film boiling heat fluxes and heat fluxes calculated as if no boiling is occurring.

7. Conclusions

The SIMMER-III film boiling model successfully reduces heat transfer coefficients in the film boiling regime for liquid sodium. The film boiling model calculates significantly more accurate heat fluxes in the film boiling regime, and around the minimum film boiling temperature, than if heat transfer were to be calculated without taking account of vaporization.

This application suggests that input variables CMFB and FILMIN should be modified slightly for sodium, as described in Section 5.3. The heat transfer coefficient in subcooled coolant may also be larger than is currently modelled, and alternative correlations to determine this HTC should be investigated.

This application also highlights the uncertainty in modelling heat transfer in the nucleate boiling regime.

8. Recommendations for Model Improvement

There are no firm recommendations for model improvement. However the suitability of the heat transfer correlation used to calculate heat transfer in the subcooled liquid and methods of treating the nucleate boiling regime should be investigated.

9. References

1) M. M. K. Farahat, D. T. Eggen and D. R. Armstrong: "Pool boiling in subcooled sodium at atmospheric pressure", Nucl. Sci. Eng. 53, p. 240-254, 1974.

2) M. M. K. Farahat: "Transient boiling heat transfer from spheres to sodium", ANL-7909, January 1972.
.

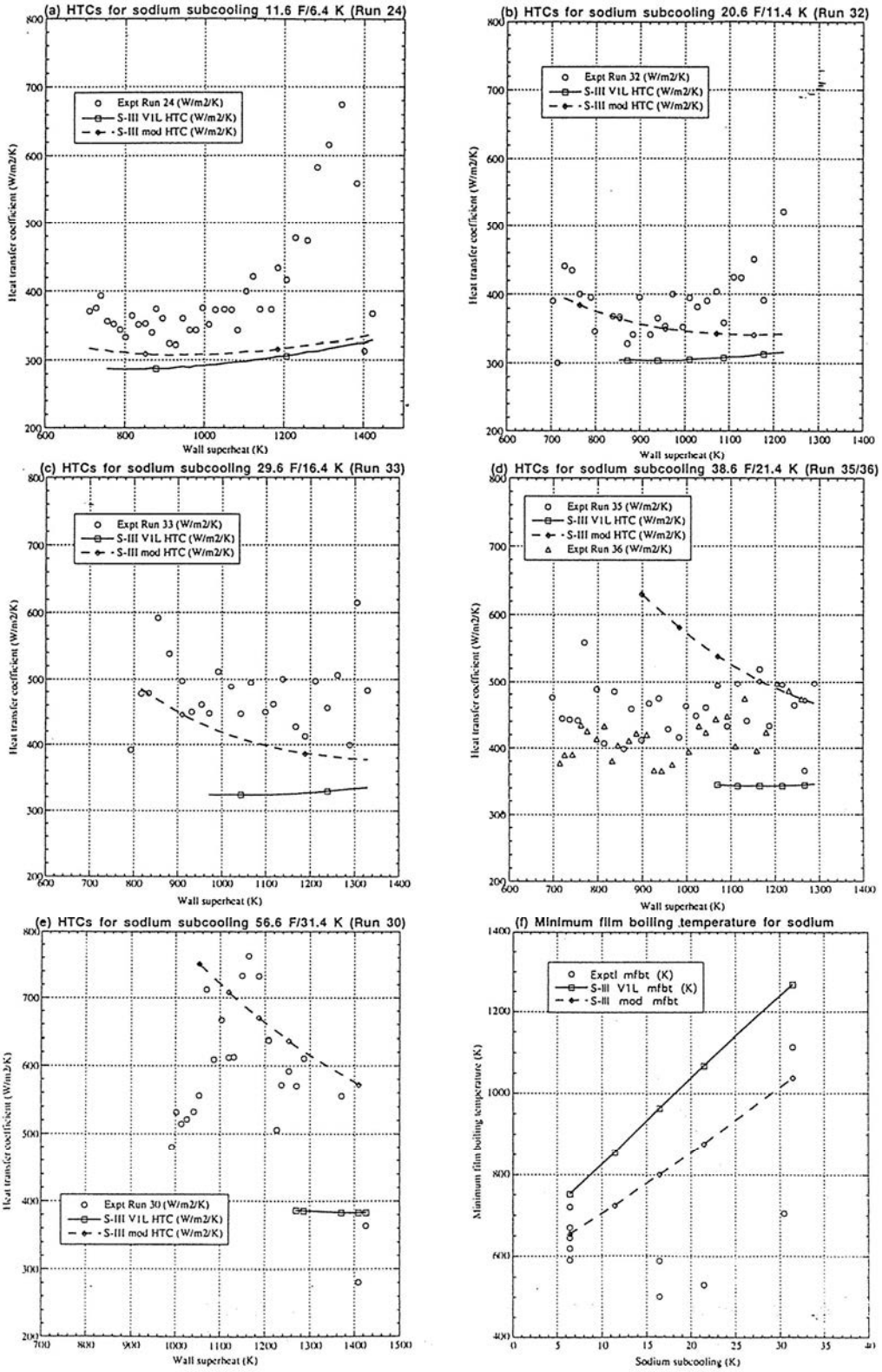

Fig. 1. Measured and calculated film boiling heat fluxes and minimum film boiling temperature.

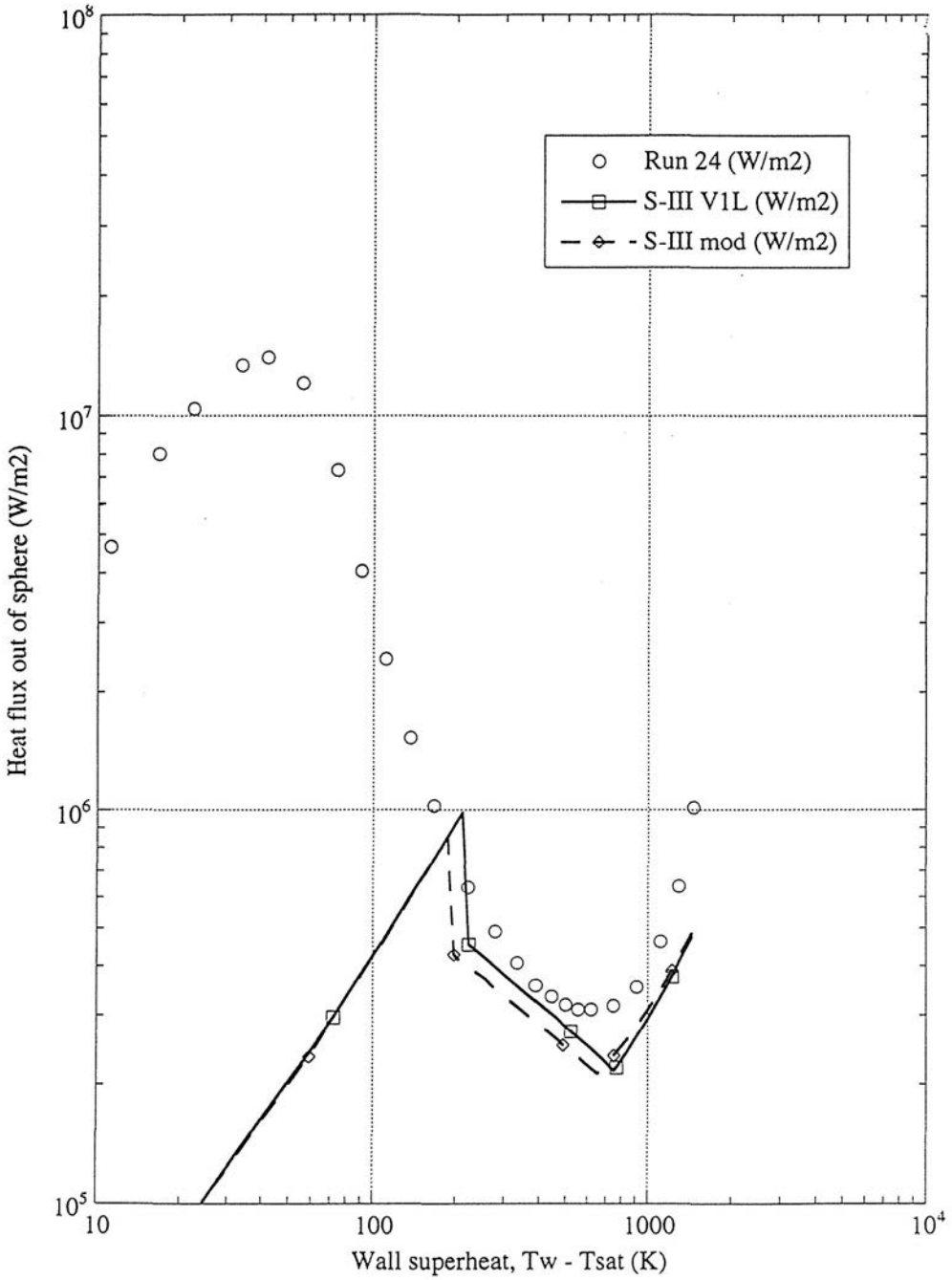

Fig. 2. Measured and calculated boiling curve for the sphere quenched in sodium subcooled by 6.4 K.

Problem 4.1: Fuel freezing: GEYSER experiments

"The Freezing of Molten Fuel in a Small Diameter Tube: Geyser Calculations"

Pierre Coste (CEA-G)

Outline of the Case

Molten UO_2 at approximately 3000°C is injected into a cold, stainless steel, 4 mm inner diameter tube. The purpose is to study the freezing, looking especially at the penetration time and length. The initial inlet velocity ranges from 1.8 to 4.1 m/s and the pressure gradients from 3×10^5 to 19×10^5 Pa.

1. Objectives of the Application

This application concentrates on a verification of the S-III melting and freezing model. It includes the description of the fuel crust growth; the can wall melting; the temperature of the liquid fuel/can wall interface; the fuel particles formation; the blockage of the flow due to the particles via the particle jamming model and the Ishi's drag coefficient.

2. Description of the Experiment

It consists in injecting molten UO_2 at approximately 3000°C in 4 mm (resp. 8 mm) inner (resp. outer) diameter stainless steel tubes.[1] The molten material transfer is initiated by the tube going down and the pressure increase in the containment. The pressure difference between the containment and the tube induces an ascending flow of the molten fuel. There was no steel melting in these tests. The flow front position is followed by the instrumentation. The penetration time *tp* and the penetration length *Lp* are reported in Table 1.

3. Analytical Solution

Some solutions can be found in the litterature in the case of crust freezing (conduction problem). In the case of bulk freezing which is what happens in all Geyser tests except G12 and G15, there is a simple relationship between the average HTC and the penetration length.[2] The HTC was evaluated with an interface resistance model expression which was obtained semi-empirically for relocation of molten UO_2 into stainless tubes for LMFBR Safety Studies.[2]

4. Understanding of Phenomena

Analysis of molten UO_2 freezing experiments was performed and it was shown that HTC between UO_2 and structures is about one order of magnitude lower than the one that can be calculated with usual turbulent forced convection correlation. This reduction was attributed to the presence of an interfacial resistance between the melt and the mold. An evaluation of this resistance was proposed.[2] But the physics

involved in these phenomena is rather complicated and there are large uncertainties. A key one is the shift between bulk and crust freezing which is governed by a competition between nucleation and turbulence phenomena.

5. SIMMER-III Representation

5.1 Geometry, Initial and Boundary Conditions for a Reference Case

A 1-D mesh was used. Pure UO_2 material is used.

The first mesh (region1) at the bottom of the tube is for molten UO_2 at the initial state. All the other meshes (region2) is full of fission gas at the initial state. The meshes size is growing going from the inlet to the outlet.

A pressure boundary condition was imposed at the top of the tube. At the bottom, the pressure and other parameters except the velocity are kept equal to their initial value. A head loss coefficient was tuned at the inlet of the tube in order to get the initial inlet velocity of the experiment at the early beginning of the transient.

5.2 Code Modifications

None.

5.3 Parametric Cases

The following parameters effects were investigated: mesh size, UO_2 liquid thermal conductivity, maximum packing fraction, heat transfer coefficients on liquid side and structure side, initial velocity, curvature effect on the structure HTC, minimum film thickness, use of the V/C, wall thermal time constant TAUST, maximum droplets and particles radii, interface temperature between liquid UO_2 and can wall. Only the most important parameters (when uncertainty/effect is high) are discussed hereafter. An interface resistance model has been implemented in several ways and tested.

6. Results

6.1 Standard S-III

S-III clearly overestimates the HTC: it finds a too low penetration length, by one order of magnitude (Table 2). Neither velocity nor pressure effects are well predicted. S-III finds bulk freezing in all the cases. Bulk freezing at the front controls the ultimate length of penetration in both S-III and tests (G4, 7, 9, 11). S-III has the very interesting ability to simulate the competition between these 2 phenomena, because it calculates at the same time:

- the crust growth by the non-equilibrium balance at the liquid fuel/can wall interface.

- the fuel particles forming from the equilibrium freezing of the liquid fuel.

But this choice is not reliable in all the situations which maybe encountered by the code, because it is too sensitive on following ill-known parameters.

6.2 Sensitive parameters

An input parameter TAUST is the time constant which gives the structure HTC by conduction. S-III default value of 10^{-3} s was chosen, but one could also take 10^{-2} s: the uncertainty reaches a factor 10. Unfortunately the consequence on the calculations can be very high when the change in structure HTC results in a different kind of freezing. When S-III chooses crust freezing the penetration length is indeed one order of magnitude higher than bulk freezing.

UO_2 liquid thermal conductivity is obviously an important parameter. The uncertainty is at least of a factor 2. Furthermore the effect can be important for a similar reason as TAUST, but in this case because of the change of HTC on liquid side.

Interface temperature between UO_2 and wall is very difficult to evaluate, especially when there is no crust and when steel melts. It is directly linked with the lack of bulk/conduction freezing map.

6.3 Interface resistance model

Generalities

The need of an interface resistance model in S-Ill in the case of bulk freezing is clear and is consistent with previous studies.[2] The first questions are: should one implement it on structure side HTC or liquid side HTC or both? What is the interface temperature? What about cases with steel melting or thin crust? Several models with the change of the HTCs and the interface temperature have been tested, giving reasonnable results. But then the second questions come: does the modifications can deteriorate the results in other configurations? Are they simple enough for a general implementation in the code? Waiting for something better, a compromise is proposed and the corresponding results are reported in Table 2.

Description

The idea is to introduce the only bulk freezing model available for LMFBR studies and to change nothing to S-III in cases where the model was not assessed, for example when steel melts. When an interface resistance is assumed, 2 interface temperatures can be calculated: $T_{I,Ki}$ on structure side and $T_{I,L1}$ on liquid side from:

$$h_{L1}(T_{L1} - T_{I,L1}) = h_I(T_{I,L1} - T_{I,Ki}) = h_{Ki}(T_{I,Ki} - T_{Ki})$$

When $T_{I,Ki}$ is higher than the steel solidus temperature the structure is expected to melt. When $T_{I,L1}$ is lower than the UO_2 nucleation temperature, liquid UO_2 is expected to freeze to crust In these 2 cases, standard SIII is used. The UO_2 nucleation temperature is estimated around 2700 K.[3]

In other cases, the interface resistance of Ref. 2) is added on liquid side. so that the total HTC between the wall *Ki* and the liquid fuel *L*l is:

$$h_{IGB} = 400\frac{2k_{L1}k_{Ki}}{k_{L1}+k_{Ki}}V_{L1}$$

where k is the thermal conpuctivity and V the velocity (m/s).

If the interface resistance is added, the interface temperature liquid fuel/can wall is calculated in crder to have neither steel melting nor crust freezing, i.e. only UO_2 particles formation:

$$T^{I}_{L1,Ki} = V_{L1}T_{Ki}$$

Results

The improvement is clear. For G9, *Lp* is still too low, because the model switches to standard S-III too quickly.

7. Conclusions

Geyser experiments which deal with molten UO_2 freezing in small steel diameter tubes were calculated with S-III. They were usefull for S-III qualification because pure UO_2 was used in a simple geometry, with well-known boundary conditions. Nevertheless the involved phenomena are rather complicated and difficult to reproduce, sometimes even qualitatively. Thus standard version of S-III finds one order of magnitude too low penetration lengths. It is consistent with previous analysis which showed the necessity of an interface resistance in the case of bulk freezing. S-III has the very interesting ability to simulate the competition between bulk and conduction freezing, but its choice is not reliable in all the cases, reflecting a lack of knowledge in this area.

8. Recommendations for Model Improvement

A bulk freezing model available for LMFBR studies is proposed. It has been successfully implemented and used to calculate the Geyser tests. It brings the minimum change to S-III, trying to keep to cases where the model was assessed, in order to not deteriorate the calculations in other configurations. The Winfith SMPR calculations reported in Problem 4.2 confirmed the Geyser results.

9. References

1) G. Berthoud, B. Duret: "The Freezing of Molten Fuel: Reflections and New Results", NURETH-4 Conference, Karlsruhe, October 10-13, 1989.

2) G. Berthoud: "The Freezing of Molten Fuel: Determination of Interface Resistance", IAEA Specialists Meeting, Oarai, Japan, June 1994.

3) A.W. Cronenberg, R.L. Coats: "Solidification Phenomena for UO_2, UC and UN Relative to Quenching in Sodium Coolant", Nucl. Eng. Design 36,261 (1976).

Table 1. Geyser experimental conditions.

test	wall temperature (°C)	ΔP (10^5Pa)	Lp (cm)	tp (msec)	$V_{initial}$ (m/s)
G4	20	3	55 (bulk)	170	3.2
G7	1000 on 30 cm	3	75 (bulk)	180	4.1
G9	20	3	45 (bulk)	320	1.8
G11	20	8	70 (bulk)	430	1.9
G12	20	19	100 (crust)	700	3.0
G15	20	8	70 (crust)	310	3.3

Table 2. S-III results versus Geyser experiments.

	Lp(cm) essai	Lp(cm)	SIII
		standard	+ interface resistance
G4	55	6	50
G7	75	6	55
G9	45	5	9
G11	70	step4 failure	40
G12	100	4	62
G15	70	4	60

Problem 4.2: Fuel freezing: SMPR experiments

"The Freezing of Molten Fuel in Small DiameterTubes: Winfrith SMPR Calculations"

Pierre Coste (CEA-G)

Outline of the Case

Molten therrnite (UO_2+Mo) at 3600 K is injected into cold, stainless steel, 3.3 and 4.9 mm inner diameter tubes. The purpose is to study the freezing, looking especially at the penetration time and length. The initial inlet velocity ranges from 0.94 to 3.3 m/s and the pressure gradient from 0.06×10^5 to 0.18×10^5 Pa.

1. Objectives of the Application

This application concentrates on a verification of the S-III melting and freezing model. It includes the description of the fuel crust growth; the temperature of the liquid fuel/can wall interface; the fuel particles formation.

2. Description of the Experiment

It consists in injecting molten thermite at 3600K in 3.3 mm and 4.9 mm inner diameter steel tubes.[1] The thermite is a mixture of UO_2 and 19% of weight of molybdenum. The penetration time *tp* and the penetration length *Lp* are reported in Table 1. The typical test scenario is the following. UO_2 is freezing to crust. Then the flow front thermal conductivity is increased by a higher Mo proportion, inducing particles formation and at the end blockage of the flow by bulk freezing.

3. Analytical Solution

Some solutions can be found in the litterature in the case of crust freezing which is a conduction problem. For bulk freezing, it is possible to have a simple relationship between the average HTC and the penetration length.[2] The HTC was evaluated with an interface resistance model which was obtained semi-empirically for relocation of molten UO_2 into stainless tubes for LMFBR Safety Studies.[2]

4. Understanding of Phenomena

The physics involved in the molten UO_2 freezing phenomena as it was investigated by Geyser experiments is already rather complicated and there are large uncertainties. In Winfrith SMPR one difficulty is added due to the use of the thermite, which is a mixture of 2 materials, with quite different properties. The liquid Mo EOS and TPP are not well established. So in comparison with Geyser it brings uncertainties and leads to quite more complex calculations and interpretation.

5. SIMMER-III Representation

5.1 Geometry, Initial and Boundary Conditions for a Reference Case

A 1-D mesh was used. UO_2 is used as material 1. Mo is introduced as material 2, but the can walls remain made of steel. All the Mo EOS and TPP properties were introduced. The first mesh (region1) at the bottom of the tube is for molten thermite at the initial state. All the other meshes (region 2) are full of fission gas at the initial state.

The meshes size is growing going from the inlet to the outlet. A pressure boundary condition was imposed at the top of the tube. At the bottom, the pressure and other parameters except the velocity are kept equal to their initial value. A head loss coefficient was tuned at the inlet of the tube in order to get the initial inlet velocity of the experiment at the early beginning of the transient.

5.2 Code Modifications

Code modifications were necessary in order to have Mo in *L*2 (metal liquid), Mo in *L*5 (metal particles), and steel in the can walls. With these materials *L*2 freezing to the can walls or can walls melting to *L*2 must be set to zero to avoid inconsistencies coming from Mo turning to steel and vice-versa. These assumptions were verified in the experiment because the can walls did not melt and the Mo did not form a crust.

5.3 Parametric Cases

The following parameters effects were investigated: use of 1 liquid field for the mixture, use of Mo, use of the V/C, wall thermal time constant TAUST, interface temperature between liquid UO_2 and can wall. An interface resistance model was implemented in several ways and tested.

6. Results

6.1 Standard S-III

The first calculations performed was with he thermite modeled by pure UO_2 with an increased liquid thermal conductivity: 10 $Wm^{-1}K^{-1}$, to take into account the main Mo effect (called "S-III stand.l", see Table 2). "S-III stand.1" found bulk freezing in all the cases. It clearly overestimated the HTC, finding a too low penetration length *Lp*.

Then another version was used: "S-III stand.2" (see Table 2). The thermite is modeled with 2 liquid fields; some modifications are included in order to have Mo in *L*2 (metal liquid), Mo in *L*5 (metal particles), and steel in the can walls. Neither velocity nor pressure effects are predicted.

For SMPR02-dl and -d2, SMPR05-1 and -2, the results remain similar to the previous ones: the bulk freezing at the front controls the ultimate *Lp* and S-III overestimates the transfer. There is no crust before the blockage.

The calculations of SMPR05-3 and -4 are different, the *Lp* is either too long or correct, because S-III chooses another path: the crust freezing, with enrichment in Mo at the front, as in the experiment

6. 2 Parameters

Time constant for the thermal penetration in the walls, TAUST: the uncertainty reaches a factor 10. It can be very sensitive because it can decide the choice between crust freezing or bulk freezing.

Mo effect: taking Mo into account increases the heat exchange in the calculation, the *Lp* being 2 times shorter. One can notice that to have this effect, V/C must be called, otherwise the exchange between liquid 1 and liquid 2 is not taken into account.

Interface resistance model: An interface resistance model in the case of bulk freezing has been implemented. Its value is taken from Ref. 2) which proposes a bulk freezing model available for LMFBR studies. The interface liquid fuel/can wall temperature is calculated so that the balance between crust growth or particles forming is the same as standard S-III. Notice that the value of the resistance model is the same as the one presented in Ref. 4):

$$h_{IGB} = 400\frac{2k_{L1}k_{Ki}}{k_{L1}+k_{Ki}}V_{L1}$$

but the way to implement it is older. The results are summarized in Table 2, "S-III modified results". The improvement is clear because even when S-III chooses the wrong way partcles/crust the calculated *Lp* remains reasonnable.

7. Conclusions

Winfrith SMPR experiments which deal with therrnite freezing in small steel diameter tubes were calculated with S-III. The therrnite is a mixture of pure UO_2 and molybdenum. It has been modeled either with 1 liquid field or 2. In the second case some modifications in the code were necessary. In the test, the UO_2 freezes to crust while the penetration length is controlled by bulk freezing at the front which is enriched in Mo. The S-III calculations find a too low penetration length when bulk freezing occurs and a reasonnable or too long penetration length when crust freezing occurs. Then an interface resistance only in the case of bulk freezing can improve the results.

8. Recommendations for Model Improvement

A bulk freezing model available for LMFBR studies[2)] has been successfully implemented and used in the case of bulk freezing to calculate the Winfrith SMPR tests. The difficulty is to make the minimum

change in S-III to keep to cases where the model was assessed, in order to not deteriorate the calculations in other configurations. The results obtained with this model on Winfrith SMPR are consistant with the results from Geyser, which is reported in Problem 4.1.

9. References

1) R.B. Tattersall, R.J. Maddison: "Experiments at AEE Winfrith on the Penetration of Molten Fuel into Pin Arrays and Tubes", 13th Meeting of the Liquid Metal Boiling Group, 27th-29th sept 1988.

2) G. Berthoud: "Relocation of Molten Fuel: Determination of the Interfacial Resistance", IAEASpecialists Meeting, Oarai, Japan, June 1994.

Table 1. Winfrith SMPR experimental conditions.

	D tube (mm)	ΔP (MPa)	V (m/s)	essai Lp(cm)
SMPR02-d1	3.3	0.18	3.3	33
SMPR02-d2	4.7	0.18	3.3	52
SMPR05-1	3.3	0.06	3.3	17
SMPR05-2	3.3	0.06	1.7	16
SMPR05-3	3.3	0.06	1.4	18
SMPR05-4	3.3	0.06	0.94	18

Table 2. S-III results.

	essai Lp(cm)	SIII stand.1 Lp(cm)	SIII stand.2 Lp(cm)	SIII modified Lp(cm)
SMPR02-d1	33	8	6	12
SMPR02-d2	52	10	9	20
SMPR05-1	17	6	6	11
SMPR05-2	16	6	7	28
SMPR05-3	18	6	26	26
SMPR05-4	18	6	20	20

S-III stand.l: S-III V1.H, 1 liquid field for the thermite, i.e. the thermite is modeled with pure UO_2 with a modified liquid thennal conductivity: 10 $Wm^{-1}K^{-1}$

S-III stand.2: S-III V1.J, 2 liquid fields for the thermite, i.e. modifications to have Mo in L2 (metal liquid), Mo in L5 (metal particles), and steel in the can walls are included

S-III modified: S-III stand.2 ce model + interface resistance model

Problem 4.3: Freezing of hot melts in tubes: THEFIS

"Penetration and Freezing of Hot Melts Into Vertical Tube Structures"

M. Flad*, W. Maschek, S. Kleinheins (FZK, *GTI)

Outline of the Case

In the framework of the SIMMER-III code assessment the freezing models and pressure losses at area changes are investigated by simulating a THEFIS experiment.[1] In the THEFIS experiments a hot Al_2O_3 thermite melt penetrates into cold tube structures leading to an increasing crust build-up at the tube walls until the cross section is blocked completely. The maximum penetration length, the penetration vs time dependence and the crust formation are compared to the data derived from the experiments.

1. Objectives of the Application

By the simulation of a hot melt penetrating a cold tube structure the heat and mass transfer models should be assessed. The penetration of the melt passing through cold tubes represents an integral test of heat transfer coefficients, melting and freezing models and pressure Joss calculations at changing area cross sections.

2. Description of the Experiment

In the THEFIS experiment series performed at FZK the freezing behaviour of a thermite melt inside cold steel/quartz tubes is investigated. At the beginning of the test the tube holds room temperature and is lowered into a crucible containing Al_2O_3 at 2300 K. Shortly after immersing into the melt a driving pressure is imposed which injects the melt up into the tube. The mass of Al_2O_3 supplied in the crucible exceeds by far the amount of material necessary to fill .the structure. The Al_2O_3 crust build-up at the colder walls gradually reduces the flow area and the flow velocity until the melt comes to a halt. For the test analysed the substrate tube consisted of quartz.

The maximum penetration length and the penetration vs time dependence is recorded. Also a post-experiment analysis of the crust is performed. The results show a deep penetration of the Al_2O_3 melt consistent with a conduction freezing behaviour.[2]

3. Analytical Solution

None.

4. Understanding of Phenomena

The large penetration length of the Al_2O_3 melt is characteristic for a conduction limited freezing behaviour. The crust growth finally leads to a closure of the flow path and a stoppage of the flow. The

maximum crust thickness and closure is reached downstream of the flow entrance when a superheated melt is regarded.

The Al_2O_3 results from a thermite reaction which does not proceed completely. Post-experiment investigations of the crust revealed some impurities originating from the basic material and the crucible. Therefore, the thermophysical properties of the Al_2O_3 melt applied differ somewhat from the values available for pure material. Previous simulations with SIMMER-II showed a distinct influence of the viscosity on the maximum penetration length.[3)]

At the beginning of the test the driving pressure increases due to the opening characteristic of the solenoid valve. After 0.4 sec the final pressure difference is achieved. As no information about the pressure transient characteristic of the valve was available a standard correlation has been applied for the simulation. Analyses with SIMMER-II demonstrated the influence of the initial pressure increase on the penetration velocity.[3)] The same holds for SIMMER-III.

5. SIMMER-ID Representation

The THEFIS test facility consisting of the quartz tube and the feeding reservoir is modelled as a one-dimensional system. One hundred axial cells are provided and split up into 10 cells for the reservoir and 90 cells for the quartz tube (Fig. 1). A high order differencing scheme is used.

For the Al_2O_3 equation-of-state the values from the THINA simulation[4)] with AFDM are applied and transformed to SIMMER-III input data with the SAEOS data converter.

5.1 Geometry, Initial and Boundary Conditions for a Reference Case

According to the experiment a vertical quartz tube with 6 mm inner diameter and 1 mm wall thickness is modeled. The tube length is 1.8 m. The reservoir is attached at the lower inlet of the tube and consists of a bottomless tank with 8 mm diameter and 0.2 m height. At the beginning of the simulation the tube structure holds 3 00 K. At the upper end of the tube a pressure of 0.1 MP a is imposed.

The reservoir contains Al_2O_3 at 2300 K (solidus temperature 2100 K). The pressure at the reservoir inlet rises within 0.4 sec from 0.1 MPa to the final value of 0.2 MPa (driving pressure difference 0.1 MPa). The pressure increase at the beginning follows an exponential law and is supposed to come close to the opening characteristic of a solenoid valve used in the experiment.

5.2 Code Modifications

This simulation is within the scope of the SIMMER-III application range. No modification of models has been required. However, some modifications had to be done to cope for floating divides which occured. In SP VITER and VITERP the determinant of the S-matrix for velocities happens to become smaller than permissible. In SP IFASRC and HTC one field element of the thermal conductivity KPLM

resp. KR was found to become zero occasionally probably resulting from an allocation error. The modifications worked well for this special 1d-case but are not meant to be a general remedy.

5.3 Parametric Cases

A parametric case with a non-superheated melt was run giving a reduction in penetration distance in accordance with Ref. 5). In this case, the maximum crust growth occurs at the tube inlet.

6. Results and Discussion

The results from the simulation show a good agreement with the data derived from the experiment. The maximum penetration length is underestimated by about 10 % (Fig. 2). Approaching the maximum penetration value the cross section is blocked to about 90 % ($\alpha_{tube} + \alpha_{crust}$) by crust formation (Fig. 3, 4).

The velocity (~ mass flow) through the inlet area is substantially decreased (about 1/80 of the maximum value), but not completely stopped (Fig. 5). As heat losses of the tube to the environment can not be considered and heat conduction in axial direction is not modeled the cooling down of the melt is delayed.

The penetration transient stays somewhat behind the values recorded in the THEFIS experiment. This was also noted in previous calculations with SIMMER-II. These calculations showed that with a different pressure characteristic for the solenoid valve (higher dp/dt) the results are improved.[3)]

Some problems arise at the very beginning of the calculation when large pressure spikes from the leading edge arrive at the reservoir and disturb the acceleration of the melt (Fig. 5). Using default input values for the momentum exchange functions the penetrating melt comes to a premature standstill. The cooling down of the melt generates particles at the leading edge causing an artificial stoppage of the flow. The low particle fraction should not be able to obstruct the flow path.

The input values for the momentum exchange functions, the maximum packing fractions for mixture and particles, ALPDM and ALPMP, respectively, had to be raised from default vahles to 0.9 to enable a further penetration of the melt into the tube. With these modifications the crust formation at the final state shows its characteristic conduction limited freezing behaviour.

In SIMMER-III correct pressure losses are obtained for the flow through an area restriction (orifice) only if the orifice region is represented by at least two meshes. In this application, area changes produced by crust formation do not differ widely from one cell to another, so that the pressure loss calculation leads to satisfactory results. The analyses of pressure losses at area changes showed that SIMMER-III gives good results for a flow through a sudden expansion. For a flow through a sudden restriction with an area change more than 50%, deviations from the handbook[6)] pressure losses are calculated.

7. Conclusions

The simulation agreed well with the data derived from the experiment. The experience from former simulations with SIMMER-II was a good support. The integral assessment proved the heat transfer coefficients and the melting/freezing models to be adequate for simulating a melt penetration with a conduction limited freezing behaviour. The dafault values for the momentum exchange functions should be raised.

8. Recommendations for Model Improvements

The acceleration of the penetrating melt is affected adversely by high pressure spikes propagating from the leading edge of the melt down to the reservoir. These spikes resulting from 'packing' problems should be smoothed.

It is desirable to remove the floating divides that occured throughout the simulation. These errors probably result from numerical rounding errors not taken into account and from an allocation error.

Concerning numerics some improvements are also desired to reduce the large CPU time necessary. The consumed CPU time of about 25 h appears to be much too high for the problem concerned.

9. References

1) G. Fieg, M. Möschke, I. Schub, H. Werle: Penetration and Freezing Phenomena of Ceramic Melts into Pin-Bundles, The 1990 Int. Conf on Fast Reactor Safety Snowbird, Utah, USA, Vol. II, 387, August 12 - 16 (1990).

2) M. Epstein, et al.: Transient Freezing of a Flowing Ceramic Fuel in a Steel Channel, Nucl. Sci. Eng. 61,310 (1976).

3) W. Maschek, G. Fieg, M. Flad: Experimental Investigations of Freezing Phenomena of Liquid/Particle Mixtures in the THEFIS Facility and Their Theoretical Interpretation, The 1990 Int. Conf on Fast Reactor Safety Snowbird, Utah, USA, Vol. I, 519, August 12 - 16 (1990).

4) D. Wilhelm: personal communication.

5) S. J. Hakim: Analyses of a Prototypic and a Simulant Experiment Related to Freezing in Flow Channels, LA-7938-C (1979).

6) I. E. Idelchik: Handbook of Hydrodynamik Resistance Berlin, Springer Verlag (1986).

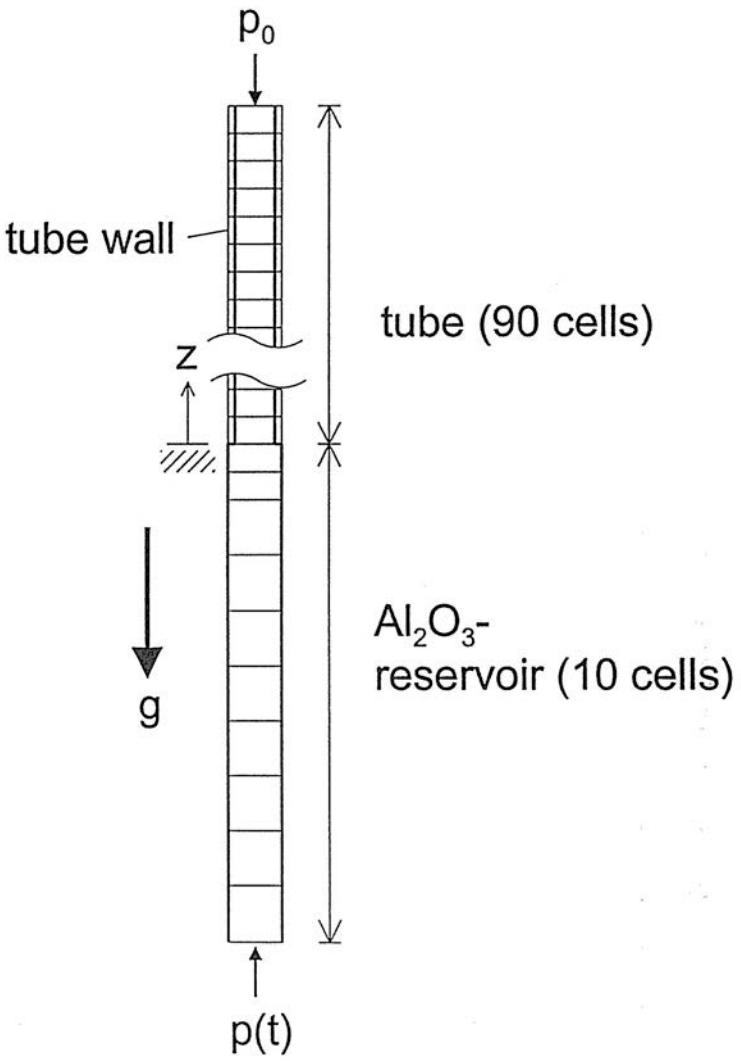

Fig. 1. SIMMER-III representation.

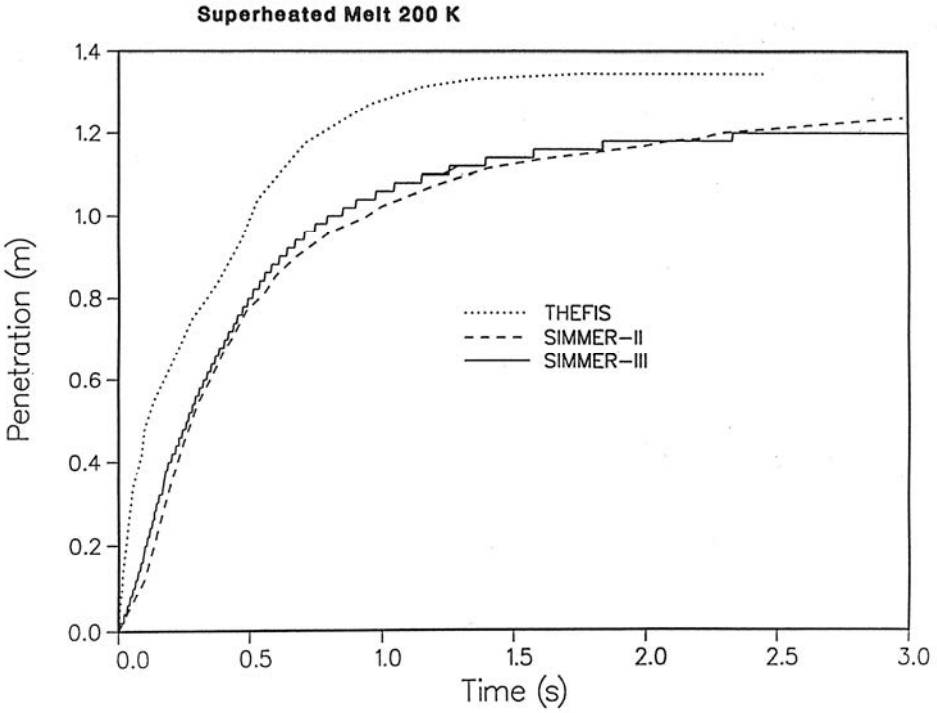

Fig. 2. Penetration length versus time.

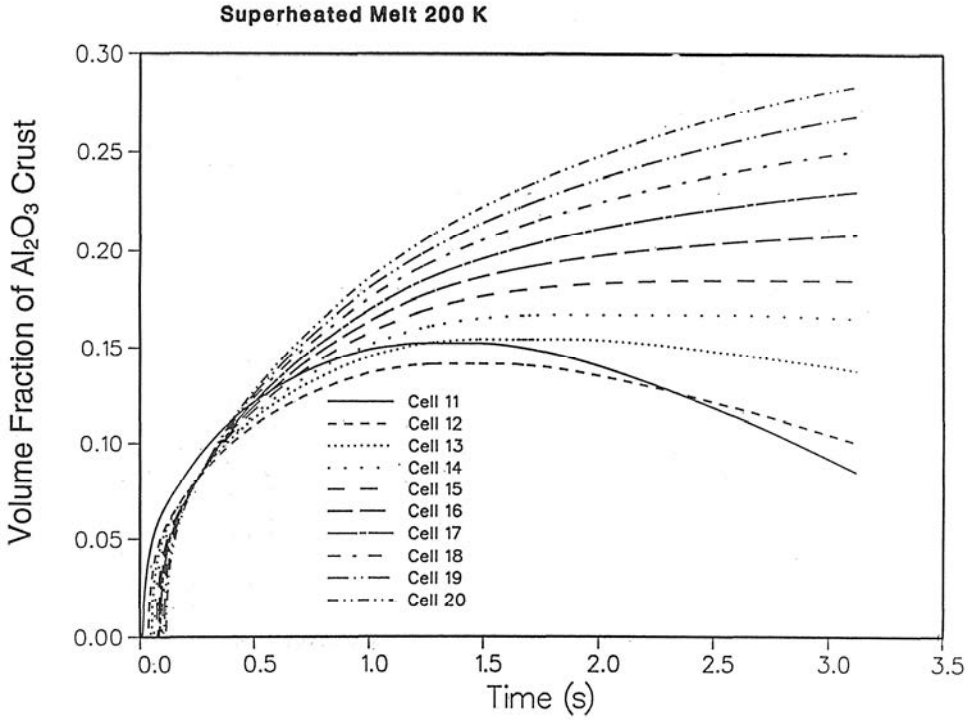

Fig. 3. Crust formation (Cells 11 to 20).

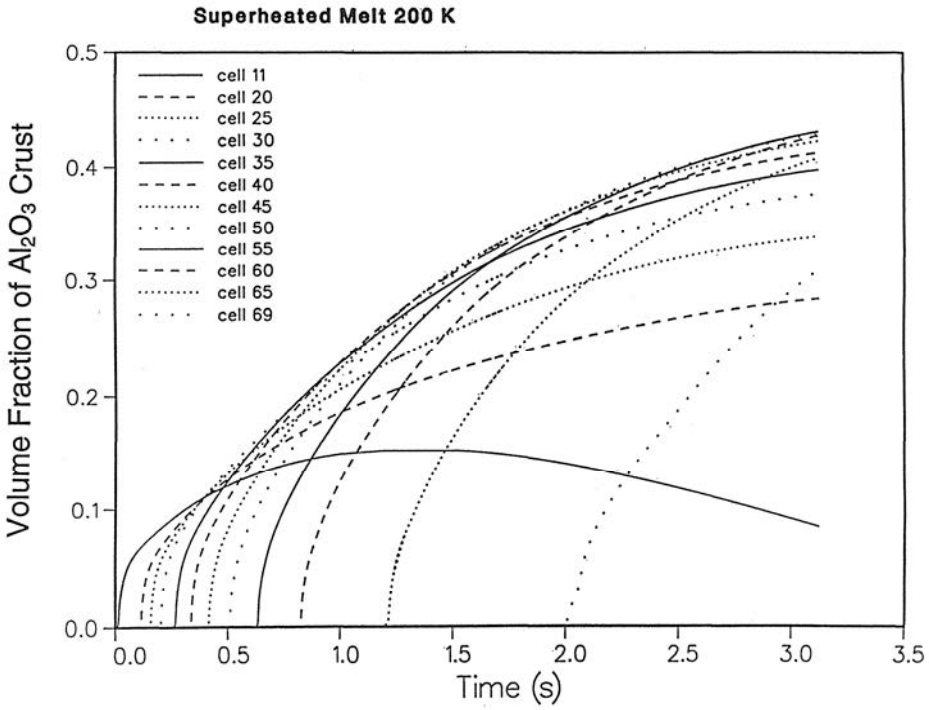

Fig. 4. Crust formation (Cells 20 to 69).

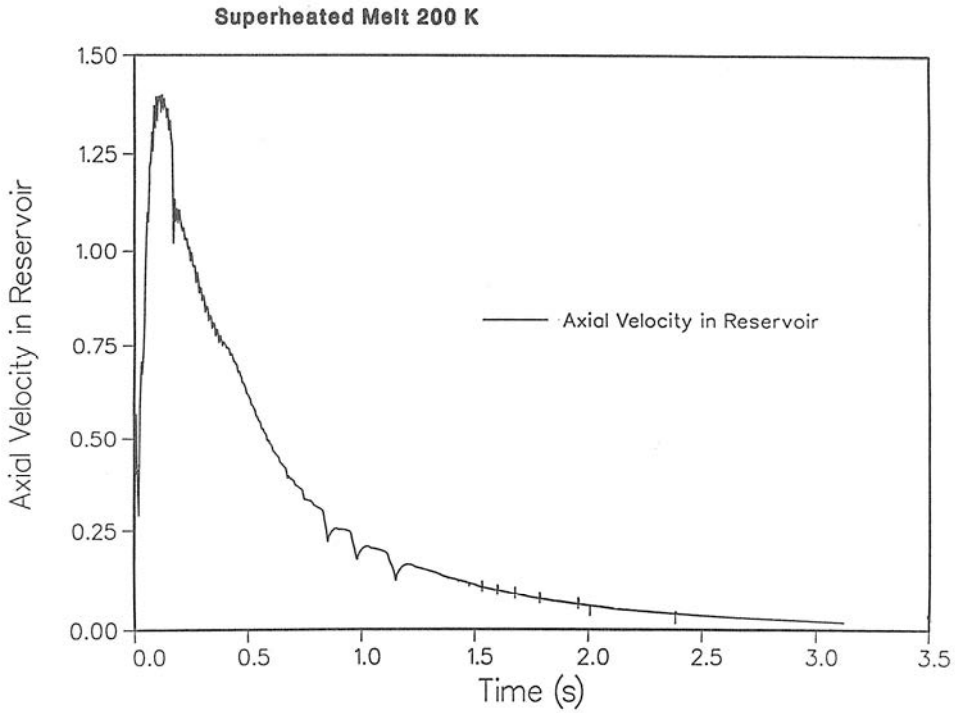

Fig. 5. Axial velocity in reservoir.

Problem 5.1: Condensation of steam on droplet

"Direct Contact Condensation of Steam on Subcooled Droplet"

David Brear and Koji Morita (PNC)

Outline of the Case

A subcooled, spherical water droplet grows due to direct condensation of steam vapor in a saturated steam atmosphere. The measured time-dependent droplet growth is compared with predictions using the SIMMER-III heat and mass transfer formulation.

1. Objectives of the Application

To verify and validate the SIMMER-III HMT and HTC models for the condensation of steam in a simple geometry using clear-cut experimental conditions.

2. Description of the Benchmark Problem

Ford and Lekic[1] performed experiments of steam condensation on single, slow-moving water droplets of three different diameters and with different initial subcoolings below the saturation temperature of steam ($T_s = 99.1℃$). The growth of the droplets during condensation was measured by high speed photography. In Ref. 1) the time-dependent radii of two representative droplets are presented. The droplets had the same initial radius, $R_0 = 0.755\,\mathrm{mm}$, but different initial subcoolings: $\Delta T = 50.0℃$ and $\Delta T = 33.7℃$, respectively. The droplet growth was measured for only 120 ms, which was insufficient for the droplets to attain thermal equilibrium with the steam atmosphere.

It is remarked in Ref. 2) that the vapor environment in the Ford and Lekic experiment can be regarded as pure steam, i.e. the presence of non-condensable gas can be neglected. The flow conditions around the droplets in the Ford and Lekic experiment are not clearly defined in Ref. 1), and it is known that droplets of the sizes used can circulate and oscillate when moving at their terminal velocity.[3] However it is considered in Ref. 1) that the droplets can be treated as rigid spheres, which implies that the droplet velocities were small during the period of measurement.

3. Analytical Solutions

Conduction (Ford and Lekic) model

Details are described in Ref. 1). The rate of condensation is controlled by heat transfer in the droplet, with negligible resistance at the droplet surface or in the vapor. Heat transfer in the droplet is due to conduction only, and the droplet is assumed to be spherically symmetric:

$$\frac{\partial T(r,t)}{\partial t} = \alpha\left(\frac{\partial^2 T}{\partial r^2} + \frac{2}{T}\frac{\partial T}{\partial r}\right) \tag{1}$$

The boundary conditions to solve Eq. (1) are that the droplet is initially at uniform temperature, and the droplet surface immediately attains the saturation temperature. The additional boundary condition is the heat balance at the interface:

$$k\left(\frac{\partial T}{\partial r}\right)_{r=R} = \lambda\rho\frac{dR}{dt} \tag{2}$$

Equation (2) effectively states that the droplet growth is caused solely by accretion of mass due to condensation. The resulting time-dependent equation for droplet growth is:

$$\frac{d(R^2)}{dt} = \frac{4k\Delta T}{\rho\lambda}\sum_{n=1}^{\infty}\exp\left(-n^2\frac{\pi^2\alpha t}{R^2}\right) \tag{3}$$

In fact Ford and Lekic used an empirical approximation to Eq. (3) when comparing their predictions with experimental results. They obtained the following equilibrium droplet radius:

$$\frac{R_\infty}{R_0} = \left(1 + \frac{c_p\Delta T}{\lambda}\right)^{1/3} \cong 1 + \frac{c_p\Delta T}{3\lambda} \tag{4}$$

Conduction model with thermal expansion

Equations (2) to (4) neglect the thermal expansion of the droplet as it heats up. If thermal expansion is taken into account, the boundary condition (2) becomes:

$$\frac{dR(\rho,\bar{T})}{dt} = \frac{\partial R}{\partial\rho}\frac{d\rho}{dt} + \frac{\partial R}{\partial\bar{T}}\frac{d\bar{T}}{dt} = \frac{k}{\lambda\rho_0}\left(\frac{\partial T}{\partial r}\right)_{r=R} + \frac{1}{3}R\beta\frac{d\bar{T}}{dt} \tag{5}$$

Equation (5) states that the droplet grows due to accretion of mass due to condensation, and due to thermal expansion of the original droplet mass as it heats up. The equation for droplet growth is:

$$\frac{d(R^2)}{dt} = \frac{4k\Delta T}{\rho\lambda}\left(1 + \frac{\beta\lambda}{c_p}\right)\sum_{n=1}^{\infty}\exp\left(-n^2\frac{\pi^2\alpha t}{R^2}\right) \tag{6}$$

The equilibrium radius taking account of thermal expansion is:

$$\frac{R_\infty}{R_0} = (1+\beta\Delta T)^{1/3}\left(1 + \frac{c_p\Delta T}{\lambda}\right)^{1/3} \cong 1 + \frac{\Delta T}{3}\left(\frac{c_p}{\lambda} + \beta\right) \tag{7}$$

Comparison of Eqs. (7) and (4) indicates that the thermal expansion enhances the droplet growth rate by about $\beta\lambda/c_p \cong 0.35$ in the conditions encountered in Ford and Lekic's experiments.

4. Understanding of Phenomena

A review of direct contact condensation of steam on subcooled water droplets is available.[3), 4)] The main uncertainty in interpreting direct condensation experiments is whether droplets are circulating or

oscillating, since both of these processes can enhance heat transfer in the droplet, and hence droplet growth, significantly. The presence of non-condensable gas in the vapor can in principle slow the condensation process, as can the molecular diffusion of steam at high condensation rates, but these processes were not thought to be operating in Ford and Lekic's experiment. A solution of Eq. (2) using a moving outer boundary affects the predicted droplet growth rate slightly, but not significant.[8] No theoretical models find it necessary to consider non-equilibrium conditions at the droplet surface.

5. SIMMER-III Representation

5.1 Geometry, Initial and Boundary Conditions for a Reference Case

In the present study a test code to solve the heat and mass transfer equations related to the problem was used to analyze the problem without directly using S-III. The use of this code has the advantage of verifying the S-III constitutive equations without uncertainties caused by another models, and especially of eliminating the error of EOS data from numerical solutions. The code calculations were performed with thermophysical properties of water supplied by a program package, PROPATH[5], which uses NBS/NRC steam tables.[6]

The falling droplet is assumed to always contact the saturated vapor, and the surface temperature of the droplet is at the steam temperature. The driving force of condensation is governed by the temperature difference between the inside and surface of the droplet. With these assumptions the S-III HMT model should solve the following conservation equations:

$$\frac{\partial \bar{\rho}}{\partial t} = \Gamma \tag{8}$$

$$\frac{\partial \bar{\rho} e}{\partial t} = \Gamma i_c + ah(T_s - \bar{T}) \tag{9}$$

where the mass-transfer rate of condensation is given by

$$\Gamma = \frac{ah(T_s - \bar{T})}{\lambda} \tag{10}$$

The HTC is given as follows from its definition:

$$h = \frac{k\left(\frac{\partial T}{\partial r}\right)_{r=R}}{T_s - \bar{T}} \tag{11}$$

In the standard S-III the HTC corresponding to Eq. (11) is expressed by:

$$h = \frac{k}{fR} \tag{12}$$

with $f = 0.2$ for a quasi steady-state profile[7], which is a standard value in S-III. In the test code, Eqs. (8) and (9) coupled with EOS were solved iteratively in the same way as the standard S-III HMT model does.

In the reference case, the growth of droplet during condensation was calculated using the steady-state HTC, Eq. (12), with $f = 0.2$.

5.2 Code Modifications

A test code was used to analyze the problem without directly using S-III.

5.3 Parametric Cases

5.3.1 Alternative Steady-State HTC

The reference case was repeated with an alternative steady-state HTC by specifying $f = 0.15$.

5.3.2. Conduction (Ford and Lekic) Model

The Ford and Lekic model is obtained by defining a constant water density and using the following transient HTC:

$$h = \frac{\pi^2 k}{3R} \sum_{n=1}^{\infty} \exp\left(-n^2 \frac{\pi^2 \alpha t}{R^2}\right) \Bigg/ \sum_{n=1}^{\infty} \frac{1}{n^2} \exp\left(-n^2 \frac{\pi^2 \alpha t}{R^2}\right) \tag{13}$$

5.3.3. Conduction Model with Thermal Expansion

The effect of thermal expansion of the droplet on the conduction model is obtained by using Eq. (13) and allowing the water density to vary according to standard thermophysical properties.

6. Results

6.1. Reference Case

The normalized radii, R/R_0, of droplet calculated by the S-III model with Eq. (12) is shown in Fig. 1 compared with the measured data for droplet subcoolings of $\Delta T = 50.0℃$ and $\Delta T = 33.7℃$, respectively. The standard S-III model, based on the steady-state HTC, considerably underestimates the transient growth of droplet over most of the period observed, especially the initial rapid increase of droplet radii.

6.2. Alternative Steady-State HTC

Figure 2 shows the normalized radii calculated by the S-III model with a steady-state HTC defined by $f = 0.15$ for a droplet subcooling $\Delta T = 50.0℃$. The calculated droplet growth is, on average, a better fit with the experimental data over the time period of interest, but underestimates the droplet growth on short timescales and overestimates the growth on long timescales.

6.3. Transient HTC based on Ford and Lekic Model

Figure 3 shows the normalized radii calculated by the S-III model with a transient HTC defined by Eq. (13) and a constant water density, for a droplet subcooling $\Delta T = 50.0℃$. The calculated droplet growth agrees well with the experimental data, and is consistent with Ford and Lekic's calculation in Ref. 1).

6.4. Transient HTC based on Conduction Model with Thermal Expansion

Figure 3 also shows normalized radii for a droplet subcooling $\Delta T = 50.0℃$ calculated by the S-III model using Eq. (13) and taking account of thermal expansion of the droplet. If thermal expansion is taken into account the droplet growth is significantly overestimated. This result suggests that the agreement of the Ford and Lekic model with the measured data is fortuitous since the non-negligible thermal expansion of droplet is ignored in their model.

7. Conclusions

The investigation of steam condensation on a single water droplet has been inconclusive since the measured growth rate of the droplet was not reproduced, and the discrepancy between theory and the experimental results has not been resolved. Nevertheless the following points can be made:

a. The standard S-III HMT model cannot simulate the transient growth of a droplet during condensation for the entire period of growth. A transient HTC in the droplet is necessary to predict the heat transfer accurately, whereas S-III is constrained to use a steady-state HTC.
b. Nevertheless the standard S-III HMT model, with a steady-state HTC in the droplet, can be used to vary the timescale in which the droplet attains equilibrium (by varying the value of the steady-state HTC).
c. The agreement of Ford and Lekic's theoretical model with the experimental result seems to be fortuitous since the thermal expansion of droplet is ignored.
d. The experimental results obtained by Ford and Lekic seem to imply that a thermal, or mass transfer, resistance is operating, though it is not clear what the resistance is due to.
e. There appears to be no critical review of the Ford and Lekic result in the heat transfer literature. This is mainly because most other experimental results pertain to flow conditions in which droplets are circulating, or oscillating, which enhances heat transfer in the droplets and results in faster condensation rates than observed in Ford and Lekic’s experiments.

8. Recommendations for Model Improvement

Although a transient HTC is required to accurately reproduce the droplet growth, it is not recommended that this capability be implemented in S-III. This is because S-III does not trace each droplet history and so the general modeling of transient HTCs is impractical in the code framework.

9. References

1) J. D. Ford, A. Lekic, “Rate of growth of drops during condensation”, Int. J. Heat Mass Transfer pp.61-64 (1973).

2) E. Kulic et al., “Heat transfer rate predictions in condensation on droplets from air-steam mixture”, Can. J. Chem. Eng., 53, 3, pp.252-258 (1975).

3) G. P. Celata, “Direct Contact Condensation of Steam on Subcooled Water”, Phase interface phenomena in multiphase flow, Hemisphere, New York (1991).

4) G. P. Celata et al., “Direct contact condensation of steam on droplets”, Int. J. Multiphase Flow, 17, 2, 191 (1991).

5) PROPATH: A Program Package for Thermophysical Properties of Fluids, Version 7.1 by PROPATH Group, Corona Publishing Co., Ltd., Tokyo (1990).

6) L. Haar et al., NBS/NRC Steam Tables, Hemisphere, New York (1984).

7) J. Berthier et al., “AFDM: An Advanced Fluid-Dynamics Model, Volume III: AFDM Heat-Transfer and Momentum-Exchange Coefficients”, LA-11692-MS, Vol. III, Los Alamos National Laboratory (1990).

8) E. A. Fischer, private communication (1993).

Nomenclature

a : smear contact area of droplet-vapor interface [1/m]

c : convective factor

c_p : heat capacity at constant pressure [J/kg/K]

e : specific internal energy [J/kg]

h : heat-transfer coefficient [W/m^2/K]

i_c : condensate enthalpy, specific enthalpy of saturated liquid [J/kg]

k : thermal conductivity [W/m/K]

r : local radius of sphere [m]

R : radius [m]

t : time [s]

T : *temperature [K]*

$\bar{T}$: average temperature [K]

ΔT : initial droplet subcooling [K] $T_s - T_0$

Greek letters

α : thermal diffusivity [m^2/s] $\dfrac{k}{\rho c_p}$

β : volumetric thermal expansion coefficient [1/K] $-\dfrac{1}{\rho}\dfrac{d\rho}{dT}$

Γ : mass-transfer rate [kg/s]

λ : latent heat of vaporization [J/kg/K]

ρ : density [kg/m^3]

$\bar{\rho}$: smear density [kg/m^3]

Subscripts

0 : reference, initial condition

s : steam, vapor

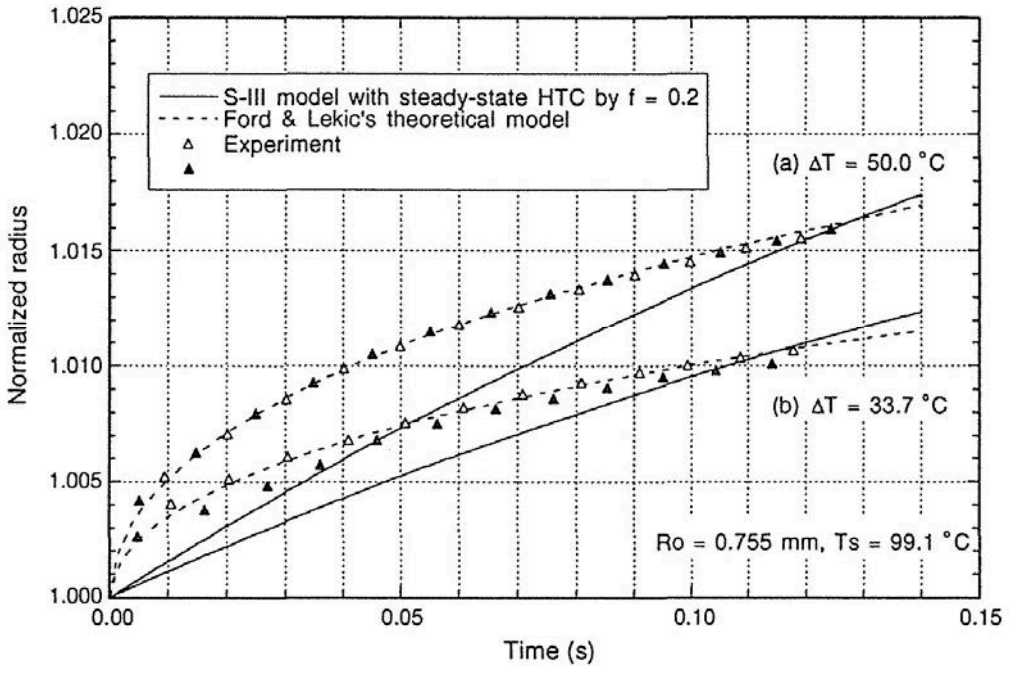

Fig. 1. Droplet radii calculated by S-III model with steady-state HTC defined by $f = 0.2$.

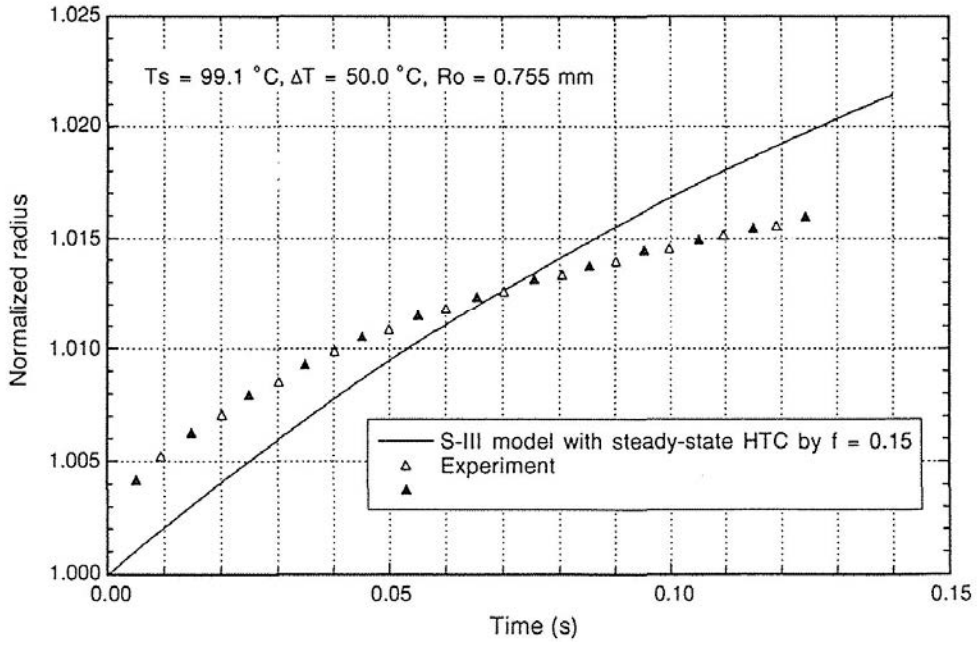

Fig. 2. Droplet radius calculated by S-III model with steady-state HTC defined by $f = 0.15$.

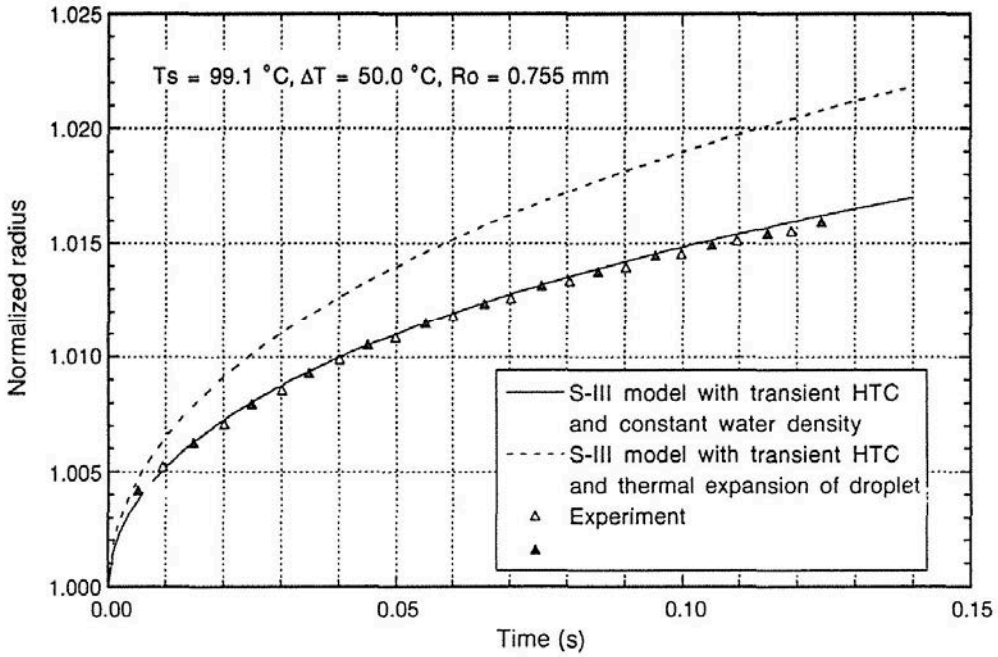

Fig. 3. Droplet radius calculated by S-III model with transient HTC.

Problem 5.2: Droplet evaporation

"Energy Conservation in Droplet Evaporation"

Yoshiharu TOBITA (PNC)

Outline of the Case

A single water droplet of 1 g at 158°C is placed in a container of 1 liter filled with saturated vapor at 100°C. The ambient pressure is 1 atm. The droplet begins to evaporate and finally the temperature of this system reaches equilibrium value of 104.7°C.

1. Objectives of the Application

This application aims at checking the energy conservation during the vaporization and condensation process in SIMMER-III. In some SIMMER-III applications to experiment analysis and reactor condition, the vapor temperature was found to increase higher than the liquid temperature by evaporation while the vaporization continues to produce the vapor. This behavior seems strange from intuition and provided the motivation to check the energy conservation during the evaporating process of a droplet placed in its own vapor.

2. Description of the Experiment

To check the energy conservation during the vaporization process, two thermodynamic states were defined.

State 1) A container of 1 liter contains water vapor of 1 atrn and liquid water of 1 g.
The temperature is 100°C.
The mass of the vapor is 1.0×10^{-3} m^3 / 1.673 m^3/kg = 5.977286×10^{-4} kg.
The total enthalpy in this system becomes
$(5.977286\times10^{-4} \times 639.5) + (1.0\times10^{-3} \times 100.092) = 0.482309$ J.

State 2) If 0.1 g of water vaporizes, the specific volume of the vapor becomes
10×10^{-3} m^3 / $(5.977286+1.0)\times10^{-4}$ kg = 1.4332220 m^3/kg.
The saturation conditions which correspond to this specific volume are:
Temperature = 104.7°C, pressure = 1.2192 atm, and
total enthalpy in the system= 0.5415136 J.

If we give water droplet the required energy to cause the transition from state 1 to state 2, the specific internal energy of the droplet becomes

$(0.5415136 - 0.482309) / 1.0\times10^{-3} + 100.092 = 159.29568$ J/kg.

The droplet temperature at this internal energy is 158°C. The preceding consideration provides the following test case to check whether the energy is conserved reasonable during the vaporization process.

Geometry : 1 mesh system with rigid wall with the volume of 1 liter.

Initial condition of liquid: volume fraction = 9.581297×10^{-4} and temperature = 158°C.

Initial condition of vapor: pressure = 1.0 atm and temperature = 100°C.

The liquid droplet begins to evaporate and the system will reach to equilibrium state with uniform temperature. The equilibrium temperature should be 104.7°C if energy is conserved during the calculation.

3. Analytical Solution

The analytical value of the equilibrium temperature is 104.7°C.

4. Understanding of Phenomena

In view of the stationary energy conservation between state 1 and state 2, the phenomena is well understood. However, the transition behavior gives rise to a complicated situation. The vapor temperature can increase even higher than the liquid temperature depending on the vaporization rate and heat transfer rate from vapor to droplet. This overheating is caused by the mechanical work done on the vapor phase by vaporization. A brief examination of this vapor temperature overshooting by Fischer is presented in Appendix.

5. SIMMER-III Representation

5.1. Geometry, Initial and Boundary Conditions for a Reference Case

A 0-D mesh was used with its radius of 5.64189 cm and height of 10 cm to make the volume 1 liter. Initial and boundary conditions are explained in section 2. The radius of the droplet is kept constant at 1.0×10^{-4} m. The total mass of vapor becomes 0.58574 kg/m^3, which is slightly lower than the value from the steam table, 0.59775 kg/m^3. However, the same initial liquid temperature of 158°C is assigned to droplet since the difference of initial vapor density is thought not to cause significant influence on the total heat balance in the system.

5.2 Code Modifications

None.

5.3 Parametric Cases

To investigate the effect of vaporization speed on the vapor temperature transient, the liquid side heat transfer coefficient is divided by 10 and 100 in case 1 and case 2, respectively. In addition a case with the droplet radius of 1.0×10^{-5} m was performed.

6. Results

The general temperature transient behaved as follows. The liquid temperature begins to decrease due to the energy loss by vaporization while the vapor temperature increases by the mechanical work done by vaporization. The saturation temperature goes up according to the pressure increase too. The vaporization ceases when the liquid temperature and saturation temperature becomes equal and thereafter the vapor and liquid temperature approach each other by heat conduction. Uniform temperature. After enough time, the system reaches thermal equilibrium with uniform temperature.

In the reference case (case 0) plotted in Figs. 1 and 2, the vapor temperature exceeds the liquid temperature at 4 ms while the vaporization continues because the liquid temperature is higher than the saturation temperature. The liquid temperature and saturation temperature become equal at about 30 ms. Thermal equilibrium is achieved after 500 ms.

In order to check the effect of vaporization speed to the transient behavior of temperature, the heat transfer coefficient in liquid droplet was divided by 10 and 100 in the cases 1 and 2, respectively. This operation reduces the vaporization speed by a factor of 10 and 100 in the framework of rate-limited vaporization model in SIMMER-III. The results of these two cases were plotted in Figs. 3 and 4. The liquid temperature transient shows the almost same behavior as Fig. 1, whereas the time scale in these graphs were 10 and 100 times larger than Fig. 1. This means that the liquid temperature change is dominated by the energy loss due to vaporization only. In contrast to the similarity in liquid temperature, the vapor temperature bebaviors show big differences between each case. This is because the slow vaporization allows the vapor to transfer the heat to the liquid surface of which temperature is assumed to be saturation temperature.

In addition to the cases discussed above, the case in which the droplet radius was divided by 10 was performed. The calculated temperatures are plotted in Fig. 5. In this case, the reduction of droplet radius changed the heat transfer rate from vapor to droplet with the same factor as vaporization rate. Therefore, the relative relationships among the liquid, vapor, and saturation temperature did not show any change from the reference case while the time scale of the phenomena was reduced by a factor of 10.

The temperatures and the macroscopic densities of liquid and vapor at the calculated thermal equilibrium condition are shown in Table 1. The mass of vaporized liquid is very close to 0.1 g and the predicted equilibrium temperature is very close to the theoretical prediction in all cases.

7. Conclusions

A vaporization of droplet was analyzed by SIMMER-III. The energy conservation during vaporization was checked by comparing the equilibrium temperature with theoretical prediction. The

calculated temperature agreed with the theoretical value in all cases performed and thus the energy conservation in the vaporization model of SIMMER-III was confirmed.

8. Recommendations for Model Improvement

None.

9. References

None.

Table 1. The comparison of SIMMER-III results and theoretical prediction.

		temperature (K)			density (kg/m3)	
		liquid	vapor	saturation	vapor	liquid
Initial condition		431.09	373.15	372.69	0.58574	0.87405
Thermal equilibrium	Theory	377.85	377.85	377.85	0.68574	0.77405
	Case 0	377.44	377.93	377.44	0.68379	0.77600
	Case 1	377.45	377.98	377.44	0.68370	0.77609
	Case 2	377.69	377.45	377.38	0.68388	0.77461
	Case 3	377.40	377.40	377.40	0.68391	0.77588

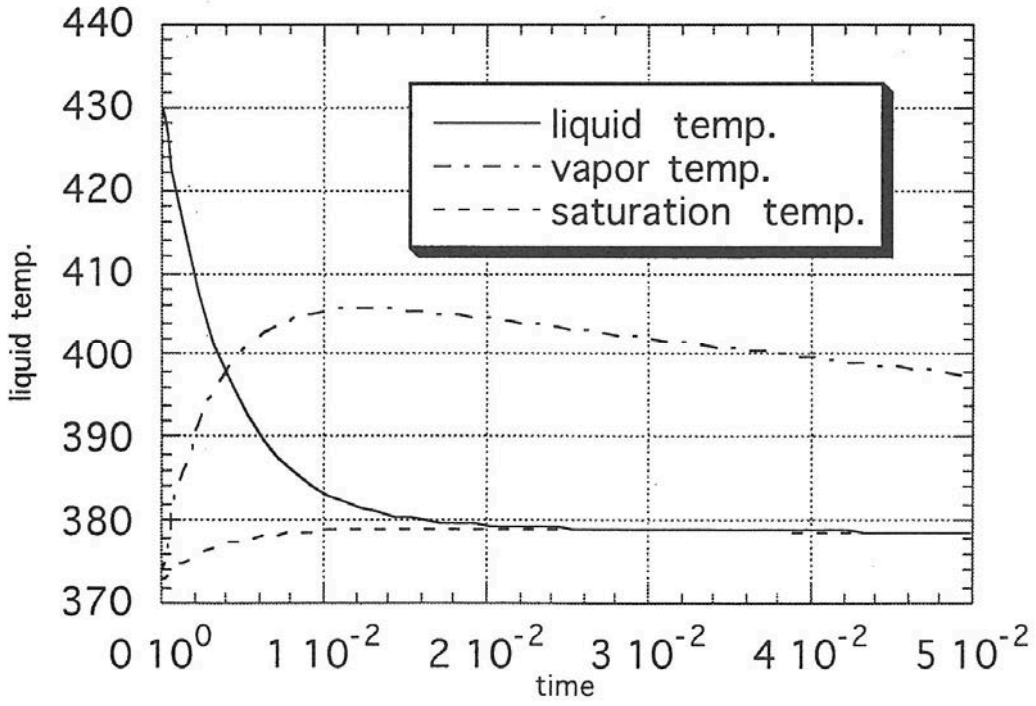

Fig. 1. Temperature transient in case 0.

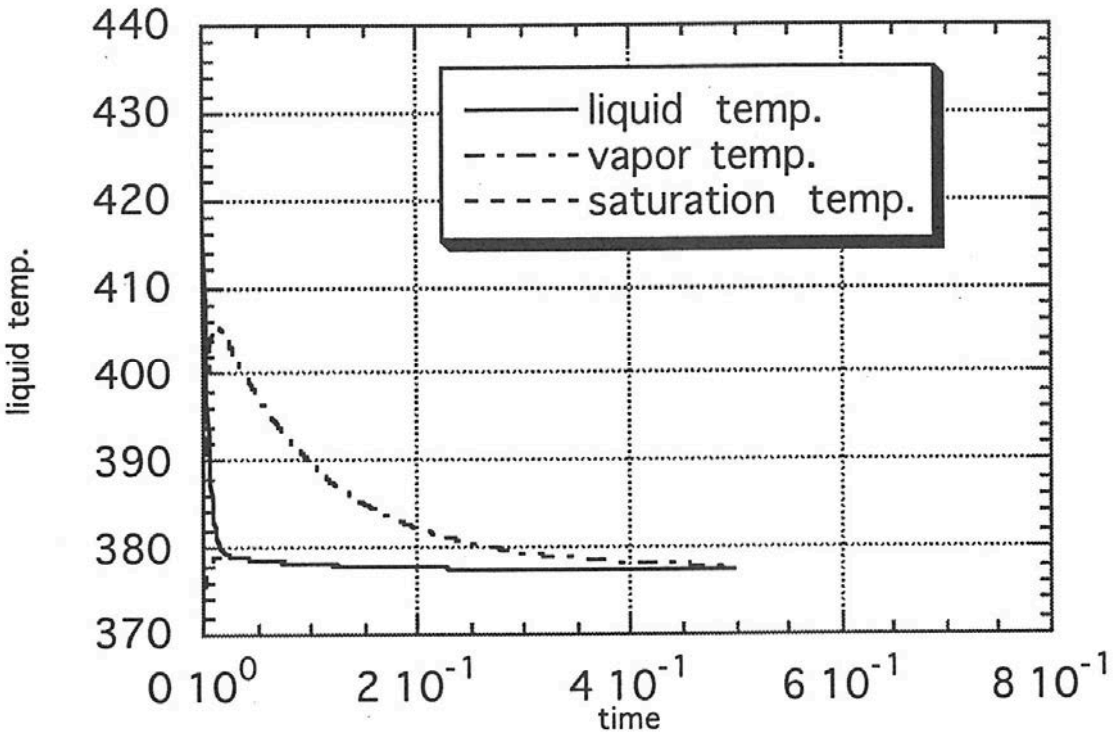

Fig. 2. Temperature transient in case 0 (from 0 s to 0.8 s).

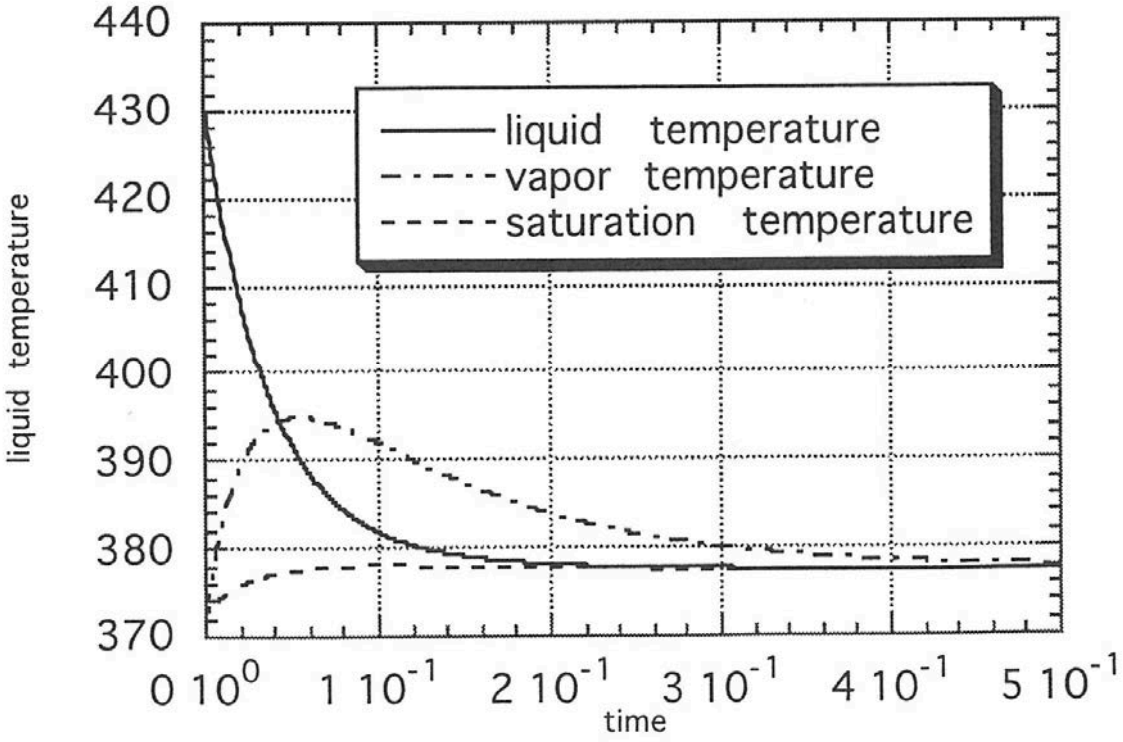

Fig. 3. Temperature transient in case 1.

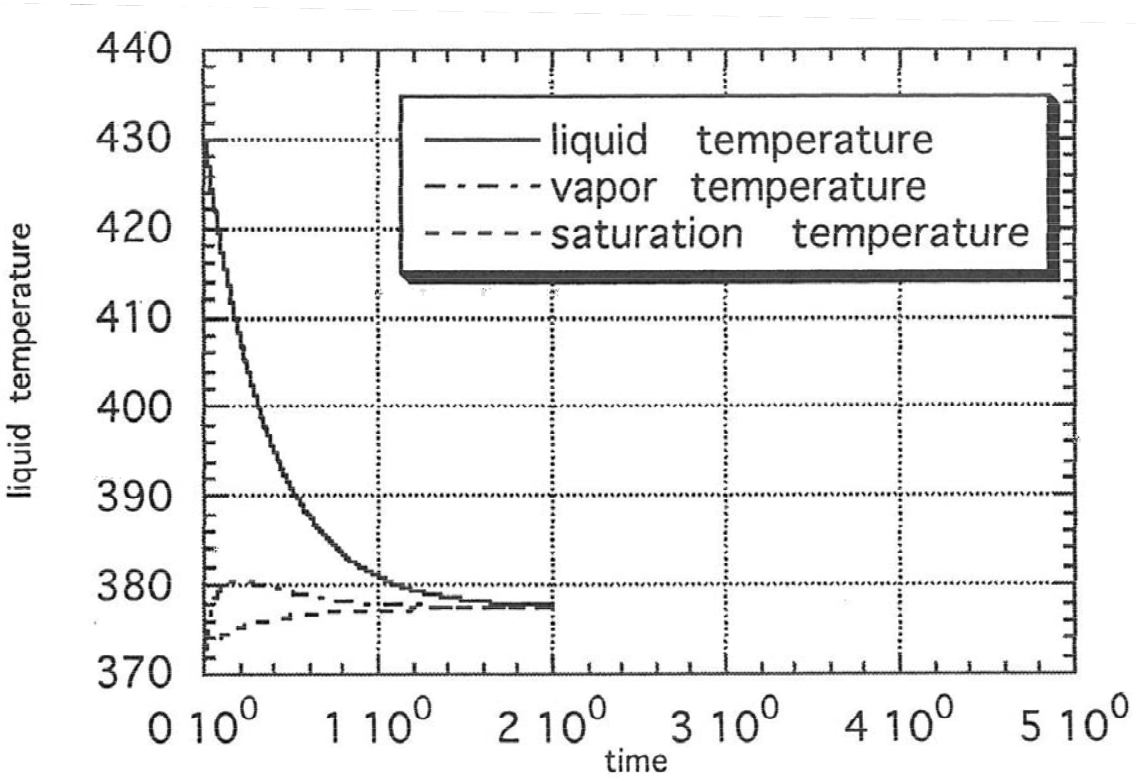

Fig. 4. Temperature transient in case 2.

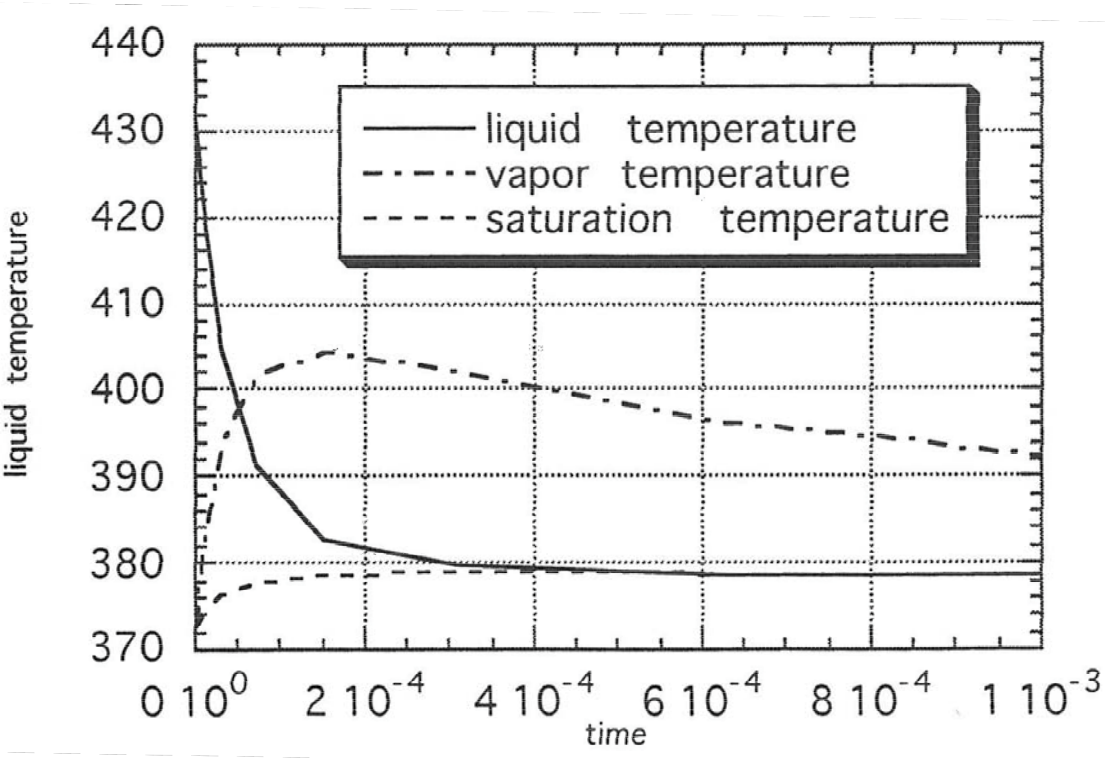

Fig. 5. Temperature transient in case 3.

Appendix to Problem 5.2 report: Comments on the V/C equations

E.A. Fischer

Vaporization and Condensation in SIMMER-III is based on a heat-flux limited mass transfer concept. S-III calculations for vaporization of a superheated liquid in a closed cell showed an overshoot in the vapor temperature, above the liquid temperature, which was not immediately understood. Seemingly, heat was transferred from a colder to a hotter medium, which contradicts the Second Law. To clarify this point, look at the S-III heat-flux limited mass transfer model for V/C.

The vaporization or condensation rates are

$$\Gamma_{gl} = \frac{q}{i_g - i_{con}} \quad \text{for } q > 0$$

$$\Gamma_{gl} = \frac{-q}{i_{vap} - i_l} \quad \text{for } q < 0$$

where the heat flux q is

$$q = ah_{lg}(T_i - T_l) + ah_{gl}(T_l - T_g)$$

These equations must be combined with the conservation equations for mass and energy The denominator is the heat of vaporization, which is the difference in enthalpy between liquid and vapor The interface temperature is defined as the saturation temperature

$$T_i = T_{sat}(p_g).$$

The same model (with minor modifications) was used in SIMMER-II, and in other codes like RELAP and TRAC. To understand the temperature overshoot, let us look at specific processes:

- Vaporization at constant pressure:

  In this case, the S-111 energy equations are equivalent to the simple heat balance equation:

$$i_g - i_l = e_g - e_l + p\left(\frac{1}{\rho_g} - \frac{1}{\rho_l}\right)$$

  No temperature change is expected in this case.

- Vaporization at constant volume

  One can think of this as a sequence of three processes:

  1) vaporization at constant pressure, using the heat of vaporization
  2) compression of the vapor to its original volume; this heats the vapor above the liquid temperature.
  3) the vapor cools to the liquid temperature by heat conduction

The first two processes occur .simultaneously, and much faster than the third one. Thus, heating of the vapor is due to compression, not to heat transfer. The vapor energy equation reads (at constant volume)

$$\rho_g \frac{de_g}{dt} = \Gamma_{lg}(i_{vap} - e_g) + ah_{gl}(T_l - T_g)$$

As $h_{lg} \gg h_{gl}$, the first term dominates at short times, leading to rather rapid vaporization, and heating of the vapor. The vapor then cools to the equilibrium temperature on a time scale determined by the second term, i.e. by h_{gl}, which is much more slowly than the initial vaporization and heating.

One further comment:

I have not found a convincing derivation of the above V/C model in the literature. One can, however, show, that the equations follow, in good approximation, from the principles of irreversible thermodynamics. The proof is too lengthy to be reproduced here.

Problem 5.3: Vapor bubble collapse

"Vapor Bubble Collapse in a Subcooled Liquid"

David Brear and Koji Morita (PNC)

Outline of the Case

A single, spherical vapor bubble collapses, driven by condensation in a slightly subcooled liquid. The bubble has a slow, constant translatory motion, contains some non-condensable gas, and remains approximately spherical during collapse. For these idealized conditions, an analytical model is available,[1)] assuming potential flow of the liquid around the bubble and collapse controlled by heat transfer, rather than by inertial effects.

The experiment was designed to approximate these conditions as well as feasible.

1. Objectives of the Application

This application concentrates on a verification of the SIMMER-III heat and mass transfer model, and of the heat transfer coefficients, because the controlling mechanism in the collapse process is heat transfer in the liquid. The application does not provide a test of the interfacial area model.

2. Description of the Experiment

The experimental conditions and the results for four translatory bubbles are described in Ref. 1). Liquid and vapour are water. The experimental procedure was basically as follows:

A bubble (initial radius between 1.4 and 3.9 mm, depending on the experiment) was released in the decompressurized test chamber with an imparted slow velocity (by having the test chamber fall under reduced gravity conditions). Then, the pressure was rapidly increased (within 2-3 ms) to atmospheric.

The bubble was continuously photographed, to obtain the radius versus time history. The motion pictures showed oscillations of the bubbles along their major and minor axes. The reported radii (Fig. 1) are averages over the oscillations. Due partly to the presence of non-condensable gas, the collapse ceased at a persistent radius.

Results for four bubbles are reported in Ref. 1). The bubble radii, the translatory motion and the subcooling varied in all four cases. In the experiment modeled with SIMMER-III, the subcooling was 4.5 K**,** the bubble was translating at 5.5 cm/*s,* its initial radius was 1.43 mm, and the collapse took about 40 ms.

3. Analytical Solution

Heat transfer in the liquid is not spherically symmetric because the bubble is moving. Two solutions for this problem are available.

First, there is a detailed solution for the problem of a heat transfer controlled collapse, described in Ref. 1). This analytic model involves the energy equation in the liquid, with non-symmetric moving boundary conditions, and also the liquid momentum equation which is written assuming potential flow around the bubble. The differential equations are coupled by the energy balance condition at the bubble surface. The system was solved numerically. The results agree rather well with the experiment, except for one run, in which the bubble exhibited highly oscillatory behavior (Run 1870 in Fig. 1).

Second, a formulation was developed to verify the SIMMER-III results by an independent calculation. This approach uses a steady-state Nusselt number heat transfer correlation and leads to a fairly simple expression for the time dependent bubble radius. The results of this calculation should agree well with the SIMMER-III calculation.

4. Understanding of Phenomena

Experimental results are consistent within acceptable errors, and there is reasonable agreement between the theoretical curves and the experimental data (see Fig. 1). Thus, the phenomena addressed in the experiment can be considered well understood (except for the initial oscillations, of the bubbles).

5. SIMMER-III Representation

5.1 Geometry, Initial and Boundary Conditions for a Reference Case

A 1-D mesh was used, with the vapour bubble located in he bottom mesh of a column of 3 meshes. The mesh scheme, geometry and initial conditions for experimental Run 1680 are illustrated in Fig. 2. A pressure boundary condition was imposed at the top surface, with continuous inflow/outflow of materials allowed.

5.2 Code Modifications

If it is attempted to directly model a translating vapour bubble using SIMMER-III, the single vapour bubble tends to break up, and vapour convects from one mesh to another, making it difficult to distinguish between vapour loss by convection and condensation.

Therefore, to simulate the heat and mass transfer aspects of the case, the heat and mass transfer routines only were coaxed into modeling single, moving bubbles. Ad-hoc change was introduced into subroutine VCHMT to: (a) collect all the vapor in the bottom cell into a single bubble, with appropriate surface area, and (b) ensure the liquid-side HTC is appropriate to the measured bubble velocity.

5.3 Parametric Cases

To estimate the influence of non-condensable gas on the bubble collapse, the contact area available for heat and mass transfer was reduced according to the non-condensable gas partial pressure (i.e. setting input data item FPG4L= 1). In addition, the influence of the time step size was investigated,

6. Results

The step change in pressure effected on the system causes temporary oscillatory befiaviour in the SIMMER-III simulation. The oscillations are inertial, and are a function of the mesh geometry used. Therefore the calculation was compared to the measured results only after the oscillations are sufficiently damped. This is still short (about 10 ms) on the timescale of the bubble collapse. It was ensured that vapour is not convected out of the bottom cell after this time.

The SIMMER-III calculation is compared with the measured results in Fig. 3. Collapse is calculated on approximately the right time scale, but the rate of collapse is underestimated by about a factor of 2 (Time-step size is influential only in the oscillatory phase). The shape of the radius versus time curve, however, differs not only from the experimental results, but also from the detailed analysis reported by Wittke and Chao (Fig. 1).

The bubble radius was calculated independent of SIMMER-III by the simple formulation described in Section 3, using the conditions measured for experimental Run 1680. The approximate fonnula reproduces the SIMMER-III results almost exactly, which verifies that there is no anomaly in the code calculations. The time-dependent temperature gradients reported by Wittke and Chao were compared with the gradients implicit in the SIMMER-III calculation. At small times the gradients calculated by Wittke and Chao are much steeper than those used in SIMMER-III. From this, it is concluded that the different shapes can be attributed to the use of steady-state, rather than transient, heat transfer coefficients in SIMMER-III. ·

The detailed analysis by Wittke and Chao calculates heat transfer based on potential flow around the bubbles, which is appropriate if there is free circulation inside the bubbles. However the HTCs calculated by SIMMER-III are based on rigid sphere empirical correlations. Therefore the simple formulation of Section 3 was used to calculate the collapse of the bubbles using a Nusselt number appropriate for a freely circulating bubble. The results are shown in Fig. 5. The calculated rate of bubble collapse is improved considerably if a Nusselt number which takes account of internal circulation is used.

The influence of the FPG4L parameter was found to be negligible (Fig. 4).

7. Conclusions

SIMMER-III has been successfully used to simulate a translating vapour bubble collapsing in subcooled liquid. The analysis has concentrated on the heat and mass transfer aspects of bubble collapse. In addition, the heat transfer behaviour of SIMMER-III has been verified by an independent calculation.

The calculated collapse is approximately on the same timescale, though somewhat slower than observed. The application provides a verification of parts of the heat and mass transfer model of the code within its known limitations. The difference between the calculated and observed collapse is partly attributed to the use of steady-state, rather than transient heat transfer coefficients in SIMMER-III, but mainly to the influence of circulation in the bubble on the external heat transfer coefficient.

The influence of non-condensable gas in reducing the rate of heat and mass transfer could not be quantified due to the small amount of gas present in the experiment. Thus, a value for input variable FPG4L cannot be recommended on the basis of these experiments.

8. Recommendations for Model Improvement

The heat transfer coefficients used to calculate heat transfer from droplets and bubbles in SIMMER-III should be modified to take account of the effect of internal circulation.

9. References

1) D. D. Wittke and B. T. Chao: "Collapse of Vapor Bubbles with Translatory Motion", J. Heat Transfer, Vol.89, pp. 17-24, Feb. 1967.

Data pertinent to the four experimental bubbles shown in Figs.

Run no.	R_0 cm	U_∞ cm/sec	T_∞ °C	ΔT °C	p_∞^* cm Hg	Δp cm Hg	γ_p	Ja (at T_{sat})	Pé	B (at T_{sat})	Average aspect ratio
1680	0.143	5.5	95.06	4.47	74.75	11.20	0.39	13.6	936	5.5×10^{-3}	1.1
1800	0.263	15.4	96.47	2.63	73.61	6.69	0.2	8.1	4820	1.4×10^{-3}	1.5
1870	0.393	2.2	93.95	5.49	74.57	13.67	0.075	16.7	1029	2.7×10^{-3}	1.1
1560	0.354	18.2	88.99	10.54	74.75	24.15	0.125	32.0	7664	8.4×10^{-3}	1.3

$\Delta T = T_{sat} - T_\infty$, $\Delta p = p_\infty^* - p_{v,0}$

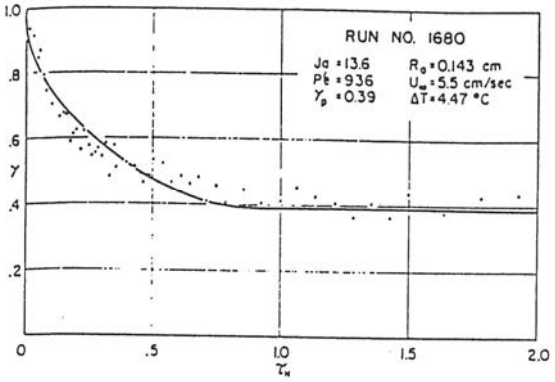

Comparison between experimental data and theory

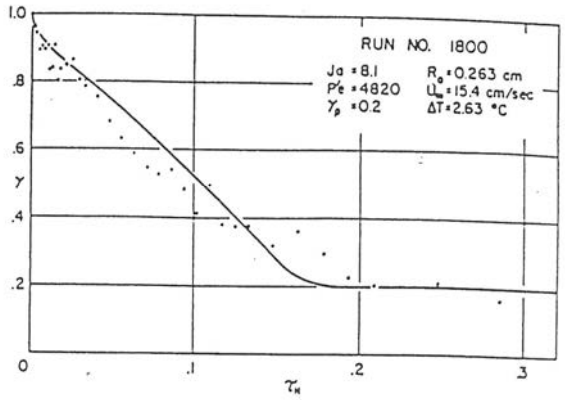

Comparison between experimental data and theory

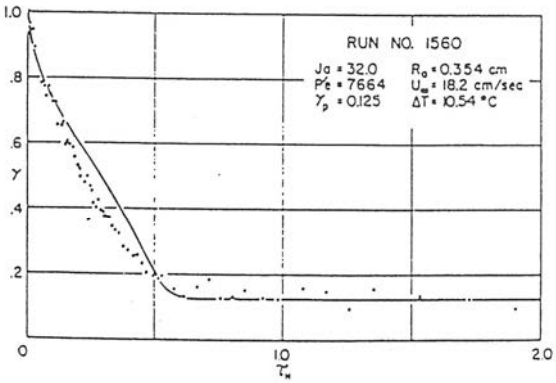

Comparison between experimental data and theory

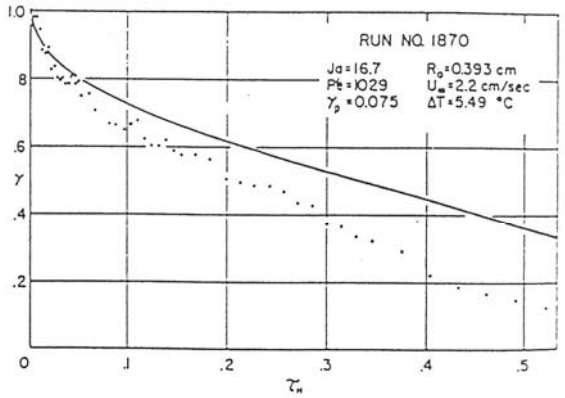

Comparison between experimental data and theory (bubble exhibited localized, irregular, oscillatory surface motion during collapse)

Dimensionless Formulation

The dimensionless bubble radius, $\gamma = R/R_0$
The dimensionless radial coordinate, $r^* = r/R_0$
The dimensionless time, $\tau = \kappa t/R_0^2$
The dimensionless temperature, $\Theta = (T - T_\infty)/(T_{sat} - T_\infty)$
The Péclet number, Pé $= 2U_\infty R_0/\kappa$
The Jakob number, Ja $= \rho c(T_{sat} - T_\infty)/\rho_v L$

$$\tau_H = \frac{4}{\pi} \mathrm{Ja}^2 \tau = \frac{4}{\pi} \mathrm{Ja}^2 \frac{\kappa t}{R_0^2}.$$

Fig. 1. Experimental conditions and results (Wittke & Chao[1]).

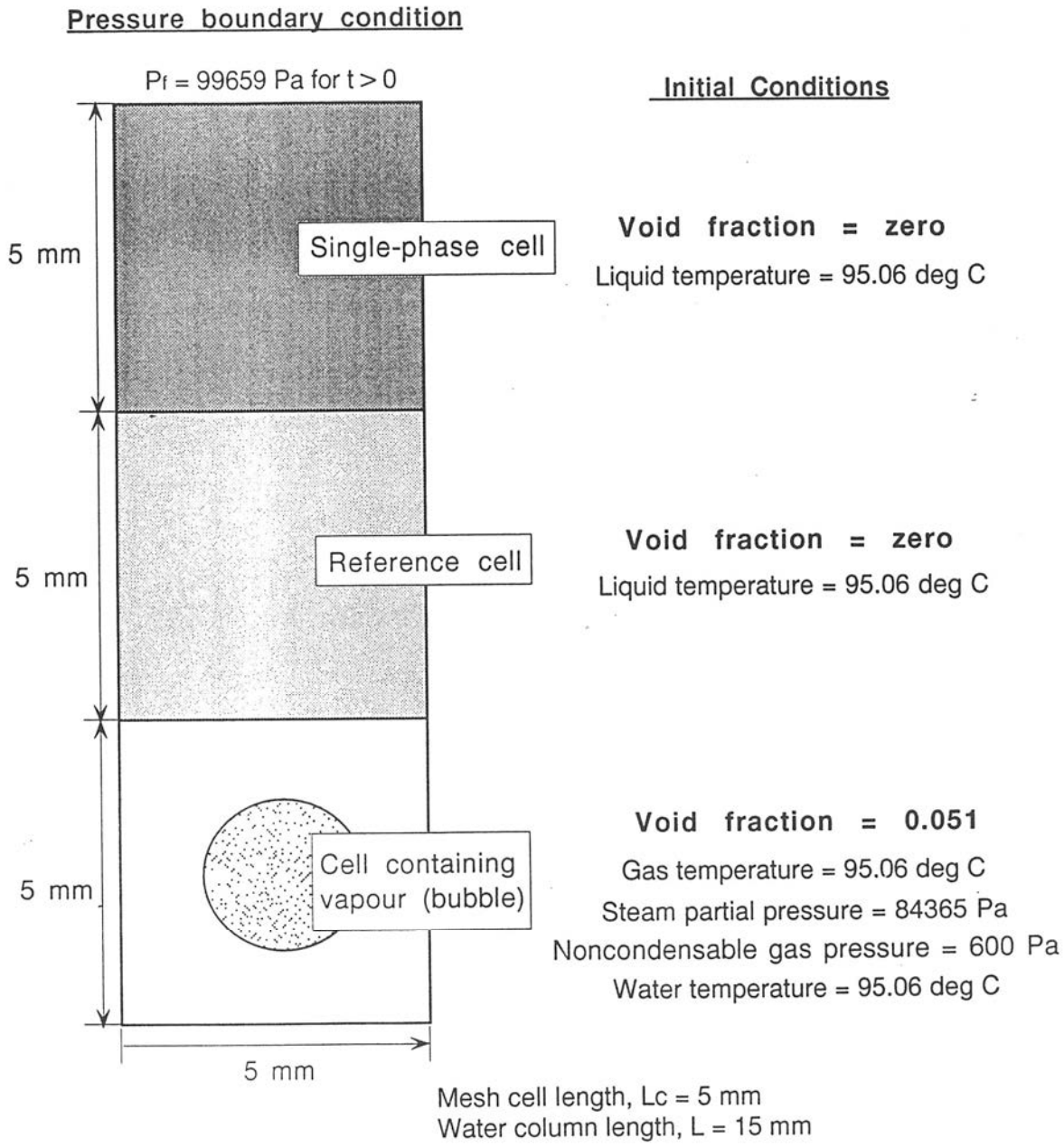

Fig. 2. Model and initial conditions for SIMMER-III representation of vapor bubble collapse in Experiment 1680.

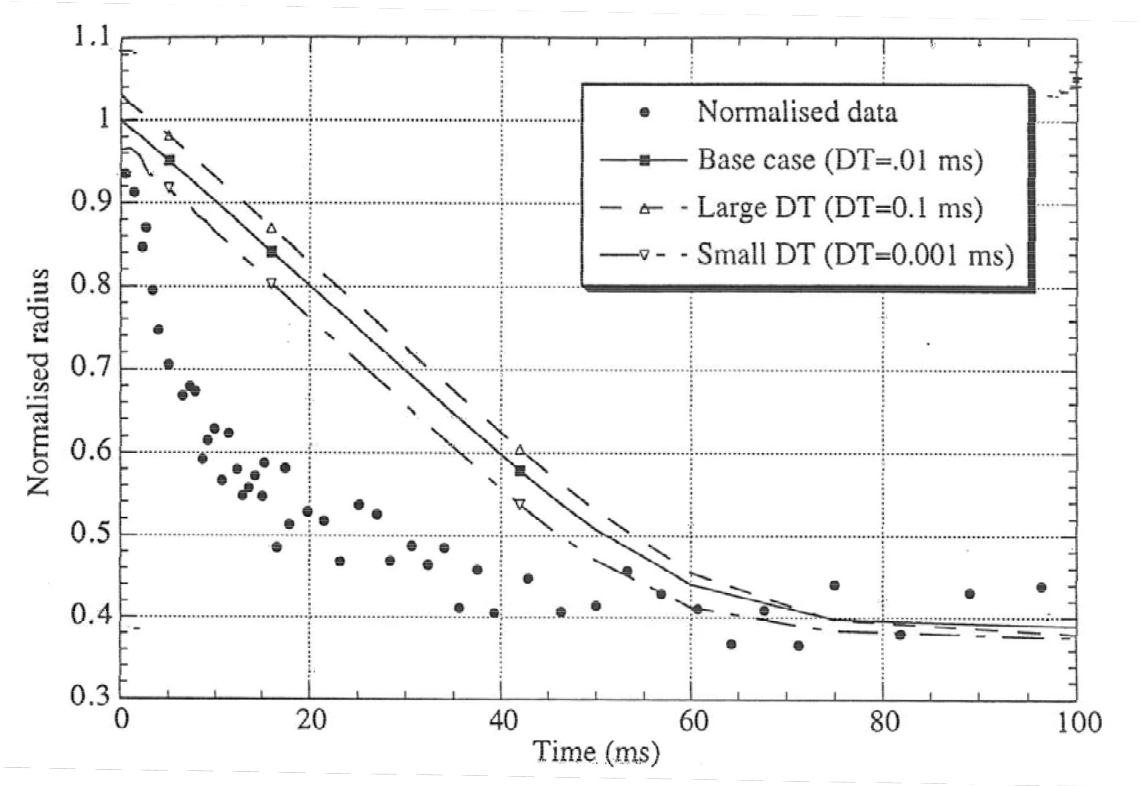

Fig. 3. Comparison of SIMMER-III calculation with experimental measurements for Run 1680.

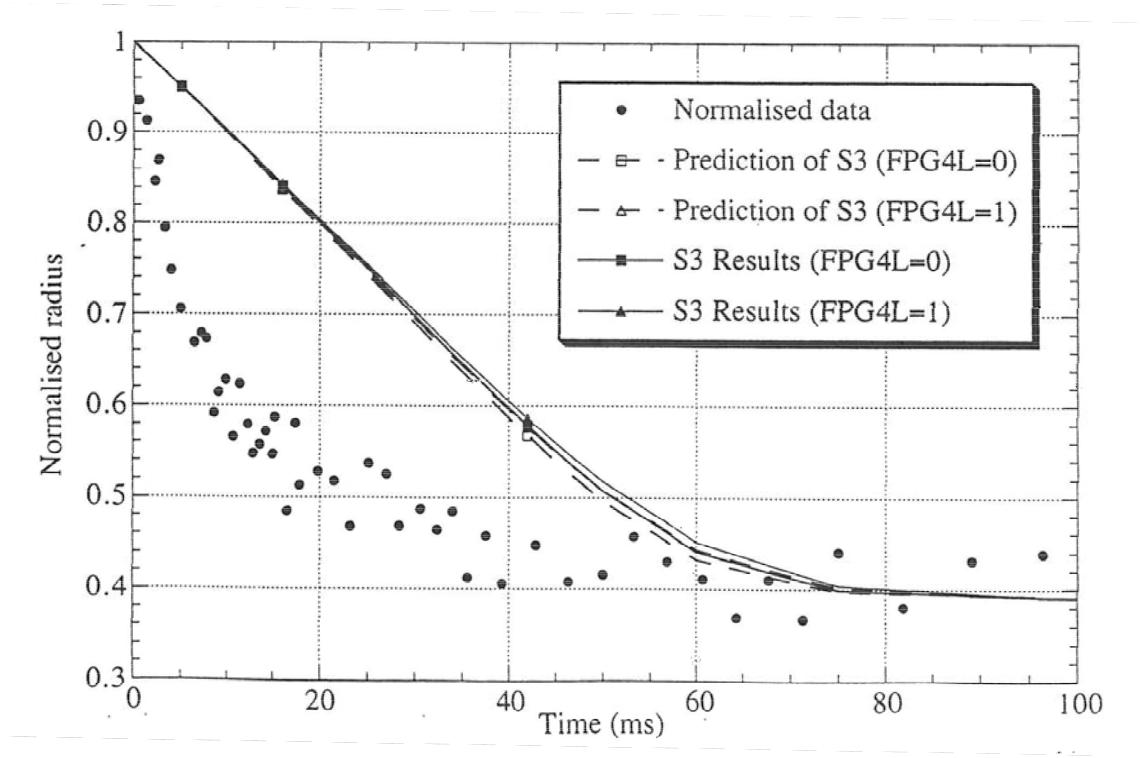

Fig. 4. Verification of SIMMER-III calculation by an independent calculation.

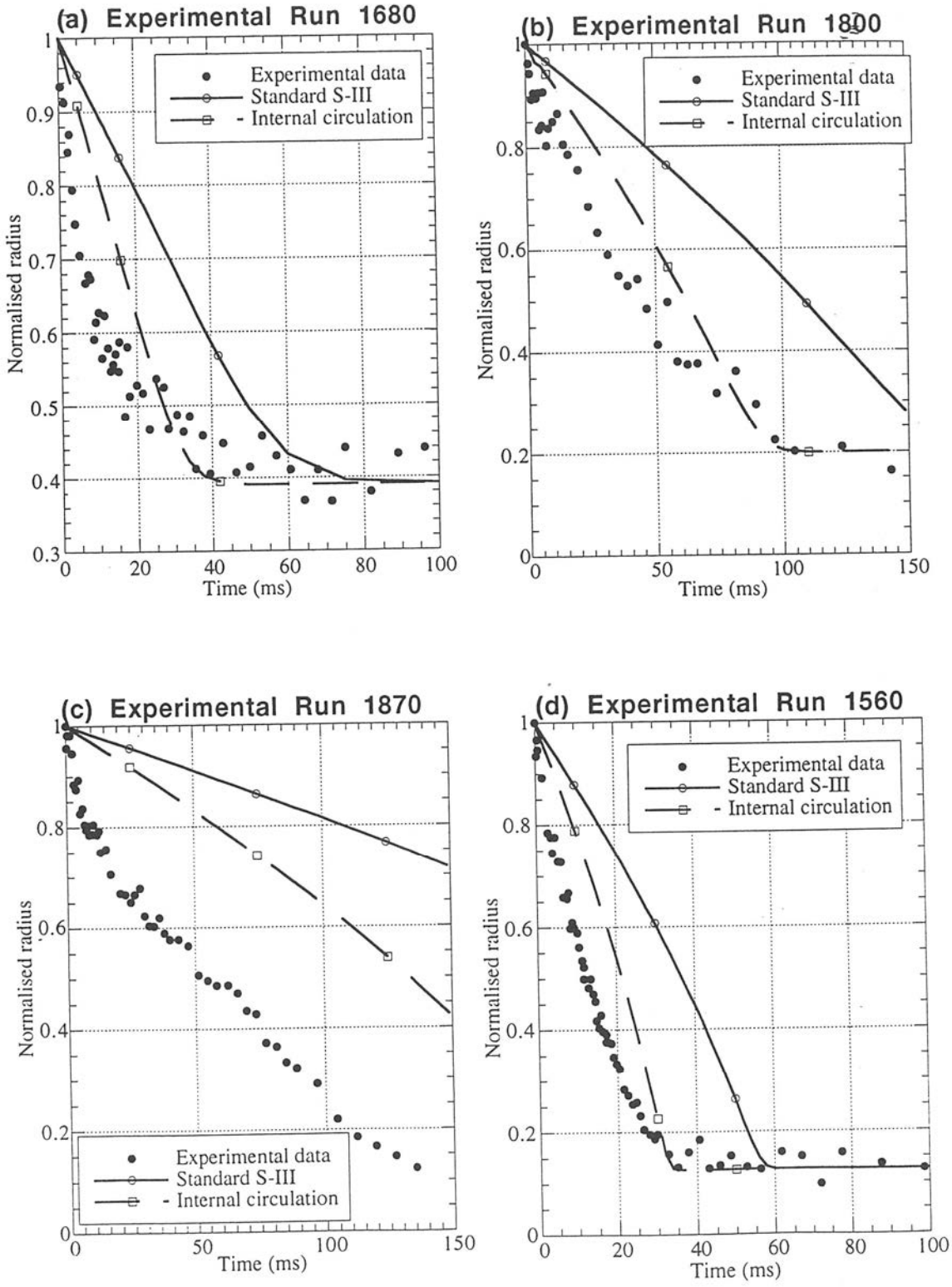

Fig. 5. Calculated collapse using a Nusselt number which takes account of circulation in the bubble.

Problem 5.4: Rapid fuel vaporization

"Rapid Fuel Vaporization"

W. Maschek, S. Kleinheins, C.D. Munz, E. Hesselschwerdt (FZK)

Outline of Case

During superprompt critical nuclear excursions the fuel is rapidly heated above its boiling point and vaporizes. The vapor pressure build-up leads to a material disassembly and to nuclear shutdown. If a significant superheating of the fuel could take place this shutdown could be delayed and the energy yield would be increased. Another mechanism which can lead to rapid material disassembly is the build-up of single phase pressures when the heated material expands and the void regions are eliminated.

The SIMMER-III Code is tested if it is capable to describe such rapid heating processes with material expansion and pressure build-up. Both theoretical considerations and experimental results from rapid vaporization tests (EEOS-12) serve as a basis for comparison.

1. Objectives of the Application

During superprompt critical nuclear excursions (e.g. caused by a recriticality) the fuel of an assembly is rapidly heated above its boiling point and vaporizes. The heating rates during such an excursion go up to a few 10^5 K/s. The vapor pressure build-up leads to an acceleration of the material and the material disassembly results into a rapid nuclear shutdown. If a significant transient superheating of the fuel could take place, the pressure build-up and the nuclear shutdown could be delayed and the energy yield of the excursion would increase. Another important mechanism which can lead to rapid material disassembly and nuclear shutdown during a nuclear excursion is the build-up of single phase pressures. Under the rapid heating the fuel expands and any void region in the material-configuration is eliminated. The SIMMER-III Code[1)] is tested if it is able to describe such rapid heating processes with pressure build-up. Both theoretical considerations[2)] and experimental results from rapid vaporization tests (equation of state experiment: EEOS-12)[3), 4)] serve as a basis for comparison.

2. Description of Experiments

In the case of a significant transient superheat the fuel vapor pressure build-up would be delayed leading also to a delay in the material disassembly process. This problem was addressed in a paper by Fischer and Maschek.[2)] In this investigation a bubble dynamics model was used to estimate the fuel superheat during an excursion for a heating rate of 400 K/ms. The results lead to the conclusion that superheat in the order of 20 K is to be expected, which is negligible in an excursion analysis. In-pile experiments by Reil and Breitung[3), 4)] showed no indication of any significant superheat and thus confirm in

a broad sense the results of Ref 2). A somewhat different situation arises when fission gas release builds up a significant pressure before the fuel vaporizes. This case occurs with irradiated fuel, and was studied in the "effective equation of state" (EEOS) series of in-pile experiments by Breitung and Wright.[5] The fission gas pressure is typically 2 to 3 MPa when the fuel reaches the liquidus point. A model for the interpretation of the EEOS experiments with irradiated fuel was developed by Fischer[6]; it is in part based on the bubble dynamics model of Ref. 2). The results of both theory and experiment are that in the initial part of the transient, the pressure is essentially determined by the fission gases. However, when the fuel reaches the boiling temperature determined by the inert gas pressure, rapid vaporization occurs, and tbe pressure then follows the fuel vapor pressure curve. It is, however, not the sum of inert gas and fuel vapor pressure.

3. Analytical Solution

None.

4. Understanding of Phenomena

Based on the experiments[5] and the analytical investigations[2] the phenomena are understood.

5. SIMMER-III Representation

Two types of SIMMER calculations were performed. In a first series of calculations vaporization into the vacuum was simulated. In a second series the evaporation into a gas atmosphere of 20 and 35 bar was simulated. In SIMMER-III the thermal expansion of fuel is treated. Thus any void space in a material probe with fixed boundaries is eliminated when the temperature increases and single phase pressures are built up. In the case of evaporating into a gas atmosphere the gas is additionally compressed during the heat-up process.

5.1 Geometry, Initial and Boundary Conditions

For the calculations a two cell geometry with rigid boundaries has been chosen with the initial liquid fuel temperature of 3100 K. The power of 8×10^8 W is deposited in a step like fashion during a time window of ~ 22 ms, a heating rate of 400 K/ms and 650 K/ms is reached in the fuel sample depending on the mass of the sample.

6. Results

6.1 Evaporation into Vacuum

By the calculations of evaporation into the vacuum the vapor equation of state should be checked and especially the resulting superheat during evaporation should be calculated.

In SIMMER-III the predicted superheat depends on the available void fraction as the available space determines the amount of fuel vapor needed to build up a certain pressure. With a higher initial void fraction

the superheat should therefore increase. In the calculations the initial void fraction is transiently reduced during the heat-up by fuel expansion.

For the current calculations two different fuel samples of the same size but with different void fractions of ~ 30% and 55% were assumed. The power input resulted in heating rates of ~ 420 K/ms and 650 K/ms, respectively.

The results of the evaporation calculations are displayed in Fig. 6.1 (pressure), Fig. 6.2 (fuel temperature), Fig. 6.3 (single phase pressure build-up) and Fig. 6.4 (superheat).

The calculations were performed with the default values of the interfacial area model, especially to mention the input quantities:

NMAX = 10^{11} (Maximum nucleation site density)

TAUNUC = 10^{-4} (Nucleation time constant)

CTHETA = 10^{5} (Coefficient in the exponenl of nucleation site density equation)

Those quantities could have a direct influence on the vaporization process.

In the Figs. 6.1 and 6.2 the pressure and temperature traces during the fuel heatup are given for both void fraction cases. With the lower void fraction the thermal expansion of the fuel leads to a rapid pressure increase by the build-up of single phase pressures after ~ 11 ms (Fig. 6.3). For the higher void fraction no single phase conditions are reached under the given conditions. The superheat developed during the excursion is displayed in Fig. 6.4 for the higher void case and shows that a superheat of approximately 30 K is calculated. The superheat is rather constant over the temperature range. This value is in quite good agreement with the predictions given by Ref. 2) where for a 400 K/s temperature ramp a superheat of 20 K is given. When calculating the saturation temperature $T_{sat} = T_{sat}(P_{sat})$ and when comparing with the relation $P_{sat} = P_{sat}(T_{sat})$ it was noted that the fit of the T_{sat} curve shows some deviations when comparing with the P_{sat} curve of up to 2%. This translates into a temperature deviation of 10 - 15 K. The above results concerning the superheat must be seen under this uncertainty range.

To check the sensitivity of the evaporation model with relation to the parameters NMAX, TAUNUC and CTHETA, the parameters were chosen as NMAX = 10^{12}, TAUNUC = 10^{-6} and CTHETA = 5000. The calculations revealed that only a negligible influence .is exerted. by these parameters in the tested .range. In an additional calculation the maximum bubble size was reduced from 10^{-3} to 10^{-6} m thus directly increasing the surface area. As expected in this case the superheat was reduced to approximately 2 K.

In conclusion one can state that the superheat is calculated in good agreement with the theoretical results of Fischer and Maschek[2] and also with the experimental evidence.

When heating up the fuel the liquid expands as is shown in Fig. 6.5. The extrapolation of the Drotning[7] data was suggested in Ref. 9):

$$\rho(T) = 8860 - 0.916(T - 3120)$$

This relation is formulated in SIMMER-III in terms of the specific volume.

6.2 Evaporation into an Inert Gas Atmosphere

In these calculations the fuel cells were pressurized with an inert gas with 20×10^5 Pa and 35×10^5 Pa at the liquidus point. Again the default values in the IFA (interfadal area) model were used for the calculations. With respect to the initial conditions and the heating rate, the calculations performed can be compared to the experiment EEOS-12 with irradiated fuel. [6), 8)] The measured pressure trace and the analysis from Ref. 6) (shaded area) are shown in Fig. 6.6. The important result is that the pressure buildup in the early part of the transient is essentially (but not completely) determined by the fission gas pressure, until the fuel starts boiling. Then, the pressure follows the vapor pressure curve of the fresh fuel.

Thus under the rapid heating conditions of the experiment, the total pressure over irradiated (U, Pu) oxide is controlled by a suppression mechanism. At any given temperature, the fission gas components suppress fuel boiling if their pressure P_{gas} is higher than the fresh fuel saturation vapor pressure P_{sat} of unirradiated fuel. If P_{sat} exceeds P_{gas}, the total pressure is, to a first approximation, equal to P_{sat}. Under the millisecond heating in the experiment, the total pressure from irradiated fuel may be taken as P_{tot} = max (P_{gas}, P_{sat}). In the EEOS-12 experiment the boiling point was reached at approximately 5150 K. The pressure then follows the vapor pressure curve.

The SIMMER-III calculated pressure-temperature dependency is plotted into the experimental pressure trace of Fig. 6.6. As can be seen the exact experimental pressure development is not fully reproduced by SIMMER-III. In the early part of the transient up to the boiling point, SIMMER-III can partly calculate the pressure increase with its thermal expansion model. When boiling is reached at 5150 K the calculated pressure is higher by approx. 40% compared to the experimental value. The difference in the pressure development between evaporation into vacuum and against a pressurized gas, as calculated by SIMMER-III can be seen in Fig. 6.7. The pressure is higher when fill gas is available because SIMMER-III considers the gas pressure and the fuel vapor pressure as partial pressures and adds them. In Fig. 6.8 and Fig. 6.9 the pressure and temperature traces are given for the evaporation into a pressurized gas atmosphere. The pressure increases slowly at the start of the power transient which is caused by a compression of the inert gas.

That the SIMMER-III results do not fully agree with the experimental results is not surprising, as the SIMMER-III code has not a detailed bubble dynamics model. In SIMMER-III the gas and vapors present in a cell are in the same bubble population, and the pressure is the sum of the partial pressures. In the early part of the transient the gas temperature in the calculations lags considerably behind the liquid fuel temperature (~ 300 K) because the large bubbles in the liquid are at rest. The heat transfer area is small and therefore the thermodynamic pressure increase due to temperature rise is not well predicted. In addition

SIMMER-III produces very little vapor below the boiling point. According to the bubble dynamics and mass transfer model in Ref. 2) nearly half of the pressure in the gas bubbles at the boiling point is due to fuel vapor.

Finally the influence of the time step size was investigated. For the calculation with 20 bars of fission gas pressure the timestep was reduced by a factor of 10. As can be seen in Fig 6.10 the influence of time step size is marginal. Thus, one can conclude that SIMMER-III simulation shows some deviations in the early part of the transient, but they can be explained by the limitations of SIMMER-III modeling. In the later part, SIMMER-III agrees well with the experiment.

7. Conclusions

The SIMMER-III code describes rapid vaporization processes with sufficient accuracy. The superheat which drives the evaporation process is calculated in good agreement with theory and experiment.

8. Recommendations

When recalculating the EEOS-12 experiment (evaporation against a fission gas pressure) the early pressure increase up to fuel boiling cannot be recalculated fully satisfactorily. A more detailed bubble dynamics model e. g. discerning between gas and vapor bubbles would be necessary to match the detailed features of the EEOS-12 experiment. Such a model is however beyond the scope of the code and might not be of importance when using the code for accident simulations.

9. References

1) Sa. Kondo, Y. Tobita, K. Morita, N. Shirakawa: SIMMER-III: An Advanced Computer Program for LMFBR Severe Accident Analysis; ANP'92, Vol. IV, 40-5, Oct. 1992, Tokyo.

2) E. A. Fischer, W. Maschek: The Role of Vapor Bubble Dynamics during Energetic Power Excursions in Fast Reactor Core Disruptive Accidents; Nucl. Technol. 71, pp.173-186 (1985).

3) W. Breitung, K. O. Reil: Vapor Pressure Measurements on Liquid Uranium Oxide and (U, Pu) mixed Oxide; Nucl. Sci. Eng. 101, pp.26-40 (1989).

4) W. Breitung, K. O. Reil: The Density and Compressibility of Liquid (U, Pu) - Mixed Oxide; Nucl. Sci. Eng. 105, pp.205-217 (1990).

5) W. Breitung, S. A. Wright: Measurements of the Total Pressure from Irradiated (U, Pu) - Mixed Oxide; Nucl. Sci. Eng.105, pp.303-318 (1990).

6) E. A. Fischer: A Model for an Effective Equation of State for Irradiated Fast Reactor Fuel; Nucl. Technol. 98, pp.100-112 (1992).

7) W. D. Drotning: Thermal Expansion of Molten Uranium Dioxide Proc. 8th Symp. Thermophysical Properties Gaithersburg, Maryland; June 15 - 18, 1981; National Bureau of Standards (1981).

8) W. Breitung: Analysis of Measured Total Pressures from Irradiated Solid and Liquid (U, Pu) - Mixed Oxide; Nucl. Sci. Eng. 108, pp.1-15 (1991).

9) E.A. Fischer: A New Evaluation of the Urania Equation of State Based on Recent Vapor Pressure Measurements; Nucl. Sci. Eng. 101, pp.97-116 (1989).

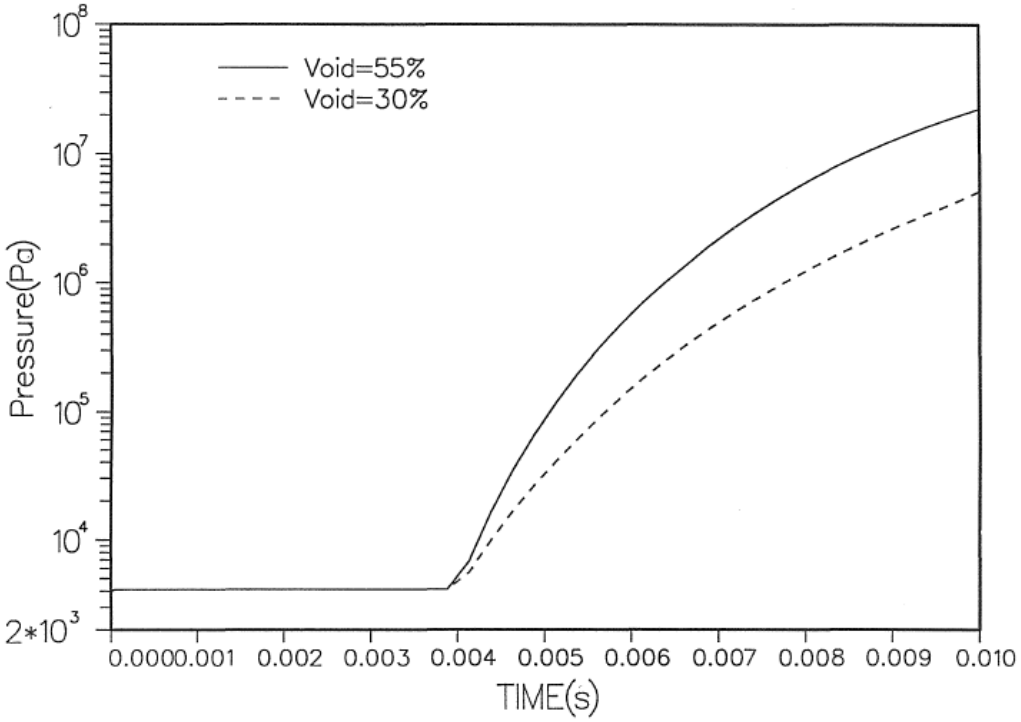

Fig. 6.1. Pressure development of the rapid vaporization test into vacuum for material void fractions of 30% and 50%.

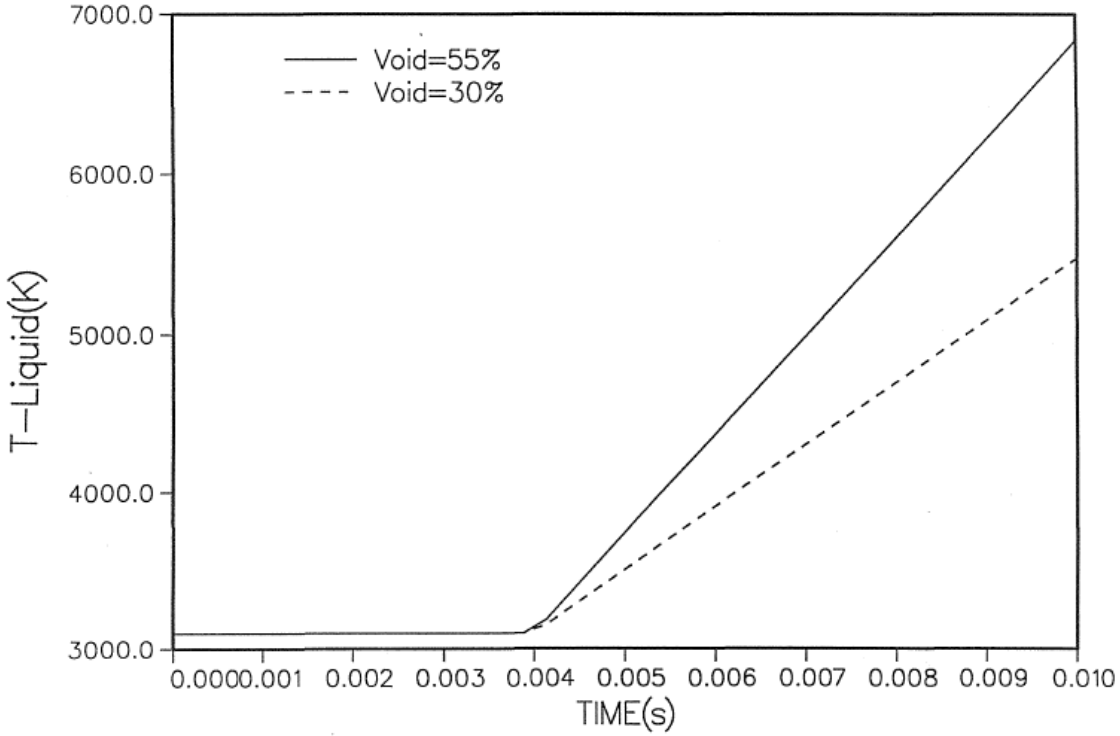

Fig. 6.2. Fuel Temperature development of the rapid vaporization test into vacuum for material void fractions of 30% and 55%.

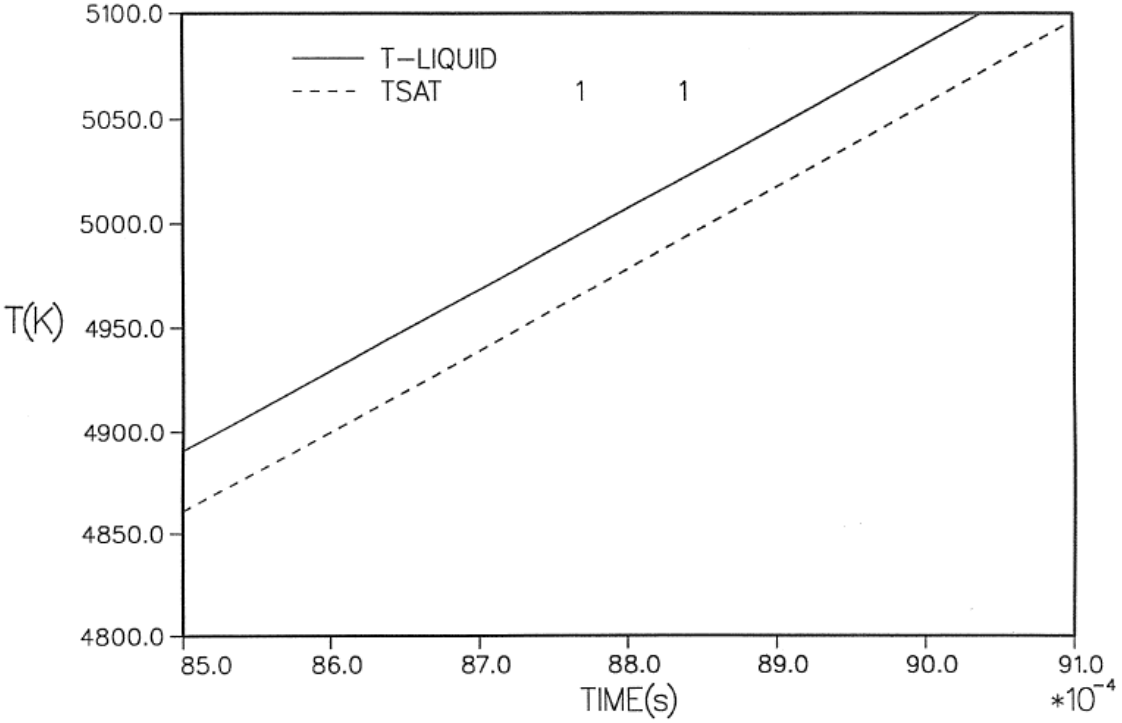

Fig. 6.3. Superheat: Liquid fuel temperature and saturation temperature development of the rapid vaporization test for material void fraction of 55%.

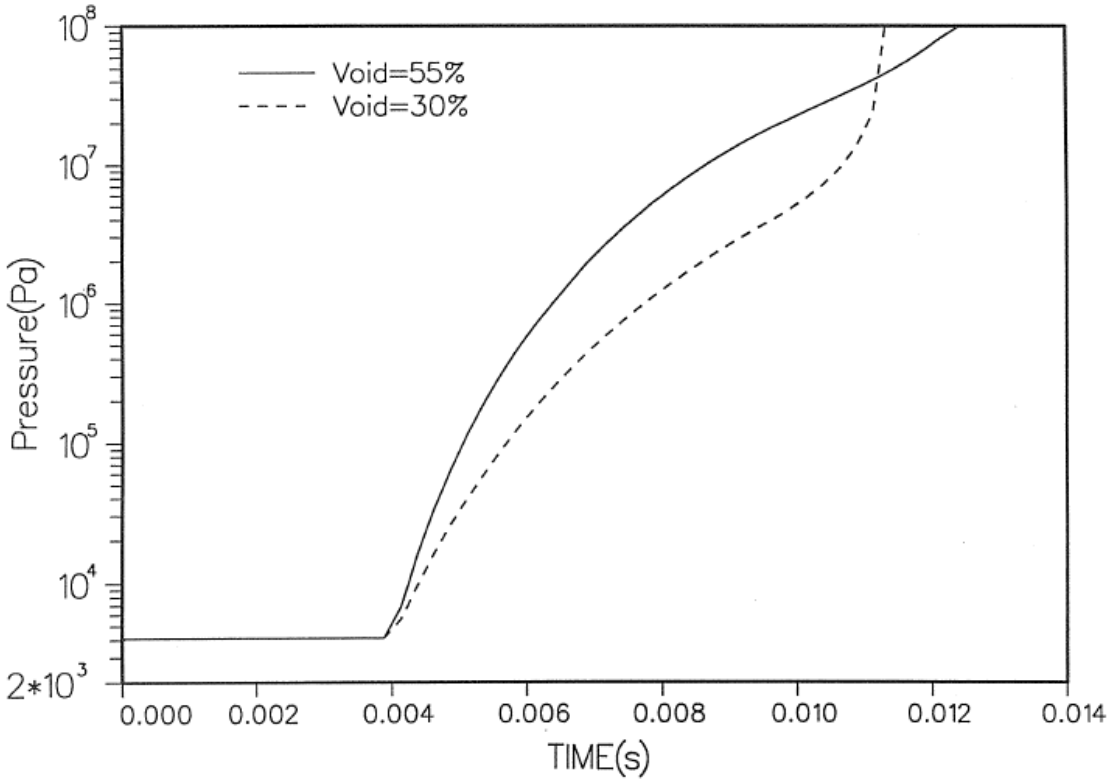

Fig. 6.4. Build-up of single-phase pressures in the 30% void fraction case.

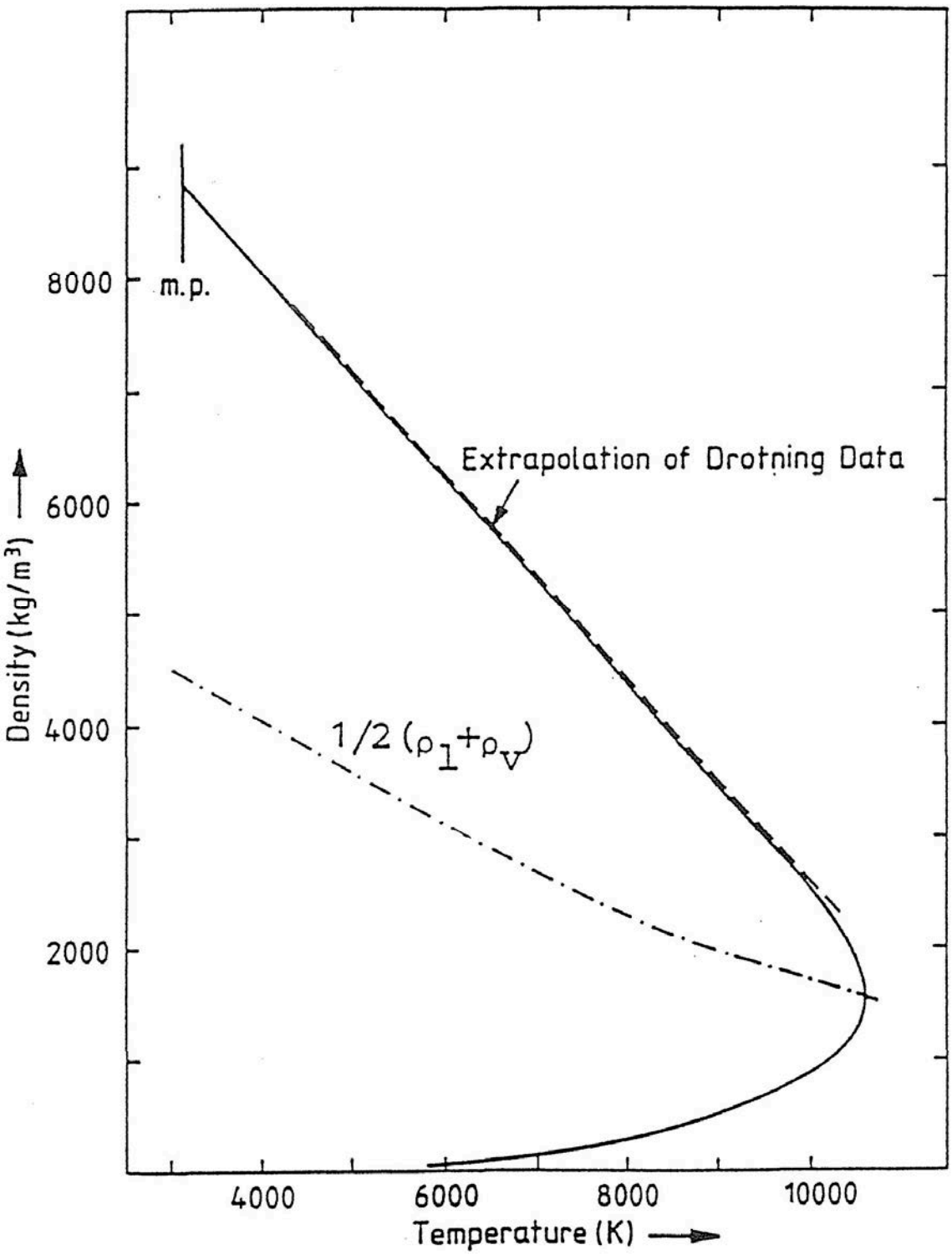

Fig. 6.5. Density of the saturated liquid and vapor.

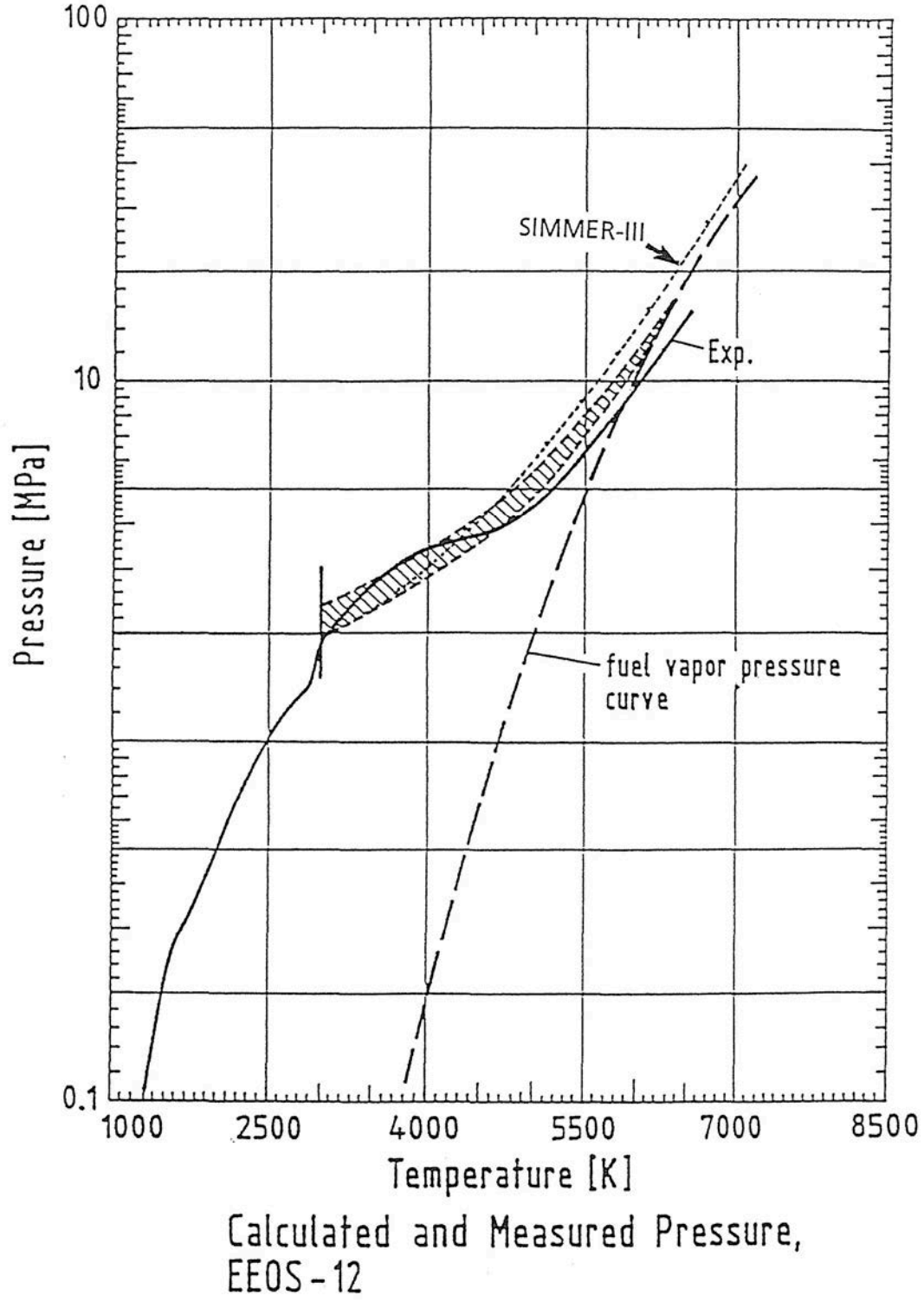

Fig. 6.6. Calculated and measured pressure of the EEOS-12 experiment.

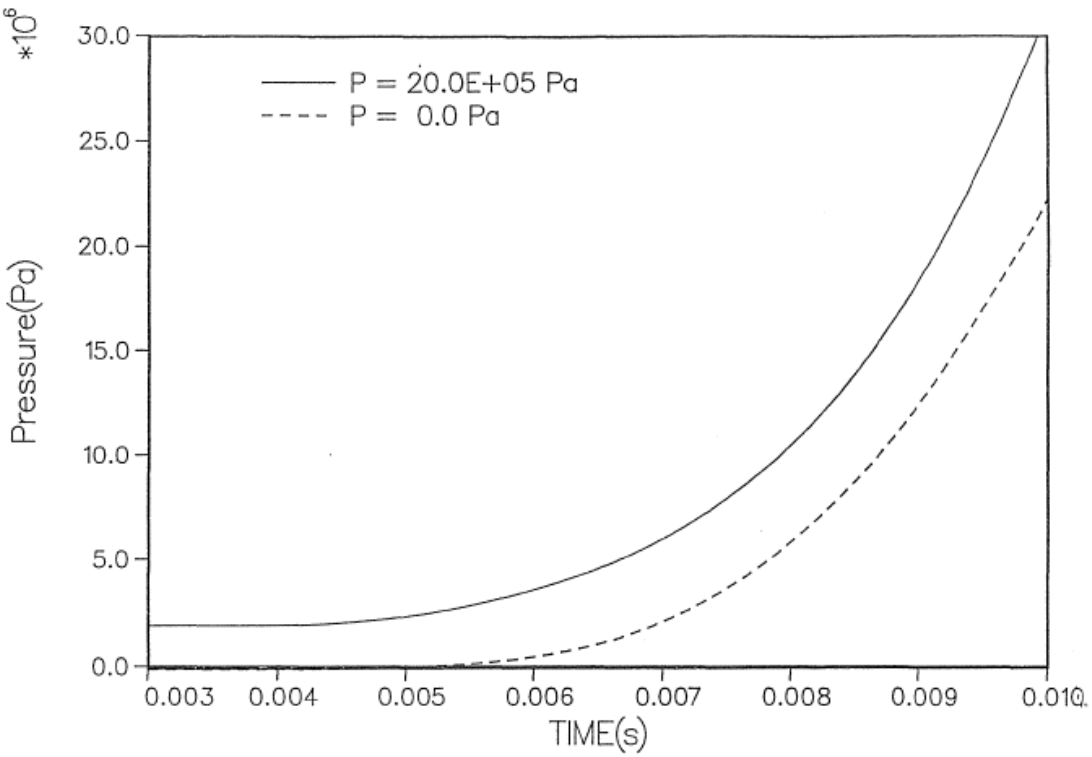

Fig. 6.7. Difference in pressure development between evaporation into vacuum and against a pressurized gas.

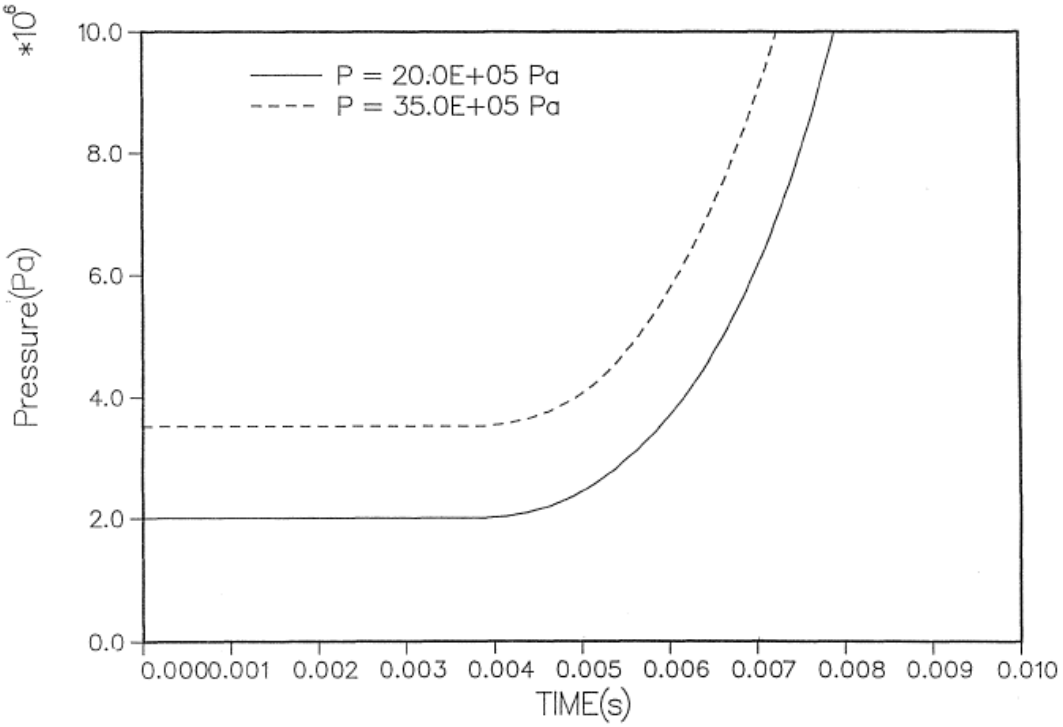

Fig. 6.8. Pressure development of the rapid vaporization test against a pressurized gas (2 and 3.5 MPa initial fission gas pressure).

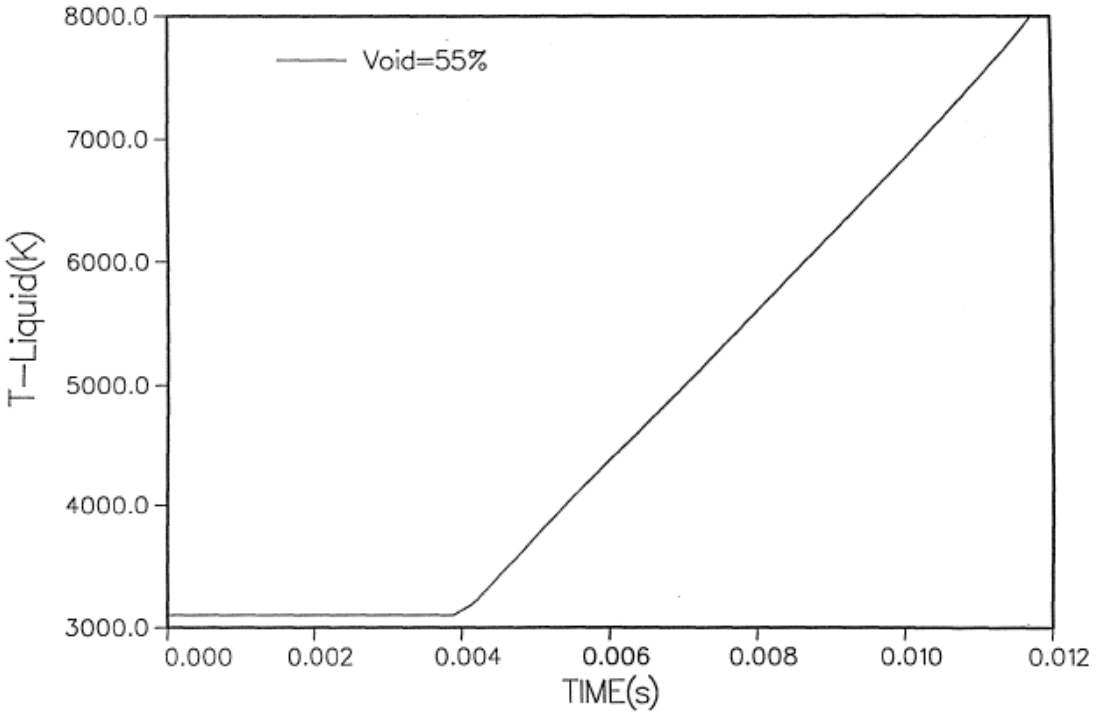

Fig. 6.9. Temperature development of the rapid vaporization test against a pressurized gas (2 and 3.5 MPa initial fission gas pressure).

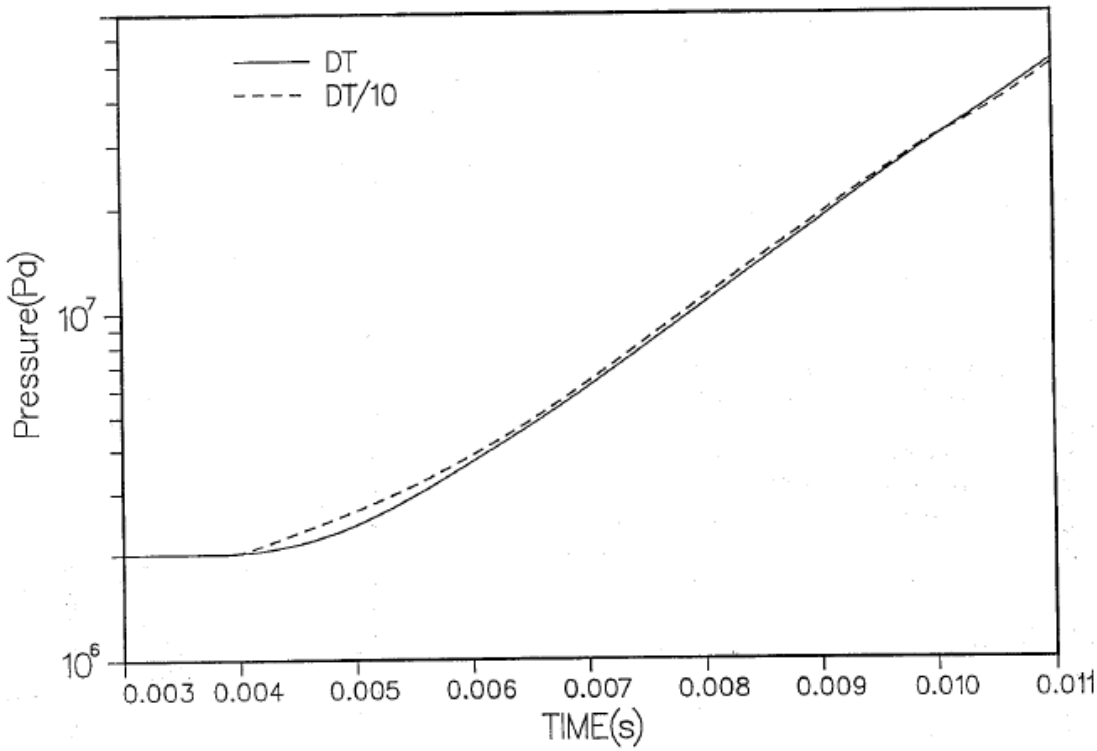

Fig. 6.10. Influence of time step size on the evaporation calculation.

Problem 5.5: Boiling in a pipe

"Boiling in Pipe"

Yoshiharu TOBITA (PNC)

Outline of the Case

This case is EPRI Numerical Benchmark Test 1.3. Saturated water enters a duct of uniform rectangular cross-section. The first quarter of its length is unheated, but heat is supplied to the remainder of the pipe at a fixed rate, causing boiling, and a consequent acceleration of both liquid and vapor.

1. Objectives of the Application

This application is aiming to test the numerical algorithm in predicting the acceleration of two phase flow by its own boiling. Since the momentum exchange function (MXF) between vapor and liquid is given as the analytical condition, this application does not provide a test of the interfacial area and MXF model.

2. Description of the problem

This case is EPRI Numerical Benchmark Test 1.3.[1)] Saturated water enters a duct of uniform rectangular cross-section. The first quarter of its length is unheated, but heat is supplied to the remainder of the pipe at a fixed rate, causing boiling, and a consequent acceleration of both liquid and vapor. Three cases are considered:

(1) in the first, the influence of gravity is totally neglected;
(2) in the second, the duct is vertical, with flow from bottom to top, and the effect of gravity is accounted for;
(3) in the third, the pipe is horizontal, and the effect of gravity is again taken into account.

The task is to predict the distributions of steam and water velocities and enthalpies, of pressure and of volume fraction, along the pipe. Special interest attaches to comparisons between the three cases. The third case was not analyzed in this study because Cartesian coordinate option had not been available at the time when this study was performed.

In order that attention can be concentrated upon other matters, the thermodynamic and other properties of the liquid and vapor are to be represented in an idealized manner. Specifically:

- the densities ρ_1 and ρ_2 are taken as 1.0 and 1.0×10^3 kg/m^3;
- the saturation enthalpies of the two fluid are regarded as independent of pressure and as therefore having constant values, namely 2.5×10^6 and 4.0×10^5 J/kg;
- the effects of viscosity and thermal conductivity, other than those introduced indirectly by way of the constitutive models (see below), are to be neglected.

Inter-phase friction is supposed to obey the law:

$$f_{12} = c\alpha_1\alpha_2\rho_2(u_2 - u_1) \quad (1)$$

where f_{12} is the force per unit volume of space exerted by phase 2 on phase 1, the value of c to be used is 50.0. Inter-phase heat transfer is to be calculated from the presumption that the phase-to-interface heat-transfer rates are equal to the corresponding enthalpy differences times $c_1 c\alpha_1\alpha_2$, and c_1 is equal to 0.01 for the vapor-to-interface transfer and to 1.0 for the liquid-to-interface transfer. The interface enthalpies are taken to have the saturation values of the phase in question.

The inter-phase mass-transfer rate is to be deduced from a heat balance over the interface, the net heat transfer being balanced by the enthalpy increase experienced by the vaporizing water.

3. Analytical Solution

None.

4. Understanding of Phenomena

Although no experimental data is available, several computer codes were applied to this problem. Despite its apparent simplicity, the differences between each code were not small. For the case of no gravity, the void fraction and vapor velocity is deduced by simple energy balance consideration by Spalding.[1] The void fraction at outlet is estimated to be 0.833 and outlet velocity 0.0501 m/1s, and the acceleration pressure loss 0.496 Pa.

5. SIMMER-III Representation

5.1 Geometry, Initial and Boundary Conditions for a Reference Case

A one-dimensional mesh was used, with 100 axial meshes as recommended by the benchmarking specification. Because the flow is in steady-state, initial conditions are not part of the problem specification. Since SIMMER-III only analyzes the transient phenomena, the calculation was started from the situation that the pipe was filled with single phase water. At the inlet to the duct, water is supplied at the mass rate of 10.0 kg/m^2/s, with a momentum per unit mass of 0.01 m/s. At the outlet from the duct, the pressure is at the reference value; this may be set to zero or at arbitrary pressure, because the absolute value of pressure has no influence upon the calculation whatsoever. The heat transfer from the pipe wall is to be presumed to enter the liquid only, at the rate of 0.5 J/kg/s; this occurs for the range $0.25 < z < 1.0$ m. In SIMMER-III representation, this heat input is supplied as volumetric heat generation per unit mass.

In the present calculations, the SAEOS model was used to evaluate the physical properties of vapor and liquid. The constant values of vapor density and saturated enthalpies of vapor and liquid cannot be reproduced by the SAEOS model. However the latent heat of vaporization was adjusted so as to be a

constant value, 2.1 MJ/kg, which is the difference between the saturated vapor and liquid enthalpies designated in the problem.

5.2 Code :Modifications

In order to realize the specifications on the material properties and constitutive models noted in section 3, some parts of the code were modified.

6. Results

The calculated pressure, void fraction, and velocity distribution is plotted for case 1 and case 2 in Figs. 1 – 8. Each case will be discussed in tum. In both cases the location at which the vaporization starts shifted slightly to downstream by 0.05 m. This is because the inlet temperature is slightly lower than the saturation temperature at the local hydrostatic pressure at 0.25 m. Though it is possible to set the boiling point to 0.25 m exactly by performing try-and-error procedure in selecting the inlet temperature, we can put up with this discrepancy because it does not affect the calculated results greatly and the try-and-error process requires enormous computer resources because the number of meshes used in this study is rather large.

Case 1. No gravity

The differences of velocity between the phases are small in this case, for the friction constant specified. The velocities calculated by SIMMER-III are in agreement with the ones by IMPI as shown in Figs. 5 and 7. The predicted void fraction distribution agreed with IMPI and PHOENICS, the pressure distribution is also close to SABENA and MINCS. However, SIMMER-III calculated the pressure gradient from the pipe inlet to 0.25 m where no velocity increase is calculated and hence the pressure must be kept constant. The cause of this problem is not clear for the moment. One explanation is the numerical precision is not enough to resolve the small pressure difference around 0.5 Pa because the system pressure in this study is set to 0.1 MPa to prevent the water boiling.

Case 2. Longitudinal gravity

The influence of gravity along the duct ensures that SIMMER-III agrees with the other codes with regard to pressure distribution (Fig. 2), no doubt because the hydrostatic influence dominates. The predicted void fraction is in agreement with MINCS. The vapor velocity distribution is in good agreement with PHOENICS and SABENA. The liquid velocity predicted by SIMMER-III is consistent with the one by PHOENICS and MINCS.

7. Conclusions

SIMMER-III has been used to simulate a boiling in a pipe flow with volumetric heating. The calculated distribution of pressure, velocities and void fraction agreed with the other codes. The self-consistency between energy deposition, fluid acceleration, and pressure loss was checked throughout the

comparison with PHOENICS code and this proved the validity of basic numerical algorithm of SIMMER-III.

8. References

1) D. B. Spalding et al., “Problem specification and collated solutions of the two-phase numerical-benchmark experience 1986-7”, DOE/EPRI Second International Workshop on Two-Phase Flow Fundamentals, 16-20 March, 1987, Troy, New York.

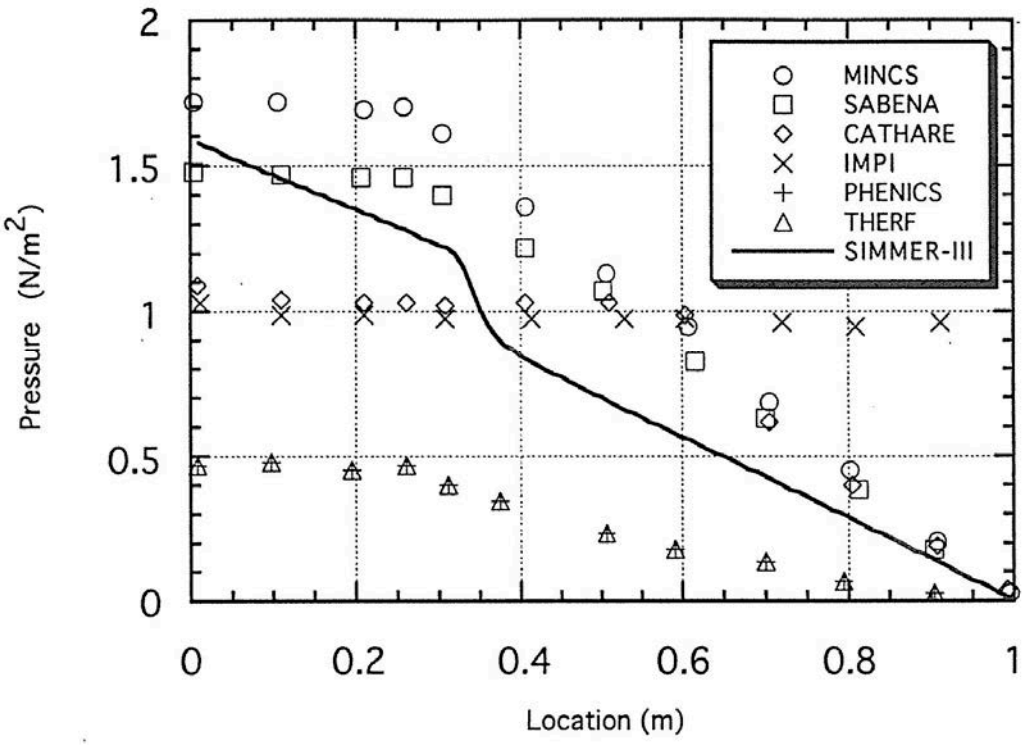

Fig. 1. Pressure distribution for case 1.

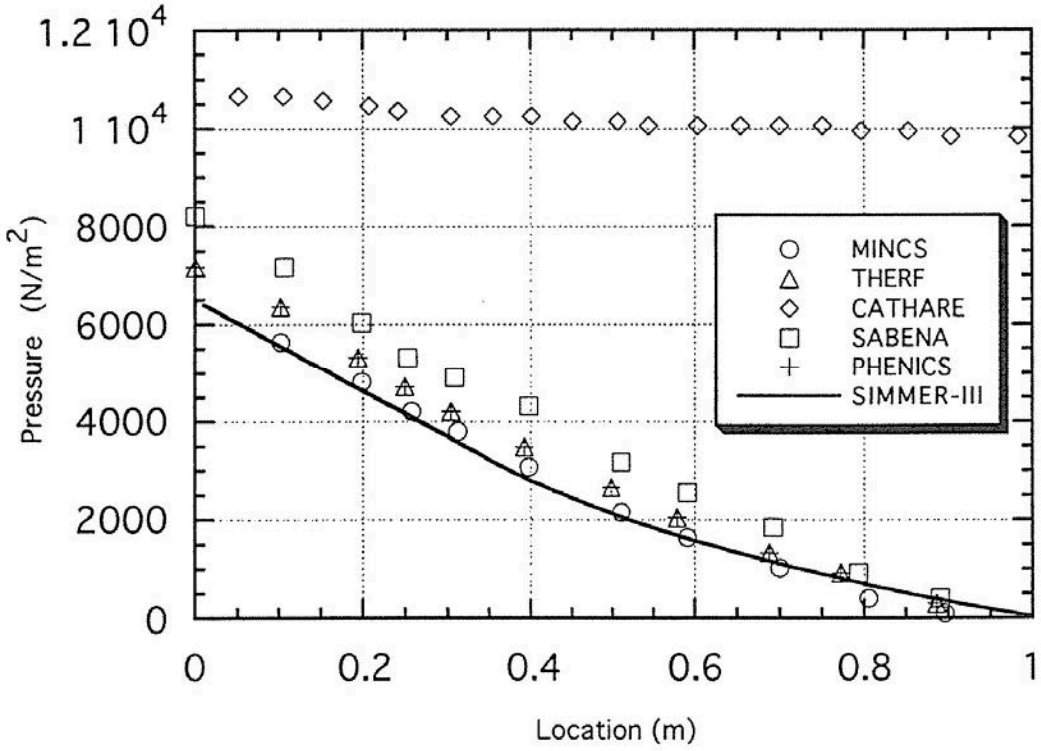

Fig. 2. Pressure distribution for case 2.

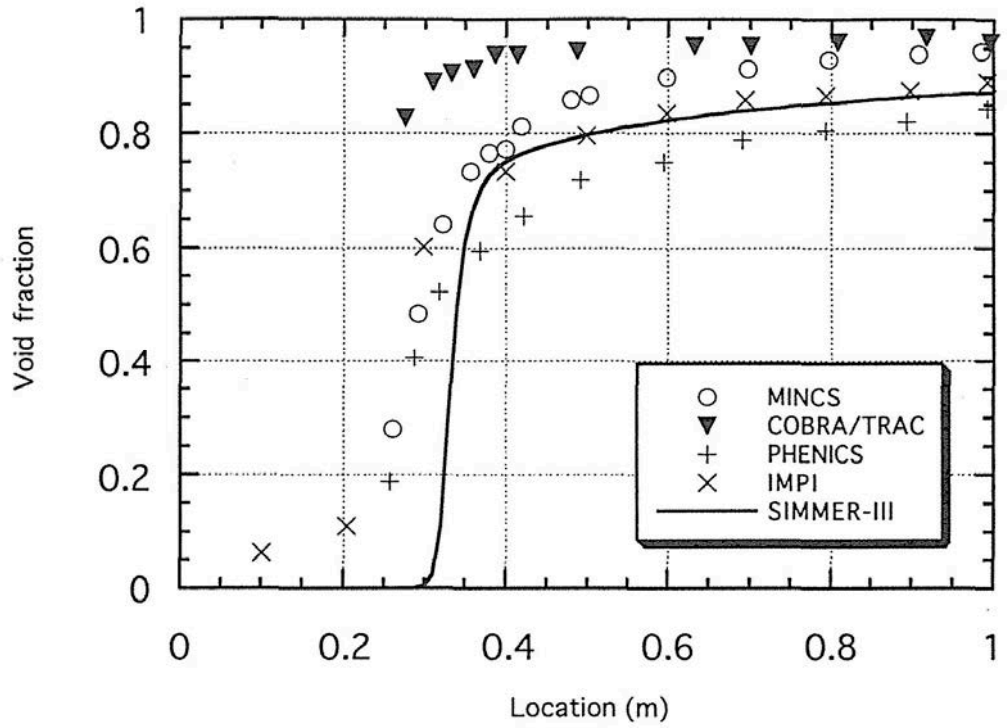

Fig. 3. Void fraction distribution for case 1 (the results of THERF, CATHARE, and SABENA are almost identical to that of PHEONICS).

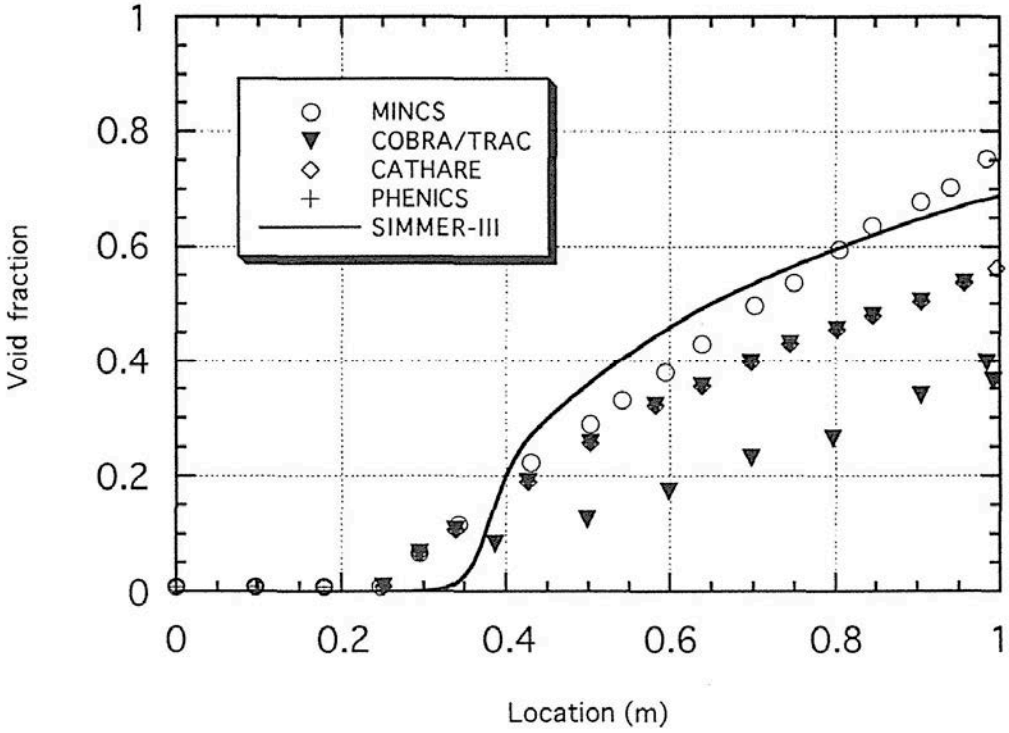

Fig. 4. Void fraction distribution for case 2. (the result of THERF is almost identical to PHEONICS and the result of SABENA is not available).

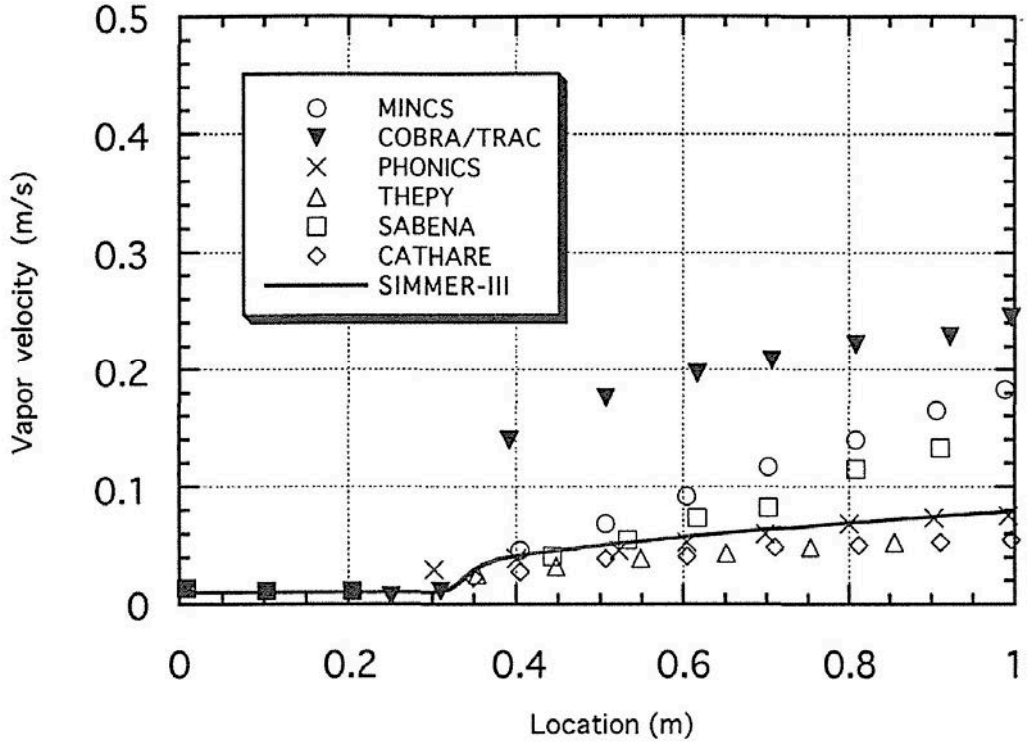

Fig. 5. Vapor velocity distribution for case 1. (the result of IMPI is almost identical to PHEONICS).

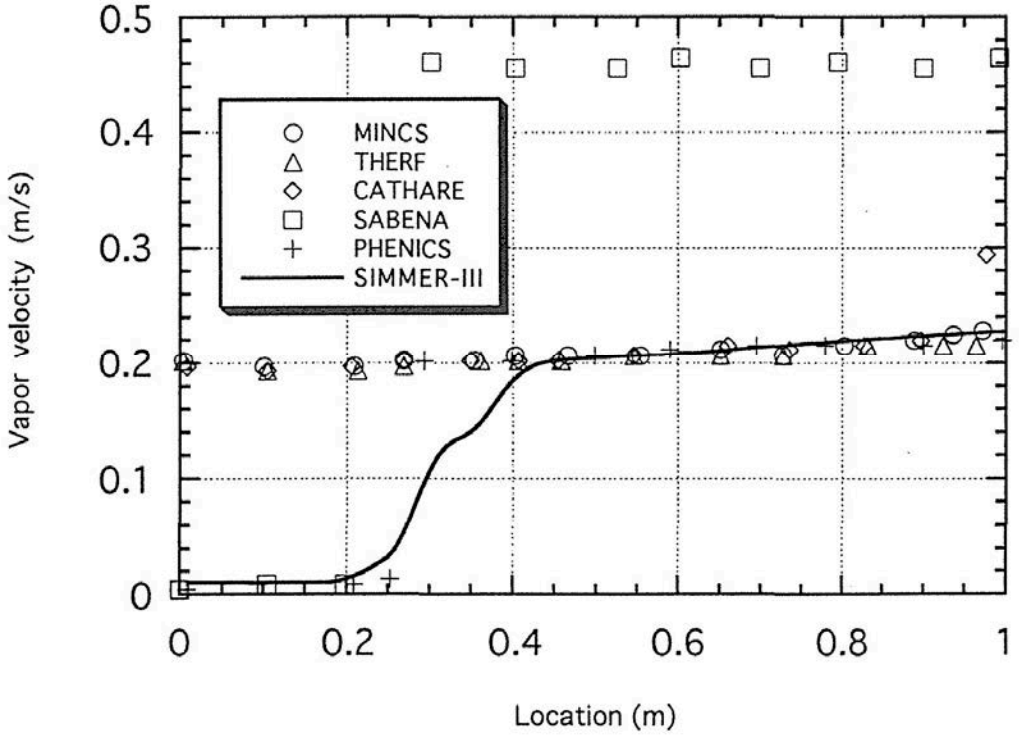

Fig. 6. Vapor velocity distribution for case 2.

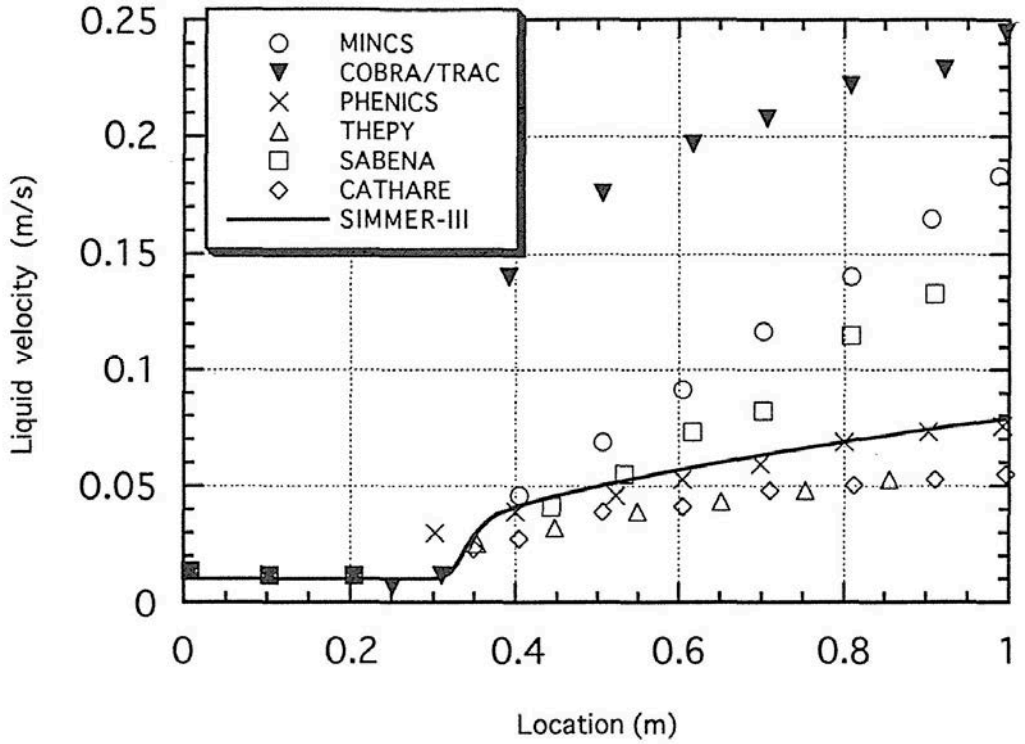

Fig. 7. Liquid velocity distribution for case 1 (the result of IMPI is almost identical to PHEONICS).

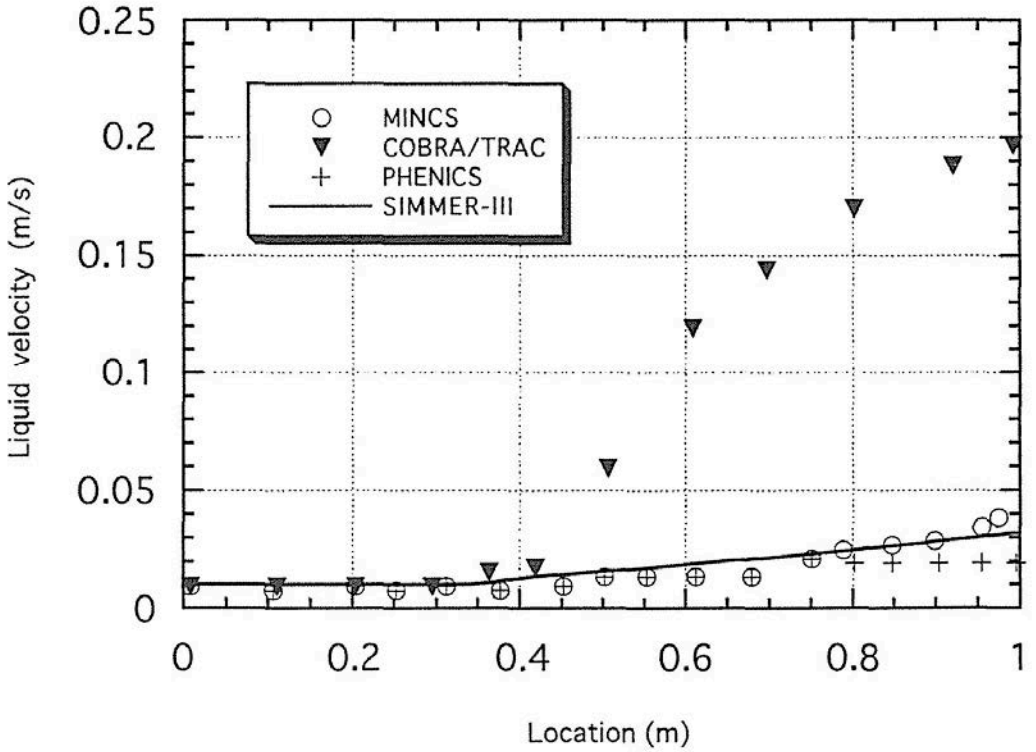

Fig. 8. Liquid velocity distribution for case 2 (the results of THERF, CATHARE, and SABENA are almost identical to that of PHEONICS).

Problem 5.6: Vapor condensation on structure

"Condensation of Vapor on Cold Structures"

Dirk Wilhelm and Fabien Boulanger (CEA-G)

Outline of the Case

In EXCOBULLE I-ter experiments, a mass of water is suddenly vaporized in the center of a cold steel box. It then condenses at the wall. The pressure transient is recorded at the wall. The calculation of this test allows to check the condensation models at walls in the code.

1. Objectives of the Application

This exercise was initiated to study the effect of condensation on structures. This effect may have been a reason for the discrepancies of heat fluxes in the cover gas region of the SEBULON experiment calculations, which is reported in Problem 5.7.

The present exercise is to recalculate two EXCOBULLE I-ter experiments in which the main expansion volume is either void or filled with a non condensable gas.[1)]

2. Description of the Experiment

The EXCOBULLE I-ter experiment consists of a cubic steel box with an open volume of 1.3×10^{-3} m^3 and with a wall at room temperature. In the center of the box, a glass sphere containing 15 cm^3 of water at 140°C and 3.7×10^5 Pa is broken at time zero to release the water which evaporates rapidly. Consequently, the water vapor condenses at the cold steel wall.

During the first 100 ms, a pressure transducer, mounted into the lateral wall, records the transient. The pressure rises shortly after the rupture of the glass sphere, and the gradually decreases, to small values if there is no non condensable gas present, to larger values if there is.

3. Analytical Solution

This basic problem is a test case for multiphase codes. A specific analytical model using the kinetic theory of condensation can be found in Ref. 1).

4. Understanding of Phenomena

The condensation rates during such an expansion with non condensable gas cannot be described by standard theory derived from the Nusselt model for liquid metals. The resistance due to the presence of non condensable gases must be expressed by the vapor diffusion through the layer of gases which accumulates at the interface.

5. SIMMER-III Representation

5.1 Geometry, Initial and Boundary Conditions

A 2-D mesh in Cartesian co-ordinates was used, as illustrated in Fig. 1. The volume inside the glass sphere is cell (1,4) in the very center. The calculations were only possible·because the single phase water which was originally confined to cell (1,4) was distributed over two cells, (1,4) and (2,4) which resulted in two-phase conditions at time zero. The initial pressure in the water cell is 3.719×10^{5} Pa by the EOS of the code. The initial code water mass is 1.614×10^{-2} kg which is larger than the 14 g water of the experiment.

5.2 Parametric Cases

Two cases were recalculated: first with non condensable gas in the box, second without. Two differencing schemes were tested.

6. Results

6.1 Case with non condensable gas

The non condensable gas pressure is set at an initial partial pressure of 0.15 bar. It was run both on higher order differencing and on donor cell differencing. Figure 2 shows a comparison of experimental pressures with the S-III result using donor-cell differencing. Higher order differencing produces a higher peak at 2 ms, the rest of the transient being very similar.

The results show that the terminal pressure is too small. The code overestimates condensation at the presence of an inert gas. This finding is conservative and should be regarded as appropriate.

6.2 Case without non condensable gas

The experimental gas pressure in the void was initially 0.1 Pa. Because of EOS limitations, this pressure had to be raised to 1000 Pa. Figure 3 shows a comparison of experimental pressures with the S-III result. The pressure peak in the beginning is calculated well, the pressure drop is slightly too fast, the terminal pressure is good. The code represents the condensation under void well.

7. Conclusions

The code overestimates condensation at the presence of an inert gas, but this is conservative and shoold be regarded as appropriate. The code represents the condensation under void well.

The recalculations of the EXCOBULLE I-ter experiments showed reasonable agreement between experimental and code pressures. This implies that rapid condensation is being modeled correctly for transients lasting several hundred milliseconds at small vapor densities.

8. Recommendations for Model Improvement

None.

9. References

1) G. Berthoud: Etudes des phenomenes de recondensation d'un fluide diphasique chaud en presence de gaz incondensables, Report CEA-R-5229, CEN/Grenoble, 1983

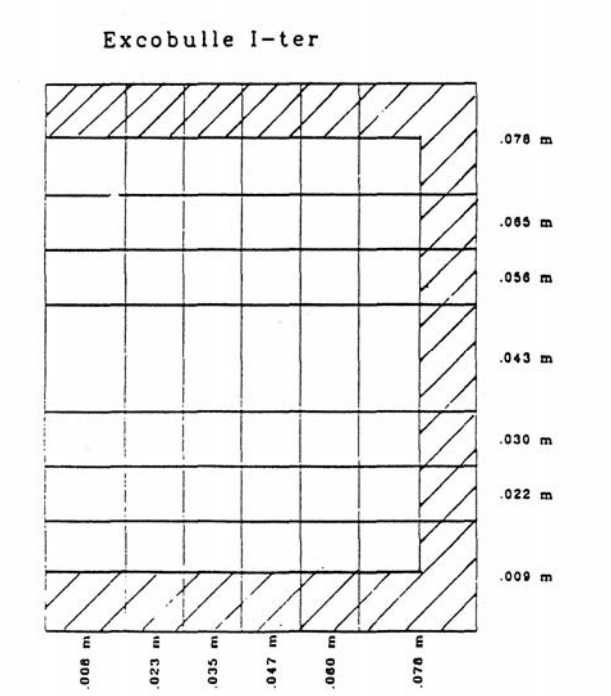

Fig. 1. Mesh cell set of Excobulle I-ter.

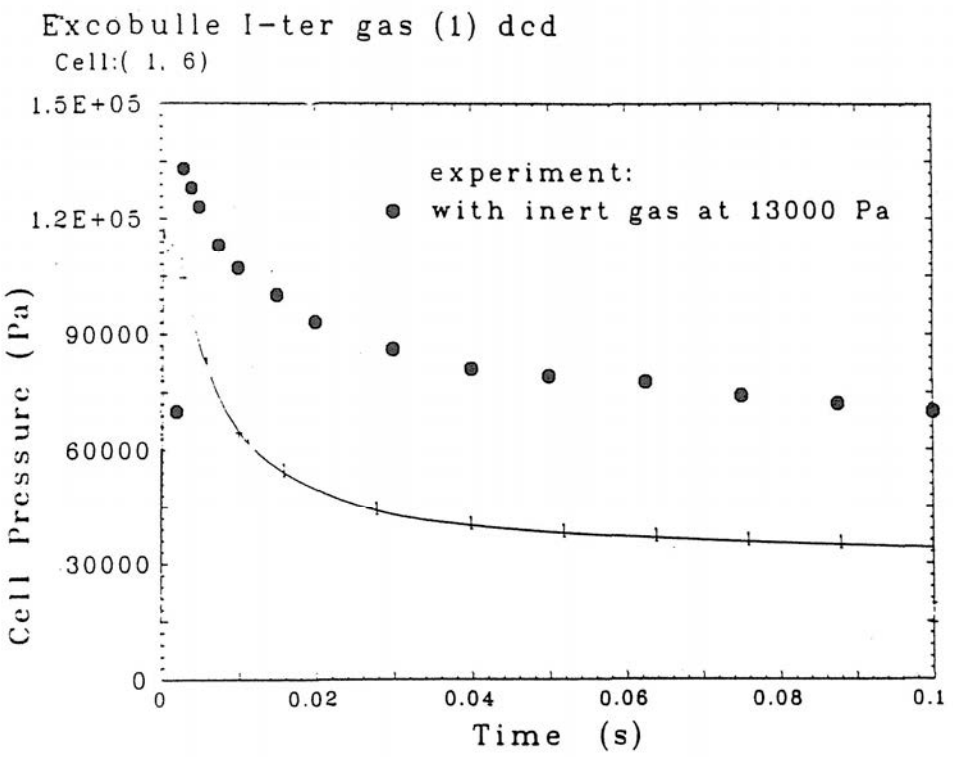

Fig. 2. S-III pressures - Excobulle I-ter with non condensable gas.

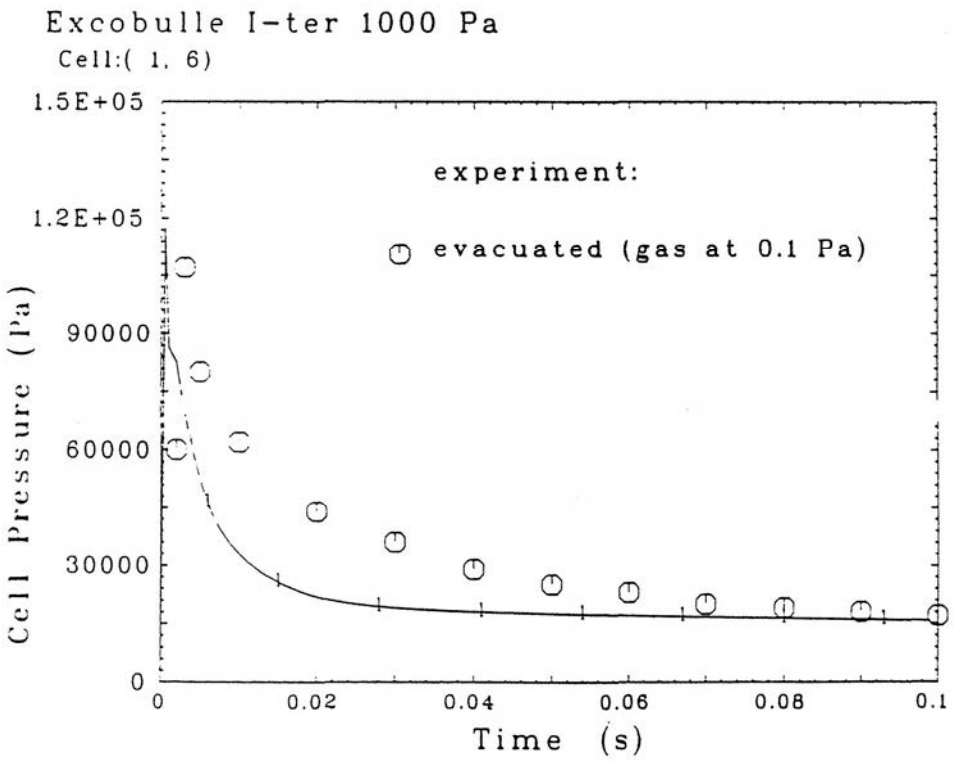

Fig. 3. S-III pressures - Excobulle I-ter without non condensable gas.

Problem 5.7: Boiling pool with wall heat transfer

"Boiling Pools with Heat Transfer to the Wall"

Dirk Wilhelm and Fabien Boulanger (CEA-G)

Outline of the Case

A UO_2 molten pool is simulated by a 2-D water pool in a laterally cooled steel box. The lateral heat fluxes are measured and the pool dynamics is visualized. A steady volumetric power is injected and the pool response is recorded. Large efforts has been devoted to analyze those experiments. They are a relevant situation to check the ability of codes to describe the complex situation encountered in boiling pool configuration.

1. Objectives of the Application

The behaviour of a boiling pool of molten core materials is subject to a large uncertainty because it is difficult to study it on a real scale. An attempt was made in the experiments SCARABEE BF2 and BF3.[1] At the same time, the SEBULON experiment was perfonned at CEA Grenoble to study the fluid dynamics boiling pool.[2]

2. Description of the Experiment

The SEBULON experiment was perfonned to study the fluid dynamics of a volume-heated boiling water pool with the advantage of being capable to visually observe the experiments and to measure the local lateral heat fluxes with a high accuracy. The experiment was set up so that the fluid flow is practically two-dimensional in a nan-ow rectangular-vessel.

The series No 4 was selected because it contains very different power levels and a good measurement of the lateral heat fluxes.[3] There were four tests being recalculated the main parameters of which are listed in Table 1. An important value for comparing basic hydrodynamics is the hold-up. It is not explicitly given in Table 1, but can easily be calculated with

$$\text{hold-up} = \frac{\text{height while boiling} - \text{initial pool height}}{\text{initial pool height}}$$

Reference to this value will be made in the following description of the recalculations.

3. Analytical Solution

There is no analytical solution available. However, boiling pools are considered as a basic test case for two-phase codes. These experiments have been recalculated with a specific code.[4] This basic code was phenomena oriented, assuming the topology of the flow which is described hereafter.

4. Understanding of phenomena

In the experiment, the pool was generally divided into four regions.[2)]

- a single phase pool at the bottom,
- a two-phase region in the center with ascending water and bubble velocities,
- a liquid boundary layer with falling water velocities at the wall,
- a zone of intennediate two-phase flow between the center and the wall in which an outward transport of mass with condensing bubbles can be observed.

This natural convection pattern is typical for boiling pool experiments, with two water vortices symmetric to the mid plane of the two-dimensional slab.

5. SIMMER-III Representation

5.1 Geometry, Initial and Boundary Conditions

A 2-D mesh in Cartesian co-ordinates was used, as illustrated in Fig. 1. Because the experiment was performed in a symmetric box the code model represents only one half of the box, from the center line to the right lateral wall. The third co-ordinate perpendicular to the drawing has the dimension of 1 m.

In the experiment, the pool thickness is only 60 mm. Therefore, the total power input in the code needs to be larger by a factor of 17 than in the experiment. In the experiment, there was a measurement of the vapor flow out of the containment. Therefore, the upper bound of the code model was closed except for the center cell to be able to compare vapor mass fluxes.

The wall at which the heat fluxes were measured is represented in the code by 30% volume of the right can wall in the rightmost cells. The wall temperature was 293 K for all tests.

5.2 Code modifications

There was a small addition to the code to keep the internal energy of the wall constant at the given value of the experiment. This is a very simple approximation, but it does not introduce a bias because S-III heat fluxes are either below or above those of the experiment. The heat fluxes were calculated within the postprocessor using the approximation:

$$\text{Flux} = \sum_{\text{gas, liquids}} \alpha h \Delta T$$

where α is the effective volume fraction, h the heat transfer coefficient, and ΔT the temperature difference between fluid and wall. The heat transfer coefficient was calculated using the Dittus-Boelter approximation:

$$h = \frac{k}{D_h}(5 + 0.025 Re^{0.8} Pr^{0.3})$$

where k is the thermal conductivity, D_h the hydraulic diameter, Re the Reynolds number, and Pr the Prandtl number.

5.3 Parametric cases

The calculation was started with the smallest energy concentration, but the four tests will be described in the order of the experimental numbers. A coarser mesh is tested for the last case.

6. Results

6.1 test 4.504

The test No. 504 was performed with a deep pool at an elevated power level (30 kW). The initial pool level is at 0.5 m. The pool boils after 2 seconds. We discuss the time after the first violent evaporation when the pool has calmed down a bit, i.e. after *5* seconds. At that time, the pool surface stays at about 0.55 m, compared to a value of 0.65 to 0.7 m of the experiment. The S-III hold-up is only 10% compared to 30% to 40% of the experiment. The deviation is substantial and has a profound effect on the redistribution of phases. Fig. 2 shows the average water volume fraction between *5* and 10 seconds for all vertical cuts. Appreciable void fractions can be found above 0.3 m, by comparison, the single phase region of the experiment extends to 0.17 m.

Fig. 3 shows the water velocities within the pool at three different times. The code calculates one or two vortices of water in the pool, depending on the progress of time. At first, the pool movement is according to that of the experiment, with water flowing down the wall. and rising in the pool center. Around 7 seconds, there are two vortices, one at the (single phase) bottom in the proper direction, and one at the pool top in the wrong direction. Finally, the vortex of the top pool extends all the way to the pool bottom.

Consequently, the heat fluxes vary substantially with time and space. During the first four seconds, the heat fluxes are often above those of the experiment. This cools down the pool, leading to a temperature drop close to the wall from 373 K to 365 K**,** and down to 368 K in the pool center. Afterwards, the heat fluxes are generally lower than those of the experiment. During periods of low heat fluxes, the temperatures of the pool rise again, within six seconds to about 370 K close to the wall, and to 373 K in the pool center.

Fig. 4 shows a comparison of experimental heat fluxes (solid squares) and S-III profiles at four different times. The code heat fluxes drop rapidly by two orders of magnitude in the cover gas region. The experimental results show much larger values. One may suspect that this is due to an undervaluation of the code condensation rate. However, the code has proven to model condensation correctly.[8] The large experimental heat fluxes in the cover gas region can be explained by the effects the violent sloshing movements have on the redistribution of the liquid phase towards the cover gas region. This helps to transport energy to the upper part of the wall. Since the code calculates rather calm pool surfaces, these effects are missing.

Figure 5 shows the vapor volume flow through the stack for the calm period of the run. The vapor mass flow through the upper exhaust changes rapidly. There is a net inflow of 2.2×10^{-6} m^3/s after *5* seconds. This value is subject to a large uncertainty because of the unsteady behaviour of the pool. The experiment states a volume outflow of 3.45×10^{-6} m^3/s.

6.2 test 4.509

The test No. 509 was performed with a very deep pool at a low power level (5.5 kW). The initial pool level is at 0.8 m. Because of the low power density, the profiles of void, velocity, and fluxes develop slowly. At first, there is a downward water flow all along the lateral wall. After four seconds, the upper region develops a behaviour different from that seen in the experiment. Figure 6 shows the water velocities inside the pool. There are two vortices, one in the two-phase region with an opposite direction to that seen in the experiment, and one in the single phase region with the proper direction. This results in a velocity minimum at the wall at 0.45 m and a distortion of the heat flux profile.

Figure 7 shows a comparison of experimental heat fluxes (solid squares) and S-III profiles at late times. The calculation was interrupted because of computer times larger than 70 hours. The figure shows that the code heat flux level is the same as that of the experiment. However, because of the presence of two vortices, there is a large variation along the lateral wall. Fluxes outside the pool are generally higher than those observed in the experiment.

The void fractions at the top of the pool are small (up to 40%) which is consistent with experimental observation. However, the liquid volume fraction above 0.8 m are too large. Figure 8 shows the distribution of the radial water volume fraction close to the pool surface at four different times. There is a pool center with less void. Above the liquid pool, the center remains liquid continuous. The pool surface is not even as seen in the experiment. This may be attributed to the presence of the stack hole in the center top. However, the mechanisms that drive this peculiar distribution are probably associated to the heat flux shape and the non-homogeneous rejection of heat inside the pool.

6.3. test 4.518

The test No. 518 was performed with a deep pool at a medium power level (10 kW). The initial pool level is at 0.5 m. The pool boils after 7 seconds. The pool surface stays rather calm and even. The pool surface is at 0.53 m, compared to the value of 0.6 to 0.64 m of the experiment. The S-III hold-up is about 10% compared to 20% to 28% of the experiment. The single phase bottom of the pool extends to about 0.3 m, compared to 0.38 m to 0.43 m of the experiment.

The code calculates two vortices of water in the pool, one at the bottom (single phase) with the proper direction, and one at the top of the pool in opposite direction of what is known through the experiment.

Consequently, the heat fluxes have a minimum around 0.3 m elevation, the value of which is close to that observed in the experiment. Figure 9 shows a comparison of experimental heat.fluxes (solid squares) and S-III profiles at late times. Because of the presence of two vortices in opposite direction, there is a substantial variation of heat fluxes calculated. The average heat fluxes are close to those of the experiment. Both, experiment and code, observe a calm pool surface with heat fluxes that decrease rapidly in the cover gas region. The mass flow through the upper exhaust changes rapidly only for the initiation of pool evaporation. The net outflow is close to zero which is consistent with experimental observation.

6.4. test 4.533

The test No. 533 was performed with a shallow pool at a high power level (20 kW). The initial pool level is at 0.2 m. The pool boils after 1 second. There is a pool collapse between 1.5 and 4 seconds. A second steady boil-up starts around 7 seconds a time at which code time steps become very small. Therefore, average data are extracted for this section of the calculation. The pool surface is at 0.28 m, compared to the value of 0.38 m of the experiment. The S-III hold-up is about 40% compared to 90% of the experiment. There is practically no single phase region in the pool, a finding that is consistent with experimental observation.

The code calculates either two or one vortices in the liquid pool. Figure 10 shows the water velocities inside the pool at two times. The sense of the water velocity vortex is generally in the proper direction, with rising water in the center, and descending water at the wall. If the void fraction of the pool decreases, there is a tendency towards the vortex in the wrong direction. Therefore, axial water velocities at the wall which should always be negative according to experimental observation, are sometimes positive.

Figure 11 shows a comparison of experimental heat fluxes (solid squares) and S-III profiles at late times. The heat fluxes vary substantially with time and space which can be explained by the violent evaporation and the resulting pool movements. In the pool region, the fluxes are similar to those of the experiment.

For this period of later times, the code calculates a substantial loss of vapor through the stack. At the average over 1.6 seconds, a vapor loss of 0.0107 kg/s has been calculated. If all this mass loss would correspond to an energy loss out of the calculational domain, the associated power would be 24 kW which would be half of the power rejected through the wall. The experiment shows a large amount of heat being rejected through the wall in the cover gas region. As for test 4.504, the violent sloshing movements lead to a redistribution of the liquid phase towards the cover gas region. This helps to transport energy to the upper part of the wall. The code does not calculate this movement, nor the resulting heat fluxes. The mass flow through the upper exhaust changes rapidly. It is therefore astonishing that the water surface calculated by the code stays rather calm. The experiment states no net mass flow through the stack, an indication of the efficiency of the steam condensation.

The test No. 533 was recalculated using a coarser mesh (3×4 cells for the initial liquid pool). The water velocity vortex is predominantly in the proper direction with water falling at the wall. However, it changes occasionally towards the wrong direction, with a more stable situation at later times.

The water velocities are smaller than those of the first run. Therefore, the heat fluxes are smaller. Figure 12 shows a comparison of experimental heat fluxes (solid squares) and S-III profiles. The S-III heat fluxes have a sharp peak close to the pool surface which does not appear in the experiment. The heat fluxes in the cover gas region are much lower than those of the experiment. The reason for this has been explained for the reference calculation. The effects of the missing pool movements are intensified. Figure 13 shows the water volume fractions along the pool at a late time. The average void fraction is substantially smaller than that of the experiment. The pool surface is remarkably smooth and stable.

7. Conclusions

The recalculations of the SEBULON experiments were characterized by the same difficulties as during the calculation of the hydrodynamics of bubble columns, which is reported in Problem 2.2. The code was found to have difficulties to calculate the natural convection pattern typical for the experiment (Section 4). Therefore, the redistribution of phases, crucial for calculating the prototypic transition phase, is subject to inconsistencies. For the prototypic case, the redistribution of materials governs the volumetric heat generated inside the pool and the contacts to the unmolten structures adjacent to the pool. The heat fluxes at the wall are dependent upon the convection patterns of the pool. The major results of the SEBULON experiments are the values for these heat fluxes. Because of the difficulties with the hydrodynamics, the code heat fluxes are subject to inconsistencies.

However, the code heat fluxes are of the same order of magnitude as those of the experiment giving rise to assume that the basic calculational code procedure to assess these fluxes is correct, with the local velocities driving the heat transfer and standard forced convection engineering correlations to approximate their magnitude. Moreover, a non-negligible influence of the cell size on the fluid velocities has been found. This may influence the heat flux calculation considerably.

In addition to those problems, the pool-averaged values of the void fraction, defined by the hold-up, are not calculated correctly. The void fractions of the code are much smaller than those of the experiment. The critics[5)] about the friction factors between the phases of the bubble columns need to be repeated. This may also influence the behaviour of the pool surface, because the code does not model the violent movement for the tests at high power densities.

8. Recommendations for Model Improvement

The hydrodynamics is important because it governs the evolution of the prototypic liquid pool which may either progress or rest locally contained. It clearly has to be improved.

During those calculations over long times, the problem of instabilities should be treated. These instabilities are not observed if there is no free pool surface. Since MC3D has similar difficulties, the reason for these instabilities can only be explained by the imperfect description of the large gradients from liquid-continuous to vapor-continuous flow at the pool surface. Indeed, first signs of instabilities have been found, in MC3D and AFDM**,** in the cells of the free pool surface. This finding has also to be seen relative to recent work that has been done to study the effects of the staggered mesh while solving the Navier-Stokes equations.[5), 6)] It is suggested to follow the development of research in this field closely, and to implement any new models to reduce code instabilities.

Given the number of unresolved problems, it would be premature to expect valuable information from a code study on transition phase pools.

9. References

1) J.P. Breton et.al.: The SCARABEE molten and boiling pool test series BF experimental results, modeling and interpretation, Proc. of the Int. Fast Reactor Safety Meeting, Snowbird, Aug. 1990, Vol. I, pp. 357-365.

2) J.M. Seiler et al.: One component, volume heated, boiling pool thennohydraulics, 14th Liquid Metal Boiling Working Group, Florence, April 16-18, 1991.

3) P. Malterre, A. Liegeois, J.M. Seiler: Compte rendu d'essais SEBULON No 4, Internal Report CEA/DRN/DTP/STI/LMSP, Oct. 1990, STI/LMSP/90.82/PM/AL/JMS/pd.

4) J.M. Seiler et al.: One component, volume heated, boiling pool thennohydraulics - part 2: modelization, AIChE Symposium series n. 288, Heat transfer, Vol.88, pp. 54-63, San Diego 1992.

5) T.F. Miller, F.W. Schmidt: Use of a pressure-weighted interpolation method for the solution of the incompressible Navier-Stokes equations on a nonstaggered grid system, Numerical Heat Transfer, Vol.14, pp.213-233, 1988.

6) S.K. Choi, H. Y. Nam, M. Cho: Systematic comparison of finite-volume calculationa1 methods with staggered and nonstaggered grid arrangements, Numerical heat Transfer, Vol. 25B, pp.205-221, 1994.

Table 1. SEBULON data and averaged SIMMER-III results.

Test No	Power	Power per initial height	Initial pool height	Height while boiling	S-III height while boiling
4.504	30000	6000	0.5	0.65-0.7	0.55
4.509	6900	6900	0.8	0.8	> 0.8
4.518	20000	20000	0.5	0.6-0.64	0.53
4.533	100000	100000	0.2	0.38	0.28
	W	W/m	m	m	m

Test No	Single phase height	S-III single phase height	Exit gas flow	S-III exit flow	Average flux at the wall	S-III aver. Flux at the wall
4.504	0.17	0.3	3.45	-2.2	238000	110000*
4.509	0.7?	0.7	0.0	> 0	66000	76000
4.518	0.38-0.43	0.3	0.0	> 0	144000	150000
4.533	0.01	0.01	0.0		239000	170000*
	m	m	cm^3/s	cm^3/s	W/m^2	W/m^2

* = value average over a late period

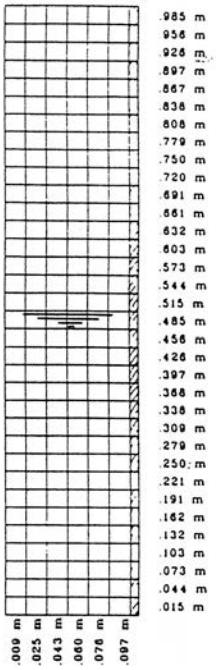

Fig. 1. Mesh cell set of SEBULON 4.504.

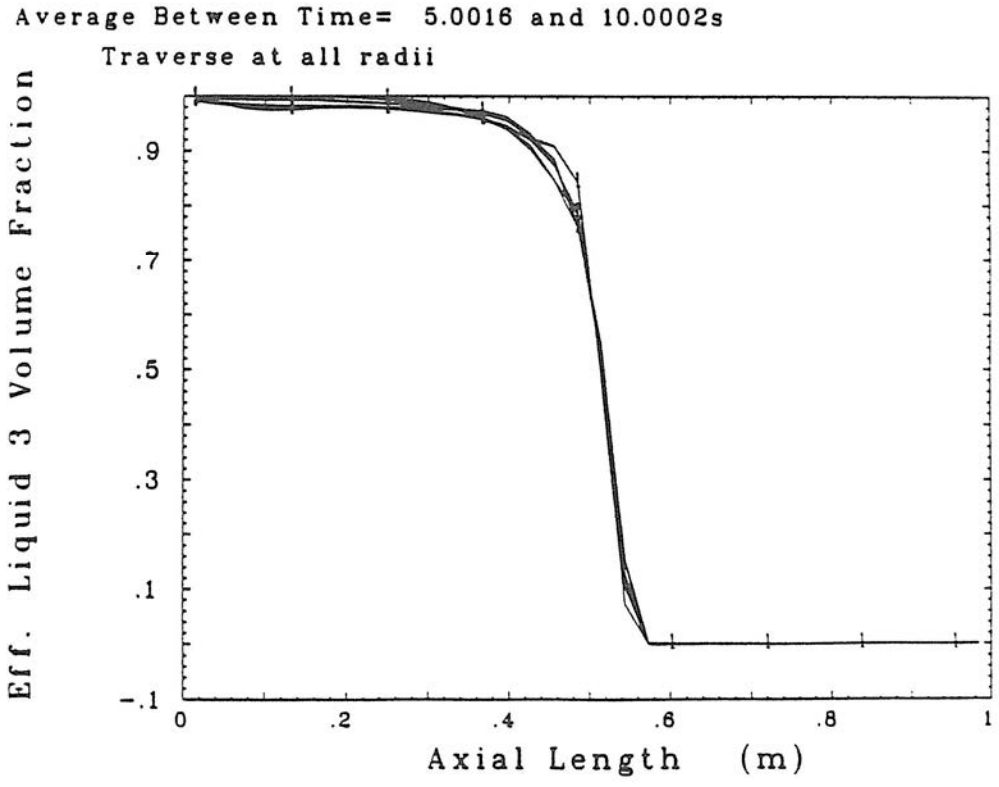

Fig. 2. Average water volume profiles along the Sebulon 4.504 test section.

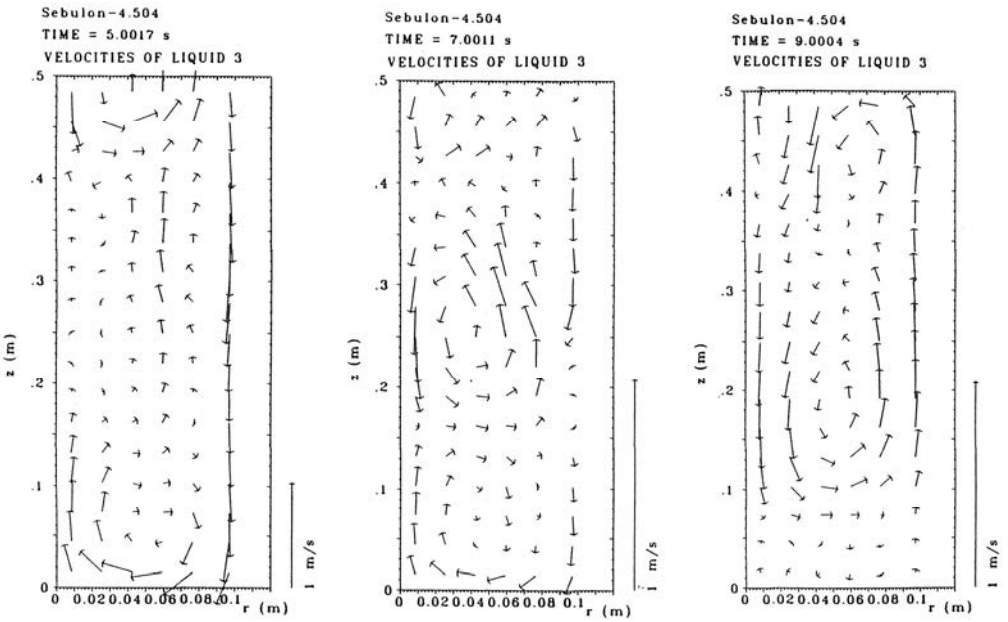

Fig. 3. Water velocities in the liquid section of Sebulon 4.504.

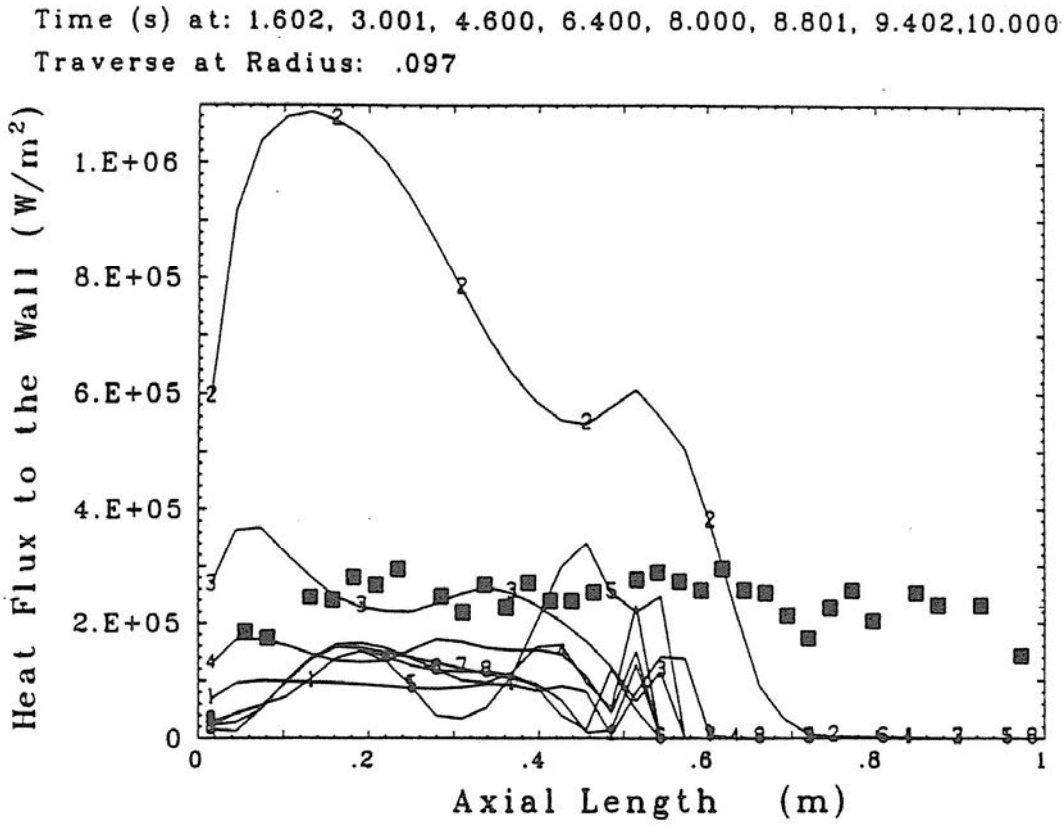

Fig. 4. Heat fluxes of S-III and Sebulon 4.504.

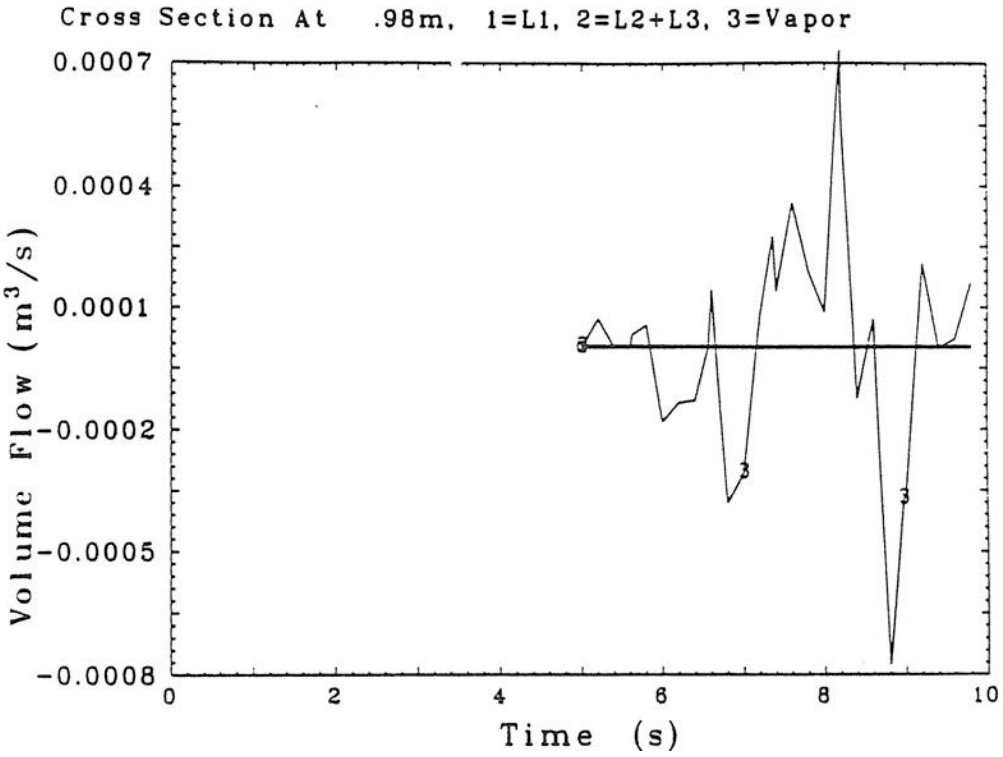

Fig. 5. Vapor volume flow at the stack of Sebulon 4.504.

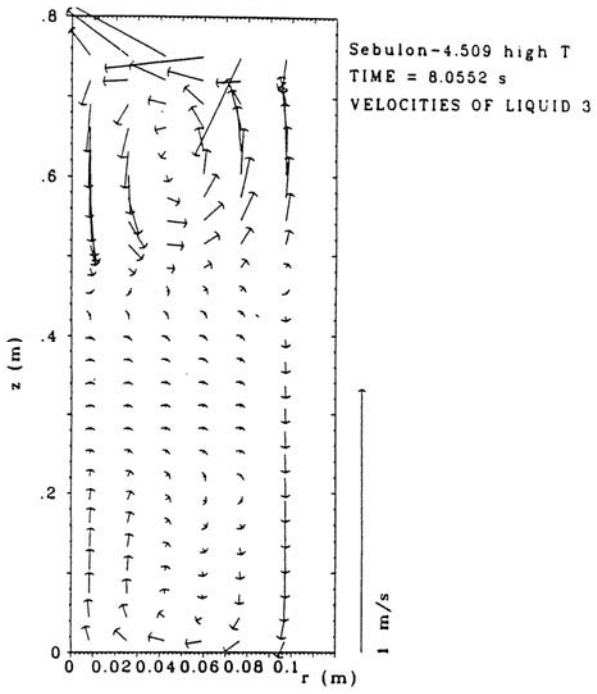

Fig. 6. Water velocities in the liquid section of Sebulon 4.509.

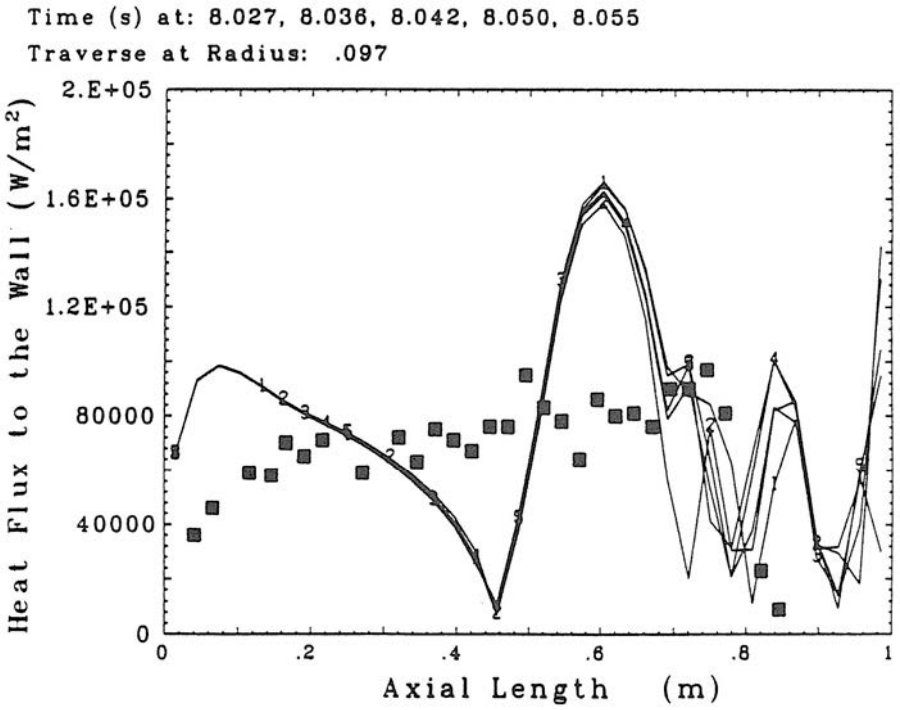

Fig. 7. Heat fluxes of S-m and Sebulon 4.509.

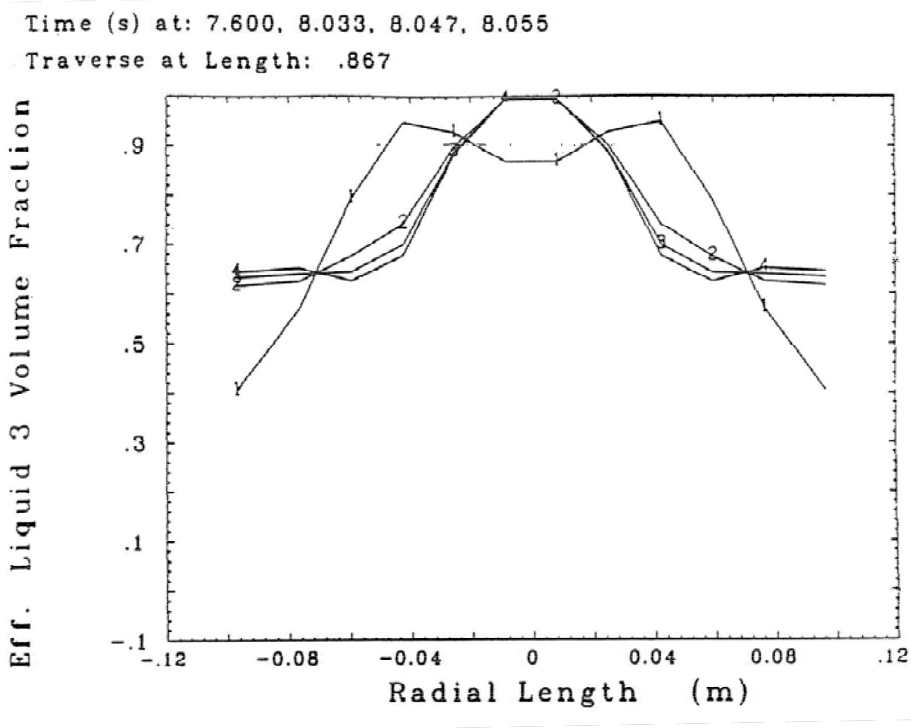

Fig. 8. Horizontal water volume fraction profiles of Sebulon 4.509.

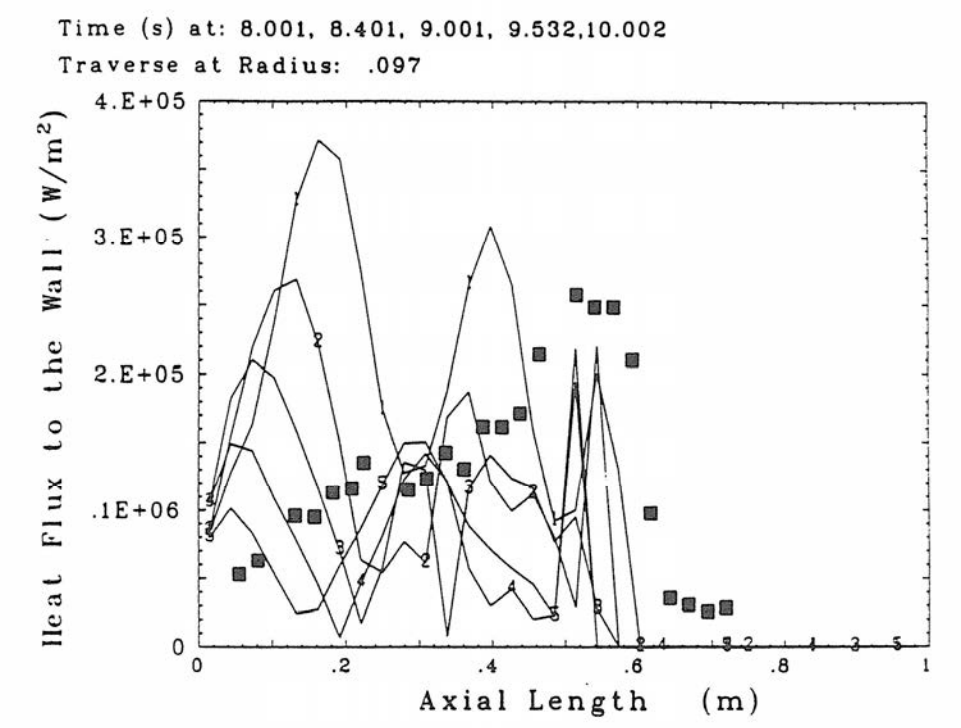

Fig. 9. Heat fluxes of s-m and Sebulon 4.5018.

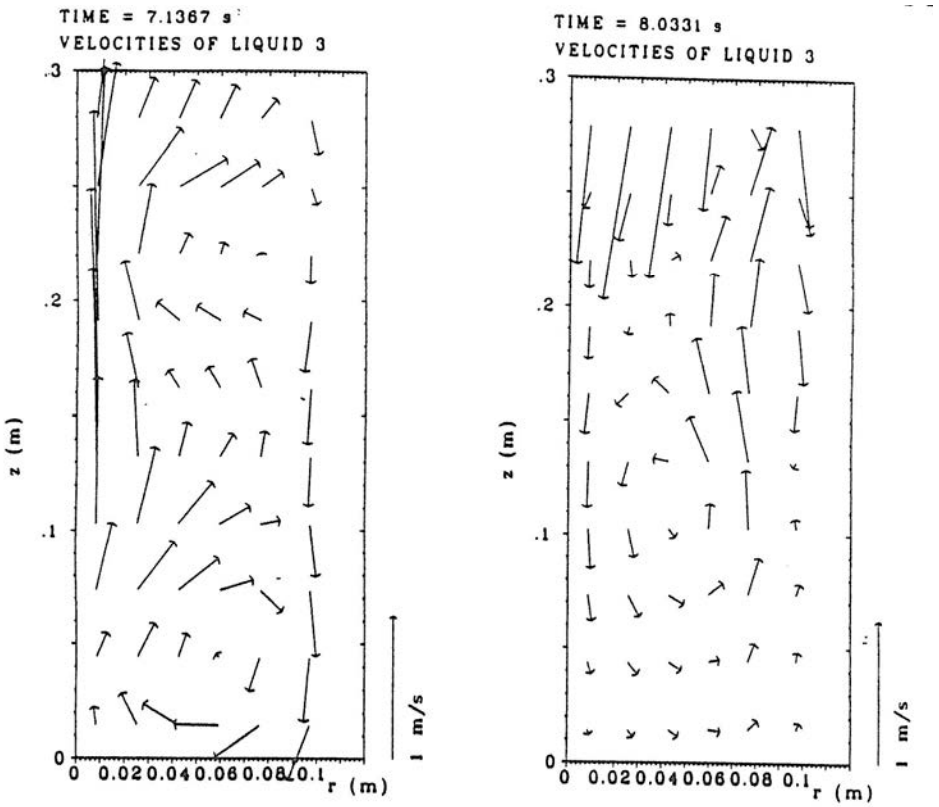

Fig. 10. Water velocities in the liquid section of Sebulon 4.533.

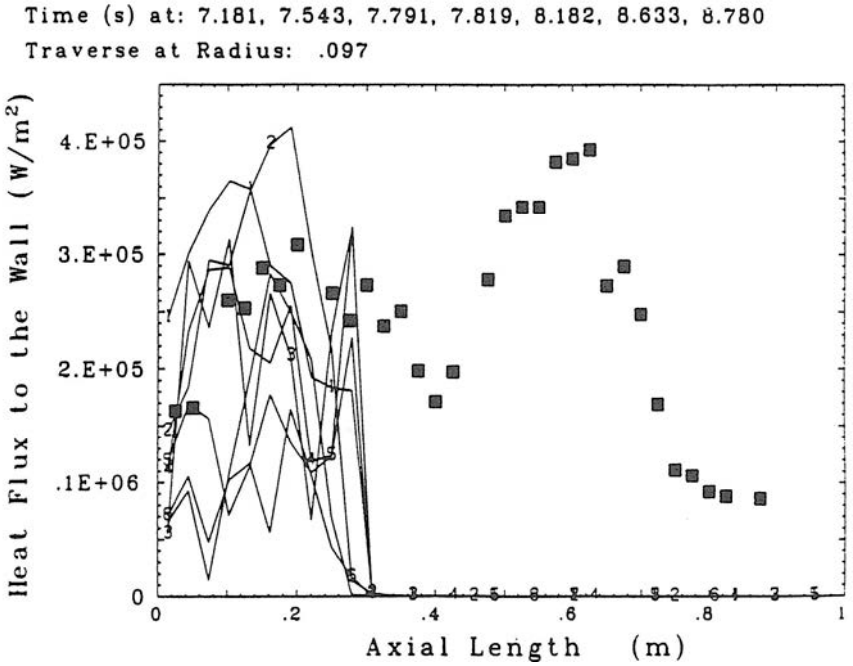

Fig. 11. Heat fluxes of S-III and Sebulon 4.533.

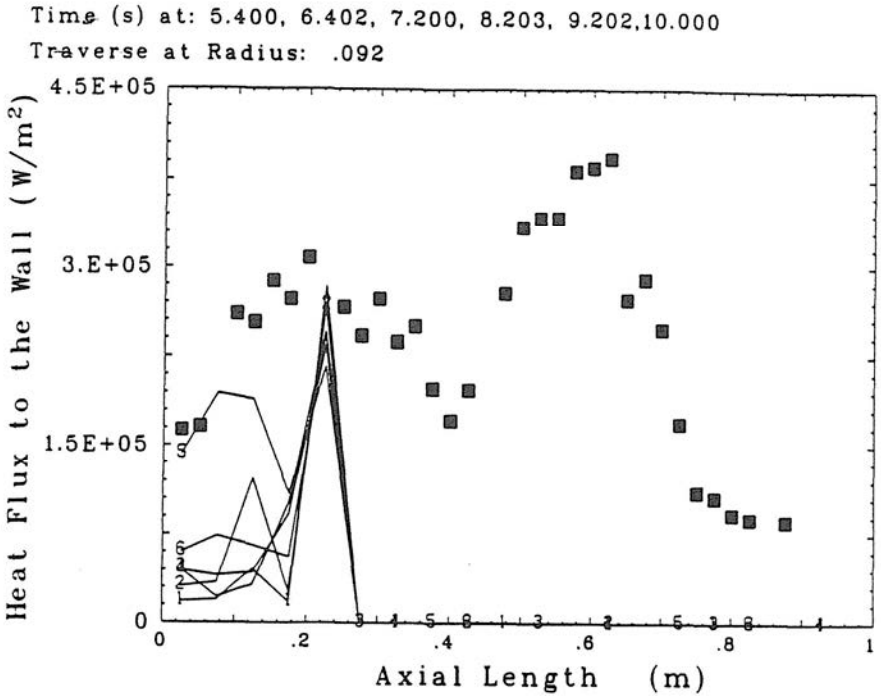

Fig. 12. Heat fluxes of S-III (Coarse mesh) and Sebulon 4.533.

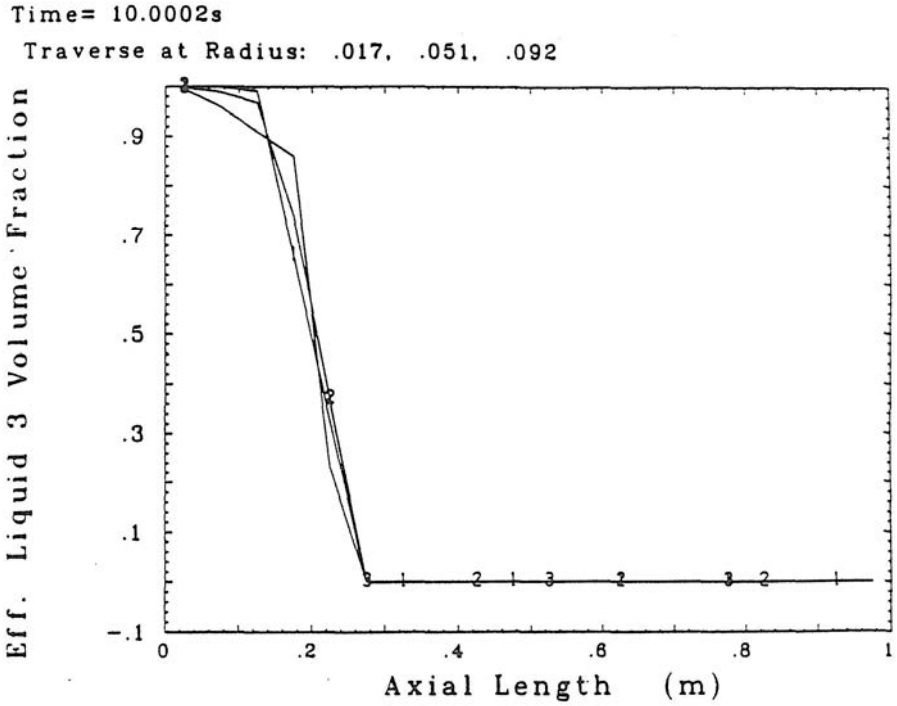

Fig. 13. Water volume profiles along the Sebulon 4.533 section (coarse mesh).

Problem 5.8: Two-phase blowdown: Bartak's pipe

“Rapid Depressurization of Superheated Liquids: Bartak' s Pipe”

Dirk Wilhelm and Fabien Boulanger (CEA-G)

Outline of the case

In Bartak's experiments, superheated water at high pressure is contained in a long pipe. One end of the pipe is connected to a pressure vessel (volume 150 liter) and a pressure holder. The other end is closed by a rupture disk. The disk is broken and the pressure is measured along the tube. A pressure wave travels from the open end to the back end of the pipe. Non-equilibrium two-phase or single phase flow may be dominant. The calculation of this transient allows to verify some characteristics of the interfacial areas models.

1. Objectives of the application

This application is designed to verify the ability of the code to compute a pressure wave in a 1-D configuration. In Bartak experiments, a non-equilibrium two-phase mixture exists at least for the higher temperature case: thus it is an occasion to test the interfacial areas models. Note: a similar application based on an other experiment is available in Problem 5.9.

2. Description of the experiment

In Bartak experiments[1)], superheated water is contained in a 1.70 m long pipe. One end of the pipe is connected to a pressure vessel of 150 liter volume and a pressure holder. The other end is closed by a rupture disk. At time zero, the disk is broken. Pressures are measured along the horizontal pipe during the first 18 ms after the rupture of the disk. Two reference experiments were recalculated:

- «low temperature test» with a reference temperature of 220°C.
- «high temperature test» with a reference temperature of 290°C.

3. Analytical solution

4. Understanding of phenomena

A remarkable difference was reported between the «low temperature test» and the «high temperature test»: The first one is characterized by a negligible pressure undershoot and pressure wave oscillations within a predominantly single-phase flow. The second one is characterized by a significant pressure undershoot and almost no pressure wave oscillations indicating that a non-equilibrium two-phase mixture exists a long the entire discharge pipe.

5. SIMMER-III Representation

5.1 Geometry, Initial and Boundary Conditions

A 2-D mesh was used, as illustrated in Fig. 1. The first volume of the pressure vessel between 1.7 m and 2.2 m/s filled with water. The pressure holder is simulated by the uppermost row·of cells. The pipe itself is introduced as a single row of cells. The derivative of the specific volume with respect to the pressure was evaluated at the given state usmg the steam tables, as already done in Ref. 1) for Edwards experiments.

5.2 Parametric cases

The two reference experiments were recalculated.

6. Results

6.1 Low temperature test (220 ℃)

The initial water pressure is 120×10^5 Pa. The derivative of the specific volume with respect to the pressure is $dv/dp = -1.2\times10^{-12}$.

Figure 2 shows the S-III pressures at three selected locations. The results may be compared to Fig. 3 in which the experimental pressures are condensed. The S-III results compare well with the experiment.

The remaining discrepancies between experiment and calculation is due to the lack of the pipe wall in the input data set, the problems during the rupture of the disk and the difficulty to describe dissipative processes in technical systems with a one-dimensional approach. The oscillation of the pressures show that the main flow is single phase.

The time the pressure wave runs from one end of the pipe to the other is calculated correctly. In spite of the lack of wall friction in the code, the decrease in the pressure amplitude is calculated correctly.

6.2 High temperature test (290 ℃)

The initial water pressure is 125×10^5 Pa. The derivative of the specific volume with respect to the pressure is $dv/dp = -3.2\times10^{-12}$.

Figure 4 snows the S-III pressures at three selected locations for the case of 290 ℃. The results may be compared to Fig. 5 in which the experimental pressures are condensed. The S-III pressures show oscillations around the saturation pressure. In the experiment, there are no such oscillations, and pressures remain well below the saturation pressure. The time the S-III pressure wave travels has changed with the value of dv/dp. The results should show substantial differences to the pressure history of the case of 220 ℃ because of the development of two-phase flow in the pipe. S-III is not capable to model the non-equilibrium two-phase mixture present in this test.

7. Conclusions

The two reference experiments of a pipe break show distinctive differences which could not be calculated by S-III. This may be due to a lack of precision in the calculation of the interfacial areas. Not only the steady state balances of interfacial surface area source terms need to be modeled correctly, but also the transient behaviour.

It is not possible to assess the appropriateness of each of the models by recalculatini a few experiments. A multitude of interactive parameters needs to be defined, many of which are unknown because there is a lack of experimental information, especially for the time constants.

8. Recommendations for Model Improvement

The calculations of the transient interfacial areas need to be revised. This should be done only during and after the revision of steady-state models on bubble columns. The major objective is to identify the orders of magnitude for the time constants of the different surface area source terms.

It is suggested to reduce the number of unknown parameters by reducing the number of models. One could take advantage on the successful recalculation of Bartak's experiment with the AFDM code in order to simplify the interfacial areas models.

9. References

1) J. Bartak: A studies of the rapid depressurization of hot water and the dynamics of vapor bubble generation in superheated water, Int. J. of Multiphase Flow, Vol.16, No.5, pp. 789-798, 1990.

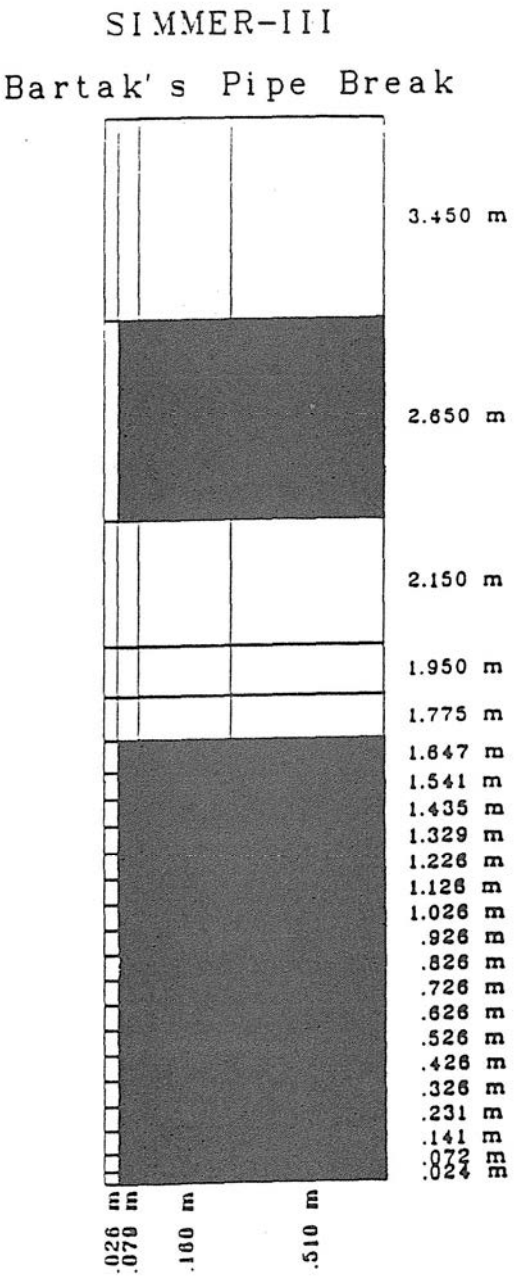

Fig. 1. Mesh cell set of Bartak's depressurization experiment.

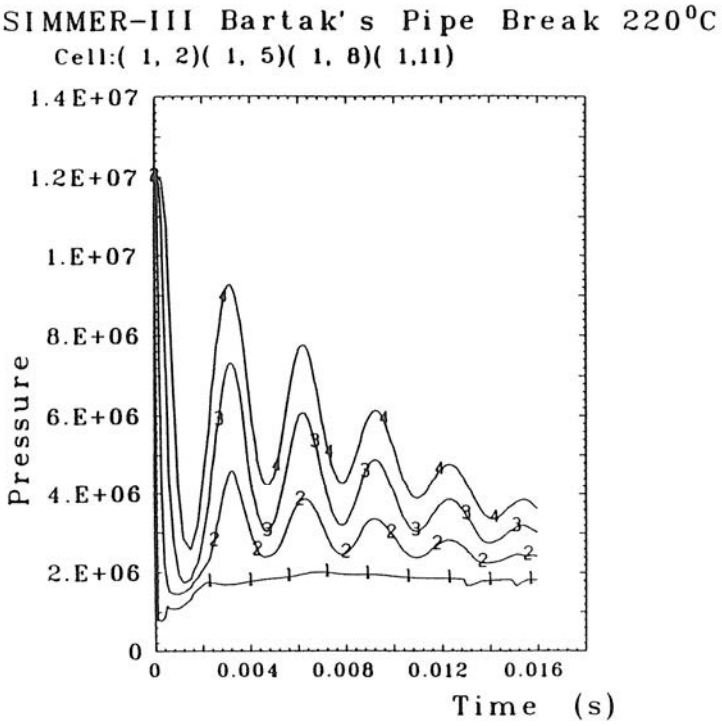

Fig. 2. Code pressures in the pipe for the single-phase depressurization.

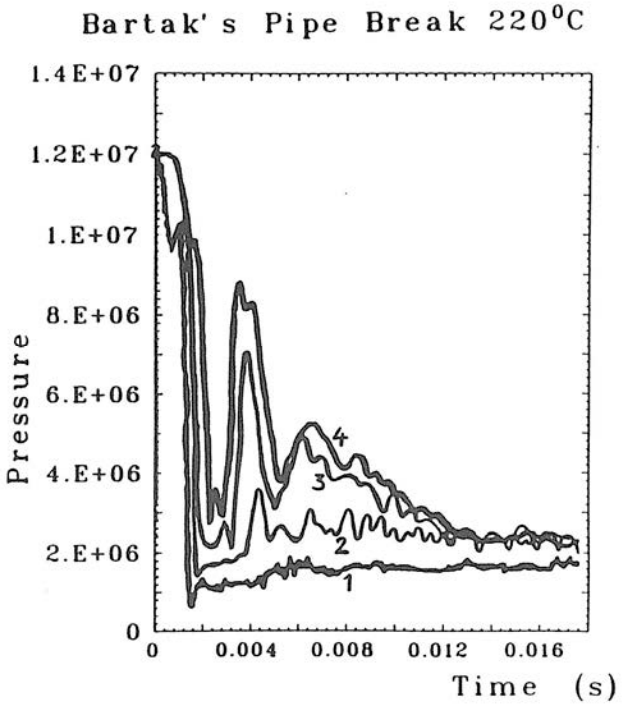

Fig. 3. Measured pressures in the pipe for the single phase depressurization.

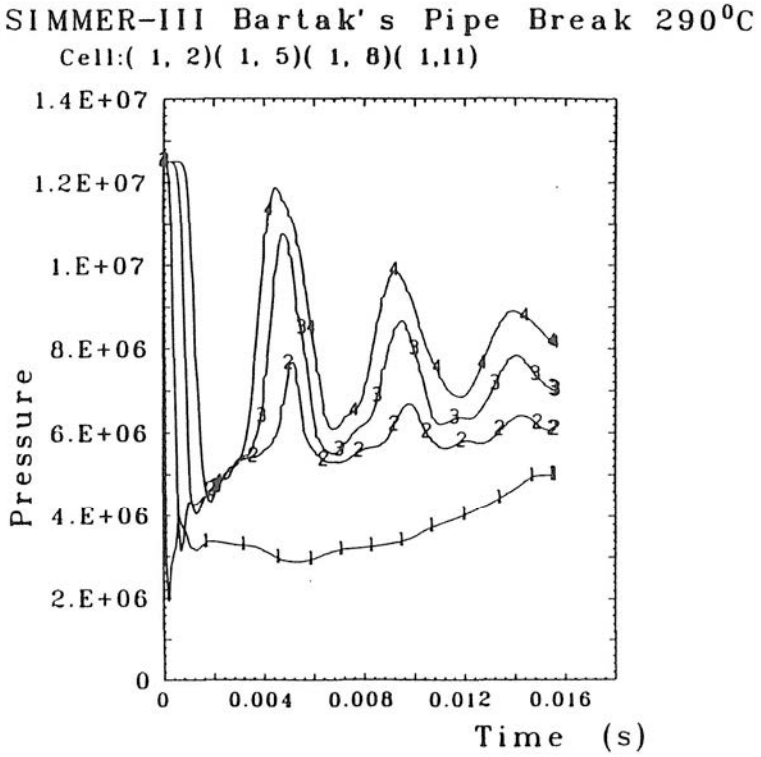

Fig. 4. Code pressures in the pipe for the two-phase depressurization.

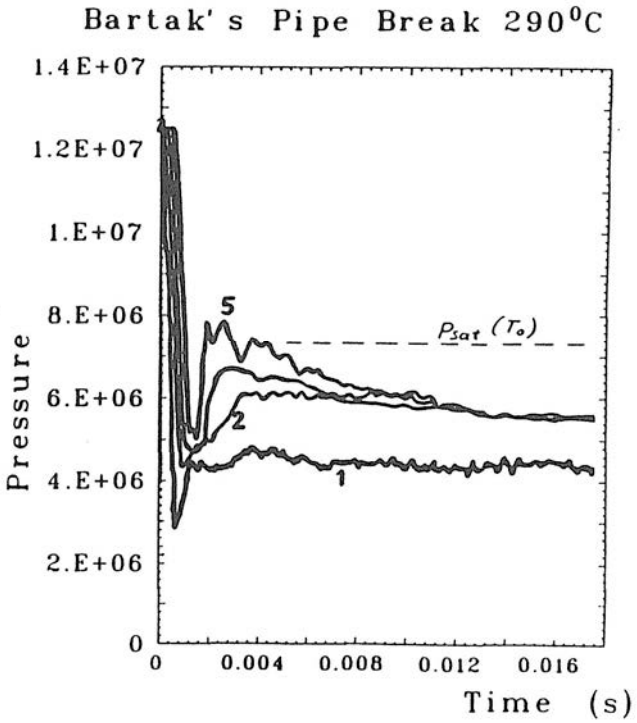

Fig. 5. Measured pressures in the pipe for the two phase depressurization.

Problem 5.9: Two-phase blowdown: Edwards' pipe (1)

“Rapid Depressurization of Superheated Liquids: Edwards' Pipe”

Dirk Wilhelm and Fabien Boulanger (CEA-G)

Outline of the case

In Edwards experiments, superheated water at high pressure is contained in a long closed pipe. One end of the pipe is then opened and the pressure is measured along the tube. A two-phase flow exits into a large discharge tank. A pressure wave travels from the open end to the closed end of the pipe in about 3.7 ms.

1. Objectives of the application

This application is designed to verify the ability of the code to compute a pressure wave in a 1-D configuration. Note: a similar application based on an other experiment is available.

2. Description of the experiment

In Edwards experiments,[1)] superheated water is contained in a 4.35 m long pipe. One end of the pipe is closed, a rupture glass is located by the other end. In the test no 1 considered, the pressure is 1000 lb/in^2-g and the temperature 467 °F. At time zero, the glass is broken. A two-phase flow exits into a large discharge tank. The pressure is recorded along the pipe. A pressure wave originated at the glass travels up to the closed end of the pipe in about 3.7 ms (Fig. 4).

3. SIMMER-III Representation

3.1 Geometry, Initial and Boundary conditions

A 1-D mesh was used, as illustrated in Fig. 1. The wall structure was not introduced because the time studied is so short that the transient can be calculated in an adiabatic way. The pipe end was simulated by two void cells with a constant pressure boundary condition.

An orifice coefficient was occasionally used at the location of the rupture glass. This does not change the transient during the first 10 ms. The initial conditions are subject to some S-III peculiarities. If the volume fraction of water in the pipe is specified to be 1.00 in order to model single phase conditions, a gas pressure must not be defined in that region. Otherwise, the volume fraction definition may be overridden by the pressure definition, and severe problems may occur after several tens of time steps.

3.2 Parametric cases

The impact of the water EOS has been tested.

4. Results

Figure 2 shows the pressure history at four different locations:

- cell (1,1) at the closed end (0.064 m),
- cell (1,10) at 1.216 m,
- cell (1,20) at 2.496 m,
- cell (1,30) at 3.776 m close to the pipe exit.

First, the standard set of water EOS are used. The code calculates the pressure wave originating from the rupture of the glass at the pipe end at time zero to arrive at the closed end of the pipe after 1 ms. There is no pressure undershoot except in regions close to the pipe exit.

Second, the results can be improved considerably by specifying the proper value for the derivative of the specific volume with respect to the pressure, dv/dp. This is a standard input to the EOS data. Figure 3 shows the pressure histories for a run with the dv/dp changed to that given by the steam tables at constant temperature, $dv/dp = -1.5 \times 10^{-12}$.[2] The results have changed substantially. They are close to those of the experiment. The pressure wave travels more than 3 ms from the rupture glass to the closed end of the pipe. There is a considerable pressure undershoot at the closed end.

A third possibility to assess the sensitive EOS parameter is to use the isentropic sound speed given as c=1265 m/s.[1] A first order approximation would yield $dv/dp = -1/(c\rho)^2$ where the density ρ at the given state is 828 kg/m^3. This would yield a value $dv/dp = -9.1 \times 10^{-13}$ instead of the default value of -10^{-13}. Figire 4 shows the comparison of the S-III result with the pressure trace of the experiment. This result could still be improved by using smaller mesh cells.

5. Conclusions

The recalculations of the Edwards' pipe blowdown showed good agreement between experimental and code pressures. This is due to specifying the appropriate value for the derivative of the specific volume with respect to the pressure which is an EOS input parameter.

6. Recommendations for Model Improvement

None.

7. References

1) A.R. Edwards: T.P. O'Brien: Studies of phenomena connected with the depressurization of water reactors, J. of Brit. Nucl. Energy Soc., No.9, pp. 125-135, 1970.

2) U. Grigull: Properties of water and steam in SI units, Berlin, Heidelberg, New York, 1989.

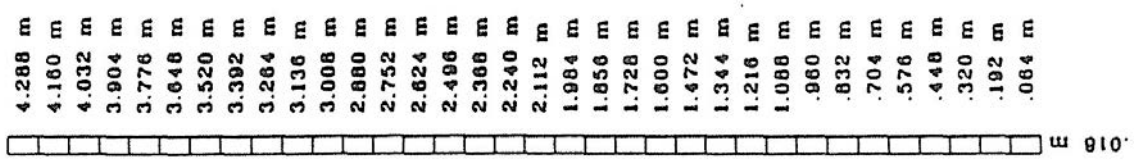

Fig. 1. Mesh cell set of Edwards' pipe.

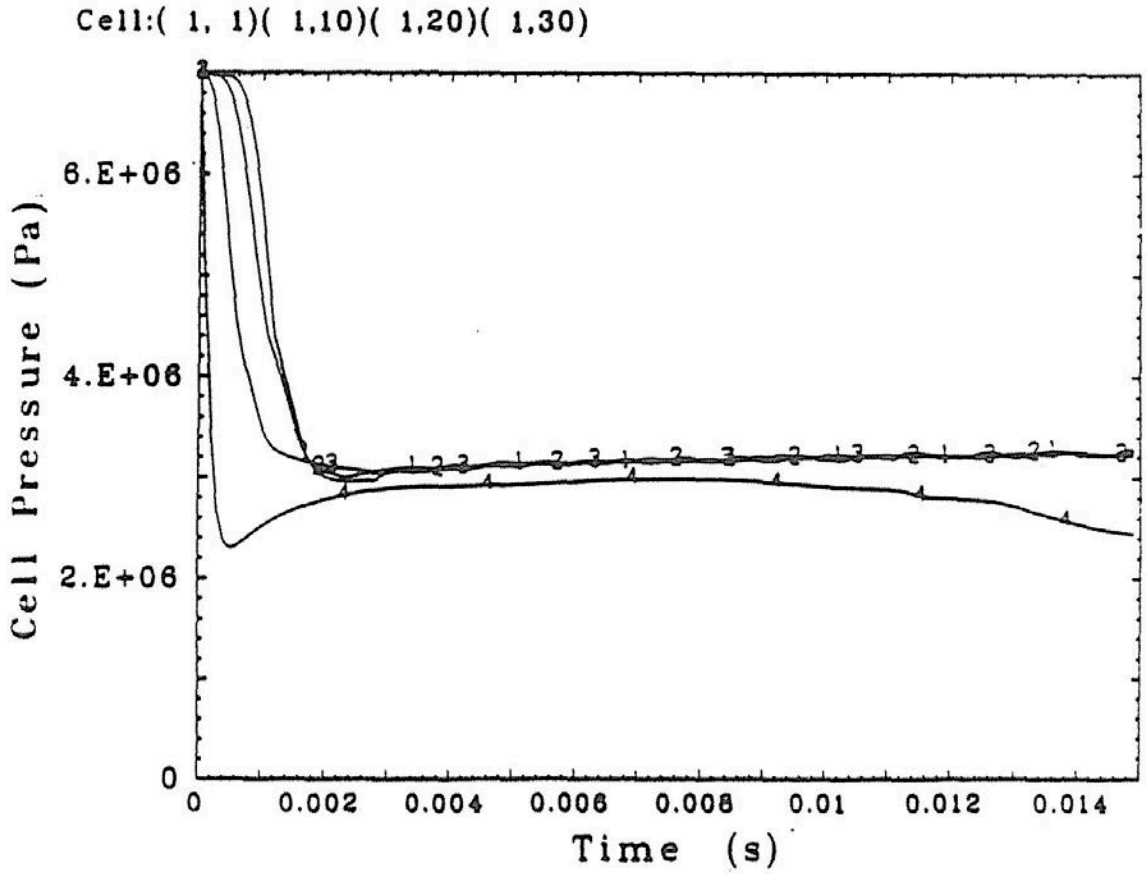

Fig. 2. Pressures in the pipe without adjusted sound velocity.

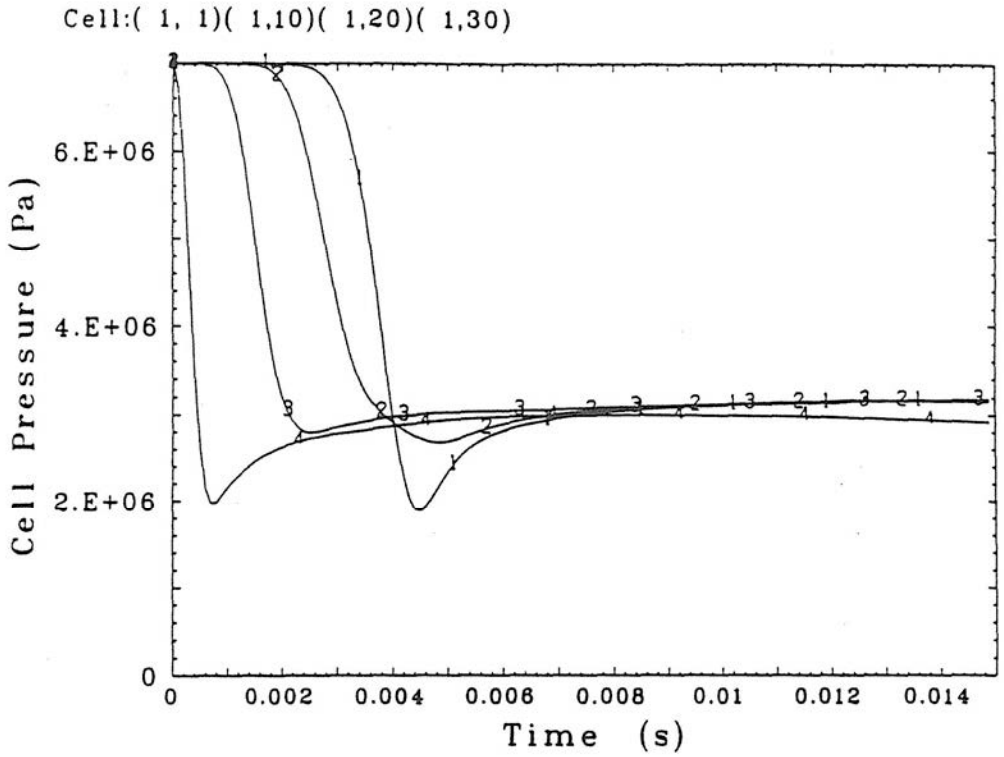

Fig. 3. Pressures in the pipe with adjusted sound velocity.

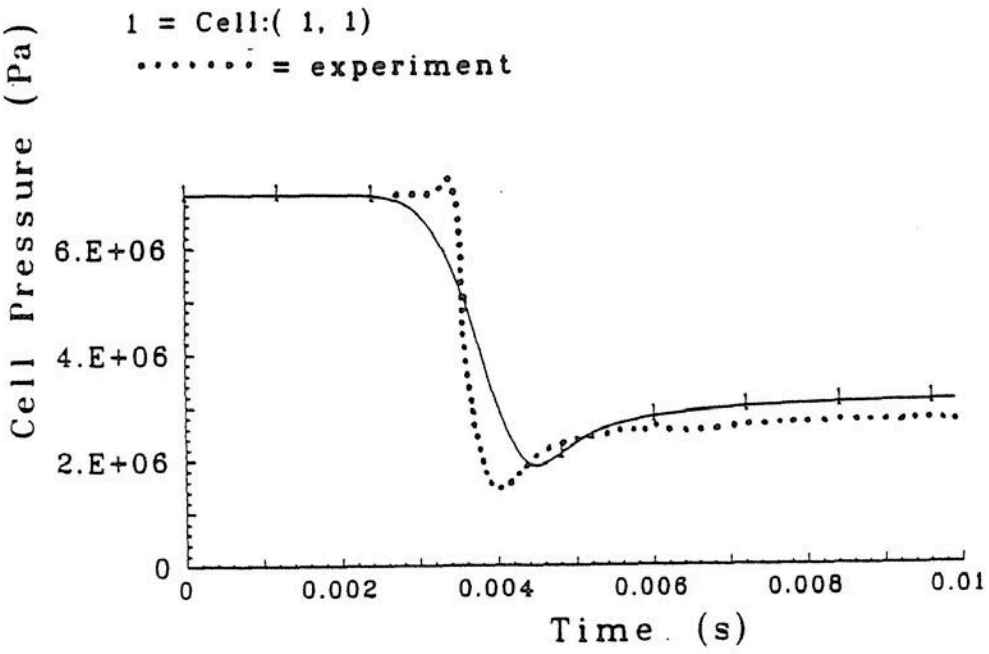

Fig. 4. Pressures of S-ill and Edwards' experiment.

Problem 5.10: Two-phase blowdown: Edwards' pipe (2)

“Edwards’ Pipe Blowdown”

Koji Morita (PNC)

Outline of the Case

The evaluation of the coolant discharge during the early stage of a loss-of-coolant accident (LOCA) has been one of major concerns in the safety of water reactors. Edwards and O’Brien[1)] have studied a rapid depressurization phenomenon of subcooled water in a long horizontal pipe to provide quantitative information on the behavior of water under blowdown conditions. Their experiments are well-known as the Edwards’ pipe problem or the NRC Standard Problem No. 1 for evaluation of reactor safety analysis codes. This problem involves the flash boiling of water from a long pipe closed at one end and suddenly opened to the atmosphere at the other by the rupture of diaphragm.

1. Objectives of the Application

The pipe blowdown experiment contains physical process to test and verify the mathematical models in the multiphase fluid-dynamic computer codes. The objective of this problem is to test the SIMMER-III (S-III) fluid dynamics modeling on several important thermal-hydraulic effects: one-dimensional two-phase flow dynamics, flow regime transition, IFA source terms, and non-equilibrium vaporization.

2. Description of the Experiment

Edwards and O'Brien[1)] experimentally studied depressurization phenomena of initially nonflowing subcooled water in a horizontal pipe. One of the experiments consists of the breaking of a rupture disk at the end of a pipe containing compressed water at 1000 lb/in^{2}g (6.99608 MPa) and 467 ºF (514.817 K). When the rupture disk breaks, a decompression wave propagates through the water, dropping the pressure to the saturation level. The water then flashes, and the two-phase fluid and superheated steam flows out the rupture until the pressure drops to the ambient conditions. In the experiment pressures were recorded at several positions along the pipe and temperature and void fraction were measured at a station near the middle of the pipe.

3. Analytical Solution

No analytical solution is available for this problem.

4. Understanding of Phenomena

The problem has been investigated using two-phase analysis codes: non-equilibrium models were proposed for flashing flow assuming a constant number of bubbles per unit volume of mixture and/or per unit mass of liquid[1), 2), 3)] and a distributed nucleation model was used in which the nucleation rate was estimated by applying correlations previously developed for the nucleation of a subcooled liquid near a heated surface.[4)] However, the modeling of the flashing of a liquid flowing in two-phase state remains a largely unresolved problem because of its mechanical and thermal non-equilibrium processes.

5. SIMMER-III Representation

5.1. Geometry, Initial and Boundary Conditions for Reference Case

The reference calculation was performed using the following specifications:

a. The horizontal pipe was modeled as one-dimensional geometry and was equally zoned with 40 mesh cells, each of length 10.24 cm. To take account of the expansion effect the ambient conditions external to the pipe were modeled as an exit region of 8 m long with 5 mesh cells, each of length 1.6 m. The acceleration constant of gravity in the axis direction was set to zero to apply the code to the horizontal system.

b. A horizontal pipe wall was simulated by setting structure components to account for the wall friction, although the wall can be treated as adiabatic due to the highly transient process during the decompression. The closed end of the pipe was set to an adiabatic wall with zero velocities across the boundary. The exit region was enclosed with a rigid and adiabatic wall except for the top boundary where a constant pressure 0.101325 MPa and continuous flow conditions were specified.

c. Edwards and O'Brien[1)] reported that the exit area was reduced by 10 to 15% due to unclean breakage of the rupture disk in the experiment. This area reduction was modeled by specifying an appropriate orifice drag at the broken end of the pipe. In S-III, the orifice coefficient c_o at the top edge of a cell is defined by the following equation:

$$\Delta p = c_o \rho |\vec{v}| \tag{1}$$

where Δp is the pressure drop across the orifice [Pa], ρ is the fluid density [kg/m^3], and $\vec{v}$ is the flow velocity [m/s]. According to Bird et al.,[2)] the mass rate of flow through a pipe which has a thin plate orifice with a hole is given by

$$w = c_d S_0 \sqrt{\frac{2\rho\Delta p}{1-\left(\frac{S_0}{S}\right)^2}} \tag{2}$$

where c_d is the discharge coefficient which approaches about 0.61 for a high Reynolds number, S is the cross-sectional area of the pipe [m^2], S_0 is the cross-sectional area of the hole of the orifice plate [m^2], and w is the mass rate of flow ($= \rho|\vec{v}|S$) [kg/s]. From Eqs. (1) and (2), c_o is expressed by

$$c_o = \frac{1}{2{c_d}^2}\left[\left(\frac{S}{S_0}\right) - 1\right] \tag{3}$$

Assuming 15% reduction of cross-sectional area, $c_o \cong 0.516$ is obtained. Although Eq. (2) may be inappropriate for two-phase flows, this orifice coefficient was approximately used at the cell of the broken end of the pipe.

d. The pipe inside initially was filled with a single-phase subcooled water at a uniform 502.2 K and 6.99608 MPa. As suggested by Hirt and Romero,[2] the lower water temperature was chosen rather than 514.817 K in the experiment to account for the difference in the local and bulk temperatures during the decompression. For the exit region air at 0.10325 MPa was initially specified.

e. The thermodynamic properties of water were calculated using the simplified analytic EOS[5] instead of the S-III standard AEOS for water. The parameters were determined based on the properties at 514.817 K.[6] This is because the temperature change in the problem is not large and the SAEOS may give more exact properties over a narrow temperature range rather than the standard AEOS.

f. The pool flow map were used for the calculation of flow topologies. The bubble nucleation was allowed as far as the bubbly flow region exists. For a flag to control the definition of $A_{CP,B\to D}$ by convection, IFAOPT(3)=3 was selected, where $A_{CP,B\to D}$ is an IFA of the continuous phase (*CP*) component which is transferred from the bubbly flow region to the dispersed flow region due to the convection between cells which have different void fraction. By this selection, the loss of $A_{G,B}$ which is caused by the reduction of bubbly flow region is compensated so that the total IFA between CP component and vapor is conserved depending on the amount of the bubbly flow region through the transfer.

g. The heat transfer empirical correlations for fluid/structure, fluid/droplet and fluid/bubble contacts were modified to be appropriate for the moderate Prandtl-number fluid, water. The heat transfer form continuous fluids to the pipe wall was calculated based on the Dittus-Boelter correlation:

$$h = \frac{\kappa}{D_h}\left(5.0 + 0.023{Re_h}^{0.8}Pr^{0.4}\right) \tag{4}$$

where D_h is the hydraulic diameter [m], h is the heat transfer coefficient [W/m-K], and κ is the thermal conductivity of continuous fluid [W/K]. Re_h and Pr are defined using the properties of continuous fluid as follows:

$$Re_h = \frac{\rho|\vec{v}|D_h}{\mu} \tag{5}$$

$$Pr = \frac{\mu c_p}{\kappa} \tag{6}$$

where c_p is the heat capacity at constant pressure [J/kg-K], $\vec{v}$ is the velocity of continuous fluid [m/s], μ is the viscosity [Pa s], and ρ is the density [kg/m^3]. The heat transfer from continuous fluids flowing around bubbles and water droplets were calculated by the following correlation given by Bird et al.[7]:

$$h = \frac{\kappa}{D_h}\left(2.0 + 0.60 {Re_d}^{0.5} Pr^{1/3}\right) \tag{7}$$

where

$$Re_d = \frac{\rho|\Delta\vec{v}|d}{\mu} \tag{8}$$

d is the diameter of bubble or water droplet [m] and $\Delta\vec{v}$ is the velocity difference between continuous and dispersed phases [m/s].

h. The calculation was performed using a constant time step of 0.1 ms as far as the numerically stable calculation was carried out.

The schematic and nodalization diagram for the reference calculation is shown in Fig. 1. Locations of the gauge stations, GS1, GS4, GS5, and GS7 are also indicated in Fig. 1. Pressures measured at GS1, GS4 and GS7 and temperature and void fraction at GS5 were compared with the calculated results.

5.2 Code Modifications

None.

5.3 Parametric Cases

5.3.1 Time and Spatial Discretization

The reference calculation was repeated with a smaller time step of 0.01 ms or with 80 mesh cells in the pipe region to eliminate time- or spatial-discretization errors or give more accurate numerical integration.

5.3.2 Flow Regime

A different flow regime map was applied to the problem. According to the discussion by Jones[8], for rapidly expanding systems the transition to slug or churn flows may be inhibited until quite large void fractions up to over 0.7: The bubbly or bubbly-slug regime is assumed to exist for void fraction under 0.8, the dispersed flow is for void fraction over 0.9, and the region between 0.8 and 0.95 is considered as a transition zone coupling slug and dispersed flows. To reproduce the above flow transition criteria on the S-III flow regime map, $\alpha_B = 0.8$ and $\alpha_D = 0.95$ were used, where α_B is the maximum void fraction in the liquid components at which the bubbly flow regime can exist, and α_D is the minimum void fraction in the

liquid components at which the dispersed flow regime can exist. The bubble nucleation was also allowed as far as the bubbly flow region exists.

5.3.3. Water temperature

In the reference calculation the initial water temperature was chosen as 502.2 K rather than 514.817 K reported by Hirt and Romero[2]. They suggested that liquid in the vicinity of a vapor bubble is somewhat cooler than the bulk of the liquid because of the loss of latent heat required for boiling. A saturation pressure corresponding to 514.817 K is above that experimentally observed after the initial depressurization and the water boiling. For the purpose of predicting the temperature difference between the bubble interface and the bulk liquid, Stuhmiller and Ferguson[9] considered a growing vapor bubble of radius $r_{G,B}$ [m] with the vapor saturated at the current liquid pressure. The thermal energy required to grow this bubble is provided by cooling of a thin liquid layer around the interface:

$$A_{G,B}\delta\rho_L c_L(T_L - T^I) = \alpha_{G,B}\rho_G h_{lg} \tag{9}$$

where $A_{G,B}$ is the IFA of vapor bubble per unit volume [m^{-1}], c_L is the specific heat of liquid [J/kg-K], h_{lg} is the latent heat of vaporization [J/kg], T_L is the bulk liquid temperature [K], T^I is the bubble interface temperature [K], $\alpha_{G,B}$ is the volume fraction of vapor bubble, δ is the effective thickness of cooled layer around a growing vapor bubble [m], ρ_L is the liquid density [kg/m^3], and ρ_G is the vapor density [kg/m^3]. Stuhmiller and Ferguson[9] obtained the following relation based on the turbulent diffusivity argument:

$$\delta \cong \sqrt{0.07}r_{G,B} \tag{10}$$

Using the relation $A_{G,B} = 3\alpha_{G,B}/r_{G,B}$, the temperature difference can be expressed by

$$T^I = T_L - 1.26\frac{\rho_G h_{lg}}{\rho_L c_L} \tag{11}$$

The essentially same equation as Eq. (11) has been derived by Alamgir et al.[10] To test the above discussion the bulk liquid temperature used for the calculation of interfacial energy balance between vapor and liquid was replaced with Eq. (11) in the S-III phase transition model. In this calculation, the initial liquid temperature was set to 514.187 K and the SAEOS parameters based on the properties at 514.817 K were used.

5.3.4 Nucleation model

A different nucleation model, which is one of the IFA source terms, was applied to the problem. Riznic and Ishii[11] proposed the following equation for the effective nucleation site density N_b [m^{-2}] for flashing flow:

$$N_b = \frac{1}{{D_d}^2}\left\{\frac{1}{\frac{D_d}{2}}\frac{2\sigma T_{sat}}{2(T_L - T_{sat})\rho_G h_{lg}}\right\}^{-4.4} f(\rho^*) \tag{12}$$

where D_d is the bubble departure diameter [m], T_{sat} is the saturation temperature [K], and σ is the surface tension between liquid and vapor [N/m]. The property function is correlated in terms of the density ratio as

$$f(\rho^*) = 2.157 \times 10^{-7}\left(\frac{\Delta\rho}{\rho_G}\right)^{-3.12}\left(1 + 0.0049\frac{\Delta\rho}{\rho_G}\right)^{4.13} \tag{13}$$

where $\Delta\rho$ is the density difference between liquid and vapor [kg/m^3]. A bubble departure diameter is determined by Kocamustafaogullari's model,[12] given by

$$D_d = 2.64 \times 10^{-5}\theta\left(\frac{\sigma}{g\Delta\rho}\right)^{0.5}\left(\frac{\Delta\rho}{\rho_G}\right)^{0.9} \tag{14}$$

where θ is the contact angle [degree] and g is the gravity [m/s^2]. The frequency of bubble departure is estimated by the expression by Zuber[13]:

$$D_d f = 1.18\left(\frac{\sigma g\Delta\rho}{{\rho_L}^2}\right)^{0.25} \tag{15}$$

where f is the frequency of bubble departure [s^{-1}]. Although originally the correlation Eq. (12) was developed for pool flow and convective boiling and the data was correlated by using different effective superheat for those two types of boiling, Riznic & Ishii generalized this correlation even for the flashing flow by introducing the appropriate superheat in the boundary layer where the bubble is generated.

According to the linearized formula of the S-III IFA source terms, the IFA source term of bubble nucleation per unit volume is expressed by

$$S_{G,B,N} = \frac{A^e_{G,B,N} - A_{G,B}}{\tau_N} \tag{16}$$

where $A^e_{G,B,N}$ is the equilibrium IFA of bubble nucleation per unit volume [m^{-1}], $S_{G,B,N}$ is the IFA source term of bubble nucleation per unit volume [m^{-1}s^{-1}], and τ_N is the time constant of bubble nucleation [s]. Using the equilibrium radius of nucleation bubble, the equilibrium IFA is given by

$$A^e_{G,B,N} = \frac{3\alpha_{G,B}}{r^e_{G,B,N}} \tag{17}$$

where $r^e_{G,B,N}$ is the equilibrium radius of nucleation bubble [m]. The bubble number density per unit volume M_b [m^{-3}] determined from the effective nucleation site density, Eq. (12), is obtained by

$$M_b = N_b\frac{4(1-\alpha_S)f_B}{D_d} \tag{18}$$

where f_B is the volume fraction of liquid-continuous region, and α_S is the volume fraction of structure field. The equilibrium radius of nucleation bubble in Eq. (17) can be defined as the bubble departure radius $D_d/2$ until the actual bubble number density determined from $\alpha_{G,B}$ and a bubble radius $r_{G,B,N}$ exceeds M_b, where $r_{G,B,N}$ is defined by

$$r_{G,B,N} = \frac{3\alpha_{G,B}}{A_{G,B,N}} \tag{19}$$

As the result the equilibrium radius of nucleation bubble is given by

$$r^e_{G,B,N} = max\left[\frac{D_d}{2}, \left(\frac{3\alpha_{G,B}}{4\pi M_b}\right)^{1/3}\right] \tag{20}$$

The time constant of bubble nucleation is simply defined using the frequency of bubble departure:

$$\tau_N = f^{-1} \tag{21}$$

In this calculation, Eq. (16) with the correlations, Eqs. (12)-(15), was used for the calculation of the IFA source term of bubble nucleation instead of the standard S-III model, which is same as the AFDM model[14].

6. Results

6.1 Reference Case

Results of the reference case are compared with the experimental data in Figs. 2. As the decompression wave passes through the pipe, the local pressure drops down to the saturation pressure and is maintained at this level until most water disappears. This initial non-equilibrium sate was generally well reproduced by the reference calculation, where the pressure goes below the saturation pressure due to the delay in vaporization. The final blowdown phase which occurs as the superheated steam flows out of the pipe shows good agreement with the experimental data. Near the open end of the pipe the calculation shows more rapid pressure drop and lower pressure than observed in the short-term behavior. This may be influenced by the unclean breakage of the rupture disk in the experiment or the numerical conditions to represent the exit region outside the pipe.

In this calculation effective IFA source terms were the bubble nucleation in the bubbly flow region and the droplet flashing in the dispersed flow region. Another terms have no contribution to IFA changes. It seems that as a bubbly mixture is filled with small bubbles flow structures may be characterized by the intensive coalescence of bubbles which results in the formation of large bubbles. However, the IFA model predicted no effect of bubble coalescence in the reference calculation.

6.2 Time and Spatial Discretization

Short-term pressure histories in the case of a smaller time step are shown in Fig.2-1 compared with the experimental data and the reference calculation. More reasonable early blowdown behavior was reproduced by more accurate time integration. In this case, no remarkable improvements was observed in the long-term behavior. On the other hand, the calculation using smaller spatial resolution gave no significant change in both short- and long-term behaviors.

6.3 Flow regime

Long-term pressure histories in the case using a different flow regime map are shown in comparison with the experimental data and the reference calculation in Fig. 2-2. Comparisons of void fraction and liquid temperature are made in Figs. 2-3 and 2-4, respectively. In this case, less difference was observed in the short-term behavior. As shown in Figs. 2-3 and 2-4, a slower discharge rate and temperature drop were predicted than the reference case and this produced a slower rate of depressurization during the late time transient. This is because the bubbly flow regime was applied to the higher void fraction flow, in which a higher vapor-liquid momentum coupling is calculated. However, the flow regime applied to this case underestimated the discharge rate than observed.

6.4 Water temperature

Results of the case using the measured initial temperate are compared with the experimental data and the reference calculation in Fig. 3. The comparison with experimental data are good for both short- and long-term blowdown histories. Another two models have been proposed to predict or represent the temperature difference in the problem: Hirt and Romero[2)] expressed the temperature difference as a function of the local Reynolds number to represent the effect of turbulence development. However, this parametric model requires an a priori knowledge of the temperature difference as an initial condition. Rivard and Torrey[3)] proposed a model based on the conduction limited model using the effective thermal conductivity of the liquid. Although the model can predict the temperature difference directly from the measured initial data model constants should be determined empirically. On the other hand the present expression Eq. (11) predicts the temperature difference theoretically and its applicability is supported by the fact that the recovery pressure level after pressure undershoot evaluated by Eq. (11) well correlates experimental data from many available sources.[10)]

6.5 Nucleation model

Results of the calculation using the different nucleation model are compared with the experimental data and the reference calculation in Fig. 4. Although the pressure undershoot due to the initial non-equilibrium state is slightly overestimated and its recovery to the saturation pressure is dull, the general short-

term blowdown behavior is reasonably simulated. In the bubble nucleation model used in the reference calculation, which is same as the AFDM model,[14] $A^e_{G,B,N}$ is determined independently of $r^e_{G,B,N}$:

$$A^e_{G,B,N} = (36\pi M_b)^{1/3}{\alpha_{G,B}}^{2/3} \tag{22}$$

where M_b is defined as a function of liquid superheat and was correlated to specific experimental data of Ref. 15). A fault in this formulation is that the model does not explicitly predict $r^e_{G,B,N}$ in a physical way. This fact can be seen in Fig. 5. The bubble radius is restricted by the input minimum bubble radius, $r_{G,B,min}$ (= 5.0×10^{-5} m), during the flow exists in the bubbly flow region. In addition, M_b in Eq. (14) reaches to the input minimum nucleation bubble density, $M_{b,max}$ (= 10^{11} m^{-3}), just after the liquid becomes the superheated state. Therefore, it can be said that the results of the reference case, which are fortuitously reasonable, were obtained under the control by the input parameters on the bubble nucleation. On the other hand, as shown in Fig. 6, in the present case the bubble radius and the bubble number density predicted by the model are used in the calculation without restrictions to their ranges. This means that the obtained results simulate the physical process on the blowdown behavior based on the experimental correlations.

7. Conclusions

The following conclusions were obtained from this assessment study:

a. The reference calculation gives relatively good agreement with experimental data and demonstrates computational capability of S-III because no attempt was made to improve the agreement adjusting model parameters.

b. It was also shown, however, that this good agreement was fortuitously obtained under the control by the input parameters that effect on the bubble nucleation behavior.

c. A parametric study indicates that the solutions during the short-term transient are sensitive to the accuracy of time integration.

d. The simplified flow regime map used in the standard S-III generally well simulates the highly transient blowdown behavior, and

e. The system pressure is largely governed by the liquid temperature due to phase transition so that the vapor state is thermally equilibrated with the liquid sate. This means that a model is required to appropriately represent the liquid temperature difference between bulk and interface.

8. Recommendations for Model Improvement

The following model improvements are recommended:

a. A proposed nucleation model in which the radius of nucleation bubble is explicitly predicted is recommended for the calculation of flashing flows. The model can estimate the nucleation rate based on the generalized correlations for pool flow and convective boiling.

b. A theoretical expression was tested to predict the liquid temperature difference between bulk and interface. Successful results were obtained by applying this expression for the calculation of interfacial energy balance between vapor and liquid in the S-III phase transition model. However, further investigation will be required so that the model describes a relaxation effect of the temperature difference as turbulence is generated.

9. References

1) A. R. Edwards and T. P. O'Brien: Studies of phenomena connected with the depressurization of water reactors, J. Br. Nucl. Energ. Soc., 9, 125-135 (1970).

2) C. W. Hirt and N. C. Romero: "Application of a Drift-Flux Model to Flashing in Straight Pipes", LA-6005-MS, Los Alamos Scientific Laboratory (1975).

3) W. C. Rivard, M. D. Torrey: "Numerical Calculation of Flashing from Long Pipes Using a Two-Field Model", LA-6104-MS, Los Alamos Scientific Laboratory (1975).

4) N. I. Kolev: "The Code IVA4: Nucleation and flashing model", Kerntechnik, 60, 157-165 (1995).

5) K. Morita and E. A. Fischer: private communication (1995).

6) L. Haar et al.: NBC/NRC Steam Tables, Hemisphere, New York (1984).

7) R. B. Bird et al.: Transport Phenomena, Wiley, New York (1960).

8) O. J. Jones: "Nonequilibrium Phase Change – 1. Flashing Inception, Critical Flow, and Void Development in Ducts", in Boiling Heat transfer: Modern Development and Advances, edited by R. T. Lahey, Jr., Elsevier Science Publishers B. V., Amsterdam (1992).

9) J. H. Stuhmiller, R. E. Ferguson: "The Role of Microscale Processes in the Modeling of Two-Phase Flow", EPRI NP-1325, Project 888-1, Interim report, Electric Power Research Institute (1980).

10) Md. Alamgir et al.: "An Experimental Study of the Rapid Depressurization of Hot Water", J. Heat Transfer, 102, 433-438 (1980).

11) J. R. Riznic and M. Ishii: "Bubble number density and vapor generation in flashing flow", Int. J. Heat Mass Transfer, 32, 1821-1833 (1989).

12) G. Kocamustafaogullari: "Pressure dependence of bubble departure diameter for water", Int. Com. Heat Mass Transfer, 10, 501-509 (1983).

13) N. Zuber: "Nucleate boiling. The region of isolated bubbles and the similarity with natural convection", Int. J. Heat Mass Transfer, 6, 53-78 (1963).

14) D. Wilhelm: “AFDM: An Advanced Fluid-Dynamics Model, Volume II: Topologies, Flow Regimes, and Interfacial Areas”, LA-11692-MS, Vol. II, Los Alamos National Laboratory (1990).

15) N. Abuaf et al.: “A study of Nonequilibrium Flashing of Water in a Converging-Diverging Nozzle”, BNL-NUREG-51317, NUREG/CR-1864, Vol. 2, Brookhaven National Laboratory (1980).

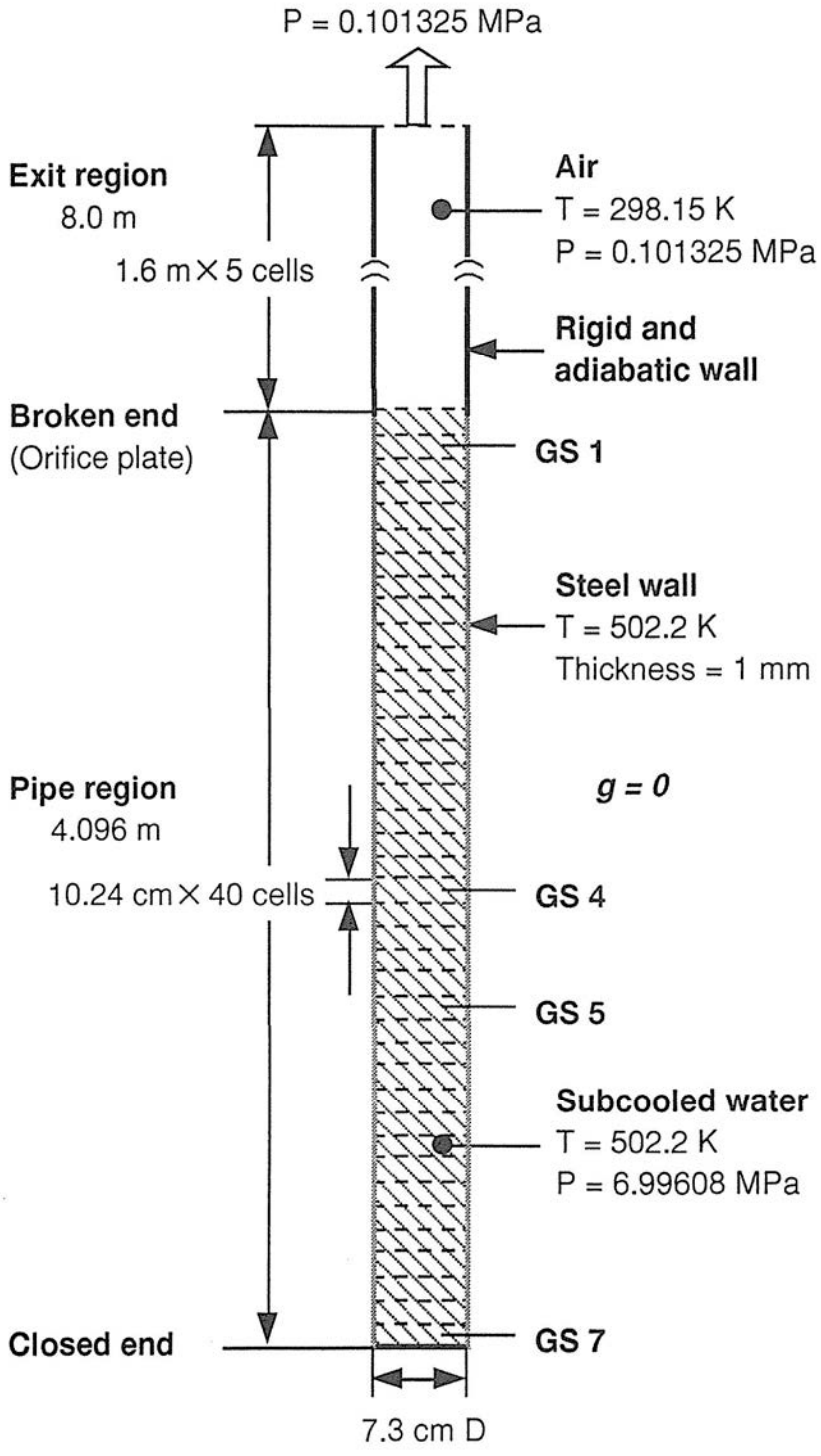

Fig. 1. Schematic and nodalization diagram for the reference case.

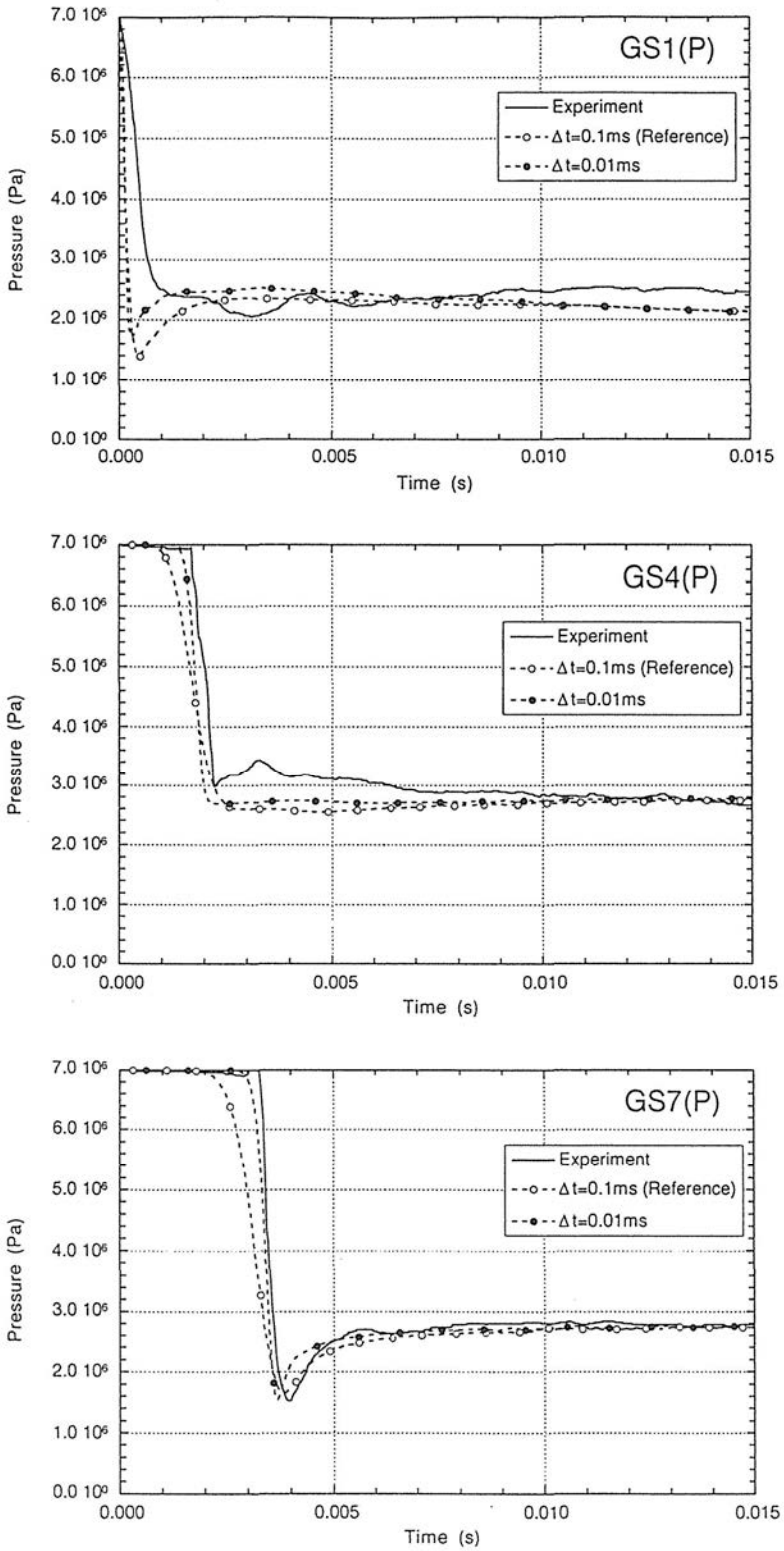

Fig. 2-1. Short-term pressure histories for two values of time step compared with experimental data.

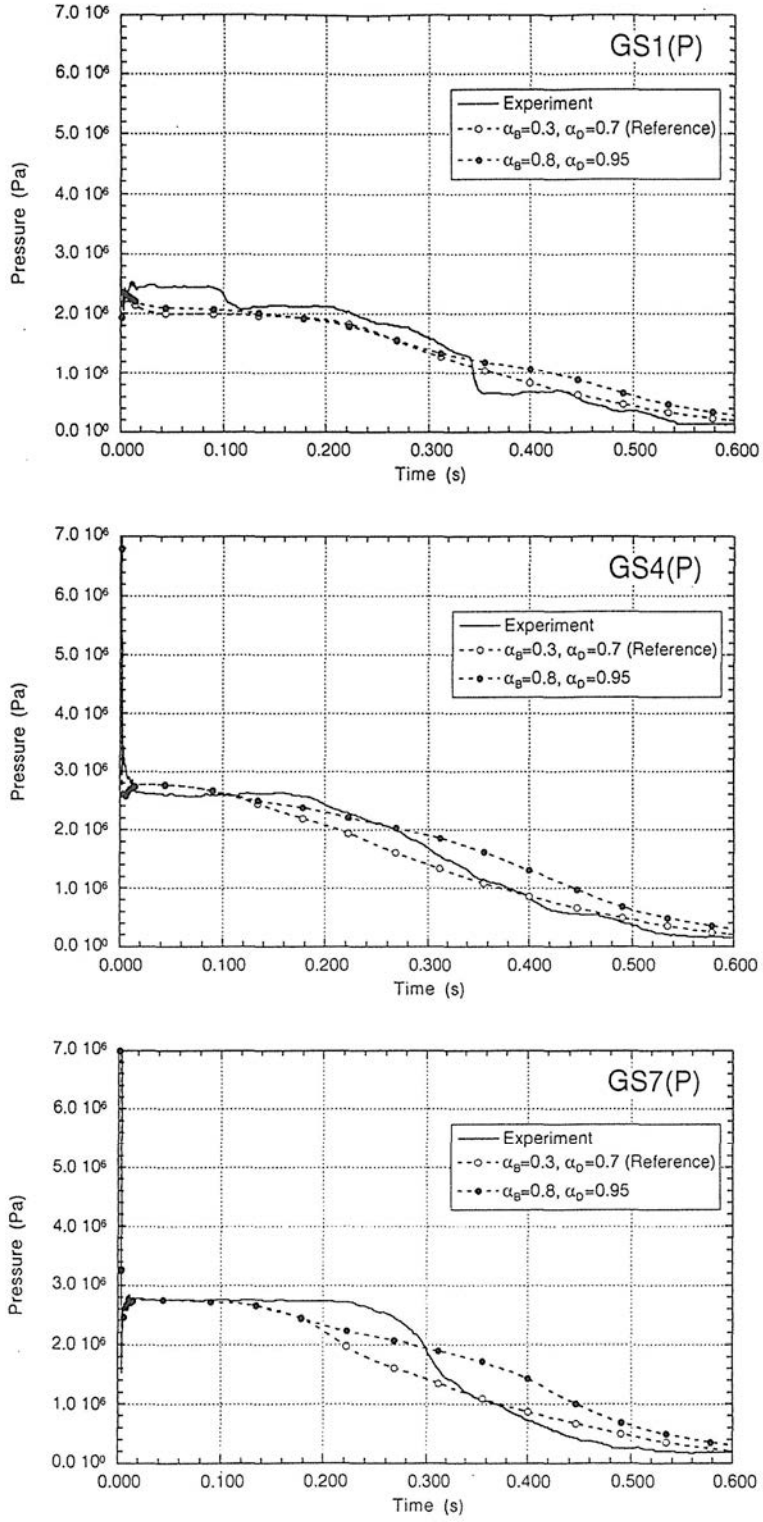

Fig. 2-2. Long-term pressure histories for two values of time step compared with experimental data.

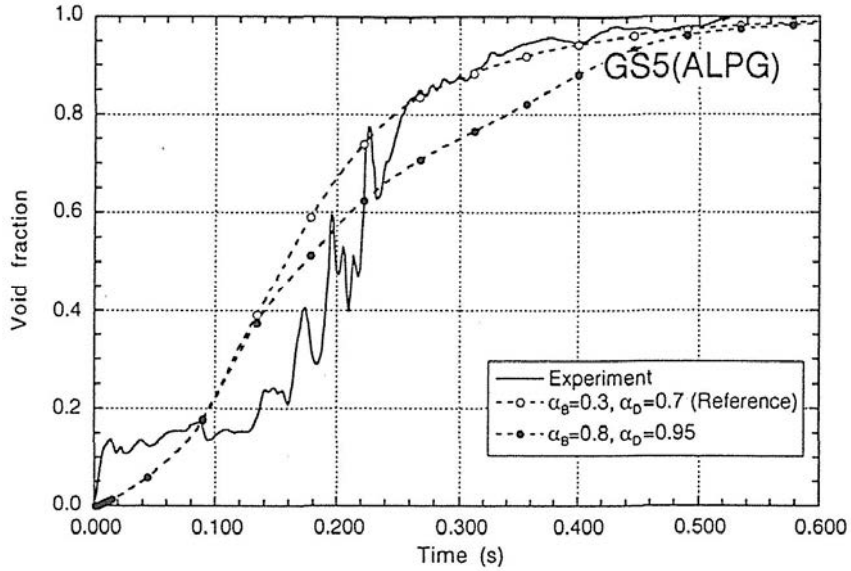

Fig. 2-3. Void-fraction histories for two flow regimes compared with experimental data.

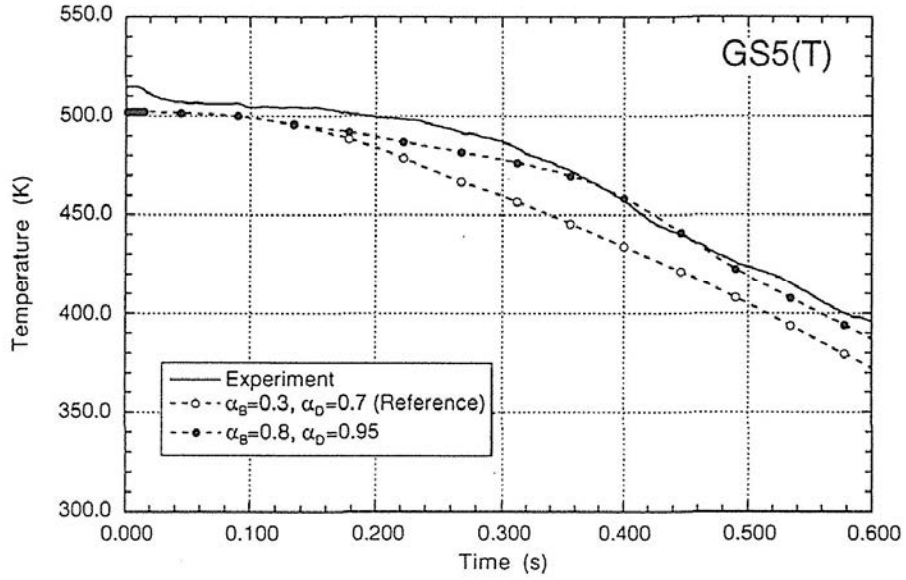

Fig. 2-4. Water-temperature histories for two flow regimes compared with experimental data.

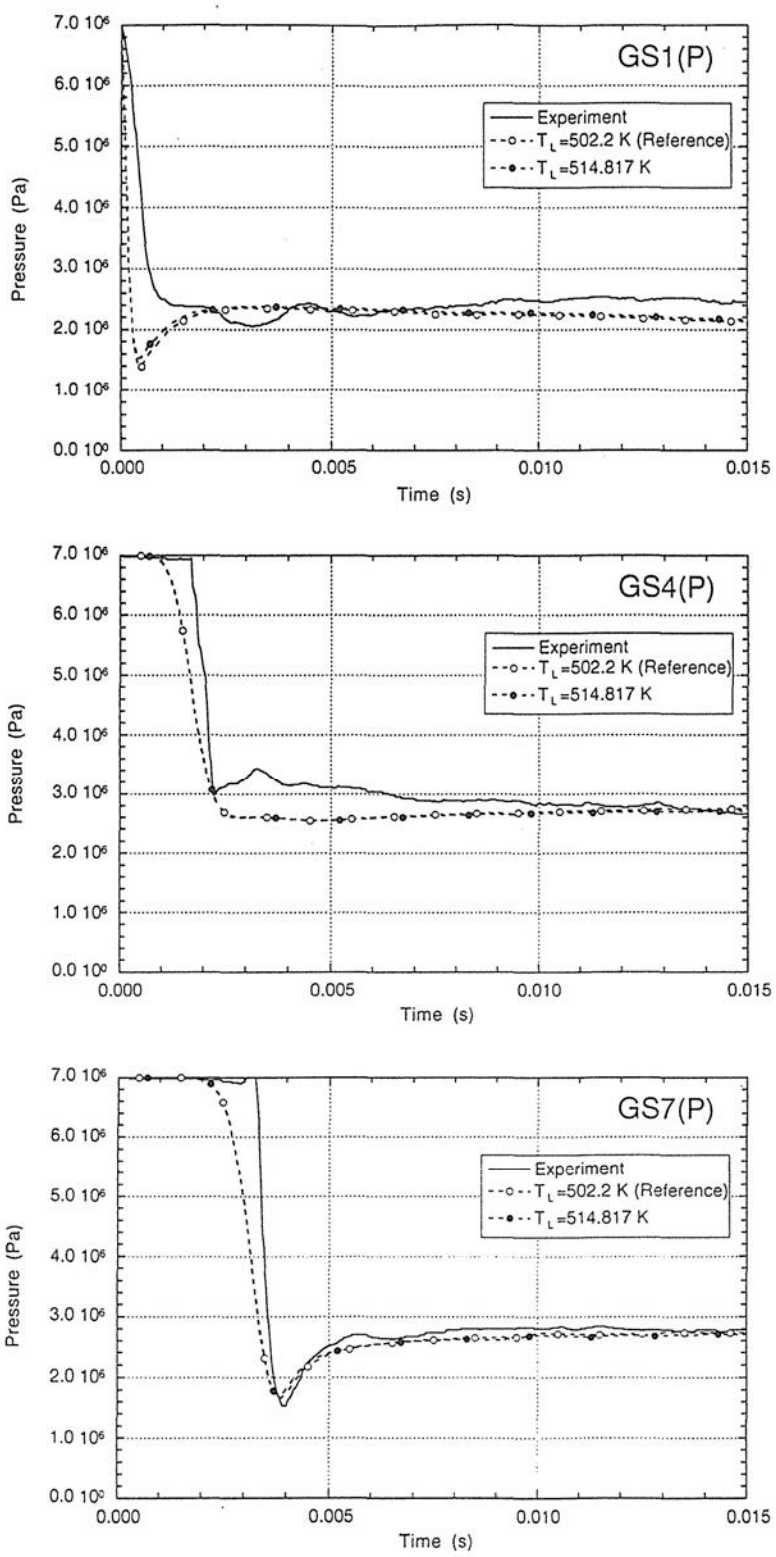

Fig. 3-1. Short-term pressure histories for two values of initial liquid temperature compared with experimental data.

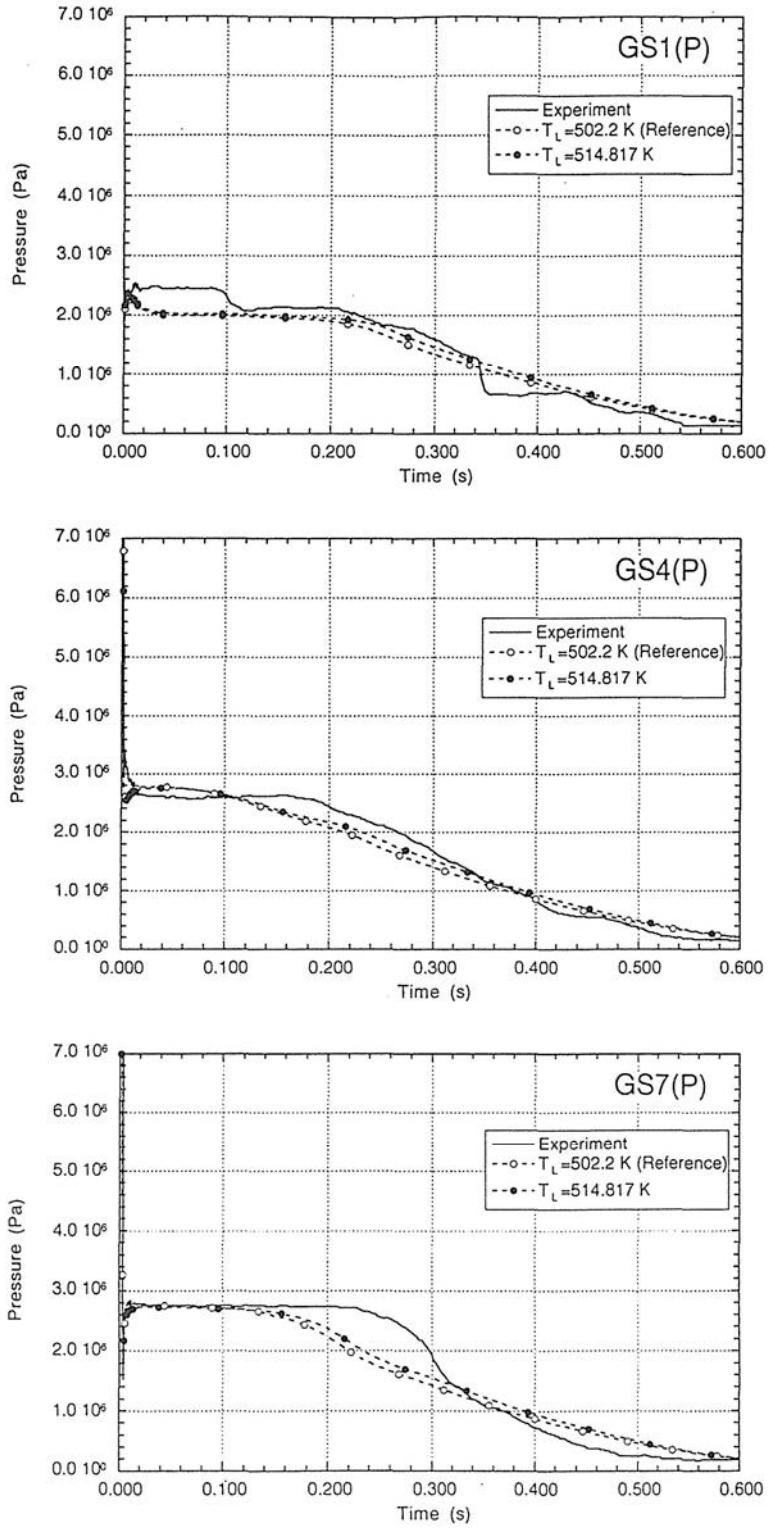

Fig. 3-2. Long-term pressure histories for two values of initial liquid temperature compared with experimental data.

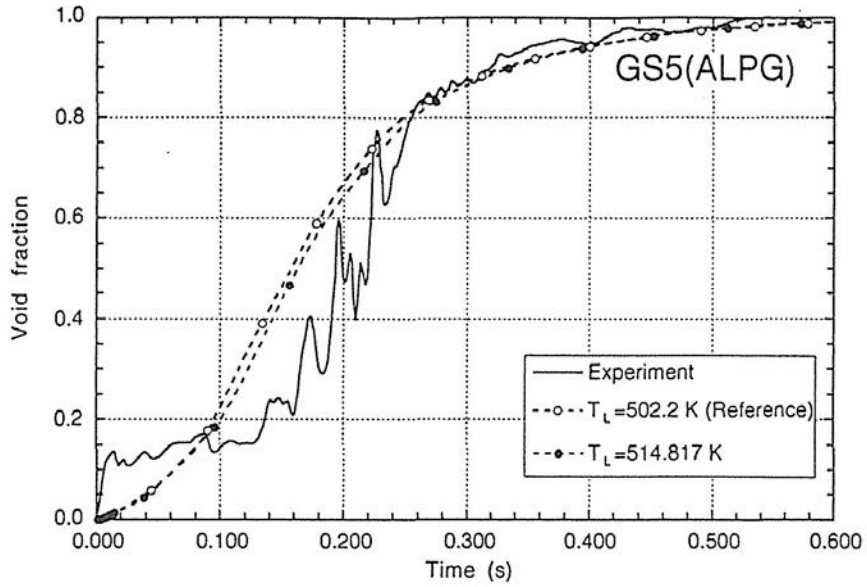

Fig. 3-3. Void-fraction histories for two values of initial liquid temperature compared with experimental data.

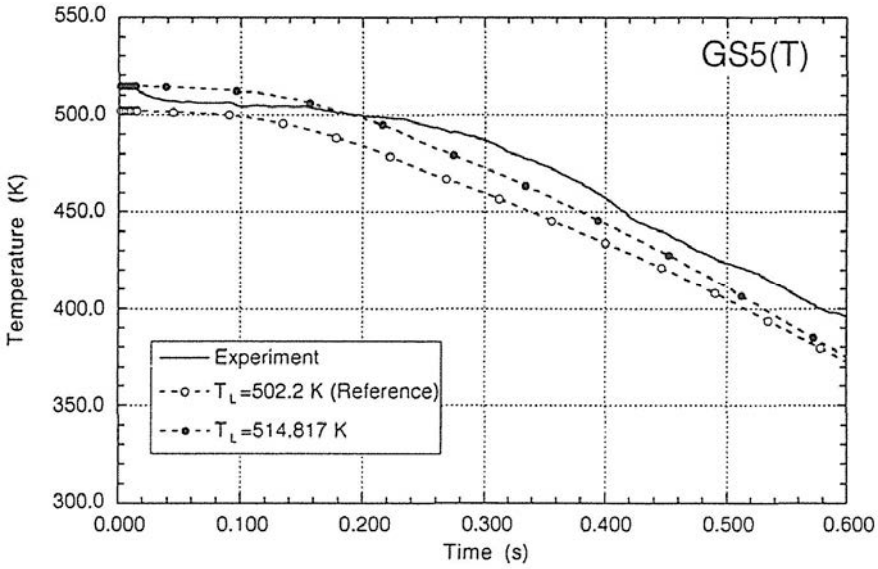

Fig. 3-4. Liquid temperature histories for two values of initial liquid temperature compared with experimental data.

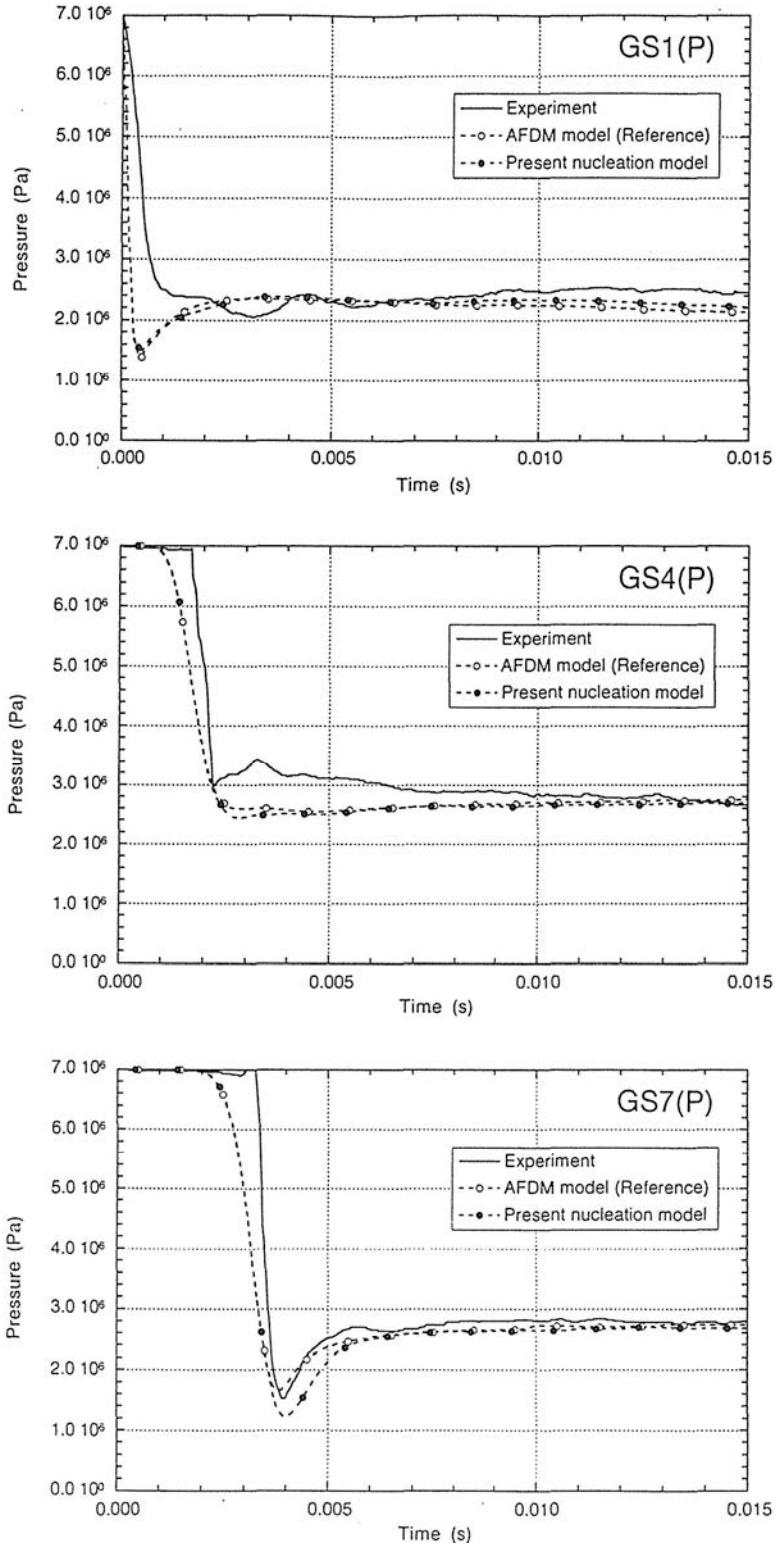

Fig. 4-1. Short-term pressure histories for two nucleation models compared with experimental data.

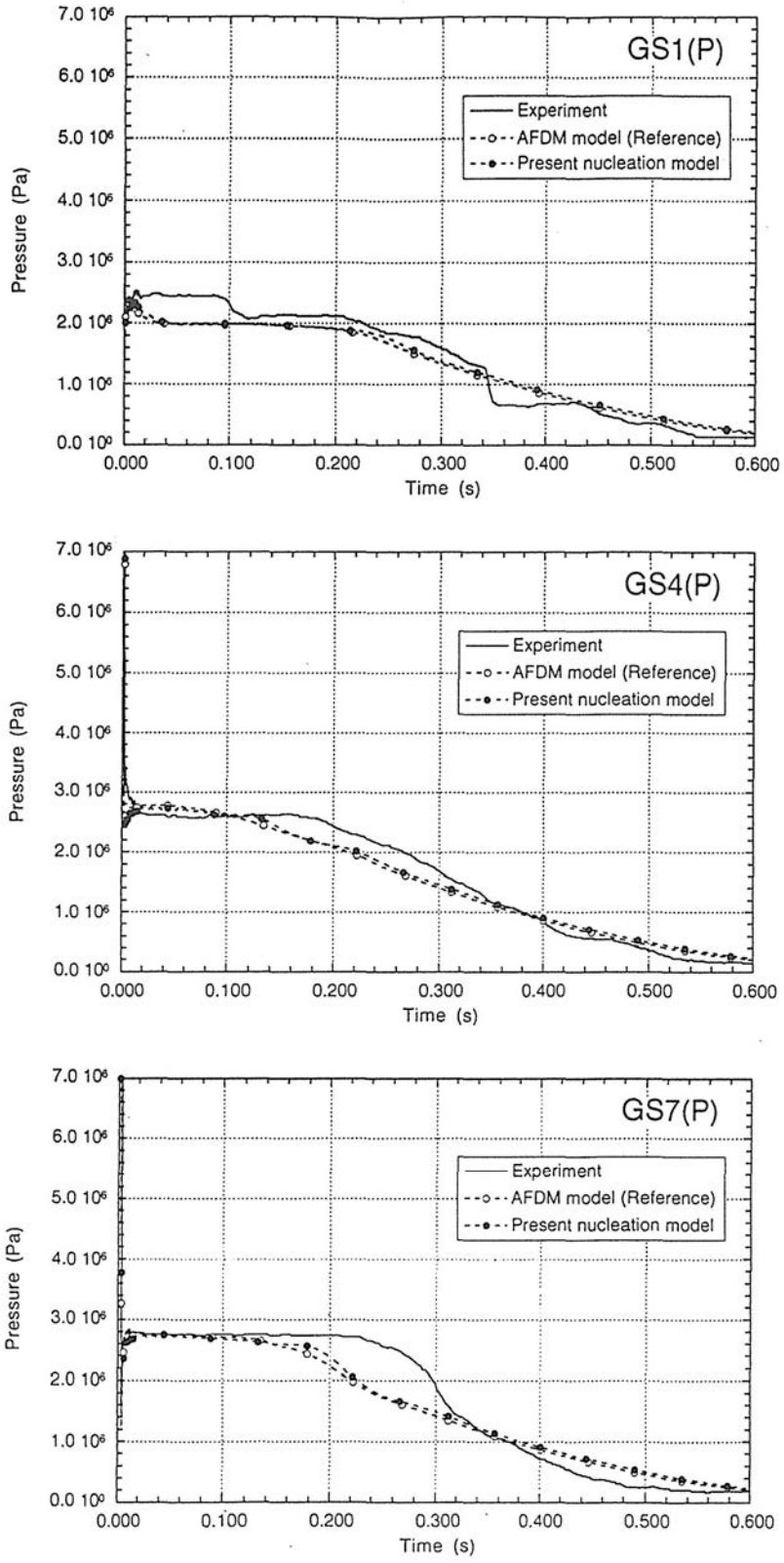

Fig. 4-2. Long-term pressure histories for two nucleation models compared with experimental data.

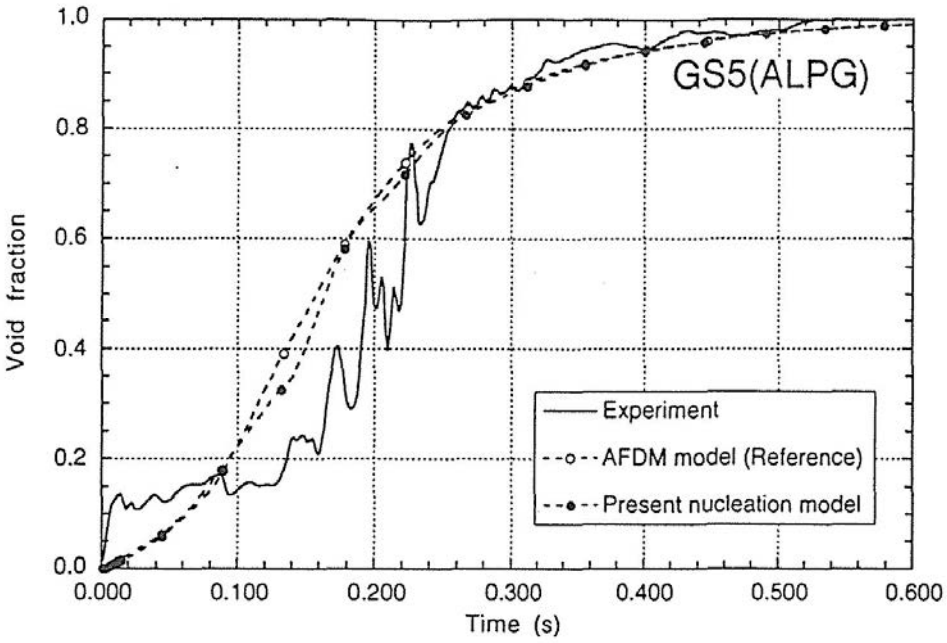

Fig. 4-3. Void-fraction histories for two nucleation models compared with experimental data.

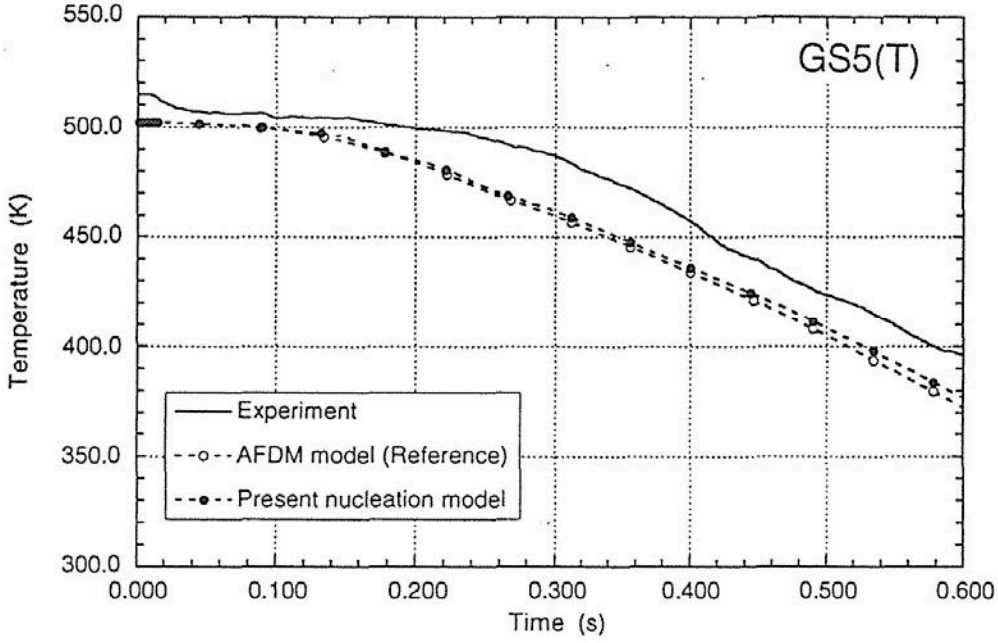

Fig. 4-4. Liquid-temperature histories for two nucleation models compared with experimental data.

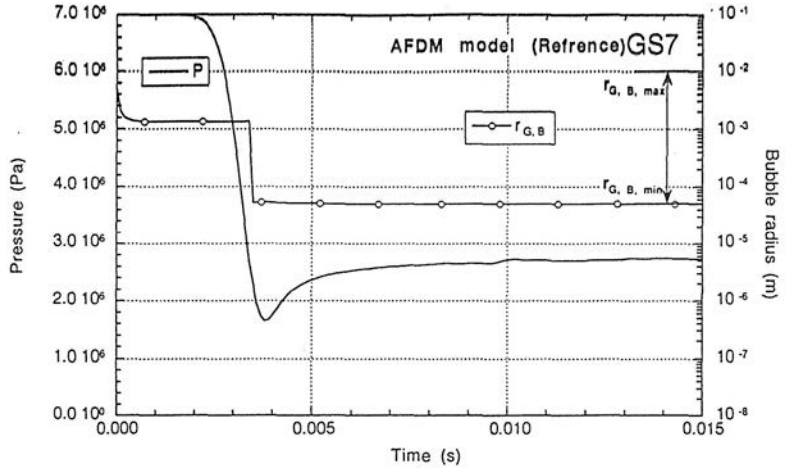

Fig. 5-1. Bubble radius and pressure histories in the reference calculation.

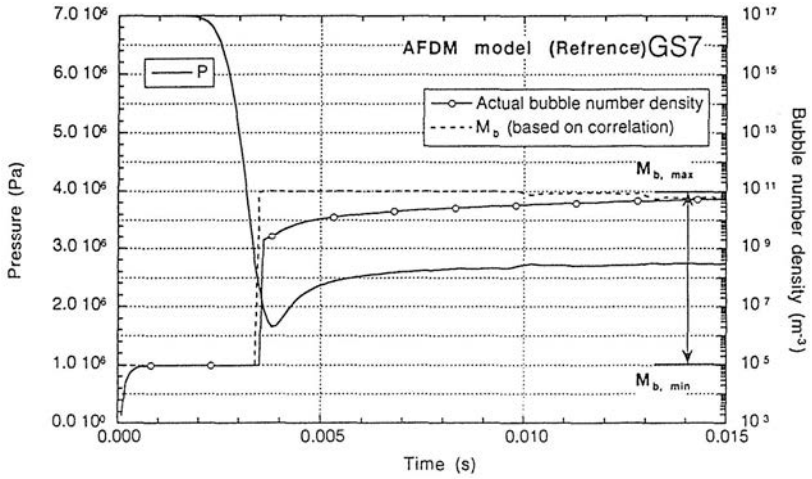

Fig. 5-2. Bubble number density and pressure histories in the reference calculation.

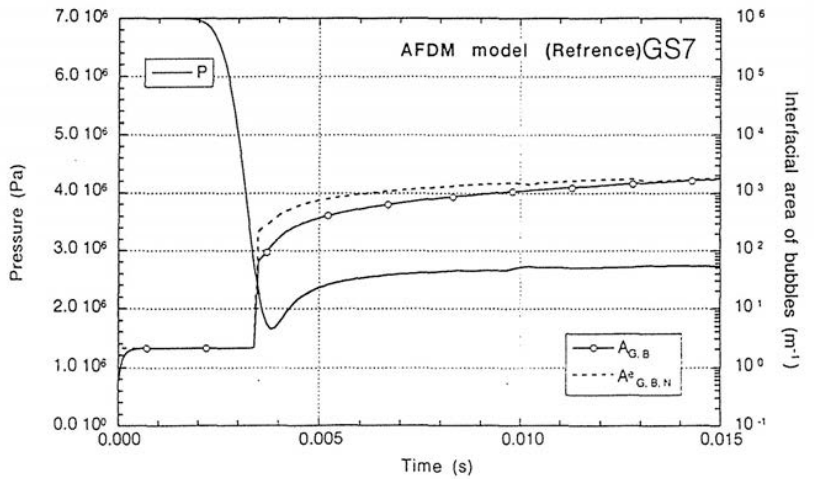

Fig. 5-3. Bubble IFA and pressure histories in the reference calculation.

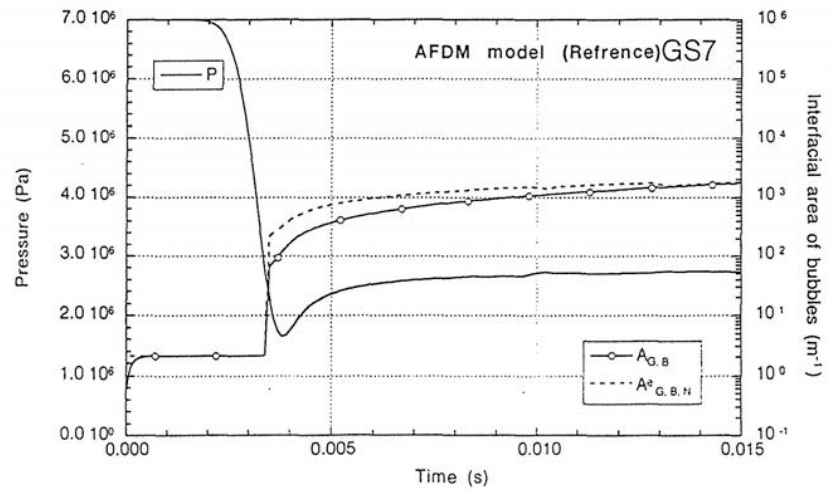

Fig. 6-1. Bubble radius and pressure histories with the present nucleation model.

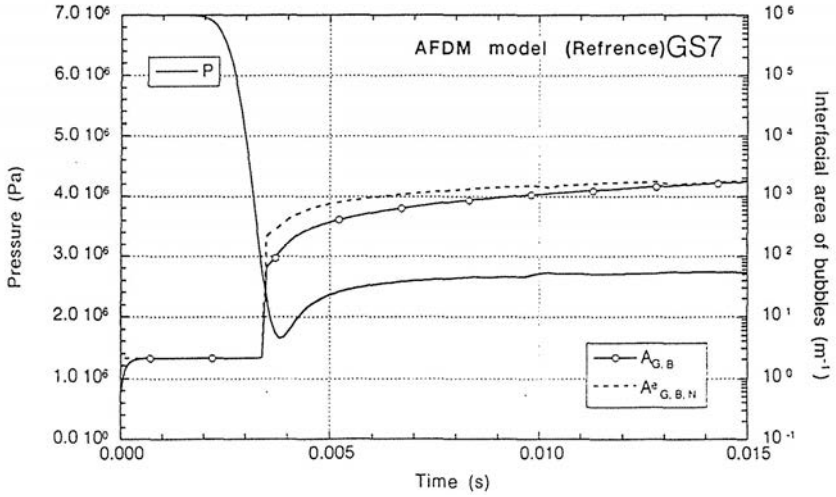

Fig. 6-2. Bubble number density and pressure histories with the present nucleation model.

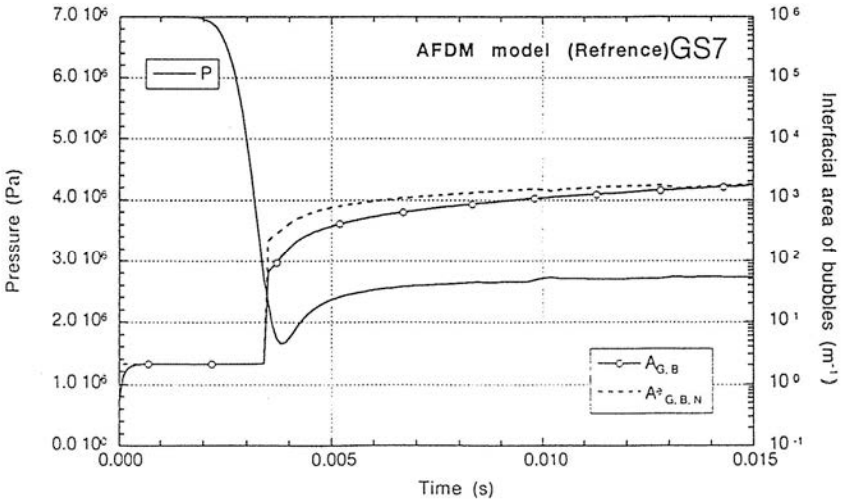

Fig. 6-3. Bubble IFA and pressure histories with the present nucleation model.

Problem 5.11: Thermite injection into sodium: THINA

"Rapid Thermite Injection into Sodium"

Dirk Wilhelm and Fabien Boulanger (CEA-G)

Outline of the Case

In THINA experiment no 564, a thennite mixture (76% iron, 24% alumina) is injected into a sodium pool. The thermal energy of the mixture is partly converted into mechanical energy. The efficiency of this conversion is measured (0.21%). Detailed injection conditions are available from the experiment and previous code studies. They are used to calculate this test.

1. Objectives of the Application

This application is to study the perfonnance of S-III on problems of fuel-coolant interactions, based on THINA 564 experiment. This has already been done[1], but the present study has been performed with more realistic initial conditions.

2. Description of the Experiment

Within the THINA apparatus, the test 564 is run using a thermite mixture of 76% iron and 24% alumina injected into the sodium pool. The thermal energy of the mixture is converted into mechanical energy. The efficiency of the conversion from thermal energy to mechanical energy was only 0.21%.

3. Analytical Solution

No analytical solution is available. But, during the course of the THINA program, the analysis of the experiments was supported by calculations with AFDM.[2] This was done to generate additional data for the experimentalists which were not available by measurements or observations.

Although the efficiency of the energy conversion was very low, it was difficult to achieve measured mechanical energies with AFDM, given the conditions of the melt injection (a compact molten thermite flow during the injection). The code injection times were much smaller than those measured in the experiment. The major reason was the observation that the injected thermite contained a residual volume fraction of non condensable gas and vapor remaining from the chemical reaction. Using this void fraction in the code, the injection procedure was slowed down and lowered the conversion efficiency.

While AFDM calculations were performed mainly to show differences using the same initial conditions for three THINA experiments, it was observed that the injection times of the code for alumina-dominated thermite were reasonable while iron-dominated thermite yielded longer injection periods compared to those of the experiment. While Ref. 2) still states that this may be due to initial bubble

diameters, it may also be due to different void fractions because the iron is at the bottom of the component separator. However, it is suggested to start SIMMER calculations with a void of 5%. The present study is to use the injection conditions which were found to be necessary for the AFDM calculation.

5. SIMMER-III Representation

5.1 Geometry, Initial and Boundary Conditions

A 2-D mesh was used, as illustrated in Fig. 1. It shows the characteristic length of the injector colwnn necessary to have inertia effects dominate the first 30 ms of the injection. As suggested, S-III calculations are started with a void of 5%.

6. Results

Due to very small time steps, the calculation of the first 200 ms took 85 hours. The run was therefore not repeated although it failed to shut the injector valve. Therefore, the calculation will only be discussed up to 140 ms.

Figure 2 shows the ejected mass with an acceleration period of about 30 ms, and a linear rise of inventory afterwards. Figure 3 shows a comparison of experimental pressures in the sodium pool (dashed lines) compared to the S-III pressure at the corresponding location. The injection time during the first 100 ms is calculated well, the experimental injection starting a little bit later due to effects of the injector nozzle. The pressure traces compare well with those of the experiment. After 100 ms, the pressures of the experiment rise considerably. This is not modeled by the code. Except for some non energetic pressures spikes, the pressures remain low.

Figure 4 shows a comparison between the pool levels of the experiment[3)] and the calculation. After 100 ms, the experimental pool level rises faster than calculated. However, there are already distinctive differences between experiment and code at earlier time, as can oo observed in Fig. 5. This figure shows the maximum extension of the two phase region in the sodium pool of the experiment (dashed line) and the sodium volume fraction contours of the code at 60 ms. The dashed line should be compared to the contour of 0.9 volume fraction. While the code predicts a reasonable radial extension, its two phase zone does not progress fast enough in axial direction. If the liquid thermite jet would be more compact in the calculation, this would probably lead to a faster axial penetration.

There are obviously substantial difficulties to describe these processes. Figure 6 shows the same contours at 140 ms, where the experimental extension of the two phase region (dashed line) is far ahead of that of the code.

To study the thermite droplet size, Fig. 7 shows these along the center line even beyond the time of the experimental injection period. It shows that the droplet radii vary between 0.1 mm and 0.6 mm. In Ref. 3), the thermite particle radii found in the post-mortem analysis were generally of the order of 0.2 mm,

with a distribution ranging from 0.02 mm to 1 mm. Therefore, the size calculated by the code seems to be reasonable, although a direct comparison of droplets early in the transient and particles late in the transient may be premature.

7. Conclusions

Using the knowledge of the experiment and the parallel analyses, it has been found necessary to model the injection process differently to the calculation performed earlier. The injection process dominates the way the thermite is distributed and thereby the contact to the volatile sodium which will ultimately lead to the conversion of thermal to mechanical energy. In this calculation, the injection and expansion processes are reasonably well calculated. Compared to the previous calculation[1)], the thermite droplet size is better predicted.

While the conversion efficiency in the experiment is already low (below 1%), the code is likely to produce even much smaller values. Not only thermite-sodium contacts at times of a larger void fraction in the sodium pool are low, they are also low from the very beginning. Since the most uncertain values which govern these contacts are the interfacial surface areas, it is likely that the code does not come close to what is needed to describe the thermal interaction.

8. Recommendations for Model Improvement

No recommendation are given from this calculation because of the integral nature of the experiment.

9. References

1) K. Morita, et al.: private communication.

2) D. Wilhelm: Numerical Simulation of the THINA Thermite Injection into Sodium with the AFDM-Code, Kernforschungszentrum Karlsruhe internal report 18.02.0lPl0A, August 1991.

3) F. Huber, A. Kaiser, D. Wilhelm: Results on the Behaviour of Thermite Melt Injected into Sodium, Experimental Thermal and Fluid Science, Vol.18, pp.48-69, September 1998.

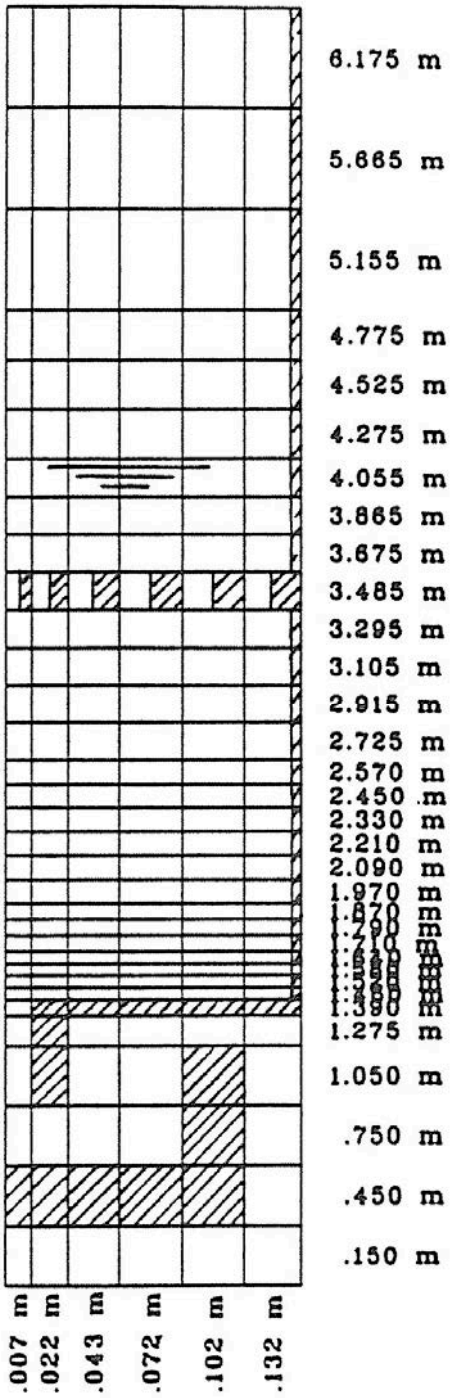

Fig. 1. Mesh cell set of the THINA experiment.

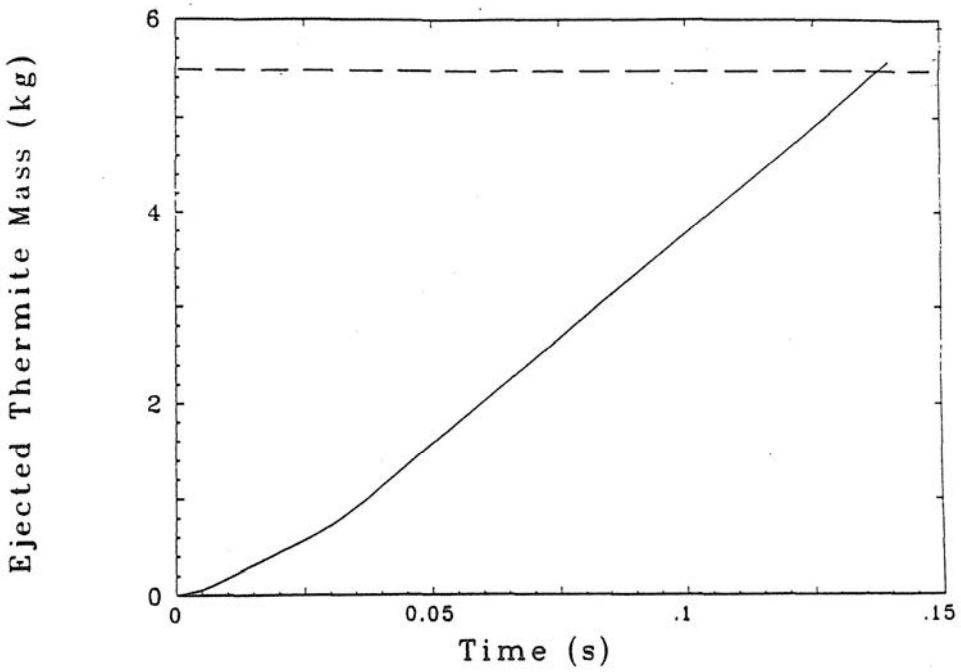

Fig. 2. Code injected mass for Thina 564 (experimental maximum at 5.5 kg).

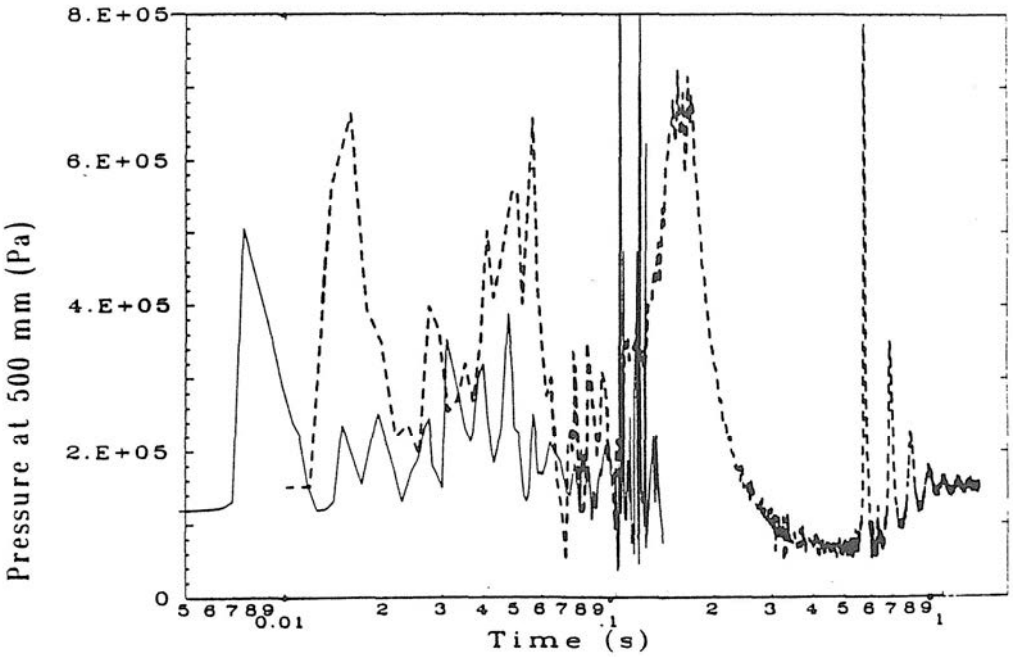

Fig. 3. Code pressure (solid line) and experiment (dashed line).

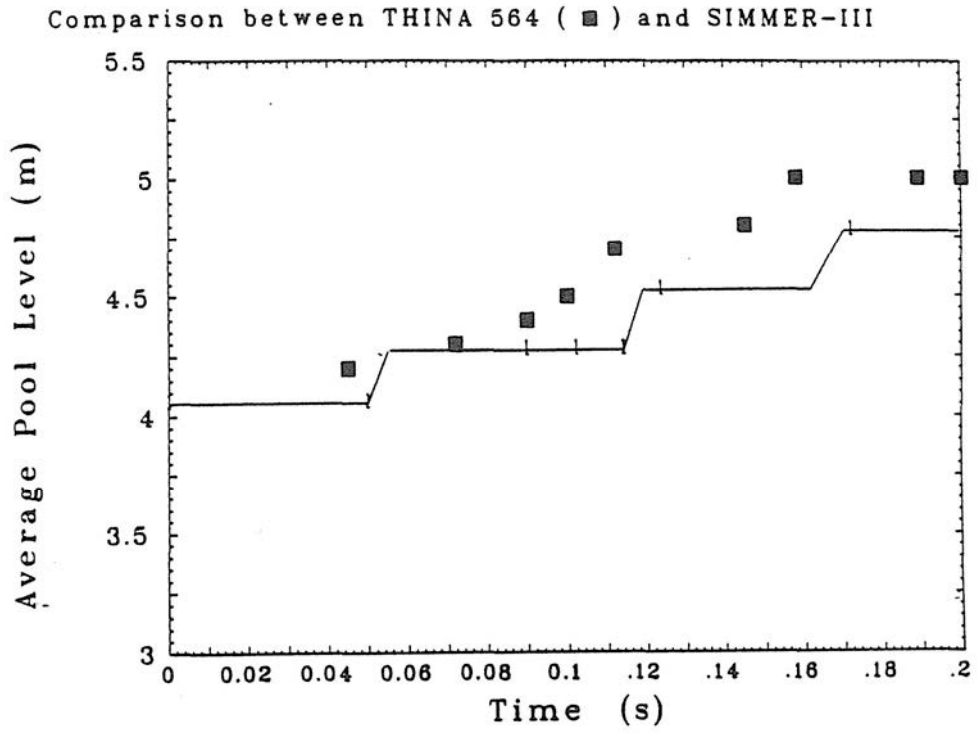

Fig. 4. Code sodium level (solid line) and experiment.

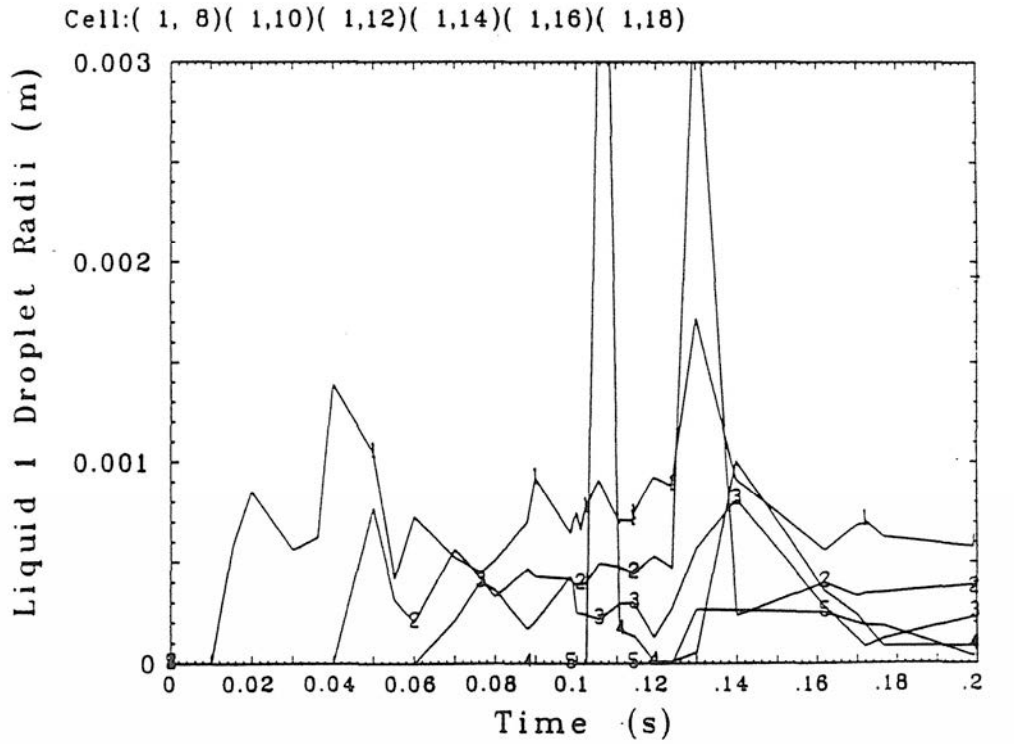

Fig. 5. Selection of code thermite droplet radii.

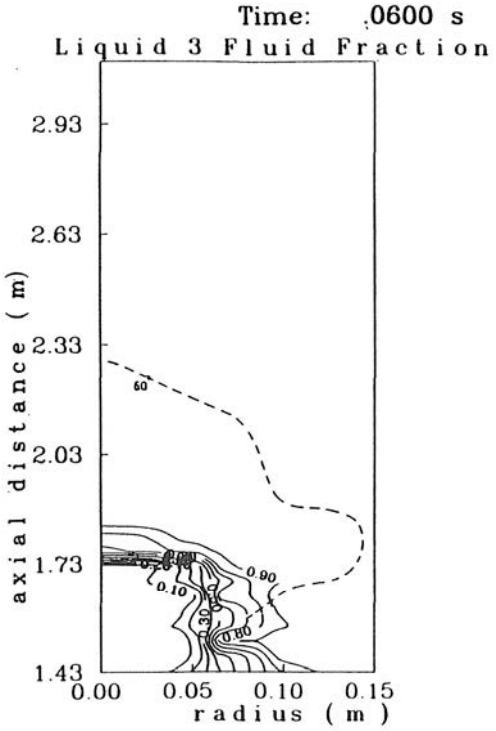

Fig. 6. Code sodium contours (solid lines) and experiment (dashed line).

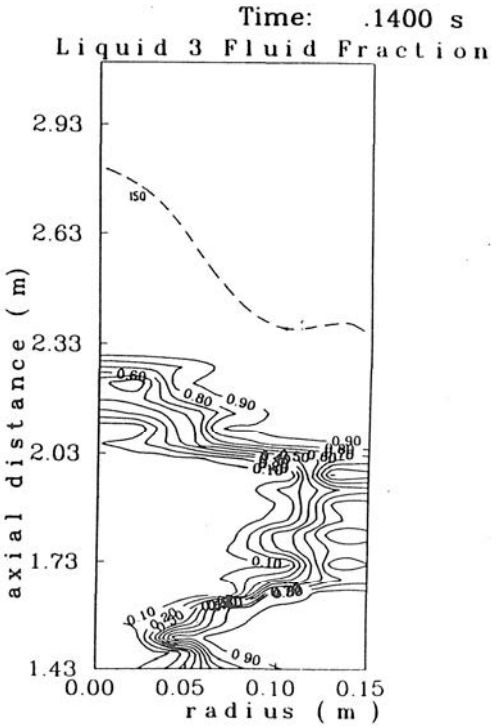

Fig. 7. Code sodium contours (solid lines) and experiment (dashed line).

国際単位系（SI）

表１．SI 基本単位

基本量	SI 基本単位	
	名称	記号
長さ	メートル	m
質量	キログラム	kg
時間	秒	s
電流	アンペア	A
熱力学温度	ケルビン	K
物質量	モル	mol
光度	カンデラ	cd

表２．基本単位を用いて表されるSI組立単位の例

組立量	SI 組立単位	
	名称	記号
面積	平方メートル	m^2
体積	立方メートル	m^3
速さ，速度	メートル毎秒	m/s
加速度	メートル毎秒毎秒	m/s^2
波数	毎メートル	m^{-1}
密度，質量密度	キログラム毎立方メートル	kg/m^3
面積密度	キログラム毎平方メートル	kg/m^2
比体積	立方メートル毎キログラム	m^3/kg
電流密度	アンペア毎平方メートル	A/m^2
磁界の強さ	アンペア毎メートル	A/m
量濃度(a)，濃度	モル毎立方メートル	mol/m^3
質量濃度	キログラム毎立方メートル	kg/m^3
輝度	カンデラ毎平方メートル	cd/m^2
屈折率(b)	（数字の） 1	1
比透磁率(b)	（数字の） 1	1

(a) 量濃度（amount concentration）は臨床化学の分野では物質濃度（substance concentration）ともよばれる。
(b) これらは無次元量あるいは次元１をもつ量であるが、そのことを表す単位記号である数字の１は通常は表記しない。

表３．固有の名称と記号で表されるSI組立単位

組立量	SI 組立単位			
	名称	記号	他のSI単位による表し方	SI基本単位による表し方
平面角	ラジアン(b)	rad	1 (b)	m/m
立体角	ステラジアン(b)	sr(c)	1 (b)	m^2/m^2
周波数	ヘルツ(d)	Hz		s^{-1}
力	ニュートン	N		$m\ kg\ s^{-2}$
圧力，応力	パスカル	Pa	N/m^2	$m^{-1}\ kg\ s^{-2}$
エネルギー，仕事，熱量	ジュール	J	N m	$m^2\ kg\ s^{-2}$
仕事率，工率，放射束	ワット	W	J/s	$m^2\ kg\ s^{-3}$
電荷，電気量	クーロン	C		s A
電位差（電圧），起電力	ボルト	V	W/A	$m^2\ kg\ s^{-3}\ A^{-1}$
静電容量	ファラド	F	C/V	$m^{-2}\ kg^{-1}\ s^4\ A^2$
電気抵抗	オーム	Ω	V/A	$m^2\ kg\ s^{-3}\ A^{-2}$
コンダクタンス	ジーメンス	S	A/V	$m^{-2}\ kg^{-1}\ s^3\ A^2$
磁束	ウエーバ	Wb	Vs	$m^2\ kg\ s^{-2}\ A^{-1}$
磁束密度	テスラ	T	Wb/m^2	$kg\ s^{-2}\ A^{-1}$
インダクタンス	ヘンリー	H	Wb/A	$m^2\ kg\ s^{-2}\ A^{-2}$
セルシウス温度	セルシウス度(e)	℃		K
光束	ルーメン	lm	cd sr(c)	cd
照度	ルクス	lx	lm/m^2	m^{-2} cd
放射性核種の放射能(f)	ベクレル(d)	Bq		s^{-1}
吸収線量，比エネルギー分与，カーマ	グレイ	Gy	J/kg	$m^2\ s^{-2}$
線量当量，周辺線量当量，方向性線量当量，個人線量当量	シーベルト(g)	Sv	J/kg	$m^2\ s^{-2}$
酸素活性	カタール	kat		s^{-1} mol

(a)SI接頭語は固有の名称と記号を持つ組立単位と組み合わせても使用できる。しかし接頭語を付した単位はもはやコヒーレントではない。
(b)ラジアンとステラジアンは数字の１に対する単位の特別な名称で、量についての情報をつたえるために使われる。実際には、使用する時には記号radおよびsrが用いられるが、習慣として組立単位としての記号である数字の１は明示されない。
(c)測光学ではステラジアンという名称と記号srを単位の表し方の中に、そのまま維持している。
(d)ヘルツは周期現象についてのみ、ベクレルは放射性核種の統計的過程についてのみ使用される。
(e)セルシウス度はケルビンの特別な名称で、セルシウス温度を表すために使用される。セルシウス度とケルビンの単位の大きさは同一である。したがって、温度差や温度間隔を表す数値はどちらの単位で表しても同じである。
(f)放射性核種の放射能（activity referred to a radionuclide）は、しばしば誤った用語で"radioactivity"と記される。
(g)単位シーベルト（PV,2002,70,205）についてはCIPM勧告2（CI-2002）を参照。

表４．単位の中に固有の名称と記号を含むSI組立単位の例

組立量	SI 組立単位		
	名称	記号	SI 基本単位による表し方
粘度	パスカル秒	Pa s	$m^{-1}\ kg\ s^{-1}$
力のモーメント	ニュートンメートル	N m	$m^2\ kg\ s^{-2}$
表面張力	ニュートン毎メートル	N/m	$kg\ s^{-2}$
角速度	ラジアン毎秒	rad/s	$m\ m^{-1}\ s^{-1}=s^{-1}$
角加速度	ラジアン毎秒毎秒	rad/s^2	$m\ m^{-1}\ s^{-2}=s^{-2}$
熱流密度，放射照度	ワット毎平方メートル	W/m^2	$kg\ s^{-3}$
熱容量，エントロピー	ジュール毎ケルビン	J/K	$m^2\ kg\ s^{-2}\ K^{-1}$
比熱容量，比エントロピー	ジュール毎キログラム毎ケルビン	J/(kg K)	$m^2\ s^{-2}\ K^{-1}$
比エネルギー	ジュール毎キログラム	J/kg	$m^2\ s^{-2}$
熱伝導率	ワット毎メートル毎ケルビン	W/(m K)	$m\ kg\ s^{-3}\ K^{-1}$
体積エネルギー	ジュール毎立方メートル	J/m^3	$m^{-1}\ kg\ s^{-2}$
電界の強さ	ボルト毎メートル	V/m	$m\ kg\ s^{-3}\ A^{-1}$
電荷密度	クーロン毎立方メートル	C/m^3	m^{-3} s A
表面電荷	クーロン毎平方メートル	C/m^2	m^{-2} s A
電束密度，電気変位	クーロン毎平方メートル	C/m^2	m^{-2} s A
誘電率	ファラド毎メートル	F/m	$m^{-3}\ kg^{-1}\ s^4\ A^2$
透磁率	ヘンリー毎メートル	H/m	$m\ kg\ s^{-2}\ A^{-2}$
モルエネルギー	ジュール毎モル	J/mol	$m^2\ kg\ s^{-2}\ mol^{-1}$
モルエントロピー，モル熱容量	ジュール毎モル毎ケルビン	J/(mol K)	$m^2\ kg\ s^{-2}\ K^{-1}\ mol^{-1}$
照射線量（X線及びγ線）	クーロン毎キログラム	C/kg	kg^{-1} s A
吸収線量率	グレイ毎秒	Gy/s	$m^2\ s^{-3}$
放射強度	ワット毎ステラジアン	W/sr	$m^4\ m^{-2}\ kg\ s^{-3}=m^2\ kg\ s^{-3}$
放射輝度	ワット毎平方メートル毎ステラジアン	$W/(m^2\ sr)$	$m^2\ m^{-2}\ kg\ s^{-3}=kg\ s^{-3}$
酵素活性濃度	カタール毎立方メートル	kat/m^3	$m^{-3}\ s^{-1}$ mol

表５．SI 接頭語

乗数	名称	記号	乗数	名称	記号
10^{24}	ヨタ	Y	10^{-1}	デシ	d
10^{21}	ゼタ	Z	10^{-2}	センチ	c
10^{18}	エクサ	E	10^{-3}	ミリ	m
10^{15}	ペタ	P	10^{-6}	マイクロ	μ
10^{12}	テラ	T	10^{-9}	ナノ	n
10^9	ギガ	G	10^{-12}	ピコ	p
10^6	メガ	M	10^{-15}	フェムト	f
10^3	キロ	k	10^{-18}	アト	a
10^2	ヘクト	h	10^{-21}	ゼプト	z
10^1	デカ	da	10^{-24}	ヨクト	y

表６．SIに属さないが、SIと併用される単位

名称	記号	SI 単位による値
分	min	1 min=60 s
時	h	1 h =60 min=3600 s
日	d	1 d=24 h=86 400 s
度	°	1°=(π/180) rad
分	’	1’=(1/60)°=(π/10 800) rad
秒	”	1”=(1/60)’=(π/648 000) rad
ヘクタール	ha	1 ha=1 $hm^2=10^4m^2$
リットル	L, l	1 L=1 l=1 $dm^3=10^3cm^3=10^{-3}m^3$
トン	t	1 t=10^3 kg

表７．SIに属さないが、SIと併用される単位で、SI単位で表される数値が実験的に得られるもの

名称	記号	SI 単位で表される数値
電子ボルト	eV	1 eV=1.602 176 53(14)×10^{-19}J
ダルトン	Da	1 Da=1.660 538 86(28)×10^{-27}kg
統一原子質量単位	u	1 u=1 Da
天文単位	ua	1 ua=1.495 978 706 91(6)×10^{11}m

表８．SIに属さないが、SIと併用されるその他の単位

名称	記号	SI 単位で表される数値
バール	bar	1 bar=0.1MPa=100 kPa=10^5Pa
水銀柱ミリメートル	mmHg	1 mmHg≈133.322Pa
オングストローム	Å	1 Å=0.1nm=100pm=10^{-10}m
海里	M	1 M=1852m
バーン	b	1 b=100fm^2=$(10^{-12}cm)^2$=$10^{-28}m^2$
ノット	kn	1 kn=(1852/3600)m/s
ネーパ	Np	SI単位との数値的な関係は、対数量の定義に依存。
ベル	B	
デシベル	dB	

表９．固有の名称をもつCGS組立単位

名称	記号	SI 単位で表される数値
エルグ	erg	1 erg=10^{-7} J
ダイン	dyn	1 dyn=10^{-5}N
ポアズ	P	1 P=1 dyn s cm^{-2}=0.1Pa s
ストークス	St	1 St =1$cm^2\ s^{-1}$=$10^{-4}m^2\ s^{-1}$
スチルブ	sb	1 sb =1cd cm^{-2}=10^4cd m^{-2}
フォト	ph	1 ph=1cd sr cm^{-2} =10^4lx
ガル	Gal	1 Gal =1cm s^{-2}=$10^{-2}ms^{-2}$
マクスウエル	Mx	1 Mx = 1G cm^2=10^{-8}Wb
ガウス	G	1 G =1Mx cm^{-2} =10^{-4}T
エルステッド(a)	Oe	1 Oe ≙ $(10^3/4\pi)$A m^{-1}

(a) ３元系のCGS単位系とSIでは直接比較できないため、等号「 ≙ 」は対応関係を示すものである。

表10．SIに属さないその他の単位の例

名称	記号	SI 単位で表される数値
キュリー	Ci	1 Ci=3.7×10^{10}Bq
レントゲン	R	1 R = 2.58×10^{-4}C/kg
ラド	rad	1 rad=1cGy=10^{-2}Gy
レム	rem	1 rem=1 cSv=10^{-2}Sv
ガンマ	γ	1 γ=1 nT=10^{-9}T
フェルミ		1 フェルミ=1 fm=10^{-15}m
メートル系カラット		1 メートル系カラット= 0.2 g = 2×10^{-4}kg
トル	Torr	1 Torr = (101 325/760) Pa
標準大気圧	atm	1 atm = 101 325 Pa
カロリー	cal	1 cal=4.1858J（「15℃」カロリー），4.1868J（「IT」カロリー），4.184J（「熱化学」カロリー）
ミクロン	μ	1 μ =1μm=10^{-6}m

（第8版，2006年）